

Fabrication of size-selected alloy nanoclusters and their applications for gas sensing

Ahmad I. Ayesh

Department of Mathematics, Statistics

and Physics

Qatar University

Doha, Qatar

Email: ayesh@qu.edu.qa

This work reports on the production of alloy Ti-Cu nanoclusters by magnetron sputtering and plasma-gas condensation inside an ultra-high compatible system. Inert-gas was introduced inside a source chamber to generate plasma, sputter material from its target, and establish plasma-gas condensation [1]. The nanocluster size and yield were controlled by adjusting the nanocluster source conditions: inert-gas flow rate f_{Ar} , aggregation length L , and sputtering discharge power P [2]. Nanoclusters were produced by three-body collision that created nanocluster embryo, and grew further by two-body collision. The dependence of nanocluster size on nanocluster source conditions was modeled using a homogeneous nucleation model where a nanocluster grows from embryo by nanocluster-nanocluster collision and vapor condensation. Controlled oxidation of ionized nanocluster was conducted in-situ which was found to affect nanoclusters' charges but retain their sizes. The nanoclusters were deposited on SiO_2/Si substrates with pre-formed metal electrodes to produce percolating nanocluster devices [3, 4]. Those devices have useful applications. Herein, we present their utilization for sensitive and selective gas sensor applications.

A. Nanocluster production

Nanoclusters were generated using dc magnetron sputtering and inert-gas aggregation inside an ultra-high vacuum compatible apparatus (UHV) made by Mantis deposition Ltd. The UHV apparatus is shown schematically in Fig. 1 [5], and it contains three main chambers: source, mass filter, and deposition chambers. Pair of turbo pumps were utilized to pump the system down to a base pressure of $\sim 10^{-6}$ Pa beforehand nanocluster generation. The nanoclusters were generated from a Cu target of purity 99.99% that was allocated on a sputter head. Both sputter head and chamber walls of the source were cooled down using water at room temperature. Sputtering was conducted by applying a dc voltage to the Cu target in existence of inert gas. Herein, argon (Ar) inert gas was presented inside the source chamber and was used to: a) generate the plasma needed for sputtering, b) allow the inert-gas condensation, and c) form pressure gradient among the source and deposition chambers that enables nanoclusters' to fly between them. The source chamber has two main nozzles on its exit with diameters of 5 and 6 mm, in order. The flow rate of inert gas (f_{Ar}) was managed using an MKS Instruments mass flow controller within the range $f_{Ar} = 0 - 100$ sccm.

A main factor that influence nanocluster size (indicated as the diameter of nanocluster presumptuous an approximately spherical shape) is the aggregation length (L) which is the distance among target surface and source exit nozzle [5].

Controlling of L could be established by shifting the sputter head that is located on a motorized linear translator. Oxidation of Cu nanoclusters was achieved either by allowing oxygen gas flow inside the source chamber or to the space among the source and mass filter chambers, see Fig 1 [4].

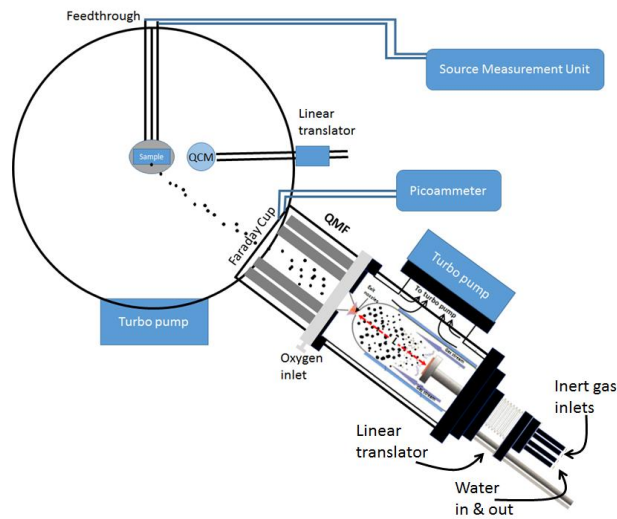


Fig. 1. Schematic diagram of the UHV system [1, 5].

REFERENCES

- [1] A.I. Ayesh, N. Qamhieh, H. Ghamlouche, a.M.E.-S. S. Thaker, Fabrication of size-selected Pd nanoclusters using a magnetron plasma sputtering source, *J. Appl. Phys.*, 107 (2010) 034317
- [2] A.I. Ayesh, H. Ahmed, F. Awwad, S. Abu-Eishah, S.T. Mahmoud, Mechanisms of Ti Nanoclusters Formation by Inert Gas Condensation, *Journal of Materials Research* 28 (2013) 2622-2628.
- [3] A.I. Ayesh, N. Qamhieh, S.T. Mahmoud, H. Alawadhi, Fabrication of size-selected bimetallic nanoclusters using magnetron sputtering, *Journal of Materials Research*, 27 (2012) 2441-2446.
- [4] A.I. Ayesh, Production of metal-oxide nanoclusters using inert-gas condensation technique, *Thin Solid Films*, 636 (2017) 207-213.
- [5] A.I. Ayesh, S. Thaker, N. Qamhieh, H. Ghamlouche, Size-controlled Pd nanocluster grown by plasma gas-condensation method, *J. Nanopart. Res.*, 13 (2011) 1125.

Ambipolar graphene-quantum dot phototransistors

L. Zheng¹, W. Zhou¹, X. -H. Cheng^{1,2}, L. -Y. Shen¹, D. -W. Xu¹, Y. -H. Yu^{1,2}

¹State Key Laboratory of Functional Materials for Informatics, Shanghai Institute of Microsystem and Information Technology, Chinese Academy of Sciences, Shanghai, China, email: zhengli@mail.sim.ac.cn

² Center of Materials Science and Optoelectronics Engineering, University of Chinese Academy of Sciences, Beijing, China

Abstract—N, S co-decorated graphene integrated with PbS colloidal quantum dots (CQDs) has been performed to fabricate a hybrid phototransistor. It demonstrates a gate-tunable ambipolar feature with a low gate bias of less than 3.3 V at room temperature in ambient. Upon SWIR light at 1550 nm, the phototransistor exhibits ultrahigh responsibility ($R=10^4 \text{ AW}^{-1}$) and specific detectivity ($D^*=10^{12} \text{ Jones}$) with a low driving voltage of 1 V. This decorated hybrid architecture illustrates the potential of graphene and CQDs to be integrated with silicon integrated circuits and open new path for ambipolar photodetectors fabrications.

I. INTRODUCTION

Recently, hybrid graphene-CQDs phototransistors have been explored to enhance both photoresponsivity and gain of the photodetector. Unlike in conventional photodetectors, the photogenerated charges transferred from CQDs to graphene can be either free or recombined and lead to a positive or negative photoresponse. However, graphene is sensitive to the external environment and always P-doped in ambient [1,2]. As a result, the required V_{BG} is usually over 20 V [1]. Moreover, the high gain value of this composite material typically relies on high source-drain bias, which will lead to high energy consumption, large leakage current, and reduced detectivity.

Herein, a hybrid N, S co-decorated graphene-PbS CQDs phototransistor is fabricated. A distinct gate-tunable ambipolar feature can be detected with a gate-bias of less than 3.3 V. This hybrid photodetector exhibits ultrahigh photodetection gain (10^5), ultrahigh R (10^4 AW^{-1}) and D^* (10^{12} Jones), and fast response (3 ms) at a low driving voltage of 1 V..

II. DEVICE FABRICAITON

The N, S co-decorated graphene is prepared by CVD. After back-gated graphene FETs building, Al_2O_3 grown by ALD is used to isolate the electrodes and CQDs. Pre- H_2O treatment is optimized to enhance the dielectric property on graphene [3]. A window is opened on the channel by Al_2O_3 etching for CQDs spin coating. CQDs were synthesized based on the protocols reported by Sargent et al [4].

III. RESULTS AND DISCUSSION

A. Transfer characteristic of N, S co-decorated graphene

For the pristine graphene in ambient, the Dirac point (V_{Dirac}) of the GFETs will shift to a conspicuous positive position [1]. As shown in Fig. 1, highly reproducible transport characteristics with negligible shift of the Dirac point are obtained from GFETs built on the N, S co-decorated graphene

at room temperature under ambient conditions, even exposed to the ambient condition for 24 hours.

B. Ambipolar feature of the hybrid phototransistor

In the hybrid phototransistor, N and S co-decorated graphene is the carrier transport channel, and PbS CQDs are used as the photon absorbing material (Fig. 2). The unique electronic properties of graphene offer a gate-tunable carrier density and polarity that can tune the sensitivity and operation speed of the detector as shown in Figs. 3-5, which shows a gate-tunable transformation of positive and negative photoresponse. Illumination causes the shift of V_{Dirac} to higher values (Fig. 6) due to photogate effect and V_{Dirac} can remain below 3.3 V when the illumination power is below 19 Wm^{-2} .

C. Photoelectric performance under SWIR illumination

R can reach its highest value of $1.8 \times 10^4 \text{ AW}^{-1}$ at a low gate bias of only 2.3 V (Fig. 7). Even if the driving bias is down to 0.1 V, R can reach $3.1 \times 10^3 \text{ AW}^{-1}$. As shown in Fig. 8, D^* can reach its maximum of $4.4 \times 10^{12} \text{ Jones}$ at a gate bias of 2.3 V and when the driving bias declines to 0.1 V, D^* can still reach a considerable value of $2.5 \times 10^{12} \text{ Jones}$.

As shown in Fig. 9a, if $V_{BG}=3$ V, the photocurrent rises fast in the ON state but its direction is negative. This anomaly can be explained by the ambipolar feature of graphene. A fast rise of 3 ms (corresponding to 63% decay) is detected (Fig. 9b) due to the built-in potential between decorated graphene and PbS CQDs. This component of temporal response is compatible with sensing and imaging, addressing a wide range of consumer applications. For the specific device, the transit time of the carriers is found to be 10 ns, which then leads to an ultrahigh gain of 3×10^5 .

IV. CONCLUSION

In summary, a hybrid graphene-PbS CQDs phototransistor is fabricated with ambipolar photodetection. A gate tunable transformation of positive and negative photoresponse is detected with a low V_{BG} (<3.3 V). The photoconductive gain is up to 10^5 with fast transient response of 3 ms. Upon SWIR light at 1550 nm, the phototransistor exhibits ultrahigh R (10^4 AW^{-1}) and D^* (10^{12} Jones) with a low driving voltage (1 V). This study shows ingenious electronic coupling of decorated graphene with CQDs will broaden applications in both photodetectors and energy-harvesting functionalities.

REFERENCES

- [1] J. Wu et al, *Adv. Mater.*, vol. 30, no. 7, 1705880, 2018.
- [2] N. Dotschuk, et al., *Nat. Commun.*, vol. 6, pp. 6563, 2015,
- [3] L. Zheng et al, *ACS Appl. Mater. Inter.*, vol. 6, no. 10, pp. 7014, 2014.
- [4] J. Tang et al., *Nat. Mater.*, vol. 10, no. 10, pp. 765, 2011.

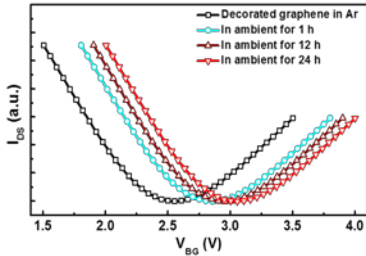


Fig. 1. Transfer characteristic curves of GFETs with N, S co-decorated graphene.

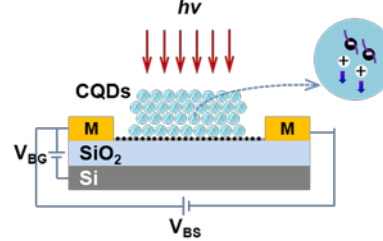


Fig. 2. Schematic of the hybrid photodetector and the electrical circuit showing the voltage bias.

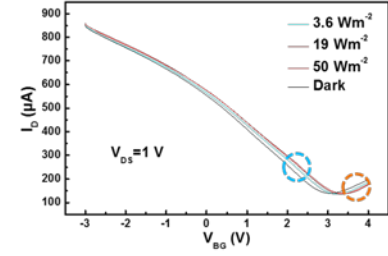


Fig. 3. Transfer curves of the hybrid phototransistor under different illumination powers with V_{DS} of 1 V.

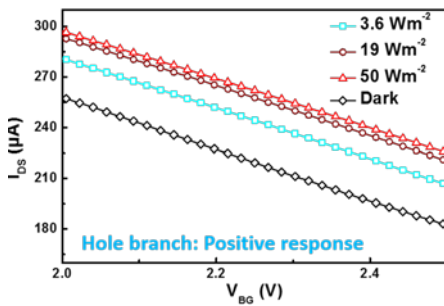


Fig. 4. Enlarged hole branches of the decorated graphene covered by PbS CQDs under different illumination powers.

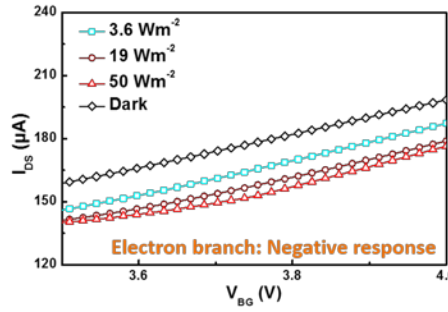


Fig. 5. Enlarged electron branches of the decorated graphene covered by PbS CQDs under different illumination powers.

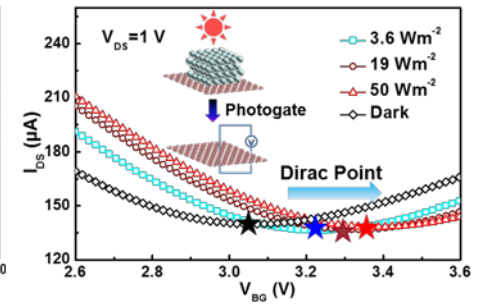


Fig. 6. Dirac Point shift induced by photogate effect of the decorated graphene covered by PbS CQDs under different illumination powers.

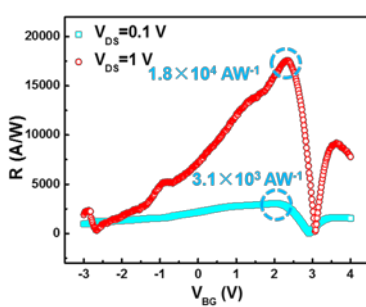


Fig. 7. Responsivity of the hybrid photodetector as a function of gate voltage for fixed driving voltage of 1 V and 0.1 V under illumination of 1550 nm, respectively.

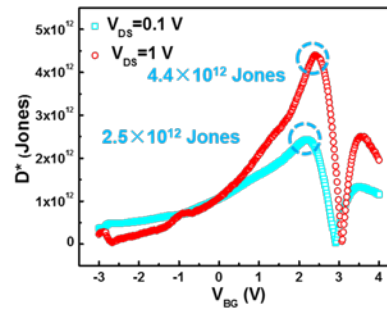


Fig. 8. Specific detectivity of the hybrid photodetector as a function of gate voltage for fixed driving voltage of 1 V and 0.1 V under illumination of 1550 nm, respectively.

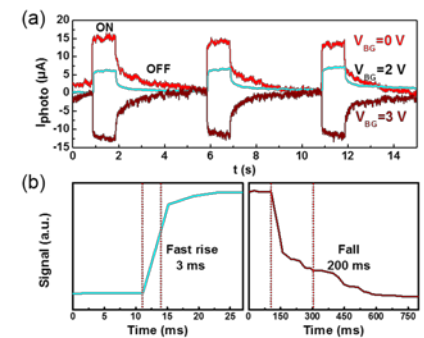


Fig. 9. Response time of the hybrid photodetector. (a) Photoswitching behavior of the hybrid photodetector under illumination of 1550 nm at $V_{BG}=0$ V (purple curve), $V_{BG}=2$ V (brown curve) and $V_{BG}=3$ V (red curve), respectively. (b) Rise and fall edges showing fast response.

Tunable fluctuation induced tunneling and pressure induced electro-switching properties of polymer based nano-graphene composites

1 Eirini Kolonelou

2 Department of Chemical Engineering
 3 National Technical University of
 4 Athens
 5 Athens, Greece
 6 email address: eiriikolone@gmail.com

7 Anthony N. Papathanassiou

8 Physics Department
 9 National and Kapodistrian University
 10 of Athens
 11 Athens, Greece
 12 email address: antpapa@phys.uoa.gr

13 Elias Sakellis

14 Physics Department
 15 National and Kapodistrian University
 16 of Athens
 17 Athens, Greece
 18 email address: e_sakel@phys.uoa.gr

19 Athanasios Zarkadoulas

20 Department of Chemistry
 21 National and Kapodistrian University
 22 of Athens
 23 Athens, Greece
 24 email address: antpapa@phys.uoa.gr

25 **Abstract**—The electrical conductivity of poly(vinyl
 26 alcohol)/poly(vinyl pyrrolidone) (1/1, w/w) and poly(vinyl
 27 alcohol) composites loaded with nano-graphene fraction, the
 28 composites operate as pressure-induced electro-switches. The
 29 functionality conductor is optimum and stable above, but close
 30 to, the percolation threshold. The semiconducting to insulator
 31 transition is signature by a drop of two orders of magnitude of
 32 the electrical conductivity. The phenomenon remains stable
 33 over tenths of degrees above room temperature. The results
 34 are interpreted through the effect of compression on the
 35 fluctuation induced tunneling of electrons through the polymer
 36 barrier separating neighbouring nano-graphene. The
 37 polarizability of the inter-graphene/polymer, which assists
 38 current flow within the tunneling region, weakens upon
 39 pressure. Subsequently, whilst the tunnelling length shortens
 40 upon compression, the enhancement of electron tunneling due
 41 to the local electric field at the polymer-graphene interfaces is
 42 suppressed.

43 **Keywords**—*nano-graphene composites, polymer composites,
 44 pressure, switches*

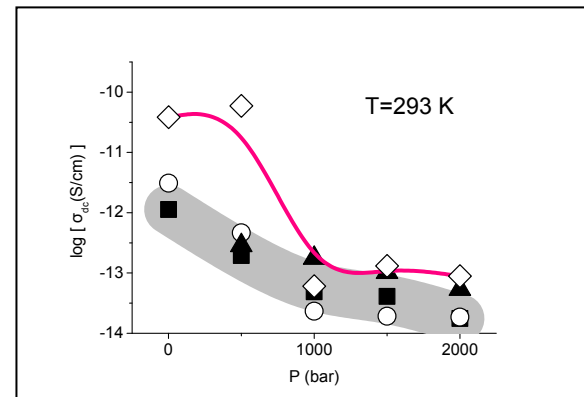


Figure 1. The logarithm of the dc-conductivity as a function of nano-graphene content: 0 w/w % (squares), 0.05 w/w % (circles), 0.1 w/w % (triangles), 0.3 w/w % (diamonds), at T=293 K. For x=0.3w/w, compression yields a step-like transition of the conductivity.

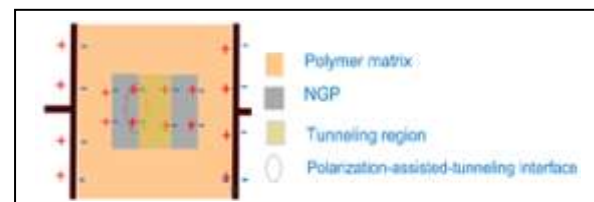


Figure 2. Line diagram of a cross section of a polymer/nano-graphene composite placed in a capacitor-type sample holder. Interfacial polarization dictates a local electric field perpendicular to the interface surface area and oriented towards the direction of the externally applied electric field. Fluctuation induced tunneling current is therefore enforced by the increased total electric pressure.

FinFET versus GAAFET Performances and Perspectives

A. Benfdila, M. Kessi and A. Lakhlef

Micro and Nanoelectronics Research Group,
Faculty of Electrical Engineering and Computer Sciences
Mouloud Mammeri University, Tizi-Ouzou, Algeria,
Email: benfdila@ummto.dz

The present paper deals with a comparative study and investigation on the performances of both gate all around field effect transistors (GAAFET) and thin fin field effect transistors (FinFET) that are considered as the next future basic logic elements for the advanced CMOS technology.

If the FinFET opened the three dimensional integration era (3D Tech), the GAAFET confirmed this 3D Tech and expended it accordingly. Furthermore, it has been developed to implement nano-electromechanical system (NEMS) technology.

The main improvement introduced by the FinFET technology is the better and maximized channel control using typical gate and channel geometries. This led to better maximization of the switching performances such as I_{ON}/I_{OFF} ratio and the operating frequencies.

The investigation on FinFET gate structure leading to better switching characteristics is presented. We have pointed out some drawbacks that might be overcome by the introduction of the GAAFET structure, that is also deeply investigated. The analyses are done using the well known device models including compact modeling.

It has been found that the I_{ON}/I_{OFF} ratio is higher for GAA compared to that of Fin structures. The frequency ranges are also different and that of GAA span much above that of FinFET. Switching leakages are higher for FinFETs and reduced for the GAAFETs.

The conclusion of our investigation is that the GAA structure gives better device performances compared to FinFET structures. However in technology point of view, FinFET structures are easily fabricated in ultra large scale integration (ULSI), whereas, GAA structures need more technology development for their generalization for integrated circuits technology.

FinFET can be used in the next decades and GAAFET will probably replace the FinFET in far times.

In any case, for the far future, substition of these nanodevices by new nanotransistor structures such as Graphene Nano Ruben Transistors (GNRT) is necessary. This will be the beginning of the next era of Nanoelectronics and future PostCMOS integrated circuits technology that may be called Carbon Electronics Era.

1

2

3

4

5

6

7

8

9

10

11

12

13

14

15

16

17

18

19

20

21

22

23

24

25

26

27

28

29

30

31

32

33

34

35

36

37

38

39

40

41

42

43

44

45

46

47

48

49

50

51

52

53

54

55

56

57

58

59

60

61

62

63

64

65

Investigation on High Switching Performances Graphene Transistors Using Band-gap Engineering

Benfdila Arezki and Lakhlef Ahcene

Micro and Nanoelectronics Research Group, Faculty of Electrical Engineering and Computer Sciences,
University M. Mammeri, Tizi-Ouzou, Algeria,
benfdila@ummto.dz

Graphene transistors are considered to be the successor's basic element for the next generation of advanced integrated circuits. The graphene suffers from the absence of a bandgap. The present paper deals with the investigation on the bandgap engineering approach aiming an increase of the switching characteristics of the graphene transistors.

INTRODUCTION

Graphene nanotransistor (GFET) is seen to be the successor of the MOS transistor as basic unit in Integrated circuits^{1,2}. These promising devices can find their application in RF circuits and amplifiers as their temperature and power sustain ability are very appreciable^{3,4}. Graphene transistors can be used in flexible and stretchable electronics as well as advanced nanosensors^{5,6}. However, their switching characteristics are strongly dependent on the graphene bandgap, which is assumed null for intrinsic graphene materials. In order to build high performance transistors, opening a bandgap for the graphene material is necessary. This is known as bandgap engineering.

BANDGAP ENGINEERING PRINCIPLES

The main obstacle for graphene transistor is the material zero bandgap that worsens the switching characteristics of the GFETs. Several techniques have been proposed to open a bandgap in graphene, among these engineering techniques, we can cite the Substrate induced bandgap, Bandgap engineering using h-BN/Ni (111). It is known that in theory a maximum of 0.50 to 0.53 eV can be obtained. Such bandgaps are observed on Graphene Bi-Layer (GBL) sheets grown on silicon carbide (SiC).

Other methods are the substitutional doping (SD), Nitrogen doping (NB). In any case graphene engineering should be considered in chemistry and physics view points. A high selective hydrogenation of graphene grown by lithography under the form of nanoruban showed a very interesting result of 0.7 eV. This process is part of selective chemical graphene functionalization techniques (SCGF).

In this paper we will deal with the graphene nanoruban and the opening of a bandgap capable of inducing an appreciable switching current ratio of at least $I_{ON}/I_{OFF} > 10^6$.

GRAPHENE FET PERFORMANCES

The Graphene Nano Ribbon (GNR) structure used in the form of GNRFET for logic circuits and RF devices combines the high field, high mobility and the possibility of opening a bandgap. The higher carrier mobility of graphene is the basis of all electrical characteristics of graphene transistors. Graphene Metal (GM) and Metal Semiconductor (MS) interfaces as well as carrier mobility are the main critical issues to improve the higher device performances. In our earlier work, we have described the Graphene Metal and Graphene Semiconductor Interfaces and their impact on resistive and schottky contacts⁷. The drain/source contact resistances introduce leakage currents that worsen the OFF state current in switching GFETs. This induce (in logic circuits) low I_{ON}/I_{OFF} ration. Lower ratio leads also to higher static power dissipation.

RESULTS AND DISCUSSION

In this paper we have used a semi-classical device model including the band to band tunneling that is described in Ref⁸ to emphasize on the bandgap engineering. Device performances are studied based on the current-voltage characteristics with respective bandgap width variations. I_{OFF} current estimated and the performance ratio deduced.

CONCLUSION

In this work the bandgap engineering using a typical technique is described. Device performances for different band with are simulated and performance parameters are deduced. It has been found that GNRFETs are the better candidate for this gap engineering. Effort should be made to overcome defects and set up an optimal gap width that allow maximum device performances

REFERENCES

1. A. C. Ferrari et al, *Nanoscale*, 7, 4598 (2015)
2. A. Benfdila et al, *J. Nano. & Optoelect.* 13, 1437 (2018)
3. H. Shu-Jen et al, *Nature Commun.*, 5, 3086 (2014)
4. J. Zheng et al, *Scientific Reports*, 3, 1314, (2013)
5. G. Fiori et al, *Nature Nanotech.*, 10 1038 (2014)
6. A. Benfante et al, *IEEE Photonics*, 10-2 (2018)
7. A. Benfdila et al, *ICFSI-16*. Germany Jul.1-7 (2017)
8. A. Paussa et al, *IEEE-TED* 61, 1567 (2014)

Black phosphorous on paper based strain sensor for human motion monitoring

1 Venkatarao Selamneni

2 Electrical and Electronics Engineering
3 Birla Institute of Technology and
4 Science Pilani, Hyderabad Campus
5 Hyderabad, India.
6

7 p20180429@hyderabad.bits-pilani.ac.in

8 Parikshit Sahatiya

9 Electrical and Electronics Engineering
10 Birla Institute of Technology and
11 Science Pilani, Hyderabad Campus
12 Hyderabad, India

13 parikshit@hyderabad.bits-pilani.ac.in

Abstract—The report demonstrates the direct growth of black phosphorous (BP) on paper with PDMS as passivation and its utilization in human motion monitoring systems. Bulk BP was obtained from red phosphorous (RP) using simple sonochemistry, followed by the exfoliation and the direct growth of BP on cellulose paper utilizing hydrothermal method. The PDMS not only hinders the oxidation of BP but also provides flexibility to the device thereby allowing the use of cellulose paper based device as strain sensor. The gauge factor calculated was 6.1 and 2000 bending cycles revealed reliability and repeatability of the fabricated device. The device was integrated onto human hand for its real time application in human motion monitoring.

Keywords—Black phosphorous, papertronics, human motion monitoring, sonochemistry, hydrothermal

I. INTRODUCTION

Even though there have many reports on BP based devices [1-2], direct growth of BP on flexible substrates still remains a challenge. The issue is intensified by the ability of the BP to oxidize when exposed to air [2]. The growth or the synthesis of BP requires high pressure processing, chemical and mechanical exfoliation which are not only low throughput process but also require a lot of post-processing for the full development of the device. Hence there is an urgent need to develop a process for the direct growth of BP on flexible substrates.

Black phosphorous possess puckered honeycomb lattice which can be visualized as rows of orthogonally coupled rings along the zigzag direction. This makes the structure BP soft, yet, mechanically strong that can withstand large strains [3]. The application of strain deforms the puckers thereby changing the P_z orbitals near the band edges which modulates the electronic properties of BP. It has been demonstrated that the application of ~ 1.2 GPa can close the bandgap which can raise the conductance by one order of magnitude [4]. The above results have hinted that the BP can be utilized as a potential candidate for the development of piezoresistive flexible strain sensors.

In this report, we demonstrate the direct growth of BP on cellulose paper by two step method - simple sonochemical followed by hydrothermal. The grown BP was passivated by PDMS for its utilization as electro-mechanical strain sensor.

II. EXPERIMENTAL SECTION

Red Phosphorous to Black Phosphorous

60 mg of RP was dispersed in 100 mL of deionized (DI) water using magnetic stirring for 1 hour. The solution was kept for ultra-sonication for 10 minutes. The ultra-sonication was repeated for 8 times which produced a higher volume of bulk

BP at the bottom of the beaker. The remaining red phosphorous solution was discarded and the bulk BP was dried and collected.

Bulk BP hydrothermal and fabrication of device

The obtained bulk BP powder was then dispersed in Dimethylformamide (DMF) to prepare a seeding solution. Cellulose paper was dipped in the seeding solution for 30 minutes followed by drying at 70°C for 10 minutes. The nutrient solution (higher concentration) and the seed coated cellulose paper were transferred to Teflon lined autoclave and hydrothermal reaction was performed at 160°C for 8 hours.

BP grown on cellulose paper with copper tape as contacts were passivated using PDMS.

III. RESULTS AND DISCUSSIONS

To confirm the growth of BP on cellulose paper and also the oxidation states of BP, XPS analysis was performed. As shown in **figure 1a**, deconvolution of P 2p peak results in doublet corresponding to 2p1/2 and 2p3/2 which can be attributed to the as grown BP [5]. The broad peak at 133.2 2V suggests the oxidation of BP thereby forming P-O and P=O bonding states. It should be noted that the BP was taken in pristine form while performing XPS which leads to the oxidation peaks. Also, Raman and XRD analysis were performed whose results suggests the successful growth of BP (Results not shown). To study the morphology of the as grown BP on cellulose paper, FESEM analysis was performed. **Figure 1b** shows the low magnification FESEM image wherein the growth of BP on cellulose paper and the microfiber morphology of the cellulose paper is visible suggesting that the growth of BP does not affect the cellulose paper substrate. **Figure 1c** shows the high magnification FESEM image wherein a connected structure of nanoparticles is visible.

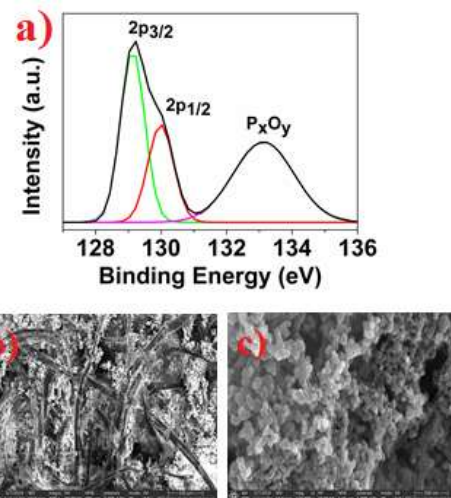


Figure 1: a) Deconvoluted XPS spectra for BP b) Low magnification FESEM image of BP growth on cellulose paper c) High magnification FESEM image.

As observed from the **figure 2a**, the device exhibited ohmic characteristics under the voltage sweep from -1V to 1V. Upon bending strain i.e. both inward and outward bending, increase in the sensor current was observed. Also, as the bending strain increases, further increment in the sensor current was observed. **Figure 2b** shows the sensitivity graph wherein a linear fit between the change in the resistance with applied strain calculates the gauge factor and was found to be 6.1. The experiment was repeated for 3 devices and similar results were obtained suggesting the repeatability of the reported process. **Figure 2c** shows the temporal response of the fabricated device under bending strain of $\sim 1.5\%$, wherein increment in the sensor current was observed. **Figure 2d** shows the temporal response of the fabricated device under increasing dynamic strain where increase in the sensor current was observed upon increasing strain. **Figure 2e** shows the temporal response for 2000 bending cycles wherein the negligible change in the sensor performance was observed suggesting the highly robust nature of the fabricated device.

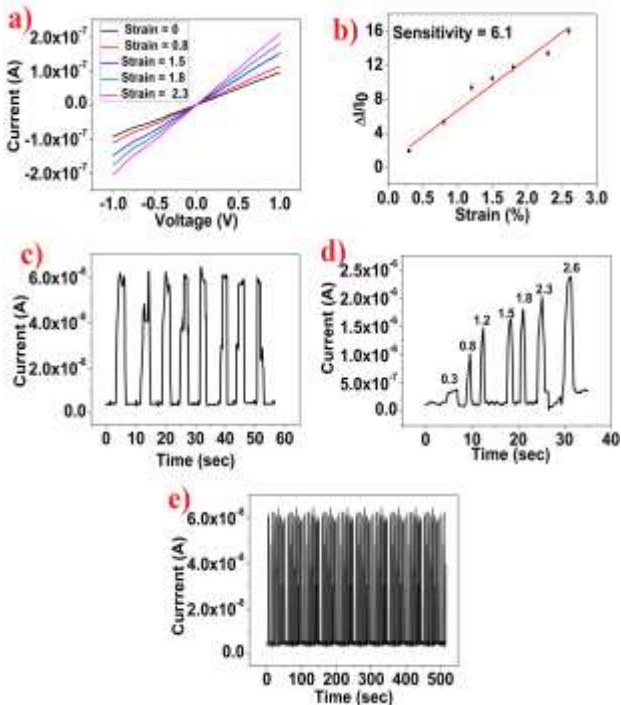


Figure 2: a) IV characteristics of the fabricated device under different bending strains b) Graph of normalized current v/s strain c) Temporal response for fixed strain of 1.2 % d) Temporal response upon increasing strain e) Temporal response for 2000 cycles.

The reason for the increment in the device current upon bending strain can be attributed to the increased connected paths between the BP nanoparticles thereby creating more paths for the current to flow. Most of the pressure sensor reports the rupture or cracks in the active materials thereby creating modulation in conductance, but, in such cases, the hysteresis of the device is poor i.e. the device resistance does not return to the initial value which affects the device

reliability. In this case, excellent hysteresis was observed which can be attributed to the non-rupture of the BP on cellulose paper. Hence the other reason for the modulation in the conduction is due to the change in the tunneling resistance between individual BP nanoparticles. Upon bending strain, the tunneling distance between individual BP nanoparticles decreases which decreases the tunneling resistance thereby increasing tunneling current.

Inspired by the excellent sensitivity and hysteresis, the fabricated device was integrated onto different parts of the human body and the corresponding motion were monitored. **Figure 3 a,b** shows the integration of fabricated device onto human hand and wrist and their corresponding response towards the respective motions.

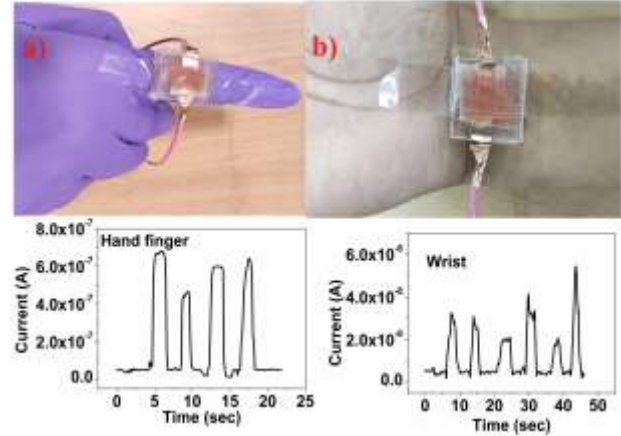


Figure 3: Fabricated device integrated onto a) human finger and b) wrist and their corresponding response.

IV. CONCLUSION

The report demonstrates the direct growth of BP on cellulose paper and its applications towards human motion monitoring. The gauge factor was calculated to be and measurements for 2000 cycles revealed excellent reliability of the fabricated sensor. The sensor was integrated onto human hand and wrist for its real time application in motion monitoring.

ACKNOWLEDGMENT

Authors thank Central Analytical Laboratory, BITS Pilani Hyderabad Campus for the assistance in material characterization.

REFERENCES

- [1] Li, L., Yu, Y., Ye, G. J., Ge, Q., Ou, X., Wu, H., and Zhang, Y. Black phosphorus field-effect transistors. *Nature nanotechnology*, 2014, vol. 9(5), pp. 372.
- [2] Du, Y., Liu, H., Deng, Y., and Ye, P. D. Device perspective for black phosphorus field-effect transistors: contact resistance, ambipolar behavior, and scaling. *ACS Nano*, 2014, vol. 8(10), pp. 10035-10042.
- [3] Jiang, J. W., and Park, H. S. Mechanical properties of single-layer black phosphorus. *Journal of Physics D: Applied Physics*, 2014, vol. 47(38), pp. 385304.
- [4] Liu, H., Neal, A. T., Zhu, Z., Luo, Z., Xu, X., Tománek, D., and Ye, P. D. Phosphorene: an unexplored 2D semiconductor with a high hole mobility. *ACS Nano*, 2014, vol. 8(4), pp. 4033-4041.
- [5] Hao, C., Wen, F., Xiang, J., Yuan, S., Yang, B., Li, L., and Tian, Y. Liquid-Exfoliated Black Phosphorous Nanosheet Thin Films for Flexible Resistive Random Access Memory Applications. *Advanced Functional Material's*, 2016, vol. 26(12), pp. 2016-2024.

Asymmetric Current-Voltage Characteristics in Graphene-hBN Dot-Ring Nanostructures - A numerical study

Siddharth Krishnan

Department of Electrical Engineering
Indian Institute of Technology Gandhinagar
Gandhinagar, India
Email: siddharth.krishnan@iitgn.ac.in

Ravi Sadananda Hegde

Department of Electrical Engineering
Indian Institute of Technology Gandhinagar
Gandhinagar, India
Email: hegder@iitgn.ac.in

Quantum dots (QD) of Graphene and other 2D materials have the potential to replace colloidal-semiconductor QDs. Dot-Ring Hetero-Nanostructures (DRN), 2D QDs surrounded by quantum rings, are a possible route towards gate-tunability in these systems. A particularly exciting feature is the asymmetric diode-like I-V characteristics of graphene-hexagonal Boron Nitride(h-BN) DRN recently predicted by Seele and coworkers¹. We build on their preliminary work, uncovering the underlying physics behind this exotic property and studying how structural and gating parameters influence the observed asymmetry.

As seen in Figure 1, the Dot-Ring nanostructure contains an inner graphene quantum dot, surrounded by two concentric ring. The inner ring is composed of h-BN while the outer is a graphene quantum ring. The device is symmetrically connected to semi-infinite zig-zag edge graphene nanoribbons, serving as the leads. In our study, we apply the gate voltage to the central dot. Through the gate voltage, we control the wave function of the electron in the device, hence controlling its transport properties. One method of fabricating nanorings of 2-dimensional structures is using Au@Pt lithography techniques².

I. RESULTS

We perform our quantum transport calculations using the Python software package Kwant³. Kwant solves the

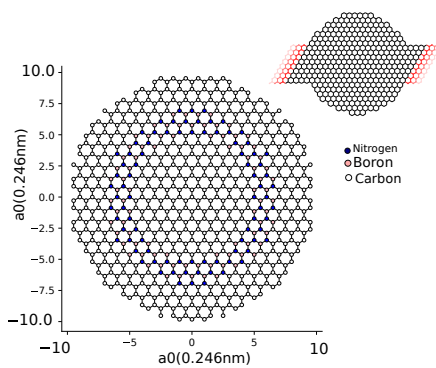


Fig. 1. The structure of the DRN with the inner graphene dot surrounded by the h-BN ring and finally the graphene ring. In the top right, we have the structure connected to semi-infinite leads of zig-zag edge graphene

scattering problem in a tight-binding system through the wave function formalism. The Hamiltonian of the system takes the form:

$$\hat{\mathbf{H}} = \sum_{i,j} H_{ij} c_i^\dagger c_j, \quad (1)$$

where c_i^\dagger and c_j are the fermionic creation and annihilation operators respectively, i and j are the degrees of freedom of the system, and H_{ij} are the elements of the infinite Hamiltonian describing the system. The Hamiltonian can also be written in the first quantization as

$$\hat{H} = \sum_{i,j} H_{i,j} |i\rangle \langle j|, \quad (2)$$

where the degree of freedom i is of the form $|i\rangle = |\mathbf{r}\alpha\rangle$, \mathbf{r} is the position of the lattice point, and α is the internal degree of freedom. The primary raw outputs of Kwant are the scattering matrix of the system and the electron wave functions. We can extract all the transport properties of the system from the scattering matrix, notably, the transmission as a function of electron energy. The I-V curves are then obtained using the LB formalism¹. Note that like Seel and coworkers, we implicitly assume that the DRN is closer to the source electrode in generating the I-V curves.

In Figure 2, we can observe the asymmetry of the I-V characteristic of the structure.

To study how the geometry of the structure affects its transport properties, we vary the central dot radius (R_d) and the h-BN ring radius. We observe that, within the range of energies the calculations were performed, the conductance peaks above the Fermi level decayed faster than those below as a function of the central dot radius and the h-BN ring radius.

We define a quantity called the **Asymmetry Factor**(Γ) given by

$$\Gamma = \frac{|I_{0.6V}| - |I_{-0.6V}|}{|I_{0.6V}| + |I_{-0.6V}|} \times \max(I_{0.6V}, I_{-0.6V})(\mu A) \quad (3)$$

to quantify the degree of asymmetry in the I-V characteristic of the structure. In Figure 4, we show the variation of Γ with R_d and t . We use this information to find the optimum geometry, which will give us the maximum asymmetry.

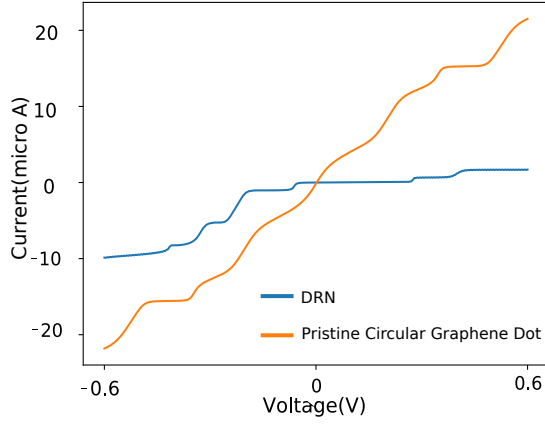


Fig. 2. The I-V characteristics for a pristine graphene dot compared to that of a DRN. The curve for the dot is symmetric while the asymmetric nature of the DRN curve is pronounced

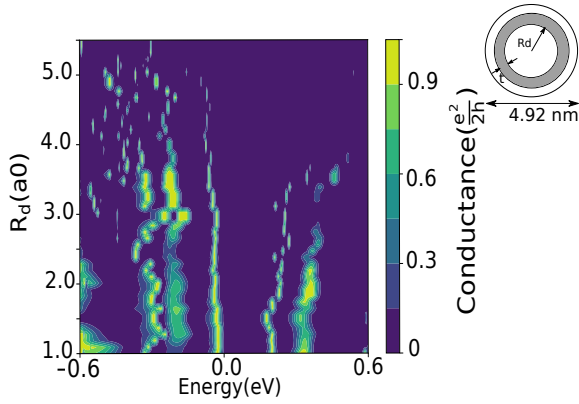


Fig. 3. Conductance contour for structures with varying central dot radius. Shown here is the contour for the conductance of the structure while varying the radius of the central dot. We observe that for small radii, a large number of states exist on both sides of the Fermi level, but for larger radii, the conductance peaks are much weaker below the Fermi level

We apply a gate voltage to the central dot and calculate the conductance as a function of gate voltage and source-drain voltage. For specific negative gate voltages, we can have a higher density of states(DOS) below the Fermi level, in our voltage range of interest. This results in a higher conductance indicated by the stronger conductance peaks in the region around $(V_{DS}, V_G) = (-0.2V, -0.35)$ in Figure 5.

CONCLUSION

In conclusion, our calculations unveil the interesting physics behind the asymmetric transport and demonstrate the possibility of control over this property through geometry and electrostatic gating. This work could entail novel devices for application in memristive and resistive memory devices.

REFERENCES

- [1] Max Seel and Ravindra Pandey. Electronic and quantum transport properties of a graphene-bn dot-ring hetero-nanostructure. *Journal of Physics Communications*, 2(4):045003, 2018.
- [2] Hee-Jeong Jang Jang, Dae Keun Park, and Wan Soo Yun. Fabrication of shape-controlled reduced graphene

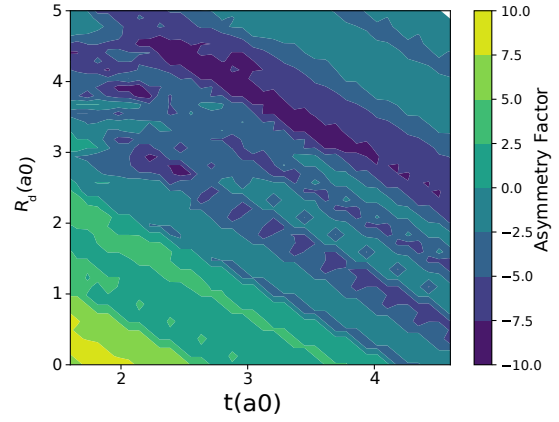


Fig. 4. Asymmetry factor as a function of the inner dot radius and the h-BN ring radius. We can see that the maximum value of the asymmetry factor is in the region coloured dark blue. This region corresponds to the geometries in Figure 3 where conductance above the Fermi level has vanished

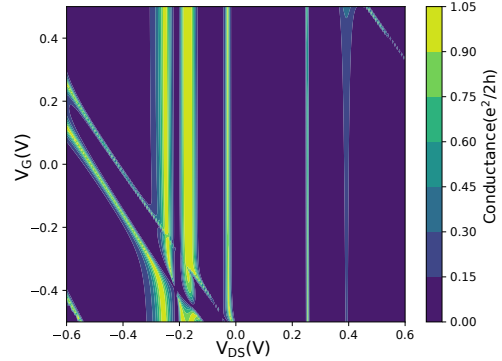


Fig. 5. Conductance as a function of gate voltage (V_G) applied to inner dot and source-drain voltage(V_{DS}) for the DRN structure with $R_d = 4.16a0$ and $t = 2.7a0$. We can see that the gate voltage is shifting certain levels(electron states in the central dot) which manifest as shifts of conductance peaks in the plot. At $-0.35V$ we can see the conductance in our range of interest is larger since both inner dot and outer ring states are participating in conduction

oxide nanorings by au@pt nanoring lithography. *Nanoscale*, Nov 2014.

- [3] Christoph W Groth, Michael Wimmer, Anton R Akhmerov, and Xavier Waintal. Kwant: a software package for quantum transport. *New Journal of Physics*, 16(6):063065, 2014.
- [4] Liang Huang, Ying-Cheng Lai, David K Ferry, Richard Akis, and Stephen M Goodnick. Transmission and scarring in graphene quantum dots. *Journal of Physics: Condensed Matter*, 21(34):344203, 2009.

Improved Microenvironments for Increased Actin-Myosin Longevity in Nano Devices

1
2
3
4
5
6
7
8
9
10
11
12
13
14
15
16
17
18
19
20
21
22
23
24
25
26
27
28
29
30
31
32
33
34
35
36
37
38
39
40
41
42
43
44
45
46
47
48
49
50
51
52
53
54
55
56
57
58
59
60
61
62
63
64
65
Aseem Salhotra

Department of Chemistry and Biomedical Sciences
Linnaeus University
Kalmar, Sweden
aseem.salhotra@lnu.se

Frida W. Lindberg

NanoLund and Solid State Physics
Lund University
Lund, Sweden
frida.lindberg@ftf.lth.se

Roman Lyttleton

NanoLund and Solid State Physics
Lund University
Lund, Sweden
roman.lyttleton@ftf.lth.se

Jingyuan Zhu

NanoLund and Solid State Physics
Lund University
Lund, Sweden
jingyuan.zhu@ftf.lth.se

Marko Usaj

Department of Chemistry and Biomedical Sciences
Linnaeus University
Kalmar, Sweden
marko.usaj@lnu.se

Marlene Norrby

Department of Chemistry and Biomedical Sciences
Linnaeus University
Kalmar, Sweden
marlene.norrby@lnu.se

Heiner Linke

NanoLund and Solid State Physics
Lund University
Lund, Sweden
heiner.linke@ftf.lth.se

Alf Måansson

Department of Chemistry and Biomedical Sciences
Linnaeus University
Kalmar, Sweden
alf.mansson@lnu.se

The in vitro motility assay (IVMA) is an effective method for functional studies of molecular motors but it is also useful as a basis for nanodevices e.g. in biocomputation and biosensing for future emerging technologies [1], [2]. In this assay, surface-adsorbed heavy meromyosin (HMM) motor fragments propel fluorescently labelled actin filaments. We have compared methods for the removal of non-functional HMM to improve the fraction of motile actin filaments (FMF) in the IVMA [3]. Additionally, it is also possible to fine-tune the velocity of the actin-myosin interaction by using pharmacological tools such as blebbistatin [4]. Here we studied actin-myosin longevity on different surfaces including reference surfaces such as silicon dioxide based chip and a regular glass coverslip. All test surfaces were silanized with trimethylchlorosilane (TMCS) in order to allow proper attachment of myosin motors for *good* functionality. CSAR 62 and PMMA are resist coating used to block the attachment of myosin in regions other than fabricated patterns. For use in nanodevices, we came across several factors, which significantly affect the longevity of actin-myosin motile function. The factors (Table I) include motility temperature (22.0–28.0 °C), surface substrate, other different effects related to the nanofabrication procedure (e.g. resists used), interaction with atmospheric oxygen (e.g. whether flow cell openings are sealed or not), size of the flow cell and type of flow cell spacers. In the latter cases we tested 3M(467MP) & 3M(Scotch) industrial grade adhesive tapes and Parafilm. Efforts to increase longevity resulted in conditions with motile function ranging between less than 20 min to more than 4 h with sealing of the flow cell and use of Parafilm as spacers, being important for favourable results. Improvements in microenvironments increasing the actin-myosin longevity in nanodevices what allow us to attain future goals in biocomputation. Similar understandings could replicate for the IVMA towards various biomedical and biosensing applications including other bio-agents such as microtubules-kinesin based nanodevices.

TABLE I. INCREASED ACTIN-MYOSIN LONGEVITY IN IVMA

TMCS coated surface	Controllable parameters in actin-myosin IVMA			
	Spacer	Temp. (°C)	Sealing	Run Time
CSAR 62 resist on SiO ₂	3M (467MP)	25.1	No	6 min
	3M (Scotch)	25.3	No	6 min
	3M (467MP)	28.0	Yes	12 min
	3M (467MP)	22.3	No	20 min
	Parafilm	25.3	Yes	240+ min
SiO ₂ (Reference)	3M (467MP)	25.3	No	12 min
	Parafilm	25.3	Yes	240+ min
PMMA resist on SiO ₂	3M (467MP)	22.0	No	12 min
	3M (Scotch)	22.1	No	12 min
Glass Coverslip (Reference)	3M (467MP)	24.9	No	20 min
	3M (Scotch)	24.9	No	60+ min
	Parafilm	25.2	Yes	240+ min

ACKNOWLEDGMENT

The authors acknowledge the EU Horizon 2020 Future and Emerging Technologies Programme of the European Union (# 732482, Bio4comp) for funding this research. Special thanks to Linnaeus University and Lund University.

REFERENCES

- [1] D. V. Nicolau *et al.*, “Parallel computation with molecular-motor-propelled agents in nanofabricated networks,” *Proc. Natl. Acad. Sci.*, vol. 113, no. 10, pp. 2591–2596, 2016.
- [2] T. Korten, A. Måansson, and S. Diez, “Towards the application of cytoskeletal motor proteins in molecular detection and diagnostic devices,” *Curr. Opin. Biotechnol.*, vol. 21, no. 4, pp. 477–488, 2010.
- [3] M. A. Rahman, A. Salhotra, and A. Måansson, “Comparative analysis of widely used methods to remove nonfunctional myosin heads for the in vitro motility assay,” *J. Muscle Res. Cell Motil.*, vol. 39, no. 5, pp. 175–187, 2018.
- [4] M. A. Rahman, M. Ušaj, D. E. Rassier, and A. Måansson, “Blebbistatin Effects Expose Hidden Secrets in the Force-Generating Cycle of Actin and Myosin,” *Biophys. J.*, vol. 115, no. 2, pp. 386–397, 2018

Structural and magnetic properties of rare earth doped cobalt ferrite nanostructures

Georgiana BULAI

Integrated Centre for Environmental Science Studies in the North-East Development Region - CERNESIM
 "Alexandru Ioan Cuza" University of Iasi
 Iasi, Romania
 georgiana.bulai@uaic.ro

Ovidiu Florin CALTUN

Faculty of Physics
 "Alexandru Ioan Cuza" University of Iasi,
 Iasi, Romania

Vasilica TRANDAFIR

Atmosphere Optics and Laser Spectroscopy Laboratory, Faculty of Physics
 "Alexandru Ioan Cuza" University of Iasi,
 Iasi, Romania

Cristian FOCSA

Physique des Lasers, Atomes et Molécules, Centre d'Etudes et de Recherches Lasers et Applications, Université de Lille
 Lille, France

Stefan Andrei IRIMICIUC

National Institute for Laser, Plasma and Radiation Physics – NILPRP
 Magurele-Bucharest, Romania

Silviu GURLUI

Atmosphere Optics and Laser Spectroscopy Laboratory, Faculty of Physics
 "Alexandru Ioan Cuza" University of Iasi,
 Iasi, Romania

Spinel ferrites are magnetic materials with important technological potential in high-frequency applications, magneto – optic devices, sensors, actuators and even drug delivery [1–3]. The spinel ferrites are promising photocatalysts in several industrial processes [4] due to their band gap valued in the range of 1.1–2.3 eV (capable of absorbing visible light) and their crystalline structure (which enhances the process efficiency due to available extra catalytic sites) [5,6].

In this study we investigated the influence of rare earth ion doping on the structural and magnetic properties of $\text{CoFe}_{2-x}\text{RE}_x\text{O}_4$ ($x = 0.01; 0.03; 0.05; 0.1; 0.2; 0.3$). Ferrite nanoparticles were obtained by coprecipitation method using carboxymethyl cellulose as natural surfactant and NaOH for pH control. After repeated washing and calcination at 500 °C for 6 h in air, the obtained nanoparticles were characterized by X-Ray Diffraction (XRD), Raman spectroscopy and Scanning Electron Microscopy – Energy Dispersive X-ray spectroscopy (SEM – EDX). The results confirm the formation of pure cobalt ferrite phase for low RE content and of residual phases when high RE concentrations were used. The crystallite sizes and lattice parameters were influenced by the presence of RE which, due to their large ionic radii determined a distortion of the spinel phase and cation redistribution between the octahedral and tetrahedral sites. Magnetic hyperthermia testing and Vibrating Sample Magnetometry (VSM) measurements were considered for all samples. An increase in saturation magnetization and specific absorption rates was observed for the doped ferrites compared to the stoichiometric CoFe_2O_4 nanoparticles.

The nanoparticles were then pressed into disks and sintered at 1250°C for 5h with a heating rate of 100°C/h. The obtained bulk materials were subsequently used as source materials in thin film growth by pulsed laser deposition. For this step of the study the targets were placed on an XY motorized stage inside a vacuum chamber. The pressure during the deposition was $\sim 10^{-2}$ Torr and a Nd-YAG laser (532 nm) was focused on the target surface. The fluence was kept at 5 J/cm^2 (50 mJ laser energy/pulse, 1 mm² spot area). The monocrystalline (100) Si substrate was placed at a distance of 5 cm in front of the target during the 60 min deposition. The XRD and Raman spectroscopy

measurements done on all thin film samples revealed an amorphous growth, thus a thermal treatment in air at 700°C for 2 h was applied on the deposited samples. Although the presence of RE elements determined the formation of residual phases in nanoparticles and bulk materials when higher RE content was used, this result was not observed for the deposited thin films. An increase in lattice parameter and decrease in crystallite size (derived from XRD measurements) was shown. Both XRD and Raman spectroscopy measurements showed a decrease in crystallinity of the films when more RE is present in the material. The thin film thicknesses were determined by stylus profilometry and the surface topography and chemical composition was studied by SEM and EDX techniques. The thickness of the thin films varied from 150 to 200 nm and the presence of droplets was observed for the investigated samples. While for the Yb doped cobalt ferrite target, Yb-rich regions at grain boundaries were identified, the thin films present a more uniform distribution of the main elements (RE, Fe, Co and O) with Co:(REFe) ratio of 0.51, 0.49 and 0.53 for the Yb, Dy and Gd doped samples (with $x=0.2$), respectively (close to the nominal value of 0.5 of the stoichiometric cobalt ferrite). The VSM results were correlated to the magnetic characteristics of the dopant. An increase of the optical band gap derived from reflectance spectra was observed.

These results are useful in understanding the influence of rare earth addition in the cobalt ferrite spinel structure as well as in studying the applicability of the obtained thin films in magneto-optic devices or as catalysts.

REFERENCES

- [1] C. Himeinschi, I. Vrejoiu, G. Salvan, M. Fronk, A. Talkenberger, D.R.T. Zahn, D. Rafaja, J. Kortus, Optical and magneto-optical study of nickel and cobalt ferrite epitaxial thin films and submicron structures, *J. Appl. Phys.*, vol. 113, pp. 084101, 2013.
- [2] S. Amiri, H. Shokrollahi, The role of cobalt ferrite magnetic nanoparticles in medical science, *Mater. Sci. Eng. C*, vol. 33, pp. 1–8, 2013.
- [3] A. Sutka, K. Arlis, A. Gross, Spinel ferrite oxide semiconductor gas sensors, *Sensors Actuators B*, vol. 222, pp. 95–105, 2016.

- [4] M. Rahimi-Nasrabadi, M. Behpour, A. Sobhani-Nasab, M.R. Jeddy, Nanocrystalline Ce-doped copper ferrite: synthesis, characterization, and its photocatalyst application, *J. Mater. Sci. Mater. Electron.*, vol. 27, pp. 11691–11697, 2016.
- [5] M. Sundararajan, V. Sailaja, L. John Kennedy, J. Judith Vijaya, Photocatalytic degradation of rhodamine B under visible light using nanostructured zinc doped cobalt ferrite: Kinetics and mechanism, *Ceram. Int.*, vol. 43, pp. 540–548, 2017.
- [6] A. V. Ravindra, P. Padhan, W. Prellier, Electronic structure and optical band gap of CoFe_2O_4 thin films, *Appl. Phys. Lett.*, vol. 101, pp. 1–5, 2012.

1
2
3
4
5
6
7
8
9
10
11
12
13
14
15
16
17
18
19
20
21
22
23
24
25
26
27
28
29
30
31
32
33
34
35
36
37
38
39
40
41
42
43
44
45
46
47
48
49
50
51
52
53
54
55
56
57
58
59
60
61
62
63
64
65

NMDC 2019 1570560242

Two-step Large-area Fabrication

of Isolated Silicon Quantum Dots

Federico Pevere
Department of engineering sciences
Uppsala University
Uppsala, Sweden
ORCID: 0000-0001-5304-913X

Hithesh Kumar Gatty
Department of engineering sciences
Uppsala University
Uppsala, Sweden
ORCID: 0000-0001-8935-2149

Jingjian Zhou
Department of applied physics
KTH Royal Institute of Technology
Stockholm, Sweden
email: jingjian@kth.se

Ilya Sychugov
Department of applied physics
KTH Royal Institute of Technology
Stockholm, Sweden
ORCID: 0000-0003-2562-0540

Jan Linnros
Department of applied physics
KTH Royal Institute of Technology
Stockholm, Sweden
ORCID: 0000-0002-5260-5322

In this work, we present a two-step fabrication method which allows to form isolated silicon quantum dots (Si-QDs) embedded in a silicon dioxide matrix over large areas (\sim mm 2). This technique could help the subsequent fabrication of resonant cavities/mirrors around single Si-QDs, as done with group III-V QDs for quantum photonic applications [1, 2]. Our approach is a combination of two methods: one which is suitable to form isolated Si-QDs but in relatively small areas (\sim μm 2) [3] and another well-established for their mass-fabrication prior to chemical surface passivation [4]. To fabricate Si-QDs, the device layer (\sim 50 nm thick) of a SOI wafer was first thinned down to \sim 10 nm using reactive ion etching (RIE) by HBr (40 mlpm), Cl₂ (15 mlpm) and O₂ (10 mlpm) gases at a pressure of 40 mTorr and a power of 300 W. The etching rate was estimated as \sim 4 nm/s and the effect of etching time on the Si thickness can be seen from the reflected white-light (WL) images of Fig. 1(a). In the second and last step, the sample was annealed at 1100 °C in Ar atmosphere with oxygen traces for 1 h. Micro-photoluminescence (μPL) measurements of the sample surface under UV excitation revealed the presence of \sim mm 2 areas full of luminescent diffraction-limited particles, as shown in the images of Fig. 1(b), suggesting them to be well-separated Si-QDs. In order to understand their physical properties, the PL of approximately 100 isolated luminescent particles was probed. Fig. 2 shows that most of the Si-QDs exhibited strong linear polarization along Si crystallographic directions [110] and [-110]. Furthermore, the emission energies of such QDs spanned over

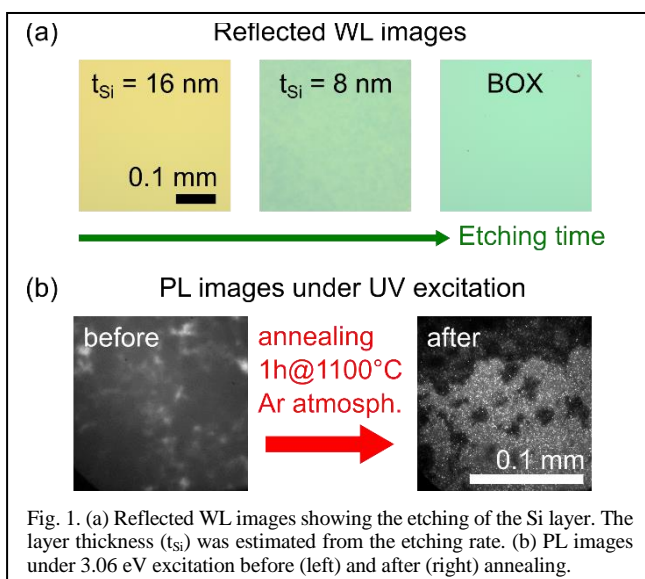


Fig. 1. (a) Reflected WL images showing the etching of the Si layer. The layer thickness (t_{Si}) was estimated from the etching rate. (b) PL images under 3.06 eV excitation before (left) and after (right) annealing.

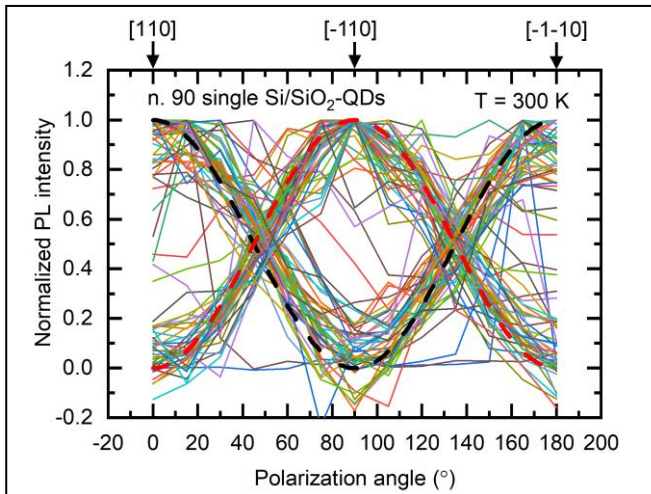


Fig. 2. Normalized PL versus polarization angle for single Si-QDs (continuous lines). Dashed lines indicate polarization along silicon [110] (black) and [-1-10] (red) directions. Excitation was 3.06 eV.

a broad range, from 1.3 to 2.0 eV as plotted in the low-temperature (10 K) spectra of Fig. 3. Single-dot spectra were typically characterized by a single emission line, usually attributed to no-phonon radiative recombination of excitons in the Si core [5]. Additionally, system resolution-limited (250 μeV) PL linewidths (FWHM) were measured for several Si-QDs at 10 K, with no clear correlation with emission energy and polarization. The repeatability of the process presented in

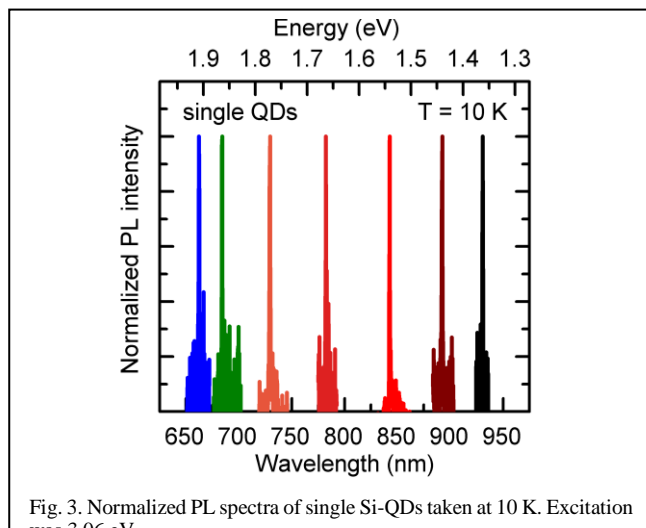


Fig. 3. Normalized PL spectra of single Si-QDs taken at 10 K. Excitation was 3.06 eV.

this work was checked by observing no significant variation in the optical properties of single Si-QDs in a batch of 10 different samples. To conclude, our two-step synthesis of isolated Si-QDs over large areas featuring linearly polarized light and narrow emission linewidths could help the future fabrication of resonant cavities/mirrors which aim to enhance the PL of individual Si-QDs for quantum photonic applications.

REFERENCES

- [1] M. Arita, F. Le Roux, M. J. Holmes, S. Kako, and Y. Arakawa, "Ultraclean Single Photon Emission from a GaN Quantum Dot," *Nano Letters*, vol. 17, no. 5, pp. 2902-2907, May 2017.
- [2] N. Somaschi *et al.*, "Near-optimal single-photon sources in the solid state," (in English), *Nature Photonics*, Article vol. 10, no. 5, pp. 340-345, May 2016.
- [3] I. Sychugov, Y. Nakayama, and K. Mitsuishi, "Sub-10 nm crystalline silicon nanostructures by electron beam induced deposition lithography," *Nanotechnology*, vol. 21, no. 28, Jul 2010.
- [4] C. M. Hessel, E. J. Henderson, and J. G. C. Veinot, "Hydrogen silsesquioxane: A molecular precursor for nanocrystalline Si-SiO₂ composites and freestanding hydride-surface-terminated silicon nanoparticles," *Chemistry of Materials*, vol. 18, no. 26, pp. 6139-6146, Dec 26 2006.
- [5] D. Kovalev, H. Heckler, M. Ben-Chorin, G. Polisski, M. Schwartzkopff, and F. Koch, "Breakdown of the k-conservation rule in Si nanocrystals," (in English), *Physical Review Letters*, vol. 81, no. 13, pp. 2803-2806, Sep 28 1998.

Fabrication of finger patterned electrode and its application by electrohydrodynamic printing

Joong Ho Lee
Department of Chemistry,
Kookmin University,
Seoul, Korea
Joongho@kookmin.ac.kr

Gang Yeol Yoo
Department of Advanced Materials
Korea University
Seoul, Korea
king2919@korea.ac.kr

Hyeongjin Lee
Department of Chemistry,
Kookmin University,
Seoul, Korea
Lhjalqp@kookmin.ac.kr

Woong Kim
Department of Advanced Materials
Korea University
Seoul, Korea
woongkim@korea.ac.kr

Young Rag Do*
Department of Chemistry,
Kookmin University,
Seoul, Korea
Joongho@kookmin.ac.kr

Given the recent growth in the display industry, the importance of fabricating patterns on lower scales has increased. There are many ways to implement electrodes on smaller scales, and here we attempt to implement Ag-fingered patterned electrodes using electrohydrodynamic jet (E-jet) printing. E-jet printing offers the advantage of higher resolutions than to ink-jet printing. Therefore, this method has the potential to fabricate electrodes as the scale of the fabrication process becomes increasingly smaller. The ink solution for fabricating electrodes is silver paste (Harima ink), which also offers the advantages of high-density Ag nano-paste and a lower curing temperature comparing to other commercial products. The diameter of the fine capillary glass nozzle used here was adjusted using a P-1000 micropipette puller, with measurements taken by an optical microscope. The voltage and frequency were optimized to fabricate an electrode with a 3.5um spacing. The width of the Ag-fingered patterned electrode and the jetting width were measured by means of scanning electron microscopy (SEM). We also measured the efficiency of the assembly of the silicon rod of the electrode and assessed the improvement of the contact resistance.

Investigation of E-Mode Beta-Gallium Oxide MOSFET for Emerging Nanoelectronics

Rajan Singh and T. R. Lenka

Department of Electronics & Communication Engineering,
National Institute of Technology Silchar
Assam, 788010, India

Email: rajan_singh@ieee.org, t.r.lenka@ieee.org

Abstract-Gallium oxide (Ga_2O_3) is an emerging material due to its suitable material properties and device characteristics. In this paper an enhancement mode ‘T’ shaped recessed gate novel Ga_2O_3 MOSFET (E-MOSFET) is designed and simulated using Atlas. The ‘T’ shape recessed gate depletes major portion of the active channel region and thus ensures off-operation at zero gate bias. The device achieves threshold voltage of 1.0 V, and R_{on} of 212 $\Omega\text{-mm}$. The simulated device results in drain current density of around 40mA/mm and I_{ON}/I_{OFF} ratio greater than 10^{10} . The device with source to drain spacing of 20 μm achieved sub-threshold swing of 123mV/dec which is the best reported value and in good agreement with experimental results.

Index Terms: *E-MOSFET, Gallium Oxide, Normally-Off, sub-threshold swing, Atlas*

I. INTRODUCTION

In power electronic applications some of the most used wide band-gap semiconductor materials are silicon carbide (SiC), gallium nitride (GaN) and diamond. In contrast, single-crystal gallium oxide (Ga_2O_3) is being given large attention as an alternative material for future power electronic devices. Gallium oxide shows band gap energy of 4.5 eV to 4.9 eV higher than of GaN (3.4-3.43 eV) [1-2].

Earlier depletion-mode single-crystal Ga_2O_3 field-plated MOSFETs (FP-MOSFETs) demonstrated breakdown voltage V_{br} of 755 V, and $I_{ON}/I_{OFF} > 10^9$ [7]. E-mode operation of Ga_2O_3 MOSFETs using wrap-gate fin arrays resulting in breakdown voltage (V_{br}) > 600 V, and I_{ON}/I_{OFF} ratio is greater than 10^5 [4]. A gate-recess e-mode Beta Gallium Oxide (BGO) showed current density (I_{DS}) up to 40 mA/mm and V_{br} exceeding 500 V for source-drain spacing (L_{SD}) of 8 μm [3].

In this paper, we have successfully demonstrated high performance E-mode MOSFET with recessed ‘T’ shaped gate showing record high I_{DS} , record low R_{on} , high I_{ON}/I_{OFF} ratio, low subthreshold swing (SS), and negligible effect of output conductance at higher gate voltage. The Atlas non-isothermal model for $\beta\text{-Ga}_2\text{O}_3$ is used for simulating the device characteristics.

II. DEVICE STRUCTURE AND SIMULATION MODEL

A semi-insulating single crystal beta- Ga_2O_3 is used as substrate, on which 300 nm thick channel of n-type Ga_2O_3 was grown. The detailed device structure and dimensions are shown in Fig. 1.

Ravi T. Velpula, Bui Ha Quoc Thang and Hieu P. T. Nguyen

Department of Electrical and Computer Engineering,
New Jersey Institute of Technology, Newark,
New Jersey, 07102, USA

Email: rv366@njit.edu, hieu.p.nguyen@njit.edu

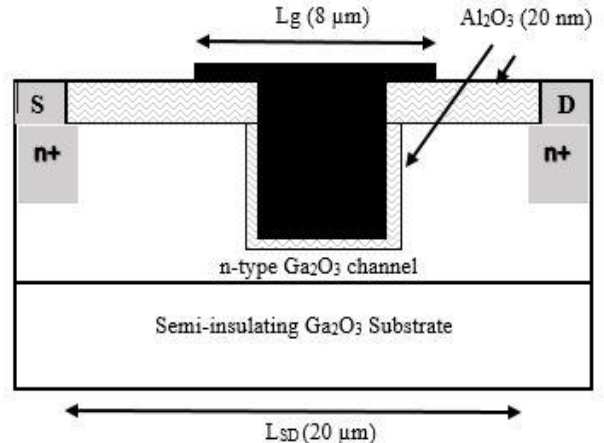


Fig. 1. Device structure and dimensions.

The channel layer has a donor concentration of $1.1 \times 10^{17} \text{ cm}^{-3}$. A highly doped n-type Gaussian type box profile of concentration $3.0 \times 10^{19} \text{ cm}^{-3}$ is made under the drain and source contact region. A gate oxide layer (Al_2O_3) of thickness 20 nm is deposited over the device with 8 μm long metal gate on the top of structure. In order to achieve E-mode operation of the device, gate is recessed upto a depth of 250 nm inside the channel. Thus leaving 50 nm of active channel thickness under the gate. The source-drain spacing (L_{SD}) is 20 μm , upper gate length (L_g) is 8 μm , gate-source spacing (L_{GS}) and gate-drain spacing (L_{GD}) of 6 μm .

A constant thermal conductivity model along with low field mobility model is used to get DC and transfer characteristics of the device. The material properties of the beta- Ga_2O_3 reported by [5-6] is used in Atlas simulation are band gap of 4.8 eV, electron mobility, μ_n of 300 cm^2/Vs , relative dielectric constant, ϵ of 10. The electron affinity of beta- Ga_2O_3 is considered as 4.0 eV and Pt/Au gate material is used with a work function of 5.23 eV [8].

The Fermi potential for n-type Ga_2O_3 is given by

$$\varphi_{Fn} = \frac{kT}{q} \ln \frac{N_D}{N_i} = 2.36 \text{ eV} \quad (1)$$

At zero gate bias, due to work function difference between metal and semiconductor (Ga_2O_3), band-bending occurs.

$$\varphi_{MS} = 5.23 - 4.17 = 1.06 \text{ eV} \quad (2)$$

So the flat-band voltage is $V_{FB} = \varphi_{MS} = 1.06 \text{ eV}$.

Depletion region width is calculated as

$$W_n = \sqrt{\frac{2 \epsilon_0 \epsilon V_{FB}}{q N_D}} = 103 \text{ nm} \quad (3)$$

III. RESULTS AND DISCUSSION

The results of DC simulation and transfer characteristics are shown in Fig. 3, Fig. 4 and Fig. 5. Fig. 3 shows the I_{DS} versus V_{DS} characteristics for a gate voltage varying from 4V to 8V in the incremental step of 1V. On-resistance (R_{ON}) is found as $207 \Omega\text{-mm}$ which is measured at lower value of V_{DS} . Fig. 4 shows the I_{DS} versus V_{GS} characteristics for $V_{DS}=15\text{V}$. The graph shows $I_{DS} \approx 40\text{mA/mm}$ and maximum transconductance of around 7mS/mm .

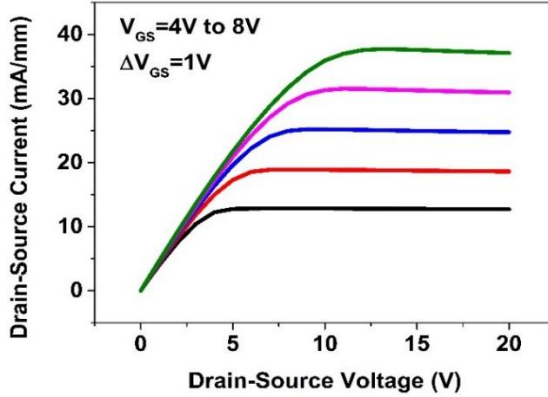


Fig. 3. Output Characteristics for $L_{SD}=20\text{um}$.

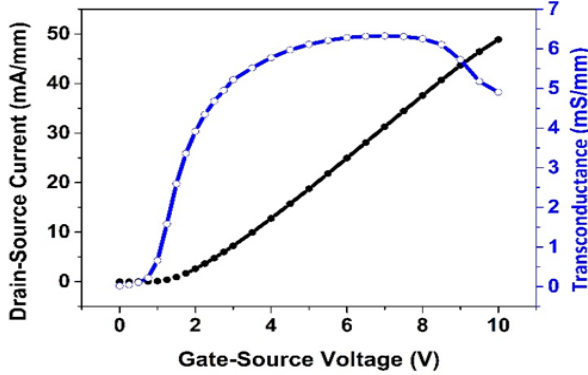


Fig. 4. Transfer Characteristics for $V_{DS}=15\text{V}$.

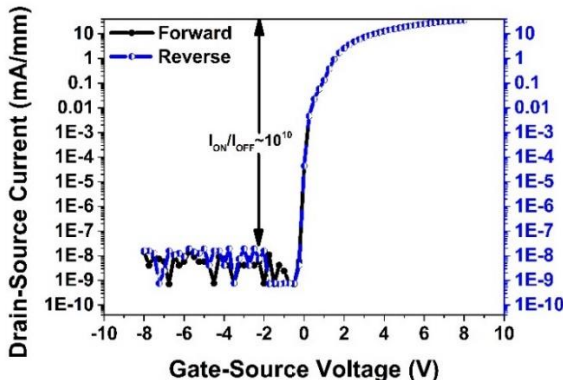


Fig. 5. Forward and reverse log transfer curves.

In Fig. 5, I_{DS} (log) versus V_{GS} is shown, which measures $I_{ON} / I_{OFF} = 10^{10}$, one order increment over latest reported

results [3]. The extracted sub-threshold-swing (SS) results in $SS=123 \text{ mV/decade}$, which is 40% improved over latest E-mode beta- Ga_2O_3 transistor [3].

The extracted parameters found in this work are summarized in Table I which are in good agreement with the reported work [3].

TABLE I. EXTRACTED DEVICE PARAMETERS

Device Parameters	I_{DS} (mA/mm)	$R_{ON} (\Omega\text{-mm})$	I_{ON}/I_{OFF}	g_m (mS/mm)	SS (mV/dec)
Ref [3]	40	215	10^9	7	183
This Work	40	207	10^{10}	7	123

IV. CONCLUSION

The design of E-mode ‘T’ shaped recessed gate gallium-oxide MOSFET was demonstrated to study its device characteristics using Atlas simulations. The extracted device parameters are in good agreement with the experimental results. With more research on novel gallium-oxide material parameters and evolution of process technology, beta- Ga_2O_3 will be the most preferred device for emerging nanoelectronics applications.

ACKNOWLEDGMENT

This publication is an outcome of the R&D work undertaken in the project under the Visvesvaraya PhD Scheme of MeitY, Govt. of India, being implemented by Digital India Corporation.

REFERENCES

- [1] H. H. Tippins, “Optical absorption and photoconductivity in the band edge of $\beta\text{-Ga}_2\text{O}_3$,” Phys. Rev., vol. 140, no. 1A, pp. A316–A319, Oct. 1965. DOI: 10.1103/PhysRev.140.A316.
- [2] M. Orita, H. Ohta, M. Hirano, and H. Hosono, “Deep-ultraviolet transparent conductive $\beta\text{-Ga}_2\text{O}_3$ thin films,” Appl. Phys. Lett., vol. 77, no. 25, pp. 4166–4168, Dec. 2000. DOI: 10.1063/1.1330559.
- [3] Kelson D. Chabak, et al., “Recessed-Gate Enhancement-Mode $\beta\text{-Ga}_2\text{O}_3$ MOSFETs,” IEEE Electron Device Lett., vol. 39, no. 1, pp. 67–70, Jan 2018. DOI: 10.1109/LED.2017.2779867.
- [4] Kelson D. Chabak, et al., “Enhancement-mode Ga_2O_3 wrap-gate fin field-effect transistors on native (100) Ga_2O_3 substrate with high breakdown voltage,” Appl. Phys. Lett., 109 213501, pp. 1–5, Nov. 2016. DOI: 10.1063/1.4967931.
- [5] M. Higashiwaki, K. Sasaki, A. Kuramata, T. Masui and S. Yamakoshi, “Gallium oxide (Ga_2O_3) metal-semiconductor field-effect transistors on single-crystal $\beta\text{-Ga}_2\text{O}_3(010)$ substrates”, Appl. Phys. Lett. 100, 013504 (2012).
- [6] M. Higashiwaki, K. Sasaki, T. Kamimura, M. H. Wong, D. Krishnamurthy, A. Kuramata, T. Masui and S. Yamakoshi, “Depletion-mode Ga_2O_3 MOSFETs”, 71st Annual Device Research Conference (DRC), 10.1109/DRC.2013.6633890.
- [7] M. H. Wong, K. Sasaki, A. Kuramata, S. Yamakoshi, and M. Higashiwaki, “Field-plated Ga_2O_3 MOSFETs with a breakdown voltage of over 750 V,” IEEE Electron Device Lett., vol. 37, no. 2, pp. 212–215, Feb. 2016, DOI: 10.1109/LED.2015.2512279.
- [8] M. Mohamed, K. Irmscher, C. Jannowitz, Z. Galazka, R. Manzke, and R. Fornari, “Schottky barrier height of Au on transparent semiconducting oxide $\beta\text{-Ga}_2\text{O}_3$,” Appl. Phys. Lett. 101, 132106 (2012).

High-sensitivity profiling of single nanoscale vesicles for cancer diagnosis

1 Federico Pevere

2 *Department of engineering sciences*
3 *Uppsala University*
4 *Uppsala, Sweden*
5 ORCID: 0000-0001-5304-913X

6 Sara Cavallaro

7 *Department of applied physics*
8 *KTH Royal Institute of Technology*
9 *Stockholm, Sweden*
10 email: saracav@kth.se

11 André Görgens

12 *Department of Laboratory Medicine*
13 *Karolinska Institutet*
14 *Stockholm, Sweden*
15 email: andre.gorgens@ki.se

11 Samir El-Andaloussi

12 *Department of Laboratory Medicine*
13 *Karolinska Institutet*
14 *Stockholm, Sweden*
15 email: Samir.El-Andaloussi@ki.se

11 Jan Linnros

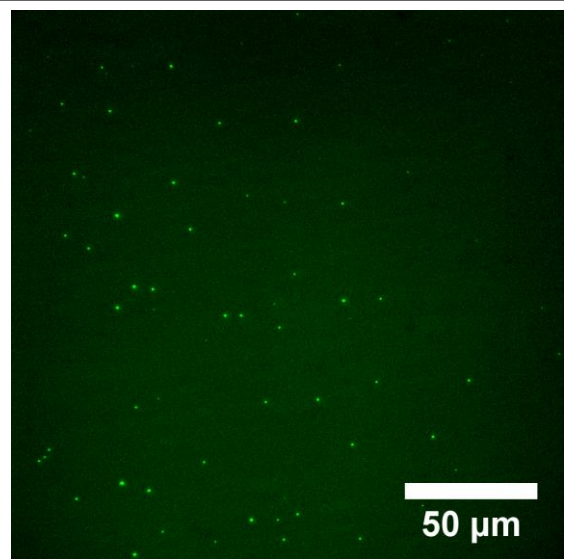
12 *Department of applied physics*
13 *KTH Royal Institute of Technology*
14 *Stockholm, Sweden*
15 ORCID: 0000-0002-5260-5322

11 Apurba Dev

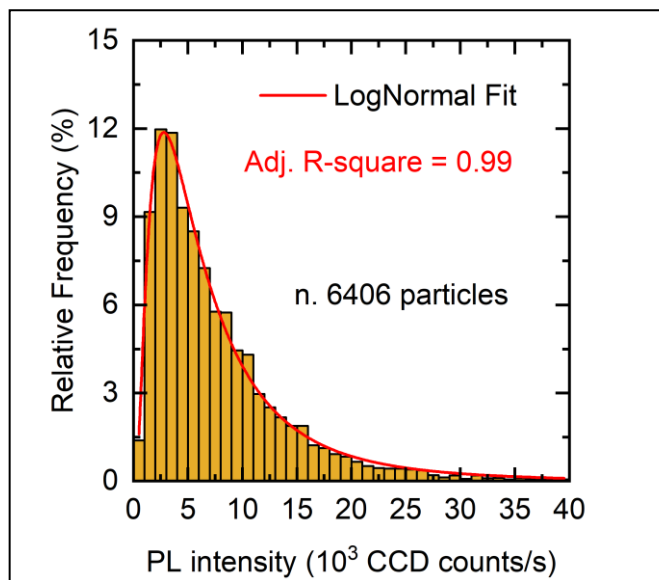
12 *Department of engineering sciences*
13 *Uppsala University*
14 *Uppsala, Sweden*
15 email: apurba.dev@angstrom.uu.se

17 Extracellular vesicles (EVs) are released by all type of
 18 cells, both healthy as well as cancer cells, and have been
 19 shown to transport molecular contents (proteins, mRNA,
 20 miRNA) related to the parent cells they originate from. By
 21 travelling in body fluids (blood, saliva, *etc.*) these "nanoscale
 22 vesicles" can carry biological information between cells in
 23 distant organs, hence they are involved in intercellular
 24 communication. For these reasons, the detection of EVs and
 25 the molecular profiling of their surface could lead to future
 26 non-invasive cancer diagnostics/therapeutics, especially for
 27 certain types of cancer (*e.g.* brain cancer) where biopsies are
 28 difficult to perform [1]. Usually, profiling is done at the
 29 ensemble level where averaged protein expression levels are
 30 qualitatively measured with a limit of detection (LOD) of 10^3
 31 EVs or more [2, 3]. However, recent studies performed at the
 32 single-vesicle level (*i.e.* LOD=1 EV) have shown great
 33 potential not only for detection of nanoscale vesicles but also
 34 for the identification of their population subtypes [4, 5].

35 In this work we present a novel platform for profiling
 36 single EVs by means of high-sensitivity fluorescence
 37 microscopy. The benefit of our approach is that no additional
 38 modification of the EV surface prior to the single-EV analysis
 39 is required, thus the technique could have potential for clinical
 40 use. By binding EV-specific antigens (CD63, CD9, CD81,
 41
 42
 43
 44
 45
 46
 47
 48
 49



50 Fig. 1. Fluorescence image showing isolated EVs from cell line HEK293
 51 with mNeonGreen-tagged CD63. The vesicles are lying on a glass
 52 surface in 1xPBS solution. The excitation was 455 nm and the emission
 53 was filtered using a standard eGFP set.



54 Fig. 2. Photoluminescence (PL) intensity distribution obtained by
 55 analyzing 6406 isolated EVs using ImageJ (orange bars). The data can be
 56 well fitted by a log-normal function (red line).

57 *etc.*) to fluorophore-tagged human antibodies, we demonstrate
 58 that it is possible to quickly profile their surface protein
 59 contents with a single-vesicle resolution. Fig. 1 shows an
 60 example of well-separated EVs, isolated from HEK293 cell
 61 line, where the antigen CD63 was tagged with mNeonGreen
 62 fluorescent protein. By using ImageJ software the distribution
 63 of the photoluminescence (PL) intensity (proportional to the
 64 expression level of CD63) can be extracted, as shown in Fig.
 65 2 for 6406 EVs. Our single-EV platform could be potentially
 66 applied to clinical samples where the identification of EV
 67 subpopulations is crucial for the future use of nanoscale
 68 vesicles as cancer markers.

REFERENCES

- [1] S. El Andaloussi, I. Mäger, X. O. Breakefield, and M. J. A. Wood, "Extracellular vesicles: biology and emerging therapeutic opportunities," *Nature Reviews Drug Discovery*, Perspective vol. 12, p. 347, 04/15/online 2013.
- [2] Z. Zhao, Y. Yang, Y. Zeng, and M. He, "A microfluidic ExoSearch chip for multiplexed exosome detection towards blood-based ovarian cancer diagnosis," *Lab on a Chip*, 10.1039/C5LC01117E vol. 16, no. 3, pp. 489-496, 2016.
- [3] H. Im *et al.*, "Label-free detection and molecular profiling of exosomes with a nano-plasmonic sensor," *Nature Biotechnology*, vol. 32, p. 490, 04/20/online 2014.

- [4] K. Lee *et al.*, "Multiplexed Profiling of Single Extracellular Vesicles," *ACS Nano*, vol. 12, no. 1, pp. 494-503, 2018/01/23 2018.
- [5] Y. T. Yang *et al.*, "Interferometric plasmonic imaging and detection of single exosomes," (in English), *Proceedings of the National Academy of Sciences of the United States of America*, Article vol. 115, no. 41, pp. 10275-10280, Oct 2018.

Modeling of AlGaN/GaN HEMT as Biosensor for Detection of Breast Cancer

¹D. K. Panda, ²R. Singh, ^{2*}T. R. Lenka, ³Ravi Teja Velpula, ³Bui Ha Quoc Thang, ^{3#}Hieu. P. T. Nguyen

¹School of Electronics, VIT-AP University, Amaravati, Andhra Pradesh, 522237, India

²Microelectronics and VLSI Design Group, Department of Electronics and Communication Engineering, National Institute of Technology Silchar, Assam, 788010, India

³Department of Electrical and Computer Engineering, New Jersey Institute of Technology, Newark, New Jersey, 07102, USA

E-mail: d.panda.2016@ieee.org¹; t.r.lenka@ieee.org^{2*}; hieu.p.nguyen@njit.edu^{3#}

Abstract—In this work a novel AlGaN/GaN HEMT based biosensor is proposed which can detect breast cancer by using protein i.e. CerbB2 in saliva instead of blood. In order to improve the sensitivity for detection, an AlN interlayer is incorporated between AlGaN and GaN layer in the device. A physics based analytical model is developed for the proposed device and validated with Atlas simulation results. The different sensing parameters such as sensing current, channel potential, and channel conductance of the device have been studied in normal and diseased condition. The biosensing performance of the device is also analyzed by varying different CerbB2 concentrations in the saliva.

Keywords - 2DEG; AlGaN/GaN; Biosensor; Biomolecules; CerbB2; HEMT

I. INTRODUCTION

Breast cancer is one of the vital causes of death in women and in excess of 135 million individuals are affected around the world. Worldwide projections recommend that the number of patients may increase to 300 million by 2025 [1]. The traditional procedure for detection of breast cancer uses protein i.e. CerbB2 which requires spearing the skin to draw the blood for testing [1]. The agony and burden of blood extraction for testing, limits the frequency of checking of cancer by detecting CerbB2, which increase the likelihood of incapability and death, and put an exceptionally overburdened budget for clinical diagnosis. Thus, it is extremely important to develop a low cost non-invasive biosensor to detect the breast cancer. Hence in order to detect accurately CerbB2 from the body fluids like saliva and serum instead of blood, a high resolution biosensor is required. AlGaN/GaN high electron mobility transistor (HEMT) is also one of the promising candidates for biosensing applications as it has a high electron sheet carrier density channel which is induced by spontaneous polarization and piezoelectric polarization of the strained AlGaN layer [2]-[3]. Counter positive charges at the surface of HEMT are induced by the 2DEG (2D electron gas) present at the interface of AlGaN/GaN. Any small changes in the ambient condition can affect the surface charge of the HEMT and hence the electron concentration in the channel changes at the AlGaN/GaN interface [3]. The standard detection time for the AlGaN/GaN HEMT based biosensor is in the range of 5 to 20 sec. In addition to this AlGaN/GaN based biosensors are highly chemically stable due to wide energy band gap of GaN material [3]. This technology can also be applied for wireless electronics.

In this paper a novel AlGaN/GaN HEMT based biosensor is proposed which can detect the breast cancer by using protein i.e. CerbB2 in saliva instead of blood. In order to make feasible modifications in device design and obtain the parameters having maximum device efficiency for a particular application, it is required to develop a reliable

physics based model. So in this paper an analytical model is developed for the proposed device which is validated with Atlas device simulation results. The different sensing parameters such as sensing current, channel potential, and channel conductance of the device are observed in normal and diseased condition. The biosensing performance of the device is also analyzed by varying the CerbB2 concentration in the saliva.

II. DEVICE STRUCTURE AND ANALYTICAL MODEL DEVELOPMENT

Figure 1 shows the proposed device structure for detection of breast cancer by using protein i.e. CerbB2 in the saliva. In order to improve the 2DEG density by excluding the charge carriers from the AlGaN barrier layer, an ultra-thin AlN spacer layer of 1 nm thickness is grown in between AlGaN and GaN layer. In this work the target biomolecule linker used as a thin layer of self-assembled thioglycolic acid (HSCH₂COOH). The self-assembly process occurs through the molecular linkage of gold electrode and thiol. In order to analyze the sensing behavior of the proposed device, a charge control model is developed for which the effective charge produced due to CerbB2 is numerically modeled. In order to perform this, the total charge due to CerbB2 molecules in saliva is calculated and applied at the gate electrode as interface charge.

Due to the change in 2DEG charge density, there will be a change in drain current and all other parameters related to 2DEG charge density [4]. For biosensing applications when the biomolecules are immobilized, the impact of applied gate bias on the device performance will be nullified. So in this work a floating gate model is developed to analyze the effect of 2DEG modulation instead of applying voltage at the gate electrode. Due to the electrostatic variation, the change in sheet charge density is modelled as follows.

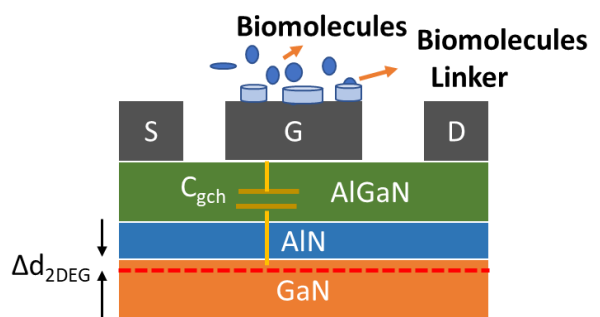


Fig. 1. Proposed device structure for CerbB2 detection

$$n_s + \Delta n_s = \frac{\varepsilon_{AlGaN}}{d_{eff}} \left(V_{GS} - \left(\psi_s + \frac{E_f - \Delta E_f}{q} + V_c \right) \right) \quad (1)$$

$$\text{Where } d_{2DEG} = t_{AlGaN} + \Delta d_{2DEG} + t_{AlGaN} \quad (2)$$

$$\Delta n_s = \frac{\varepsilon_{AlGaN}}{d_{eff}} \left(- \frac{d_{2DEG}}{d_{eff}} V_{GS} \right) \quad (3)$$

Using the above equation (1) the change in drain current is modelled as

$$I_D + \Delta I_D = q \frac{\varepsilon_{AlGaN}}{d_{eff}} \left(E_f - \left(\frac{\Delta E_c + \frac{q^2}{\varepsilon_{AlGaN}} \sigma_{AlN}^2 t_{AlN}}{q} \right) + V_c \right) - \frac{d_{2DEG}}{d_{eff}} V_{GS} W \frac{v_{sat} E(x)}{\sqrt{E^2(x) + \left(\frac{v_{sat}}{\mu_0} \right)^2}} \quad (4)$$

III. RESULTS AND DISCUSSION

Figure 2 shows the change in drain current (sensing current ΔI_D) variation with respect to different gate bias for different CerbB2 concentrations. It shows that the sensing current increases with increase in concentration of charged target biomolecules. From the figure it is also observed that the simulation and model results nearly match each other for different CerbB2 concentrations in saliva.

The variation of electrostatic channel potential for different CerbB2 concentrations in saliva is shown in Figure 3. It shows that the channel potential reduces by nearly 50 mV when peak CerbB2 concentration in saliva changes from normal condition to diseased condition.

Channel conductance is an important performance metric for good sensing performance of the device by ensuring high channel conductance. Figure 4 shows the variation of channel conductance with respect to different drain bias. It shows that, with increase in gate surface charge due to bio immobilization the channel conductance (g_d) decreases. From this it is clear that, the device resistance is increased in linear region, since the capacitive coupling of additional charge applied near the gate electrode.

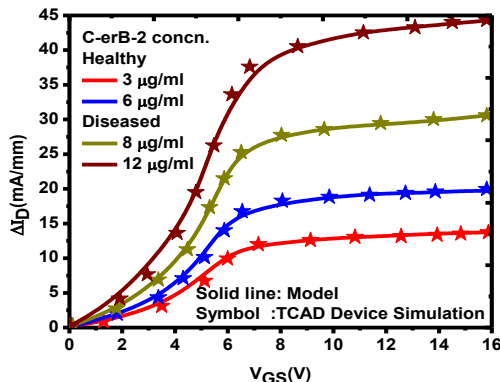


Fig. 2. Sensing current variation in saliva for different concentration of CerbB2.

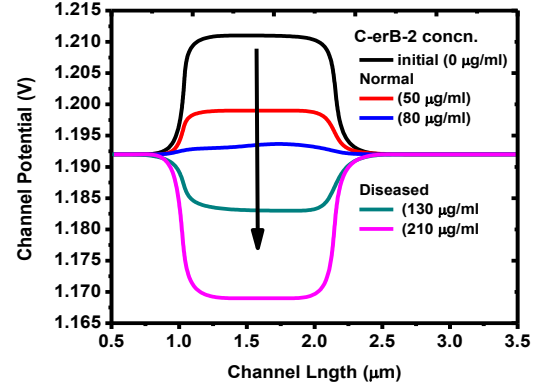


Fig. 3. Channel potential variation in saliva for different concentration of CerbB2.

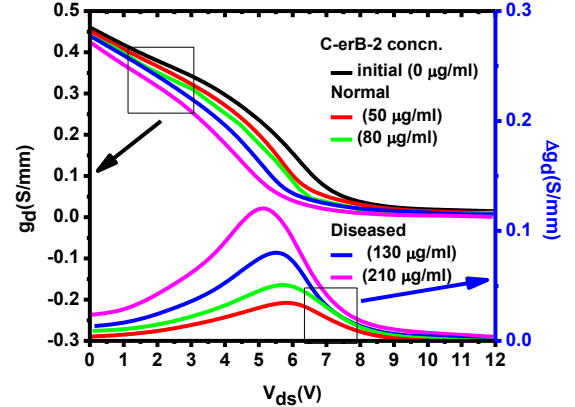


Fig. 4. Channel Conductance variation in saliva for different concentration of CerbB2.

IV. CONCLUSION

A physics based analytical model of AlGaN/GaN HEMT is developed and calibrated with TCAD device simulation results for detection of CerbB2 in saliva for breast cancer diagnosis. Different sensing parameters such as sensing current, channel potential, and channel conductance of the device are realized for normal and diseased condition with different concentrations of CerbB2 in the saliva. From the interesting results, it is concluded that the proposed device can be used as a potential biosensor for breast cancer detection as compared to other FET based biosensors.

ACKNOWLEDGMENT

This publication is an outcome of the R&D work undertaken in the project under the Visvesvaraya PhD Scheme of MeitY, Govt. of India, being implemented by Digital India Corporation.

REFERENCES

- [1] K. H. Chen *et al.*, “C-erbB-2 sensing using AlGaN/GaN high electron mobility transistors for breast cancer detection,” *Applied Phy. Lett.*, vol.92, pp. 192103-1-3, 2008.
- [2] S. Yang *et al.*, “Disposable Gate AlGaN/GaN High-Electron- Mobility Sensor for Trace-Level Biological Detection,” *IEEE Electron Device Letters*, vol. 39, no. 10, pp. 1592-1595, Oct. 2018.
- [3] D. K. Panda and T. R. Lenka, “A Compact Thermal Noise Model for Enhancement mode N-Polar MOSHEMT including 2DEG Density Solution with Two Sub-bands,” *IET Circuits, Devices & Systems*, 2018. DOI: 10.1049/iet-cds.2017.0226.
- [4] F. M. Yigletu, B. Iñiguez, S. Khandelwal and T. A. Fjeldly, “A compact charge-based physical model for AlGaN/GaN HEMTs,” *2013 IEEE 13th Topical Meeting on Silicon Monolithic Integrated Circuits in RF Systems*, Austin, TX, 2013, pp. 174-176.

Compact Drain Current Model of Silicon-Nanotube-based Double Gate-All-Around (DGAA) MOSFETs Incorporating Short Channel Effects

Arun Kumar, P S T N Srinivas, and Pramod Kumar Tiwari

Department of Electrical Engineering, Indian Institute of Technology Patna, Bihta, Bihar, 801103, India

Email: arun.pee16@iitp.ac.in, surya_1821ee04@iitp.ac.in, pktiware@iitp.ac.in

Abstract—This paper reports a compact drain current model of silicon-nanotube-based ultra-thin DGAA MOSFET incorporating short channel effects (SCEs). The drain current equation is expressed as a function of charge density, which is derived using the unified surface potential expressions and Gauss' law. The proposed compact model also takes into account of quantum confinement effects which is significant in devices with the ultra-thin channel region. Results obtained from the proposed compact drain current model have been validated with TCAD results obtained from the Sentaurus device simulator.

Keywords— DGAA MOSFETs, compact model, surface potential, drain current, quantum confinement effects

I. INTRODUCTION

The continuous downscaling of the planar MOSFET down under sub-22 nm regime becomes a challenging task because of device vulnerability to the severe short channel effects (SCEs) and loss of electrostatic control all over the charge carriers in the active channel region. Recently, double gate-all-around (DGAA) MOSFETs has generated much interest owing to their excellent immunity to SCEs and improved electrostatic dominance over the channel region [1]. Fahad *et al.* [1] presented the DGAA MOSFET structure back in 2011, followed by registering a patent to his credit in 2015. A rigorous analysis of device electrical performance was undertaken by many research group across the globe supporting the fact that DGAA MOSFETs offers better device characteristics and enhanced drive current capability over the nanowire GAA MOSFET having plagued with low drive current [1-2]. A unified drain current model for DGAA MOSFET was presented in our earlier work which is inherently analytical and also captures the quantum confinement effects [2]. However, the developed model was only applicable to a long channel device structure. Therefore, in this work, we present a compact model of drain current for ultra-thin DGAA MOSFET that incorporates the SCEs. The second order physical effects like threshold voltage roll-off, velocity saturation, DIBL, velocity overshoot effects, channel length modulation (CLM), and mobility degradation which dominates at short channel length are well incorporated in the developed model to predict the device output and transfer characteristics correctly. In order to check the accuracy of the proposed compact model, results obtained from the compact drain current model have been validated with TCAD results obtained from the Sentaurus device simulator [3].

II. DEVICE STRUCTURE AND MODEL FRAMEWORK

The DGAA MOSFET structure considered for the analysis is shown in Fig. 1. The channel thickness, thickness of gate oxide, and length of inner and outer channel surfaces

from the center of the device structure are noted as t_{si} , t_{ox} , r_1 and r_2 respectively.

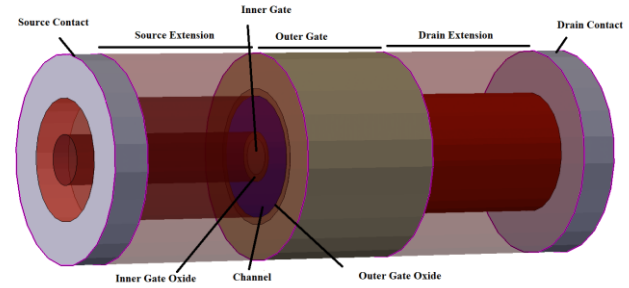


Fig. 1: 3-D view of simulated DGAA MOSFET device structure

A. Surface potential formulation

The surface potential expression which is continuous from the subthreshold region to the above threshold-voltage regime is already formulated in our earlier work employing an interpolation function as follows [2]

$$\varphi_s = \frac{1}{2}(\varphi_a + \varphi_b - \sqrt{(\varphi_a - \varphi_b)^2 + \alpha\varphi_a\varphi_b}) \quad (1)$$

B. Unified drain current

The normalized drain current flowing through the device can be described as

$$I_{ds} = Q \cdot v(E_z) \quad (2)$$

The carrier velocity is calculated using the following model

$$v(E_z) = \begin{cases} \mu_n \frac{dV(z)}{dz} & E_z < E_{sat} \\ v_{sat}, & E_z \gg E_{sat} \end{cases} \quad (3)$$

Where, μ_n denotes the low-field electron mobility, $E_{sat} = \frac{2v_{sat}}{\mu_n}$ is saturation electric field with $v_{sat} = 2.5 \times 10^7 \text{ cm/s}$ being the saturation velocity. Under linear region, (2) can be integrated in terms of charge density from source to drain region which leads to [4]

$$I_{ds} = \frac{\mu_n}{L} \left(\frac{Q_S^2 - Q_D^2}{2C_{ins}} \right) \quad (4)$$

where, Q_S and Q_D are charge densities available at the source side and drain side respectively and can be evaluated using the surface potential expression of (1) and Gauss' law. In the saturation region, with the concept of velocity saturation effect, the drain current can be written as [4]

$$I_{dsat} = v_{sat} \cdot C_{ins} (V_{gs} - V_{fb} - \varphi_s - V_{dsat}) \quad (5)$$

Replacing V_{ds} and I_{ds} with V_{dsat} and I_{dsat} in (4), V_{dsat} can be obtained as

$$V_{dsat} = V_{gs} - V_{fb} + V_T \cdot \ln \left(\frac{c_1}{v_{sat} LC_{ins} D \mu_n - D \sqrt{(v_{sat} LC_{ins} \mu_n)^2 + Q_s^2}} \right) \quad (6)$$

The effective drain biasing voltage $V_{dseff} = f(V_{ds}, V_{dsat})$ continuing from linear to saturation region is introduced using a stitching function as follows

$$V_{dseff} = \frac{1}{2} (V_{ds} + V_{dsat} - \sqrt{(V_{ds} - V_{dsat})^2 + \alpha V_{ds} V_{dsat}}) \quad (7)$$

Thus, a unified, compact drain current model which is continuous from linear to saturation region for ultra-thin DGAA MOSFETs is given by integrating charge density at both inner surface and outer surface as follows

$$I_{ds} = \frac{2\pi r_1 \mu_n}{L} \left(\frac{Q_{S1}^2 - Q_{BS1}^2}{2C_{ox1}} \right) + \frac{2\pi r_2 \mu_n}{L} \left(\frac{Q_{S2}^2 - Q_{BS2}^2}{2C_{ox2}} \right) \quad (8)$$

where $Q_{S1,2} = C_{ox1,2}(V_{gs} - V_{fb} - \varphi_{s1,2})$ and

$$Q_{DS1,2} = C_{ox1,2}(V_{gs} - V_{fb} - \varphi_{s1,2} - V_{dseff})$$

C. Short channel corrections

The mobility dependence on lateral electric field and velocity overshoot effects are incorporated by the following relation

$$\mu_{eff} = \frac{\mu_n}{\sqrt{1 + \left(\frac{\mu_n V_{dseff}}{v_{sat} L} \right)^2}} + \frac{\lambda_a}{L} \quad (9)$$

Here, λ_a is the velocity overshoot parameter. Above saturation, the channel length modulation (CLM) makes the channel length shorter by $L_{eff} = L - \nabla L$. This effect is included through the following equation

$$\nabla L = \delta \lambda_C \times \sinh^{-1} \left(\frac{V_{ds} - V_{dsat}}{E_{sat} L_C} \right) \quad (10)$$

where, λ_C is the characteristics length of DGAA MOSFETs and ∇L is the distance from drain end where pinch-off occurs. In the proposed compact model in order to include the threshold voltage roll-off and DIBL, the gate voltage V_{gs} is replaced with an effective gate voltage [4]

$$V_{gseff} = V_{gs} + \varphi_{min} \quad (11)$$

$$\text{where, } \varphi_{min} = [2\sqrt{C_3 C_4} + \sigma_1][1 - \epsilon_r(a - br + cr^2)]$$

$$+ (V_{gs} - V_{fb})\epsilon_r[n - pr + qr^2] \quad (12)$$

φ_{min} is the minimum potential value and is already evaluated in our earlier work [5]. Effective gate voltage model captures not only the DIBL effect but also the subthreshold slope degradation and threshold voltage roll-off simultaneously [4].

III. RESULTS AND DISCUSSION

In order to test the accuracy of the proposed drain current model, the results obtained from the proposed model are compared with the TCAD results obtained from Sentaurus device simulator [3]. The output characteristic of the DGAA MOSFET at different gate bias voltages is demonstrated in Fig. 2. As can be noticed from Fig.2, the proposed model results have a good agreement with the TCAD results at 20nm channel length, thus properly capturing the short channel device behavior inclusive of carrier velocity saturation. The transfer characteristic of DGAA MOSFET for different channel thickness is shown in Fig 3. The drain current increases nearly by three times with

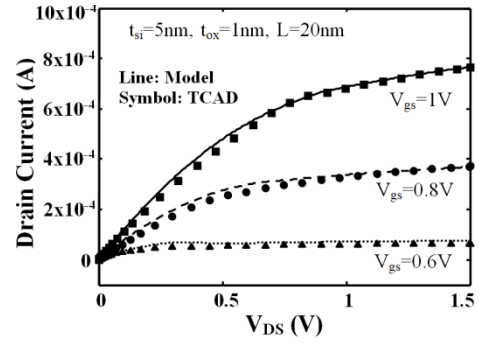


Fig. 2: Drain Current (A) variation with respect to the varying drain voltage (V) for different gate voltage values.

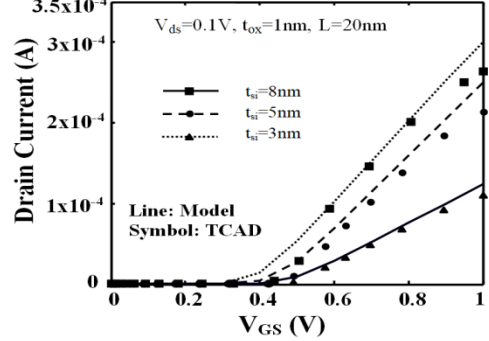


Fig. 3: Drain Current (A) variation with respect to the varying gate voltage (V) for different values of channel thickness.

an increase in channel thickness from 3nm to 8nm. At higher channel thickness, more carriers can participate in the current conduction, thus enhancing the drain current value. Moreover, a lesser drain current value at 3nm is also partially attributed to the quantization of carriers in the ultra-thin channel region. The proposed model results also have a good agreement with the TCAD results and are properly replicating the short channel drain current behavior for the entire region of operation.

IV. CONCLUSION

In summary, an explicit, unified, compact drain current model of silicon-nanotube-based ultra-thin DGAA MOSFET incorporating short channel effects is presented. The saturation voltage is evaluated based on two piece-wise drain current models for the linear and saturation case separately. The SCEs are well incorporated in the developed model to predict the device output and transfer characteristics correctly. Results obtained from the proposed compact drain current model have been validated with TCAD results obtained from the Sentaurus device simulator.

REFERENCES

- [1]. H. M. Fahad, C. E. Smith, J. P. Rojas, and M. M. Hussain, "Silicon nanotube field effect transistor with core-shell gate stacks for enhanced high-performance operation and area scaling benefits," *Nano Lett.*, vol.11, no. 10, pp. 4393-4399, Sep. 2011.
- [2]. A. Kumar and P. K. Tiwari, "An Explicit Unified Drain Current Model for Silicon-Nanotube-Based Ultrathin Double Gate-All-Around MOSFETs," *IEEE Trans. Nanotech.*, vol. 17, no. 6, pp. 1224-1234, Nov. 2018.
- [3]. *Sentaurus Device User Guide, Version N-2017.09*, Synopsys, Mountain View, CA, USA, 2016.
- [4]. R. D. Trevisoli, R. T. Doria, M. de Souza, S. Das, I. Ferain, M. A. Pavanello, "Surface-potential-based drain current analytical model for triple-gate junctionless nanowire transistors", *IEEE Trans. Electr. Devices*, vol. 59, no. 12, pp. 3510-3518, Dec. 2012.
- [5]. A. Kumar, S. Bhushan, P. K. Tiwari, "A Threshold voltage model of silicon-nanotube based ultra-thin double gate-all-around (DGAA) MOSFETs incorporating quantum confinement effects", *IEEE Trans. Nanotech.*, vol. 16, no. 5, pp. 868-875, Sep. 2017.

Highly selective and sensitive distinct flower-like ZnO microstructure based gas sensor with optimized CTAB concentration for detection of NOx at room temperature

*Note: Sub-titles are not captured in Xplore and should not be used

12 Srijita Nundy¹

13 School of Advanced material science
14 engineering

15 Sungkyunkwan University
16 Suwon 16419, Republic of Korea
17 srijita.31121990@gmail.com

18 Tae-yil Eom²

19 line 2: dept. name of organization
(of Affiliation)

20 Sungkyunkwan University
21 Suwon 16419, Republic of Korea
22 ety1106@naver.com

23 Joon-Shik Park^{*}

24 Smart Sensor Research Center
Korea Electrical Technology Institute
(KETI)
Seongnam Gyeonggi, Republic of
Korea
jspark@keti.re.kr

25 Hoo-Jeong Lee^{*}

26 line 2: dept. name of organization
(of Affiliation)

27 Sungkyunkwan University
28 Suwon 16419, Republic of Korea
29 hlee@skku.edu

A. Introduction

Nitrogen oxides (NOx) is considered as a highly toxic gas causing harm not only to human body but also to the environment. [1]. Real time monitoring along with accurate and selective detection of such gases at low concentration (ppm) and at room temperature is of pressing need at present. Sensors based on metal oxide semiconductors for detection of NOx has gained a lot of attention these days due to its easy synthesis, low cost fabrication and bulk availability. Among the MOS family , ZnO , due to its variety of remarkable properties have been the most studied and promising n-type semiconductor sensing material. However, still these ZnO based gas sensors suffers some major drawbacks due to its high operating temperature ($>200^{\circ}\text{C}$) and poor selectivity which limit its commercial application. Thus, to overcome such difficulties use of various dopants, surface modifications, UV illumination , heterojunction are been used which can affect the RT gas sensing performance and enhance its selective property. Out of various possible ways , the most effective one is synthesizing unique 3D microstructure with careful optimization which will greatly facilitate the gas sensing response [2]. In this work, we investigated the role of Cetyltrimethylammonium Bromide (CTAB) on the formation of various ZnO morphologies , from nanorods to distinct flower-like microstructure. This provided a better understanding of the growth mechanism of such microstructure and studied morphology dependent gas sensing behaviour of ZnO microstructures. The application of flower-ZnO in fabricating a highly selective, selective and sensitive gas sensor towards NOx operating at room temperature has been reported. Detailed possible mechanism of higher sensing response and selectivity at room temperature for NOX compared to reducing gases (NH₃, C₆H₅CH₃, CO, CH₃COCH₃, and C₂H₅OH) of this flower-like ZnO sensor had also been demonstrated.

B. Results and Discussions

By tuning the synthesis parameters, effect on the morphology was investigated which showed that CTAB concentration played a great role in morphology control of ZnO. Figure 1 shows the variation of the morphology for different CTAB concentrations, displaying that nanorods assemble to form a flower-like morphology with the CTAB concentration increasing from 0M up to 0.005M. ZnO nanorods (formed in the absence of CTAB, figure 1a) assembled together to form mixed morphology of small flower-like assemblies and nanorods (figure 1b) with 0.001 M concentration of CTAB which further fused together to form flower-like microstructures at a CTAB concentration of 0.005 M (figure 1c). But with further increase in the concentration of CTAB (0.01 M to 0.05 M), formation of disrupted flower-like aggregates (0.01 M) (figure 1d) were noticed and ZnO nanorods were reobtained with 0.035M (figure 1e) and the nanorods appeared to grow more in length with decreased diameter with 0.05 M concentration of CTAB (figure 1f).

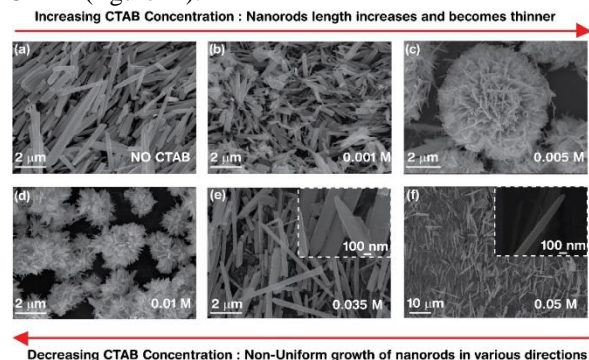


Fig. 1. Effect of CTAB concentration variation (no CTAB, 0.001M, 0.1M, 0.35M, and 0.5M) on the morphology of the ZnO microstructures for the formation of Flower-like ZnO.

CTAB not only act as a proter or ionic carrier but also act as soft template for the formation of various morphologies which showed different gas response trend towards NOx at room temperature (fig 2a). CTAB has a tendency of forming rod micelles at higher concentration (0.035 M and 0.05 M) and spherical micelles at lower concentration (0.001 M and 0.005 M).

The graph shows the sensitivities to NOX gas (0.74 ppm) of the materials at various operation temperatures (25, 43, 72, and 150°C). The graph clearly demonstrates the effects of the morphology on the sensing behavior with temperature: for ZnO with a flower-like morphology, the sensitivity is quite high (nearly 29) at 25°C and drops sharply with the temperature increasing, sharply different from the typical volcano-type behavior. The sample synthesized at a low CTAB concentration (0.001M, with a mixed morphology of small flower-like assemblies and nanorods) shows a trend

similar but with much lower sensitivities at low temperatures. For the nanorod sample (CTAB concentration=0M), the temperature behavior switches to a volcano-type one, in which the sensitivity is low at a low temperature and increases gradually with the temperature increasing. Figure 2 b shows gas response to NOX gas (0.74 ppm) for the flower-like sample, displaying a stable operation. In addition, it should be noted that the sensitivity at room temperature for the flower-like sample is notably high in comparison with other literature data. Thus, a relation between morphology, sensing response and its mechanism was established. Also, the effects of NOX concentration(0.25 to 1 ppm), and the elapsed time on the device for 140 days were investigated in terms of gas response properties. Besides this high response at room temperature, this Flower-like ZnO showed super selectivity to NOx as compared to other reducing gas species (NH3, C6H5CH3, CO, CH3COCH3, and C2H5OH) at room temperature (Figure 2c).

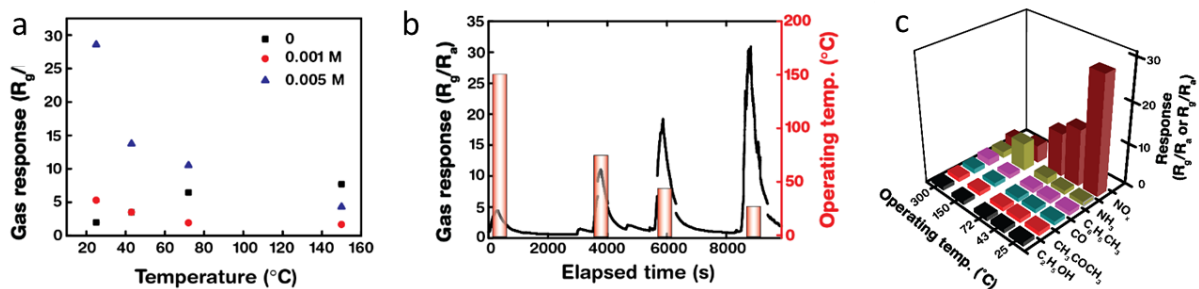


Fig. 2. Sensing response of (a) samples with all CTAB concentration variations to NOX gas (0.74 ppm) with different operating temperatures (25 °C, 43 °C, 72 °C, and 150 °C), (b) 0.005 M CTAB concentration sample and (c) 0.005 M CTAB concentration sample (a) to NOX (0.74 ppm), NH₃ (25 ppm), C₆H₅CH₃ (25 ppm), CO (25 ppm), CH₃COCH₃ (1 ppm), and C₂H₅OH (1 ppm) at different operating temperatures (25 °C, 43 °C, 72 °C, 150 °C, 300 °C

C. Conclusion

We synthesized FZO microstructures at a low temperature (90 °C) for NOx sensors and evaluated their gas sensing ability. With the increasing CTAB concentration, the morphology changed from nanorods to FZO. Thus, CTAB played a role of soft template and promoter in the morphology control. The Flower-like ZnO gas sensor produced showed high sensitivity and high

selectivity towards NOx amongst NH₃, C₆H₅CH₃, CO, CH₃COCH₃, and C₂H₅OH gases at 25 °C. Therefore, our Flower-like ZnO microstructure at 0.005 M of CTAB concentration demonstrated a very high sensitivity to NOX (oxidizing gas) at low temperatures and stability up to 140 days.

ACKNOWLEDGMENT

J.-S. Park was partially supported by Project No. P0006858 of International Collaboration Program by KIAT and MOTIE in Rep. Korea

References

- [1] M.J.S. Spencer, "ZnO Nanostructures for Gas Sensing: Interaction of NO₂, NO, O, and N with the ZnO(10̄0) Surface", *J. Phys. Chem. C*. vol. 114, pp. 10881–10893, 2010.
- [2] A. Afzal, "NOx sensors based on semiconducting metal oxide nanostructures: Progress and perspectives", *Sensors Actuators B Chem.* pp. 171–172, (2012)
- [3] P. Rai "Citrate-assisted hydrothermal synthesis of single crystalline ZnO nanoparticles for gas sensor application", *Sensors Actuators, B Chem.* pp. 173:58–65, 2012
- [4] C. Baratto, "Low temperature selective NO₂ sensors by nanostructured fibers of ZnO", *Sensors Actuators B Chem.* vol.100, pp. 261–265, 2004.
- [5] X. Pan, "A fast-response/recovery ZnO hierarchical nanostructure based gas sensor with ultra-high room-temperature output response", *Sensors Actuators B Chem.* vol.206, pp.764–771, 2015.

1
2
3
4
5
6
7
8
9
10
11
12
13
14
15
16
17
18
19
20
21
22
23
24
25
26
27
28
29
30
31
32
33
34
35
36
37
38
39
40
41
42
43
44
45
46
47
48
49
50
51
52
53
54
55
56
57
58
59
60
61
62
63
64
65

A novel Luminescent Terbium Metal Organic Framework composite based conductive ink for application in OLEDs: From synthesis to thin film fabrication through inkjet printing

Harmeet Kaur^{1,2}, Divya Sharma^{1,3} Amit L Sharma¹, Akash Deep¹

¹CSIR - Central Scientific Instruments Organisation, Chandigarh, India - 160030

² AcSIR - Academy of Scientific and Innovative Research, Chandigarh, India - 160030

³PEC – Punjab Engineering College, Chandigarh, India – 160030

Abstract

Metal Organic Frameworks (MOFs) are a versatile class of hybrid materials drawing large research attention worldwide on account of ultra-high porosity, variable topological aspects and large scale tunability. These materials exhibit eminent electrical and optical behaviour based on intelligent selection of building organic and inorganic moieties showing potential applicability in diverse opto-electronic avenues. Conductive Inks based on luminescent MOFs and their composites may prove to be highly promising

materials for fabrication of future electronic devices. The present work focuses on synthesis of a novel Tb-MOF composite based ink through preparation of a stable precursor solution. Further, Luminescent thin-film of the as-synthesized ink has been fabricated using ink-jet printing technique. The fabricated conductive luminescent thin films exhibit high emission lifetime, quantum yield as well as long term stability supporting their candidature for applicability in organic light emitting devices.

Excitons Bound to Defect States in 2D Semiconductors

Oleg Gridenco^{1*}, Sven Mehrkens¹, Kathrin Sebald¹, Christian Tessarek², Martin Eickhoff² and Jürgen Gutowski¹

¹Semiconductor Optics, ²Solid State Materials, Institute of Solid State Physics, University of Bremen, Otto-Hahn-Allee 1, D-28359 Bremen, Germany

[*gridenco@ifp.uni-bremen.de](mailto:gridenco@ifp.uni-bremen.de)

In 2D semiconducting transition metal dichalcogenides (TMDs), lattice point defects can trap free charge carriers and localize excitons. In this work we investigate how focused gallium ion irradiation affects the luminescence properties of atomically thin layers. Since these materials become direct band gap semiconductors with relatively high PL intensity in the monolayer (ML) limit, defect effects can easily be optically monitored. We found that irradiation with Ga^+ ions introduces additional defect states which trap excitons. When these recombine radiatively, light emission occurs at energies below the band-edge optical transition energy. Exfoliated MoS_2 monolayers were irradiated at controlled doses. The density of defects was changed by varying the Ga^+ ion dose starting from $2 \cdot 10^{10}$ ions/cm² until the PL signal completely vanished at $2 \cdot 10^{13}$ ions/cm². Figure 1 (a) shows typical PL spectra measured at 4 K from a pristine ML compared to a ML after Ga^+ ion irradiation with a dose of $5.5 \cdot 10^{11}$ ions/cm². The PL spectrum of the pristine layer is dominated by a broad peak at 1.92 eV (marked A) corresponding to an exciton (X_A) – trion (T) superposition. After Ga^+ ion irradiation at different doses, the PL changes significantly as shown in Fig. 1 (b). The A band emission is suppressed and a new peak D emerges at 1.76 eV assigned to a bound exciton. This broad peak is red shifted by $\Delta E \sim 170$ meV with respect to the neutral exciton X_A emission and remains optically active up to 200 K. We could demonstrate that localized defects induced by FIB create trapping potentials in which bound exciton complexes are formed.

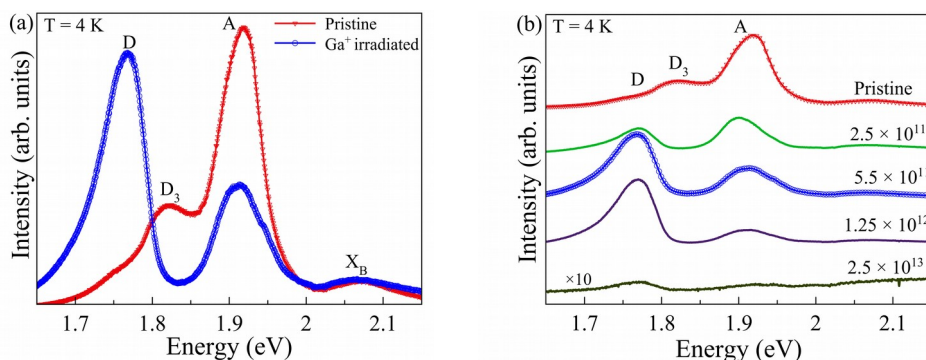


Figure 1. Photoluminescence spectra of a one ML MoS_2 sample measured at 4 K. (a) Pristine ML (red line) and a ML after Ga^+ ion irradiation with a dose of $5.5 \cdot 10^{11}$ ions/cm² (blue line). (b) Spectra of pristine and Ga^+ irradiated MLs at different ion doses.

Additionally, with regard to the emission linewidth, PL at low temperatures shows a neutral exciton linewidth as broad as 70 meV being close to charged exciton (trion) emission band. Encapsulating the ML MoS_2 into hBN drastically reduces the inhomogeneous contribution to the exciton linewidth [1]. The possibilities of tailoring optically active defect centers in 2D MoS_2 to even host single-photon emitters will be discussed.

References

[1] E. Courtade et al., Appl. Phys. Lett. **113**, 032106 (2018).

Modeling of DC and RF Characteristics of Single and Double Gate AlGaN/GaN MOS-HEMTs

¹D. K. Panda, ²R. Singh, ^{2*}T. R. Lenka, ³Ravi Teja Velpula, ³Bui Ha Quoc Thang, ^{3#}Hieu. P. T. Nguyen

¹School of Electronics, VIT-AP University, Amaravati, Andhra Pradesh, 522237, India

²Microelectronics and VLSI Design Group, Department of Electronics and Communication Engineering, National Institute of Technology Silchar, Assam, 788010, India

³Department of Electrical and Computer Engineering, New Jersey Institute of Technology, Newark, New Jersey, 07102, USA
E-mail: d.panda.2016@ieee.org¹; t.r.lenka@ieee.org^{2*}; hieu.p.nguyen@njit.edu^{3#}

Abstract - In this work, a 60 nm double gate GaN Metal Oxide Semiconductor High Electron Mobility Transistor (MOS-HEMT) is proposed and different electrical characteristics such as DC, small signal and RF performances of the device are characterized using look up table (LUT) based Verilog A model and Atlas simulations. It is observed that the double gate GaN MOS-HEMT shows good subthreshold slope (78.5 mV/dec), improved ON current, SCE immunity and also improvement in RF performance (f_{max} =220 GHz, f_c =170 GHz).

Keywords: GaN, MOS-HEMT, SCE, RF

I. INTRODUCTION

GaN based HEMTs have emerged as promising candidate for microwave and low noise applications due to their inherent remarkable material properties [1-4]. These devices have tremendously attracted to RF circuit design engineers to design both power amplifiers (PAs) [5] and low noise amplifiers (LNAs) [6] for RF front end transceivers. To enable high frequency and low noise operation of the device the gate length of the device has to be scaled down [7]. But with decrease in gate length there is a significant increase in gate leakage current and also rise in different short channel effects (SCEs) such as drain induced barrier lowering (DIBL), channel length modulation (CLM) [7]. Here a short channel 60 nm double gate GaN MOS-HEMT is proposed for the first time and the TCAD device simulation results are compared with available experimental data of single gate GaN MOS-HEMT [8].

II. DEVICE STRUCTURES

Fig. 1 and Fig. 2 represent 2D device structure of single and double gate GaN MOS-HEMT respectively. In order to reduce different parasitic capacitances and resistances a double decked T-shaped gate is proposed for both the structures. The device has a gate length (L_g), gate to source spacing (L_{gs}), gate to drain spacing (L_{gd}), and gate recess depth of 60 nm, 0.9 μ m, 0.9 μ m and 15nm respectively.

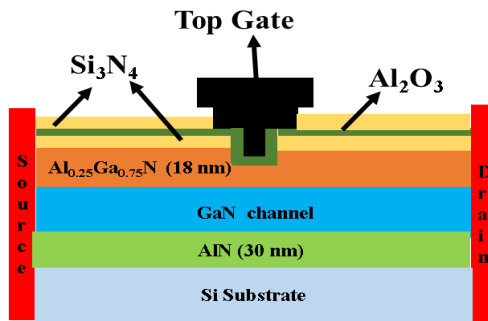


Fig. 1. 2D device structure of single gate GaN MOS-HEMT.

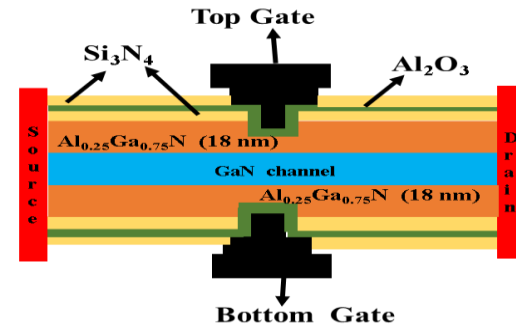


Fig. 2. 2D device structure of double gate GaN MOS-HEMT.

III. RESULTS AND DISCUSSION

Fig. 3 represents the DC transfer characteristics for single and double gate GaN MOS-HEMT at a drain voltage $V_{ds} = 1$ V. Similarly, Fig. 4 shows the sub-threshold behaviour of both devices. It shows that single gate MOS-HEMT has poor subthreshold characteristics as compared to double gate MOS-HEMT due to poor restrain to SCE [9].

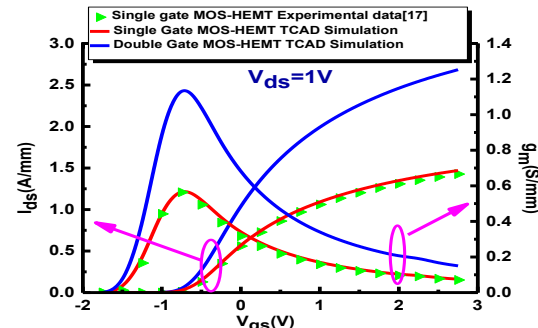


Fig. 3. Transfer characteristics comparison of single and double gate GaN MOS-HEMT at $V_{ds} = 1$ V.

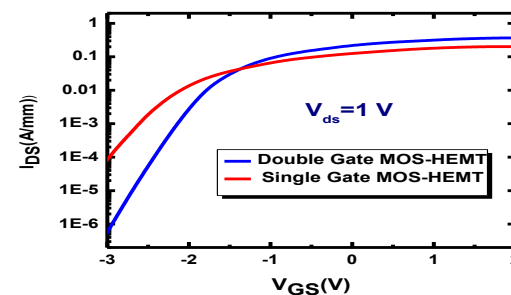


Fig. 4. Sub-threshold current comparison of single and double gate GaN MOS-HEMT in log scale.

The average value of sub-threshold slope (SS) extracted for single and double gate MOS-HEMT to be 96.3 mV/dec and 78.5 mV/dec respectively. Fig. 5 represents I_d - V_{ds}

characteristics of each device. It shows that the double gate structure has higher ON current as compared to single gate structure. AC simulation of both the devices has been carried out and the different small signal parameters are extracted by the procedure described in [10].

Fig.6 shows the parasitic capacitance comparison between single and double gate GaN MOS-HEMT with respect to different drain current density. It shows that the double gate MOS-HEMT has significant increment of gate to source (C_{gs}) and gate to drain (C_{gd}) capacitance as compared to single gate MOS-HEMT which indicates that, there is an effective control of gate over the charge in the channel.

The unity gain cut-off frequency (f_T) and maximum oscillation frequency (f_{max}) are plotted with respect to different current density in Fig.7. It shows that the double gate MOS-HEMT gives comparatively lower value of f_T as compared to single gate MOS-HEMT which is due to significant rise in C_{gg} and g_m . In case of double gate MOS-HEMT since both the gates are connected in parallel, thus the gate resistance (R_g) value is very less as compared to single gate MOS-HEMT. Due to higher electron density in the channel, the source resistance is also lower in case of double gate MOS-HEMT. So f_{max} is comparatively high in this case.

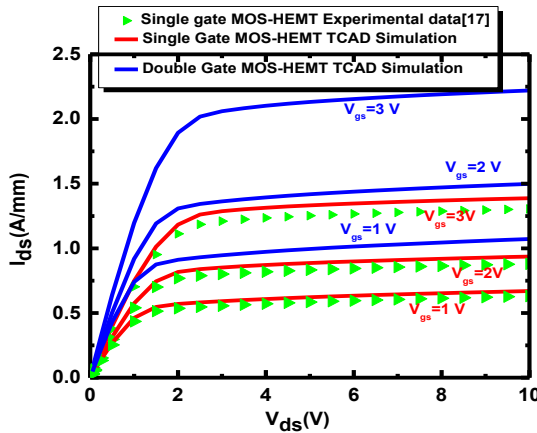


Fig. 5. Output characteristics comparison of single and double gate GaN MOS-HEMT.

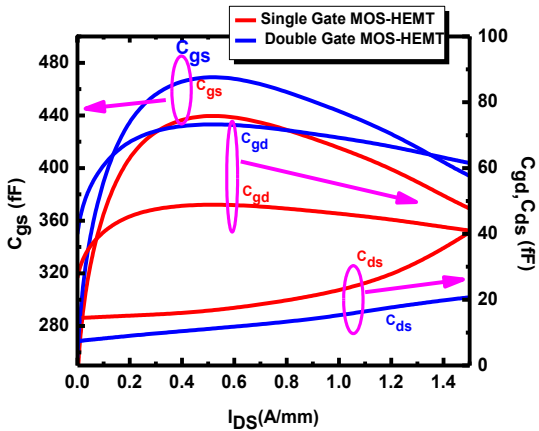


Fig. 6. Parasitic capacitance comparison of single and double gate GaN MOS-HEMT with respect to different drain currents.

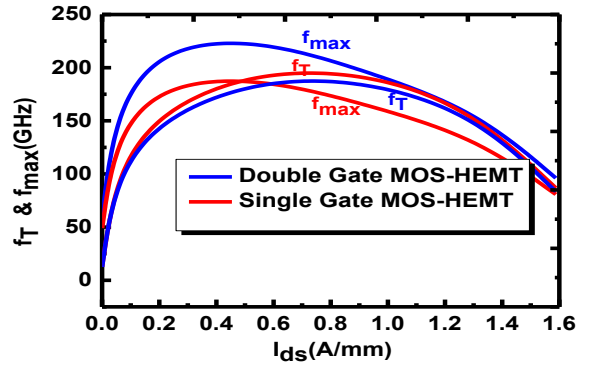


Fig. 7. f_T and f_{max} comparison between single and double gate GaN MOS-HEMT with respect to different drain currents.

IV. CONCLUSION

A 60 nm double gate GaN MOS-HEMT device structure is simulated and different electrical characteristics such as DC, small-signal and RF results are compared with the experimental data of single gate GaN MOS-HEMT having similar gate length. It is reported that the double gate GaN MOS-HEMT shows better DC and RF performance as compared to single gate GaN MOS-HEMT.

ACKNOWLEDGEMENT

This Publication is an outcome of the R&D work undertaken in the project under the Visvesvaraya PhD Scheme of Ministry of Electronics & Information Technology, Govt. of India, being implemented by Digital India Corporation.

REFERENCES

- [1] D. K. Panda, T. R. Lenka, "Compact thermal noise model for enhancement mode N-polar GaN MOS-HEMT including 2DEG density solution with two sub-bands," *IET Circuits, Devices & Systems*. (2018), DOI: [10.1049/iet-cds.2017.0226](https://doi.org/10.1049/iet-cds.2017.0226).
- [2] M. N. Khan, U. F Ahmed, M. M Ahmed, et al., "n improved model to assess temperature-dependent DC characteristics of submicron GaN HEMTs," *J Comput Electron* 17: 653. (2018).
- [3] D. K. Panda, T. R. Lenka, "Modeling and simulation of enhancement mode p-GaN Gate AlGaN/GaN HEMT for RF circuit switch applications," *Journal of Semiconductors*, 38(6) 1-6 (2017).
- [4] D. K. Panda, T. R. Lenka, "Oxide thickness dependent compact model of channel noise for E-mode AlGaN/GaN MOS-HEMT," *AEU - International Journal of Electronics and Communications*, 82:467-473. (2017)
- [5] D. Schwantuschke, C. Haupt, R. Kiefer, P. Bruckner, E. M. Seelmann, A. Tessmann, R. Quay, "A high-gain high-power amplifier MMIC for V-band applications using 100 nm AlGaN/GaN dual-gate HEMTs. International," *Journal of Microwave and Wireless Technologies*, 4:3, 267-274. (2012).
- [6] B. T. Venkatesh Murthy & I. Srinivasa Rao, "Highly linear dual capacitive feedback LNA for L-band atmospheric radars," *Journal of Electromagnetic Waves and Applications*, 30:5, 612-625 (2016).
- [7] H. Sun, D. Marti, S. Tirelli, A. Alt, H. Benedickter, & C. Bolognesi, "Millimeter-wave GaN-based HEMT development at ETH-Zürich," *International Journal of Microwave and Wireless Technologies*, 2:1, 33-38. (2010).
- [8] Y. K. Lin, S. Noda, C C Huang, H C Lo, C H Wu, Q H Luc, et al., "High-performance GaN MOSHEMTs fabricated with ALD Al₂O₃ dielectric and NBE gate recess technology for high frequency power applications," *IEEE Electron Device Letters*, 38, 771–774.
- [9] R. Gupta, S. Rathi, M. Gupta, R. S. Gupta, "Microwave performance enhancement in double and single Gate HEMT with channel thickness variation," *Superlattices and Microstructures*, 47 ,779–94. (2010).
- [10] G. Amarnath, D. K. Panda and T. R. Lenka, "Microwave frequency small-signal equivalent circuit parameter extraction for AlInN/GaN MOSHEMT," *International Journal of RF and Microwave Computer Aided Engineering*, e21179. (2017).

Interfacing scalable photonic platforms: solid-state based multi-photon interference in a reconfigurable glass chip

1 Carlos Antón-Solanas

2 C2N, Center of Nanosciences and
3 Nanotechnology, Université Paris-
4 Saclay, Route de Nozay, 91460
5 carlos.anton-solanas@c2n.upsaclay.fr

6 Juan Carlos Loredo

7 C2N, Center of Nanosciences and
8 Nanotechnology, Université Paris-
9 Saclay, Route de Nozay, 91460

10 Guillaume Coppola

11 C2N, Center of Nanosciences and
12 Nanotechnology, Université Paris-
13 Saclay, Route de Nozay, 91460

14 Helene Ollivier

15 C2N, Center of Nanosciences and
16 Nanotechnology, Université Paris-
17 Saclay, Route de Nozay, 91460

18 Niko Viggianello

19 Dipartimento di Fisica, Sapienza
20 Università di Roma, Piazzale Aldo
21 Moro 5, Roma I-00185, Italy

22 Abdelmounaim Harouri

23 C2N, Center of Nanosciences and
24 Nanotechnology, Université Paris-
25 Saclay, Route de Nozay, 91460

26 Niccolo Somaschi

27 Quandela, SAS, 86 Rue de Paris, 91400
28 Orsay, France

29 Andrea Crespi

30 Istituto di Fotonica e Nanotecnologie,
31 Consiglio Nazionale delle Ricerche,
32 Dipartimento di Fisica, Politecnico di
33 Milano, P. Leonardo da Vinci, 32,
34 Milano I-20133, Italy

35 Isabelle Sagnes

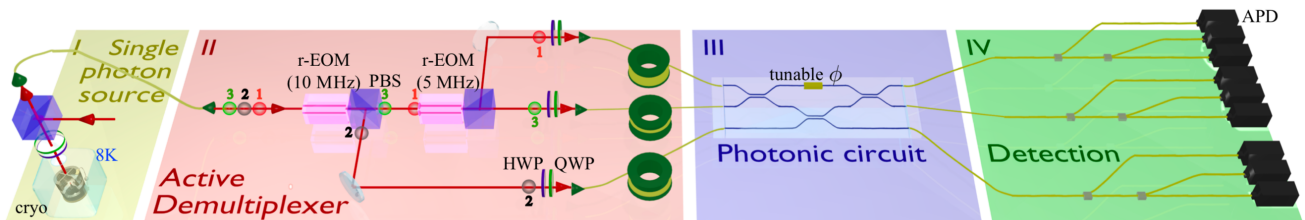
36 C2N, Center of Nanosciences and
37 Nanotechnology, Université Paris-
38 Saclay, Route de Nozay, 91460

39 Aristide Lemaître

40 C2N, Center of Nanosciences and
41 Nanotechnology, Université Paris-
42 Saclay, Route de Nozay, 91460

43 The development of optical quantum technologies relies
44 on the use of many single photons to solve milestone problems
45 spanning from quantum metrology, secure quantum
46 communication and distributed quantum computing. This
47 requires efficient sources producing highly indistinguishable
48 single photons as well as photonic circuits showing high
49 reconfigurability, phase stability and low losses.

50 Integrated photonics circuits on glass have been
51 demonstrated to be an excellent platform to tackle a vast
52 variety of complex quantum operations such as Boson
53



54 Fig. 1. **Experimental scheme of the efficient three photon coalescence.** (I) Generation of single-photon from a QD-micropillar de- vice under resonant
55 fluorescence excitation. (II) Preparation of the three photon trains (in the scheme depicted with colored spheres, each of them containing a train of 16 single
56 photons temporally distributed every 3 ns) simultaneously arriving to the tritter input via active demultiplexing. (III) Circuit of the tritter providing the three
57 photon coalescence. (IV) Detection of the quantum state of light at the output of the tritter via pseudo number-resolving measurements.

58 Sampling [1], quantum Fourier transforms [2], quantum
59 random walks [3,4]. So far, these photonic chips have been
60 operated with heralded single photon sources that show
61 limited efficiency: because the probability of generating more
62 than one heralded photon scales as the source brightness, the

63 source with an integrated photonic tritter in order to
64 investigate the genuine quantum interference of three
65 indistinguishable single photons.

66 The quantum dot cavity device is resonantly excited under
67 pulsed excitation (at a high repetition rate of 324 MHz) to
68 generate a stream of single photons with $g(2)(0) < 5\%$ and

indistinguishability >85% (between 80 ns delayed photons). We have developed a fast active demultiplexer to distribute three temporally distant single photons into three spatial fiber modes.

The output of the time to spatial demultiplexer renders a three-single-photon generation rate of 3.9 kHz, three orders of magnitude higher than the same experiment performed with heralded single photon sources [6]. The three photons are injected in the reconfigurable photonic tritter where their coalescence is implemented.

The output quantum state of light is collected in three fibers where pseudo-photon number resolving detection is performed with standard Silicon avalanche photodiodes with efficiency around 30% (see Fig. 1). The combined detection of three photon coincidences in the nine detectors allows the final reconstruction and characterization of the multi-photon coalescence state.

ACKNOWLEDGMENT

The authors acknowledge financial support by the QuantERA ERA-NET Cofund in Quantum Technologies, project HIPHOP. P.S. acknowledges further support by the ERC Starting Grant No. 277885 QD-CQED, the French Agence Nationale pour la Recherche (grant ANR SPIQE and

USSEPP), the French RENAT- ECH network, a public grant overseen by the French National Research Agency (ANR) as part of the “Investissements d’Avenir” programme (Labex NanoSaclay, reference: ANR-10-LABX-0035). C.A. and J.C.L. acknowledge support from Marie Skłodowska- Curie Individual Fellowships SQUAPH and SMUPHOS, respectively. R.O. acknowledges support from the ERC Advanced Grant CAPABLE (grant no. 742745).

REFERENCES

- [1] N. Spagnolo, et al., “Experimental validation of photonic boson sampling” *Nature Photon.* 8, 615 (2014).
- [2] A Crespi et al., “Suppression law of quantum states in a 3D photonic fast Fourier transform chip” *Nature Commun.* 7, 10469 (2016).
- [3] L. Sansoni, et al., “Two-Particle Bosonic-Fermionic Quantum Walk via Integrated Photonics” *Phys. Rev. Lett.* 108, 010502 (2012).
- [4] A. Crespi, et al., “Anderson localization of entangled photons in an integrated quantum walk” *Nature Photon.* 7, 322 (2013).
- [5] N. Somaschi, et al., “Near-optimal single-photon sources in the solid state” *Nature Photon.* 10, 340 (2016).
- [6] N. Spagnolo, et al., “Three-photon bosonic coalescence in an integrated tritter” *Nature Commun.* 4, 1606 (2013).

Graphene Based Self-Powered Mini-Spectrometer

1
2
3
4
5
6
7
8
9
10
11
12
13
14
15
16
17
18
19
20
21
22
23
24
25
26
27
28
29
30
31
32
33
34
35
36
37
38
39
40
41
42
43
44
45
46
47
48
49
50
51
52
53
54
55
56
57
58
59
60
61
62
63
64
65
Yu Liu
Institute of Microelectronics
Tsinghua University
Beijing, China
y-liu-17@mails.tsinghua.edu.cn

Linyuan Zhao
Institute of Microelectronics
Tsinghua University
Beijing, China
756595890@qq.com

Renrong Liang
Institute of Microelectronics
Tsinghua University
Beijing, China
liangrr@mail.tsinghua.edu.cn

Jing Wang
Institute of Microelectronics
Tsinghua University
Beijing, China
wang_j@mail.tsinghua.edu.cn

Jun Xu
Institute of Microelectronics
Tsinghua University
Beijing, China
junxu@mail.tsinghua.edu.cn

Abstract—We present a mid-infrared self-powered mini-spectrometer based on the surface plasmon polaritons (SPP) of graphene. The minimum pixel is a wavelength-selectivity photodetector (filter and photodetector in 1 device) with graphene/monolayer MoS₂ vertical heterostructure. A significant amount of electron-hole pairs are produced in graphene ribbons with optical absorption, separated by the built-in electric field across the graphene/MoS₂ heterojunction. The response frequency of the filter can be tuned from 8 μm to 12 μm by changing the layers and dimensions of graphene ribbons. Multiple spectral bands are divided and detected with one filter and one detector, respectively. The pixel array allowing the process to be efficiently repeated using different filters with different wavelength to obtain sufficient information for computational reconstruction of the target spectrum.

Keywords—Graphene, SPP, mini-spectrometer

INTRODUCTION

Spectroscopy is widely used in a lot of fields when light interacts with matter, such as diagnostics, food quality assessment, environmental sensing and pharmaceutical testing [1]. However, most spectrometers are expensive, bulky and unavailable out of industrial or laboratory. As a result, much studies have been invested in cheap, miniaturized and easy-to-use systems. Most of the current mini-spectrometer designs are based on interferometric optics, limiting their resolution and spectral range [2]. Although colloidal quantum dots have been proved overcome these limitations, the complex manufacture (195 different types of quantum dots) is badly for commercial production [3].

Nowadays, graphene and graphene-like two-dimensional (2D) materials have attracted much attention in optoelectronic applications such as photodetection [4]. Furthermore, SPP of graphene are attractive due to the tunability by voltage, dimension or number of layers. Graphene has been proved to be a very promising candidate for mid-infrared to terahertz applications where its plasmonic resonance resides. We have demonstrated graphene based voltage tunable mini-spectrometer for the first time in 2018 [5]. But the energy-efficient mini-spectrometer is also important in a lot of areas. Here, we proposed a self-powered mini-spectrometer which can be tuned by changing the layers and dimensions of graphene ribbons. The absorption cover a spectral ranging from 8~12 μm. The graphene mini-spectrometers are expected to be useful in minimizing size, weight, cost and complexity of the spectrometer.

RESULTS AND DISCUSSION

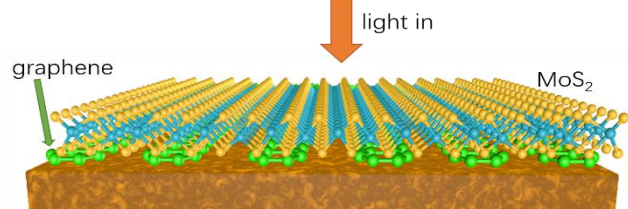


Fig. 1. The structure of the graphene based 2 in 1 mini-spectrometer.

The graphene mini-spectrometer (filter and photodetector in 1 device) is illustrated in Fig. 1. Single-layer MoS₂ film was covered on the periodic monolayer graphene ribbons deposited on Si/SiO₂ substrate. The SPP was excited by the periodic graphene ribbons, and a great amount of e-h pairs were generated and separated by the built-in field at the interface of graphene and MoS₂. The responsivity of the photodetector can be calculated by

$$R_{ph} = GI/P_{in} \quad (1)$$

where G is the photogain. I is the photocurrent. P_{in} is the source power [5]. And the theoretical photoresponsivity can reach 10⁸ A/W. The resonance occurs when the incident light frequency match with the oscillation frequency of electrons and can be described as [5]:

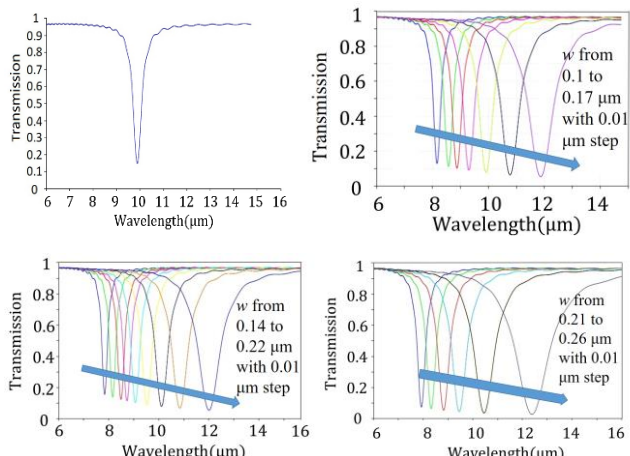


Fig. 2. The normal-incidence transmission spectra when the period of graphene ribbons is 300 nm. (a) The width is 150 nm. (b) The transmission spectra of 2 layers device when the width change from 0.1 to 0.17 μm with 0.01 μm step. (c) The transmission spectra of 3 layers device when the width change from 0.14 to 0.22 μm with 0.01 μm step. (d) The transmission spectra of the 4 layers device when the width change from 0.21 to 0.26 μm with 0.01 μm step.

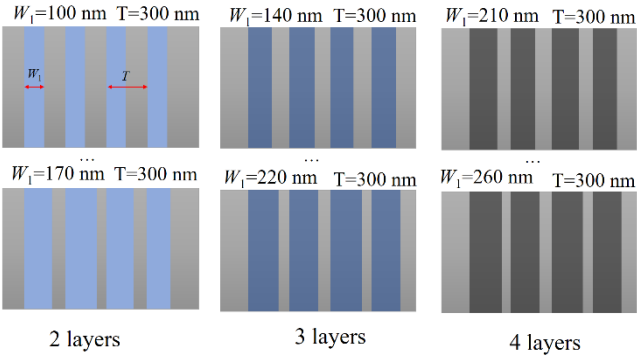


Fig. 3. The diagram of the self-powered device. The layer and width of graphene can be tuned to change the resonant wavelength.

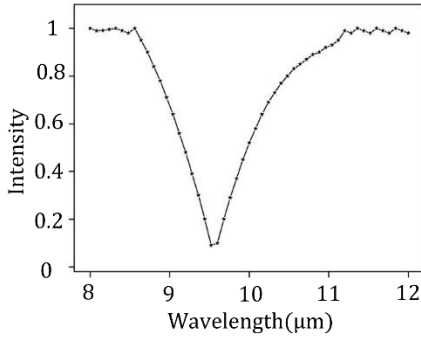


Fig. 4. The reconstructed spectra by self-powered graphene spectrometer.

$$\operatorname{Re}(\beta(\omega)) - \frac{\omega}{c} \sin \theta = \frac{2\pi}{T} \quad (2)$$

where ω is the angular frequency of the incident light. $\beta(\omega)$ is the wavevector of SPPs in graphene. θ is the incident angle. c is the speed of light and T is the grating period. The normal-incidence transmission spectra is shown in Fig. 2(a), where the period of graphene ribbons is 300 nm and the width is 150 nm. Sharp notch is seen at 10 μm , which corresponds to the calculation results of equation 2. As a result, a sharp notch optical filter was created. The resonant frequency can be tuned fast and conveniently by changing the layers and dimensions of graphene ribbons. When the size or layer is changed, the resonant wavelength changes correspondingly, as shown in Fig. 2(b) to Fig. 2(d), covering the spectrum from 8~12 μm discretely.

The interval structure of the mini-spectrometer is illustrated in Fig. 3. Each detector is unique, as a result of tuning the graphene size or layer. The measured spectrum by a graphene spectrometer is based on the measurement of the total transmitted intensity (current intensity). This intensity

Table I. Comparison of the performance metrics of different mini-spectrometer.

Structure	Resolution	Range
This work	~10 nm	8 μm -12 μm
Colloidal crystal, Ref [2]	~16 nm	490 nm-630 nm
Quantum dots, Ref [3]	~1 nm	390 nm-690 nm
Integrated sensor, Ref [6]	~1 nm	1310 nm-1340 nm

measurement is repeated with different Fermi level of the graphene filter, resulting in a set of measured current intensity. Spectral is reconstructed by linear regression, making the sum of the squares of the differences between the set of measured intensities and a set of standard intensities minimized.

To illustrate the above method mathematically and distinctly, consider an incident-light spectrum $\phi(\lambda)$ (where λ is the wavelength) that is transmitted through a graphene detectors, a Fermi level at a time. Then the Fermi level was changed, resulting in measured current intensities I_i , (where $I = 1, 2, \dots, n$ is the measured number), shown as:

$$I_i = \sum_{\lambda} \phi(\lambda) T_i(\lambda), \quad i = 1, 2, \dots, n \quad (3)$$

where $T_i(\lambda)$ is the transmission spectrum of graphene detector, which is predetermined. I_i is the measured value and can be described as:

$$I_i = Vq\mu\Delta n \quad (4)$$

where V is the applied bias on p-n junction. q is the elementary electron charge. μ is the charge carrier mobility. Δn is the photon induced carriers density. The only unknown variable is $\phi(\lambda)$, which corresponds to a set of n variables.

Considering the limit of photolithography (10 nm), the width of the spectrometer was changed 10 nm each time. The arbitrary spectra and corresponding reconstructed spectrum (50 types detector) is shown in Fig. 4, representing nearly all the major features of the spectra. The comparison of the performance metrics of different mini-spectrometer was shown in table 1. The resolution of these designs can satisfy the accuracy of a lot of application. Comparing with the graphene spectrometer, the operation ranges of colloidal crystal, quantum dots and integrated sensor are narrow. Therefore, the SPP based graphene mini-spectrometer is promising and attractive.

ACKNOWLEDGMENT

This work was supported by the National Key Research and Development Program of China under Grant 2016YFA0200400 and Grant 2016YFA0302300, the National Science and Technology Major Project of China under Grant 2016ZX02301001, the National Natural Science Foundation of China under Grant 61306105.

REFERENCES

- [1] A. J. Das, A. Wahi, I. Kothari, and R. Raskar, "Ultra-portable, wireless smartphone spectrometer for rapid, non-destructive testing of fruit ripeness," *Scientific Reports*, vol. 6, no. 1, Sep. 2016.
- [2] H. Ding, C. Liu, H. Gu, Y. Zhao, B. Wang, and Z. Gu, "Responsive Colloidal Crystal for Spectrometer Grating," *ACS Photonics*, vol. 1, no. 2, pp. 121–126, Jan. 2014.
- [3] J. Bao and M. G. Bawendi, "A colloidal quantum dot spectrometer," *Nature*, vol. 523, no. 7558, pp. 67–70, Jul. 2015.
- [4] Y. Liu, W. Huang, T. Gong, Y. Su, H. Zhang, Y. He, "Ultra-sensitive near-infrared graphene photodetectors with nanopillar antennas," *Nanoscale*, vol. 9, pp. 17459–17464, Oct. 2017.
- [5] Y. Liu, T. Gong, Y. Zheng, X. Wang, J. Xu, Q. Ai, "Ultra-sensitive and plasmon-tunable graphene photodetectors for micro-spectrometry," *Nanoscale*, vol. 10, pp. 20013–20019, Oct. 2.
- [6] Z. Wang, S. Yi, A. Chen, M. Zhou, T. S. Luk, A. James, "Single-shot on-chip spectral sensors based on photonic crystal slabs," *Nature Communications*, vol. 10, no. 1, Mar. 2019.

A New Method for Fabricating Graphene-Based Field-Emission Air-Channel Photodetector

1
2
3
4
5
6
7
8
9
10
11
12
13
14
15
16
17
18
19
20
1
2
3
4
5
6
7
8
9
10
11
12
13
14
15
16
17
18
19
20
21
22
23
24
25
26
27
28
29
30
31
32
33
34
35
36
37
38
39
40
41
42
43
44
45
46
47
48
49
50
51
52
53
54
55
56
57
58
59
60
61
62
63
64
65
Yu Liu

*Institute of Microelectronics
Tsinghua University
Beijing, China
y-liu-17@mails.tsinghua.edu.cn*

Linyuan Zhao

*Institute of Microelectronics
Tsinghua University
Beijing, China
756595890@qq.com*

Renrong Liang

*Institute of Microelectronics
Tsinghua University
Beijing, China
liangr@mail.tsinghua.edu.cn*

Wenjie Chen

*Institute of Microelectronics
Tsinghua University
Beijing, China
chen-wj15@mails.tsinghua.edu.cn*

Jun Xu

*Institute of Microelectronics
Tsinghua University
Beijing, China
junxu@mail.tsinghua.edu.cn*

Abstract—We firstly present a graphene based field emission air channel transistors by wet transfer method and electron beam lithography (EBL) processing. The air gap between two graphene electrodes is obtained by focused ion beam (FIB). The width of the air-channel is about 40 nm. The current can be tuned by changing the bias voltage applied to the Si substrate and graphene electrodes. The ON/OFF current ratio reaches up to 10^4 which is larger than graphene gap transistors. The currents increased when graphene electrode are under illumination. The fermi energy of graphene can be tuned by illumination and the field emission enhanced as a result. The responsivity, detectivity and response time under 850 nm are 0.056 mA/W, 1.4×10^4 Jones and < 2 ms, respectively. This device is more stable and easier for preparation than Heterojunction. We believe the low dark current, high speed, scattering-free transport and radiation resistance photodetector can be widely used in a lot of areas.

Keywords—Graphene, air-channel, photodetector

INTRODUCTION

Graphene have attracted wide research interest in photodetection due to the high carriers mobility and silicon compatible fabrication. Furthermore, the most attractive advantages of graphene based photodetectors is the broad wavelength absorption from ultraviolet to terahertz for the zero band gap. However, on the other hand, this advantage hinder its application in logic switching and low power consumption devices. The high dark current and low photoresponsivity also limit the practical application of graphene based photodetectors [1-3].

The demonstration of quantum dot and localized surface plasmon resonance (LSPR) introduced an ultra-high photoresponsivity [1]. But the ultra-high dark current (several tens of μ A) and low signal-to-noise-ratio are still serious problems. The demonstration of graphene/MoS₂ or graphene/perovskite Heterojunction device suppressed the dark current effectively [4]. However, a good contacted Heterojunction is difficult for large-scale preparation. Moreover, many efforts have been devoted to introduce an energy gap in graphene, including chemical doping, electric field doping, fabricating narrow graphene nanoribbons. But the successful introduction of an energy gap simultaneously sacrificed the carrier mobility and wide spectrum response.

Vacuum electronic devices have a theoretical charge carriers velocity of 3×10^8 m/s, which can also suppress the dark current effectively due to the tunneling transport [5]. Here, we present a graphene based field emission air channel transistor with low dark current and fast response. The currents increased when graphene electrode are under illumination because the energy band changed by photo-generated carriers. The photodetector with low dark current and high speed can be widely used in a lot of areas.

PROCESS

The preparation process are shown in Fig. 1. Firstly, a monolayer graphene was transferred to Si/SiO₂ substrate by wet transfer method. Then, the graphene electrodes were defined by electron beam lithography (EBL). Subsequently, 40-nm-thick aluminum (Al) were deposited by thermal evaporation, and the rest of the graphene were removed by oxygen plasma. Then aluminum above photoresist were lifted off by acetone. After that, the air channel were obtained by focused ion beam (FIB). Finally, the aluminum was removed by corrosive solution. The structure of the graphene based air-channel photodetector is shown in Fig. 2(a). Fig. 2(b) shows the Raman spectrum of the graphene based field-emission photodetector, indicating its monolayer character. The scanning electron microscope (SEM) images of the center part of the channel etching by FIB is shown in Fig. 2(c). The width of the air-channel is about 40 nm.

RESULTS AND DISCUSSION

Electrical measurements are conducted in air conditions by Keysight 1500B semiconductor parameter analyzer. The devices are connected with three terminals including a back-gate, emitter/source and collector/drain. The output characteristics of the device is shown in Fig. 3. The source-drain current achieved 5 nA when the drain voltage was 10 V and gate voltage was 0 V. The response of the device under 850 nm are shown in Fig. 4. Energy band diagram of tunneling mechanism for graphene without and with illumination is shown in Fig. 5(a) and Fig. 5(b), respectively. The photogenerated carriers promote the Fermi level of graphene in drain electrode and enhanced the tunneling current as a result.

The photoresponsivity (R) is an important parameter for photodetectors, which can be calculated by:

$$R = \frac{I_P}{P} \quad (1)$$

where I_P is the photocurrent, P is the optical power. The detectivity (D^*) is another important factors to show the sensitivity of the photodetector and can be calculated by the following equations:

$$D^* = \frac{\frac{1}{RA^2}}{(2eI_{dark})^{\frac{1}{2}}} \quad (2)$$

where R is the photoresponsivity, A is the photosensitive area of the detector, e is the unit charge, I_{dark} is the dark current. The response time is also an important index. These parameters under 850 nm are 0.056 mA/W, 1.4×10^4 Jones and < 2 ms, respectively.

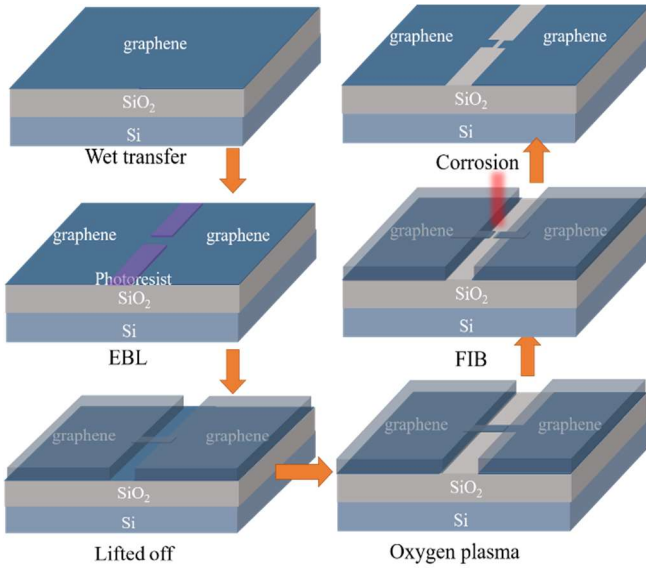


Fig. 1. The preparation process of our device. The main steps include wet transfer, EBL, lifted off, oxygen plasma, FIB and corrosion.

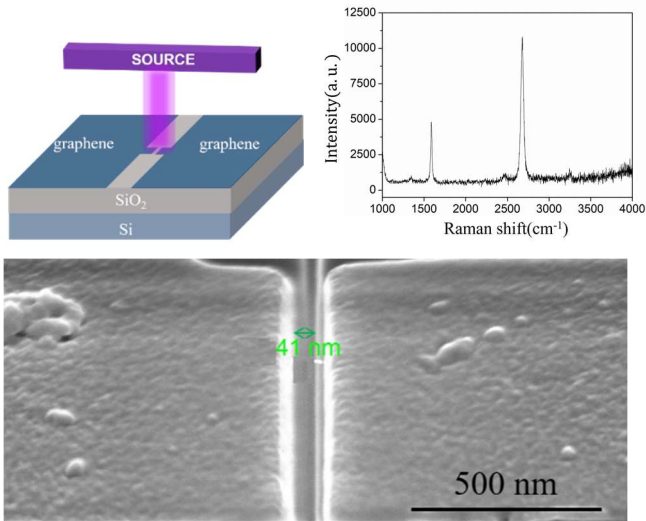


Fig. 2. (a) The structure of the graphene based air-channel photodetector. (b) The Raman spectrum of the graphene. (c) The SEM images of the center part of the channel.

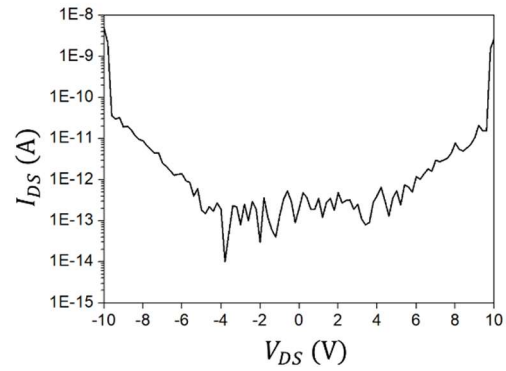


Fig. 3. The output characteristics of the device.

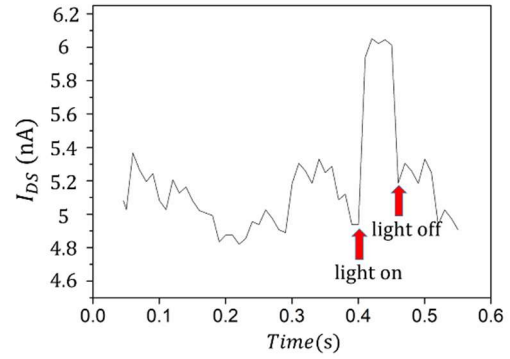


Fig. 4. The response of the device under 850 nm.

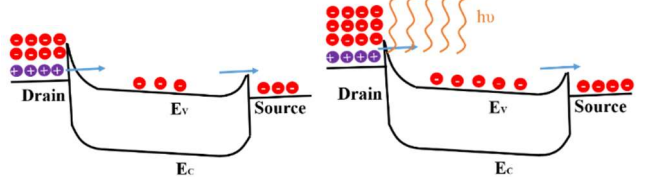


Fig. 5. Energy band diagram of tunnelling mechanism for graphene (a) without and, (b) with illumination.

ACKNOWLEDGMENT

This work was supported by the National Key Research and Development Program of China under Grant 2016YFA0200400.

REFERENCES

- [1] Z. Sun and H. Chang, "Graphene and Graphene-like Two-Dimensional Materials in Photodetection: Mechanisms and Methodology," *ACS Nano*, vol. 8, pp. 4133–4156, Apr. 2014.
- [2] Y. Liu, W. Huang, T. Gong, Y. Su, H. Zhang, Y. He, "Ultra-sensitive near-infrared graphene photodetectors with nanopillar antennas," *Nanoscale*, vol. 9, pp. 17459–17464, Oct. 2017.
- [3] Y. Liu, T. Gong, Y. Zheng, X. Wang, J. Xu, Q. Ai, "Ultra-sensitive and plasmon-tunable graphene photodetectors for micro-spectrometry," *Nanoscale*, vol. 10, pp. 20013–20019, Oct. 2018.
- [4] M. Long, P. Wang, H. Fang, and W. Hu, "Progress, Challenges, and Opportunities for 2D Material Based Photodetectors," *Adv. Fun. Mat.*, vol. 29, p. 1803807, Sep. 2018.
- [5] G. Wu, X. Wei, Z. Zhang, Q. Chen, and L. Peng, "A Graphene-Based Vacuum Transistor with a High ON/OFF Current Ratio," *Adv. Fun. Mat.*, vol. 25, pp. 5972–5978, Aug. 2015.
- [6] S. Nirantar, T. Ahmed, G. Ren, P. Gutruf, C. Xu, M. Bhaskaran, "Metal–Air Transistors: Semiconductor-Free Field-Emission Air-Channel Nanoelectronics," *Nano Letters*, vol. 18, pp. 7478–7484, Nov. 2018.

Negative capacitance line tunneling TFET with a ferroelectric capacitor

Weijun Cheng^{1,2}, Renrong Liang^{1,2*}, Gaobo Xu³, Jun Xu^{1,2*}

1. Institute of Microelectronics, Tsinghua University, Beijing, China

2. Beijing National Research Center for Information Science and Technology (BNRist), Beijing, China

3. Key Laboratory of Microelectronics Devices & Integrated Technology, Institute of Microelectronics, Chinese Academy of Sciences, Beijing 100029, China.

* Renrong Liang: liangrr@mail.tsinghua.edu.cn and Jun Xu: junxu@mail.tsinghua.edu.cn

Abstract—We develop a novel steep slope hybrid TFET by introducing a ferroelectric HfZrO capacitor to the silicon line tunneling TFET (LT-TFET). The ferroelectric capacitor was fabricated with the Zr doped HfO₂, compatible with CMOS technology. The as prepared LT-TFET exhibits a high drive current of 13 μ A/ μ m with a $V_{DS}=V_{GS}=0.5$ V. Due to the negative capacitance voltage amplification, SS is improved significantly from \sim 80 mV/dec to \sim 59 mV/dec with the drain current from 5 pA/ μ m to 500 pA/ μ m in the hybrid TFET compared to the baseline LT-TFET. The most improved SS was realized with a Zr content of 40% and the hysteresis was experimentally demonstrated to be reduced by properly negative capacitance matching.

Index terms— steep slope, TFET, line tunneling, HfZrO, negative capacitance.

I. INTRODUCTION

The high performance CMOS technology and new high-volume applications of Internet-of-Things (IoT) demand low-cost and ultralow-power CMOS compatible technology, thus needing further reducing the supply voltage [1]. In order to achieve the ultralow power operation, there have been extensive studies on the steep subthreshold slope (SS) transistors, such as tunnel FET (TFET) [2, 3] and negative capacitance FET (NCFET) [4, 5]. TFET is a promising structure to break the limitation of Boltzmann's tyranny, less than 60mV/decade at room temperature (RT). However, TFET suffers the low on-state current and the limited current range below 60 mV/dec. By introducing the negative capacitance as the performance booster, both the SS and overdrive current of TFET are expected to be improved due to the voltage amplification of negative capacitance effect.

II. DEVICE FABRICATION

The schematic of the prepared silicon LT-TFET is plotted in Fig. 1(a). The device was fabricated using a P-type Si substrate. A Local Oxidation of Silicon (LOCOS) and P-well implantation were formed to isolate the active region. Then, the P⁺ source was formed by using BF₂ implantation. In the P⁺ source region, an ultra-shallow N⁺ pocket with high surface concentration and large strain effect was formed by Ge preamorphization implantation (PAI) plus As ultra-low energy implantation combined with spike annealing [6, 7]. As shown in Fig. 1 (b), the depth and length of the pocket are 30 nm and 600 nm, respectively. After the N⁺ pocket formation, SiO₂ and ploy-Si were deposited on the Si substrate using Low Pressure Chemical Vapor Deposition (LPCVD) at low temperature to avoid the further increase of the N⁺ pocket junction. Ploy-Si gate etching was performed in the Cl₂/HBr/O₂ chemistry. The gate stack has an overlap with the N⁺ pocket and local P⁺ source, providing a vertical tunneling path. After gate patterning, the N⁺ drain was

formed by As implantation. Spike annealing was conducted to activate the doping ions. After the formation of spacer, the contact and metallization were performed. The ferroelectric capacitor was fabricated with a TiN/HfZrO/TiN stack. The 10 nm HfZrO film was deposited by using atomic layer deposition (ALD). Then, it was annealed in N₂ ambient under 550 °C for 30 s.

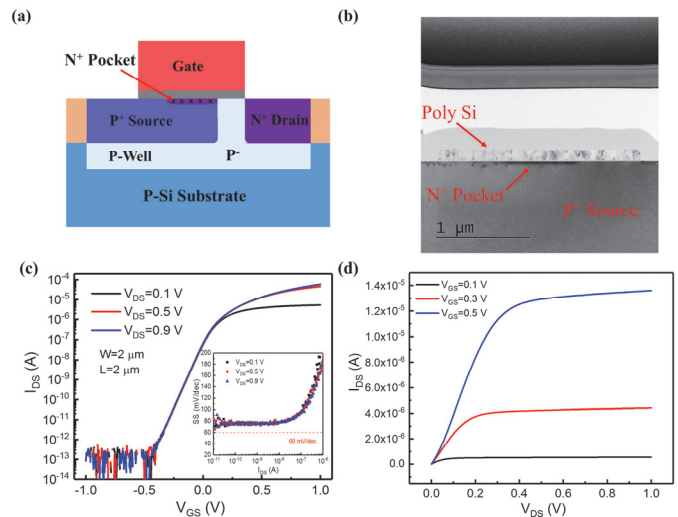


Fig. 1. (a) The schematic of the fabricated LT-TFET. The pocket under the gate overlap enabling a line tunneling aligned with the gate electric field. (b) The cross-sectional TEM image of the gate stack covering the pocket. The depth and length of the pocket are 30 nm and 600 nm, respectively. (c) The measured transfer characteristic of the LT-TFET at RT with a gate width and length of 2 μ m and 2 μ m, respectively. The inset image plots the corresponding SS versus the drain current. (d) The output characteristics, indicating a good linear onset and saturation.

III. RESULTS AND DISCUSSION

The Si LT-TFET proposed here exhibited high drive current capability and a constant SS value over a wide current range. Fig. 1(c) shows the transfer characteristic of the fabricated LT-TFET at RT. The measured on-state current is 30 μ A/ μ m with $V_{GS}=1$ V, $V_{DS}=0.9$ V. With a low voltage supply $V_{GS}=V_{DS}=0.5$ V, the on-state current is 13 μ A/ μ m. As shown in the inset figure of Fig. 1(c), the minimum SS is 65 mV/dec and SS maintains almost constant from 5 pA/ μ m to 5 nA/ μ m. The average SS over 4 current decades is around 80 mV/dec. The pre-implanted Ge interacted with the surface Si lattice and formed an amorphous thin layer, as shown in Fig. 1(b). Then the implanted As ions would pile up at the thin layer to form an ultra-narrow PN junction. Meanwhile, Ge PAI induces a uniaxial compressive stress in the pocket, thus reducing the bandgap. Due to the pocket and the Ge PAI, the tunneling efficiency and tunneling area are improved significantly. The

output characteristics show good current saturation, suggesting a high output impedance, as shown in Fig. 1(d).

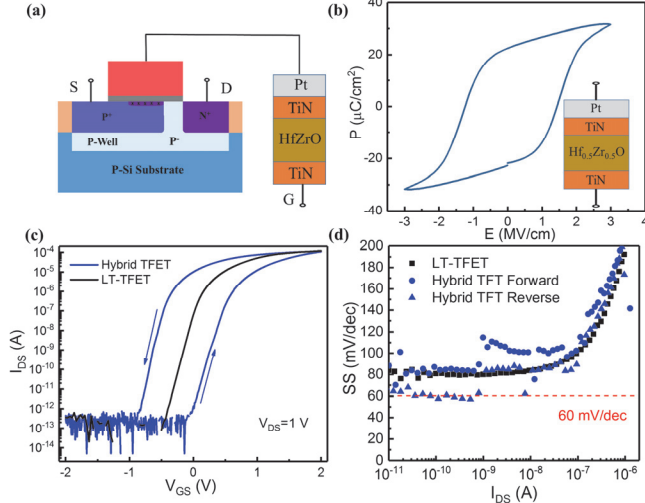


Fig. 2. (a) The configuration of the proposed hybrid TFET: a ferroelectric HfZrO capacitor is externally connected to the gate of the LT-TFET. The capacitor consists of a TiN/HfZrO/TiN/Pt structure deposited on a heavily doped P-type silicon substrate with thicknesses of 20 nm, 10 nm, 20 nm and 60 nm for each layer. (b) P-E characteristics of the HfZrO capacitor. The relative permittivity, coercive field (E_c) and remnant polarization (P_r) of the HfZrO film are 32, 1.4 MV/cm, and 22 μ C/cm², respectively. The HfZrO capacitor implemented is with a Hf and Zr ratio of 6:4 and area of 50×50 μ m². (c) The transfer characteristics of the hybrid TFET compared to the baseline LT-TFET. The hysteretic window is due to the unstable gate capacitance. The transfer curve becomes steeper during the reverse sweeping. (d) Corresponding SS of the hybrid TFET compared to the baseline LT-TFET. SS is improved significantly for drain current from 10 pA to 1 nA and a minimum SS of 57 mV/dec is achieved.

Fig. 2(a) shows the configuration the developed hybrid TFET. NC effect is realized by connecting a ferroelectric HfZrO capacitor externally to the gate of the LT-TFET. The external connections offer the flexibility of the capacitance matching between the ferroelectric capacitance and the gate capacitance of the baseline LT-TFET. The ferroelectric of the HfZrO film is demonstrated by the P-E characteristics, as shown in Fig. 2(b). Fig. 2(c) shows the transfer characteristics of the hybrid TFET and baseline LT-TFET. SS is improved significantly from ~80 mV/dec to ~59 mV/dec when the drain current ranges from 5 pA/ μ m to 500 pA/ μ m during the reverse sweeping. The Zr content dependent transfer characteristics and SS of the reverse sweeping are shown in Fig. 3(a) and Fig. 3(b). The hybrid TFET shows the most improved SS and on-state current with the Zr content of 40%, with which the ferroelectric capacitor exhibits the highest coercive field, as shown in Fig. 3(c). A high coercive field is reported to be an appropriate choice for high I_{on}/I_{off} at ultralow voltage in NCTFET by the simulation study, which follows the same design guideline as NCFET [8]. The total gate capacitance of the hybrid TFET is expressed as $C_g = (C_{FE}^{-1} + C_{MOS}^{-1})^{-1}$, where C_{FE} and C_{MOS} denote the capacitance of ferroelectric film and MOS capacitance of the LT-TFET. When $|C_{FE}| < C_{MOS}$, the total gate capacitance is negative and the whole device system is unstable and this lead to a hysteresis [4]. The hysteresis can be eliminated out by increasing the negative capacitance to make the total gate capacitance positive. A series of different size square capacitors are taken to combine with the LT-

TFET as shown in Fig. 3(d). The on-state currents increases from 36 μ A/ μ m to 60 μ A/ μ m when the capacitor area increases from 50×50 μ m² to 200×200 μ m² and non-hysteretic is realized with an area of 200×200 μ m².

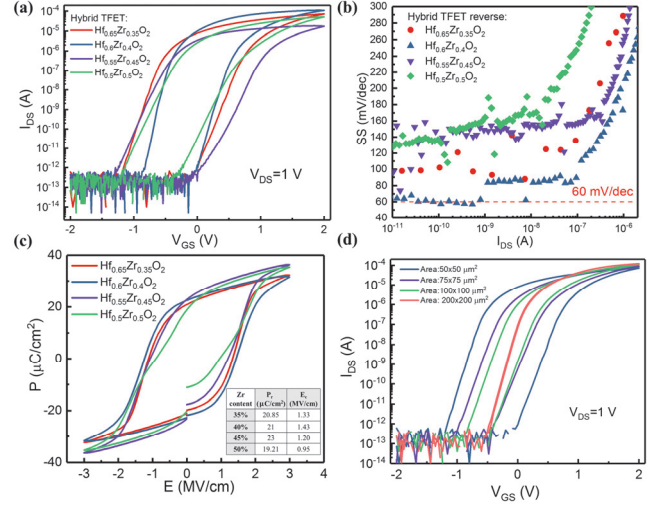


Fig. 3. (a) The transfer characteristics of the hybrid TFET with different Zr contents capacitor with a area of 50×50 μ m². (b) Corresponding SS with different Zr contents of the reverse sweeping, indicating the best SS improvement with a Zr content of 40%. (c) P-E characteristics of the HfZrO capacitor with different Zr contents with a area of 50×50 μ m². The 40% Zr content HfZrO exhibits the largest coercive field. (d) The transfer characteristics with different square area's capacitors with a Zr content of 35%. The hysteretic window can be eliminated out by properly matching the negative capacitance with the MOS capacitance of the LT-TFET.

IV. CONCLUSION

We investigated a steep subthreshold slope hybrid TFET by introducing negative capacitance to the line tunneling pocket TFET. A high drive current and SS below 60 mV/dec over two current decades are realized with a hysteresis. We also studied the effect of the ferroelectric HfZrO capacitor's area value and the Zr content on the hybrid TFET.

REFERENCES

- [1] Sakurai, T.: 'Perspectives of low-power VLSI's', IEICE transactions on electronics, 2004, 87, (4), pp. 429-436.
- [2] A. Bowonder, P. Patel, K. Jeon, J. Oh, P. Majhi, H.-H. Tseng, and C. Hu, "Low-voltage green transistor using ultra shallow junction and hetero-tunneling," in Extended Abstracts-2008 8th International Workshop on Junction Technology (IWJT'08), 2008, s. 93-96: IEEE.
- [3] Ionescu, A.M., and Riel, H.: 'Tunnel field-effect transistors as energy-efficient electronic switches', nature, 2011, 479, (7373), pp. 329.
- [4] Salahuddin, S., and Datta, S.: 'Use of negative capacitance to provide voltage amplification for low power nanoscale devices', Nano letters, 2008, 8, (2), pp. 405-410.
- [5] Wong, J.C., and Salahuddin, S.: 'Negative Capacitance Transistors', Proceedings of the IEEE, 2019, 107, (1), pp. 49-62.
- [6] G. Xu, Q. Xu, H. Yin, H. Zhou, G. Wang, C. Li, J. Liu, J. Li, W. Xiong, D. Wang, J. Li, and C. Zhao, "Study of Si Green Transistor with an Ultra-Shallow Pocket Junction," *ECS Transactions*, 2014, 60, (1), pp. 85-89.
- [7] Q. Xu, X. Duan, H. Liu, Z. Han, and T. Ye, "Low-Cost and Highly Manufacturable Strained-Si Channel Technique for Strong Hole Mobility Enhancement on 35-nm Gate Length pMOSFETs," *IEEE Transactions on Electron Devices*, 2007, 54, (6), pp. 1394-1401.
- [8] M. Kobayashi, K. Jang, N. Ueyama, and T. Hiramoto, "Negative capacitance as a performance booster for tunnel FET," in 2016 IEEE Silicon Nanoelectronics Workshop (SNW), 2016: IEEE, pp. 150-151.

Enhanced near-infrared photoresponsivity of MoTe₂ phototransistors by using an Al₂O₃ high- κ gate dielectric

1 Wenjie Chen

2 Institute of Microelectronics

3 Tsinghua University

4 Beijing, China

5 chen-wj15@mails.tsinghua.edu.cn

6 Renrong Liang

7 Institute of Microelectronics

8 Tsinghua University

9 Beijing, China

10 liangrr@mail.tsinghua.edu.cn

11 Jun Xu

12 Institute of Microelectronics

13 Tsinghua University

14 Beijing, China

15 junxu@mail.tsinghua.edu.cn

Abstract—We have fabricated high performance molybdenum ditelluride (MoTe₂) transistors on an Al₂O₃ high- κ dielectric and systematically investigated the electronic and optoelectronic properties. A high current on/off ratio around 10⁶ and the hole mobility of 41 cm²V⁻¹s⁻¹ are achieved in the Al₂O₃-based MoTe₂ transistors. Furthermore, the efficient near-infrared light detection of Al₂O₃-based MoTe₂ phototransistors has been demonstrated under the illumination of a 915 nm laser. The device shows good photoresponse capabilities with a photoresponsivity of 2934 AW⁻¹, a detectivity of 8.3×10¹¹ Jones, and a response time of 13 ms. These results reveal the application potential of the devices for next generation photodetectors.

Keywords—MoTe₂ phototransistors, high- κ , near-infrared light detection

I. INTRODUCTION

MoTe₂, a typical member of the large family of semiconducting transition-metal dichalcogenides (TMDCs), has been attracting attention widely due to its favorable optical and electronic properties in recent years [1]. Monolayer MoTe₂ exhibits a direct bandgap of 1.1 eV, while its bulk form shows an indirect bandgap of 0.83 eV. The smaller bandgap compared to other TMDCs such as molybdenum disulfide (MoS₂) and tungsten diselenide (WSe₂) renders it promising candidates for high performance near-infrared photodetectors. Photodetectors based on MoTe₂ phototransistors have been investigated, however, most of them are fabricated on SiO₂ dielectric [2]. The enhanced photoresponsivity of Al₂O₃-based MoTe₂ phototransistors under 405 nm light has been demonstrated in our previous work [3]. However, the near-infrared photoresponsivity of Al₂O₃-based MoTe₂ phototransistors has not been investigated carefully yet. In this work, near-infrared photoresponse properties of Al₂O₃-based MoTe₂ phototransistors were investigated in detail. Under a 915 nm laser illumination, the MoTe₂ photodetector shows a high photoresponsivity of 2933 AW⁻¹, a high detectivity of 8.3×10¹¹ Jones, and a short response time of 13 ms. These results suggest that the MoTe₂ phototransistors with Al₂O₃ high- κ gate dielectric has significant applicability in future high-performance near-infrared photodetectors.

II. EXPERIMENTAL DETAILS

Fig. 1(a) shows the schematic illustration of the Al₂O₃-based MoTe₂ phototransistors. First, few-layers MoTe₂ materials are produced from a semiconducting 2H-MoTe₂ bulk crystal by mechanical exfoliation method. Then, the MoTe₂ materials are transferred to a heavily doped silicon substrate covered with 30 nm Al₂O₃ deposited by atomic layer deposition (ALD). Electron-beam lithography (EBL) is

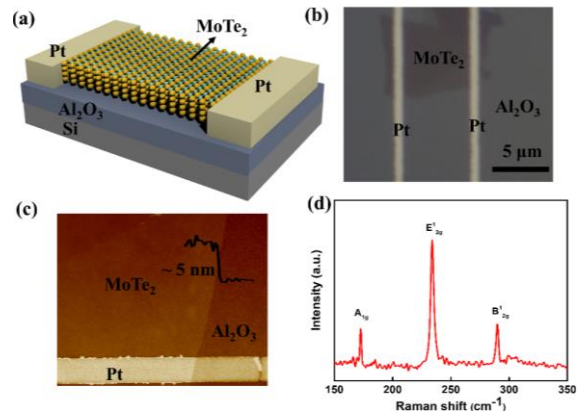


Fig. 1. (a) Schematic diagram of the Al₂O₃-based MoTe₂ phototransistor. (b) Optical image of the device. (c) AFM image of MoTe₂ flake. (d) Raman spectrum of MoTe₂ flake.

used to pattern the source/drain electrodes, followed by sputtering of 40 nm-thick Pt. After lift-off process, the MoTe₂ phototransistors are fabricated. The optical image of the as-fabricated device is shown in Fig. 1(b). Fig. 1(c) shows the atomic force microscopy (AFM) image and the thickness of MoTe₂ flake is measured to be around 5 nm. Raman spectroscopy with a wavelength of 532 nm is shown in Fig. 1(d). The electrical and optical properties are characterized with a Keithley 4200A-SCS parameter analyzer under a probe station in ambient air at room temperature. The photoresponse is measured under illumination of a laser with wavelength of 915 nm.

III. RESULTS AND DISCUSSIONS

The transfer characteristics (I_{ds} - V_{gs}) of Al₂O₃-based MoTe₂ transistors are shown in Fig. 2(a). MoTe₂ transistors with Pt contacts display p-type dominated conduction characteristics and excellent switching characteristics of a high current on/off ratio around 10⁶ in the hole accumulation regime. The mobility is extracted according to the equation:

$$\mu_{FE} = \frac{L}{W} \frac{dI_{ds}}{C_g V_{ds} dV_{gs}} \quad (1)$$

where L and W are the length and width of channel, respectively, C_g is the capacitance per unit area of the corresponding gate dielectric layer, and $g_m = dI_{ds}/dV_{gs}$ is the extrinsic transconductance. The hole mobility of MoTe₂ transistors based on Al₂O₃ dielectric is calculated to be 41 cm²V⁻¹s⁻¹, which is higher than that of the reported SiO₂-based devices [4]. To investigate the near-infrared photoresponsivity of Al₂O₃-based MoTe₂ phototransistors, we test the device illuminated by a 915 nm laser. The I_{ds} - V_{gs} curves under different light intensities are shown in Fig. 2(b).

At a fixed V_{ds} of -1 V, the photocurrent increases significantly with the increasing light intensity, which indicates good photoresponse capability. Furthermore, the threshold voltage shifts with the increase of light intensity, which could be explained by the photogating effect. The photogating effect is that the photoexcited holes/electrons will be trapped by the trap states located at the defects and/or at the surface adsorbates of MoTe₂ and then the trapped photoexcited holes/electrons will act as local gates and effectively modulate the conductance of MoTe₂ channel. Consequently, dramatic injected electrons/holes will lead to the shift of I_{ds} - V_{gs} curves. In addition to the photogating effect, the traditional photoconductive effect also contributes to the photoconductivity. Hence, prominent photocurrent under illumination can be achieved for the Al₂O₃-based MoTe₂ phototransistors. The photocurrent dependence on light intensity of the Al₂O₃-based MoTe₂ phototransistors is plotted in Fig. 2(c). The photocurrent of 3 μ A is observed using 30.9 mW/cm² illumination at V_{gs} = -12 V. Moreover, as critical parameters for phototransistors, photoresponsivity (R) and detectivity (D^*) are estimated respectively. Photoresponsivity is calculated by the formula:

$$R = \frac{I_{ph}}{PS} \quad (2)$$

where $I_{ph} = I_{light} - I_{dark}$, I_{light} and I_{dark} represent the I_{ds} at illuminated and dark states, respectively, P is the light intensity, and S is the effective illumination area. The photoresponsivity under different powers of light intensity is displayed in Fig. 2(d). The biggest photoresponsivity is calculated to be about 2923 AW⁻¹ when the power of the incident light is 1.09 mW/cm² and V_{gs} is -16 V for the Al₂O₃-based MoTe₂ phototransistors, compared to 1479 AW⁻¹ for SiO₂-based MoTe₂ devices in our previous work [5]. Hence, the photoresponsivity could be significantly enhanced by using an Al₂O₃ high- κ gate dielectric. The detectivity is calculated by:

$$D^* = \frac{RS^{1/2}}{(2qI_{dark})^{1/2}} \quad (3)$$

where q is the electron charge. A maximum detectivity of 8.3×10^{11} Jones is obtained when the power of the incident light is 1.09 mW/cm² and V_{gs} is -12 V.

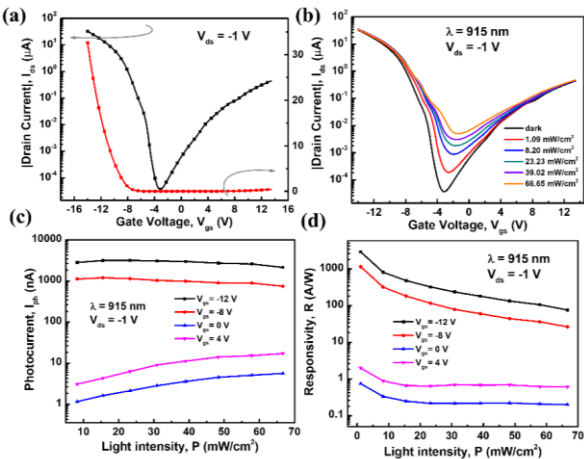


Fig. 2. (a) Transfer characteristics of the Al₂O₃-based MoTe₂ transistor. (b) Transfer characteristics of Al₂O₃-based MoTe₂ phototransistors under light illumination with different light intensities. (c) The extracted photocurrents and (d) photoresponsivities of Al₂O₃-based MoTe₂ phototransistors depend on the light intensity at different V_{gs} .

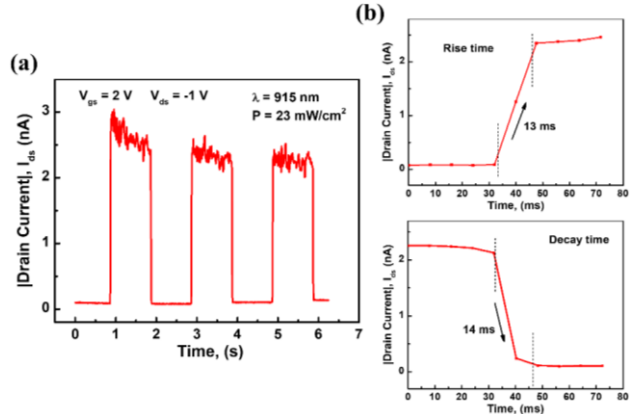


Fig. 3. (a) The continuous current-time cycles of the Al₂O₃-based MoTe₂ phototransistors. (b) The enlarged regions where I_{ds} rises and falls with time.

The response time is also one crucial factor in photodetector performance. Fig. 3(a) shows several complete current-time cycles of the Al₂O₃-based MoTe₂ phototransistors, indicating the good photoswitching stability. Fig. 3(b) shows the enlarged regions where I_{ds} rises and falls with time. The rise time (t_R) and the decay time (t_D) are defined as the time taken to go from 10% to 90% and from 90% to 10% of the total photocurrent, respectively. The rise and decay times are 13 and 14 ms for the Al₂O₃-based MoTe₂ phototransistors, respectively.

IV. CONCLUSION

In summary, the optoelectronic properties of MoTe₂ transistors based on Al₂O₃ dielectric have been systematically studied under the illumination of 915 nm laser. The Al₂O₃-based MoTe₂ phototransistors show good optoelectronic performances with photoresponsivity and detectivity of as high as 2934 AW⁻¹ and 8.3×10^{11} Jones, respectively. Furthermore, the rise time of 13 ms and the decay times of 14 ms are attained for the Al₂O₃-based MoTe₂ phototransistors. These results make MoTe₂ become a promising material for next generation electronic and optoelectronic devices in the future.

ACKNOWLEDGMENT

This work was supported by the National Key Research and Development Program of China under Grant 2016YFA0200400 and Grant 2016YFA0302300.

REFERENCES

- [1] S. Fathipour, N. Ma, W. S. Hwang, et al. "Exfoliated multilayer MoTe₂ field-effect transistors," *Appl. Phys. Lett.*, vol. 105, pp. 192101, November 2014.
- [2] Y. Lin, Y. Xu, S. Wang, et al. "Ambipolar MoTe₂ transistors and their applications in logic circuits," *Adv. Mater.*, vol. 26, pp. 3263-3269, April 2014.
- [3] W. Chen, R. Liang, J. Wang, S. Zhang, J. Xu, "Enhanced photoresponsivity and hole mobility of MoTe₂ phototransistors by using an Al₂O₃ high- κ gate dielectric," *Sci. Bull.*, vol. 63, pp. 997-1005, August 2018.
- [4] N. R. Pradhan, D. Rhodes, S. Feng, et al. "Field-effect transistors based on few-layered α -MoTe₂," *ACS Nano*, vol. 8, pp. 5911-5920, May 2014.
- [5] W. Chen, R. Liang, J. Wang, S. Zhang, et al. "Ultrasensitive near-infrared photodetectors based on MoTe₂ transistors with tunable photoresponse time," *J. Appl. Phys.*, in press.

Signal and Noise Properties of Translocation Current in Multiple-Nanopore Sensors

1 Chenyu Wen

2 *Division of Solid-State Electronics,
3 Department of Engineering Sciences*

4 Uppsala University

5 Uppsala, Sweden

6 chenyu.wen@angstrom.uu.se

7 Shuangshuang Zeng

8 *Division of Solid-State Electronics,
9 Department of Engineering Sciences*

10 Uppsala University

11 Uppsala, Sweden

12 shuangshuang.zeng@angstrom.uu.se

13 Zhen Zhang

14 *Division of Solid-State Electronics,
15 Department of Engineering Sciences*

16 Uppsala University

17 Uppsala, Sweden

18 zhen.zhang@angstrom.uu.se

19 Shi-Li Zhang

20 *Division of Solid-State Electronics,
21 Department of Engineering Sciences*

22 Uppsala University

23 Uppsala, Sweden

24 shili.zhang@angstrom.uu.se

This paper presents a novel approach for nanopore sensing by analyzing the translocation behavior of nanoparticles through multiple nanopores. A multiple-pore device is characterized by higher sensitivity and lower detection limit than a traditional single-pore counterpart. In addition, it offers more information about target molecules by deciphering the translation current in terms of average I_{ave} , standard deviation, STD, and power spectrum density, PSD, along with more flexibility such as changing size and number of nanopores, involving pores of different diameters in one device, *etc.* A model and a simulation platform are established to describe the stochastic group translocation behavior and to excavate signal and noise properties of the multiple-pore devices.

A. Introduction

Nanopore-based sensors have been widely used in many fields for both biological/medical studies and industrial/clinical applications, such as DNA sequencing, protein profiling, nanoparticle detection, *etc.*, owing to the simple device structure and working principle [1-2]. In a nanopore system, current blockage can be generated during the translocation of target molecules/nanoparticles because of their steric occupation of the pore volume. Hence, information of the target can be inferred by analyzing the current changes. Nanopore research has thus far mainly focused on single-pore devices. Although multiple-pore systems promise high throughput and low cost due to parallelization capability, their study begin to emerge in the literature with a focus on individually addressable nanopore arrays [3-4]. However, the complexity of read-out electronics and microfluidic cells imposes a severe challenge with respect to the integration of such a nanopore array in a high-density format. To alleviate this challenge, we explore an alternative approach with the multiple-pore system measuring the superposition of ionic currents from all pores present, as schematically shown in Fig. 1 [5].

B. Method

Ionic current collected by the Ag/AgCl electrodes placed in the upper and lower reservoirs is the superposition of all current components from all pores in the multiple-pore system. It carries information of the translocated nanoparticles. It also reflects the stochastic group translocation behavior of target nanoparticles, which presents an overall representation of many factors including size and number of nanopores, spacing and pattern of nanopores,

diameter and concentration of nanoparticles, bias voltage, pH and electrolyte concentration. By deciphering the characteristics of the group translocation current, such as I_{ave} , STD, and PSD, the properties of target nanoparticles can be inferred, such as their diameter and concentration. Furthermore, the multiple-pore device offers flexible configurations, such as tuning the size/number of nanopores, to yield additional information of target nanoparticles. In this system, noise is an important issue as it defines the sensing resolution (*i.e.* signal-to-noise ratio, SNR) and the manipulation margin (*e.g.* maximum number/size of pores). A model is established to describe the properties of group translocation behavior and to analyze its noise characteristics for different number and size of pores, capture probabilities, and size of nanoparticles.

C. Experimental results

The translocation experiments are taken on SiN_x nanopores of 400 nm in diameter. Fig. 2(a) shows current traces for the group translocation of 160 nm SiO₂ nanoparticles through a 7-pore device at different nanoparticle concentrations. Fig. 2(b) and (c) show, respectively, PSD and variation of I_{ave} and STD with nanoparticle concentration. The results indicate that the concentration of nanoparticles can be gauged by these current parameters. By adopting the signal and noise models [6], the SNR can be calculated for various sensing situations, including different capture probabilities, number of nanopores and diameter of nanoparticles (Fig. 3 and Fig. 4). Moreover, with the assistance of MATLAB simulation, the signal properties are compared between an N-small-pore system and one-big-pore system (Fig. 5).

ACKNOWLEDGMENT

The authors would like to thank Dr. Ralph Scheicher and Shiyu Li for fruitful discussions. This work was financially supported by the Swedish Research Council (621-2014-6300) and Stiftelsen Olle Engkvist Byggmästare (2016/39).

REFERENCES

- [1] A. H. Laszlo, I. M. Derrington, B. C. Ross, H. Brinkerhoff, A. Adey, I. C. Nova, *et al.*, “Decoding long nanopore sequencing reads of natural DNA” *Nat. Biotechnol.*, vol. 32(8), pp. 829–833, June 2014.
- [2] R. Wei, V. Gatterdam, R. Wieneke, R. Tampé, U. Ran, “Stochastic sensing of proteins with receptor-modified solid-state nanopores” *Nat. Nanotechnol.*, vol. 7(4), pp. 257–263, March 2012.

- [3] E. N. Ervin, R. J. White, H. S. White, "Sensitivity and signal complexity as a function of the number of ion channels in a stochastic sensor" *Anal. Chem.*, vol. 81 (2), pp. 533–537, December 2008.
- [4] S. Magierowski, Y. Huang, C. Wang, E. Ghafar-Zadehet, "Nanopore-CMOS interfaces for DNA sequencing" *Biosensors*, vol. 6 (3), pp. 42, August 2016.
- [5] C. Wen, S. Zeng, Z. Zhang, S.-L. Zhang, "Group behavior of nanoparticles translocating multiple nanopores" *Anal. Chem.*, vol. 90 (22), pp. 13483–13490. October 2018.
- [6] C. Wen, S. Zeng, K. Arstila, T. Sajavaara, Y. Zhu, Z. Zhang, *et al.*, "Generalized noise study of solid-state nanopores at low frequencies" *ACS Sens.*, vol. 2 (2), pp. 300–307. February 2017.

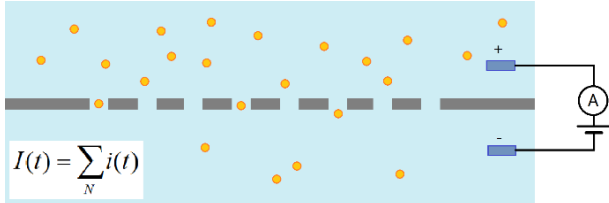


Figure 1: Schematic structure of a multiple-nanopore sensor.

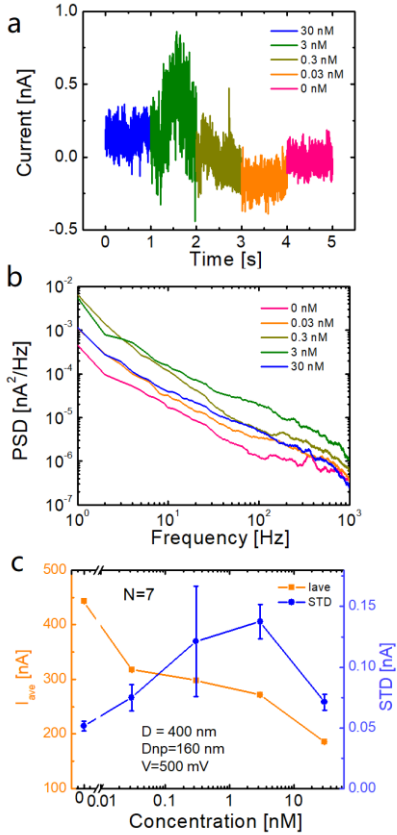


Figure 2: Group translocation characteristics of 160 nm-diameter SiO_2 nanoparticles through a 7-pore device with nanopores of 400 nm in diameter biased at 500 mV. (a) Current traces and (b) their PSD for different nanoparticle concentrations. (c) Variation of I_{ave} and STD with nanoparticle concentration

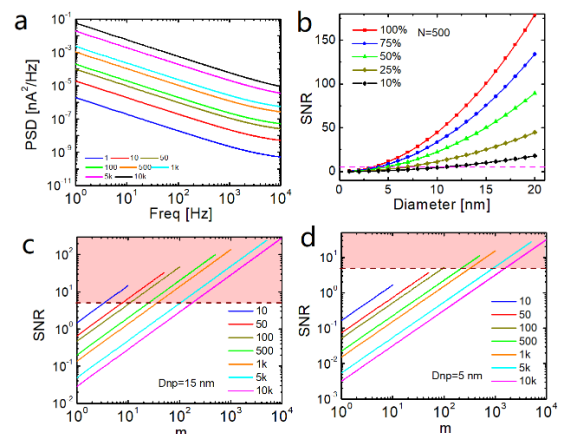


Figure 3: Signal and noise characteristics of multiple pores. (a) Noise PSD of the device with different number of pores. (b) Variation of SNR with diameter of nanoparticles and their occupancy rate. (c, d) Variation of SNR with the nanoparticle occupancy rate and number of pores for 15 nm and 5 nm particles, respectively.

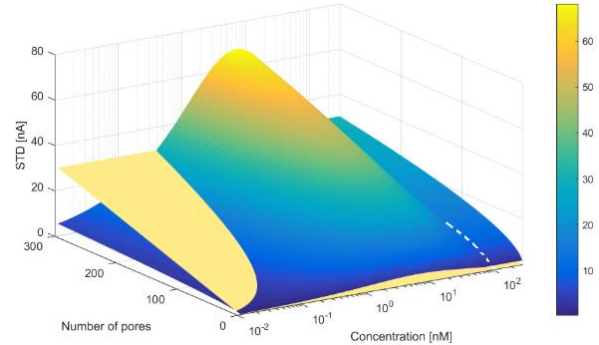


Figure 4: Variation of STD and noise of multiple pores with the nanoparticle concentration and number of pores.

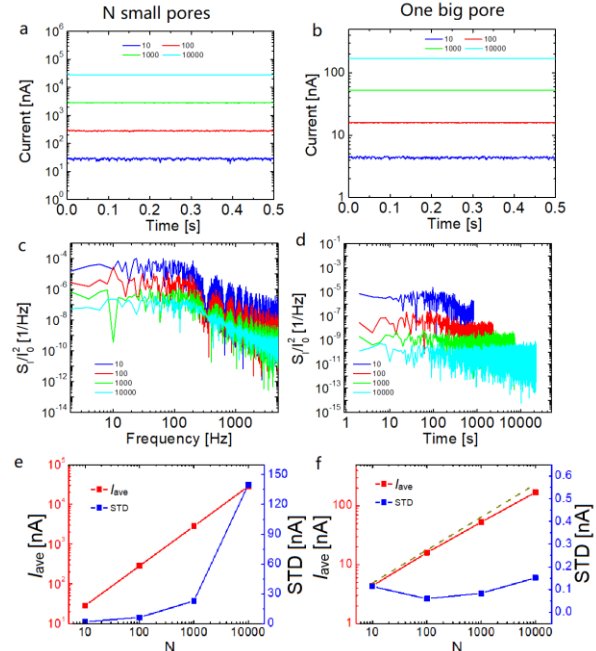


Figure 5: Comparison of the group translocation properties between an N -small-pore system and a one-big-pore system for different pore number/area. (a, b) Translocation current traces; (c, d) Normalized PSD; (e, f) I_{ave} and STD .

Fabrication of stable and efficient emissive films with core/shell perovskite nanoparticles

line 1: Hyeongjin Lee
line 2: *Department of Applied Chemistry*
line 3: *Kookmin University*
line 4: Seoul, Korea
line 5: lhjalqp@kookmin.ac.kr

line 1: Hee Chang Yoon
line 2: *Department of Applied Chemistry*
line 3: *Kookmin University*
line 4: Seoul, Korea
line 5: pdown123@kookmin.ac.kr

line 1: Joongho Lee
line 2: *Department of Applied Chemistry*
line 3: *Kookmin University*
line 4: Seoul, Korea
line 5: Joongho@kookmin.ac.kr

line 1: Young Rag Do
line 2: *Department of Applied Chemistry*
line 3: *Kookmin University*
line 4: Seoul, Korea
line 5: lhjalqp@kookmin.ac.kr

In this study, we synthesized green (G) $\text{CsPbBr}_3/\text{CsPb}_2\text{Br}_5$ and red (R) $\text{CsPb}(\text{Br}_{0.35}\text{I}_{0.65})_3/\text{CsPb}_2\text{Br}_5$ core/shell perovskite nanoparticles (PeNPs) and fabricated stable and efficient emissive films with green and red (GR) core/shell PeNPs. The photoluminescence quantum yields (PLQYs) for colloidal G and R core/shell PeNPs reached nearly 77.4% and 78.9%, respectively. The corresponding conversion efficiency rates of the core/shell G and R PeNPs films were 42.0% and 44.3%. The photo-stability, water resistance and thermal stability of the core/shell G and R PeNPs films are superior to those of GR core PeNP films. The GR colloidal PeNPs and the fabricated PeNP-films were analyzed by TEM, XRD, and EDX to assess their structural properties and by PL and EL with an integrating sphere to measure their optical properties.

Theory for Silicon-based light emitting

1
2
3
4
5 Jun-Wei Luo
6
7
8
9
10
11
12

State Key Laboratory for Superlattices
and Microstructures
Institute of Semiconductors, Chinese
Academy of Sciences
Beijing, China
jwluo@semi.ac.cn

We recently developed an unified theory for explaining why diamond, Si, Ge, and Al-containing group III-V semiconductors have indirect band gap, and the remaining common semiconductors, except GaP, have direct band gaps. We found that either the lack of, or the low-lying position of, the occupied d orbitals in cations of diamond, Si, Ge, and Al-containing group III-V semiconductors is responsible for their nature of indirect band gap, since the symmetry allowed p-d and p-s couplings at the X and L points push the X- and L-valley of the conduction band up but leave the Γ -valley intact. We propose a new pathway toward direct band gap Ge for CMOS-compatible on-chip laser. By inserting external atoms into interstitial sites of Ge lattice, which grows on Si substrate through SiGe buffer layer, impurity-induced effective tensile uniaxial strain transfers Ge from indirect bandgap to direct bandgap. Because our proposed scheme is fully compatible with CMOS technology, our new pathway would be a solution for on-chip lasers.

Although the direct or indirect nature of the band-gap transition is an essential parameter of semiconductors for optoelectronic applications, the understanding why some of the conventional semiconductors have direct or indirect band-gaps remains ambiguous. We have revealed that the existence of the occupied cation d bands is a prime element in determining the directness of the band-gap of semiconductors through the s-d and p-d couplings, which push the conduction band energy levels at the X- and L-valley up, but leaves the Γ -valley conduction state unchanged as shown in Fig. 1 [1]. This unified theory unambiguously explains why Diamond, Si, Ge, and Al-containing group III-V semiconductors, which do not have active occupied d bands, have indirect band-gaps and remaining common semiconductors, except GaP, have direct band-gaps. Besides s-d and p-d couplings, bond length and electronegativity of anions are two remaining factors regulating the energy ordering of the Γ -, X-, and L-valley of the conduction band, and are responsible for the anomalous band-gap behaviors in GaN, GaP, and GaAs that have direct, indirect, and direct band-gaps, respectively, despite the fact that N, P, and As are in ascending order of the atomic number. This understanding will shed light on the design of new direct band-gap light-emitting materials. For example, this theory unravels that it is impossible to make allotropes of Si and compounds consisting by Si mixed together with other elements high efficient direct bandgap light emitting.

Interface and quantum confinement in low-dimensional Si nanostructures are two knobs to relax the momentum conservation law of optical transition. We find the high-energy Γ - Γ direct band gap transition in Si quantum dots is slightly blue-shifted to higher energy [2] instead of being rapidly red-shifted with reduced dot size as suggested by T. Gregorkiewicz and his co-workers [3]. Our theory confirms

that the light emission efficiency of Si quantum dots increases exponentially as reducing dot size, but its highest reachable efficiently is still two orders of magnitude smaller than that of direct bandgap InP and GaAs.

Fortunately, we discovered that Si/Ge magic sequence superlattices exhibit orders more efficient at emission light than their existing counterpart records and approach more than 10% brightness of real direct gap materials, such as GaAs [4]. Furthermore, regarding the direct bandgap is only 140 meV above the indirect bandgap in Germanium (Ge), it is well established that a tiny (1-2%) extensile strain could render an indirect-to-direct bandgap transition and makes it direct bandgap. However, there is no feasible way to create such extensive strain on Ge since the lattice parameter of Ge is even 4.3% larger than Si. We have proposed to insert external atoms into interstitial sites of Ge lattices, which grows on Si substrate through SiGe buffer layer, to induce an effective tensile uniaxial strain on Ge, a new pathway toward direct band gap Ge. We predicted that 6% atom concentration of Li or 1% atom concentration of Ar insertion into the Ge to make it a transition from indirect bandgap to direct bandgap, as shown in Fig. 2. Because our proposed scheme is fully compatible with CMOS technology, our new pathway would be a solution for on-chip lasers.

A. Figures and Tables

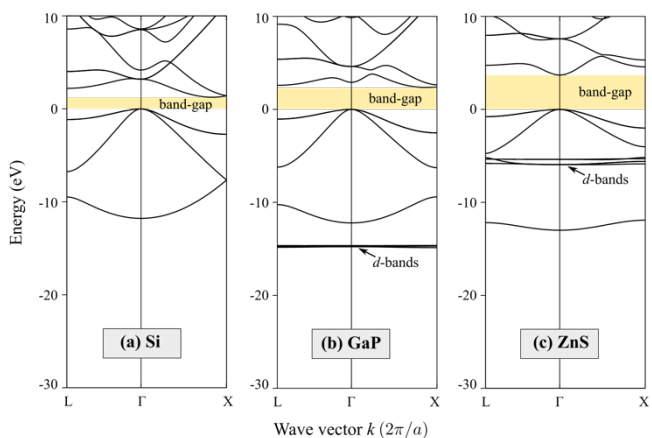


Fig. 1. Band structure of (a) Si, (b) GaP, and (c) ZnS predicted by the mBJ-GGA approach without considering the spin-orbit interaction. Yellow area indicates the band-gap. All energies are relative to the valence band maximum (VBM), which are set to zero. The lattice constants of Si, GaP, and ZnS are very similar.

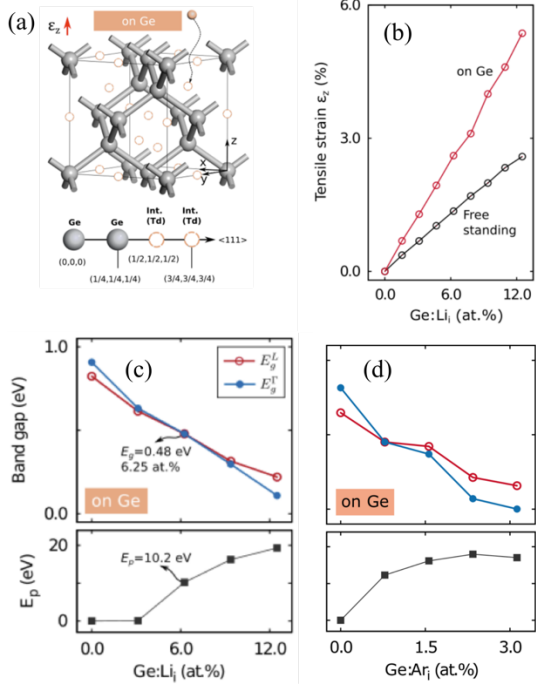


Fig. 2. Inserting impurity atoms into lattice interstitial sites provides uniaxial strain to Ge to make it a transition from indirect bandgap to direct bandgap. (a) Schematic diagram of interstitial sites of Ge lattice. (b) The strain induced by inserting Li atoms into Ge lattice. (c) The direct and indirect bandgaps and dipole matrix element of bandgap transition as a function of Li atom concentration. (d) The direct and indirect bandgaps and dipole matrix element of bandgap transition as a function of Ar atom concentration.

ACKNOWLEDGMENT (Heading)

J.W.L. thanks Prof. Alex Zunger, Prof. Jan. Linnros and Prof. I. Sychugov for a long-term cooperation. This work was supported by the National Natural Science Foundation of China (NSFC) under the joint China-Sweden Mobility program "Nanostructures by Design".

REFERENCES

- [1] L.D. Yuan, H.X. Deng, S.S. Li, S.H. Wei, and J.W. Luo, "Unified theory of direct or indirect band-gap nature of conventional semiconductors," *Phys. Rev. B* 98, 245203 (2018). *Phil. Trans. Roy. Soc. London*, vol. A247, pp. 529–551, April 1955. (*references*)
- [2] W. D. A. M. de Boer, D. Timmerman, K. Dohnalova, I. N. Yassievich, H. Zhang, W. J. Buma and T. Gregorkiewicz, "Red spectral shift and enhanced quantum efficiency in phonon-free photoluminescence from silicon nanocrystals," *Nature Nanotechnology* vol. 5, pp. 878 (2010).
- [3] J.W. Luo, S.S. Li, I. Sychugov, F. Pevere, J. Linnros, and A. Zunger, "Absence of red-shift in the direct band gap of silicon nanocrystals with reduced size", *Nature Nanotechnology* vol. 12, pp. 930 (2017).
- [4] M. dAvezac, J.W. Luo, T. Chanier, and A. Zunger, "Genetic-Algorithm Discovery of a Direct-Gap and Optically Allowed Superstructure from Indirect-Gap Si and Ge Semiconductors", *Phys. Rev. Lett.* vol. 108, pp. 027401 (2012).
- [5] R. Nicole, "Title of paper with only first word capitalized," *J. Name Stand. Abbrev.*, in press.
- [6] Y. Yorozu, M. Hirano, K. Oka, and Y. Tagawa, "Electron spectroscopy studies on magneto-optical media and plastic substrate interface," *IEEE Transl. J. Magn. Japan*, vol. 2, pp. 740–741, August 1987 [Digests 9th Annual Conf. Magnetics Japan, p. 301, 1982].
- [7] M. Young, *The Technical Writer's Handbook*. Mill Valley, CA: University Science, 1989.

GaN Silicon-on-Insulator (SOI) N-Channel FinFET for High-Performance Low Power Applications

Ajay Kumar^{1*}, Shrey Kumar Tripathi¹, Neha Gupta², Madan Mohan Tripathi³ and Rishu Chaujar³

^{1*}Department of Electronics and Communication Engineering, JIIT Noida, India.

²ASH Department, ADGITM (IPU), Delhi, India.

³Department of Electrical Engineering and Applied Physics, Delhi Technological University, Delhi, India

Abstract— This work presents, a novel Gallium Nitride (GaN) Silicon-on-Insulator (SOI) N-channel FinFET with 8 nm gate length with Zirconium dioxide (ZrO_2 , $\kappa = 25$) a high- κ gate dielectric material as the gate insulator. Gallium Nitride (GaN) is a binary III/V direct bandgap semiconductor having a wide bandgap of 3.4eV, greater than that of silicon whose band gap is only 1.1eV hence GaN can sustain higher voltages than silicon. GaN semiconductors have higher electron mobility than silicon; current can run faster through the device, they are also able to operate at higher temperatures while still maintaining their characteristics (up to 400k). It is found that the proposed device enhances on-current (I_{ON}) by four times and thereby transconductance, have been improved at ultra-low voltage power supply ($V_{DS} = 0.1$ V). Thereafter, a significant increase of 187.47% in the electric field and subthreshold swing of the GaN-SOI FinFET is 81% less than that of the Bulk device which points to the reduction of the short channel effects, better gate controllability and hence better overall performance of the GaN-SOI FinFET. Thus, the improved electrical performance of GaN-SOI FinFET makes it suitable for low power and high-performance CMOS circuits.

Investigation of Interface Characteristic in P(VDF_{0.75}-TrFE_{0.25}) Organic Ferroelectric Capacitor

Yu-Chia Chen¹, Po-Han Chen¹, Jay Chieh², Chih-Ting Lin^{1,*}

¹*Graduate Institute of Electronics Engineering*

²*Department of Material Science and Engineering*

National Taiwan University

Taipei, Taiwan

*timlin@ntu.edu.tw

Abstract—The electrical characteristics of metal-ferroelectric-oxide-semiconductor (MFOS) and metal-ferroelectric-semiconductor (MFS) capacitors are compared in this paper. The molecular chains are constrained by the restrictive force from the substrate surface. It results in an equivalent interface layer of lower dielectric constant between the ferroelectric and semiconductor. Comparing these two experiment results, we find low-k interface layer between the ferroelectric and semiconductor which is reduced efficiently by using high quality 2.5nm SiO₂ as buffer layer. The dielectric constant of MFOS capacitor also remarkable larger than MFS capacitor when the poly(vinylidene fluoride-trifluoroethylene) (P(VDF-TrFE)) copolymer thickness thinner than 300 nm. It is worth noting that the current density rises drastically at + 1.33 MV/cm electric field in the MFOS and MFS device structure. This phenomenon especially obvious in MFOS capacitor. Therefore, we propose a mechanism that causing the leakage current increase drastically should be the oxygen vacancies. The oxygen vacancies exist between P(VDF-TrFE) and SiO₂ junction.

Keywords—Ferroelectric, Dielectric constant, P(VDF-TrFE), metal-ferroelectric-semiconductor (MFS) capacitor.

I. INTRODUCTION

In recent years, the organic thin film materials have attracted extensive attention owing to there have advantages of low cost, near room temperature process abilities, large-area coverage, and flexibility. The organic material poly(vinylidene fluoride-trifluoroethylene) (P(VDF-TrFE)) has ferroelectricity and high dielectric constant [1]. Because of these characteristics, they are used in numerous applications, including organic thin film transistors (OTFT) [2] and ferroelectric field-effect transistors (FeFET) [3]. It should be noted that there are some papers have been indicated that the dielectric constant of P(VDF-TrFE) would be decreased with thickness decreased [1]. This phenomenon is caused by the capacitance of the interfacial layer in series with dielectric capacitance. In this study, we use the 2.5 nm SiO₂ as a buffer layer between P(VDF-TrFE) and silicon interface. The electrical characteristics compare with the MFS structure. Moreover, we also study the other effects which are caused by using SiO₂ as a buffer layer.

II. EXPERIMENTAL DETAILS

For the experiments, the MFOS capacitors were fabricated on p-type Si substrates. The 2.5 nm SiO₂ was grown on the substrate by anodic oxidation in deionized water with a DC voltage of 15V for 7.5 min at room temperature. Rapid thermal process in N₂ ambient at 950 °C for 15 s was used for post-oxidation anneals. Afterward, the high quality SiO₂ was formed [4]. Utilizing spin coating method to fabricated a different thickness of dielectric layer in MFOS capacitor

structure. After spin coating, the dielectric film was annealed in vacuum oven (at 140 °C for 10 h). Afterwards, the 250 nm Al film deposited on insulator layer as the top electrode and the back of the substrate as back contact to constitute the MFOS capacitor structure. In order to compare the different characteristics that with or without SiO₂ buffer layer, we also fabricated the MFS device structure. The electrical characteristics were measured by Agilent B1500A.

III. RESULTS AND DISCUSSION

Fig. 1 shows the dielectric constant which is extracted from the C-V characteristics. The dielectric constants do not decrease much seriously as the thickness decreases in the MFOS capacitor. The reverse relationship between capacitance and thickness for MFS and MFOS capacitors as shown in Fig. 2. It means that the effect of low-k interfacial layer is reduced by using SiO₂ as a buffer layer. Fig. 3 shows the polarization characteristic in MFM structure. The remnant polarization and coercive field can be approximately estimated as $\pm 3.39 \mu\text{C}/\text{cm}^2$ and $\pm 0.54 \text{ MV}/\text{cm}$ at 2μm. Fig.4(a)&(b) shows the I-V plot of the MFS and MFOS capacitors. The current density of both structures only rises drastically at + 1.33 MV/cm electric field (The peak current does not appear in negative electric field). The MFS capacitor $J_{1\text{st, peak}}/J_{2\text{nd, peak}}$ ratio is smaller than the switching current from other reference [5]. Furthermore, there are also some studies which indicate that the coercive field depends on the thickness of P(VDF-TrFE) [6]. For the reasons given above, these current peaks are not caused by dipole switching. The switching current should occur in a larger positive and negative electric field. It should be noted that the $J_{1\text{st, peak}}/J_{2\text{nd, peak}}$ ratio in the MFOS capacitor is higher than that in the MFS capacitor. Therefore, we suggest that this phenomenon is related to the electrons trapped and de-trapped by the oxygen vacancies. Fig. 5 shows the mechanism of the electron trapping ($V < 0$) and de-trapping ($0 < V$) due to oxygen vacancies.

IV. CONCLUSION

In summary, we prove the MFOS device which has better electrical characteristics than MFS device by using C-V measurement method. However, the oxygen vacancies exist between P(VDF-TrFE) and SiO₂ junction. The electrons will be trapping in and de-trapping out of oxygen vacancies under bias voltage. This phenomenon may result in misreading of memory state in the FeFET memory applications. Therefore, it is a major issue to select suitable material as buffer layer for P(VDF-TrFE) based ferroelectric field-effect transistor.

REFERENCES

- [1] Q.M. Zhang, H. Xu, F. Fang, Z.Y. Cheng, F. Xia, H. You, "Critical thickness of crystallization and discontinuous change in ferroelectric behavior with thickness in ferroelectric polymer thin films", *J. Appl. Phys.*, vol. 89, no. 5, pp. 2613–2616, Mar. 2001.
- [2] S.W. Jung, J.K. Lee, Y.S. Kim, S.M. Yoon, I.K. You, B.G. Yu, Y.Y. Noh, "Top-gate ferroelectric thin-film-transistors with P(VDF-TrFE) copolymer", *Current Appl. Phys.*, vol. 10, pp. 58–61, Jan. 2010.
- [3] R.G. Naber, C. Tanase, P.M. Blom, G. Gelinck, A. Marsman, F. Touwslager, S. Setayesh, D.D. Leeuw, "High-performance solution-processed polymer ferroelectric field-effect transistors", *Nature Materials*, vol. 4, pp. 243–248, Mar. 2005.
- [4] H.W. Lu, J.G. Hwu, "Roles of interface and oxide trap density in the kinked current behavior of Al/SiO₂/Si(p) structures with ultra-thin oxides", *Appl. Phys. A*, vol. 115, pp. 837–842, June 2013.
- [5] R. Kalbitz, P. Frübing, R. Gerhard, D.M. Taylor, "Stability of polarization in organic ferroelectric metal-insulator-semiconductor structures", *Appl. Phys. Lett.*, vol. 98, pp. 033303-1–033303-3, 2011.
- [6] N. Tsutsumi, A. Ueyasu, W. Sakai, C.K. Chiang, "Crystalline structures and ferroelectric properties of ultrathin films of vinylidene fluoride and trifluoroethylene copolymer", *Thin Solid Films*, vol. 483, pp. 340–345, July 2005.

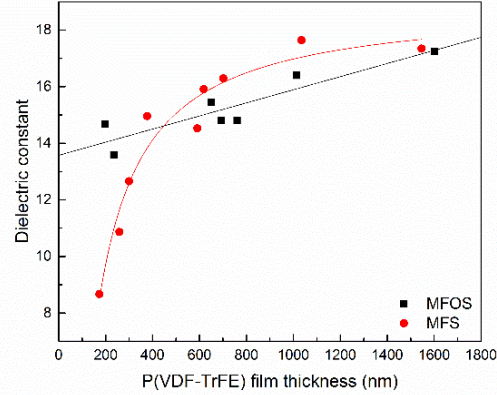


Fig. 1. The thickness dependence dielectric constant characteristics of MFOS and MFS capacitors.

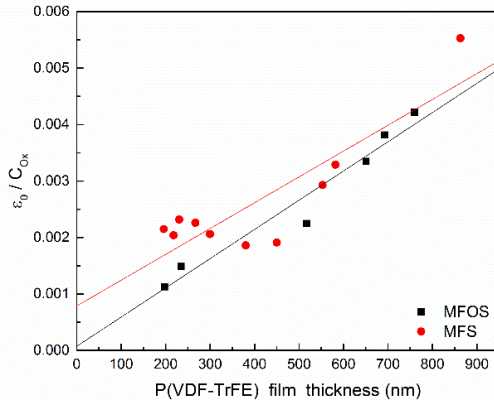


Fig. 2. The relationship between inverse of capacitance and thickness for MFS and MFOS capacitors.

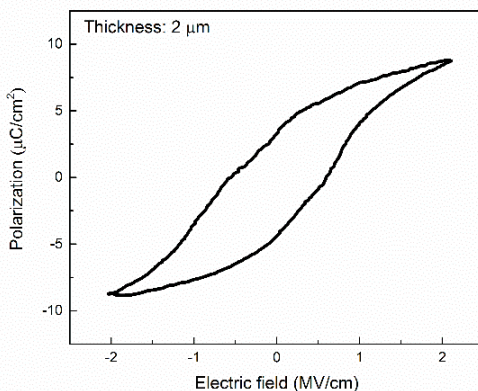


Fig. 3. The MFM structure of P (VDF-TrFE) capacitor polarization characteristic.

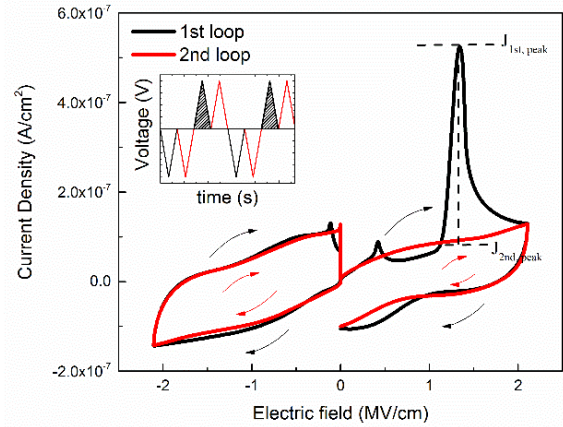
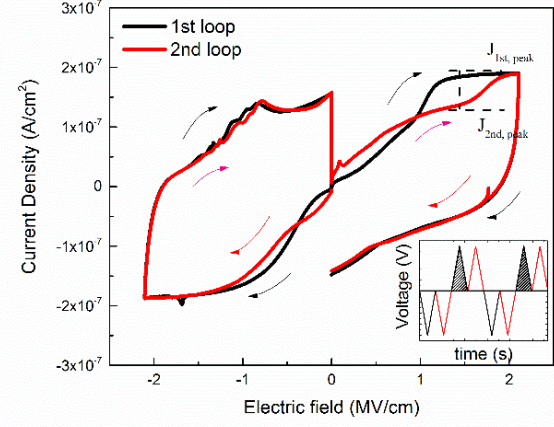


Fig. 4. (a) & (b) The I-V plot (sweep rate: 0.57 V/s) of MFS and MFOS capacitors with a 190 nm thick P(VDF-TrFE) ferroelectric insulator. The insets in (a) and (b) show the sequence of the applied unipolar/bipolar voltage sweeps in the range $V = \pm 40$ V. The gray area of triangle wave represents the peak of the I-V curve.

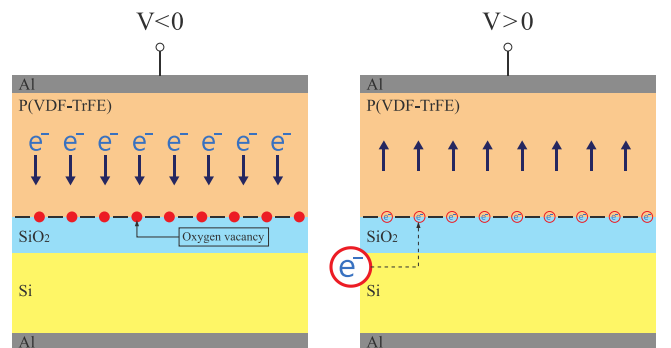


Fig. 5. The schematics of the electrons are trapped and de-trapped by oxygen vacancies.

Comparison between direct graphene growth and exfoliation process on Anodic Alumina Oxide membrane

1 Aamna AlShehhi

2 Electrical Engineering and Computer
3 Science4 Khalifa University Of Science and
5 Technology

6 Abu Dhabi , UAE

7 aamna.ralshehhi@ku.ac.ae

8 Irfan Saadat

9 Electrical Engineering and Computer
10 Science11 Khalifa University Of Science and
12 Technology

13 Abu Dhabi , UAE

14 irfan.saadat@ku.ac.ae

Abstract— This paper will present the analysis of direct growth for graphene material into AAO using CVD. Graphene peaks D, G and 2D has been detected using Raman Spectroscopy to be 1350 cm^{-1} , 1612 cm^{-1} and 2686 cm^{-1} respectively for direct graphene growth. Various growth environment will further be displayed in the conference. This comparison will further analyze the ability to choose the appropriate method for the targeted application.

Keywords—Graphene, AAO, Exfoliation

I. INTRODUCTION

Most of the recent studies focus on directly growing graphene films into different types of substrates either to be dielectric, semiconductor or metal, which will lead to simplify a lot of process in the manufacturing. In this work, we quantify the van der Waals force of direct graphene growth and exfoliation process into porous Anodic Alumina Oxide (AAO) membrane forces using Hamker parameters extracted from Atomic Force Microscopic (AFM) tool. This property is considered as one of the critical physical properties to study the adhesion of chemically inert components that will be used for the functionalized the structure. CVD planar tech tool is used for graphene growth into AAO and Cu substrates, which will be then used in the graphene exfoliation process. Our results demonstrated the results for multilayer graphene in both processes; exfoliation or directly growth.

II. LITERATURE REVIEW

Since the discovery and isolation of 2D monolayer graphene, the last decade has seen different applications that came about where this 2D pristine graphene film is used as active layer taking advantage of its unique layers [1].

“ The van der Waals heterostructure “ concept is one of the interesting areas to study this 2D material in which this material stakes with a

specific orientation to obtain the desired properties, for instance, the electrical properties where the bandgap can be changed based on the orientation of the layers[2].

In this study we quantify the material based on the process of graphene growth /exfoliation by understanding the concept of the VdW process and how is it necessary for the material interaction forces. It represented by Hamaker coefficient that defines the strength of these interactions. This coefficient referring to a demonstration of splitting the force strength into components depends on the material chemistry such as polarization and densities of the atoms.

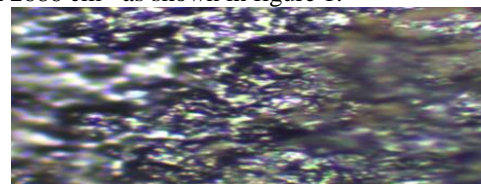
III. METHODOLOGY

This paper tackles the growth and optimization of graphene directly on manufactured AAO films and conventional transfer graphene, using Chemical vapor deposition. However, in the transfer process, CVD technique is used for graphene growth on copper substrate considering the number of layers either to be monolayer or multilayer. After that, it was transferred to the AAO through precise process.

IV. RESULTS AND DISCUSSION

Graphene layers is grown directly on AAO with various pores size 200, 160 and 120 (nm) with a thickness of 50 μm using the CVD planar tech process tool. The pore size can potentially play a critical role in the environment of graphene growth.

Our current results shows growth of graphene via Raman spectroscopy with a laser wavelength of 532 nm. The D-mode, appears at approximately 1350 cm^{-1} , and the G-mode appears at approximately 1612 cm^{-1} and 2D mode is shown in 2686 cm^{-1} as shown in figure 1.



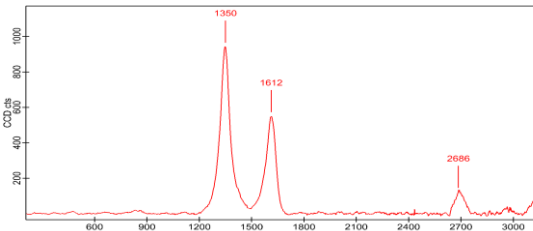


Figure 1: a) Optical Image b) Graphene Peaks (D, G, 2D) using 532 nm laser Raman Spectroscopy

Raman Spectroscopy is an impressive technique for graphene characterization. The graphene quality can be studied using Raman with analysis of the number of growth layers; single, double or multilayer. Peak Intensity, Position and width are used in the analysis. The preliminary calculation shows that I_D/I_G ratio is almost 0.84 which is referring to multilayer growth [3,4].

Electrical conductivity is another critical measurement for this kind of application and the recent results have demonstrated the capability of graphene film to be used as a conductive material for nonporous membrane. Conductive – Atomic Force Microscopy (C-AFM) tool is used for conductivity measurements. Below images are been taken using AFM.

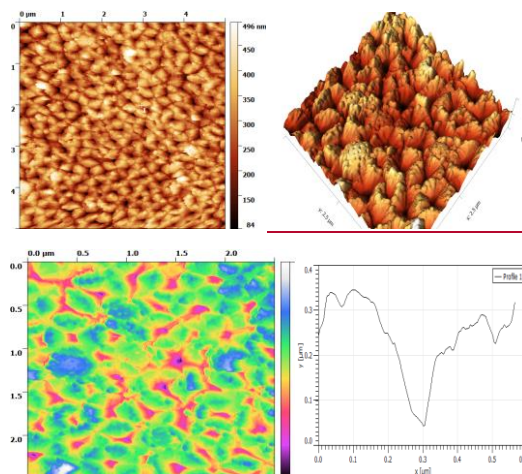


Figure 2: Graphene Growth on AAO Characterization using Non-contact Mode; a) 2D-AFM b) 3D-AFM c) AFM image with different heights d) Profile of the pore

Also, Scanning Electron Microscopy (SEM-EDS) is used for surface analysis and identifies the difference between the growth conditions. Figures 3 & 4 show some of preliminarily scan images. It shows the difference in the contrast between the AAO and AAO with direct graphene growth.

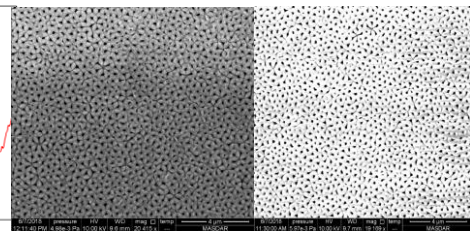


Figure 3: SEM Images; a) AAO with Graphene Growth b) AAO without graphene

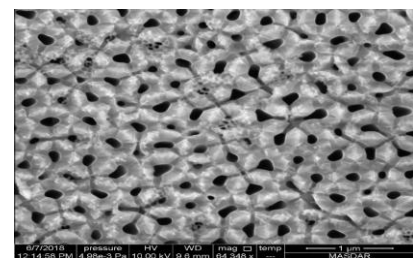


Figure 4: SEM Image for graphene growth on AAO with small scale

V. CONCLUSION

Ongoing activities include the CVD growth optimization along with various characterizations that will be reported in the full manuscript.

VI. REFERENCES

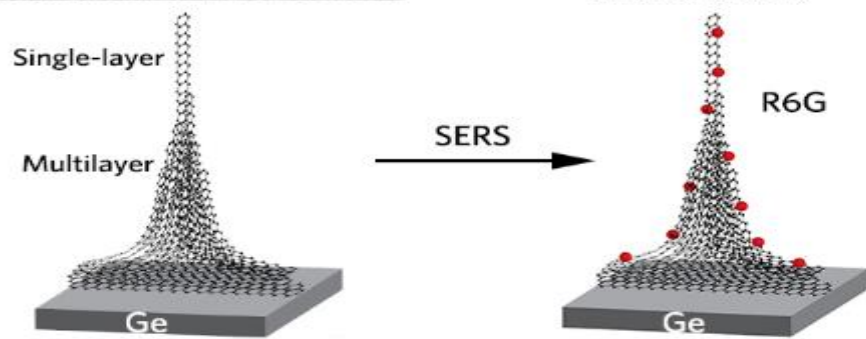
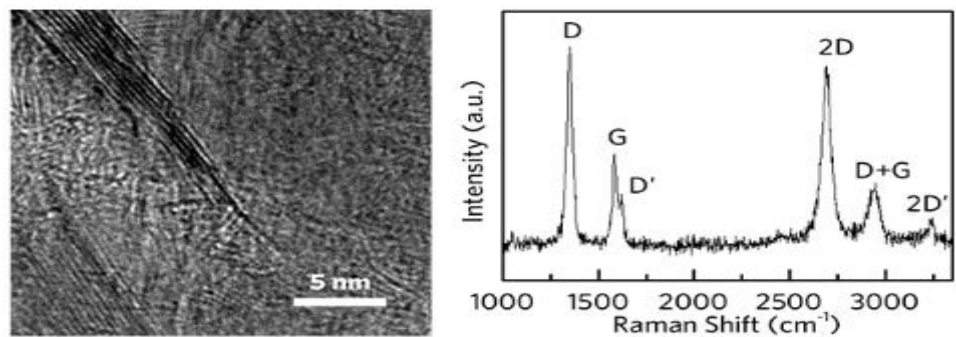
- [1] J. S. Stankovich, D. A. Dikin, G. H. Domke, K. M. Kohlhaas, E. J. Zimney, E. A. Stach, et al., "Graphene-based composite materials," *Nature*, vol. 442, pp. 282-286, 2006
- [2] Chiou, Y. C., Olukan, T. A., Almahri, M. A., Apostoleris, H., Chiu, C. H., Lai, C. Y., ... & Chiesa, M. (2018). Direct Measurement of the Magnitude of the van der Waals Interaction of Single and Multilayer Graphene. *Langmuir*, 34(41), 12335-12343.
- [3] Ying Mei, Chuyang Y. Tang "Recent developments and future perspectives of reverse electrodialysis technology: A review" *Desalination* ,Volume 425, 1 January 2018, Pages 156-174
- [4] Mark Wall, Ph.D., Thermo Fisher Scientific, Madison, WI, USA "The Raman Spectroscopy of Graphene and the Determination of Layer Thickness "

Direct Growth of Single-layer Terminated Vertical Graphene Array on Germanium by Plasma Enhanced Chemical Vapor Deposition

Abdulrahman Al-Hagri , Ru Li, , Shan Cong, Nitul Rajput, Jin-You Lu, Matteo Chiesa and Amal Al Ghaferi**

Keywords: direct growth, vertical nanographene, semiconducting substrate, plasma enhanced chemical vapor deposition

Vertically aligned graphene nanosheet arrays (VAGNAs) exhibit large surface area, excellent electron transport properties, outstanding mechanical strength, high chemical and thermal stability, and enhanced electrochemical activity, which makes them highly promising for application in supercapacitors, batteries, fuel cell catalysts. It is shown that VAGNAs terminated with a high-quality single-layer graphene sheet, can be directly grown on germanium by plasma enhanced chemical vapor deposition without an additional catalyst and at low temperature, which is confirmed by high-resolution transmission electron microscopy and large-scale Raman mapping. The uniform, centimeter-scale VAGNAs can be used as a surface-enhanced Raman spectroscopy substrate providing evidence of enhanced sensitivity for rhodamine detection down to 1×10^{-6} mol L⁻¹ due to the existed abundant edges.



Design and Fabrication of Micro fluidic Device for Optical Detection of Heavy Metal Ions in Potable Water

Owing to existing diverse reasons i.e. environment pollution, bio-fuel overuses, world-climate alteration, irrigation growth, as well as, fast-industrialization in developing-countries; demand for contamination-free water has been rapidly increasing. Further, the heavy metals ions, present even in lesser concentrations in water, are non-degradable and extremely toxic; and hence pose a great threat to living organisms. To fulfill the requirement for water free from the contagion of heavy metal ions, the cost-efficient detection of heavy metal ions in potable water, can extremely persuade the emerging world's wellbeing, primarily the children; and is promised to have a huge market. Conventional and existing detection method for heavy metal ions such as Pb^{2+} , Cd^{2+} , Hg^{2+} and Cr^{3+} ions etc. are extremely costly, time-consuming and relatively lesser-sensitive. In this paper, a simple and cost-effective method has been proposed for detecting heavy metal ions present in any water sample. A micro fluidic channel embedded with optical fiber coupler structures has been fabricated using a simple soft lithography based micro fabrication technique. Further, different concentration of Cr^{3+} , Hg^{2+} , Pb^{2+} ions in aqueous solution were passed through the micro channel, and respective optical absorbance (at 250 nm to 600 nm wavelength) were recorded via the optical fiber (coupled to aforesaid optical fiber coupler structures) and attached spectrophotometer; to obtain a standard calibration curve for a defined device's experimental set-up. The device characterization reveals that it is capable of detecting a minimum concentration of 0.036829, 0.03753 and 0.03074 M, for Cr^{3+} , Hg^{2+} , Pb^{2+} , ions in an aqueous solution, respectively. Furthermore, the device required only a minimum sample volume of 0.1ml and 5 seconds of minimum time to forecast the unknown concentration introduced into it. Additionally, in current future, it is expected that the present device may be coupled to a suitable light source and a photodiode, via the optical fibers, for developing a much compact and cost-effective tool, for the aforesaid reasons.

Polyimide-based Nanocomposites as Low-temperature Dielectrics

Harrison M. Hones
Mechanical Engineering
Rowan University
Glassboro, NJ, USA
honesh1@students.rowan.edu

Michael J. McCaffrey
Electrical and Computer Engineering
Rowan University
Glassboro, NJ, USA
dothemook@gmail.com

Jordan T. Cook
Mechanical Engineering
Rowan University
Glassboro, NJ, USA
cookj4@students.rowan.edu

Thomas J. Bielicki
Chemical Engineering
Rowan University
Glassboro, NJ, USA
bielickit4@students.rowan.edu

Richard Chao
Mechanical Engineering
Rowan University
Glassboro, NJ, USA
chaor6@students.rowan.edu

Robert R. Krchnavek
Electrical and Computer Engineering
Rowan University
Glassboro, NJ, USA
krchnavek@rowan.edu

Wei Xue
Mechanical Engineering
Rowan University
Glassboro, NJ, USA
xuew@rowan.edu

Nanocomposites made of polymers and nanomaterials have attracted considerable attention in the past two decades. Adding nanomaterials such as nanoparticles, nanowires, or nanotubes into host polymers, typically inert or “passive”, can drastically change their properties and behaviors. The resulted nanocomposites not only can possess enhanced electrical, mechanical, and thermal properties, but also can act as “active” functional materials suitable for a wide variety of new applications [1, 2].

Polyimide (PI) is an inert polymer commonly used for applications in insulation, passivation, and packaging. It is mechanically strong, thermally stable, highly flexible, and has excellent chemical resistance [3-5]. PI, as the insulation material, is well suited for power electronic devices and energy systems, due to its outstanding dielectric properties. In addition, it has a wide temperature window for operation, e.g., Kapton® from DuPont remains stable from -269°C to 400°C, making it a promising candidate as a strong dielectric for cryogenic applications [6].

In this paper, we report the investigation and findings of PI-based nanocomposites as low-temperature dielectrics. Silicon dioxide (SiO_2) nanoparticles, generated through a sol-gel process, are added to the host polymer as nanoscale fillers. The sol-gel process results in uniformly distributed SiO_2 nanoparticles in the host polymer. To evaluate the effect of fillers, nanocomposites with various concentrations of SiO_2 in the PI are fabricated and then tested as dielectrics at room temperature (300 K) and cryogenic temperature (164 K). The dielectrically broken down samples are inspected with scanning electron microscopy (SEM) and optical microscopy. The findings from this project can help advance our understanding of PI-based nanocomposites, especially on how nanofillers can change the overall material properties, eventually leading to better designed materials suitable for specific applications.

The host polymer PI is prepared through the reduction of polyamic acid (PAA) using a thermal imidization process. The SiO_2 nanoparticles are generated inside a material mixture using a well-studied sol-gel process. Four precursor materials that include tetraethyl orthosilicate (TEOS), hydrochloric acid

(HCl), ethyl alcohol, and water are used to form the sol-gel. Kapton®, a pure PI polymer, is used as the control material for performance comparison with the nanocomposites.

Fig. 1(a)-(d) illustrates the preparation process of the PI/ SiO_2 nanocomposites. The two starting materials, PAA and sol-gel precursors, are mixed in a glass beaker. The mixture is stirred with a magnetic bar rotating at 50 rpm for 4 hours. Next, the mixture is applied to a glass slide and then spin coated into a thin film. Afterward, the sample is heated to 250°C for 30 min for imidization. The heating process converts the initial PAA to PI by removing water molecules from the molecular chains. The treated sample can be easily peeled off from the glass slide and used as a standalone film for further testing, as shown in Fig. 1(e).

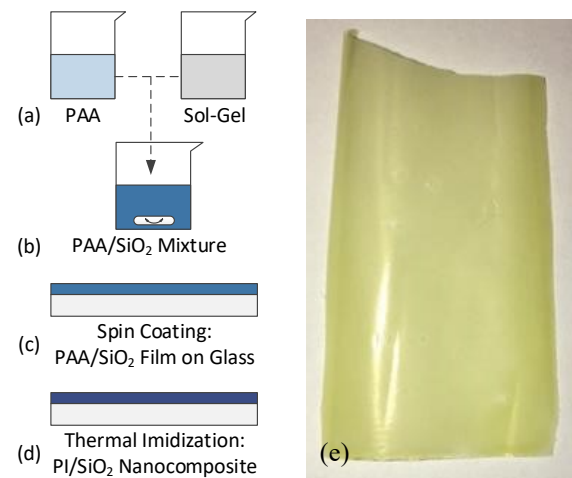


Fig. 1. Preparation of PI/ SiO_2 nanocomposites. (a)-(d) Fabrication process of the nanocomposite using PAA and sol-gel precursors. (e) A cured, imidized PI/ SiO_2 film peeled off from the glass slide.

SEM is used to inspect the overall quality of the film and the dispersion of nanoparticles in the nanocomposite. Fig. 2(a) shows that the SiO_2 nanoparticles are uniformly distributed in the host polymer without agglomerations. The particle sizes range from 50 nm to 500 nm, as a result of the particle formation and growth at different times in the sol-gel process.

The dielectric strengths of the thin-film samples are obtained using high-voltage DC breakdown tests. The testing process and related parameters follow the ASTM-D3755 standard for dielectric breakdown measurements. After a sample is broken down at a high DC voltage, it is inspected with both SEM and optical microscopy to ensure that the dielectric breakdown occurs through the thickness direction of the sample, instead of through flash over (across the sample surface) or spark over (through the air). Fig 2(b) shows an SEM image of a breakdown point in a nanocomposite sample. The diameter of the through hole is approximately 50 μm . However, the affected area is much large, approximately 100 μm in diameter.

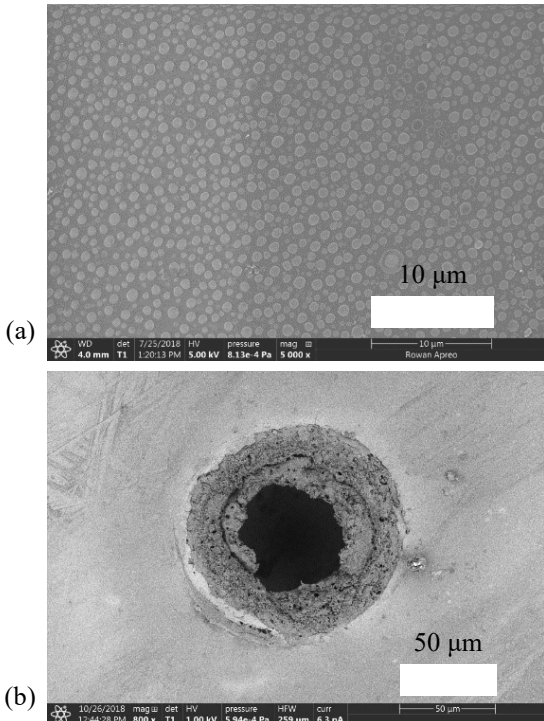


Fig. 2. SEM inspection of the samples. (a) PI/SiO₂ nanocomposite with 10 wt.% SiO₂ nanoparticles. (b) Dielectric breakdown point in a sample.

Two groups of PI/SiO₂ nanocomposite samples with 4 wt.% and 10 wt.% nanoparticles, along with Kapton[®], are tested at both room temperature (300 K) and cryogenic temperature (164 K). Fig. 3 shows the dielectric performance of these samples. Kapton[®] samples show an average dielectric strength of 295 kV/mm at room temperature, which is similar to the reported value from its datasheet. The dielectric strengths of 4 wt.% and 10 wt.% SiO₂ nanocomposites are measured as 147 kV/mm and 159 kV/mm, respectively. The reduced values can be explained by the lower dielectric strength of SiO₂ (10-100 kV/mm) as compared to the host PI (100-300 kV/mm). Interestingly, the performances of these three samples at 164 K show reversed trends. The dielectric strengths of Kapton[®], 4 wt.% SiO₂, and 10 wt.% SiO₂ samples are obtained as 262 kV/mm, 184 kV/mm, and 230 kV/mm, respectively. It proves that the behavior of a nanocomposite could be drastically different from its host polymer.

Although the dielectric strength of the nanocomposites is lower than the pure polymer, other potential features such as enhanced mechanical strength and modified thermal properties can bring unique advantages to the host material. The ability to tune a material's properties alone already is a

valuable tool for designing nanocomposites for specific applications.

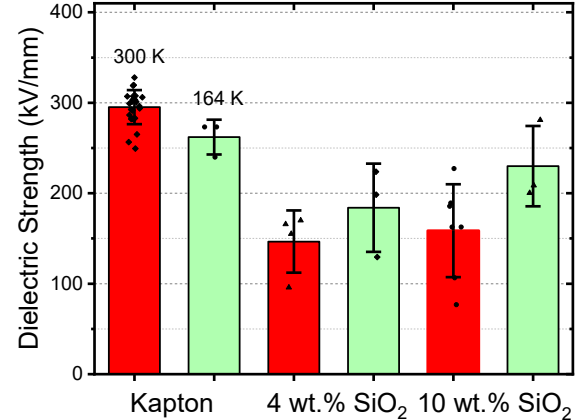


Fig. 3. Dielectric strengths of Kapton[®] and PI/SiO₂ nanocomposite at two different temperatures.

In the full-length paper, we will first expand the discussion on material preparation, sample quality, and dielectric testing results. Second, we will show material performance with more SiO₂ concentration values. Third, we will perform low-temperature testing in a wider range of temperatures. These results will show how nanocomposites perform under different conditions and how their performance differs from the pure polymer counterparts. This study will help advance our knowledge on nanocomposite research.

ACKNOWLEDGMENT

This work was supported by the Department of Defense under the Naval Engineering Education Consortium (NEEC) with the grant number NSWC IHEODTD N00174-17-1-0008 and the National Science Foundation with the grant number CBET #1625816. The authors would like to thank the Applied Superconductivity Team at the Naval Surface Warfare Center Philadelphia Division (NSWCPD) for their helpful discussion on cryogenic testing of dielectrics.

REFERENCES

- [1] K. Müller, E. Bugnicourt, M. Latorre, M. Jorda, Y. Echegoyen Sanz, J. M. Lagaron, O. Miesbauer, A. Bianchin, S. Hankin, U. Bötz, G. Pérez, M. Jesdinszki, M. Lindner, Z. Scheuerer, S. Castelló, and M. Schmid, "Review on the Processing and Properties of Polymer Nanocomposites and Nanocoatings and Their Applications in the Packaging, Automotive and Solar Energy Fields," *Nanomaterials*, vol. 7, p. 74, 2017.
- [2] S. Fu, Z. Sun, P. Huang, Y. Li, and N. Hu, "Some basic aspects of polymer nanocomposites: A critical review," *Nano Materials Science*, vol. 1, pp. 2-30, 2019.
- [3] X. Cui, G. Zhu, W. Liu, K. Wang, F. Ren, H. Fu, and X. Yan, "Mechanical and dielectric properties of polyimide/silica nanocomposite films," *Plastics, Rubber and Composites*, vol. 44, pp. 435-439, 2015.
- [4] S. Diahiam, S. Zelmat, M. L. Locatelli, S. Dinculescu, M. Decup, and T. Lebey, "Dielectric breakdown of polyimide films: Area, thickness and temperature dependence," *IEEE Transactions on Dielectrics and Electrical Insulation*, vol. 17, pp. 18-27, 2010.
- [5] J. Engel, J. Chen, and C. Liu, "Development of polyimide flexible tactile sensor skin," *Journal of Micromechanics and Microengineering*, vol. 13, p. 359, 2003.
- [6] Y. H. Zhang, Y. Li, S. Y. Fu, J. H. Xin, W. A. Daoud, and L.F. Li, "Synthesis and cryogenic properties of polyimide–silica hybrid films by sol–gel process," *Polymer*, vol. 46, pp. 8373-8378, 2005.

Gradual RESET modulation by intentionally oxidized titanium oxide for multilayer-hBN RRAM

Po-An Chen

Institute of Microelectronic,

Department of Electrical Engineering

National Cheng Kung University

Tainan, Taiwan

q18041129@mail.ncku.edu.tw

Wei-Chou Hsu

Institute of Microelectronic,

Department of Electrical Engineering

National Cheng Kung University

Tainan, Taiwan

wchsu@eembox.ee.ncku.edu.tw

Meng-Hsueh Chiang

Institute of Microelectronic,

Department of Electrical Engineering

National Cheng Kung University

Tainan, Taiwan

mhchiang@mail.ncku.edu.tw

Abstract – Hexagonal boron nitride (hBN) has recently become a promising material for being utilized as switching layer while resistive random-access memory (RRAM) continues to emerge. In this work, the insertion of intentionally oxidized titanium oxide between multilayer hBN and top electrode modulates the RESET characteristic into gradual RESET, which can promote the reliability for multilayer-hBN RRAM. The consistency of high resistance state (HRS) can be improved by preventing the RRAM devices from abrupt RESET, and then the good uniformity of SET and RESET voltages can be obtained. The effective modulation can be attributed to the multiple thin conductive filaments, and the inhibition for Ti penetration. Significant reliability improvement for multilayer-hBN RRAM can be achieved through the demonstrated simple process control.

Keywords—RRAM, hBN, reliability, gradual RESET, 2D materials.

A. Introduction

The demand for non-volatile memory from edge computing in applications of artificial intelligence (AI) and internet of things (IoTs) has increased rapidly. Researchers are eager to search for promising memories while scaling challenges of conventional non-volatile memories are waiting to be solved. Among the emerging memory devices, resistive random access memory (RRAM) is considered to be the great candidate due to its several advantages, such as simple structure, high operation speed, low power consumption, and CMOS compatible process [1-5]. Various materials have been utilized as the switching layer of RRAM, and 2D materials have become the novel competitor in the past few years [6-9].

Among the various 2D materials, hexagonal boron nitride (hBN) has been known as the most optimum 2D material for serving as switching layer because of its insulative characteristic. In addition, stable chemical characteristic and good mechanical strength of hBN make it much advantageous. Therefore, hBN has gained the most publications of the applications in RRAM among 2D materials, including the implementation in electronic synapses in the recent years [6-7, 9]. It looks like hBN can serve as a good switching layer, combined with the atomistic thickness of 2D materials. However, the investigation of reliability for hBN RRAM has not been addressed in detail.

In this work, we found that two types of RESET characteristics, abrupt RESET and gradual RESET, existing during the operation of multilayer-hBN RRAM (multi-hBN RRAM). For abrupt RESET, the resistance state changes from low resistivity back to high resistance state (HRS) drastically and randomly, which leads to bad reliability. In contrast, gradual RESET could achieve a much consistent HRS and the uniform distribution of SET and RESET voltages, resulting in good endurance as well. For this reason, we modulated the switching layer of multi-hBN RRAM with an intentionally

oxidized titanium oxide to achieve the controllable gradual RESET. An effective modulation can be implemented through a simple experiment process flow, and finally the multi-hBN RRAM with better reliability performance can be obtained.

B. Experiment processes and DC measurement

a) Experiment processes: Multilayer hBN was synthesized on the copper foil through CVD, and then the multi-hBN RRAM was fabricated on the copper foil directly without a transfer to avoid the uncertainties associated with additional process steps. A thin titanium metal with 3 nm thickness was deposited on the multilayer hBN by e-beam evaporator. After the deposition, the sample was placed on the hot plate at 120 °C for 1 hour, and stored in the ambient of clean room overnight to oxidize the thin titanium metal into titanium oxide. The device fabrication was then completed by the deposition of Ti (7nm) and Al (100 nm) with shadow mask to pattern the top electrode. The top view of as-fabricated modulated multi-hBN RRAM with different area sizes for top electrodes and the device structure are shown in Fig. 1 (a) and Fig. 1 (b) respectively. The numbers (light color to the left) in Fig. 1 (a) represent the sizes of the top electrode in μm^2 .

b) DC measurement: During the DC measurement for multi-hBN RRAM, the thick aluminum metal served as the top electrode (TE), and the copper foil served as the bottom electrode (BE) directly. The voltage stress was always given to the top electrode, and the bottom electrode was always grounded. The compliance current was set to 1 mA during the SET operation to prevent from permanent breakdown.

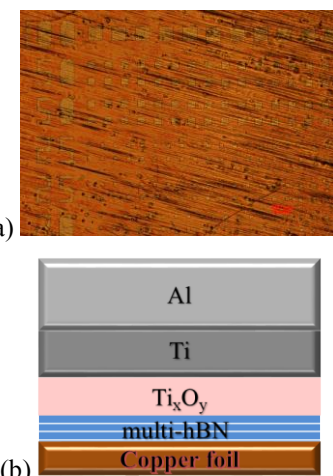


Fig. 1. (a) Top view of the as-fabricated and (b) the device structure of titanium-oxide modulated multi-hBN RRAM.

C. Results and discussion

The IV results shown in this work were all measured from $25\text{-}\mu\text{m}^2$ multi-hBN RRAM devices. An effective modulation by titanium oxide can be observed in Fig. 2 (a). After initial positive-bias forming process, the IV characteristics of the modulated multi-hBN RRAM between each cycle is uniform and stable. The RESET characteristic of the modulated devices is gradual RESET, in which the resistance state is gradually stressed back to high resistance state by negative bias. The mechanism for gradual RESET can be attributed to the one-by-one rupture of multiple thin filaments within the switching layer. This mechanism can be proven by the step-by-step RESET through increasing RESET voltage as shown in Fig. 2 (b). The gradual RESET can gently recover the resistance state back to HRS, and also make the HRS more controllable.

In contrast, the IV characteristics of the multi-hBN RRAM without titanium-oxide modulation shows an unstable and non-uniform IV distribution, which can be observed in Fig. 3. The clear difference is the characteristic of abrupt RESET, leading to substantial RESET and random distribution of HRS. Usually, abrupt RESET is caused by the rupture of a single thick filament within the switching layer by joule heating. For the multi-hBN RRAM without titanium-oxide modulation, the thick filament has been proven to be the penetration of Ti atoms from top electrode [6]. Therefore, we can conclude that the effective modulation can be achieved by the insertion of titanium oxide which can inhibit excessive Ti atom penetration, and modulate the RESET process from abrupt into gradual RESET, resulting in uniform IV distribution and better reliability with good endurance.

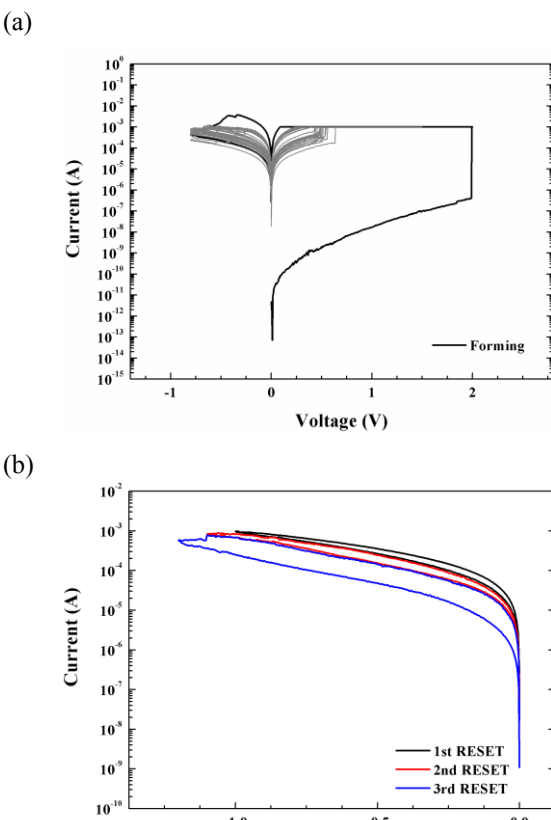


Fig. 2. (a) The IV characteristics of the multi-hBN RRAM with titanium-oxide modulation, which shows good uniformity and good endurance with gradual RESET. (b) The multiple RESET for multi-hBN RRAM with titanium-oxide modulation.

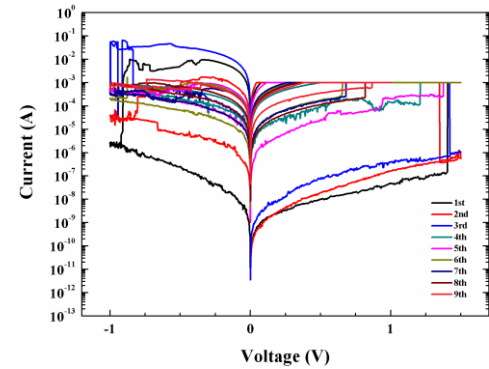


Fig. 3. The IV characteristics of the multi-hBN RRAM without titanium-oxide modulation, which shows poor uniformity and poor endurance with abrupt RESET.

D. Conclusion

The effective RESET modulation can be achieved by the insertion of an intentionally oxidized titanium oxide between multilayer hBN and active top electrode. The modulated multi-hBN RRAM shows uniform IV distribution and good endurance with gradual RESET characteristic. The effective modulation can be attributed to the multiple thin filaments and the inhibition for Ti penetration. Through the demonstrated simple process control, the multi-hBN RRAM with good reliability can be obtained.

ACKNOWLEDGMENT

This work was supported in part by the Ministry of Science and Technology and Taiwan Semiconductor Research Institute for technical support.

REFERENCES

- [1] F. Pan, et al. "Nonvolatile resistive switching memories-characteristics, mechanisms and challenges." *Progress in Natural Science: Materials International* 20 (2010): 1-15.
- [2] F. Pan, S.Gao, C.Chen, C.Song, and F.Zeng, "Recent progress in resistive random access memories: materials, switching mechanisms, and performance." *Materials Science and Engineering: R: Reports* 83 (2014): 1-59.
- [3] T.C. Chang, K.C. Chang, T.M. Tsai, T.J. Chu, Simon M.Sze, "Resistance random access memory." *Materials Today* 19.5 (2016): 254-264.
- [4] L. Zhu, J. Zhou, Z. Guo, and Z. Sun, "An overview of materials issues in resistive random access memory." *Journal of Materomics* 1.4 (2015): 285-295.
- [5] D. Ielmini, "Resistive switching memories based on metal oxides: mechanisms, reliability and scaling." *Semiconductor Science and Technology* 31.6 (2016): 063002.
- [6] C. Pan, et al. "Coexistence of grain - boundaries - assisted bipolar and threshold resistive switching in multilayer hexagonal boron nitride." *Advanced Functional Materials* 27.10 (2017): 1604811.
- [7] X. Wu, et al. "Thinnest Nonvolatile Memory Based on Monolayer h - BN." *Advanced Materials* (2019): 1806790.
- [8] R. Ge, et al. "Atomristor: nonvolatile resistance switching in atomic sheets of transition metal dichalcogenides." *Nano letters* 18.1 (2017): 434-441.
- [9] Y. Shi, et al. "Coexistence of volatile and non-volatile resistive switching in 2D h-BN based electronic synapses." *2017 IEEE International Electron Devices Meeting (IEDM)*. IEEE, 2017.

Understanding low-frequency noise in ion-sensitive field-effect-transistor sensors operating in electrolytes

Zhen Zhang

Abstract: Electronic sensing of ions in electrolytes using ion sensitive field-effect transistor (ISFET) technology finds a vast variety of applications in chemistry and biomedicine. Low-frequency noise (LFN) of an ISFET-based sensor is of significant implications for the sensor signal-to-noise performance in real sensing applications. The LFN of the ISFET sensor is contributed internally from both the solid/liquid (liquid noise) and solid/solid interfaces (device noise), and externally from environmental interferences. In this talk, I will present our understanding of the LFN in the ISFET-based sensors and propose possible solutions to control the LFN. I will start with our systematic investigation of the solid/liquid interfacial noise¹⁻³ especially its relation to the surface binding/de-binding dynamic properties. Insights into how detailed surface properties may affect the noise performance of an ion sensor operating in electrolytes will be provided. For the well-understood solid/solid interfacial noise, I will show a novel Schottky junction gate design for the silicon ISFET sensor, where carrier trapping/detrapping processes at the conventional noisy gate oxide/semiconductor interface are eliminated⁴⁻⁶. Our sensor with the new gate junction exhibits significantly reduced noise compared to the reference conventional ISFET devices operated at both inversion and depletion modes. Then, I will turn to our strategy in suppressing the environmental interferences by intimately integrating a bipolar amplifier with the ISFET for an immediate amplification of the ISFET current⁷. Two different bipolar amplifier device designs will be presented⁷⁻⁸. Finally, I will conclude my talk by giving some perspectives of single charge detection using the ISFET-based sensor.

Other contributing authors: D. Zhang, X. Chen, S. Chen, Q. Hu, H. Norström, S.-L. Zhang, P. Solomon (IBM)

1. Da Zhang, Indrek Must, Nathan L. Netzer, Xingxing Xu, Paul Solomon, Shi-Li Zhang, and Zhen Zhang, ‘Direct assessment of solid–liquid interface noise in ion sensing using a differential method’, *Appl. Phys. Lett.*, 108, 151603 (2016)
2. Da Zhang, Paul Solomon, Shi-Li Zhang, and Zhen Zhang, ‘An impedance model for the low-frequency noise originating from the dynamic hydrogen ion reactivity at the solid/liquid interface’, *Sensors and Actuators B: Chemical*, 254, 363 (2018), DOI:10.1016/j.snb.2017.07.054.
3. Da Zhang, Paul Solomon, Shi-Li Zhang, and Zhen Zhang, ‘Correlation of Low-Frequency Noise to the Dynamic Properties of the Sensing Surface in Electrolytes’ *ACS Sensors*, 2 (8), 1160 (2017) DOI:10.1021/acssensors.7b00285

4. Xi Chen, Si Chen, Qitao Hu, Shi-Li Zhang, Paul M Solomon, and Zhen Zhang, ‘Device noise reduction for silicon nanowire field-effect-transistor based sensors by using a Schottky junction gate’, *ACS Sensors* (2019), DOI: 10.1021/acssensors.8b01394
5. Xi Chen, Si Chen, Shi-Li Zhang, Paul M Solomon, and Zhen Zhang, ‘Low Noise Schottky Junction Tri-gate Silicon Nanowire Field-effect Transistor for Charge Sensing’, *IEEE transaction on electron devices* (under revision).
6. Xi Chen, Si Chen, Paul M Solomon, and Zhen Zhang, ‘Top-bottom gate coupling effect on low frequency noise in a Schottky junction gated silicon nanowire field-effect transistor’, *IEEE Journal of the Electron Devices Society* (under review)
7. Da Zhang, Xindong Gao, Si Chen, Hans Norström, Ulf Smith, Paul Solomon, Shi-Li Zhang, Zhen Zhang, “An ion-gated bipolar amplifier for ion sensing with enhanced signal and improved noise performance”, *Appl. Phys. Lett.*, 105, 082102 (2014)
8. Qitao Hu, Xi Chen, Hans Norström, Shuangshuang Zeng, Yifei Liu, Fredrik Gustavsson, Shi-Li Zhang, Si Chen, and Zhen Zhang, ‘Current gain and low-frequency noise of symmetric lateral bipolar junction transistors on SOI’, *48th European Solid-State Device Research Conference (ESSDERC)*, September 3 - 6, 2018, DRESDEN, Germany

Device Modeling for High Efficiency Lead Free Perovskite Solar Cell with Cu₂O as Hole Transport Material

A. C. Soibam

*Microelect. and VLSI Design Group
Dept. of Elect. and Comm. Engineering
National Institute of Technology
Silchar, 788010
Assam, India
arunasoibam@gmail.com*

M. Thway

*Solar Energy Research Institute of
Singapore, Department of Electrical
and Computer Engineering,
National University of Singapore
Singapore, 117574
thway@nus.edu.sg*

T. R. Lenka

*Microelect. and VLSI Design Group
Dept. of Elec. and Comm. Engineering
National Institute of Technology
Silchar, 788010
Assam, India
t.r.lenka@ieee.org*

K. Dey

*Cavendish Laboratory
Department of Physics
University of Cambridge
JJ Thomson Avenue, CB3 0HE
Cambridge, UK
kd426@cam.ac.uk*

F. Lin

*Solar Energy Research Institute of
Singapore
National University of Singapore
Singapore, 117574
lin.fen@nus.edu.sg*

Abstract—In this work the device simulation of lead-free perovskite solar cell with CH₃NH₃SnI₃ as absorber perovskite material was performed. The parameters which affect the overall performance were investigated and it was found that absorber thickness, doping concentrations of HTM, ETM and perovskite and the temperature influence the solar cell performance. The optimized performance of the perovskite solar cells with PCE of 30.59%, was obtained when the thicknesses of perovskite was 300nm and the doping concentrations of Cu₂O, PCBM and perovskite were 9×10²¹cm⁻³, 1×10²¹cm⁻³ and 1×10¹³cm⁻³ respectively.

Keywords—Perovskite, Lead free, Copper oxide, SCAPS

I. INTRODUCTION

In recent years, organic-inorganic metal halide perovskites have attracted significant attention as absorber materials for solar cells, owing to their excellent optoelectronic properties, low cost fabrication and high photovoltaic performance [1]. In most of the conventional perovskite (bandgap ~ 1.6 eV) solar cells, APbX₃ (A=CH₃NH₃⁺, HC(NH₂)₂⁺, Cs⁺, Rb⁺; X= I⁻, Br⁻, Cl⁻) is used as the active layer for absorption of incoming sunlight [2,3]. However, the well-known toxicity of lead (Pb) possess serious concerns regarding the possible health and ecological hazards [1]. Hence, in order to avoid toxicity, CH₃NH₃SnI₃ is being used here as the absorber material having a direct bandgap of 1.30eV which is close to the ideal bandgap as postulated by the Shockley-Queisser limit [4]. Moreover, among all the CH₃NH₃BX₃ (B = Sn, Pb and X = Cl, I, Br) compounds, CH₃NH₃SnI₃ has the highest light absorption range and most appropriate optical properties to use in optoelectronic applications. In this work, Cu₂O is employed as the hole transport material (HTM) and PCBM as the electron transport material (ETM). The proposed perovskite solar cell device is explored using inverted planar (p-i-n) type structure which is more desirable due to its less current hysteresis, low temperature and simple fabrication process [5].

II. DEVICE STRUCTURE AND SIMULATION

SCAPS is a 1D simulation software which primarily analyses the device performance by solving the three important semiconductor equations viz. Poisson's equation, carrier-continuity equation and drift diffusion equation [8]. The simulated device structure for lead-free perovskite solar cell proposed in this study is shown in Fig. 1.

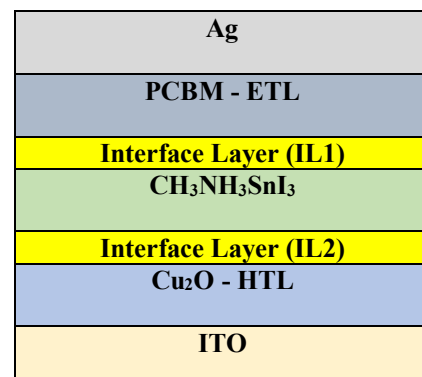


Fig. 1. Simulated device structure of PSC.

TABLE I. SIMULATION PARAMETERS OF THE LEAD-FREE PEROVSKITE SOLAR CELL

Parameter	Cu ₂ O	IL1	CH ₃ NH ₃ SnI ₃	IL2	PCBM
Thickness (nm)	10	1	300	1	50
E _g (eV)	2.17 [2]	1.3	1.3 [1]	1.3	2 [5]
χ (eV)	3.2 [2]	4.2	4.2 [1]	4.2	3.9 [5]
ε _r	7.11 [2]	10	10 [1]	10	4 [5]
N _c (cm ⁻³)	2.02×10 ¹⁷ [2]	1×10 ¹⁸	1×10 ¹⁸	1×10 ¹⁸	1×10 ²¹ [5]
N _v (cm ⁻³)	1.1×10 ¹⁹ [2]	1×10 ¹⁹	1×10 ¹⁹	1×10 ¹⁹	2×10 ²⁰ [5]
μ _n (cm ² /Vs)	2.0×10 ² [2]	2	2 [6]	2	0.01 [5]
μ _p (cm ² /Vs)	8.0×10 ¹ [2]	2	2 [6]	2	0.01 [5]
N _d (cm ⁻³)	-	-	-	-	1×10 ²¹
N _a (cm ⁻³)	9×10 ²¹	1×10 ¹³	1×10 ¹³	1×10 ¹³	-
N _i (cm ⁻³)	-	1×10 ¹⁸	2.5×10 ¹³	1×10 ¹⁸	-

III. RESULTS AND DISCUSSION

The effect of material parameters and temperature to the power conversion efficiency (PCE) of the solar cell is shown in the following graphs. The response of the solar spectrum which affects the efficiency of the solar cell is largely influenced by the thickness of the absorber perovskite material. In order to investigate its effect, the thickness is varied from 100nm to 500nm and observed that the optimized value of PCE is obtained as 30.59% at perovskite material thickness of 300nm in Fig. 2.

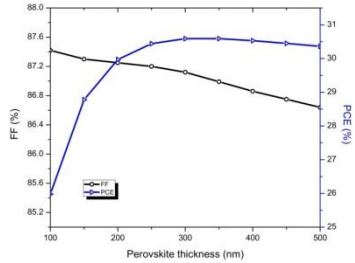


Fig. 2. FF and PCE as a function of perovskite absorber layer thickness.

The doping concentration of the materials are related to the energy band and recombination rate, thereby it decides the electrical behavior of the device, hence it has a considerable influence on solar cell performance as shown in Fig. 3, 4 and 5. A heavily p-type doped perovskite material short circuited the solar cell and does not work as an effective absorber hence a sharp decline in the curve of PCE is observed in Fig. 5.

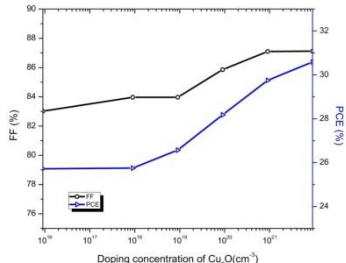


Fig. 3. FF and PCE as a function of Cu_2O doping concentration.

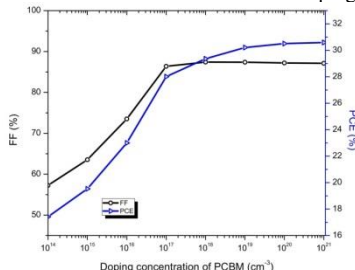


Fig. 4. FF and PCE as a function of PCBM doping concentration.

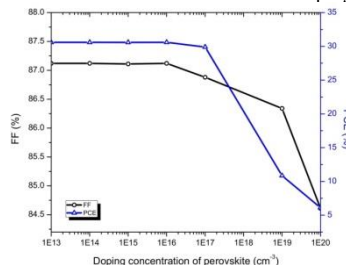


Fig. 5. FF and PCE as a function of perovskite doping concentration.

The effect of temperature to the performance of solar cell is necessary to be discussed as the solar cell is kept exposed to the environment where a wide range of temperature variations occur. In Fig. 6, it is shown that FF and PCE decrease very rapidly due to the increase in recombination rate.

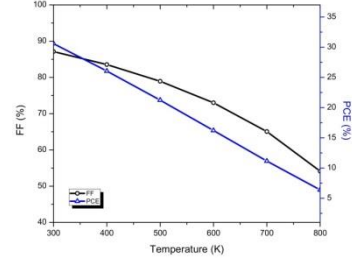


Fig. 6. FF and PCE as a function of temperature.

IV. CONCLUSION

A highly efficient as well as lead free perovskite solar cell based on $\text{CH}_3\text{NH}_3\text{SnI}_3$ as absorber material with Cu_2O as hole transport material and PCBM electron transport layer was investigated and shown that it can achieve high power conversion efficiency of above 30%. Some factors which influence the device performance were discussed and the maximum value of PCE is obtained as 30.59% by optimizing the values of absorber thickness and the doping concentrations of HTM, ETM and perovskite material. These results show that this lead-free perovskite solar cell can be a potential choice of achieving high efficiency and toxic free solar cell.

ACKNOWLEDGMENT

The authors acknowledge Dr. Marc Burgelman, University of Gent for providing SCAPS-1D solver to carry out the research work. This publication is an outcome of the R&D work undertaken in the project under the Visvesvaraya PhD Scheme of Ministry of Electronics & Information Technology, Government of India, being implemented by Digital India Corporation.

REFERENCES

- [1] F. Anwar, R. Mahbub, S. S. Satter, and S. M. Ullah, "Effect of Different HTM Layers and Electrical Parameters on ZnO Nanorod-Based Lead-Free Perovskite Solar Cell for High-Efficiency Performance," International Journal of Photoenergy, vol. 2017. DOI: 10.1155/2017/9846310.
- [2] M. I. Hossain, F. H. Alharbi, N. Tabet, "Copper oxide as inorganic hole transport material for lead halide perovskite based solar cells," Solar Energy, pp. 370–380, Aug 2015.
- [3] X. Wei, X. Wang, H. Jiang, Y. Huang, A. Han, Q. Gao, J. Bian, Z. Liu, "Numerical simulation and experimental validation of inverted planar perovskite solar cells based on NiOx hole transport layer," Superlattices and Microstructures, pp. 383-393, Sept 2017.
- [4] W. Shockley, and H. J. Queisser, "Detailed Balance Limit of Efficiency of p-n Junction Solar Cells," Journal of Applied Physics, 32, 510, 1961.
- [5] P. Zhao, Z. Liu, Z. Lin, D. Chen, J. Su, C. Zhang, J. Zhang, J. Chang, Y. Hao, "Device simulation of inverted $\text{CH}_3\text{NH}_3\text{PbI}_{3-x}\text{Cl}_x$ perovskite solar cells based on PCBM electron transport layer and NiO hole transport layer," Solar Energy, pp. 11–18, April 2018.
- [6] T. Minemoto, and M. Murata, "Device modeling of perovskite solar cells based on structural similarity with thin film inorganic semiconductor solar cells," Journal of Applied Physics, August 2014.

Graphene Assisted Chemical Nucleation of Diamond

Yonhua Tzeng, Fellow, IEEE
 Institute of Microelectronics
National Cheng Kung University
 One University Road
 Tainan, Taiwan
tzengyo@mail.ncku.edu.tw

This paper reports a breakthrough diamond CVD technology. Diamond is a strategic electronic, optical, and chemical material. Coating of diamond films on non-diamond substrates requires diamond nuclei to be formed first. Diamond nucleation is achieved by either bias enhanced nucleation or inserting diamond debris or diamond nanoparticles made from detonation or crushing of larger diamond particles in the substrate. The diamond seeding process relies on existing diamond. It avoids the need for nucleating diamond on the substrate where a diamond film is to be coated. However, to insert diamond seeds in complicated substrate surfaces is not an easy job. For example, the side walls of a trench and the internal surfaces of a small tubing are difficult to reach for inserting high density diamond seeds. The seeding is usually conducted in an ultrasonic bath to agitate diamond particles for them to impact the substrate for diamond particles to adhere to the substrate surfaces. This is not an easy job for substrates of a very large area. The consumption of diamond particles and the space it takes for the equipment are also expensive.

Bias enhanced diamond nucleation relies on an applied negative bias at the substrate to accelerate positive ions from the plasma to bombard the substrate surface where carbon atoms are deposited and trying to form various carbon phase. Ion bombardment results in a wide variety of carbon bonds between carbon atoms and carbon structures of different phases including sp₃ bonded diamond phase. By chemically or physically suppressing the growth of non-diamond carbon phase and promoting the growth of diamond, diamond nuclei are formed while non-diamond carbons are etched away. The diamond nuclei thus formed are subjected to proper environments for the growth into larger diamond grains. Neighboring diamond grains join each other to form grain boundaries. Many diamond grains thus form a continuous diamond film.

We have demonstrated that by transferring graphene on a substrate with a tungsten coating and letting the graphene coated tungsten be subjected to the typical diamond plasma assisted CVD conditions in 1-2% methane diluted by hydrogen diamond nucleation succeeds without diamond seeding nor bias enhanced nucleation process. Subsequent growth of diamond resulted in the formation of a continuous diamond film. This is the first time that a diamond film is grown from chemical nucleation of diamond. It is thus an exciting advancement in the development of diamond CVD technology. However, transferring a pre-synthesized graphene on a destination substrate is tedious. It is desirable that transfer-free graphene can results in the chemical nucleation of diamond on the substrates where diamond films are to be deposited. This paper reports graphene induced diamond nucleation and state-of-the-art of transfer-free graphene assisted diamond nucleation.

Diamond has been successfully grown on silicon by transferred or transfer-free graphene induced chemical

nucleation without bias enhanced nucleation nor seeding by diamond nanoparticles. Raman spectrum of diamond grown on a non-diamond substrate using the transfer-free graphene induced chemical nucleation method shows clearly a diamond Raman peak at 1332 cm⁻¹. This accomplishment is currently patent pending. Extensive research and development is currently undertaken to explore this new means of synthesizing diamond and coating of diamond on practically useful substrates.

ACKNOWLEDGMENT

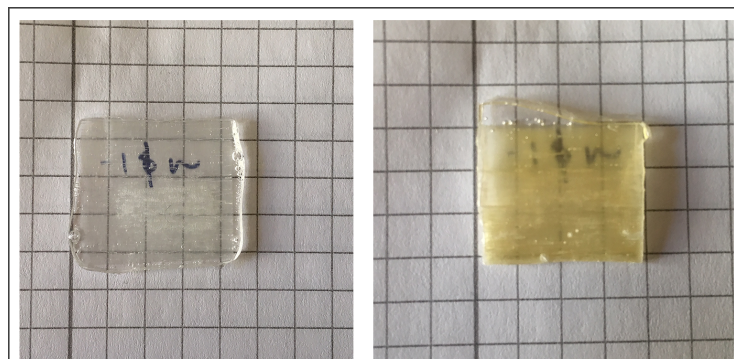
This work is partially supported by the Ministry of Science and Technology in Taiwan under the grant MOST 106-2221-E-006-173-MY3.

REFERENCES

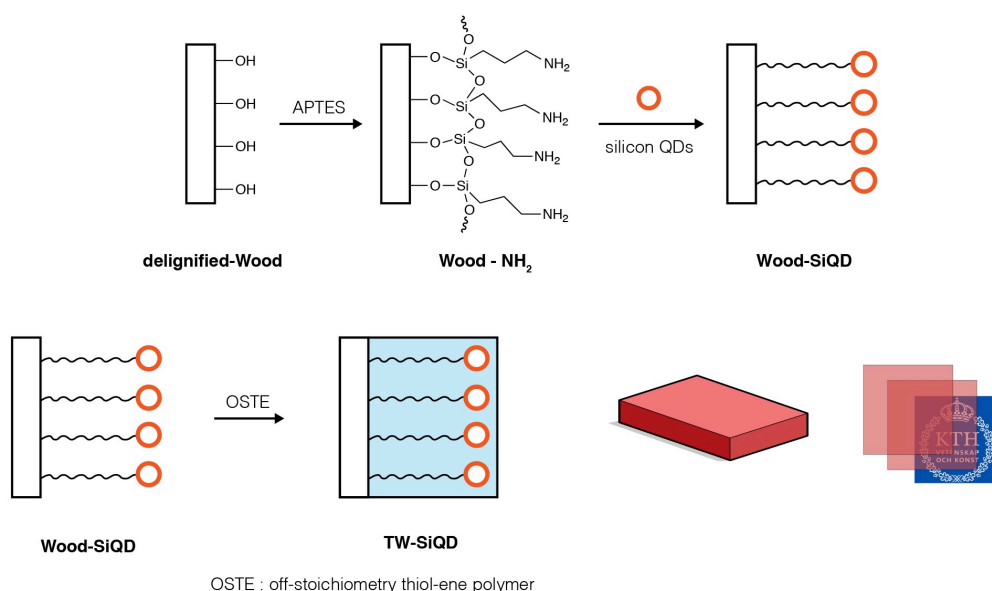
- [1] Yonhua Tzeng, Orlando H. Auciello, Chuan-Pu Liu, Chi-Kai Lin Yin-Wei Cheng. Diamond Film Coated Electrode for Battery. US Patent #9,196,905, November 24, 2015.
- [2] Yonhua Tzeng, Wai-Leong Chen. Method of Transferring a Graphene Film. US Patent #9,181,100, November 10, 2015.
- [3] Yonhua Tzeng, Graphene and Its Growth. US patent #8,865,105, Oct. 21, 2014.
- [4] Y. Tzeng, Method of Plasma Enhanced Chemical Vapor Deposition of Diamond Using Methanol-based Solutions. US Patent #7,622,151, November 24, 2009.
- [5] Y. Tzeng, Method of hot-filament chemical vapor deposition of diamond. US Patent #6,558,742, May 6, 2003.
- [6] Yonhua Tzeng, Ji-Heng Jiang, Method of Diamond Growth. ROC patent # I447253, August 1, 2014.
- [7] Y. Tzeng and C. Wu. Method of diamond nucleation. ROC patent #I429779, March 11, 2014.

1
2
3
4
5
6 Multifunctional SiQD-embedded transparent wood (TW)
7 Alden M. Clemments, Ilya Sychugov

8
9
10
11
12
13
14
15
16
17
18
19
20 Owing to its unique physical structure, wood is an ideal template for embedding a variety of
21 nanomaterials, such as quantum dots (QDs), metal nanoparticles, catalysts, etc. Bulk porosity,
22 fiber alignment and orientation, high strength, and low thermal conductivity are but a few of the
23 properties that make it a suitable scaffold for nanoparticle support. Of the many applications,
24 quantum dot/wood composites have recently received much interest for their potential use as light
25 harvesters. By impregnating quantum dots along the cell wall and throughout the lumen, high
26 payloads and optimal distribution/dispersion can be achieved. Synthetically, this remains
27 challenging due to the delicate organic framework. Additionally, in order to optimize the
28 optical/electronic output, wood must first be made transparent. This is accomplished by removing
29 lignin and other light-absorbing compounds. What remains is structurally similar to that of the
30 native material, but void of color. Transparency is achieved by subsequently filling the porous
31 cavities with a refractive index matching polymer (**Figure 1**). Here, we demonstrate that by
32 employing a variety of chemical methods (**Figure 2**), improvements in QD loading, distribution,
33 and ultimately optical output are drastically improved.



34
35
36
37
38
39
40
41
42
43 **Figure 1** Comparison of TW (left) and SiQD-embedded TW



55
56
57
58
59
60
61
62
63
64
65 **Figure 2** Synthesis of SiQD-embedded transparent wood.

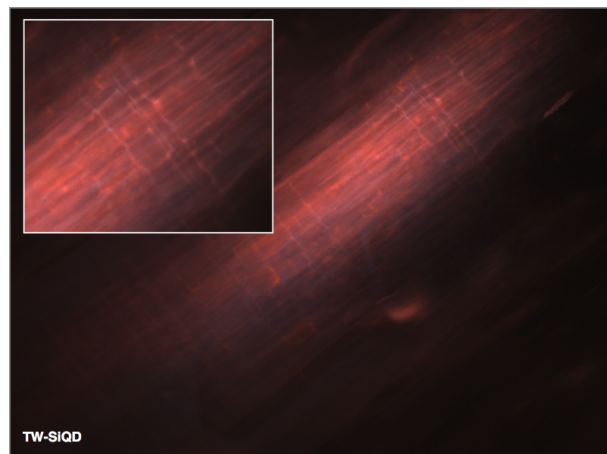


Figure 2 photoluminescent image of SiQD-embedded TW.
Distribution of SiQDs along the fibers can be observed.

Modeling Photon Migration in Nanostructured Organic Materials

1 Adil Baitenov

2 *Applied Physics*3 *KTH*

4 Stockholm, Sweden

5 baitenov@kth.se

6 Hui Chen

7 *Fibre and Polymer Technology*8 *Wallenbergs Wood Science Center, KTH*

9 Stockholm, Sweden

10 huch@kth.se

11 Elena Vasileva

12 *Applied Physics*13 *KTH*

14 Stockholm, Sweden

15 vasileva@kth.se

16 Lars Berglund

17 *Fibre and Polymer Technology*18 *Wallenberg Wood Science Center, KTH*

19 Stockholm, Sweden

20 blund@kth.se

21 Sergei Popov

22 *Applied Physics*23 *KTH*

24 Stockholm, Sweden

25 sergeip@kth.se

26 Max Yan

27 *Applied Physics*28 *KTH*

29 Stockholm, Sweden

30 miya@kth.se

31 Ilya Sychugov

32 *Applied Physics*33 *KTH*

34 Stockholm, Sweden

35 ilyas@kth.se

In this work we present an analytical solution of diffusion model and a set of experiments that allow the determination of macroscopic properties, such as scattering and absorption coefficients, for a scattering and absorbing media. In particular, anisotropic transparent wood with micro- and nano-porosity was investigated.

Transparent wood (TW) is a highly scattering anisotropic material with aligned micro- (10 – 70 μm diameter fibers) and nano-structures ($\sim 5 \text{ nm}$ diameter nanofibrils). It is produced by removing lignin and infiltrating an index matching polymer. As it can be seen from fig. 1, TW has a

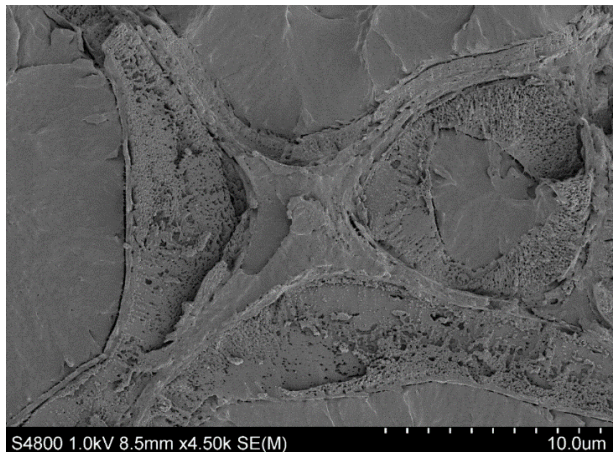


Fig. 1. Cross-sectional SEM image of a transparent wood sample revealing wood morphology and polymer filling cell lumens.

nonhomogeneous structure with scattering interfaces between fibers and cell walls, as well as between cell walls and the embedded polymer [1].

In order to describe propagation of light inside and through the TW, we implement the diffusion equation. It is widely used for highly scattering materials, for thicknesses where photon propagation becomes randomized [2]. The photon propagation can be described using a standard diffusion equation with a sink:

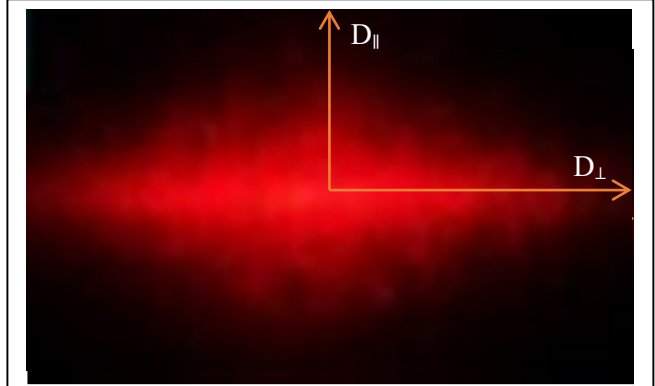


Fig. 2. Experimental light distribution after the TW sample for a normally impinging laser beam. As can be seen the scattering is anisotropic. Sample was placed with fibers aligned vertically.

$$\frac{\partial}{\partial t} p(x, y, z, t) = \left(D_{\perp} \cdot \left(\frac{\partial^2}{\partial x^2} + \frac{\partial^2}{\partial y^2} \right) + D_{\parallel} \frac{\partial^2}{\partial z^2} \right) p(x, y, z, t) - c \cdot \mu_a \cdot p(x, y, z, t), \quad (1)$$

where $D_{\parallel, \perp}$ is a diffusion coefficient, corresponding to the direction parallel and perpendicular to the fiber direction (fig. 2), c is a speed of light, μ_a is an absorption coefficient and p is a probability to locate a photon at time t at a position with (x, y, z) coordinates.

Diffusion coefficient depends both on the scattering coefficient μ_s and the absorption coefficient μ_a :

$$D = \frac{c}{3(\mu_a + \mu_s)} \quad (2)$$

In order to obtain these values, a dedicated experiment was performed. The scattering coefficient was measured by finding the fraction of ballistic photons passing through the sample. The measurement setup included the 633 nm He-Ne laser source, a sample placed perpendicularly to the incident beam, and an optical fiber placed 200 μm away from the sample output facet, which gathered light to the spectrometer for analysis. After performing measurements for different

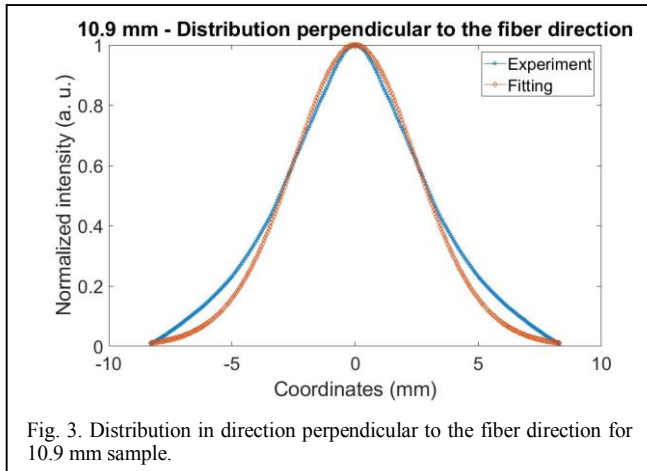


Fig. 3. Distribution in direction perpendicular to the fiber direction for 10.9 mm sample.

thicknesses, the scattering coefficient was found using a purely random process model with a constant rate μ_s :

$$T_{ballistic} = \exp(-\mu_s d) \quad (3)$$

where d is a sample thickness.

Diffusion coefficient is obtained from photon distribution after the TW sample by fitting distributions (fig. 3.). A scanning of the collection fiber was implemented to obtain spatial distribution of the light at the output facet of the sample. The following solution to the equation (1) is used to extract the diffusion coefficient value:

$$p(x, d) = \frac{1}{2\pi D} K_0 \left(\sqrt{\frac{c \cdot \mu_a}{D} \cdot (x^2 + d^2)} \right), \quad (4)$$

where K_0 is a hyperbolic Bessel function.

After obtaining diffusion and scattering coefficients the absorption coefficient can be calculated from (2).

Presented method allows predicting photon distribution and transmission, as well as effective path length in anisotropic highly scattering materials (especially biological tissues) analytically, with less initial data than other methods (for example Monte Carlo method that requires scattering and absorption coefficients as inputs) [3-5].

REFERENCES

- [1] Li, Y.; Yang, X.; Fu, Q.; Rojas, R.; Yan, M.; Berglund, L. A. "Towards Centimeter Thick Transparent Wood through Interface Manipulation," *J. Mater. Chem. A*, 6, 1094–1101, Dec 13 2017.
- [2] Johnson, P. M.; Bret, B. P. J.; Rivas, J. G.; Kelly, J. J.; Lagendijk, A. "Anisotropic Diffusion of Light in a Strongly Scattering Material," *Phys. Rev. Lett.*, 89 (24), 1–4, Dec 9 2002.
- [3] V. V. Tuchin, "Laght scattering study of tissues," *Physics-Uspekhi*, vol. 40, no. 5, pp. 495-515, May 1997.
- [4] Q. Fang, D. A. Boas, "Monte Carlo simulation of photon migration in 3D turbid media accelerated by graphics processing units," *Optics Express*, vol.17, no. 22, Oct 26 2009.
- [5] D. A. Boas, J.P. Culver, J. J. Stott, A. K. Dunn, "Three dimensional Monte Carlo code for photon migration through complex heterogeneous media including the adult human head," *Optics Express*, vol. 10, no. 3, pp. 159-170, Feb 2002.

Ligand Influence of Si Quantum Dots on Light Scattering of Quantum Dots-Polymer Composites

1 Jing Huang

2 Department of Applied Physics
 3 KTH-Royal Institute of Technology
 4 Stockholm, Sweden
 5 ORCID: 0000-0001-6005-2302

6 Jingjian Zhou

7 Department of Applied Physics
 8 KTH-Royal Institute of Technology
 9 Stockholm, Sweden
 10 ORCID: 0000-0002-6623-2491

11 Tommy Haraldsson

12 Department of Micro and Nanosystems
 13 KTH-Royal Institute of Technology
 14 Stockholm, Sweden
 15 tommyhar@kth.se

16 Jan Linnros

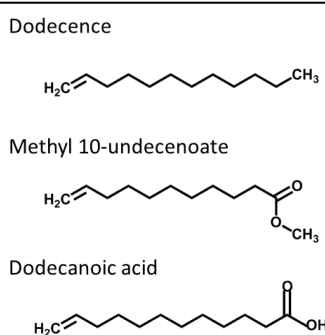
17 Department of Applied Physics
 18 KTH-Royal Institute of Technology
 19 Stockholm, Sweden
 20 ORCID: 0000-0002-5260-5322

21 Ilya Sychugov

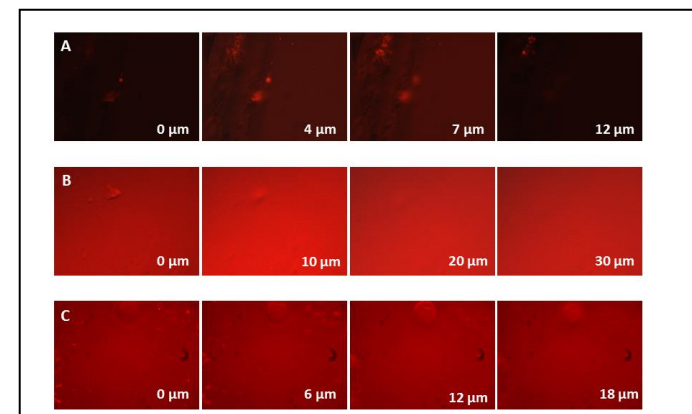
22 Department of Applied Physics
 23 KTH-Royal Institute of Technology
 24 Stockholm, Sweden
 25 ORCID: 0000-0003-2562-0540

26 Luminescent solar concentrator (LSC) is a promising
 27 technology to integrate semi-transparent PV glazing system
 28 into modern buildings and achieve the desired goal of the so-
 29 called ‘nearly zero energy building’ decreed by EU.[1-3]
 30 Silicon quantum dots (QDs) are good candidates as
 31 fluorophores in LSCs, due to their small overlap between
 32 absorption and emission spectra, potential to achieve high
 33 quantum yield, low toxicity and element abundance.[4, 5]
 34 Furthermore, our previous results showed that embedding Si
 35 QDs into off-stoichiometric thio-ene polymer (OSTE) can
 36 indeed enhance the photoluminescence quantum yield
 37 (PLQY) of Si QDs, indicating that Si QDs/OSTE composite
 38 is promising to be applied in LSCs.[6] However, in addition
 39 to high PLQY and small reabsorption loss of fluorophores,
 40 scattering loss is also needed to be suppressed to fabricate
 41 efficient LSCs with large size, since the luminescent light
 42 propagation toward the edge can be disrupted by the scattering
 43 in the waveguide. However, the polarity mismatch between Si
 44 QDs surface and OSTE always induce obvious agglomerates
 45 and serious scattering loss. Therefore, in order to improve
 46 performance of the LSCs, tuning the surface polarity of the Si
 47 QDs to be compatible with OSTE is significant.

48 In this work, three different kinds of molecules were
 49 employed as ligand for Si QDs, which are dodecene, methyl
 50 10-undecenoate and dodecanoic acid, as shown in Fig 1. The
 51 corresponding QDs will be labeled as alkane-Si QDs, ester-Si
 52 QDs and acid-Si QDs, respectively. Due to gradually
 53 increased dielectric constant of the ligands, the surface
 54 polarity of alkane-Si QDs, ester-Si QDs and acid-Si QDs
 55 increased gradually. From the micro-PL photographs of the Si
 56 QDs-OSTE composites (Fig. 2) we can find there are some
 57 agglomerates from the composites with alkane-Si QDs and



64 Fig 1. Molecular structures of the three different ligands.



65 Fig 2. Real color micro-PL photographs of Si QDs-polymer composites
 66 fabricated from Si QDs with different ligand (A: alkane-Si QDs; B: ester-Si
 67 QDs; C: acid-Si QDs) with taken at a different depth.

68 acid-Si QDs, while no obvious agglomerate could be observed
 69 from the composite with ester-Si QDs, indicating that the
 70 surface polarity of ester-Si QDs is more close to the polarity
 71 of the OSTE polymer. The scattering measurement (Table 1)
 72 also shows that the composite with ester-Si QDs has the
 73 lowest scattering cross section, and the value with acid-Si QDs
 74 is slightly higher, while that with the most used alkane-Si QDs
 75 is even much more higher. Consequently, among the three
 76 kinds of QDs, ester-Si QDs is the most compatible with the
 77 OSTE to fabricate nanocomposite with low scattering loss for
 78 LSCs.

ACKNOWLEDGMENT

79 This project is supported by Swedish Energy Agency
 80 (46360-1), and Jingjian Zhou also thanks the support from the
 81 China Scholarship Council.

82 QDs	83 Concentration of QDs 84 ($\times 10^{-9}$ 85 mol/ml)	86 Scattering 87 coefficient of 88 QDs in OSTE 89 (cm^{-1})	90 Scattering 91 cross section 92 of QDs in 93 OSTE ($\times 10^{-17} \text{ cm}^2$)
94 alkane-Si QDs	95 0.7	96 0.318	97 76
98 ester-Si QDs	99 7.45	100 0.062	101 1.4
102 acid-Si QDs	103 3.7	104 0.076	105 3.4

REFERENCE

- [1] F. Meinardi, F. Bruni, S. Brovelli, Luminescent solar concentrators for building-integrated photovoltaics, *Nature Rev. Mater.*, vol. 2, pp. 17072, 2017.
- [2] F. Meinardi, H. McDaniel, F. Carulli, A. Colombo, K.A. Velizhanin, N.S. Makarov, R. Simonutti, V.I. Klimov, S. Brovelli, Highly efficient large-area colourless luminescent solar concentrators using heavy-metal-free colloidal quantum dots, *Nature Nanotech.*, vol. 10, pp. 878-886, 2015.
- [3] M.R. Bergren, N.S. Makarov, K. Ramasamy, A. Jackson, R. Guglielmetti, H. McDaniel, High-Performance CuInS2 Quantum Dot Laminated Glass Luminescent Solar Concentrators for Windows, *ACS Energy Lett.*, vol. 3, pp. 520-525, 2018.
- [4] F. Meinardi, S. Ehrenberg, L. Dhamo, F. Carulli, M. Mauri, F. Bruni, R. Simonutti, U. Kortshagen, S. Brovelli, Highly efficient luminescent solar concentrators based on earth-abundant indirect-bandgap silicon quantum dots, *Nat. Photonics*, vol. 11, pp. 177-186, 2017.
- [5] S.K.E. Hill, R. Connell, C. Peterson, J. Hollinger, M.A. Hillmyer, U. Kortshagen, V.E. Ferry, Silicon Quantum Dot–Poly(methyl methacrylate) Nanocomposites with Reduced Light Scattering for Luminescent Solar Concentrators, *ACS Photonics*, vol. 6, pp. 170-180, 2019.
- [6] A. Marinins, R. Zandi Shafagh, W. van der Wijngaart, T. Haraldsson, J. Linnros, J.G.C. Veinot, S. Popov, I. Sychugov, Light-Converting Polymer/Si Nanocrystal Composites with Stable 60–70% Quantum Efficiency and Their Glass Laminates, *ACS Appl. Mater. Interfaces*, vol. 9, pp. 30267-30272, 2017.

Study of stiffness and its correlations with the flexible sensing performance of piezo polymer PVDF

Ronit Ganguly

Department of Electrical
Engineering, Indian
Institute of Technology,
Hyderabad,
Kandi, Sangareddy,
Telangana, India-502285
ee15resch02014@iith.ac.in

Korla Rajesh

Department of Materials
Science and
Metallurgical Engineering,
Indian Institute of
Technology Hyderabad,
Kandi,
Sangareddy, Telangana,
India-502285
rajeshk@iith.ac.in

Amit Acharyya

Department of Electrical
Engineering, Indian
Institute of Technology
Hyderabad, Kandi,
Sangareddy, Telangana,
India - 502285
amit_acharyya@iith.ac.in

Ranjith Ramadurai

Department of Materials
Science and
Metallurgical
Engineering, Indian
Institute of Technology
Hyderabad, Kandi,
Sangareddy, Telangana,
India- 502285
ranjith@iith.ac.in

Abstract —Free standing PVDF thin films synthesized from varying precursor viscosities was fabricated through solution casting method. The films prepared from relatively higher precursor viscosity, were found to have relatively larger Young's modulus. These films were also found to possess a dominant planar piezo-response (displacement amplitude ~800 mV). The dominant planar response was also confirmed by the presence of planar ferroelectric domains which are out of phase by 180° with amorphous region between them. These domains induce electrostatic force between the crystalline regions, which in turn is expected to provide resistance against the deformation of carbon chain in the polymer film and give rise to higher Young's modulus. Hence samples with large stiffness exhibits larger piezoelectric property and thereby largest voltage response.

Keywords— PVDF, piezopolymer, flexural response, PFM, Young's modulus

I. INTRODUCTION

Piezoelectric materials are most widely used because of their wide bandwidth, fast electromechanical response, relatively low power requirements, and high generative forces [1]. There are ceramic and polymer based piezoelectric in which piezoelectric polymers are considered to be much more sensitive and durable in responding to deformations and electric fields [2]. There has been upsurge in studies of mechanical as well as ferroelectric properties of such piezo polymers as these properties plays a major role in deciding the commercial application of a material.

PVDF is a semi-crystalline polymer that has five polymorphs α , β , γ , δ and ϵ of which α , β and γ of major interest. The α -phase is readily formed during crystallization from melt. Its conformation is arranged in Trans -gauche -(TG + TG-), where the net dipole moment is zero due to its antiparallel arrangement two chain in unit cell and as a result of the non-piezoelectric form [3]. This is also called as form II. Form I or β -phase has all-trans (TT) conformation. All chains of the unit cell have dipoles pointed in the same direction, arranged in a non centro-symmetric crystal resulting in β -phase with piezoelectric property. Among all polymorphs, β -phase is the most popular because of its higher piezoelectric and pyroelectric properties [4].

The SS (Switching spectroscopy) in a piezoresponse force microscope(PFM) are usually preferred to study the material in nanoscale dimension, understand the polarization orientation and switching property of thin films[5]. It is known that the processing condition has an impact on the ferroelectric polarization of PVDF [6]. Similarly, the processing condition can influence the mechanical properties of PVDF thin film [7]. Since both the ferroelectric polarization as well as mechanical properties are effected by processing conditions, there exists a correlation between them. In this study, we prepare PVDF films with different processing conditions and study its effect on the polarization and mechanical properties (mainly Young's modulus). An attempt has been made to study and correlate the polarization influence on device performance as well as on mechanical properties.

II. EXPERIMENTAL SECTION

A. Sample Preparation

Commercially available PVDF (Sigma Aldrich) powders and N-Methyl-2-pyrrolidone (NMP) (Sigma Aldrich) solvent with appropriate weight proportion were mixed in a magnetic stirrer to obtain the solution of PVDF with varying viscosity. These films were casted on borosilicate glass by the conventional doctor blade technique and further annealed at 90°C. More details of synthesis procedure has been reported earlier. [6] The viscosities considered in the present studies are 2.4, 2.9, 4.6, 8.1 Pa.s and labeled as PVDF 2.4, PVDF 2.9, PVDF 4.6, PVDF 8.1 respectively.

III. RESULTS AND DISCUSSION

A. X Ray Diffraction and Piezoresponse Force Microscopy

The X-ray diffraction of all PVDF samples were studied and confirmed the presence of β -phase in PVDF films along with the small percentage of γ -phase [8].

Fig. 1(a) shows the in-plane (IP) phase image of PVDF 4.6 sample. It reveals the presence of paired regions with opposite domains oriented either left or right with respect to the probe tip confirms the presence of dominant In-Plane (IP) polarization components. A detail study of this can be found elsewhere [6].

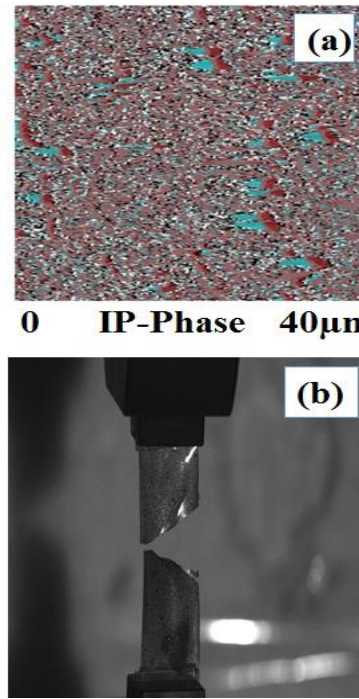


Fig. 1. (a) In-Plane PFM Phase of Pure PVDF (b) PVDF sample subjected to tensile measurement .

B. Tensile Studies and Device Performance

It has been evident from above PFM studies that PVDF samples has dominant planar domains indicating higher piezoelectric response. This was demonstrated with the help of planar based energy harvester fabricated from higher viscosity sample (in this case PVDF 4.6 sample). When tapping forces due to fingerpad in the range of ~ 5 (weak force) - 20N (moderate force) [9], were applied over the harvester, a spike in the voltage is observed as a response. The maximum voltage for our samples was found to be ~800mV.

Since the PFM measurement shows predominant planar response, mechanical behavior in planar direction can be of major interest. All the free standing films were prepared in accordance to ASTM D882 standards for tensile measurement and was performed using Instron 5969 universal testing machine (Fig 1(b)) at an initial strain rate of 10^{-3} s⁻¹. Fig. 2 represents the stress - strain curves of PVDF films with different viscosities: 2.4/2.9 and 4.6/8.1 Pa.s. It was observed that with increase in precursor viscosity Young's modulus increases, which can be attributed to increase in film density due to high precursor viscosity as well as the increasing electrostatic interactions due to in-plane polarization component, (PVDF 4.6 sample).

The above measurement points towards a correlation between the stiffness and device performance. This correlation can be attributed to the presence of ferroelectric polarization domains which are uniformly distributed through the sample. Aforementioned electrostatic force due to these domains opposes any deformation of the film results in increasing the film stiffness. These forces restrict the movements of carbon backbone and holds it tightly enough to avoid bond breaking and thereby breaking of films.

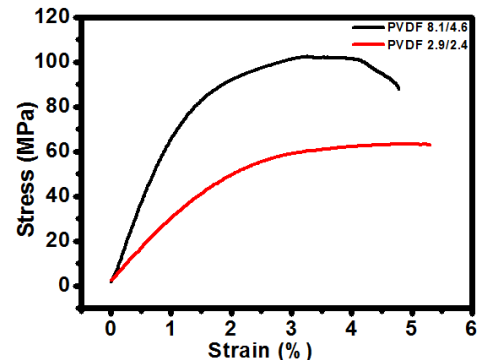


Fig. 2. Strain-Stress plot of PVDF 8.1/4.6 and 2.9/2.4 Sample.

IV. CONCLUSION

We look into the polarization behavior of PVDF film over a viscosity range and verify it by performance of devices fabricated from these viscosity range. Tensile measurement was performed to determine the stiffness of the film. We attempt to correlate the stiffness of the films to the device performance based on these films. The polarization component plays a major role in determining the elastic property of the PVDF films.

ACKNOWLEDGMENT

Mr. Ronit Ganguly acknowledges the Visvesvaraya Ph.D. Scheme MEITY. Dr. Amit Acharyya's acknowledges the support by the "Visvesvaraya Young Faculty Fellowship Scheme" by MEITY, GOI".

REFERENCES

- [1] J. S. Harrison and Z. Ounaias, "Encyclopedia of Polymer Science and Technology," vol. 3, pp. 474-498, 2002.
- [2] M. Shahinpoor, Y. Bar-Cohen, T. Xue, J. O. Simpson and J. Smith, "Ionic Polymer-Metal Composites (IPMC) As Biomimetic Sensors and Actuators - Artificial Muscles," Proc. Ann. Int. Symp. on Smart Mater. Struct., pp. 3324-327, March 1998.
- [3] S. Weinhold, M. H. Litt and J. B. Lando, "The Crystal Structure of the γ Phase of Poly(vinylidene fluoride)," Macromolecules, vol.13, no. 5, pp. 1178-1183, 1980.
- [4] F. Mokhtari, M. Latifi and M. Shamshirsaz, "Electrospinning/electrospray of Polyvinylidene fluoride (PVDF): Piezoelectric Nanofibers," The Journal of The Textile Institute, vol. 107, no. 8, pp. 1037-1055, 2016.
- [5] A. L. Kholkin, S. V. Kalinin, A. Roelofs, A. Gruverman, Scanning Probe Microscopy: Electrical and Electromechanical Phenomena at the Nanoscale, vol. 2, Springer, 2007, pp. 173-214.
- [6] R. Ganguly, S. Bhattacharjee, K. Miriyala, V. Gunasekaran, S. Bhattacharya, A. Acharyya and R. Ramadurai, "Tunable Polarization Components and Electric Field Induced Crystallization in Polyvinylidenefluoride: A piezo polymer," Polymer Crystallization. vol. 2, no. 1, pp.10027, 2019.
- [7] J. Liu, X. Lu and C. Wu, "Effect of Preparation Methods on Crystallization Behavior and Tensile Strength of Poly(vinylidene fluoride) Membranes," Membranes, vol. 3, no. 4, pp. 389-405, 2013.
- [8] M. Kanik, O. Aktas, H. S. Sen, E. Durgun and M. Bayindir, "Spontaneous High Piezoelectricity in Poly(vinylidene fluoride) Nanoribbons Produced by Iterative Thermal Size Reduction Technique," ACS Nano, vol. 8, no.9, pp. 9311-9323, 2014.
- [9] K. Shima, Y. Tamura, T. Tsuji, A. Kandori, M. Yokoe, and S. Sakoda "Estimation of Human Finger Tapping Forces Based on a Fingerpad-Stiffness Model," Annu. Int. Conf. IEEE Eng. Med. Bio. Soc., pp. 2663-2667, 2009.

Plasmonic Profile Optimization of Organic Solar Cells for Maximum Conversion Efficiency

Muath Bani Salim
Sustainable Energy Systems
Engineering Program
Texas A&M University –Kingsville
Kingsville, TX, USA
muath_naser.bani_salim@students.tamuk.edu

Reza Nekovei
Department of Electrical Engineering
and Computer Science
Texas A&M University –Kingsville
Kingsville, TX, USA
Reza.Nekovei@tamuk.edu

Amit Verma
Department of Electrical Engineering
and Computer Science
Texas A&M University –Kingsville
Kingsville, TX, USA
Amit.Verma @tamuk.edu

Abstract— This paper explores the optimization of the plasmonic shape to maximize the organic photovoltaic cells (OPV) conversion efficiency (PCE). The optimization aims to find the best plasmonic profile for the hole transfer layer of the OPV. Also, this paper compares different plasmonic cases to the regular case in which no plasmonic is used. The optimization is done with the help of a Genetic Algorithm and by considering the PCE as the primary objective function. The results show that the optimum active layer thickness with no plasmonics is 118 nm, and it gives 3.79% PCE. While at one of the best optimized plasmonic cases, the PCE is 4.16% with a 107 nm active layer thickness.

I. INTRODUCTION

Organic photovoltaic cells (OPV) is one of the emerging PV types that use organic semiconductors (OSC) to convert solar power to electricity [1]. Recently, several methods and technologies have been used to enhance the OPV conversion efficiency (PCE) such as the light trapping techniques and plasmonics which aim to trap more light in the OPV active layer to get higher PCE at a lower active layer thickness [2]. Plasmonics can be done by having repeated non-flat material at the top of the OPV device, typically in the hole transfer layer (HTL) [3] as shown in Figure 1. This paper makes a comparison between four different plasmonic cases to find the optimum active layer that will give the maximum PCE. The plasmonic is implemented in the HTL layer which is made from Poly polystyrene sulfonate (PEDOT: PSS). The other layers are made from the following: the transparent anode is Indium tin oxide, the active layer is P3HT: PCBM, Zinc oxide is used as the electron transfer layer (ETL), and Ag in the cathode as shown in Figures 1&2.

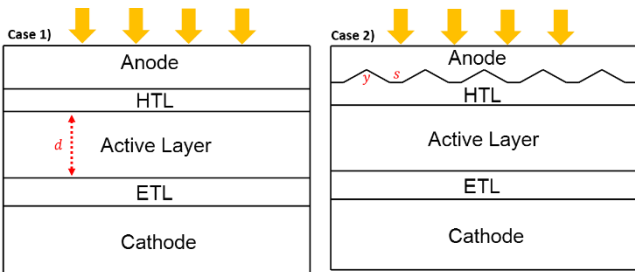


Fig. 1. OPV morphology for Cases 1&2 in this study

II. METHODS

Four different OPV cases have been tested to find the best plasmonic profile that will give the maximum PCE. A Genetic Algorithm (GA) was used [4] with the help of MATLAB software [5] to maximize the PCE by finding the best plasmonic profile dimensions for each case. Case 1 is the regular type of OPV without any plasmonics, as shown in Figure 1. The optimization, in this case, aims to find the best active layer thickness (d) that will give the maximum PCE.

Case 2 is uses plasmonics with repeated and identical isosceles triangles that have the same height (y) and the same horizontal spacing (s) in between as shown in Figure 1. All triangles have the same base width in this case. This case aims to find the best triangles height (y) and the optimum active layer thickness that will give the maximum PCE value.

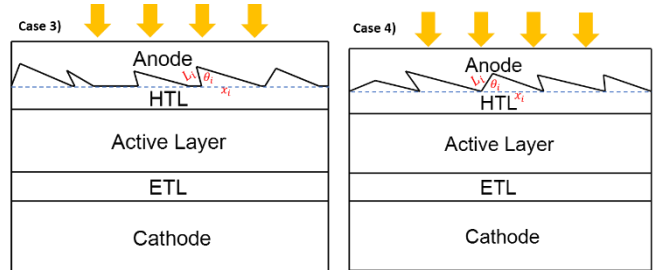


Fig. 2. OPV morphology for Cases 3&4 in this study

Case 3 uses plasmonics with the i^{th} repeated and non-identical triangles with some horizontal spacing (s_i) as shown in Figure 2. This case aims to find the best dimensions for the triangles (L_i, x_i, θ_i) and the active layer thickness that will give the maximum PCE value. This paper considered five triangles ($i=5$), so there are 16 independent variables for this case of optimization. Case 4 is the same as case 3, but there is no horizontal spacing between the five triangles.

For all cases, the amount of the absorbed power and the short circuit current I_{sc} are found by using an electromagnetic simulation with the help of COMSOL Multiphysics software [6] and under AM1.5 illumination as in (1)-(2), where v is the volume, q is the elementary charge,

h is the Planck's constant, the material's relative permittivity. The PCE is found from the I-V curve and with the help of the OPV single diode model as in (3), where n is the ideality factor, V_t is the thermal voltage, R_s and R_p are the series and parallel resistances respectively.

$$\nabla \times \vec{E}_{opt} = -j \frac{2\pi c \mu_0 H_{opt}}{\lambda} \quad (1)$$

$$I_{sc} = q \int_{\lambda_1}^{\lambda_2} \int \frac{\pi \epsilon_2 \epsilon_0}{h} |E_{opt}|^2 dv d\lambda \quad (2)$$

$$I = I_{sc} - I_0 \times \exp\left(\frac{V + IR_s}{nV_t} - 1\right) - \frac{V + IR_s}{R_p} \quad (3)$$

Figure 3 shows the optimization process flow for each case.

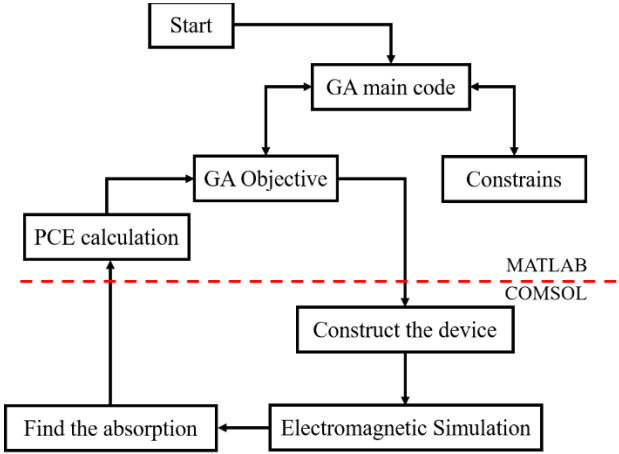


Fig. 3. Plasmonic optimization block diagram

III. RESULTS

The optimization results for case 1 show that the maximum PCE is 3.79% at the active layer thickness of 118 nm as shown in TABLE I and Figure 4.

TABLE I. TABLE TYPE STYLES

	Thickness(nm)	Jsc	V	PCE%
Case 4	107	8.06	0.62	4.16
Case 3	107	7.98	0.62	4.12
Case 2	117	7.98	0.62	4.12
Case 1	118	7.34	0.62	3.79

The optimization results for case 2 show that with triangle height of $y=39$ nm, the maximum PCE is 4.12%, which is higher than case 1, as shown in Figure 4 (a)-(b).

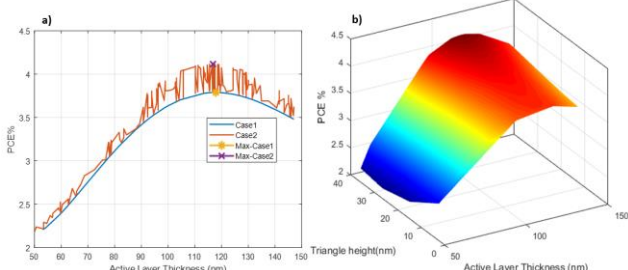


Fig. 4. a) PCE for case 2 vs the active layer thickness b)PCE as function of the active layer thickness and the triangle height

Figure 4 (b) shows the relation between the active layer thickness and the dimension y in case 2. The results show that case 3 required 107 nm active layer thickness to give 4.12% PCE, as shown in Figure 5 (a), which is same as case 2 but with less active layer thickness. Case 4, is the best case at which we get the highest efficiency (4.16%) as shown in Figure 5 (b), which is the result of the optimum plasmonic shape which was expected during the optimization process

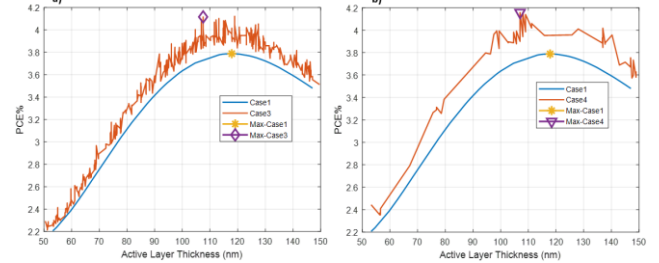


Fig. 5. a) PCE for case 3 vs the active layer thickness b) PCE for case 3 vs the active layer thickness

TABLE II shows the triangles dimesions results at the optimum points of case 3&4.

TABLE II. TABLE TYPE STYLES

	L_1	L_2	L_3	L_4	L_5
Case 3	38	26	26	32	32
Case 4	32	38	34	30	28
x_1	x_2	x_3	x_4	x_5	
Case 3	56	16	48	56	50
Case 4	70	60	62	60	44
θ_1	θ_2	θ_3	θ_4	θ_5	
Case 3	78	104	98	98	70
Case 4	36	110	70	102	92

IV. CONCLUSIONS

Plasmonics are a useful technology that can be used to harvest more power from PV cells by trapping more light inside the cell. This work shows how to maximize the cell's PCE by finding the optimum plasmonic profile. Comparisons between four different plasmonic cases were carried out in this paper to find the most compelling case and profile. This study will expand to find the maximum PCE for plasmonics with other materials rather than PEDOT: PSS in the HTL layer.

REFERENCES

- [1] J. Bergqvist *et al.*, "Asymmetric photocurrent extraction in semitransparent laminated flexible organic solar cells," *npj Flexible Electronics*, vol. 2, no. 1, p. 4, Feb. 2018.
- [2] K. Yao *et al.*, "Plasmonic Metal Nanoparticles with Core–Bishell Structure for High-Performance Organic and Perovskite Solar Cells," *ACS Nano*, vol. 13, no. 5, pp. 5397–5409, May 2019.
- [3] G. Capizzi, G. Lo Sciuto, C. Napoli, R. Shikler, and M. Woźniak, "Optimizing the Organic Solar Cell Manufacturing Process by Means of AFM Measurements and Neural Networks," *Energies*, vol. 11, no. 5, p. 1221, May 2018.
- [4] S. Jafar-Zanjani, S. Inampudi, and H. Mosallaei, "Adaptive Genetic Algorithm for Optical Metasurfaces Design," *Scientific Reports*, vol. 8, no. 1, p. 11040, Jul. 2018.
- [5] "MATLAB - MathWorks." [Online]. Available: <https://www.mathworks.com/products/matlab.html>.
- [6] "COMSOL Multiphysics® v. 5.4. www.comsol.com. COMSOL AB, Stockholm, Sweden. .

Nanoscale electrical characterization of organized GaAsP nanowires for photovoltaic energy harvesting

O. Saket¹, C. Himwas^{1,2}, A. Cattoni¹, S. Collin¹, F. Oehler¹, F. H. Julien¹, J. C. Harmand¹, M. Tchernycheva¹

1 :Centre de Nanosciences et de Nanotechnologies, UMR 9001 CNRS, Univ. Paris Sud, Univ. Paris-Saclay, 10 Boulevard Thomas Gobert, F-91120 Palaiseau Cedex, France.

2: Semiconductor Device Research Laboratory, Department of Electrical Engineering, Faculty of Engineering, Chulalongkorn University, 254 Phayathai Road, Bangkok 10330, Thailand

Email: omar.saket@c2n.upsaclay.fr

Keywords: III-V nanowire, molecular beam epitaxy, electron beam induced current, solar cells

Among the renewable sources of energy, solar energy represents the largest part, which makes solar panels the most promising energy harvesters. Today, single-junction solar cells have reached their maturity, and the efficiency of these devices start to approach the theoretical limit [1] with a record of conversion of 29.1% for GaAs [2] and 26.7% for Si device [2]. The efficiency can be highly improved using a tandem architecture, however the widespread of the most efficient multi-junction devices is limited by the high cost of III-V substrates, and by the difficulty to deal with the lattice mismatch. In this context, nanowires (NWs) have recently emerged as a good alternative for solar cell devices. NWs can be grown on lattice mismatching substrates without creating dislocations, thanks to the strain relaxation by their free lateral surface [3]. With the objective to reduce the cost and improve the efficiency of single-junction devices, a hybrid solar cell was proposed by LaPierre *et al.* [4], which consists in a combination of a Si bottom-cell with a III-V NW cell grown on top. Theoretical calculations for this device predict an efficiency of 42.3% under 500 sun [4].

In this contribution, we report on the growth, the electrical characterization of single NWs and on the fabrication and characterization of the devices composed of GaAsP NWs. Organized GaAsP NWs were grown on a patterned $\text{SiO}_2/\text{Si}(111)$ substrate by Ga-catalyzed molecular beam epitaxy. The GaAsP composition (probed by EDX) was adjusted to achieve a bandgap close to 1.7 eV, which is the optimal value for III-V on Si tandem device [4]. Axial p-i-n junctions were grown using Be and Si as doping sources for p-type and n-type doping, respectively. The morphology of the organized NW array is illustrated in the scanning electron microscopy (SEM) image of fig.1.a). Single NWs are probed under different external biases by electron beam induced current microscopy (EBIC) to extract the minority carrier diffusion lengths and the extension of the collection region along the NW axis. From the EBIC mapping and the SEM contrast, the junction is found to be localized at the interface between the p-doped and the intrinsic region which reveals a residual n-type doping of the intrinsic segment (see fig.1.b). Individual NW IV characteristics are recorded in dark and under electron beam irradiation, showing a measurable open circuit voltage for the irradiated curve. NW arrays were processed into solar cells by encapsulating the wires in a dielectric matrix, and by adding an indium tin oxide top contact. Top view EBIC analyses were applied to investigate the electrical wire-to-wire homogeneity of the NW array.

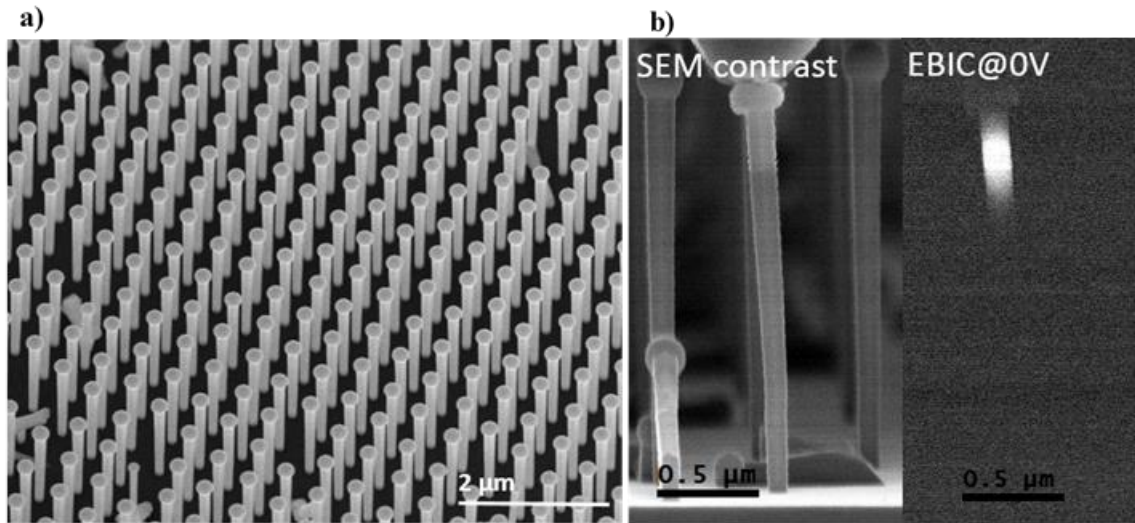


Figure 1.a) SEM image of organized GaAsP NWs; b) SEM image of individual NWs contacted on the top with a tungsten nano-probe and the corresponding EBIC map.

References

- [1] W. Shockley et H. J. Queisser, « Detailed Balance Limit of Efficiency of p - n Junction Solar Cells », *Journal of Applied Physics*, vol. 32, n° 3, p. 510-519, mars 1961.
- [2] M. A. Green *et al.*, « Solar cell efficiency tables (Version 53) », *Prog Photovolt Res Appl*, vol. 27, n° 1, p. 3-12, janv. 2019.
- [3] F. Glas, « Critical dimensions for the plastic relaxation of strained axial heterostructures in free-standing nanowires », *Phys. Rev. B*, vol. 74, n° 12, p. 121302, sept. 2006.
- [4] R. R. LaPierre, « Theoretical conversion efficiency of a two-junction III-V nanowire on Si solar cell », *Journal of Applied Physics*, vol. 110, n° 1, p. 014310, juill. 2011.

Self-assembled monolayer passivation for improving semiconductor stability

1 Sung-Eun Lee

2 Program in Nano Science and
3 Technology, Graduate School of
4 Convergence Science and Technology
5 Seoul National University
6 Seoul, Republic of Korea
7 ronny.lee@snu.ac.kr

8 Jintaek Park

9 Program in Nano Science and
10 Technology, Graduate School of
11 Convergence Science and Technology
12 Seoul National University
13 Seoul, Republic of Korea
14 zintaek@snu.ac.kr

15 Eun Goo Lee

16 Program in Nano Science and
17 Technology, Graduate School of
18 Convergence Science and Technology
19 Seoul National University
20 Seoul, Republic of Korea
21 agcu82@snu.ac.kr

22 Hyunjae Na

23 Program in Nano Science and
24 Technology, Graduate School of
25 Convergence Science and Technology
26 Seoul National University
27 Seoul, Republic of Korea
28 now6143@snu.ac.kr

29 Kyungho Kim

30 Program in Nano Science and
31 Technology, Graduate School of
32 Convergence Science and Technology
33 Seoul National University
34 Seoul, Republic of Korea
35 leopa@snu.ac.kr

36 Prof. Youn Sang Kim

37 Program in Nano Science and
38 Technology, Graduate School of
39 Convergence Science and Technology
40 Seoul National University
41 Seoul, Republic of Korea
42 younskim@snu.ac.kr

43 Indium gallium zinc oxide (IGZO) semiconductor for
44 display has been intensively studied for decades because of its
45 high mobility, high on/off ratio, and relatively lower process
46 temperature than Si-based semiconductor devices [1-3].
47 However, in the case of top gate structure, as there is a risk of
48 semiconductor damage due to ionic bombardment when
49 deposition of gate dielectrics on the front channel occurred,
50 the use of bottom gate structures is widely recommended [4,5].
51 But in the bottom gate structure, the stability problem is still
52 constantly raised due to the back channel region which is
53 exposed to the atmosphere. In particular, it is well known that
54 back channels are exposed to the atmosphere with the bottom
55 gate structure, therefore water or oxygen molecules can be
56 easily adsorbed or desorbed on the back channel surface to
57 accumulate or deplete electrons in the back channel region
58 [6,7]. Therefore, with these unsuitable phenomena, the
59 degradations such as decreased stability and hysteresis of the
60 IGZO oxide semiconductor device could occur.

61 Herein, we studied the self-assembled monolayer (SAM)
62 of the silane head group, which can be used as a protective
63 layer on the back channel surface of the bottom gate structure
64 to improve the stability of the IGZO semiconductor. Although,
65 previous studies have shown that the use of SAM to block
66 adsorption and desorption of back channel surface of water
67 and oxygen molecules in the atmosphere has been reported
68 [8,9], the results on SAM functional groups by water contact
69 angles are very few. Our study showed that the positive bias
70 stress (PBS) could be improved with an increment of the water
71 contact angle of SAM functional group as seen in table 1. It
72 can be inferred that the accumulation and depletion
73 phenomena of electrons are significantly reduced due to the
74 decrease of adsorption and desorption of water and oxygen
75 molecules on the back channel surface, resulting in improved
76 stability of IGZO. In addition, after SAM treatment, the TFT
77 characteristics such as mobility, drain current on/off ratio and
78 subthreshold swing showed almost no change or even an
79 improvement (table 1), indicating that it is quite an excellent
80 treatment method as a back channel protective layer which
81 does not damage the semiconductor at all.

Sample	Measurement result				
	Water contact angle	PBS ΔV_{th} (3600sec)	Mobility	I_{on}/I_{off}	S.S.
Reference	-	12.46 V	12.1 cm ² /Vs	10 ⁸	0.18 V/dec
NH ₂ SAM	63.9 °	2.47 V	12.3 cm ² /Vs	10 ⁸	0.17 V/dec
CF ₃ SAM	77.2 °	0.32 V	12.4 cm ² /Vs	10 ⁸	0.17 V/dec

Table 1. IGZO semiconductor positive bias stress (PBS, gate bias = 20 V, drain bias = 10.1 V, 3600 sec) stability results and TFT characteristics according to the water contact angle of SAM passivation. As the SAM water contact angle is increased, the PBS stability is improved, but the deterioration of the TFT characteristics is not found at all.

Also, SAM has another great advantage of not using sputtering or chemical vapor deposition (CVD) processes that require some conditions of extremely high vacuum or high temperature post heat treatment because SAM is processed at low vacuum and low temperature of 70 °C. Therefore, it certainly can be much more excellence in case of applying to a solution or low-temperature process oxide semiconductor. In other words, it can be used to utilize the atmospheric pressure treatment and the low-temperature treatment, which are advantages of the solution process and the manufacturing process of the low-temperature process device. Thus, the SAM treatment can be used as a very efficient and economical back channel protective layer for semiconductor processes such as solution or low-temperature. In addition, we are still trying to confirm that it could be a universal treatment method that is applicable to various semiconductor materials such as organic semiconductor device by identifying the stability improvement. The results of this additional study will be continuously reported to academia in order to contribute to the stability improvement of semiconductors.

ACKNOWLEDGMENT

This research was supported by the Basic Science Research Program through the National Research Foundation of Korea (NRF) funded by the Ministry of Science and ICT (MSIT) (2017R1A2B3005482).

REFERENCES

[1] K. Nomura, H. Ohta, A. Takagi, T. Kamiya, M. Hirano, H. Hosono, "Room-temperature fabrication of transparent flexible thin-film

transistors using amorphous oxide semiconductors", *Nature* vol.432, pp. 488-492, 2004.

[2] T. Kamiya, K. Nomura, H. Hosono, "Present status of amorphous In-Ga-Zn-O thin-film transistors", *Sci. Technol. Adv. Mater.*, vol. 11, pp. 044305-044327, 2010.

[3] L. Lan, N. Xiong, P. Xiao, W. Shi, M. Xu, W. Xu, R. Yao, J. Peng, "A low-cost low-temperature thin-film-transistor backplane based on oxide semiconductor", *J. Soc. Inf. Disp.*, vol. 20, pp. 175-177, 2012.

[4] W.K. Lin, K.C. Liu, J.N. Chen, S.C. Hu, S.T. Chang, "The influence of fabrication process on top-gate thin-film transistors", *Thin Solid Films*, vol. 519, pp. 5126-5130, 2011.

[5] Xiao, P., Huang, J., Dong, T., Yuan, J., Yan, D., Xie, J., Tan, H., "X-ray photoelectron spectroscopy analysis of the effect of photoresist passivation on InGaZnO thin-film transistors", *Applied Surface Science*, vol. 471, pp. 403-407, 2019.

[6] J. Park, J. Jeong, H. Chung, Y. Mo, H. Kim, "Electronic transport properties of amorphous indium-gallium-zinc oxide semiconductor upon exposure to water" *Appl. Phys. Lett.*, vol. 92, pp. 072104, 2008.

[7] D. Kang, H. Lim, C. Kim, I. Song, J. Park, Y. Park, "Amorphous gallium indium zinc oxide thin film transistors: sensitive to oxygen molecules" *Appl. Phys. Lett.*, vol. 90, pp. 192101, 2007.

[8] Xiao, P., Lan, L., Dong, T., Lin, Z., Sun, S., Song, W., Peng, J., "InGaZnO thin-film transistors modified by self-assembled monolayer with different alkyl chain length", *IEEE Electron Device Letters*, vol. 36, pp. 687-689, 2015.

[9] Du, X., Flynn, B. T., Motley, J. R., Stickle, W. F., Bluhm, H., Herman, G. S., "Role of self-assembled monolayers on improved electrical stability of amorphous In-Ga-Zn-O thin-film transistors. *ECS Journal of Solid State Science and Technology*, vol. 3, pp. 3045-3049, 2014.

Control of Bias Stress Stability in IGZO Thin-Film Transistors by Atmospheric Pressure Plasma

Eun Goo Lee

Program in Nano Science and Technology, Graduate School of Convergence Science and Technology
Seoul National University
Seoul, Republic of Korea
agcu82@snu.ac.kr

Jintaek Park

Program in Nano Science and Technology, Graduate School of Convergence Science and Technology
Seoul National University
Seoul, Republic of Korea
zintaek@snu.ac.kr

Sung-Eun Lee

Program in Nano Science and Technology, Graduate School of Convergence Science and Technology
Seoul National University
Seoul, Republic of Korea
ronny.lee@snu.ac.kr

Hyunjae Na

Program in Nano Science and Technology, Graduate School of Convergence Science and Technology
Seoul National University
Seoul, Republic of Korea
now6143@snu.ac.kr

Kyungho Kim

Program in Nano Science and Technology, Graduate School of Convergence Science and Technology
Seoul National University
Seoul, Republic of Korea
leopa@snu.ac.kr

Prof. Youn Sang Kim

Program in Nano Science and Technology, Graduate School of Convergence Science and Technology
Seoul National University
Seoul, Republic of Korea
younskim@snu.ac.kr

Amorphous metal oxide semiconductors have attracted much attention as candidates for driving devices of next-generation display due to their high electrical characteristic and excellent uniformity in large areas [1]. In particular, amorphous indium gallium zinc oxide (IGZO) is a practical channel material for driving devices in industrial fields because it has high optical transparency, high mobility, high on/off ratio and low-temperature processability compared to conventional amorphous silicon [2]. Despite these advantages, amorphous metal oxide semiconductors still suffer from intrinsic defects, resulting in stability issues due to the external environment [3]. In addition, since the driving devices used in the active matrix of the display are used not only as switching parts but also as current supplying parts, a channel material having almost no threshold voltage change due to bias stress is required [4]. There are two approaches to solve this problem: 1) depositing a thin film on the back channel of the active layer to prevent contact with the atmosphere, 2) reducing the intrinsic defect of the amorphous metal oxide semiconductor by surface treatment on the back channel [5],[6]. The first method requires an additional process for depositing a dielectric material to passivate the active layer, while the second method increases the bias stress stability through direct treatment on the back channel of the active layer, but requires large equipment and long processing time.

In this study, we propose an atmospheric plasma treatment that can treat the back channel surface in an in-line process and in a short time by generating high energy radical to solve the above problem. The atmospheric pressure plasma treatment improves the electrical properties as well as the stability of negative bias stress and positive bias stress of the semiconductor. Most conventional plasma processes are performed under a pressure lower than atmospheric pressure, whereas atmospheric plasma does not require a vacuum system, thereby simplifying the structure of the entire system and reducing the cost and processing objects of various shapes. In addition, atmospheric plasma can react strongly with high energy radicals directly to the surface of the sample, resulting in strong surface treatment in a short time. The intrinsic defects existing on the surface of the amorphous metal oxide semiconductor are removed by reaction with high

energy radical, which serves to enhance the stability of the semiconductor. As shown in Fig. 1 (a), before the atmospheric pressure plasma treatment, the threshold voltage gradually increases toward the negative direction as time passes by negative bias. On the other hand, as shown in Fig. 1 (b), the negative threshold voltage shift is significantly

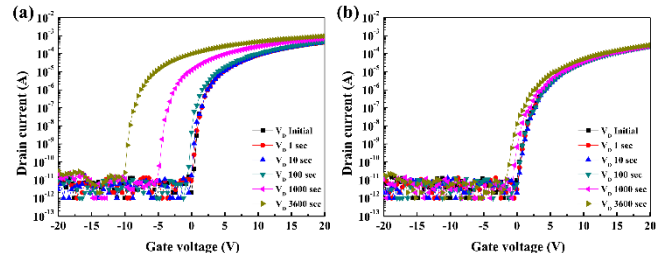


Fig. 1. The variation of time-dependent transfer curves under negative bias stress stability test of IGZO TFTs, (a) without atmospheric pressure plasma treatment, (b) with atmospheric pressure plasma treatment for 20 min (gate bias = -20 V, drain bias = 10.1 V)

reduced after atmospheric plasma treatment for 20 minutes.

As a result, negative and positive bias stress stability were decreased from -10.8V to -2V and from +5V to +1V, respectively, by applying atmospheric pressure plasma treatment to the back channel of the active layer. In addition, the electrical mobility also increased from 10 to 15 cm²/Vs, which was confirmed to increase due to the variation of the valance band offset by affecting the semiconductor internal structure through the atmospheric plasma treatment. By using the atmospheric plasma, the surface of the metal oxide semiconductor can be treated easily and quickly, thereby reducing the defects of the semiconductor and improving the stability as well as the electrical characteristics.

ACKNOWLEDGMENT

This research was supported by the Basic Science Research Program through the National Research Foundation of Korea (NRF) funded by the Ministry of Science and ICT (MSIT) (2017R1A2B3005482).

REFERENCES

[1] K. Nomura, H. Ohta, A. Takagi, T. Kamiya, M. Hirano, and H. Hosono, "Room-temperature fabrication of transparent flexible thin-film

transistors using amorphous oxide semiconductors,” *Nature*, vol. 432, no. November, p. 488, 2004

[2] J. K. Jeong, J. H. Jeong, H. W. Yang, J. S. Park, Y. G. Mo, and H. D. Kim, “High performance thin film transistors with cosputtered amorphous indium gallium zinc oxide channel,” *Appl. Phys. Lett.*, vol. 91, no. 11, pp. 11–14, 2007.

[3] H.L. Chen, T.C. Chang, T.F. Young, T.M. Tsai, K.C. Chang, R. Zhang, S.Y. Huang, K.H. Chen, J.C. Lou, M.C. Chen, C.C. Shih, S.Y. Huang, and J.H. Chen, “Ultra-violet light enhanced super critical fluid treatment in In-Ga-Zn-O thin film transistor,” *Appl. Phys. Lett.*, vol. 104, no. 24, pp. 1–5, 2014.

[4] C. Lin, C. Hung, P. Kuo, and M. Cheng, “Display Technology Letters,” *J. Disp. Technol.*, vol. 8, no. 12, pp. 681–683, 2010.

[5] J. Park, S. Kim, C. Kim, S. Kim, I. Song, H. Yin, K.K. Kim, S. Lee, K. Hong, J. Lee, J. Jung, E. Lee, K.W. Kwon, and Y. Park, “High-performance amorphous gallium indium zinc oxide thin-film transistors through N₂O plasma passivation,” *Appl. Phys. Lett.*, vol. 93, no. 5, pp. 2006–2009, 2008.

[6] Y.K. Moon, S. Lee, W.S. Kim, B.W. Kang, C.O. Jeong, D.H. Lee, and J.W. Park, “Improvement in the bias stability of amorphous indium gallium zinc oxide thin-film transistors using an O₂ plasma-treated insulator,” *Appl. Phys. Lett.*, vol. 95, no. 1, pp. 93–96, 2009.

Optical and Electrical Properties of RF-PECVD Germanium Spin Coated with 40nm Silver Nanoparticles

1
2
3
4
5
6
7
8
9
10
11
12
13
14
15
16
17
18
19
20
21
22
23
24
25
26
27
28
29
30
31
32
33
34
35
36
37
38
39
40
41
42
43
44
45
46
47
48
49
50
51
52
53
54
55
56
57
58
59
60
61
62
63
64
65
Khadija Jumaa
Khaflia University
Abu Dhabi UAE
khadija.jumaa@ku.ac.ae

Aamenah Siddiqui
Khaflia University
Abu Dhabi UAE
aamenah.siddiqui@ku.ac.ae

Ghada Dushaq
New York University
Abu Dhabi UAE
ghd1@nyu.edu

14
15
16
17
18
Mahmoud Rasras
New York University
Abu Dhabi UAE
mr5098@nyu.edu

Ammar Nayfeh
Khaflia University
Abu Dhabi UAE
ammar.nayfeh@ku.ac.ae

Abstract— In this work, the effect of spin coating 40 nm silver nanoparticles on RF-PECVD grown Ge-on-Si films has been investigated. The samples used in this work are 700 nm of germanium deposited on p-type silicon which were then spin coated with colloidal silver nanoparticle solution. The distribution of the nanoparticles is determined using SEM images and ImageJ image analysis software. The effect of introducing the silver nanoparticles on the optical reflectance, and sheet resistance of the germanium layers is investigated.

1. INTRODUCTION

Germanium (Ge) is one of the promising semiconductors for photovoltaic applications such as solar cells, owing to its high electron and hole mobility [1], and its high absorption in the infrared region. Several research groups have demonstrated Ge-based solar cells [2], in fact, Germanium-based solar cells already account for more than 80% of satellite applications [3]. Though the main limitation in the commercialization of Ge-based solar cells is the high wafer cost. Moreover, the 4.2% lattice mismatch in the Ge layers grown on low cost substrates such as silicon, also presents a major challenge. However, recently, good quality Ge-on-Si films fabricated using RF-PECVD (at $T < 600$ °C) were demonstrated [4]-[6], paving the way for their use in photovoltaic applications. In terms of optical properties, Ge has a high index of refraction and 60% normal incidence reflection which leads to high reflection and hinder its use in solar cells without employing anti-reflective coatings (ARC). Indium Tin oxide (ITO) is a popular ARC material, however, it is costly. Other materials such as ZnO has also found its way as an ARC but multiple layers are needed to minimize reflection at multiple wavelengths. Therefore, the use of metal nanoparticles, such as silver, is a low-cost and viable alternative to improve the optical and electrical properties of Ge-on-Si films for solar cell applications. Metallic nanoparticles such as silver can be used to assist solar cells in the process of converting light into electricity where the absorption is improved by the trapped light from the nanoparticles, a process known as plasmon excitation or surface-plasmon resonance. Metal nanoparticles are strong scatterers of light at wavelengths near their resonant frequency [7]. This work studies the effect of spin coating of 40 nm silver

nanoparticles on 700 nm of Ge-on-Si films grown using RF-PECVD. The optical properties such as reflectance and electrical properties such as sheet resistance of the films after spin coating the samples with 10 ml and 20 ml of 40 nm silver nanoparticle colloidal solution are studied and compared to the film properties with no nanoparticles present. The concentration of silver nanoparticles in the aqueous buffer solution is 0.02 mg/ml, provided by Sigma-Aldrich.

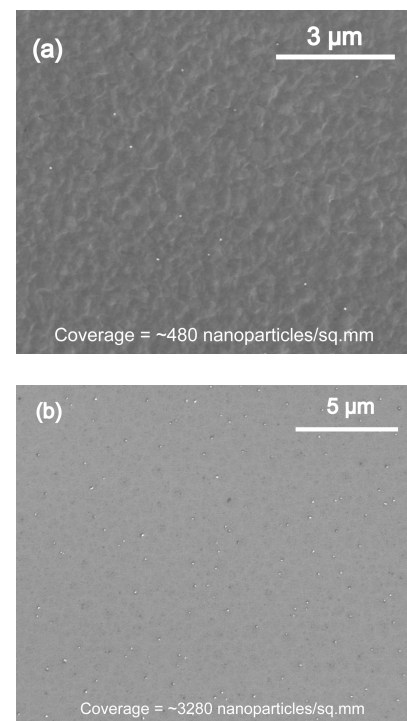


Fig. 1. SEM images of Ge-on-Si films spin coated with (a) 10 ml and (b) 20 ml of silver nanoparticle solution. The corresponding coverage density determined from Image J is 0.047% (~ 480 nanoparticles/mm 2) and 0.33% (~ 3280 nanoparticles/mm 2), respectively.

Experimental method

Ossila Personal Spin coater was used for spinning 40 nm of silver nanoparticles on RF-PECVD deposited 700 nm Ge-on-Si films [4]-[6], where the spinning was performed for 45 seconds at 2000 rpm. Three samples of Ge films were used,

one sample is left as a reference sample and the other two are coated with 10 ml and 20 ml of the silver nanoparticles colloidal solution, respectively, which was dispersed using a pipette. Using ImageJ image analysis tool the spinning led to the deposition of ~ 480 nanoparticles/mm² (0.047%) surface coverage and ~ 3280 nanoparticles/mm² (0.328%) coverage. Fig.1(a) and Fig. 1(b) show the SEM image of the top surface for both cases. The samples were then characterized for optical reflectance and sheet resistance.

2. Optical and Electrical Properties

The optical and electrical properties of Ge-on-Si films with and without silver nanoparticles were analyzed. The reflectance was measured using LAMBDA 1050 UV/Vis/NIR Spectrometer. Fig. 2 shows the reflectance on the surface of the three samples versus photon energy.

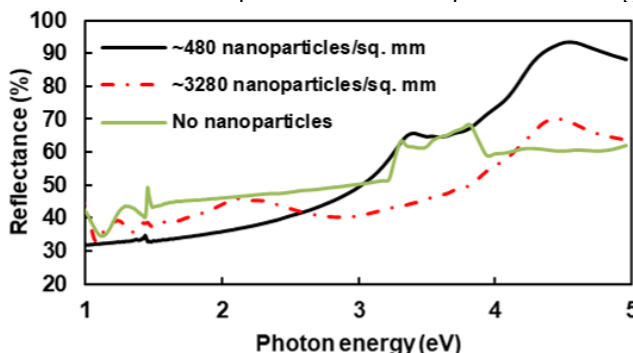


Fig. 2. Effect of silver nanoparticles on the reflectance of Ge-on-Si films.

Results showed that presence of nanoparticles reduced the amount of the reflected light due to plasmon effect which enhance the light absorption in the visible and near-infrared region. The electrical properties of the samples are studied based on the changes of their sheet resistance using four probe LakeShore 7607 Hall Measurement System, and the results are shown in Fig. 3. The sample with no nanoparticles exhibited the highest sheet resistance ($200 \Omega/\square$) whereas the sample with ~ 480 and ~ 3280 nanoparticles/mm² appeared to have the lower sheet resistance (60 and $1.5 \Omega/\square$, respectively), which is $>95\%$ less than the sample without any nanoparticles, showing promising film properties for device applications.

3. Conclusion

In conclusion, spin coating 40 nm silver nanoparticles on Ge-on-Si thin films is demonstrated. Results indicate that

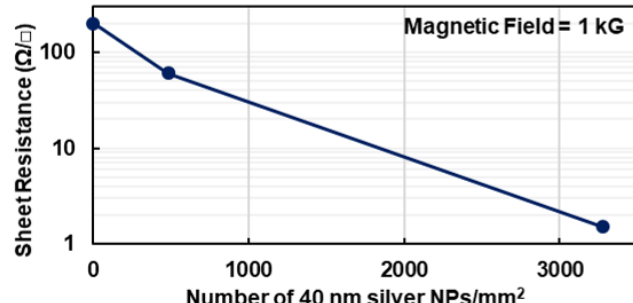


Fig. 3. Effect of silver nanoparticles on the sheet resistance of Ge-on-Si films. Sheet resistance declines significantly as the number of nanoparticles rise.

the presence of nanoparticles enhanced the optical and electrical performance of Ge films by reducing the sheet resistance significantly and lowering reflectance in the visible and near infrared regions. Moreover, this finding validates the

potential of using spin coated nanoparticles as a low-cost alternative to conventional ARC layers for photovoltaic applications.

4. Acknowledgements

We gratefully acknowledge financial support for this work provided by Khalifa University

REFERENCES

- [1] J. Wang and S. Lee, "Ge-Photodetectors for Si-Based Optoelectronic Integration", *Sensors*, vol. 11, no. 12, pp. 696-718, 2011.
- [2] D. Kim, Y. Choi, E. Do, Y. Lee and Y. Kim, "High efficiency silicon and Germanium stack junction solar cells", *2012 International Electron Devices Meeting*, 2012.
- [3] Germanium solar cells fuel greener future - Eco-innovation Action Plan - European Commission", *Eco-innovation Action Plan*, 2018. [Online].
- [4] Ghada H. Dushaq, Mahmoud S. Rasras, Ammar M. Nayfeh, "Low temperature deposition of germanium on silicon using Radio Frequency Plasma Enhanced Chemical Vapor Deposition," *Optics Express* Vol. 25, Issue 25, pp. 32110-32119 (2017).
- [5] Ghada H. Dushaq, Mahmoud S. Rasras, Ammar M. Nayfeh, "Low temperature deposition of germanium on silicon using Radio Frequency Plasma Enhanced Chemical Vapor Deposition," *Thin Solid Films*, page 585-592, 2017.
- [6] Ghada H. Dushaq, Mahmoud S. Rasras, Ammar M. Nayfeh, "Germanium MOS capacitors grown on Silicon using low temperature RF-PECVD," *J. Phys. D: Appl. Phys.* 50 405107.
- [7] F. Lenzmann, M. van Lare, J. Salpakari, P. Spinelli, J. Notta, M. Dörenkämper, N. Bakker, A. Weeber and A. Polman, "Plasmonic light-trapping in a-Si:H solar cells by front-side Ag nanoparticle arrays: A benchmarking study", *physica status solidi (a)*, vol. 210, no. 8, pp. 1571-1574, 2013.

Effect of atmospheric-pressure plasma treatment for solution-processed oxide thin-film transistors

Jintaek Park

Program in Nano Science and Technology, Graduate School of Convergence Science and Technology
Seoul National University
Seoul, Republic of Korea
zintaek@snu.ac.kr

Sung-Eun Lee

Program in Nano Science and Technology, Graduate School of Convergence Science and Technology
Seoul National University
Seoul, Republic of Korea
ronny.lee@snu.ac.kr

Eun Goo Lee

Program in Nano Science and Technology, Graduate School of Convergence Science and Technology
Seoul National University
Seoul, Republic of Korea
ronny.lee@snu.ac.kr

Hyunjae Na

Program in Nano Science and Technology, Graduate School of Convergence Science and Technology
Seoul National University
Seoul, Republic of Korea
now6143@snu.ac.kr

Kyungho Kim

Program in Nano Science and Technology, Graduate School of Convergence Science and Technology
Seoul National University
Seoul, Republic of Korea
younskim@snu.ac.kr

Prof. Youn Sang Kim

Program in Nano Science and Technology, Graduate School of Convergence Science and Technology
Seoul National University
Seoul, Republic of Korea
younskim@snu.ac.kr

Solution-process have drawn considerable attention as a thin-film deposition method for thin-film transistor (TFT), because they do not require cumbersome equipment compared to the vacuum process such as radio frequency magnetron sputtering, atomic layer deposition and pulsed laser deposition [1-3]. Therefore, oxide semiconductors and oxide dielectrics using solution-process method have been studied in a simple and inexpensive process [4,5]. However, the application of solution-processed TFTs to the industry is still difficult because of the insufficient electrical properties as compared with a vacuum-processed thin film. Thus, many researches have been conducted to improve the properties of solution-processed thin films. Among them, conventional plasma treatment in vacuum conditions has been studied since oxygen plasma treatment controls the oxygen vacancy [6-8]. Unfortunately, introduction of the vacuum treatment makes it difficult to apply the plasma treatment to the solution-treated thin film because the advantage of the solution process is lost. Accordingly, there is a growing demand for a technique suitable for application to solution-treated thin films in an industrial field.

Herein, we present an atmospheric-pressure plasma (APP) treatment technique for improving the electrical performance of solution-processed films. Firstly, we have implemented improvements in important TFT parameters, V_{on} and the on/off current ratio, which still keep up the high field-effect mobility, by introducing the APP treatment into solution-processed InO_x TFTs (Figure 1 a). Secondly, AlO_x dielectric film using aqueous route method was deposited by a solution process and its characteristics were improved. Characteristic changes through APP treatment were observed by measurement of capacitance-frequency and breakdown voltage. It was observed that the breakdown voltage of AlO_x thin film was increased by APP treatment (Figure 1 b)). To investigate the changes of binding relationship according to APP treatment time, X-ray photoelectron spectroscopy (XPS) was performed. TFTs were fabricated by depositing a solution-processed InO_x with a semiconductor film, and the characteristics were evaluated. The field-effect mobility was increased compared to the untreated samples. Thin-film deposition including semiconductor and gate dielectric and

plasma treatment were performed in a non-vacuum environment. The process temperature was below 250 °C.

In summary, we newly introduce the potential of APP treatment that can simply control the carrier concentration of solution-processed OS thin film and improve the breakdown voltage of solution-processed gate dielectric thin film. This APP technique can provide advances toward industrial applications of solution-processed TFTs, while maintaining the advantages of the solution process.

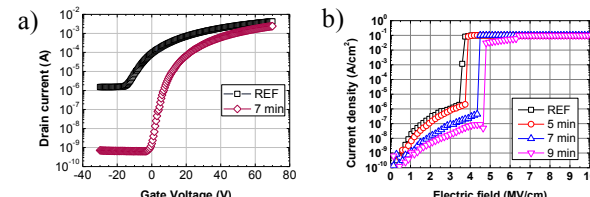


Figure 1. a) I-V characteristic of InO_x semiconductors varying atmospheric-pressure plasma treatment time. b) Electric field vs. current density of AlO_x dielectric films varying atmospheric-pressure plasma treatment time.

ACKNOWLEDGMENT

This research was supported by the Basic Science Research Program through the National Research Foundation of Korea (NRF) funded by the Ministry of Science and ICT (MSIT) (2017R1A2B3005482).

REFERENCES

- [1] Fortunato, E.; Barquinha, P.; Martins, R. Oxide semiconductor thin-film transistors: A review of recent advances. *Adv. Mater.*, vol 24, pp. 2945–2986, 2012.
- [2] Park, S. Y.; Kim, B. J.; Kim, K.; Kang, M. S.; Lim, K. H.; Lee, T. i.; Myoung, J. M.; Baik, H. K.; Cho, J. H.; Kim, Y. S. Low-temperature, solution-processed and alkali metal doped ZnO for high-performance thin-film transistors. *Adv. Mater.*, vol 24, pp. 834– 838, 2012.
- [3] Nayak, P. K.; Wang, Z.; Alshareef, H. N. Indium-free fully transparent electronics deposited entirely by atomic layer deposition. *Adv. Mater.*, vol 28, pp. 7736–7744, 2016.

- [4] Lim, K.-H.; Lee, J.; Huh, J.-E.; Park, J.; Lee, J.-H.; Lee, S.-E.; Kim, Y. S. A systematic study on effects of precursors and solvents for optimization of solution-processed oxide semiconductor thin-film transistors. *J. Mater. Chem. C*, vol 5, pp. 7768–7776, 2016.
- [5] Lee, D. H.; Chang, Y. J.; Herman, G. S.; Chang, C. H. A general route to printable high-mobility transparent amorphous oxide semiconductors. *Adv. Mater.*, vol 19, pp. 843–847, 2007.
- [6] Kim, J. S.; Joo, M. K.; Xing Piao, M.; Ahn, S. E.; Choi, Y. H.; Jang, H. K.; Kim, G. T. Plasma treatment effect on charge carrier concentrations and surface traps in a-InGaZnO thin-film transistors. *J. Appl. Phys.*, vol 115, No. 114503, 2014.
- [7] Pu, H.; Zhou, Q.; Yue, L.; Zhang, Q. Investigation of oxygen plasma treatment on the device performance of solution-processed a-IGZO thin film transistors. *Appl. Surf. Sci.*, vol 283, pp. 722–726, 2013.
- [8] Park, J. S.; Jeong, J. K.; Mo, Y. G.; Kim, H. D.; Kim, S.-I. Improvements in the device characteristics of amorphous indium gallium zinc oxide thin-film transistors by Ar plasma treatment. *Appl. Phys. Lett.*, vol 90, No. 262106, 2007.

Efficient contact resistance extraction from individual device characteristics of graphene FETs

Anibal Pacheco-Sanchez

Departament d'Enginyeria Electrònica
Universitat Autònoma de Barcelona
Bellaterra, Spain
AnibalUriel.Pacheco@uab.cat

David Jimenez

Departament d'Enginyeria Electrònica
Universitat Autònoma de Barcelona
Bellaterra, Spain
david.jimenez@uab.cat

Abstract—Practical contact resistance extraction methods have been applied to fabricated graphene field-effect transistors from different technologies. In contrast to other characterization techniques which require either the fabrication of additional test structures or elaborated models requiring internal quantities and a few number of fitting parameters, the methods used here enable a straightforward extraction of contact resistance values from the electrical characteristics of individual devices within the linear transistor operation using a drift-diffusion approach. Results are validated with other experimental characterization methods and with different sophisticated models.

Index Terms—graphene field-effect transistor, contact resistance, parameter extraction

I. INTRODUCTION

The most common method of contact resistance R_C characterization in GFETs is the transfer length method (TLM) [1]–[5]. While TLM has been verified with physics-based models of GFETs [1], it involves the fabrication of additional dedicated test structures and the obtained values might differ for other individual devices due to reproducibility issues present at this stage of the technology [5], [6]. Analytical and compact models make use of certain fitting parameters, including the contact resistance, to describe experimental data of a certain GFET technology [2], [7]–[9]. However, these are useful but technology-specific procedures and their validity depends on the physical basis of the models and on the fitting parameters. Alternative extraction methods in which contact resistance values can be obtained for individual transistors are required in order to ease device and technology evaluation. In this work, such efficient extraction methods, based on the Y -function [10], are presented and applied to experimental data.

II. EXTRACTION METHODOLOGY

The Y -function is a combination of a drift-diffusion (DD) drain current I_D equation at the linear region and its correspondence transconductance g_m such as $Y = I_D / \sqrt{g_m}$ [10]. In this work, values of R_C have been extracted with Y -function based methods (YFMs) considering [11], [12], [28]

$$I_D \approx \beta \frac{\left(V_{GS} - V_{th} - \frac{V_{DS}}{2}\right)}{1 + \theta \left(V_{GS} - V_{th} - \frac{V_{DS}}{2}\right)} V_{DS}, \quad (1)$$

where V_{GS} and V_{DS} are the gate-to-source and drain-to-source extrinsic voltages, respectively, V_{th} is the charge threshold voltage [10] and $\theta = \theta_0 + R_C \beta$ is the extrinsic mobility

degradation [10], [13] with θ_0 as the intrinsic mobility degradation coefficient due to vertical fields and $\beta = \mu_0 C_{ox} w_g / L_g$ embraces the low-field mobility μ_0 , the oxide capacitance C_{ox} , the gate width w_g and the gate length L_g . Transport in graphene transistors of different channel and gate lengths has been successfully described by the DD approach [14]–[19].

A Y -function and an X -function ($X = 1/\sqrt{g_m}$) using Eq. (1) have been considered for the extraction of R_C either at a single bias point (BP) [11] or at the bias range (BR) [12], [28] in which the corresponding method has been applied. In this work, contact resistance values obtained with the first approach are labeled as $R_{C,BP}$ [11] while $R_{C,BR}$ identifies the values extracted with the second one [12], [28]. $R_{C,BP}$ can be used for immediate technology evaluation whilst $R_{C,BR}$ reveals more information on internal physical phenomena at the metal-graphene interface.

III. RESULTS AND DISCUSSION

Contact resistance values have been extracted with YFMs [11], [12], [28] for different graphene transistor technologies [2], [4], [20]–[27]. The methods have been applied here to the dominant branch of the transfer characteristic in each device. The values of the extracted parameters, including $R_{C,BP}$ and $R_{C,BR}$ have been substituted into Eq. (1) and the results have been compared to the corresponding experimental data of each device within the bias range selected for the extraction. Fig. 1 shows the good match between experimental data of devices with different gate lengths (100 nm [4] and 5 μm [24]) and Eq. (1) using the corresponding extracted parameters.

The extracted contact resistivity $R_{C,BP} w_g$ the device length and device width for the different GFETs under study are summarized in Table I where the reported values of the contact resistivity $R_{C,\text{ref}} w_g$, obtained with other methods, such as TLM or by fitting analytical/compact models (AMs/CMs), are listed as well. YFMs have been applied within the same bias region in which the values of $R_{C,\text{ref}}$ have been reported. The extracted values here are close to the reference data. In contrast to contact resistance values obtained by fitting a CM, YFMs can extract values for different technologies without adjusting further parameters. While physics-based AM are more accurate to describe the device performance, they result impractical for immediate characterization since they require information regarding intrinsic physical device quantities, e.g.,

charge carrier density [2], [20]. Therefore, the Y -function based methods are an alternative for an efficient contact resistance extraction. Furthermore, the channel phenomena have no impact on the extraction since the same value of $R_{C,BP}$ is extracted for scattering-affected transistors with identical device architecture and materials but different L_g [4].

The evolution of $R_{C,BR}w_g$ over V_{GS} for each studied device is presented in Fig. 2 where $|V_{GS,0}|$ is the lowest limit of the bias region used for the extraction. In general, $R_{C,BR}w_g$ of most of the analyzed devices slightly decrease at higher $|V_{GS}|$ as expected in the linear operation regime. The almost constant values indicate a good contact transparency in the studied bias region. The lowest $R_{C,BR}w_g$ have been found for fabricated devices intended for RF applications [4], [20]–[22]. The channel to contact resistance ratio shown also in Fig. 2 (right) indicates how dominant are these parameters for the RF devices [4], [20]–[22]. The pronounced decrease of the curves is due to the V_{GS} -dependence of R_{ch} rather than that of $R_{C,BR}$. The contact resistance is extremely dominant for three devices [4], [21], [22]. The curve of the 2 μm -long device [20] shows a non-monotonical decrease suggesting non-trivial internal mechanisms. Additionally, since the ratio is close to unity, both channel and contact resistances are relevant for the performance of this studied transistor [20].

REFERENCES

[1] F. Xia et al., *Nat. Nanotechnol.*, vol. 6, pp. 179–184, 2011.
[2] A. D. Smith et al., *Solid-State Electron.*, vol. 108, pp. 61–66, 2015.
[3] L. Anzi et al., *2D Materials*, vol. 5, no. 2, 025014, 2018.
[4] H. Lyu et al., *Scientific Reports*, vol. 6, 35717, 2016.
[5] S. Venica et al., in *Proc. IEEE ICMTS*, Austin, TX, USA, 2018.
[6] A. D. Smith et al., *IEEE Trans. Electron Dev.*, vol. 64, no. 9, pp. 3919–3926, 2017.
[7] J. D. Aguirre-Morales et al., *IEEE Trans. Electron Dev.*, vol. 64, no. 10, pp. 4302–4309, 2017.
[8] G. M. Landauer et al., *IEEE Trans. Nanotechnol.*, vol. 13, no. 5, pp. 895–904, 2014.
[9] D. Jimenez et al., *IEEE Trans. Electron Dev.*, vol. 58, no. 11, pp. 4049–4052, 2011.
[10] G. Ghibaudo, *Electron. Lett.*, pp. 543–545, vol. 24, no. 9, 1988.
[11] A. Pacheco-Sanchez et al., *Solid-State Electron.*, vol. 126, pp. 161–166, 2016.
[12] A. Pacheco-Sanchez et al., (submitted), *Appl. Phys. Lett.*, 2019.
[13] C. Hao et al., *Solid-State Electron.*, vol. 28, no. 10, pp. 1025–1030, 1985.
[14] E. G. Marin et al., *IEEE Trans. Electron Dev.*, vol. 65, no. 10, pp. 4167–4179, 2018.
[15] M. G. Ancona, *IEEE Trans. Electron Dev.*, vol. 57, no. 3, pp. 681–689, 2010.
[16] G. Fiori et al., *Proc. IEEE*, vol. 101, no. 7, pp. 1653–1669, 2013.
[17] V. E. Dorgan et al., *Appl. Phys. Lett.*, vol. 91, no. 8, 082112, 2010.
[18] S. Wang et al., *J. Phys. D. Appl. Phys.*, vol. 49, 425103, 2016.
[19] P. C. Feijoo et al., *IEEE Trans. on Electron Dev.*, vol. 66, no. 3, pp. 1567–1573, 2019.
[20] A. Hsu et al., *IEEE Electron Dev. Lett.*, vol. 32, no. 8, pp. 1008–1010, 2011.
[21] R. Cheng et al., *PNAS*, vol. 109, no. 29, pp. 11588–11592, 2012.
[22] L. Sang et al., *IEEE Trans. Circuits-I*, vol. 65, no. 8, pp. 2559–2570, 2018.
[23] A. D. Smith et al., *IEEE Trans. Electron Dev.*, vol. 64, no. 9, pp. 3927–3933, 2017.
[24] H. Wang et al., *IEEE Trans. on Electron Dev.*, vol. 58, no. 5, pp. 1523–1533, 2011.
[25] M. Iannazzo et al., *IEEE Trans. Electron Dev.*, vol. 62, no. 11, pp. 3870–3875, 2015.
[26] J. Kedzierski et al., *IEEE Electron Dev. Lett.*, vol. 30, no. 7, pp. 745–747, 2009.
[27] W. Wei et al., in *Proc. IEEE EuMC*, Rome, Italy, pp. 367–370, 2014.
[28] A. Pacheco-Sanchez, *Determination of key device parameters for short- and long-channel Schottky-type carbon nanotube field-effect transistors*, Ph. D. Dissertation, TU Dresden, TUD-press, 2019.

TABLE I
REPORTED (OBTAINED WITH OTHER METHODS) AND EXTRACTED
CONTACT RESISTIVITY OF FABRICATED GFETs.

[ref.]	w_g (μm)	L_g (nm)	$R_{C,ref}w_g$ ($\text{k}\Omega \mu\text{m}$)	$R_{C,BP}w_g$ ($\text{k}\Omega \mu\text{m}$)
[4]	–	100	1.1 with TLM	1.4
[22]	12	150	0.08 with CM	0.25
[4]	–	300	1.1 with TLM	1.4
[27]	12	300	4.6 with CM in [7]	4.3
[21]	5	300	–	0.5
[20]	10	2000	1.2 with AM	1.4
[2]	80	2000	20 with AM & TLM	22
[25]	40	4000	16 with CM	20
[24]	25	5000	7 with CM in [8]	10
[26]	5	10 000	3 with CM in [9]	3.2

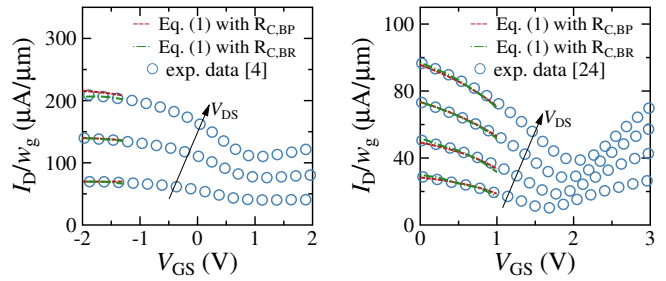


Fig. 1. Experimental and calculated (with Eq. (1) considering extracted parameters) transfer characteristics of fabricated GFETs with different L_g : (left) 100 nm [4], $V_{DS}=0.1$ V, 0.2 V and 0.3 V and (right) 5 μm [24], $V_{DS}=0.35$ V, 0.6 V, 0.85 V and 1.1 V.

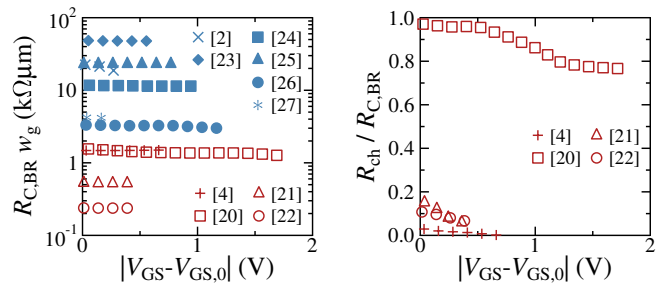


Fig. 2. Left: Extracted V_{GS} -dependent contact resistivity of fabricated GFETs. Right: ratio between channel resistance and extracted contact resistance for selected devices. All curves correspond to the lowest reported V_{DS} .

Effect of temperature on the tribo-mechanical properties of cooper oxide thin films prepared by different oxygen pressure for TEG application

C. Birleanu*, M. Pustan*, V. Merie*, D. Marconi**, L. Barbu-Tudoran**

*Technical University of Cluj-Napoca, Faculty of Building Machine, 103-105, Bd. Muncii, 400641, Cluj-Napoca, Romania

**National Institute for Research and Development of Isotopic and Molecular Technologies, 67-103 Donath Street, 400293, Cluj-Napoca, Romania

E-mail: Corina.Barleanu@omt.utcluj.ro

Copper oxides are semiconductor materials that have been studied due to the natural abundance of copper (Cu) raw material; ease of production by oxidation with Cu; their non-toxic character and the good mechanical properties of Cu_2O [1, 2].

Cooper oxides thin film have been studied in this paper for applications including thermoelectric generator (TEG) which is a thermal energy harvesting source used to convert heat into electricity. The scope of this paper is to investigate the operating temperature effect on the tribo-mechanical properties of cooper dioxide (Cu_2O) thin films used to fabricate micro- thermoelectrical generator (micro- TEG). Energy harvesting is an alternative source for Microelectromechanical Systems (MEMS) devices driven by the desire to provide long lifetime power source especially in application where the maintenance is difficult or not possible. The temperature needed to actuate a micro-TEG changes the mechanical behavior of the thermoelectrical materials. The mechanical stability and thermal performance of a micro- TEG are strongly dependent on the material properties. Testing the micro-TEG materials behavior at different temperatures will improve the system reliability and performance.

The deposition method and certain particular conditions have a significant influence on the physical properties of thin copper oxide films. These are sensitive to the detailed arrangement of Cu and O atoms, which in turn is influenced by the deposition method. Many methods can be used to obtain thin copper oxide films. For most of applications, it is important to grow a high-quality, stoichiometric thin film of a single phase of copper oxide. For this reason, in the present work, we deposited thin films of $\text{Cu}_2\text{O}/\text{MgO}/\text{Si}$ by Pulsed Laser Deposition (PLD) on silicon substrates under different O_2 pressure. The structure and composition of these films were determined by X-ray Diffraction (XRD) analysis as the major tool for identification of phases of the as-prepared copper oxide films.

During the deposition process, the temperature of the substrate was maintained at 700°C. Laser fluency was set to 2J/cm² with a frequency of 5Hz. Deposition time was set of 1 hour. In order to optimize the structural, morphological, mechanical properties of the investigated Cu₂O thin films, the oxygen pressure in the deposition chamber was 1×10⁻⁵mbar, 5×10⁻⁵mbar, 1×10⁻⁴mbar, and 2×10⁻⁴mbar, respectively. The oxygen pressure during deposition has influence on the thickness of Cu₂O thin films as well as the roughness parameters.

The AFM scanning mode of the edge of thin films provides information about the film thickness and roughness (fig. 1).

The measured thickness of the thin films is between 171.1nm and 814nm while the R_a - roughness is between 47nm and 161nm. This effect to obtain high thickness and roughness is based on obtaining higher particle sizes at low deposition oxygen pressures. Moreover, the modulus of elasticity and hardness increase if the oxygen pressure decreases to vacuum during deposition. The operating temperature applied on a micro-TEG to generate electricity decrease the modulus of elasticity and the hardness based on thermal relaxation of material. The experimental tests were performed using an atomic force microscope (AFM) with a temperature-controlled stage which give us the possibility to monitor the temperature of investigated thin films during testing between 20°C and 100°C. For this thin film the hardness decreases with 15% if the testing temperature increases from 20°C to 100°C and the modulus of elasticity decreases with 10.5% for the same testing conditions. The same tendency was experimentally determined for all investigated samples.

The variation of the nanohardness and Young modulus reveal that the elastic deformation and ductility of Cu₂O films increase with decrease the deposition pressure. The tribological behavior of films is not yet fully satisfactory. The friction coefficient and wear rate of the Cu₂O films are still relatively high at this preliminary

stage of the research program. Additional measurements regarding in particular, the microstructure, morphology, nanohardness and tribological properties of Cu_2O films are in progress.

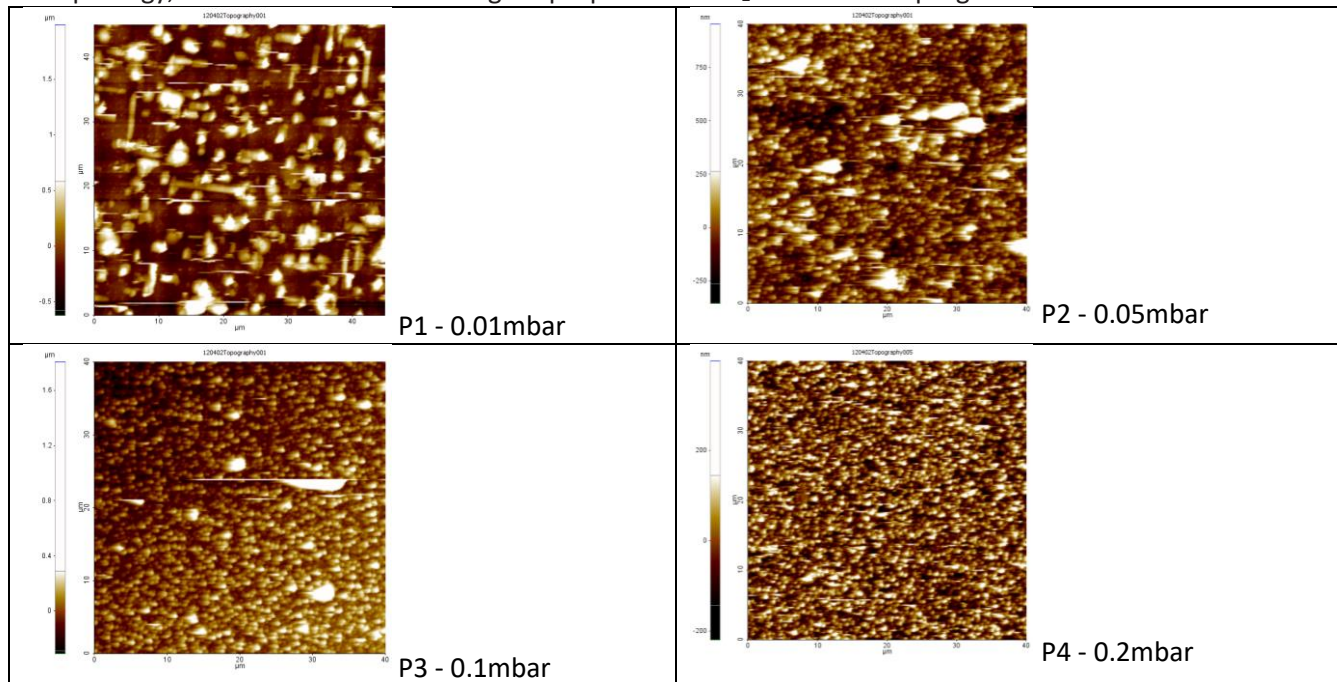


Fig. 1 AFM images for $\text{Cu}_2\text{O}/\text{MgO}/\text{Si}$ thin films investigated

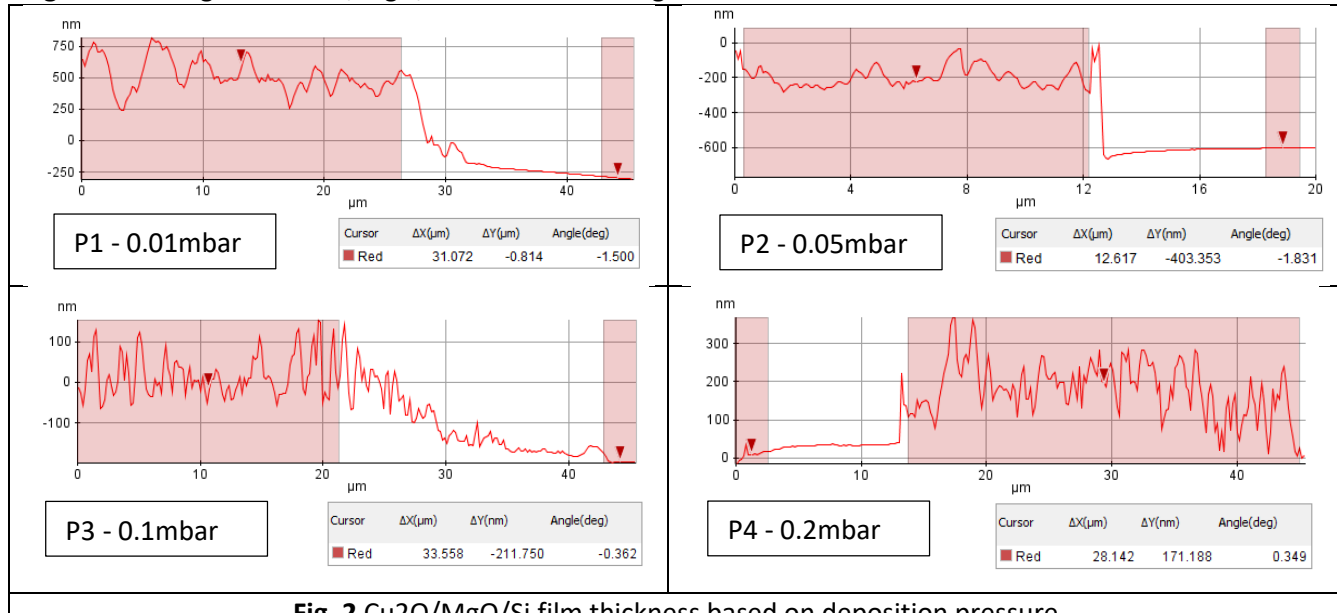
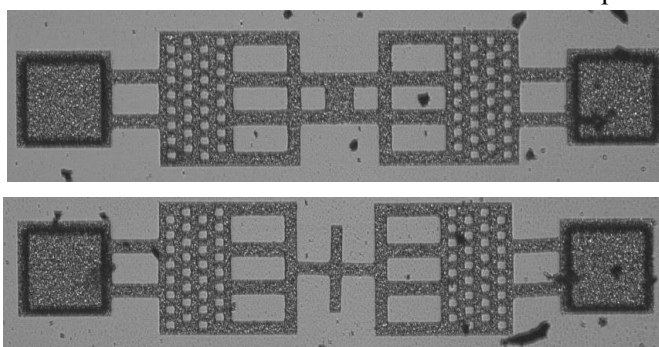


Fig. 2 $\text{Cu}_2\text{O}/\text{MgO}/\text{Si}$ film thickness based on deposition pressure

Results - $\text{Cu}_2\text{O}/\text{MgO}/\text{Si}$ Thin films

Deposition pressure O_2	Investigated parameters*			
	h [nm]	R_a [nm]	E [GPa]	H [GPa]
2×10^{-1} mbar	171.1	47.57	51	1.47
1×10^{-1} mbar	211.7	59.65	59.6	1.84
5×10^{-2} mbar	403.3	73.60	64.3	2.45
1×10^{-2} mbar	814	161.42	76	3.59

* h - the thickness of the film, R_a - roughness, E - modulus of elasticity, H - hardness.

1
2 **Reliability characterization of flexible MEMS micromembranes for the out-of-plane displacement**
34
5 Marius Pustan, Corina Birleanu, Cristian Dutescu, Camelia Rancea
67 Technical University of Cluj-Napoca, Faculty of Building Machine, 103-105, Bd. Muncii, 400641, Cluj-
8 Napoca, Romania
910 E-mail: Marius.Pustan@omt.utcluj.ro
11
1213 The scope of this paper is orientated to investigate MEMS micromembranes with high mobility for the out-
14 of-plane displacement. These micromembrane can be implemented in optical applications. The mobility of
15 MEMS membranes is provided by the geometry of hinges and their reliability depends on the geometrical
16 dimensions and the material behavior. The out-of-plane deformation of micromembrane gives the rise to
1723 Fig.1 Micromembranes fabricated from gold for the
24 out-of-plane displacement
25
2627 The occurrence of complex efforts that can
28 reduce the operation time especially if one
29 considers that, in optical applications, an
30 additional stress state is also provided by the
31 thermal effects. Two different micromembranes
32 are considered for investigations (Fig.1). The
33 difference between micromembranes consists in
34 the geometry of the central plate which is moved
35 toward substrate. These micromembranes are
36 fabricated from gold on a silicon substrate. By
37 using an atomic force microscope, the out-of-
38 plane displacement of flexible part of
39 micromembrane is experimentally monitored. A
40 controlled force given by the bending deflection of AFM probe and its stiffness, is applied in the mid-
41 position of micromembranes and the deflect these toward substrate. After, the out-of-plane stiffness is
42 determined and compared with numerical results. Moreover, the adhesion between micromembrane and
43 substrate is investigated using the spectroscopy-in-point of AFM. Adhesion force is influenced by the
44 testing conditions, the geometry of micromembrane as well as the contact surfaces roughness. For reliability
45 characterizations of micromembrane operating in optical applications, the temperature effect on the
46 micromembrane response must be determined. During testing, a thermal gradient is applied on investigated
47 micromembrane and the variation of stiffness is monitored. The temperature increases from 20°C to 100°C.
48 As temperature increases, the stiffness decreases based on the thermal relaxation of micromembranes
49 material. The results in terms of stiffness agreed with numerical simulation. In finite element analysis the
50 real value of modulus of elasticity is used which was experimentally determined by nanoindentation. The
51 research results are useful to MEMS designers in order to fabricate reliable MEMS for applications where
52 a thermal gradient occurs.
53
54
55
56
57
58
59
60
61
62
63
64
65

Electromigration induced break junction for nanometers-sized EGOFET fabrication

line 1: Matteo Parmeggiani
 line 2: *Center for sustainable Future Technologies*
 line 3: *Italian Institute of Technology*
 line 4: Torino, Italy
 line 5: *Department of Applied Science and Technology (DISAT)*
 line 6: *Politecnico di Torino*
 line 7: Torino, Italy
 line 8: matteo.parmeggiani@polito.it

line 1: Matteo Cocuzza
 line 2: *Department of Applied Science and Technology (DISAT)*
 line 3: *Politecnico di Torino*
 line 4: Torino, Italy
 line 5: *Istituto dei Materiali per l'Elettronica ed il Magnetismo*
 line 6: *IMEM-CNR*
 line 7: Parma, Italy
 line 8: matteo.cocuzza@infm.polito.it

line 1: Alberto Ballesio
 line 2: *Department of Applied Science and Technology (DISAT)*
 line 3: *Politecnico di Torino*
 line 4: Torino, Italy
 line 5: alberto.ballesio@polito.it

line 1: Candido Fabrizio Pirri
 line 2: *Center for sustainable Future Technologies*
 line 3: *Italian Institute of Technology*
 line 4: Torino, Italy
 line 5: *Department of Applied Science and Technology (DISAT)*
 line 6: *Politecnico di Torino*
 line 7: Torino, Italy
 line 8: fabrizio.pirri@polito.it

line 1: Alessio Verna
 line 2 *Department of Applied Science and Technology (DISAT)*
 line 3: *Politecnico di Torino*
 line 4: Torino, Italy
 line 5: alessio.verna@polito.it

line 1: Simone Luigi Marasso
 line 2: *Department of Applied Science and Technology (DISAT)*
 line 3: *Politecnico di Torino*
 line 4: Torino, Italy
 line 5: *Istituto dei Materiali per l'Elettronica ed il Magnetismo*
 line 6: *IMEM-CNR*
 line 7: Parma, Italy
 line 8: simone.marasso@polito.it

Short Abstract

In this study we fabricated nanometers-sized Electrolyte Gated Organic Field Effect Transistors (EGOFETs) by means of a room temperature electromigration induced break junction (EIBJ) of gold microwires [1]. A 10 nm titanium layer was used for gold adhesion and oxidized with a rapid thermal annealing process after nanogaps fabrication. The current-voltage characteristic of the obtained electrodes show the typical signature of Fowler-Nordheim tunneling [2][3]. Poly-3-hexylthiophene (P3HT) with backbones length comparable to nanogaps dimension was used as organic semiconductor for EGOFETs fabrication. The devices were characterized using D.I. water as electrolyte and a Ag/AgCl reference electrode as gate electrode and were able to operate in a narrow gate voltage windows of less than 500 mV.

Extended Abstract

Organic Field Effect Transistor (OFET) are becoming a promising tool for sensing applications in many different research areas, ranging from environmental monitoring to biosensing [4]. EGOFETs exploit the high dielectric constant of aqueous solutions in order to achieve a good control of charge carrier concentration inside the conductive channel [5], allowing for very high sensitivity in chemical and biological sensing [6].

In polymeric organic semiconductor the current is usually dominated by the hopping mechanism of charge carriers from adjacent polymer chains [7]. In this study we exploited electromigration of Au wires to fabricate EGOFETs with channel lengths ranging from 15 to 60 nm, aiming to study the conduction properties of poly-3-hexylthiophene (P3HT) on the same scale length of the polymer backbone. We used P3HT with average molecular weight of 37 kDa (regioregularity > 96%, RMI-001EE, Rieke Metals), corresponding to chain lengths of the order of 80-100 nm.

Ti adhesion layer (10 nm) and Au (100 nm) have been e-beam evaporated on Si/SiO₂ substrate and patterned via

standard UV-photolithography and wet etching, in order to obtain gold microwires 6 μ m long and 2 μ m wide. The gold electrodes have been passivated with polyamide (Asahi Kasei AM-271) in order to prevent short circuit of the devices when operated in liquid. The passivation has been deposited via spin coating and UV-photolithography, followed by a hard bake at 350 °C for one hour on hot plate. The microwires were not covered by the passivation, in order to allow the nanogap formation and polymer deposition.

Nanometer-sized channels have been obtained via electromigration induced break junction of the gold microwires. The EIBJ process has been performed with repeated voltage sweep allowing to flow in the microwires a current density of the order of 10⁷ A/cm². The process was stopped as soon as a sudden drop in the current was measured (Fig. 1).

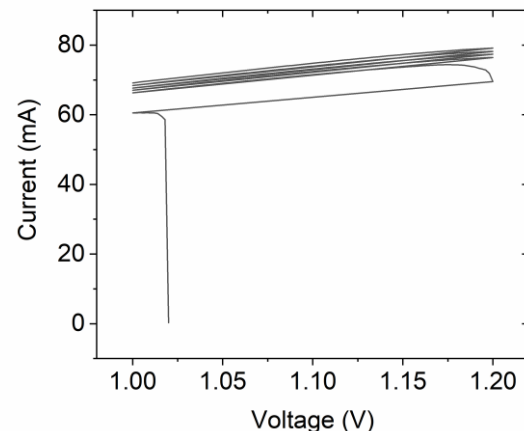


Fig. 1. Current measurement during electromigration process. The process is stopped when the complete fracture of the Au wire is obtained.

The present work was performed in the framework and financed by POLITO BIOMed LAB, financed by Politecnico di Torino, and DEFLeCT ("Advanced platform for the early detection of not small cells lung cancer") project, financed by Piedmont Region in the framework of "Health & WellBeing" Platform project.

In order to remove any conductive paths due to residual Ti adhesion layer inside the nanogap, a rapid thermal annealing in oxygen atmosphere has been performed (300 °C for 80 s, O₂ flow = 2 SLM). This allowed to oxidize the Ti film, avoiding the short circuit of the electrodes. Fig. 2 shows a SEM image of a nanogap obtained via EIBJ, with shorter dimension of 16 nm.

Finally P3HT dissolved in oDCB (2.5 mg/ml) was spin coated on the devices at 2000 rpm for 30 s and dried at 90 °C under vacuum for 1 hour.

We characterized the electrical resistance of nanogaps before and after polymer deposition. Fig. 3 shows the typical signature of Flower-Nordheim (FN) tunneling for the bare nanogap (black line). In the inset is visible the FN representation, showing the transition from direct tunneling to FN tunneling at 0.35 V. The presence of P3HT inside the nanogap allows the conduction along the polymer backbones (red line), resulting in a linear IV characteristic in the region previously dominated by direct tunneling.

Transfer-characteristic of the nanogap-EGOFET have been measured in D.I. water with leak-free Ag/AgCl reference electrode as gate electrode. Fig. 4 shows the transfer-characteristic for a device operating in a very narrow gate potential window between -200 mV and +200 mV at different drain voltages. The drain voltages were kept lower than the transition voltage for Flower-Nordheim tunneling.

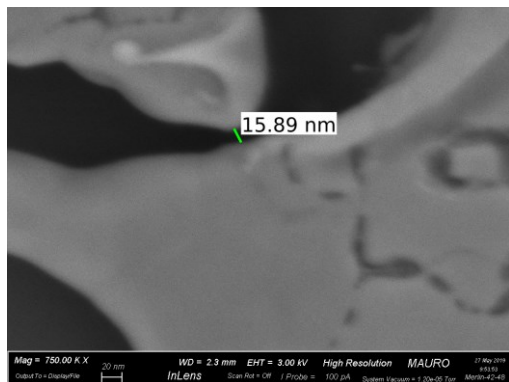


Fig. 2. SEM image of a nanogap fabricated via EIBJ method. The shorter distance between the two electrodes is of the order of 16 nm.

REFERENCES

- [1] D. Demarchi, P. Civera, G. Piccinini, M. Cocuzza, and D. Perrone, "Electrochimica Acta Electrothermal modelling for EIBJ nanogap fabrication," vol. 54, pp. 6003–6009, 2009.
- [2] N. Prokopuk and K. Son, "Fowler – Nordheim Tunneling in Electromigrated Break Junctions with Porphyrin Molecules," 2007.
- [3] A. Phys, "Fabrication of reproducible sub-5 nm nanogaps by a focused ion beam and observation of Fowler-Nordheim tunneling," vol. 103108, no. June, 2015.
- [4] S. G. Surya, H. N. Raval, P. Sonar, K. N. Salama, and V. R. Rao, "Trends in Analytical Chemistry Organic field effect transistors (
- [5] B. L. Kergoat *et al.*, "COMMUNICATION A Water-Gate Organic Field-Effect Transistor," pp. 2565–2569, 2010.
- [6] P. Seshadri *et al.*, "Biosensors and Bioelectronics Low-picomolar, label-free procalcitonin analytical detection with an electrolyte-gated organic field-effect transistor based electronic immunosensor," *Biosens. Bioelectron.*, vol. 104, no. December 2017, pp. 113–119, 2018.
- [7] V. Coropceanu, A. Demetrio, S. Filho, Y. Olivier, R. Silbey, and J. Bre, "Charge Transport in Organic Semiconductors," pp. 926–952, 2007.

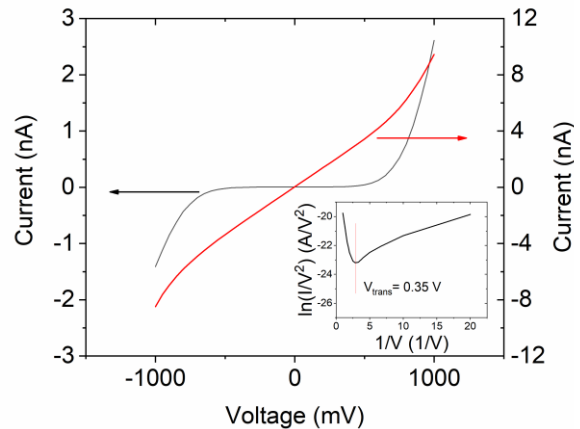


Fig. 3. Current-voltage characteristic of a bare nanogap (black line) showing typical signature of Flower-Nordheim tunneling, and of a nanogap filled with P3HT (red line), showing a linear resistive behaviour. The inset shows the Flower-Nordheim representation for the bare nanogap IV curve, with a transition voltage of 0.35 V.

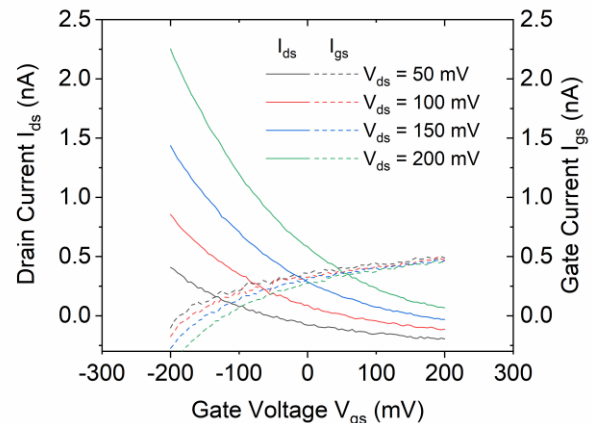


Fig. 4. Transfer-characteristic of a nanogap-EGOFET measured in D.I. water with a leak free Ag/AgCl reference gate electrode. Solid lines show the drain current flowing through the organic semiconductor channel, dashed lines are the leakage current flowing through the gate.

OFETs) in environmental sensing and health monitoring : A review," vol. 111, pp. 27–36, 2019.

- [5] B. L. Kergoat *et al.*, "COMMUNICATION A Water-Gate Organic Field-Effect Transistor," pp. 2565–2569, 2010.
- [6] P. Seshadri *et al.*, "Biosensors and Bioelectronics Low-picomolar, label-free procalcitonin analytical detection with an electrolyte-gated organic field-effect transistor based electronic immunosensor," *Biosens. Bioelectron.*, vol. 104, no. December 2017, pp. 113–119, 2018.
- [7] V. Coropceanu, A. Demetrio, S. Filho, Y. Olivier, R. Silbey, and J. Bre, "Charge Transport in Organic Semiconductors," pp. 926–952, 2007.

Memory effect in MIS structures with embedded all-inorganic colloidal silicon carbide (SiC) nanocrystals

Andrzej Mazurak, Robert Mroczynski

Warsaw University of Technology

Institute of Microelectronics and Optoelectronics

Koszykowa 75, 00-662 Warsaw, Poland

Abstract – Colloidal all-inorganic silicon carbide (SiC) nanocrystals (NCs) have been introduced into Metal-Insulator-Semiconductor (MIS) structures with HfO_x gate dielectric layers. The fabricated MIS structures were characterized by means of stress-and-sense measurements in terms of device capacitance, flat-band voltage shift, and retention time. Presented results have shown the feasibility of the application of SiC-NCs in memory structures.

Keywords – silicon carbide (SiC) nanocrystal; memory; metal-insulator semiconductor structure; electrical characterization; high- k dielectrics

I. INTRODUCTION

Nowadays, the ongoing investigations of the structures with nanocrystals (NCs) embedded in dielectric layers due to their potential applications in the field of modern optoelectronics and photonics can be clearly noticed [1]. The literature reports mostly the application of silicon (Si) nanocrystals in various semiconductor devices and structures, e.g. Field-Effect Light-Emitting Devices (FELEDs) [2], photovoltaics [3], memory structures based onto photoluminescence (PL) [4], or Non-Volatile Semiconductor Memory (NVSM) devices [5, 6]. However, in the last two decades, it can be clearly observed the noticeable growth of interest of other types of semiconductor NCs or all-inorganic perovskite NCs [7]. In this work, the technology of the metal-insulator-semiconductor (MIS) structures with silicon-carbide (SiC) nanocrystals embedded in dielectric layers is presented. The fabrication of SiC-NCs was based on the reactive bonding method followed by electroless wet chemical etching [8]. The results of the electrical characterization of the fabricated test structures are discussed. Comparative electrical measurements of the MIS structures with and without NCs proved the essential difference resulting from the charging/discharging processes of the nanocrystals, relatively high retention, and the feasibility of application of the studied MIS structures in memory devices.

II. EXPERIMENTAL

In this study silicon (Si) substrates with the resistivity of $1\text{--}10 \Omega\text{cm}$ were used. The processing sequence of SiC-NCs MIS structures was as follows: Si substrates were cleaned by means of a modified RCA method (Piranha + SC1 + SC2 + HF dipping). In the first step, 10 nm or 20 nm bottom hafnium oxide (HfO_x) layer was deposited. In the next step, the SiC-NCs spinning off on top of the hafnia surface was performed followed by 20 nm top HfO_x layer deposition. Two types of colloidal nanocrystals were used, i.e. with the dimensions of $1\text{--}3$ and $4\text{--}6$ nm. After the formation of SiC-NCs embedded in dielectric layer ensembles, the aluminum contact pads were formed by means of the standard UV photolithography process and wet etching. Hafnium oxide and aluminum layers

were deposited in Pulsed-DC reactive magnetron sputtering process. Split experiments with the post-metallization annealing (PMA) at 300°C in vacuum atmosphere were performed. For the sake of comparison, reference MIS structures (without the SiC-NCs introduction) were also fabricated. The schematics of the studied in this work MIS stacks have been presented in Fig. 1.

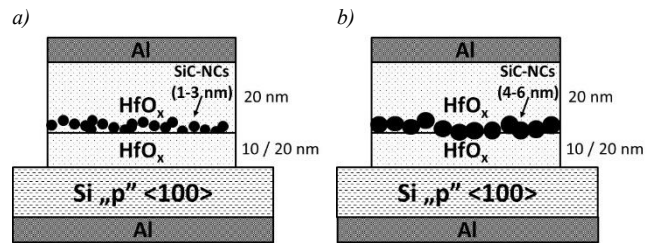


Fig. 1. The test structures investigated in this work: schematic cross-section of MIS stacks with the dimensions of SiC-NCs $1\text{--}3$ nm (a) and $4\text{--}6$ nm (b).

The measurement procedure used to investigate the fabricated devices consists of charging pulses and measurements performed in a staggered manner. At the very beginning, the fresh device is measured. Then, charging bias pulses (electrical stress) followed by measurements (capacitance or current) are applied. The charging bias pulse may be implied by a voltage or a current source. In the program-erase voltage analysis voltage pulses of opposite values are subsequently applied. The measurement may be taken in a sweep or sampling mode. The MIS capacitors with the gate area of $A = 1.8 \times 10^{-4} \text{ cm}^2$ were used. They have allowed the determination of basic electrical properties of the investigated structures. The quality and electrical parameters of obtained MIS structures were examined with the Keithley 4200 semiconductor characterization system equipped with SUSS PM-8 probe station.

III. RESULTS & DISCUSSION

The results presented in Fig. 2 show the CV characteristics of MIS structures with SiC-NCs compared to the reference devices. The significant different magnitude of frequency dispersion of presented curves suggesting the charge build-up in MIS structures with NCs can be clearly noticed. Such an effect is due to the NCs presence between hafnia films, and the formation of quantum well allowing charge carriers trapping.

The memory effect in examined MIS structures has been studied by the determination of flat-band (V_{fb}) voltage value from the C-V characteristic analysis by applying appropriate voltage stress. The V_{fb} value can be assumed as the characteristic for the MIS structure, similarly as the threshold

voltage (V_{th}) value of the particular MOSFET. And thus, the investigations of V_{fb} changes of MIS structures at specific stress conditions can be valuable for memory effects characterization. Based on the V_{fb} evaluation from the C-V characteristics after stressing (i.e., after excitation at particular voltage value), the “hysteresis loop” of the particular MIS structure $V_{fb} = f(V_{p/e})$ was obtained, as presented in Fig. 3.

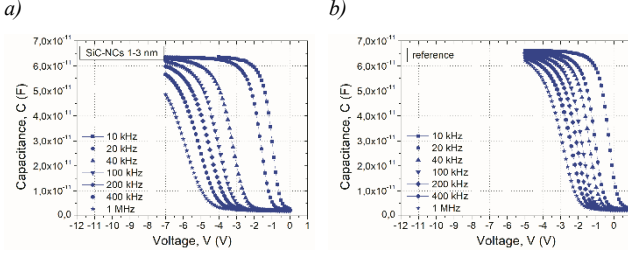


Fig. 2. High-frequency C-V characteristics of MIS structures with SiC-NCs (a) compared to a reference device (b), i.e. without NCs embedded in hafnia films.

The results presented in Fig. 3 have demonstrated relatively large hysteresis. The measurements were performed towards negative, as well as positive $V_{p/e}$ values, and repetitive behavior of obtained dependences was proved. In the case of MIS structures with 10 nm bottom HfO_x the change of V_{fb} of the order of 7.8 V, and 4.1 V, for NCs with the dimensions of 1÷3 nm, and 4÷6 nm, respectively, have been obtained. The application of thicker (i.e. 20 nm) bottom HfO_x layer has not influenced significantly the obtained memory window.

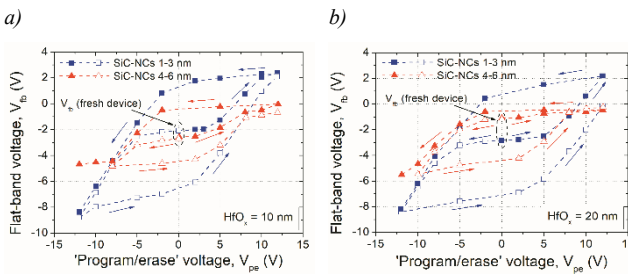


Fig. 3. Comparison of memory windows (expressed as V_{fb} change) of MIS structures with SiC-NCs and bottom HfO_x of the thickness of 10 nm (a) and 20 nm (b); $V_{p/e} = 0 \pm 12$ V, and stress time = 1s were used.

However, the further performed examination of the stability of introduced charge into investigated SiC-NCs MIS has confirmed the improvement of the retention after the application of thicker bottom HfO_x layer. These results have been depicted in Fig. 4. The observed retention time of V_{fb} extrapolated to ten years exhibits increased stability. In the case of MIS structures with NCs with the dimensions of 1÷3 nm the improvement is of the order of 15 %, while in the case of NCs of 4÷6 nm, the retention has been maintained at a similar level. The observed effect can be justified by the less likely tunneling of charge carriers through the thicker HfO_x dielectric film. The split experiment performed with the PMA was aimed at the further improvement of dielectric films quality and the clearly identification of the influence of SiC-NCs onto memory characteristics of investigated test structures. Our previous works have shown that the annealing of MIS stacks improves not only the contact properties, but also the quality and interfacial properties of Si/ HfO_x system [9].

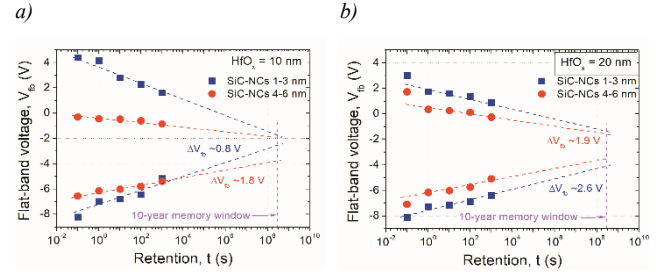


Fig. 4. Comparison of retention (expressed as V_{fb} change) of MIS structures with SiC-NCs and bottom HfO_x of the thickness of 10 nm (a) and 20 nm (b); $V_{p/e} = 0 \pm 12$ V, and stress time = 1s were used.

As the consequence, the application of PMA slightly reduced the memory windows, but significantly improved the retention characteristics of obtained SiC-NCs MIS structures (to be shown).

IV. CONCLUSION

The feasibility of application of colloidal SiC-NCs in MIS devices has been demonstrated. The large hysteresis of V_{fb} values of fabricated MIS stacks, the relatively large retention, and improved stability of introduced charge after the application of thicker bottom hafnia films, were observed. Presented in this work findings have clearly proved the potential applications of silicon carbide nanocrystals in several types of memory structures, especially in the Nonvolatile Semiconductor Memory (NVSM) and Resistive Random Access Memory (RRAM) devices.

ACKNOWLEDGMENT

This work has been supported by The National Centre for Research and Development (NCBiR) under grant No. V4-Jap/3/2016 (“NaMSeN”) in the course of “V4-Japan Advanced Materials Joint Call”.

REFERENCES

- [1] F. Priolo, T. Gregorkiewicz, M. Galli, and T.F. Krauss, *Nature Nanotechnology* 9, 19–32 (2014), DOI:10.1038/nnano.2013.271.
- [2] R. J. Walters, J. Carreras, T. Feng, L. D. Bell, and H. A. Atwater, *IEEE J. of Selected Topics in Quantum Electronics*, Vol. 12, No. 6, November/December 2006.
- [3] G. Conibeer, M.A. Green, D. Konig, I. Perez-Wurfl, S. Huang, X. Hao, D. Di, L. Shi, S. Shrestha, B. Puthen-Veetil, Y. So, B. Zhang, Z. Wan, *Prog. Photovolt. Res. Appl.* 19 (2011) 813–824.
- [4] R. J. Walters, P. G. Kik, J. D. Casperton, H. A. Atwater, R. Lindstedt, M. Giorgi, and G. Bourianoff, *Appl. Phys. Lett.* Vol. 85, No 13 (27) (2004), 0003-6951.
- [5] A. Mazurak, R. Mroczynski, J. Jasiński, D. Tanous, B. Majkusiak, S. Kano, H. Sugimoto, M. Fujii, J. Valenta, *Microelectron. Eng.* 178 (2017) 298–303.
- [6] A. Mazurak, R. Mroczynski, *Solid-State Electron.* *in press* (2019), DOI: 10.1016/j.sse.2019.03.050.
- [7] C. de Weerd, L. Gomez, A. Capretti, D.M. Lebrun, E. Matsubara, J. Lin, M. Ashida, F.C.M. Spoor, L.D.A. Siebbeles, A.J. Houtepen, K. Suenaga, Y. Fujiiwara, and T. Gregorkiewicz, *Nature Communications* (2018) 9:4199, DOI: 10.1038/s41467-018-06721-0.
- [8] D. Beke, Z. Szekrenyes, I. Balogh, M. Veres, E. Fazakas, L.K. Varga, K. Kamaras, Z. Czigany, and A. Gali, *App. Phys. Lett.* 99, 213108 (2011), DOI: 10.1063/1.3663220.
- [9] A. Taube, R. Mroczynski, K. Korwin-Mikke, S. Gierałtowska, J. Szmidt, A. Piotrowska, *Mat. Scienc. Eng. B* 177 (2012) 1281–1285, DOI:10.1016/j.mseb.2011.12.010.

Spin Hall nano-oscillators as gigahertz neurons

1 Mohammad Zahedinejad

2 Department of physics

3 University of Gothenburg

4 Gothenburg, Sweden

5 mohammad.zahedinejad@physics.gu.se

6 Ahmad A. Awad

7 Department of physics

8 University of Gothenburg

9 Gothenburg, Sweden

10 ahmad.awad@physics.gu.se

11 Shreyas Muralidhar

12 Department of physics

13 University of Gothenburg

14 Gothenburg, Sweden

15 shreyas.muralidhar@physics.gu.se

16 Himanshu Fulura

17 Department of physics

18 University of Gothenburg

19 Gothenburg, Sweden

20 himanshu.fulura@physics.gu.se

21 Roman Khymyn

22 Department of physics

23 University of Gothenburg

24 Gothenburg, Sweden

25 roman.khymyn@physics.gu.se

26 Johan Åkerman

27 Department of physics

28 University of Gothenburg

29 Gothenburg, Sweden

30 johan.akerman@physics.gu.se

31 Spin transfer torque oscillators (STO) are one of the
 32 promising platforms for bioinspired computing and
 33 microwave signal generation. Thanks to nanoscale
 34 dimensions, ease of fabrication, and CMOS compatibility
 35 they have shown superior performance in recognition tasks.
 36 An ensemble of STOs can interact with neighboring
 37 oscillators via exchange and dipolar coupling imitating the
 38 neuronal activity and connectivity in human brains. Neural
 39 oscillations and synchronization have been shown to be the
 40 main phenomena behind many cognitive functions such as
 41 memory, vision, and perception [1]. Using the same
 42 analogy, the spintronic community has been looking to
 43 harness synchronization for auto associated memory [2], the
 44 Ising machine [3], vertex coloring [4], and recognition tasks
 45 and computation. Recent researches have shown by using
 46 reservoir computing with only one STO one could achieve
 47 85% recognition rate in spoken vowels [5]. Using four
 48 mutually synchronized STOs with individual electrical
 49 access up to 90% recognition rate was achieved which is
 50 comparable to the state of art CMOS base classifiers [6].
 51 However, in order to do more complex tasks, larger scale
 52 synchronized oscillators are needed which with the current
 53 approaches does not seem to be feasible.

54 Spin Hall nano – oscillators (SHNO) are the branch of
 55 STOs driven by pure spin current provided by a heavy
 56 nonmagnetic layer injected to adjacent ferromagnetic layer
 57 exciting a sustainable precession of magnetization moment
 58 at microwave frequencies. SHNOs placed next to each other
 59 can operate in unison once they are provided with enough
 60 coupling by tuning the applied direct-current (DC) and
 61 applied magnetic field [7].

62 In this abstract, We demonstrate 2D arrays of SHNOs
 63 fabricated in $\text{Ni}_{80}\text{Fe}_{20}(3)$ Hf(0.5)/Pt(5) tri-layers (numbers
 64 in parenthesis indicate thickness in nm). Figure 1 shows a
 65 schematic of a 4 x 4 SHNOs array. An external magnetic
 66 field (H) was applied during the microwave measurements
 67 with an out of plane (OOP) angle θ and an in-plane (IP)
 68 angle ϕ as shown in Fig.1.

69 The nano-constriction width was varied from $w = 50$ to 120
 70 nm while the pitch size (p) in both the x and the y directions
 71 was set to 100, 140, 200 and 300nm, to modify the dipolar
 72 and exchange coupling. We also fabricated the arrays to
 73 accommodate more number of SHNOs from 2x2 (4 SHNO)
 74 to 8x8 (64 SHNO) and studied their frequency behaviors.

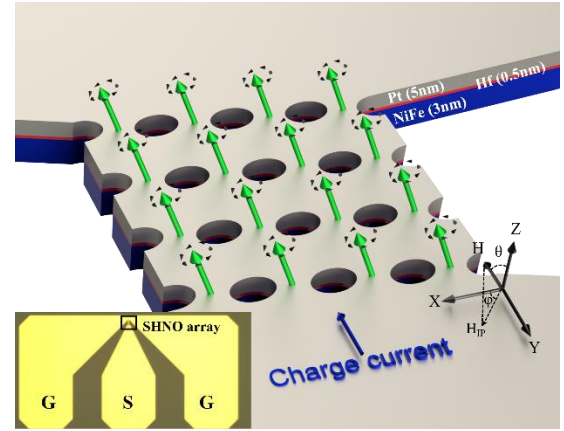


Fig.1 Schematic representation of a 4x4 SHNO array. The schematic shows the direction of the applied magnetic field. The green arrows indicate the precessing magnetization of each nano-constriction. The Pt, Hf, and NiFe layers are highlighted by gray, red, and blue colors with corresponding thicknesses in nm. The inset shows an optical microscopy image of the ground-signal-ground co-planar wave guide used for electrical measurements.

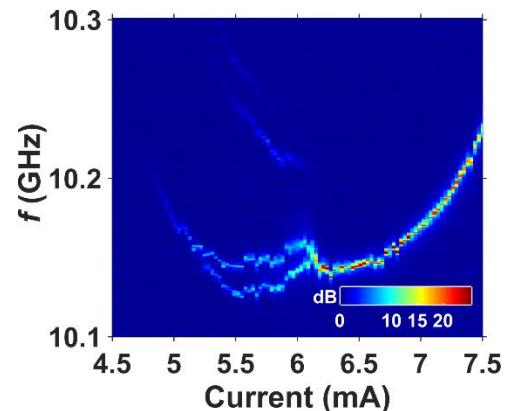


Fig.2. PSD plot of a 4x4 SHNO arrays with $(w, p) = (120, 200)$ nm. As the applied dc current provides enough coupling, the frequency branches approach to each other and eventually operate as an ensemble in unison.

Fig.2 shows the power spectral density (PSD) of a 4x4 SHNO array with $(w, p) = (120, 200)$ nm. As the applied current increases, the oscillators eventually find common ground to operate at synchronized frequency. Fig.3 Shows

the linewidth and peak power values for the arrays which could reach a synchronized state, and for different (w, p) versus the array size (# of SHNOs). As it can be seen, all the arrays with (w, p) = (50, 100) nm synchronize for different array sizes. However, for larger w and p values the applied field and current may fail to be provided by enough coupling. Therefore larger arrays fail to synchronize as the array grows in size. According to synchronization theory, the linewidth of the synchronized state is inversely proportional to the number of oscillators contributing the synchronization. Fig.3a shows the linewidth values (green squares) for arrays with (w, p) = (50, 100) nm are in an excellent agreement with 1/N fitted curve (dashed black line). Our largest array accommodating 64 SHNOs operating at 10 GHz achieves a record value of 170,000 for quality factor (Q) among all spintronic based microwave oscillators. Also, the peak power of an ensemble of oscillators in the synchronized state scales up with N^2 scaling factor if there is no phase difference between the oscillators. Fig.3b shows the peak power values corresponding to the points shown in Fig.3b, where the green squares show a rollover in the peak power at the array size scale. This behavior could be explained by introducing a relative phase difference between the oscillators, which prevents the peak power scale up as N^2 . By introducing the phase difference parameter as a fitting factor, experimental data can be explained by the dashed black line in Fig.3b, which corresponds to a relative phase difference of $\phi = 16^\circ$.

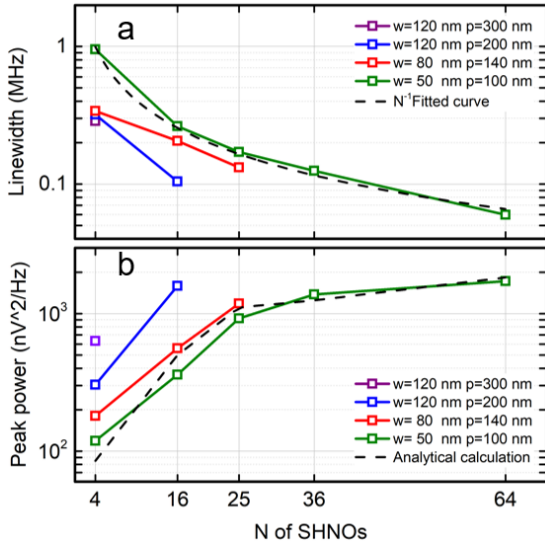


Fig.3 (a) Linewidth values obtained for arrays with different (w, p)s and sizes. All data points shown in squares correspond to a synchronized state is achieved by the array. (b) the peak power values corresponding to all data points shown in (a). An apparent rollover for the power is observed at the array size scales.

Each oscillator within the array can be considered as an artificial neuron imitating oscillatory behavior while it is coupled to the neighboring neurons through dipolar and exchange interactions. The frequency of each oscillator and the coupling between neighboring oscillators can be tuned globally by changing the applied magnetic field strength and dc current.

Moreover, the couplings and frequencies can be tunable by introducing other magnetic materials in which precession can be tuned over a wide frequency range [8], the magnetization and perpendicular magnetic anisotropy can be tuned via applying a local electric field by gating means.

In conclusion, we have pushed the boundaries toward realizing massive oscillatory networks are CMOS compatible and scalable in size down to 50 nm individual oscillator's footprint hard to achieve with any other technology. We believe our 2D SHNO arrays can pave the way for emerging bio-inspired computing paradigms operating at ultrahigh frequencies.

References

- [1] Gouwens, Nathan W., et al. "Synchronization of firing in cortical fast-spiking interneurons at gamma frequencies: a phase-resetting analysis." *PLoS computational biology* 6.9 (2010): e1000951.
- [2] Nikonorov, Dmitri E., et al. "Coupled-oscillator associative memory array operation for pattern recognition." *IEEE Journal on Exploratory Solid-State Computational Devices and Circuits* 1 (2015): 85-93.
- [3] Wang, Tianshi, Leon Wu, and Jaijeet Roychowdhury. "New Computational Results and Hardware Prototypes for Oscillator-based Ising Machines." *Proceedings of the 56th Annual Design Automation Conference 2019*. ACM, 2019.
- [4] Parihar, Abhinav, et al. "Vertex coloring of graphs via phase dynamics of coupled oscillatory networks." *Scientific reports* 7.1 (2017): 911.
- [5] Vodenicarevic, Damir, et al. "Nano-oscillator-based classification with a machine learning-compatible architecture." *Journal of Applied Physics* 124.15 (2018): 152117.
- [6] Romera, Miguel, et al. "Vowel recognition with four coupled spin-torque nano-oscillators." *Nature* 563.7730 (2018): 230.
- [7] Awad, A. A., et al. "Long-range mutual synchronization of spin Hall nano-oscillators." *Nature Physics* 13.3 (2017): 292.
- [8] Zahedinejad, M., et al. "CMOS compatible W/CoFeB/MgO spin Hall nano-oscillators with wide frequency tunability." *Applied Physics Letters* 112.13 (2018): 132404.

Effect of Polymer Blend on Electrical Performance and Photo-Response of TIPS-Pentacene OFETs

Ajay Kumar Mahato, Vivek raghuwanshi, Deepak bharti, Ishan Varun, and Shree Prakash Tiwari

Department of Electrical Engineering,
Indian Institute of Technology Jodhpur

Jodhpur, India
Email: sptiawari@iitj.ac.in

In this work, we have explored the effect of TIPS-pentacene:polystyrene blend on electrical performance and photo-response of solution processed organic field-effect transistors (OFETs). It was observed that though the blend OFETs show better electrical performance, the photo-responsivity (R) of neat TIPS-pentacene OFETs was significantly better. This study was performed for different color lights such as blue, red, and green, as well as for ultraviolet light (UV). R was highest for blue color (~ 2600 mA/W for neat, ~ 230 mA/W for blend), and smaller for other cases. Low R value in blend devices is contributed to less trapping of photo-generated charge carriers during photo-illumination compared to their neat counterparts.

Blending of TIPS-pentacene with polystyrene offers enhancement in the performance of solution-processed OFETs [1]. However, reports on effects of blend on the photo-response performance of OFETs are scarce [2]. Here, we have demonstrated the effect of polymer blend on the photo-response of TIPS-pentacene OFETs, fabricated on heavily doped (n^+) silicon with 300 nm thermal SiO_2 and Au top contacts. Gate capacitance density values were measured to be 10.5 and 2.7 nF/cm² at 1 KHz from metal-insulator-semiconductor structure respectively for neat and blend devices. Photo-response were obtained as reported earlier [3]. Table I summarizes the electrical performance of fabricated OFETs.

TABLE I. COMPARISON OF ELECTRICAL PARAMETERS OF NEAT TIPS-PENTACENE AND TIPS-PENTACENE: PS BLEND DEVICE

Dev.	$\mu_{\text{max}}, \mu_{\text{avg}}$ (cm ² V ⁻¹ s ⁻¹)	$V_{\text{TH,avg}}$ (V)	SS_{avg} (V/dec.)	$D_{\text{it,avg}} \times 10^{12}$ (cm ⁻² eV ⁻¹)
Neat	0.3, 0.2 ± 0.1	-0.9 ± 0.7	1.4 ± 0.3	1.4 ± 0.3
Blend	0.8, 0.6 ± 0.3	-0.8 ± 0.3	1.1 ± 0.6	0.3 ± 0.2

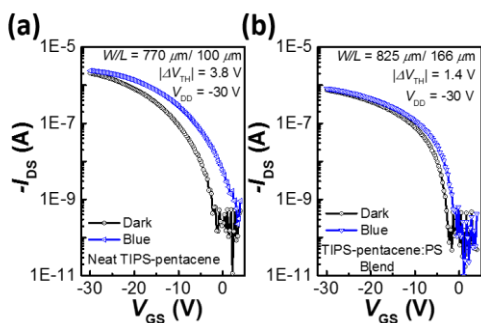


Fig. 1 Effect of blue light on the transfer characteristics of (a) neat, and (b) blend top-contact TIPS-pentacene OFETs.

Fig. 1 shows the transfer characteristics for Blue color for representative neat and blend devices. Plots for photocurrent modulation (P) and R are shown in Fig 2. It can be seen that R from neat devices is about ~ 10 times

higher than blend devices. Less trapping of photo-generated charge carriers during photo-illumination in blend devices resulted in less photo-responsivity.

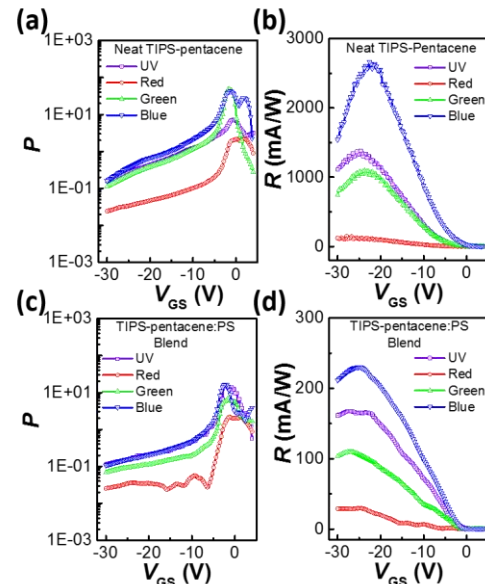


Fig. 2 Photocurrent modulation (P), and photo-responsivity (R) plots of representative neat (a, b) and blend (c, d) OFETs.

In summary, neat and TIPS-pentacene:polystyrene blend OFETs were studied for their electrical performance and photo-response. It was found that the blend OFETs exhibited better electrical performance compared to neat devices; however, lesser trapping of photo-generated charge-carrier significantly reduced the photo-responsivity.

ACKNOWLEDGMENT

This work is supported by Science and Engineering Research Board (SERB), India (EMR/2017/003766).

REFERENCES

- [1] Bharti, D., and Tiwari, S.P., "Phase separation induced high mobility and electrical stability in organic field-effect transistors," *Synthetic Metals*, 2016, 221, pp. 186-191
- [2] Ljubic, D., Smithson, C.S., Wu, Y., and Zhu, S., "Highly UV-Sensitive and Responsive Benzothiophene/Dielectric Polymer Blend-Based Organic Thin-Film Phototransistors," *Advanced Electronic Materials*, 2015, 1, (8), pp. 1500119
- [3] Mahato, A.K., Raghuwanshi, V., Bharti, D., Varun, I., Prasad, N., Roy, M.S., and Tiwari, S.P., "TIPS-pentacene/Copper (II) phthalocyanine bi-layer photo sensitive organic field-effect transistors," *Synthetic Metals*, 2019, 248, pp. 110-119

Nanomembranes for a Noiseless Airplane Cabin

1 Elvis C. Monteiro

2 Graduate Studies Program on
3 Mechanical Engineering

4 Universidade Federal de Minas Gerais

5 Belo Horizonte, Brazil

6 elvis.c.monteiro@hotmail.com

7 Matheus M. Norton

8 Graduate Studies Program on
9 Mechanical Engineering

10 Universidade Federal de Minas Gerais

11 Belo Horizonte, Brazil

12 mtmello11@hotmail.com

13 Antonio Avila

14 Department of Mechanical
15 Engineering

16 Universidade Federal de Minas Gerais

17 Belo Horizonte, Brazil

18 avila@ufmg.br

The aeronautic industry is constantly looking for ways of improving cabin comfort to compete in the global market. Moreover, this “search for a noiseless cabin” is constrained by requirements of weight and production costs. As discussed by Leylekian et al [1], the aircraft noise can be divided into two major sources, i.e. external and internal. According to Casalino et al [2], in general, engines and airframe are responsible for external noise, while internal noise are basically due to interactions between internal components such as intra-panels and secondary structure vibrations, as well internal systems, e.g. air-condition and ventilation. A comprehensive study on noise sources and its effects on airplane cabin’s was developed by Johansson et al [3]. As discussed by these authors, the engine type and location affects the cabin noise. Turboprop engines produce frequencies into the range of 60-400 Hz, while jet aircrafts with tail mounted engines create noise into the 100-500 Hz frequency range. Furthermore, boundary layer noise, or wind noise, is audible in into the entire cabin and it is, in general, above the 400 Hz range. Wilby [4] went further, as his established the narrow-band interior noise spectrum for a business jet up to 800 Hz. For commercial mid-size, up to 140 passengers, this band interior noise spectrum can be expanded to 1000-1200 Hz limit. Therefore, this research focuses on the 400-1200 Hz range.

As discussed by Petrone et al [5], a potential material for cabin noise reduction can be based on nanomembranes prepared by electrospinning. They developed a “blanket” based on electrospun fibers made of polyvinyl pyrrolidone (PVP). According to them, their results were encouraging and can be applied from the 200-1600 Hz range. In this research, however, a polyvinylidene fluoride co-polymer (PVdF-TrFe), which have also piezoelectric properties was selected. The key issue here is to couple the piezoelectric effect and the acoustic absorption properties. The electrospinning parameter employed were an applied voltage of 1.0 KV/cm, a flow rate of 2.0 ml/h, and a DMAc/PVdF-TrFe solution of 15 % v/w.

Figure 1 shows two samples of PVdF-TrFe nanomembranes, the first one with carbon nanotubes (CNT), while the second one was doped with 0.6% w/w of CNT functionalized with Sodium dodecyl benzene sulfonate (SDBS) at 100 ppm concentration. As it can be observed in Figures 1a-b the CNT addition not only promote a decrease on fiber diameter (around 48%) but it is also changed the overall morphology. Once the fibers’ morphology was established, the next step was the acoustic properties prediction. As the fibers’ porosity is higher than 80%, see Figure 2, the Langmuir model based on drag forces was employed for predicting the airflow resistivity. According to

Pellegrinis et al [6], the Langmuir airflow resistivity (σ) can be calculated by the following equation (1):

$$\sigma = \frac{16\mu(1-\phi)}{d^2 \left[-\ln(1-\phi) - 1.5 + 2(1-\phi) - \frac{(1-\phi)^2}{2} \right]} \quad (1)$$

where ϕ is the fiber porosity (for such membranes $\sim 92\%$), μ is the air dynamics viscosity and d is the fiber diameter. As the ratio between the frequency and the airflow resistivity is smaller than $0.01 \text{ m}^3/\text{kg}$. Furthermore, according to Othmani et al [7] suggested Komatsu model for calculating the complex wave propagation constant and the characteristic impedance. These properties are critical for computing the noise absorption coefficient as function of frequency (f). Hurrel et al. [8] describes the complex wave propagation constant (γf) and the characteristic impedance (Z_c) using Komatsu equations (2) and (3) as:

$$\gamma_f = \frac{2\pi f}{c_a} [0.0069b^{4.1} + i(1 + 0.0004b^{6.2})] \quad (2)$$

and

$$Z_c = \rho_a c_a [1 + 0.00027b^{6.2} - i(0.0047b^{4.1})] \quad (3)$$

where C_a is the sound velocity at air at 20°C (343 m/s), ρ_a is the air density at 20°C (1.213 kg/m^3), and b is an auxiliary variable defined as:

$$b = 2 - \log \frac{f}{\sigma} \quad (4)$$

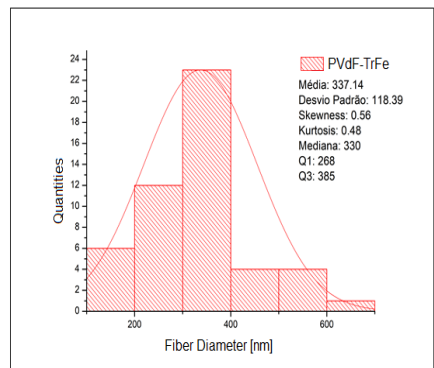
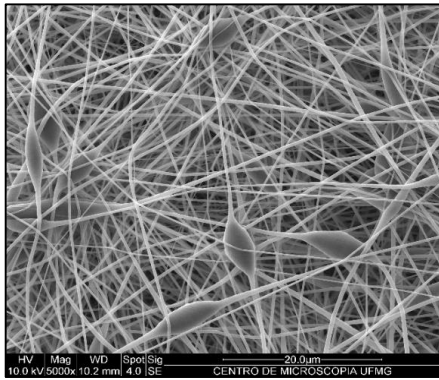
Following Jones and Kessissoglou [9], the noise absorption coefficient (α) can be calculated as described in equation (5):

$$\alpha = 1 - \left| \frac{Z_p - \rho_a c_a}{Z_p + \rho_a c_a} \right|^2 \quad (5)$$

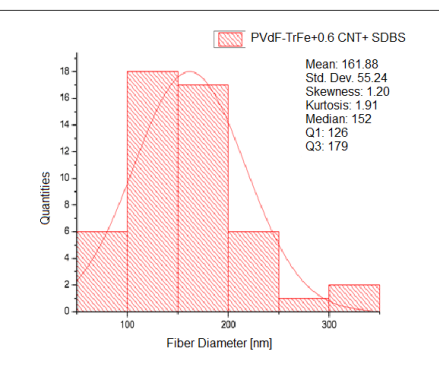
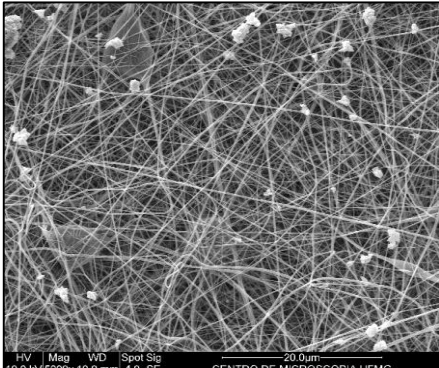
Another important issue is the nanomembrane thickness, in this case, it was assumed a constant thickness of 50 mm. Note that according to Pellegrinis et al [6], as the thickness increases α will also increase. However, as the final objective is to keep the overall weight small, the 50 mm thickness was assumed. Figure 3 shows the absorption coefficient as a function frequency range.

The sound absorption coefficient is highly dependent of the fiber diameter, fiber porosity and frequency. Larger diameters appear to lead to better sound absorption coefficient. The electrospinning technique seems to produce fibers with large porosity and variable diameters. It could be

tailored to produce nanomembranes with light weight and good acoustic properties.



(a)



(b)

Figure 1: Nanomembranes: (a) without CNT, (b) with 0.6% w/w + SDBS

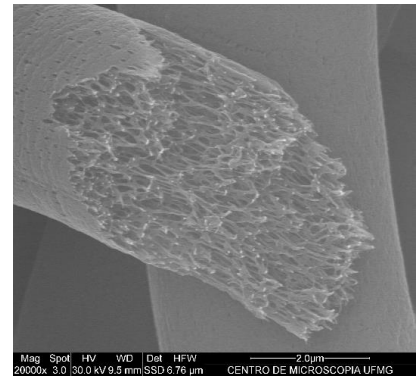


Figure 2: Nanofiber porosity observation by high resolution scanning microscope

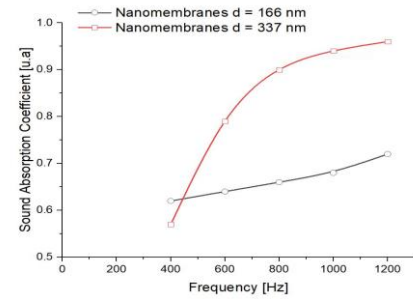


Figure 3: Sound Absorption Coefficient

ACKNOWLEDGMENT

The authors would like to acknowledge the financial support provided by the Brazilian Research Council under grant 304556/2018-1.

REFERENCES

- [1] L. Leylekian, M. Lebrun, P. Lempereur. "An overview of aircraft noise reduction technologies". *J. of AerospaceLab*, Vol. 7, pp. 1-15, 2014.
- [2] D. Casalino, F. Diozzi, R. Sannino, A. Paonessa. "Aircraft noise reduction technologies: A bibliographic review". *Aerospace Science and Technology*, Vol. 12, pp. 1-17, 2008.
- [3] S. Johansson, L. Hakansson and I. Claesson, "Aircraft cabin noise and vibration prediction and active control", In: *Handbook of Noise and Vibration Control*, Malcolm J. Crocker (editor), Chapter 100, John Wiley, 2007.
- [4] J.F. Wilby, "Aircraft cabin noise and vibration prediction and active control", In: *Handbook of Noise and Vibration Control*, Malcolm J. Crocker (editor), Chapter 99, John Wiley, 2007.
- [5] G. Petrone, J. Avossa, F. Branda, F. Marulo, "New polyvinylpyrrolidone (PVP) based soundproofing materials through electrospinning", In: *Proceedings of the Inter-Noise Conference*, 2016, Hamburg, Germany
- [6] M. T. Pelegrinis, K. V. Horoshenkov, A. Burnett. "An application of Kozeny–Carman flow resistivity model to predict the acoustical properties of polyester fibre". *Appl. Acoustics* Vol. 101, pp.1-4, 2016.
- [7] C. Othmani, M. Taktak, A. Zein, T. Hentati, T. Elnady, T. Fakhfakh, M. Haddar. "Experimental and theoretical investigation of the acoustic performance of sugarcane wastes based material". *Appl. Acoustics* Vol. 109, pp.90-96, 2016.
- [8] A.I. Hurrell, K.V. Horoshenkov, M.T. Pelegrinis. "The accuracy of some models for the airflow resistivity of nonwoven materials". *Appl. Acoustics*. Vol. 130, pp. 230-237, 2018.
- [9] P. W. Jones and N. J. Kessissoglou. "Simplification of the Delany–Bazley approach for modelling the acoustic properties of a poroelastic foam". *Appl. Acoustics*, Vol. 88, pp. 146-152, 2015.

Differentiating complexation with GGH peptide and non-specific adsorption of copper ions on gold with Si-nanoribbon ISFET biosensors

Olena Synhaiwska ^{1,2}, Yves Mermoud ^{1,2}, Masoud Baghernejad ^{1,*}, Israel Alshanski ³, Mattan Hurevich ³, Shlomo Yitzchaik ³, Mathias Wipf ¹, and Michel Calame ^{1,2}

¹ Transport at Nanoscale Interfaces Laboratory, Empa – Swiss Federal Laboratories for Materials Science and Technology, Duebendorf, Switzerland; olena.synhaiwska@empa.ch, yves.mermoud@empa.ch, mathias.wipf@empa.ch, michel.calame@empa.ch

² Department of Physics, University of Basel, Basel, Switzerland

³ Institute of Chemistry, The Hebrew University of Jerusalem, Jerusalem, Israel; israel.alshanski@mail.huji.ac.il, mattan.hurevich@mail.huji.ac.il, shlomo.yitzchaik@mail.huji.ac.il

* Current affiliation: Max Plank Institute for Polymer Research, Mainz, Germany; baghernejad@mpip-mainz.mpg.de

In this work we focus on detection of copper, which is essential for the human organism, but becomes harmful at certain concentrations, due to its ability to form complexes with peptides and therefore cause modification of molecular structure of proteins. This leads to various health problems like Parkinson, Alzheimer disease, Menkes syndrome, myeloid leucosis, liver cirrhosis etc. [1]. Therefore, development of a precise, easy in operation and low-cost device is necessary in order to monitor Cu levels in ground water and blood.

We have developed a sensor based on Si-nanoribbon (Si-NR) ion-sensitive field-effect transistors (ISFETs) [2–4]. ISFETs are very promising candidates for sensing purposes, as they provide high sensitivity to various targets which is achieved with receptor molecules. The fabrication process of ISFETs is CMOS compatible, which will set a low production cost of a device.

Using an ISFET, the change in surface potential at the gate is measured. In this work the gate is functionalized with a self-assembled monolayer of Glycyl-Glycyl-Histidine (GGH) (Fig. 1) [5]. Using peptides for ion detection gives us an opportunity to mimic biological systems and to understand important processes, relevant for biological and chemical applications. For example, GGH peptide is a model of the copper-binding site of human serum albumin, a major copper transporting path in blood [6].

Besides detection of copper, it's also important to understand the interaction between the peptide and the ion, as it strongly depends on the factors like composition, ionic strength and pH of the media. Monitoring potential at the surface gives us an opportunity to study the net charge of the system receptor-target in different conditions.

Our results provide an explanation of the GGH peptide–copper ion complexation process, considering reactions which can happen in different conditions. We perform differential measurements to compare the response from functionalized and non-functionalized Si-NRs. Such measurements are important in order to eliminate contributions from non-specific signals. We also demonstrate the impact of non-specific adsorption of copper ions or its hydrolysis products on gold. This effect is not well studied yet, but affects the obtained result, and it's highly important to distinguish this signal from specific binding of Cu ions to GGH.

We aim at modelling the response of our device for different conditions using the site-binding model, in order to find optimal conditions for efficient copper detection.

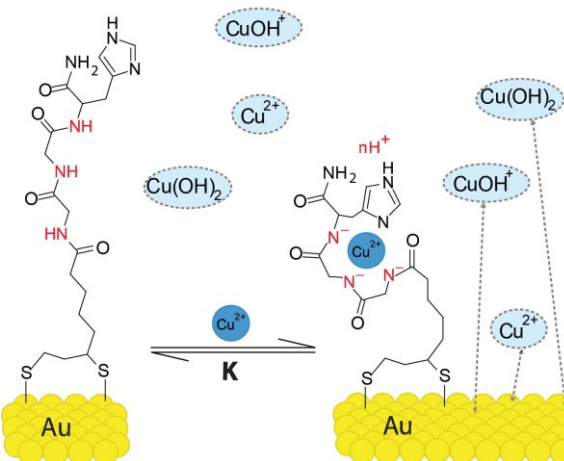


Fig. 1. Schematics of complexation of peptide GGH and copper. Arrows indicate non-specific adsorption of copper and its hydrolysis products on gold.

ACKNOWLEDGMENT

We gratefully acknowledge the support by EU Horizon 2020 FET Open project “Reservoir Computing with Real-time Data for future IT” (RECORD-IT) under grant agreement 664786.

REFERENCES

- Angelova, M.; Asenova, S.; Nedkova, V.; Koleva-Kolarova, R. Copper in the human organism. *Trakia Journal of Sciences* **2011**, *9*, 11.
- Wipf, M.; Stoop, R.L.; Navarra, G.; Rabbani, S.; Ernst, B.; Bedner, K.; ... Calame, M. Label-Free FimH Protein Interaction Analysis Using Silicon Nanoribbon BioFETs. *ACS Sens.* **2016**, *1*, 781–788.
- Wipf, M.; Stoop, R.L.; Tarasov, A.; Bedner, K.; Fu, W.; Wright, I.A.; ... Schönenberger, C. Selective Sodium Sensing with Gold-Coated Silicon Nanowire Field-Effect Transistors in a Differential Setup. *ACS Nano* **2013**, *7*, 5978–5983.
- Stoop, R.L.; Wipf, M.; Müller, S.; Bedner, K.; Wright, I.A.; Martin, C.J.; ... Calame, M. Implementing Silicon Nanoribbon Field-Effect Transistors as Arrays for Multiple Ion Detection. *Biosensors* **2016**, *6*, 21.
- Mervinetsky, E.; Alshanski, I.; Hamo, Y.; Sandonas, L.M.; Dianat, A.; Buchwald, J.; ... Yitzchaik, S. Copper Induced Conformational Changes of Tripeptide Monolayer Based Impedimetric Biosensor. *Scientific Reports* **2017**, *7*, 9498.
- Lau, S.-J.; Kruck, T.P.A.; Sarkar, B. A Peptide Molecule Mimicking the Copper(II) Transport Site of Human Serum Albumin. *J. Biol. Chem.* **1974**, *249*, 5878–5884.

Wet-Chemical Techniques for Etching and Metallizing X-Ray Zone Plate Nanostructures

1
2
3
4
5
6
7
8
9
10
11
12
13
14
15
16
17
18
19
20
21
22
23
24
25
26
27
28
29
30
31
32
33
34
35
36
37
38
39
40
31
32
33
34
35
36
37
38
39
40
41
42
43
44
45
46
47
48
49
50
51
52
53
54
55
56
57
60
61
62
63
64
65
Rabia Akan

Department of Applied Physics
KTH Royal Institute of Technology
Stockholm, Sweden
rabiaa@kth.se

Thomas Frisk

Department of Applied Physics
KTH Royal Institute of Technology
Stockholm, Sweden
tfrisk@kth.se

Ulrich Vogt

Department of Applied Physics
KTH Royal Institute of Technology
Stockholm, Sweden
ulrich.vogt@biox.kth.se

Zone plates are diffractive focusing optics used in x-ray microscopes. A zone plate consists of concentric rings, i.e. zones, with decreasing line widths from its center to its outermost part. Two main characteristics in the design are important to consider when fabricating zone plates: outermost zone width and zone thickness. The width of the outermost zone defines the resolution of the zone plate and the thickness defines the x-ray focusing efficiency. Especially for use in the hard x-ray regime, zone plates with thicknesses of several micrometers are required. Therefore, high aspect ratio nanostructures are needed and are the biggest challenge in the fabrication of high resolution, high efficiency zone plates. The purpose of the study is to facilitate the zone plate fabrication process via wet-chemical methods in achieving high-aspect ratio zone plate nanostructures. In this study, we investigate alternative processes to reactive ion etching (RIE) and atomic layer deposition (ALD).

RIE is often used to create the deep trenches in the zone plate material [1]. Limitations in achievable aspect ratios and etching verticality is, however, present with this dry etching technique. As an alternative to RIE, Chang and Sakdinawat introduced a wet etching method, metal assisted chemical etching (MACE), to transfer a metal zone plate pattern into a silicon substrate [2]. We further identified and optimized the involved MACE process parameters in achieving vertical, dense and deep silicon nanostructures within a few minutes at ambient processing conditions [3].

To use silicon itself requires extremely large depths in order to serve as a sufficiently efficient zone plate device. Too large depths cause mechanical instability of the nanostructures. Instead, MACE-processed silicon zone plate structures can serve as molds for heavy metals, while not having to be as thick (Fig. 1).

So far, ALD was used for the metallization of MACE-produced zone plates [2], [4]. Unfortunately, ALD is a slow and rather expensive process. On the other hand, wet-metallization techniques, such as electrodeposition (ED) and electroless deposition (ELD), are relatively simple, cheap and readily available techniques with flexibility in metals of choice and could serve as potential alternatives to ALD. Here, we show our initial results on ED and ELD of different heavy metals in silicon zone plate nanostructures produced by MACE. The fabricated zone plates are several micrometers thick and their outermost zone widths are <100 nm.

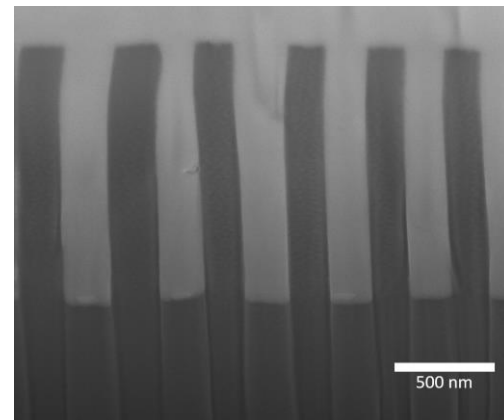


Fig. 1. SEM micrograph of metal-assisted chemical etching produced and electroless deposition metallized zone plate section. The dark parts correspond to silicon and the light parts to metal.

REFERENCES

- [1] K. Parfeniuks et al., "Improved tungsten nanofabrication for hard X-ray zone plates", *Microelectron. Eng.*, vol. 152, pp. 6-9, December 2015.
- [2] C. Chang and A. Sakdinawat, "Ultra-high aspect ratio high-resolution nanofabrication for hard X-ray diffractive optics", *Nat. Commun.*, vol. 5, pp. 1-7, June 2014.
- [3] R. Akan, K. Parfeniuks, C. Vogt, M. S. Toprak and U. Vogt, "Reaction control of metal-assisted chemical etching for silicon-based zone plate nanostructures", *RSC Adv.*, vol. 8, pp. 12628–12634, March 2018.
- [4] K. Li et al., "Fabrication of hard x-ray zone plates with high aspect ratio using metal-assisted chemical etching", *J. Vac. Sci. Technol., B*, vol. 35, pp. 06G901 1-9, Nov/Dec 2017.

An Electrically Controlled Heat Rectifier using Graphene Nanoribbons

Daryoush Shiri¹, IEEE Member, Andreas Isacsson²

Department of Physics, Chalmers University of Technology, SE 41296 Gothenburg, Sweden

¹ORCID: 0000-0001-6115-5821

²ORCID: 0000-0001-6908-5696

Abstract— Using Molecular Dynamics (MD) simulations we propose that splitting a graphene nano-ribbon into two unequal strained sections using external force leads to large asymmetry in the forward and reverse heat fluxes. We find that the corresponding rectification ratio (RR) is enhanced to 60% compared to previous proposals. More importantly, the polarity of the proposed heat diode is controllable on-the-fly i.e. by changing the position where force is applied. This technique obviates the complex nano-patterning and lithography required to pattern graphene every time a new rectification value or sign is sought for and opens a route to simpler fabrication of phononic devices in 2D materials.

I. INTRODUCTION

Graphene is a promising candidate for micro and nano-scale heat management applications [1-4]. By nanoscale patterning, the material properties can be adjusted for required transport characteristics. In the context of heat transport, this patterning is done to locally modify the phonon dispersion relation and the corresponding research area, phononics, is sharply on the rise [5-7]. Phononics aims at engineering devices to control transport and detect phonons (heat carriers) in the same way electrons carry information in electronics. Just as the semiconductor diode plays a fundamental role integrated electric circuits, efforts to construct efficient acoustic and thermal diodes aim at a similar revolution in phononics [6]. In a thermal diode, or rectifier, the magnitude of the heat flux resulting from a temperature difference applied at the two terminals differ depending on which terminal is the hotter [7, 8]. An important figure of merit is the rectification ratio, RR, defined as the relative difference between these two heat fluxes (currents). However, in contrast to acoustic diode proposals, the implementation of thermal diodes is not as straightforward as the heat is carried by many acoustic modes i.e. a wide spectrum of phonons. The necessary conditions for a device to display rectification are nonlinearity of the inter-atomic potential and broken mirror symmetry. If this leads to a temperature dependent mismatch of the vibrational density of states (vDOS) between the left and right regions, thermal rectification may ensue. Most proposals relating to carbon nano tubes [9, 10] and graphene based thermal rectifiers have thus far focused on symmetry-breaking geometries which may be hard to realize experimentally [11-16]. Here we show that simply using two weakly connected graphene ribbon segments of unequal length can provide sufficient mismatch of vDOS for significant thermal rectification to emerge. We attribute this to the temperature dependency of the vDOS which emanates from the non-linearity of atomic potentials as well as the length difference. This leads to different vDOS overlaps for thermal bias in the forward and the backwards directions. This, in turn,

results in a highly asymmetric flow of heat. Chief among our results is that the rectification ratio and its sign can be adjusted by changing the length of the short and long nanoribbon sections on-the-fly using electric field-induced strain. The value of RR is enhanced to 60% which is comparable or better than some of the proposals based on more elaborate nano-patterning methods.

II. METHODS

The molecular dynamics simulation is performed using LAMMPS package [17-18]. The graphene nano ribbons are rectangular and their widths and lengths are 10 nm and 100 nm, respectively along x and y directions. The size of the simulation box along the z direction is ± 50 Å to avoid interaction of the device with its periodic replica. The energy of the ribbon is minimized under periodic boundary conditions in all directions using Conjugate Gradient (CG) algorithm with *box/relax* command by Tersoff many-body potential. The integration time step is 0.5 fsec. To achieve the equilibration temperature with zero pressure, the NPT ensemble is used together with Nose-Hoover thermostat and barostat for time duration of 500 psec. The time constants, τ , for temperature and pressure settling are 0.05 and 0.5, respectively. Another round of NVT ensemble i.e. constant volume and temperature is used while both ends of graphene nano ribbons are fixed using zero force and velocity at all time steps. The fixed edges are 10 Å wide stripes of atoms and are called Hot and Cold for which nonequilibrium method is applied to sustain a temperature gradient along the ribbon. After this the boundary conditions are changed to fixed boundary along x direction while keeping the boundary along y to be periodic to avoid edge effects. The NVE (constant energy and volume) ensemble is used for 10 nsec for the Middle section which is the nano ribbon excluding fixed, Hot and Cold sections. The temperature of Hot and Cold sections is controlled by Nose-Hoover thermostats. After the initial 10 nsec, heat flux, velocity auto correlation function (VACF) and temperature are window averaged and recorded for 20 nsec. The Fast Fourier Transform (fft) of VACF data returns the vDOS spanning from zero to 60 THz. Application of force (max 0.05 eV/Å) to the chosen area is done using *addforce* and *efield* commands.

III. RESULTS AND DISCUSSION

Based on the above, we simulate our proposed adjustable heat rectifier setup as shown in Figure 1. Applying electric field to the selected electrode in z direction, divides the nano ribbon into a short and long section with unequal amount of stresses. The magnitude of forces used in the simulations are of the order nN, characteristic for nano-electromechanical devices. The recorded values of average heat fluxes are shown in Table I and they suggest rectification ratios of 35 % and 42 % for

temperature/gradient values of $300 \text{ K} \pm 100 \text{ K}$ and $300 \text{ K} \pm 50 \text{ K}$, respectively (Figure 2a). If the position of force is changed and it is moved to the right-side (see Figure 2b), the same values as above are obtained for the rectification ratios however, with the reversed sign. We also examined the change of base temperatures to 200 K and 400 K for reversed bias case.

TABLE I. HEAT FLUXES J^\pm , RECTIFICATION RATIOS RR AND RECTIFICATION DIRECTION (SHORT \rightarrow LONG) FOR THE TUNABLE CONFIGURATION IN FIGURE 2. THE TOP TWO ROWS CORRESPOND TO CONFIGURATION IN PANEL (A), WHILE THE MIDDLE TWO ROWS CORRESPOND TO PANEL (B).

$T_{L,R}$ (K)	J^+, J^- (eV/ps Å ²)	RR (%) $\frac{ J^+ - J^- }{\max(J^+, J^-)}$	Rect. dir.
300 ± 50	5191, 2998	42	S \rightarrow L
300 ± 100	6451, 4201	35	S \rightarrow L
200 ± 50	1542, 3903	60	L \leftarrow S
400 ± 50	3822, 4931	22	L \leftarrow S
300 ± 50	2345.5, 2201	6.5	Symmetric
300 ± 100	3840.5, 3904	1.6	Symmetric

As can be seen from Table I, the value of the rectification ratio changes. In case of $T_{L,R} = 400 \text{ K} \pm 50 \text{ K}$ and $T_{L,R} = 200 \text{ K} \pm 50 \text{ K}$, the RR values are 60 % and 22 %, respectively. To verify that the rectification is indeed induced from asymmetric division of the nano ribbon section, we also applied the force symmetrically, dividing the ribbon into two equal partitions. The resulting flux differences for imposed temperature differences of $\Delta T = 50 \text{ K}$ and $\Delta T = 100 \text{ K}$ corresponded to $RR = 6 \%$ and $RR = 1 \%$, respectively as shown in the last rows of Table I. This corroborates that the large asymmetry in the values of heat flux stems from the strain induced asymmetry in the nano ribbon. The significance of this work lies in its flexibility of changing the value and sign of heat rectification without resorting to a newly nano-patterned and/or functionalized graphene. It is also possible to generalize the proposed principle to other two dimensional materials using not only the electric field but also magnetic field with proper electrode designs [19].

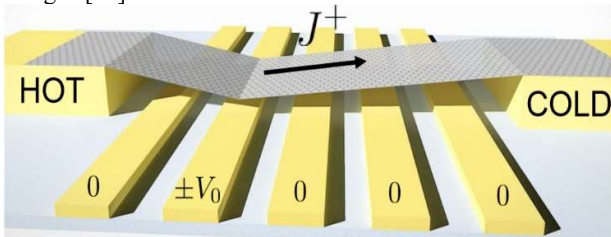


Figure 1. Proposal for a tunable thermal diode where the sign and value of rectification ratio is controlled by applying electric field to the chosen gate electrode underneath a thermally biased graphene nano ribbon.

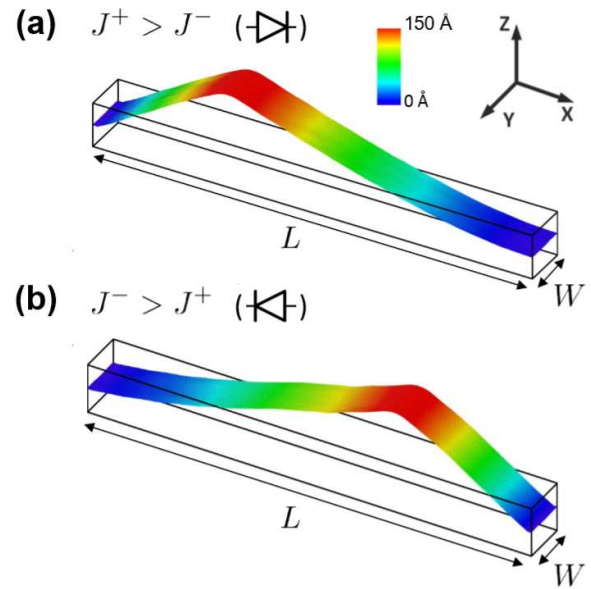


Figure 2. Adjustable heat rectification by asymmetric application of electric field-induced force to a $100 \text{ nm} \times 10 \text{ nm}$ graphene nanoribbon. (a) Schematic shows the rectification direction of the heat diode when the force is applied to the left section. (b) When the force is applied to the right section, rectification direction is reversed.

ACKNOWLEDGMENT

Access to supercomputing facilities of The Swedish National Infrastructure for Computing (SNIC) and C3SE at Chalmers University of Technology is greatly acknowledged.

REFERENCES

- [1] D. G. Cahill, et al, *Applied Physics Reviews* 1, 011305 (2014).
- [2] E. Pop, V. Varshney, and A. K. Roy, *MRS Bulletin* 37, 12731281 (2012).
- [3] D. L. Nika and A. A. Balandin, *Journal of Physics: Condensed Matter* 24, 233203 (2012).
- [4] A. A. Balandin, *Nature Materials* 10, 569 (2011).
- [5] S. Hu, M. An, N. Yang, and B. Li, *Nanotechnology* 27, 265702 (2016).
- [6] N. Li, J. Ren, L. Wang, G. Zhang, P. Hänggi, and B. Li, *Rev. Mod. Phys.* 84, 1045 (2012).
- [7] T.-M. Shih, Z. Gao, Z. Guo, H. Merlitz, P. J. Pagni, and Z. Chen, *Scientific Reports* 5, 12677 (2015).
- [8] G. Wu and B. Li, *Physical Review B* 76, 085424 (2007).
- [9] X. Ni, G. Zhang, and B. Li, *Journal of Physics: Condensed Matter* 23, 215301 (2011).
- [10] N. Yang, G. Zhang, and B. Li, *Applied Physics Letters* 95, 033107 (2009).
- [11] S. Hu, M. An, N. Yang, and B. Li, *Small* 13, 1602726 (2017).
- [12] J. Hu, X. Ruan, and Y. P. Chen, *Nano Letters* 9, 2730 (2009).
- [13] N. Yang, G. Zhang, and B. Li, *Applied Physics Letters* 95, 033107 (2009).
- [14] W. Xu, G. Zhang, and B. Li, *Journal of Applied Physics* 116, 134303 (2014).
- [15] Y. Wang, A. Vallabhaneni, J. Hu, B. Qiu, Y. P. Chen, and X. Ruan, *Nano Letters* 14, 592 (2014).
- [16] G. Zhang and H. Zhang, *Nanoscale* 3, 4604 (2011).
- [17] S. Plimpton, *J. Comp. Phys.* 117, 1 (1995).
- [18] D. Shiri and A. Isacsson, *Journal of Applied Physics* 125, 125101 (2019).
- [19] D. Shiri and A. Isacsson, *arXiv:1707.06572* (2017).

*Rania E. Adam, Magnus Willander and Omer Nur

Department of Sciences and Technology, Linköping University, Campus Norrköping, SE-601 74
Norrköping, Sweden

Abstract

In the present work, we report on synthesis of plasmonic ZnO/GR/Ag/AgI nanocomposites as a novel photocatalyst with highly enhanced photocatalytic performance under solar irradiation. The plasmonic ZnO/GR/Ag/AgI nanocomposites were investigated by different characterization techniques, which confirm a successful formation of the nanocomposite. Using Congo red as a model dye molecule, our results on photodegradation of the dye molecule demonstrated photodegradation efficiency up to 90% after one hour under solar irradiation. Whereas the photodegradation efficiency of the pure ZnO, ZnO/GR was found to be 58%, and 75%, respectively. The significantly enhanced photodegradation efficiency is attributed to the improvement on the electronic properties of the nanocomposites due to the hybridization by graphene, where carbon acts as an efficient electron acceptor with good conductivity, which significantly increases the charge carrier collection efficiency. Moreover, the addition of Ag/AgI generates a strong surface plasmon resonance effect in the metallic silver with a redshift of the optical absorption into the visible light region which further enhances the photocatalytic performance. This result is important to understanding the photocatalytic mechanism of ZnO/GR/Ag/AgI nanocomposites which can lead to further development of novel efficient photocatalyst materials.

Keywords: ZnO, Graphene, photocatalytic, Plasmonic, Congo red, Solar light,
Nanocomposite.

*Corresponding author: rania.elhadi.adam@liu.se, reery111@hotmail.com

Reliable bipolar resistive switching in solution processed $\text{BiFe}_{0.99}\text{Cr}_{0.01}\text{O}_3$ thin films

Chandni Kumari

Department of Physics

Indian Institute of Technology Jodhpur

Jodhpur, India

kumari.3@iitj.ac.in

Ishan Varun

Department of Electrical Engineering

Indian Institute of Technology Jodhpur

Jodhpur, India

varun.1@iitj.ac.in

Shree Prakash Tiwari

Department of Electrical Engineering

Indian Institute of Technology Jodhpur

Jodhpur, India

sptiwari@iitj.ac.in

Ambesh Dixit

Department of Physics

Indian Institute of Technology Jodhpur

Jodhpur, India

ambesh@iitj.ac.in

I. INTRODUCTION

Resistive random access memories have attracted significant attention in the research community because of their potential for non-volatile memory device owing to its low power consumption, scalability, high speed and higher integration capability. BiFeO_3 (BFO) is a multiferroic perovskite material, showing room temperature magnetoelectric properties. BFO based RRAMs exhibit both unipolar and bipolar characteristics and different switching mechanisms are attributed for these characteristics [1]. However, BFO suffers from high leakage current because of intrinsic oxygen vacancies and Fe mixed valence states. Hence, doping at Fe site may improve the electric and magnetic properties and also lead to significant improvement in switching characteristics [2]. Chromium doped BFO material is reported to show significant improvement in magnetic and electric properties owing to its robust isovalent 3+ nature [2]. However, these doping in BFO are generally achieved by pulsed laser deposition (PLD) or other vacuum assisted deposition techniques.

PLD needs high vacuum system and imposes limitations for easy fabrication. That's why a low cost solution process is usually preferred. However, the solution processed films require higher crystallization temperature and especially in case of BFO, may lead to the secondary phases because of volatile nature bismuth even at lower temperatures [3]. Hence, optimization of individual synthesis step is essential for phase pure Cr doped BFO thin films. Here, we report the synthesis of $\text{BiFe}_{1-x}\text{Cr}_x\text{O}_3$ (BFCO) with $x = 0.01$ thin films and their RRAM characteristics together with silver as top (TE) and FTO as bottom (BE) electrodes.

II. RESULTS AND DISCUSSIONS

The structural and microscopic characterizations support the formation of phase pure BFCO thin films on FTO substrates. Further, silver contacts are deposited to realize $\text{Ag}/\text{BiFe}_{0.99}\text{Cr}_{0.01}\text{O}_3/\text{FTO}$ RRAM device structures and $-2.2 \text{ V} \rightarrow 0 \text{ V} \rightarrow 1.7 \text{ V} \rightarrow 0 \text{ V} \rightarrow -2.2 \text{ V}$ potential bias is applied across the device to understand the electrical performance. Further, a compliance current of 10 mA is applied to protect the device from permanent break down. Initially, the resistance starts decreasing after applying the positive bias at TE and current abruptly increases at the set voltage, turning

the device ON. When the polarity of applied voltage is reversed, current starts decreasing and thus, bringing the device in OFF states at reset voltage, figure 1(a). These RRAM devices showed bipolar RRAM characteristics and the observed set (V_{set}) and reset (V_{reset}) voltages are 1.5 V and -1.46 V, respectively. The estimated $I_{\text{on}}/I_{\text{off}}$ ratio is ~ 80 at 0.2 V.

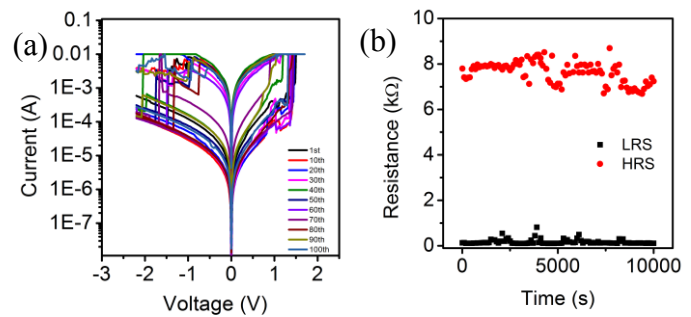


Figure 1: (a) resistive switching upto 100 cycle and (b) retention curve for $\text{Ag}/\text{BiFe}_{0.99}\text{Cr}_{0.01}\text{O}_3/\text{FTO}$ RRAM device

The device showed reproducible RRAM behavior for 100 cycles, figure 1(a). The retention curve of the device is shown in figure 1(b), indicating that the device is able to maintain LRS and HRS states for 10000 s without any significant variation and thus, preserving the non-volatile characteristics. The endurance characteristics for 200 cycles ensures the stability of the device, further, conduction mechanism is attributed to filament formation and switching mechanism is assigned to migration of silver ion inside the film.

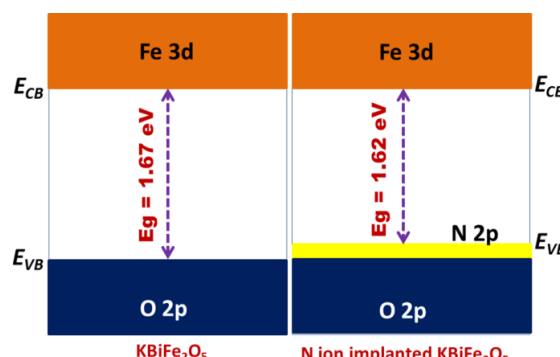
REFERENCES

- [1] C. Kumari, I. Varun, S. Prakash Tiwari, and A. Dixit, "Robust non-volatile bipolar resistive switching in sol-gel derived BiFeO_3 thin films," *Superlattices Microstruct.*, vol. 120, pp. 67–74, Aug. 2018.
- [2] Y. Sharma *et al.*, "Studies on structural, optical, magnetic, and resistive switching properties of doped $\text{BiFe}_{1-x}\text{Cr}_x\text{O}_3$ thin films," *J. Appl. Phys.*, vol. 120, no. 19, p. 194101, Nov. 2016.
- [3] Q. Zhang, D. Sando, and V. Nagarajan, "Chemical route derived bismuth ferrite thin films and nanomaterials," *J. Mater. Chem. C*, vol. 4, no. 19, pp. 4092–4124, 2016.

1 2 3 4 5 6 7 8 9 Local electronic structure engineering in new 10 multifunctional brownmillerite KBiFe_2O_5 for 11 efficient solar energy harvesting applications

12 *Durga Sankar Vavilapalli*13 *Crystal Growth Centre*14 *Anna University*15 *Chennai 600025, India*16 *v.durgasankar@yahoo.com*17 *Asokan Kandasami,*18 *Inter-University Accelerator Center*19 *Aruna Asaf Ali Marg, New Delhi, 110067, India*20 *asokaniuac@gmail.com*21 *Shubra Singh*22 *Crystal Growth Centre*23 *Anna University*24 *Chennai 600025, India*25 *Shubra6@gmail.com*

Abstract: KBiFe_2O_5 (KBFO) is a new brownmillerite structured multiferroic compound with potential for solar energy harvesting applications. The multifunctionality of multiferroics, including KBiFe_2O_5 , with potential coupling between ferroelectric and magnetic order parameters, can lead to application in photovoltaics since these compounds have narrow band gap (~ 1.67 eV) and large absorption coefficient. The narrow band gap as compared to conventional perovskite multiferroics, for example BiFeO_3 , is due to the influence of magnetic ordering on electron - electron interaction. [1-3]. Brownmillerite structured KBFO consists of alternate layers of FeO_6 and FeO_4 polyhedra. The oxygen vacancies in these compounds are distributed orderly in the two-dimensional FeO_4 tetrahedral layer. Nitrogen (N) substitution in FeO_{4-x} leads to further changes in optical properties and narrowing its bandgap owing to the lower electronegativity of N as compared to O. In this work we have implanted the nitrogen ions on KBFO film to engineer its local electronic structure. Ion implantation on KBFO, also results in the narrowing the bandgap further enabling it to absorb more sunlight from solar spectra for efficient solar energy harvesting applications.



46 **Figure 1:** Schematic representation of electronic structure of KBiFe_2O_5 with and without N ion implantation

47 References:

48 [1] V. D. Sankar and S. Singh, Optical Properties of Fe Based Perovskite and Oxygen Deficient Perovskite
49 Structured Compounds: A Comparison, Cham, 2019.

50 [2] D. S. Vavilapalli, A. A. Melvin, S. Kavita, A. K. Yadav, S. N. Jha, D. Bhattacharyya, S. C. Sarma, S. C. Peter,
51 M. S. Ramachandra Rao and S. Singh, Solar Energy Materials and Solar Cells, 2019, 200, 109940.

52 [3] D. S. Vavilapalli, K. Srikanti, R. Mannam, B. Tiwari, M. K. K, M. S. R. Rao and S. Singh, ACS Omega, 2018,
53 3, 16643-16650.

Towards Ballistic Silicon Nanowire Transport

1
2
3
4
5
6
7
8
9
10
11
12
13
14
15
16
17
18
19
20
21
22
23
24
25
26
27
28
29
30
31
32
33
34
35
36
37
38
39
40
41
42
43
44
45
46
47
48
49
50
51
52
53
54
55
56
57
58
59
60
61
62
63
64
65
Nivedha Radhakrishnan
James Watt School of Engineering
University of Glasgow
Glasgow, United Kingdom
N.Radhakrishnan.1@research.gla.ac.uk

Muhammad Mirza
James Watt School of Engineering
University of Glasgow
Glasgow, United Kingdom
Muhammad.Mirza@glasgow.ac.uk

Douglas Paul
James Watt School of Engineering
University of Glasgow
Glasgow, United Kingdom
Douglas.Paul@gla.ac.uk

INTRODUCTION

In the last two decades, research into silicon nanowires has seen major advancements for a wide range of applications. These include the next generation of CMOS electronics [1], opto-electronics, sensing applications [2], and metrology [3]. For such high performance devices, excellent electrostatic control of the channel is required. This has resulted in a shift from the conventional Metal-oxide-semiconductor field effect transistor (MOSFET) to other structures such as FinFETs and the use of multiple wrap around gates. Short channel effects, however, persist in devices scaled to below 10 nm.

One method to improve device performance requires the utilisation of quantum mechanical effects such as ballistic conduction. This is a transport regime where the mean free path λ_{MFP} is comparable to the channel length L , and is expected to enhance the drain-voltage characteristics [4]. A few one dimensional nanowire transistors have shown ballistic conductance [4], however, they are grown using bottom up methods, or they utilise materials like carbon nanotubes both of which are incompatible with industrial CMOS foundries.

METHODOLOGY AND DISCUSSION

In previous work, Mirza et al. demonstrated top-down fabricated junction-less nanowire transistors with mean widths down to 4 nm and a channel length L of 150 nm [5]. The resistivity, carrier density and mobility were directly measured using Hall bar structures rather than inferred from the conductivity. The transport in the nanowires were shown to staircase from 3D (12 nm) to 1D (7 nm) and showed quasi-ballistic characteristics. To achieve fully ballistic conduction the condition $L < \lambda_{MFP}$ should be met. This can be achieved by reducing the channel length L or by increasing the mean free path dependent on various scattering processes described by Matthiessen's law. In the junction-less devices the most significant scattering process was due to neutral impurities due to an optimised etch process. This value cannot be increased due to the devices high doping requirements of the junction less transistor.

In this study we investigate top-down fabricated Si nanowire transistors doped with phosphorus with a large range from $7 \times 10^{19} \text{ cm}^{-3}$ to $2 \times 10^{17} \text{ cm}^{-3}$, resulting in Fermi wavelengths from 9.5 nm to 65 nm respectively. Devices with a channel length down to 50 nm have been fabricated in the pursuit of ballistic conduction at lower doping. Devices were measured at a range of temperatures and a comparison made

of the I_{on}/I_{off} ratio with the previous 150 nm devices, simulations [6] to the 50 nm transistors fabricated in this study. The mobility, resistivity and carrier densities of the nanowires will also be analysed via direct four probe measurements of 50 nm Hall bar structures.

FABRICATION TECHNIQUE

Devices have been made using top-down fabrication techniques to make it easy to transfer the process to industry. Firstly, a 55 nm silicon on insulator (SOI) substrate was implanted with a range of phosphorous doping discussed above. Contact regions were then implanted considering the thermal budget to ensure an Ohmic contact. Using a previously established low energy etch process and a high quality surface passivation [7], the nanowires transistors and Hall bars were fabricated and thermally oxidised forming a 5 nm SiO_2 dielectric. The optimised fabrication ensures scattering from surface roughness is small compared to other mechanisms. A 50 nm wrap around gate was then patterned using an optimised cold development lift off process. Finally, a top metal control gate is patterned onto the devices, separated by an insulating SiO_2 PECVD layer to ensure good electrostatic control of the spacers to the contacts.

REFERENCES

- [1] J. Appenzeller, J. Knoch, M. T. Björk, H. Riel, H. Schmid and W. Riess, "Toward nanowire electronics," *IEEE Trans. Elec. Dev.* 55, 2827–2845 (2008).
- [2] C. Busche, L. Vilà-Na-dal, J. Yan, H. N. Miras, et al., "Design and fabrication of memory devices based on nanoscale polyoxometalate clusters," *Nature* 515(7528), pp. 545–549 (2014).
- [3] G. Yamahata, S. P. Giblin, M. Kataoka, T. Karasawa and A. Fujiwara, "High-accuracy current generation in the nanoampere regime from a silicon single-trap electron pump" *Sci. Reports* 7, 45137 (2017).
- [4] K. Natori, Y Kimura and T. Shimizu, "Characteristics of a carbon nanotube field-effect transistor analyzed as a ballistic nanowire field-effect transistor," *J. Appl. Phys.* 97, 034306 (2005).
- [5] M. M. Mirza, F.J. Schupp, J. A. Mol, D. A. MacLaren, A. D Briggs and D. J. Paul, "One dimensional transport in silicon nanowire junction-less field effect transistors," *Sci. Reports* 7, 3004 (2017).
- [6] V. P. Georgiev, A-I. Dochioiu, F. Adamu-Lema, S. Berrada, M. M. Mirza, D. Paul and A. Asenov, "Variability study of high current junctionless silicon nanowire transistors," In: 12th IEEE NMCD conference, Singapore, 2-4 Oct (2017).
- [7] M. M. Mirza, D. A. MacLaren, A. Samarelli, B. M. Holmes, H. Zhou, S. Thoms, D MacIntyre, and D. J. Paul, "Determining the electronic performance limitations in top-down-fabricated Si nanowires with mean widths down to 4 nm," *Nano. Letters* 14 (11), 6056-6060 (2014).

GaN Highly Selective Split Drain Transistor

J.-F. Millithaler, N. Hossain¹, H. Wang, M. Margala
*Department of Electrical and Computer Engineering,
 University of Massachusetts, Lowell, MA 01854, USA*
 jeanfrancois_millithaler@uml.edu

I. Iñiguez-de-la-Torre, J. Mateos, T. González
*Applied Physics Department, Salamanca University,
 Plaza de la Merced s/n, 37008 Salamanca, Spain*

The Ballistic Deflection Transistor (BDT) [1] has been developed to provide an alternative to CMOS technology. The BDT combines the properties of III-V heterostructure, like a very high electron mobility in the two-dimensional gas (2DEG), and a unique planar design offering two distinct output drains for one source contact and two lateral gates in push-pull configuration. The idea is to steer electrons towards one drain while closing the path of the other drain, and being able to change this state by inverting gate polarizations. This device has been experimentally validated at room temperature [2] and numerous publications have shown its potential in very high frequency and low power logic design [3]. One of the BDT's problem is its lack of selectivity, one drain channel not being fully opened when the other is being closed. The aim of the work is to provide an alternative solution to the BDT with an updated geometry and improved performances. We call this new device Split Drain Transistor (SDT).

For this work, we used an ensemble Monte Carlo (MC) simulator self-consistently coupled with a 2D Poisson solver to perform simulations of electrons dynamics. This tool has already proven its validity [1] and considers all necessary models to correctly reproduce the non-linear behavior we can find in this kind of unusual device. In particular, surface charges are self-consistently adapting themselves with the surrounding electron density. We chose GaN as material for the 2DEG with a sheet density of 10^{17} m^{-2} .

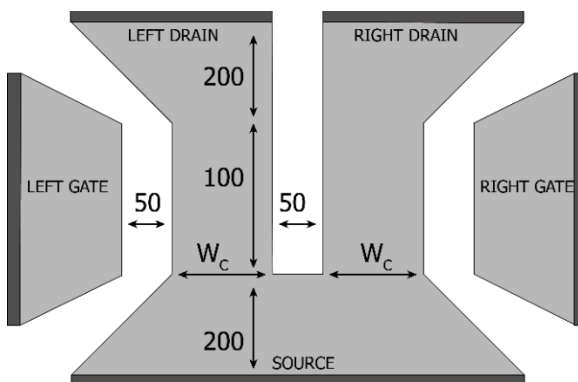


Fig. 1. Fig 1: Sketch of Transistor. The drain is split in two drains. The two gates are operating in push-pull configuration VLG=VRG. All lengths are in nanometer. Proportions have not been respected.

Figure 1 presents the sketch of the SDT. The source channel is split in two left and right drain channels and the two lateral gates are still in push-pull configuration (VLG = - VRG). Dimensions are given in nanometer and the only variable for this work is the channel width W_c going from 100 nm to 1 μm .

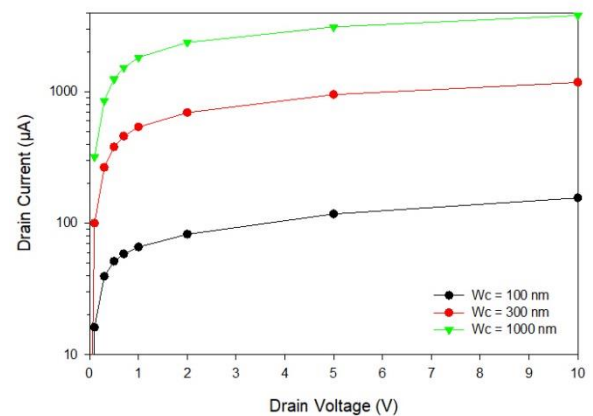


Fig. 2. Fig 2: ID-VD characteristics, for different channel widths $W_c = 100, 300$ and 1000 nm

Figure 2 shows the left drain current versus drain voltage with gates at equilibrium ($VG = 0\text{V}$). The device being symmetric, we show only one drain current. The use of GaN allows reaching high current values, which is consistent with previous work on same material [4].

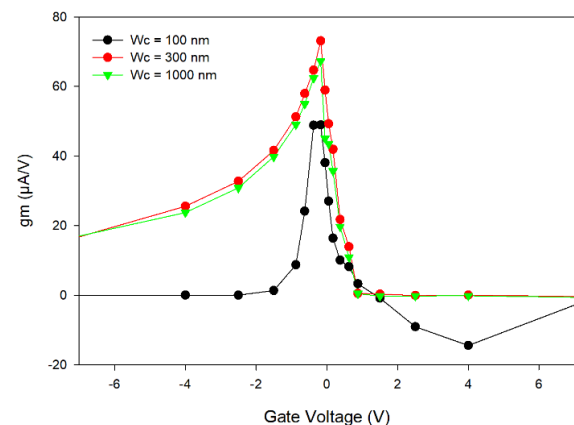


Fig. 3. Fig 4: Transconductance for three channel widths $W_c = 100, 300$ and 1000 nm

Figure 3 presents the transfer characteristics ID-VG when 1 V is applied on drains, for two channel width $W_c = 100$ and 300 nm. Further investigation will be performed for VD in the saturation region, around 10 V. We can observe a similar behavior than the BDT with one enhancement: when one drain is fully closed, its current reaching 0 A, the other drain remains completely open with a maximum current. For $W_c = 100$ nm it happens at $|VG| = 2$ V and for $W_c = 300$ nm at $|VG| = 15$ V. When the negative bias of one gate is sufficiently high, it begins to deplete the other drain, reducing its current. It happens for $W_c = 100$ nm when $|VG| > 2$ V and it fully closes the other channel at $|VG| = 10$ V. The same effect occurs for $W_c = 300$ nm when $|VG| > 15$ V but these values have not been reported here. The whole point of this device is not the close both drains, but to get one ‘off’ and the other one ‘on’.

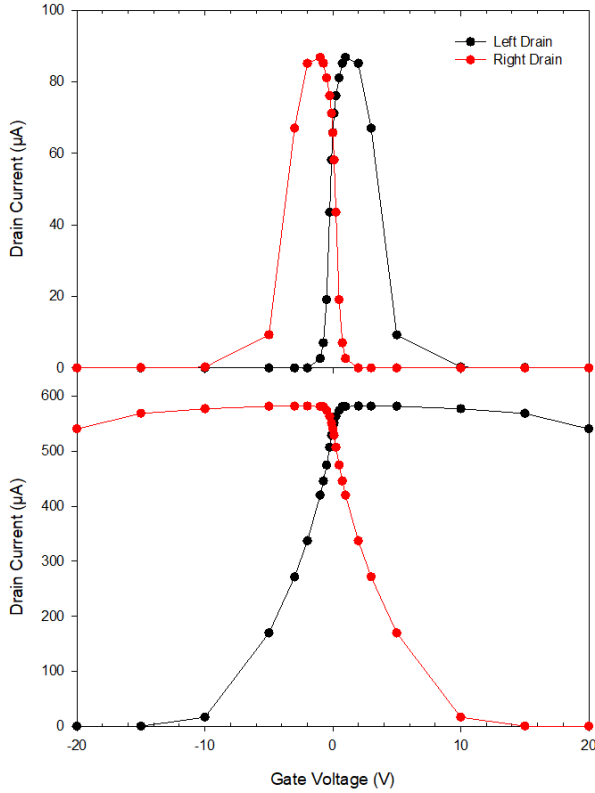


Fig. 5. Fig 3: ID-VG Transfer characteristics for two different channel width $W_c = 100$ and 300 nm.

The left drain transconductance gm has been reported on Figure 4. The right one being symmetric, it has not been reported for more clarity. We can observe a maximum around 70 μ A/V for both widths $W_c = 300$ and 1000 nm, near the equilibrium.

On the last Figure 5 we show the time response of the device under high frequency sweep of gate bias. The device has a channel width $W_c = 300$ nm and the

excitation is applied on the gates between -15 to $+15$ V, with a frequency of 100 GHz. In this case one current is maximum and the other is 0 A. The whole modeling procedure can be found in [1]. This result shows that this device has a time response around 2 ps to switch from one state to the other and could operate at a frequency higher than 200 GHz.

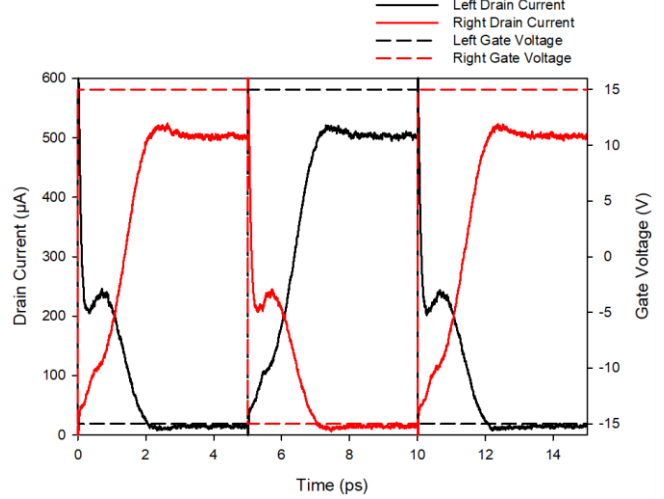


Fig. 4. Current response for the $W_c = 300$ nm device under a 100 GHz excitation of gate voltage between -10 V to $+10$ V

We plan to perform further investigations on optimizing the design, modifying polarizations, determining the highest operating frequency, implementing multiple structures, fabricating a real device, and so on. We believe the SDT could be in the future an emerging device for high power high frequency logic operations.

REFERENCES

- [1] J.-F. Millithaler et al., *Nanotechnology*, **26**, 485202 (2015).
- [2] V. Kaushal et al., *Solid-State Electronics* **56** (2011) 120–129
- [3] P. Marthi et al., *IEEE Transactions on Circuits and Systems I*, **63**, 12 (2016)
- [4] J.-F. Millithaler et al., *Appl. Phys. Lett.* **104**, 073509 (2014)

Stimulated k-vector selective magnon excitation in NiFe films using femtosecond-laser pulse trains

1 Ahmad . A. Awad

2 *department of physics*

3 University of Gothenburg

4 Gothenburg, Sweden

5 ahmad.awad@physics.gu.se

6 Shreyas Muralidhar

7 *department of physics*

8 University of Gothenburg

9 Gothenburg, Sweden

10 shreyas.muralidhar@physics.gu.se

11 Ademir Aleman

12 *department of physics*

13 University of Gothenburg

14 Gothenburg, Sweden

15 ademir.aleman@physics.gu.se

16 Roman Khymyn

17 *department of physics*

18 University of Gothenburg

19 Gothenburg, Sweden

20 roman.khymyn@physics.gu.se

21 Mykola Dvornik

22 *department of physics*

23 University of Gothenburg

24 Gothenburg, Sweden

25 mykola.dvornik@physics.gu.se

26 Johan Åkerman

27 *department of physics*

28 University of Gothenburg

29 Gothenburg, Sweden

30 johan.akerman@physics.gu.se

Spinwaves (magnons) provide an immense potential to replace the existing Si-based technology with faster, smaller and energy-efficient devices due to its low power operation and easy tunability. Sustained SWs could be excited electrically using microwave sources or direct current and more directly by focused optical pulses [1] in a thin magnetic film. It has been observed that the optical excitation happens a few orders of magnitude faster than electrical excitation [2]. However, due to the fast decay time of the SWs, the optically induced emission of SWs is not continuous. To obtain sustainable spinwaves, we have to use repetitive pulses with a very short time period between pulses. There are still very few works addressing such an option [3]. So far, optical pump-probe measurements have primarily been based on Magneto-Optical Kerr Effect (MOKE) microscopy using low repetition rate. Here, we instead attempt to investigate the optically excited spin dynamics using a μ -focused Brillouin light scattering (BLS) technique with much higher sensitivity to coherent and, additionally, incoherent SWs.

We show that stimulated emission of SWs at multiple harmonics of a 1 GHz repetition rate of the pulsed laser. The high sensitivity of detection scheme, using scanning micro-Brillouin Light Scattering (BLS), shows both localized and propagating spinwave emission in the spatial profile measurements. Tuning the applied magnetic field magnitude, we can furthermore choose which wave vector to coherently amplify. Our results clearly indicate that it is possible to create and control SWs of high amplitude using a high-repetition-rate femtosecond pulsed laser. Additionally, by rotating the in-plane component of the applied field, we can also control the direction of the propagating spin waves.

We believe that our approach of using high rep-rate ultrafast laser, will enable efficient use of not just BLS technique but also other time-averaged techniques which will shed further light on fs-laser induced demagnetization and associated effects, and will enable whole new platform for magnonics.

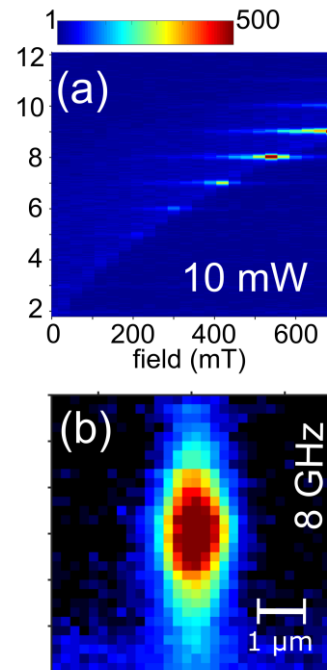


Fig. 1. (a) BLS signal as a function of frequency and the applied field on Py thin film sample. (b) Spatial profile of spinwaves in Py thin film at $H = 600$ mT.

REFERENCES

- [1] M. van Kampen et. al., "All-optical probe of coherent spin waves" Phys. Rev. Lett. 88, 22 (2002).
- [2] B. Koopmans et. al., "Explaining the paradoxical diversity of ultrafast laser-induced demagnetization" Nat. Mats. volume 9, pages 259–265 (2010).
- [3] M. Jäckl et. al. "Magnon Accumulation by Clocked Laser Excitation as Source of Long-Range Spin Waves in Transparent Magnetic Films" Phys. Rev. X, 7, 021009 (2017).

A single layer self-assembled radiative cooler

1 J. Jaramillo Fernandez

2
3
4
5
6
7
8
9
Catalan Institute of Nanoscience and
Nanotechnology (ICN2), CSIC and The
Barcelona Institute of Science and
Technology

Campus UAB, Barcelona, Spain.
juliana.jaramillo@icn2.cat

10 P.D Garcia

11
12
13
14
15
16
17
Catalan Institute of Nanoscience and
Nanotechnology (ICN2), CSIC and The
Barcelona Institute of Science and
Technology

Campus UAB, Barcelona, Spain.
david.garcia@icn2.cat

18 G. L. Whitworth

19
20
21
22
23
24
25
26
27
Catalan Institute of Nanoscience and
Nanotechnology (ICN2), CSIC and The
Barcelona Institute of Science and
Technology

Campus UAB, Barcelona, Spain.
guy.whitworth@icfo.eu

28 C. López,

29
30
31
32
33
34
35
36
37
38
39
Materials Science Factory, Instituto de
Ciencia de Materiales de Madrid
(ICMM), c/Sor Juana Ins de la Cruz 3,
28049 Madrid, Spain c.lopez@csic.es

40 A. Blanco

41
42
43
44
45
46
47
48
49
50
51
52
53
54
55
56
57
58
59
Materials Science Factory, Instituto de
Ciencia de Materiales de Madrid
(ICMM), c/Sor Juana Ins de la Cruz 3,
28049 Madrid, Spain

60
61
62
63
64
65
ablanco@icmm.csic.es

C. M. Sotomayor Torres

70
71
72
73
74
75
76
77
Catalan Institute of Nanoscience and
Nanotechnology (ICN2), CSIC and The
Barcelona Institute of Science and
Technology

Campus UAB, Barcelona, Spain.
ICREA Pg. Lluís Companys 23, 08010
Barcelona, Spain

78 Phonons, the quasi-particles that carry heat and sound, are practically involved in all kind of mechanical, optical, and thermal phenomena. By micro or nano-structuring a surface, phonons can be engineered to make them interact resonantly with photons and achieve interesting effects such as radiative cooling, which involves decreasing the temperature of a body without using electricity or any other kind of extra energy input. Radiative cooling has gained attention recently, because modern cooling technologies are particularly energy-consuming and a ten-fold grow in the energy demand associated to them is expected in the next 30 years, due to global warming. To address this global challenge, we propose a thermo-functional material that is capable of removing heat passively from devices or surfaces that undergo critical heating during operation. Our solution is based on a self-assembled single-layer array of SiO_2 microspheres on a soda-lime slab. The working principle of the proposed cooling device is based on the interaction of the transverse optical phonons and equally polarized electromagnetic waves, which results in an intense evanescent field confined at the surface of a polar-dielectric interface. Such surface excitations, so called surface phonon polaritons (SPhP), have the ability to enhance thermal energy conduction [1] and, in the presence of a grating, they can be

80 diffracted to the far-field as infrared thermal energy [2]. Thus, we engineer the thermo-optical properties of our device to be a visibly translucent thermal blackbody. This in order to remove heat and evacuate it through the transparent infrared atmospheric window as infrared thermal energy to then deposit it into the outer space at 3K which acts as a heat sink. In this work, we will present how the temperature of a crystalline silicon wafer is lowered in average 14C during daytime when the self-assembled single-layer cooler is placed on its surface, providing experimental evidence of above-ambient daytime radiative cooling.

[1] Tervo, E. J., Adewuyi, O. S., Hammonds, J. S. & Cola, B. A. High thermal conductivity in polaritonic SiO_2 nanoparticle beds. *Mater. Horiz.* 3, 434–441, 2016.

[2] Joulain, K., Mulet, J.-P., Marquier, F., Carminati, R. and Greffet, J.-J. Surface electromagnetic waves thermally excited: Radiative heat transfer, coherence properties and Casimir forces revisited in the near field. *Surf. Sci. Rep.* 57, 59112, 2005

Symmetric Lateral Bipolar Transistors as Low Noise Signal Amplifier

1 Qitao Hu

2 *Department of Engineering Sciences*
 3 *Uppsala University*
 4 *Uppsala, Sweden*
 5 *qitao.hu@angstrom.uu.se*

6 Shi-Li Zhang

7 *Department of Engineering Sciences*
 8 *Uppsala University*
 9 *Uppsala, Sweden*
 10 *shili.zhang@angstrom.uu.se*

11 Si Chen

12 *Department of Engineering Sciences*
 13 *Uppsala University*
 14 *Uppsala, Sweden*
 15 *si.chen@angstrom.uu.se*

16 Zhen Zhang

17 *Department of Engineering Sciences*
 18 *Uppsala University*
 19 *Uppsala, Sweden*
 20 *zhen.zhang@angstrom.uu.se*

21 Bipolar junction transistors (BJTs) are characterized by
 22 superior high frequency and low noise performance in
 23 comparison with metal-oxide-semiconductor field-effect
 24 transistors (MOSFETs). A lateral version of the BJT (LBJT)
 25 fabricated on silicon-on-insulator (SOI) substrates with a
 26 fully CMOS-compatible and low cost process has large
 27 potential to improve the power performance of traditional
 28 bipolar circuits [1]. Meanwhile, BJTs with high current gain
 29 (β) can serve as a local signal amplifier and are of
 30 considerable interest in sensor applications. It has been
 31 demonstrated that an intimate integration of BJTs with FET-
 32 based biosensors for immediate sensing signal amplification
 33 can significantly suppress the interference from
 34 environmental noise and therefore improve overall signal-
 35 to-noise ratio of the biosensors [2]. Such noise mitigation
 36 approach is particularly important for FET biosensor with
 37 downsized channel, *e.g.*, silicon nanowire (SiNW), aiming
 38 for large surface-to-volume ratio and therefore high charge
 39 sensitivity, as the SiNWFET biosensor operates at low
 40 current level and are extremely vulnerable to environmental
 41 noise. The LBJT is well-suited in this circumstance as its
 42
 43
 44
 45
 46
 47
 48
 49
 50
 51
 52
 53
 54
 55
 56
 57
 58
 59
 60
 61
 62
 63
 64
 65

50 fabrication can share the same process as that for the
 51 SiNWFET sensor.

52 In this work, we demonstrate NPN-type LBJTs on SOI
 53 wafers with $\beta > 60$ using a fully CMOS-compatible process
 54 [3]. Systematic investigation on the substrate voltage
 55 modulation effects on current-voltage characteristics and low
 56 frequency noise of the LBJT will be presented. Potential
 57 benefit on β and noise of the LBJT from the substrate voltage
 58 modulation will also be analyzed and discussed.

REFERENCES

- [1] Tak H. Ning, “A perspective on SOI symmetric lateral bipolar transistors for ultra-low-power systems,” *IEEE J. Electron Devices Soc.*, vol. 4, no. 5, pp. 227-235, 2016.
- [2] Da Zhang *et al.*, “An ion-gated bipolar amplifier for ion sensing with enhanced signal and improved noise performance,” *Appl. Phys. Lett.*, vol. 105, no. 8, p. 082102, 2014.
- [3] Qitao Hu *et al.*, “Current gain and low-frequency noise of symmetric lateral bipolar junction transistors on SOI,” *48th European Solid-State Device Research Conference*, 3-6 Sept. 2018.

Electric Field Enhancement Factor defined by nanoprotrusions on the electrode surface in microgaps in needle-plate configuration

1 Fathur Rahman

2 *LAPLACE, Université de Toulouse,*
 3 *CNRS, UPS, INPT*
 4 *Toulouse, France*
 5 *Bandung Institute of Technology*
 6 *Bandung, Indonesia*
 7 *PT. PLN Persero*
 8 *Jakarta, Indonesia*
 9 *fathur.rahman@ieee.org*

10 Ngapuli I. Sinisuka

11 *Bandung Institute of Technology*
 12 *Bandung, Indonesia*
 13 *n.irmea@gmail.com*

14 Jean-Pascal Cambronne

15 *LAPLACE, Université de Toulouse,*
 16 *CNRS, UPS, INPT*
 17 *Toulouse, France*
 18 *cambronne@laplace.univ-tlse.fr*

19 Antoine Belinger

20 *LAPLACE, Université de Toulouse,*
 21 *CNRS, UPS, INPT*
 22 *Toulouse, France*
 23 *belinger@laplace.univ-tlse.fr*

24 Kremena Makasheva

25 *LAPLACE, Université de Toulouse,*
 26 *CNRS, UPS, INPT*
 27 *Toulouse, France*
 28 *makasheva@laplace.univ-tlse.fr*

29 **Abstract**—Proper description of the electrical behavior of
 30 miniaturized devices requires better understanding of the
 31 breakdown phenomena in microgaps ($< 10\mu\text{m}$) at atmospheric
 32 pressures. In microgaps the breakdown characteristics deviate
 33 from those defined by the Paschen's law. It is now well
 34 accepted that the departure from Paschen's law is due to the
 35 contribution of field electron emission. Apart from the small
 36 distance, the presence of protrusions on the cathode surface
 37 can largely intensify this phenomenon. In this work, the
 38 electric field distribution is simulated in needle-plate
 39 configuration in presence of various nanoprotrusions on the
 40 cathode surface. The purpose is to find conditions when the
 41 nanoprotrusions can initiate field electron emission due to a
 42 local enhancement of the electric field. The maximum electric
 43 field is determined by the location and the geometry of the
 44 nanoprotrusions. Surprisingly, for a semi-circle shape of
 45 nanoprotrusions, the maximum electric field does not depend
 46 on the size of nanoprotrusions.

47 **Keywords**— *microgaps, nanoprotrusions, FEMM, Electric*
 48 *Field Enhancement Factor (EFEF), breakdown*

I. INTRODUCTION

49 In many electrical applications (microelectronics, micro-
 50 switches, etc.) the aim to reduce the device size often leads to
 51 a reduction of the distance between two parts at different
 52 electrical potentials. Frequently, the gas remains the only
 53 insulator between these two parts and breakdown phenomena
 54 are observed. Decreasing the device dimensions with the
 55 same operating voltage undoubtedly results in an increase of
 56 the electric field. For example, the exploration of gas
 57 breakdown phenomena at micro-scale gaps has been a great
 58 challenge in microelectromechanical switches (MEMS). The
 59 breakdown in gases is generally due to the contribution of
 60 two ionization processes: (i) ionization of gas molecules by
 61 electron collision in the volume and (ii) release of electrons
 62 from the cathode surface after ion impact (secondary electron
 63 emission). The Paschen's curve considers both mechanisms
 64 and uniquely relates the breakdown voltage and the pressure
 65 times distance ($p \times d$) product. According to the Paschen's
 66 law, at atmospheric pressure and for microscale distances,
 67 the breakdown voltage should be very high [1]. However
 68 experimentally observed breakdown voltages are much lower
 69 than the ones expected from the Paschen's law for microgaps
 70 ($< 10 \mu\text{m}$). The idea of modifying the Paschen curve

71 appeared in a series of papers from BELL laboratories
 72 through Germer's study [2], and Boyle and Kisliuk [3] who
 73 were the first researchers to explore the field electron
 74 emission as an additional mechanism. They conclude that
 75 this process has a key role in discharge ignition in micro- and
 76 submicron electrode separations. In 1999 Torres *et al.* [4]
 77 showed experimental evidences of departure from Paschen's
 78 law on the left branch of the curve. The same was confirmed
 79 by other researchers [5],[6],[7]. It is now generally accepted
 80 that the field electron emission is at the origin of the
 81 departure from Paschen's law for atmospheric pressure and
 82 small inter-electrode spacing. Recently Fu *et al.* have
 83 theoretically studied the effect of microprotrusions (100 –
 84 200 μm) in 100 μm inter-electrode distances [8], [9]. They
 85 demonstrate that at atmospheric pressure the discharge
 86 ignition is mainly determined by the shortest inter-electrode
 87 distance with a contribution of the electric field enhancement
 88 due to the protrusions.

89 When the gap between the electrodes is of only a few μm ,
 90 the electrode roughness can also be seen as a kind of
 91 protrusion. Then it could change the electric field distribution
 92 and, in turn, the breakdown characteristics. In this work, we
 93 study a needle-plate geometry where the plan electrode is the
 94 cathode and the needle is the anode. We show that a
 95 nanoprotrusion located on the plate electrode change
 96 drastically the electric field distribution and thus the
 97 breakdown conditions. We limit the presentation here to a
 98 single semi-circle protrusion. The effect of many
 99 nanoprotrusions acting together is also studied.

II. SIMULATION GEOMETRY AND METHOD

100 All simulations are performed with FEMM software (ver
 101 4.2). It is suited to solve electrostatic problems using finite
 102 element method. FEMM solves the nonlinear differential
 103 equation, for the potential V , over the user-defined domain
 104 with user-defined sources and boundary conditions. It
 105 discretizes the problem's domain using triangular elements,
 106 which form a mesh consisting of a large number of nodes.
 107 The solution over each element is approximated by linear
 108 interpolation of the values of potential at the three vertices
 109 of the triangle. Figure 1 presents the geometry of the simulated
 110 device in this work. The anode is a needle and the cathode is
 111 a plate electrode. The anode curvature radius is kept $r=5 \mu\text{m}$

and the gap is fixed to 5 μm . A semi-circle protrusion is located on the cathode. The two-dimensional planar electrostatic problem has been defined, with a solver precision value of 10^{-8} . In order to fix the voltage, Dirichlet conditions have explicitly been defined in the problem's domain. The applied voltage is on the anode $V_{\text{anode}} = 300 \text{ V}$, while the cathode is grounded ($V_{\text{cathode}} = 0 \text{ V}$).

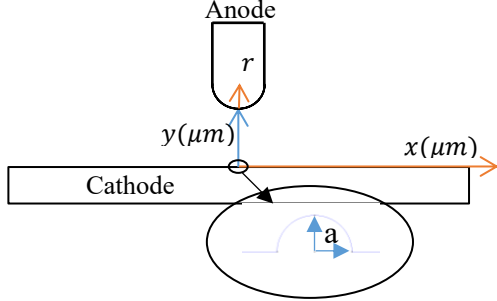


Fig. 1: Sketch of the simulated configuration.

III. RESULT AND DISCUSSION

For a semi-circle protrusion, we change the size (a) and the position of the protrusion (x_p). The zero position is when the protrusion faces the anode. Figure 2 presents the maximum electric field for three protrusion sizes at different protrusion locations. The maximum electric field is always found to be located on the top of the protrusion.

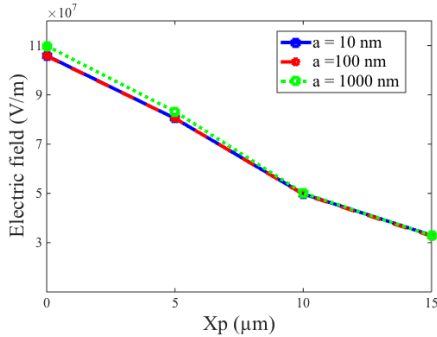


Fig. 2: Electric field versus position of the protrusion for different size of protrusion (10, 100 and 1000 nm).

Firstly the electric field decreases with the position of the protrusion. As expected, the far away the protrusion from the anode, the lowest the maximum electric field is. Secondly, the electric field is hardly modified by the size of the protrusion, in the range 10-1000 nm. This result is particularly surprising but can be explained as follow. On one hand, an increase of the size of the protrusion changes the distance between the electrodes. For a constant applied voltage, it tends toward an increase of the electric field. On the other hand, an increase of the protrusion size diminishes the curvature of the protrusion. Then, the electric field lines are less contracted close to the protrusion. Both phenomena counterbalance themselves. However it would be hasty to conclude that the protrusions have no effect on the electric field.

We have defined the Electric Field Enhancement Factor (EFEF) as the ratio of the maximum electric field on the surface with protrusion to the electric field without protrusion:

$$\beta' = \frac{E_p}{E_0} \quad (1)$$

To keep the difference clear with the field enhancement factor usually extracted from an experimental Fowler-Nordheim plot (the β factor, voltage-to-barrier field conversion factor or geometric factor, used to account for the existence of local emitting spots with field enhancement) the EFEF in our case is called β' .

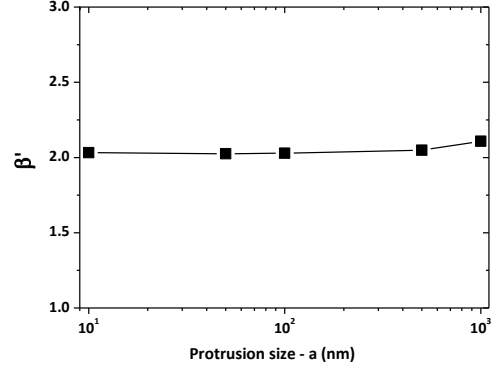


Fig. 3: Electric Field Enhancement Factor for semi-circle protrusions with different size. The protrusion is located at $x_p = 10 \text{ nm}$.

As observed in Fig. 3 the electric field enhancement is not modified by the size of the protrusion. However, the simple presence of one protrusion in the plate electrode doubles the electric field at that point ($\beta' = 2$). It can be enough to drastically increase the field electron emission at the protrusion location and to provoke unexpected breakdown.

IV. CONCLUSION

The effect of nanoprotrusions on the cathode surface in a needle-plate configuration is simulated in microgaps ($< 10 \mu\text{m}$). For a semi-circle protrusion, the presence of a protrusion doubles the electric field but the size of the protrusion does not affect the electric field. To get closer to the reality and takes into account the roughness of a surface, the effect of many protrusions acting together will be presented in a full version of the paper.

REFERENCES

- [1] F. Paschen, "Ueber die zum Funkenübergang in Luft, Wasserstoff und Kohlensäure bei verschiedenen Drucken erforderliche Potentialdifferenz," Ann. Phys., vol. 273, no. 5, pp. 69–96, 1889.
- [2] L. H. Germer and F. E. Haworth, "A low voltage discharge between very close electrodes," Physical Review, vol. 71, p. 1121, 1948.
- [3] W. S. Boyle and P. Kisliuk, "Departure from Paschen's law of breakdown in gases," Phys. Rev., vol. 97, no. 2, pp. 255–259, 1955.
- [4] J. M. Torres and R. S. Dharwal, "Electric field breakdown at micro-metre separations," Nanotechnology, vol. 10, no. 1, pp. 102–107, 1999.
- [5] P. G. Slade and E. D. Taylor, "Electrical breakdown in atmospheric air between closely spaced (0.2 μm -40 μm) electrical contacts," IEEE Trans. Components Packag. Technol., vol. 25, no. 3, pp. 390–396, 2002.
- [6] C. H. Chen, J. A. Yeh, and P. J. Wang, "Electrical breakdown phenomena for devices with micron separations," J. Micromechanics Microengineering, vol. 16, no. 7, pp. 1366–1373, 2006.
- [7] A. Peschot, N. Bonifaci, O. Lesaint, C. Valadares, and C. Poulain, "Deviations from the Paschen's law at short gap distances from 100 nm to 10 μm in air and nitrogen," Appl. Phys. Lett., vol. 105, p. 123109, 2014.
- [8] Y. Fu, P. Zhang and J.P. Verboncoeur, "Paschen's curve in microgaps with an electrode surface protrusion", Appl. Phys. Lett., vol 113, p. 054102, 2018
- [9] Y. Fu, P. Zhang, J. Krek and J.P. Verboncoeur, "Gas breakdown and its scaling law in microgap with multiple concentric cathode protrusions", Appl. Phys. Lett., vol 114, p. 014102, 2019

Impact of Effective Mass on Transport Properties and S/D tunneling in Ultrascaled Double Gate Devices: a 2D MS-EMC study

Cristina Medina-Bailon

School of Engineering

University of Glasgow

Glasgow, United Kingdom

Cristina.MedinaBailon@glasgow.ac.uk

Jaehyun Lee

School of Engineering

University of Glasgow

Glasgow, United Kingdom

jaehyun1986.lee@gmail.com

Carlos Sampedro

Departamento de Electrónica y

Tecnología de los Computadores

Universidad de Granada

Granada, Spain

csampe@ugr.es

José Luis Padilla

Departamento de Electrónica y

Tecnología de los Computadores

Universidad de Granada

Granada, Spain

jluispt@ugr.es

Luca Donetti

Departamento de Electrónica y

Tecnología de los Computadores

Universidad de Granada

Granada, Spain

donetti@ugr.es

Vihar P. Georgiev

School of Engineering

University of Glasgow

Glasgow, United Kingdom

Vihar.Georgiev@glasgow.ac.uk

Francisco Gamiz

Departamento de Electrónica y

Tecnología de los Computadores

Universidad de Granada

Granada, Spain

fgamiz@ugr.es

Asen Asenov

School of Engineering

University of Glasgow

Glasgow, United Kingdom

Asen.Asenov@glasgow.ac.uk

Abstract— *In the simulation based research of aggressively scaled CMOS transistors, it is mandatory to combine advanced transport simulators and quantum confinement effects with first-principle techniques which accurately reproduce the electronic structure at the nanometer scale. This work investigates the impact of extracted effective masses in DGSOI transistors and FinFETs considering the Source-to-Drain tunneling (S/D tunneling) using a 2D Multi-Subband Ensemble Monte Carlo (MS-EMC) simulator. The results show that in the subthreshold regime the effective mass variation increase the tunneling probability for the DGSOI transistor leading to a current degradation. However, this difference is reduced and even reversed for the FinFET.*

I. INTRODUCTION

In the simulation frameworks, approaches incorporating quantum phenomena into semi-classical models have become popular due to their reduced computational cost. Source-to-Drain tunneling (S/D tunneling) starts to play important role degrading the subthreshold behavior when the channel length is reduced below 10nm [1-2]. The electronic structure model must accurately reproduce the experimental energy gaps and effective masses for the most relevant subbands. In this work, we study the impact of the effective mass on the transport properties and on the S/D tunneling in Double-Gate Silicon-On-Insulator (DGSOI) and FinFET devices. We compare the use of bulk (m_{bulk}) effective masses and those extracted from first principle simulations (m_{eff}) by means of a 2D Multi-Subband Ensemble Monte Carlo (MS-EMC) tool.

II. METHODOLOGY

This 2D MS-EMC simulator [3-4] solves the Schrödinger equation in the confinement direction and the Boltzmann Transport Equation (BTE) in the transport plane (Fig. 1). The system is coupled by solving the Poisson equation in the whole 2D simulation domain.

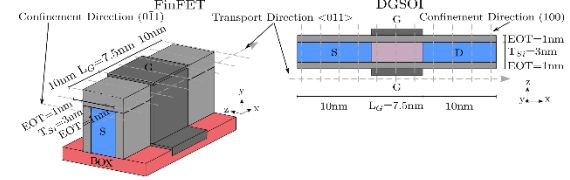


Fig. 1. DGSOI and FinFET structures herein analyzed with $L_G=7.5\text{nm}$ and $T_{Si}=3\text{nm}$. Schrödinger equation is solved for each grid point in the transport direction and BTE is solved by the MC method in the transport plane.

The realistic conduction band structure of the 2D devices has been taken into consideration by extracting accurately m_{eff} using density functional theory (DFT) simulations included in QuantumATK of Synopsys [5]. Table I summarizes the values of the masses for the DGSOI and FinFET devices studied here with silicon thickness $T_{Si}=3\text{nm}$.

TABLE I. EFFECTIVE MASSES FOR THE DGSOI AND FINFET DEVICES HEREIN STUDIED WITH SILICON THICKNESS $T_{Si}=3\text{nm}$ CONSIDERED BOTH THE BULK (m_{bulk}) AND THE EXTRACTED (m_{eff}) EFFECTIVE MASSES.

	Device	Valley	m_x	m_y	m_z
m_{bulk}	DGSOI	Δ_2	0.193 m_0	0.193 m_0	0.912 m_0
	(100)<011>	Δ_4	0.319 m_0	0.552 m_0	0.193 m_0
	FinFET	Δ_2	0.193 m_0	0.912 m_0	0.193 m_0
		Δ_4	0.552 m_0	0.193 m_0	0.319 m_0
m_{eff}	DGSOI	Δ_2	0.144 m_0	0.144 m_0	1.002 m_0
	(100)<011>	Δ_4	0.252 m_0	0.573 m_0	0.144 m_0
	FinFET	Δ_2	0.15 m_0	1.134 m_0	0.15 m_0
		Δ_4	0.642 m_0	0.15 m_0	0.265 m_0

Furthermore, we have activated the S/D tunneling module in our simulations [4] to reproduce properly the nanometer transistor behavior. This phenomenon is implemented as a stochastic mechanism evaluated for each particle at the end of the MC cycle. The tunneling probability, calculated by the WKB approximation [6], mainly depends on: (i) the carrier

position, (ii) the transport effective mass, and (iii) the subband profile that determines the shape of the tunneling barrier. Accordingly, the modification of the band structure obtained from the first principle simulations alters the tunneling probability and so the device electrostatics.

III. RESULTS

Fig. 1 shows the device parameters for the silicon DGSOI and FinFET analyzed here. Fig. 2 depicts the I_D vs. V_{GS} characteristics for both devices at $V_{DS}=0.5V$ obtained from ballistic and diffusive simulations and considering four different combinations: m_{bulk} with and w/o S/D tunneling; and m_{eff} with and w/o S/D tunneling. In general, the current decreases when m_{eff} is included in the case without S/D tunneling. However, for the simulation with S/D tunneling, the current is higher when m_{eff} is included in the DGSOI device, whereas the opposite trend is observed in the FinFET.

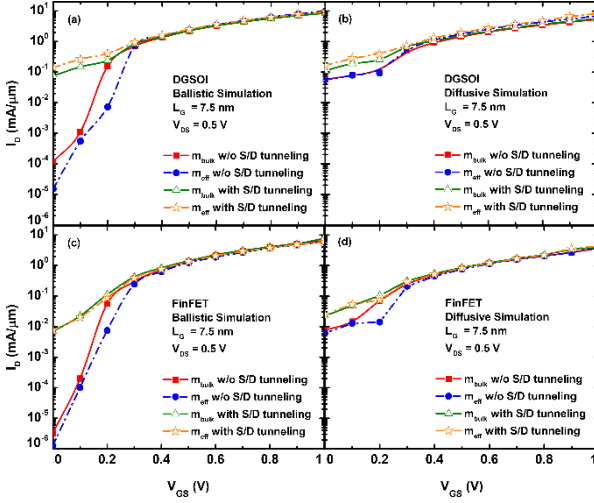


Fig. 2. I_D vs. V_{GS} in the DGSOI and FinFET devices for (a)/(c) ballistic and (b)/(d) diffusive simulations, respectively, at $V_{DS}=0.5V$ considering four different combinations: bulk (m_{bulk}) effective masses with and w/o S/D tunneling; and extracted (m_{eff}) effective masses with and w/o S/D tunneling.

The tunneling probability increases for lower effective mass and/or potential barrier. This is the case for the DGSOI transistor in which the transport m_{eff} of the dominant valley (Δ_2) is smaller than m_{bulk} (Table I). For the FinFET, the transport m_{eff} of the dominant valley (Δ_4) is higher than m_{bulk} (Table I), thus decreasing the tunneling probability and thereby the current. Consequently, the percentage of particles affected by S/D tunneling among those near the potential barrier with energy below the barrier top (Fig. 3) is higher for m_{eff} in the DGSOI, whereas it is lower for the FinFET.

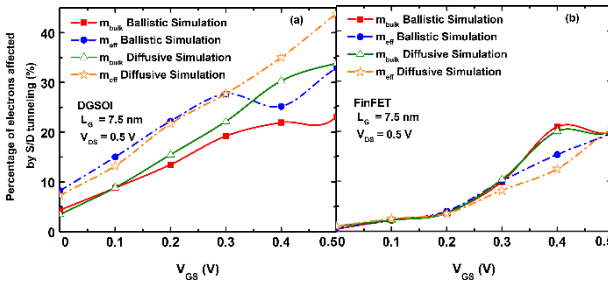


Fig. 3. Percentage of electrons affected by S/D tunneling as a function of V_{GS} in the DGSOI (a) and FinFET (b) devices at $V_{DS} = 0.5V$ from ballistic and diffusive simulations for bulk (m_{bulk}) and extracted (m_{eff}) effective masses.

This trend can also be explained referring to Fig. 4, where the energy level for the top barrier in the center of the device is shown for the first subband of Δ_2 and Δ_4 valleys. The difference between the top barrier energy of the dominant valley is higher in the diffusive simulation compared to the ballistic case, being less pronounced for the S/D tunneling model. This difference is negligible for the FinFET.

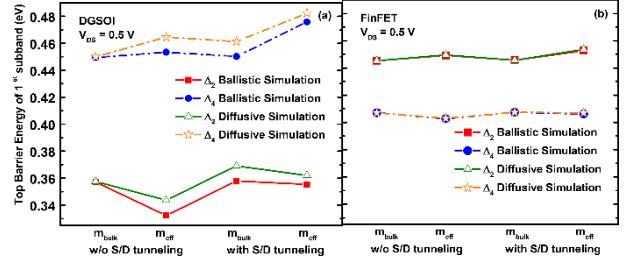


Fig. 4. Top barrier energy of the first subband of the Δ_2 and Δ_4 valleys for DGSOI (a) and FinFET (b) devices at $V_{DS}=0.5V$ considering ballistic and diffusive simulations and four different combinations: bulk (m_{bulk}) effective masses with and w/o S/D tunneling; and extracted (m_{eff}) effective masses with and w/o S/D tunneling.

Finally, Fig. 5 shows the difference in the threshold voltage (ΔV_{TH}) between simulations without and with S/D tunneling for the four different configurations of the two devices with different gate lengths. ΔV_{TH} is much more noticeable for m_{eff} in the DGSOI transistor than in the FinFET and, as expected, for the diffusive simulation compared to the ballistic one.

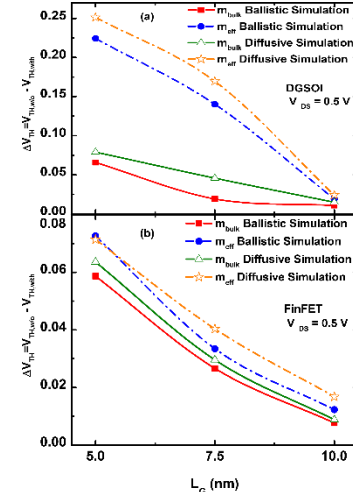


Fig. 5. Threshold voltage variation (ΔV_{TH}) between simulations w/o and with S/D tunneling as a function of L_g in the DGSOI (a) and FinFET (b) devices at $V_{DS} = 0.5V$ obtained from ballistic and diffusive simulations for bulk (m_{bulk}) and extracted (m_{eff}) effective masses.

REFERENCES

- [1] J. W. J. Wang and M. Lundstrom, "Does source-to-drain tunneling limit the ultimate scaling of MOSFETs?" Digest. International Electron Devices Meeting, pp. 707–710, 2002.
- [2] H. Iwai, "Future of nano CMOS technology," Solid-State Electronics, vol. 112, pp. 56–67, 2015.
- [3] C. Sampedro et al., "On the extension of ET-FDSOI roadmap for 22 nm node and beyond," Solid-State Elec., vol. 90, pp. 23–27, 2013.
- [4] C. Medina-Bailon et al., "Source-to-Drain Tunneling Analysis in FDSOI, DGSOI and FinFET Devices by Means of Multi-Subband Ensemble Monte Carlo," IEEE Trans. on Elec. Devices, vol. 65, no. 11, pp. 4740–4746, 2018.
- [5] QuantumATK version O-2018.06. Synopsys, inc., 2018
- [6] D. J. Griffiths, "The WKB approximation," in Introduction to Quantum Mechanics. New Jersey: Prentice Hall, ch. 8, pp. 274–297, 1995.

Impact of Silver Nanoparticles on Current Transport in CVD Mono-layer Graphene/Si Junctions

Badreyya Al Shehhi

EECS Dept

Khalifa University, Abu Dhabi, UAE

badreyya.shehhi@ku.ac.ae

Irfan Saadat

EECS Dept

Khalifa University, Abu Dhabi, UAE

Ayman Rezk

Department of Physics

Khalifa University, Abu Dhabi, UAE

ayman.rezk@ku.ac.ae

Ammar Nayfeh

EECS Dept

Khalifa University, Abu Dhabi, UAE

ammar.nayfeh@ku.ac.ae

Yawar Abbas

Department of Physics

Khalifa University, Abu Dhabi, UAE

Moh'd Rezeq

Department of Physics

Khalifa University, Abu Dhabi, UAE

mohd.rezeq@ku.ac.ae

Abstract— In this work the impact of adding silver Nanoparticles (Ag NPs) on CVD graphene monolayer Si junctions is presented. The vertical and lateral/surface current transport properties for different Si-substrate samples (varying top Si surface treatment) are studied using Conductive mode Atomic Force Microscope (C-AFM) and micro-probe station. The studies indicate the presence of NP's creates a localized electrical field enhancement that lowers the tunneling barrier for reserve biased Schottky Barrier (SB) junctions. Additionally, the presence of NP's modulates the surface conductivity of the graphene layers. The presence of thin 2nm Al₂O₃ Atomic Layer Deposition (ALD) film over the Si substrate enhances the transport across the junction by providing an effective lower contact resistance for nano-SB junction. The combination of NP's size and types will allow for custom tuning of the nano-SB properties for the desired applications.

Keywords—Nanoparticles, Graphene, C-AFM, 2D materials

I. INTRODUCTION

Nano interfaces, nanostructures and Nanoparticles (NPs) exhibit unique electrical and optical properties that is leading the way for future optoelectronic and electronic nano-devices [1]. Atomic Force Microscopy (AFM) plays a key role in exploring the basic principles underlying the functionality of two- dimensional (2D) materials along with NPs interfaces [2]. The NPs have an important effect in the current transport and electrical field enhancement [3-5]. Furthermore, combination of noble metal NPs on graphene has been demonstrated to provide outstanding optical and transport properties of graphene [1]. In this work, the impact of NPs on CVD mono-layer graphene transport has been assessed using lateral (surface) and vertical conductivity experiments, where C-AFM and micro-probe station measurements are used.

II. FABRICATION AND CHARACTERIZATION

Different test structures are fabricated where Ag NPs (~40 nm in diameter) are spun coated and dispersed on top of CVD mono-layer graphene, which were exfoliated on top of different surface treated n-type Si substrates. Table 1 summarizes the stacks of the three fabricated structures along with the associated schematic diagram for each. Sample 1 (S₁) is HF treated to remove any native oxide prior to graphene exfoliation, S₂ has native oxide (no HF treatment); and S₃ has 2nm Al₂O₃ ALD film. The top metal electrode of 10nm Ti/200nm Al is E-beam evaporated. Fig.1 shows the IV test setups for lateral and vertical current transport measurements using probe station (25um W tip) and the AFM. The AFM provides information on the size and dispersion of NP's along with the electrical properties using C-AFM. The Si tip is coated with Ti/Ir (5/20) and has diameter of 25nm.

III. RESULTS

First, baseline line measurement to assess the impact of Ag NPs on n-Si substrates to done. The vertical conductance of n-Si samples, with (w) and without (w/o) NPs, are tested via C-AFM. The C-AFM tip plays a critical role in enhancing the electrical field (vs. probe station's larger tip), which lowers the barrier for tunneling current [3-4]. The result indicates that the NPs play a major role in the current transport as expected. The NPs forms tunneling paths connecting the Si substrate to the AFM tip, resulting in large current due to the local field enhancement between the NPs and the substrate interface [5]. While adding a graphene, under the Ag NPs, enhances the tunneling current further as shown in Fig.2.

The AFM and probe station measurements are done for the three samples w and w/o the Ag NPs in the vertical and lateral/surface transport configurations. For the devices w/o NP's, the probe station based electrical response for S₁ and S₂ devices in lateral configuration exhibits an ohmic behavior (voltage sweeps of +2.5 to -2.5V). While there is no enhancement in the current in devices w NPs. However, in case of AFM surface measurement, the presence of NPs on graphene is lowering the current (vs. graphene only) in all the samples regardless the Si substrate condition/layer. This indicates that the presence of NP's on the graphene modulates the conductivity of the graphene by lowering it. Whereas the vertical current is more pronounced using the AFM measurement, where there is an enhancement of the tunneling current especially in S₃ by lowering the barrier due to the presence of the nm scale high bandgap insulation layer [6]. Fig.3 and Fig.4 show the comparison between the vertical and lateral AFM and micro-probe current density vs. voltage measurements along with associated explanations.

IV. CONCLUSION

In summary, three device types are fabricated and characterized using C-AFM and micro-probe station. The results reveal that the presence of Ag NPs on CVD graphene

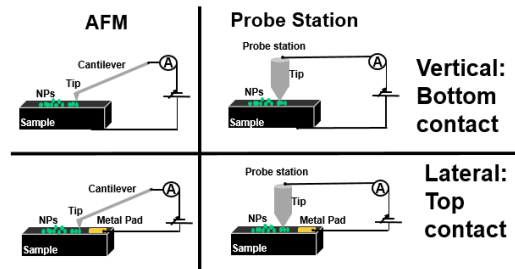
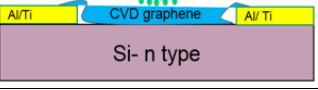
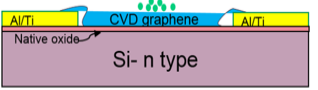
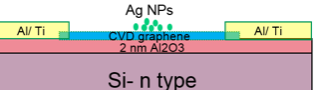


Fig. 1. The two main configuration current-voltage test.

is retarding the lateral mode conduction of graphene. For the vertical conduction, the Ag NPs increase the tunneling current by lowering the barrier and enhancing the electrical field on graphene layer. Additionally, the presence of a thin insulation layer under the graphene enhances the transport across junctions. These studies provide an approach for optimizing nano-SB devices for targeted optical/electronic operations.

TABLE I. HETERO-JUNCTIONS STRUCTURE

Sample #	Structure	Cross section
S ₁	n-Si, 210nmAl/Ti, HF,graphene, Ag NPs	
S ₂	n-Si, 210nmAl/Ti, graphene,Ag NPs	
S ₃	n-Si, HF,2nmAl ₂ O ₃ , graphene,210nm Al/Ti, Ag NPs	

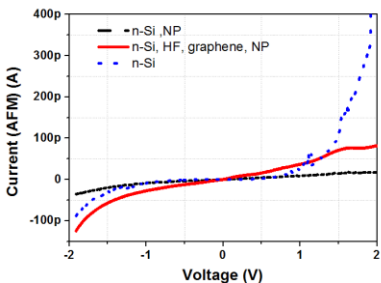


Fig. 2. The current enhancement due to presence of graphene layer (solid red line).

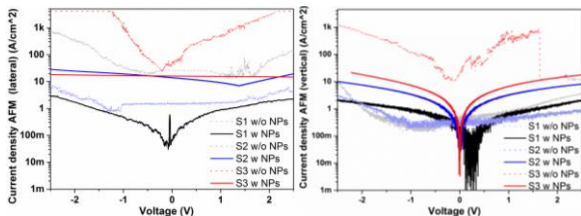


Fig. 3. The AFM lateral and vertical current transports for S₁,S₂ and S₃ w (solid line) and w/o (dotted line) Ag NPs. The presence of Ag NPs with graphene, results in lowering the conductivity of graphene across the three samples regardless the insulation layer, which indicate that the current is going through the surface of the mono-layer of graphene only, however there is an enhancement of the current in the vertical transports due the presence of Ag NPs.

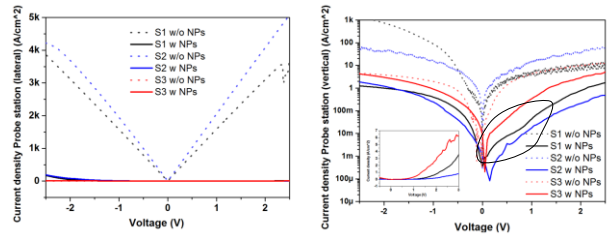


Fig. 4. Probe station lateral vertical current transports for S₁,S₂ and S₃ w (solid line) and w/o (dots line) Ag NPs. The presence of Ag NPs results in enhancing the current and shows resonance/negative-conduction response due to resonant tunneling effect (especially for S₃) compared to smoother normal rectifying behavior w/o Ag NPs for all of the three samples. The inset shows linear IV scale for the elliptical shape which has the resonant tunneling response.

REFERENCES

- [1] Jimenez-Villacorta, F., Climent-Pascual, E., Ramirez-Jimenez, R., Sanchez-Marcos, J., Prieto, C., & De Andrés, A. (2016). Graphene–ultrasmall silver nanoparticle interactions and their effect on electronic transport and Raman enhancement. *Carbon*, 101, 305–314.
- [2] H. Zhang, J. Huang, Y. Wang, R. Liu, X. Huai, J. Jiang, et al., "Atomic force microscopy for two-dimensional materials: a tutorial review," *Optics Communications*, vol. 406, pp. 3-17, 2018.
- [3] Rezeq M., Ali, A., Patole, S. P., Eledlebi, K., Dey, R. K., & Cui, B. (2018). The dependence of Schottky junction (I–V) characteristics on the metal probe size in nano metal–semiconductor contacts. *AIP Advances*, 8(5), 055122.
- [4] Rezeq M., Eledlebi,K.,Ismail,M.,Dey, R. K., & Cui, B. (2016). Theoretical and experimental investigations of nano-Schottky contacts. *Journal of Applied Physics*, 120(4), 044302.
- [5] Rezk,A.,Abbas,Y.,Saadat,I.,Nayfeh,A.,& Rezeq, M. D. (2019). Effect of Silver Nanoparticles on the Electrical Characteristics of Oxide/Semiconductor Heterojunctions. *ECS Transactions*, 89(3),133-136.
- [6] Alnuaimi, A., Almansouri, I., Saadat, I., & Nayfeh, A. (2018). High performance graphene-silicon Schottky junction solar cells with HfO₂ interfacial layer grown by atomic layer deposition. *Solar Energy*,164, 174-179.

Fabrication and Characterization of Carbon Based Interconnects for 3D ICs

Andreas Nylander, Marlene Bonmann, Jie Zhao, Andrei Voroblev, Yifeng Fu, Zhibin Zhang and Johan Liu

Moore's law has pushed the development of performance and profitability regarding integrated circuits (ICs) in an exponential fashion over the last couple of decades. With the scaling now reaching critical dimensions where quantum effects starts to become noticeable, this development is starting to slow down. The ITRS roadmap has stated More Moore, More than Moore, 3D packaging and heterogeneous integration as strategies for a continued development of IC devices where the miniaturization potential is in focus without increasing the IC footprint. However, to reach the full potential these strategies offer, new materials and design methodologies are required.

According to the ITRS, Cu interconnects face acute resistivity issues when scaling down to cross sectional dimensions below 40 nm with severe performance and reliability impacts as a result. Instead, nanomaterials like graphene and carbon nanotubes have been proposed for use as new interconnect materials for VLSI due to their intrinsic material properties that allows them to scale further than Cu.

In this paper we demonstrate CPW (coplanar waveguide) line test structures based on inkjet-printed graphene including Multi Walled Carbon Nanotubes (MWCNT) filled VIAs on SiO₂ / high resistive Si substrates. These test structures are characterized at DC and in the frequency range 1-50 GHz. Analysis allows for evaluation of the CPW intrinsic attenuation coefficient and contribution of parasitics. Preliminary results show that the graphene-based CPWs, with 0.37 mm long signal line, demonstrate insertion loss down to $S_{21} = -2$ dB at frequency of 1 GHz, which is less than that of previously published graphene-based CPW lines. The work presented here is an important step towards the realization of the full carbon 3D ICs that will provide more performance and functionality for the next generation of electronic devices.

Silicon Nanophotonics for Light Manipulation and Photodetection

Daixin Dai*, and Jiang Li.

Centre for Optical and Electromagnetic Research, State Key Laboratory for Modern Optical Instrumentation, Zhejiang Provincial Key Laboratory for Sensing Technologies, Zhejiang University, Zijingang, Hangzhou 310058, China
dxdai@zju.edu.cn

Abstract: A review is given on recent progresses of silicon nanophotonics for light manipulation and photodetection, including the following parts. The first one is for passive silicon nanophotonic devices, such as asymmetric nanophotonic waveguide structures for on-chip polarization-handling, mode-manipulation, and wavelength-filtering. The second part is for the realization of waveguide photodetectors on silicon by combining two-dimensional materials and silicon nanophotonic waveguides.

Keywords: silicon photonics, optical waveguides, switches, modes, polarization.

Optical Monitoring of Single Nanoparticle Capture in a Solid-State Nanopore Array

1
2
3
4
5
6
7
8
9
10
11
12
13
14
15
16
17
18
19
20
21
22
23
24
25
26
27
28
29
30
31
32
33
34
35
36
37
38
39
40
41
42
43
44
45
46
47
48
49
50
51
52
53
54
55
56
57
58
59
60
61
62
63
64
65
Shiyu Li

Department of Engineering Sciences
Uppsala University
Uppsala, Sweden
shiyu.li@angstrom.uu.se

Shuangshuang Zeng

Department of Engineering Sciences
Uppsala University
Uppsala, Sweden
shuangshuang.zeng@angstrom.uu.se

Zhen Zhang

Department of Engineering Sciences
Uppsala University
Uppsala, Sweden
zhen.zhangi@angstrom.uu.se

Klas Hjort

Department of Engineering Sciences
Uppsala University
Uppsala, Sweden
klas.hjort@angstrom.uu.se

Shi-Li Zhang

Department of Engineering Sciences
Uppsala University
Uppsala, Sweden
shili.zhang@angstrom.uu.se

Abstract—Solid-state nanopore arrays hold promises for high-throughput optical or electrical analysis of nanoscale entities. Here, we demonstrate an optical monitoring system for investigation of the capture process of single nanoparticles driven by electrophoretic force in a nanopore array. Over 50% of the single nanoparticle capture events are achieved by controlling the applied voltage across the nanopore membrane with a tailored nanopore size. We find that at a certain voltage bias, the capture of single nanoparticles is a self-termination process.

Keywords—nanopore array, nanoparticle, electrophoresis, optical sensing.

I. INTRODUCTION

Nanopore devices have been widely used as a powerful analytical tool for studying the kinetics of nanoscale entities passing through the pores in a resistive pulse principle [1-3]. Apart from the translocation-based sensing, capture or trapping of the target analyte with a larger size than the nanopore orifice has also been studied for various applications, such as precise positioning of single-molecules [4-5] or nanopore force spectroscopy [6]. Particularly, detection or assembly of nanoscale particles with unique luminescent, magnetic, or electronic properties is of importance for the development of nanopore-based sensors [7-8]. Moreover, with the flexibility of designing various configurations, solid-state nanopores offer a versatile platform to investigate the electrophoretic capturing process of single nanoparticles, e.g., by specifically controlling the size of individual nanopore and the inter-distance of multiple pores. However, while much attention has been focused on electrical read-out of nanoparticle capture in solid-state nanopores, there has been less emphasis on the equally important optical read-out of nanopore arrays.

Here, we demonstrate an optical sensing system for parallelized monitoring of single polystyrene nanoparticles captured by a nanopore array in a SiN_x membrane driven by an electrophoretic force. The individual nanopore size is tailored to be suitable for efficient trapping of single nanoparticles. Figure 1 shows a schematic presentation of the optical read-out setup for monitoring the nanoparticle capture in the SiN_x nanopore array using a conventional wild-field fluorescence microscope.

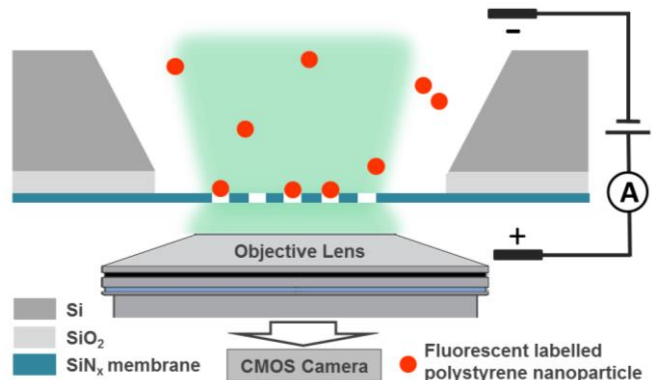


Fig. 1. Schematic of the optical read-out setup for monitoring nanoparticle capture in a nanopore array using an inverted microscope.

II. MATERIALS AND METHODS

A. Fabrication of nanopore array

The nanopore fabrication started from a 300 μm double side polished (100) silicon wafer covered with a 25-nm thick low-stress SiN_x layer grown by means of low pressure chemical vapor deposition (LPCVD) on top of a 50-nm thick thermally grown SiO_2 . Both SiN_x and SiO_2 were present on the two sides of the wafer. Etched alignment marks were first defined to ensure accurate placement. Nanopore arrays were patterned on the front side with electron beam lithography (EBL) and then transferred to the device layer SiN_x by reactive ion etching (RIE). Next, a 150 μm window was opened from the rear side of the wafer using deep reactive ion etching (DRIE) and KOH etching to reach the SiO_2 layer on the front side. This oxide was then stripped off in buffered hydrofluoric acid (BHF). This process completed the generation of nanopore arrays in the free-standing SiN_x membrane on the front side of the wafer.

B. Optical monitoring setup

A SiN_x membrane chip with a 10×10 nanopore array was mounted on a homemade fluidic cell chamber with two pseudo reference Ag/AgCl electrodes to form a closed electrical loop through electrolyte. The nanoparticles used were 100 nm fluorescent carboxylate-modified nanoparticles (Ex/Em : 580 nm/605 nm, Fisher Scientific). They were added to the top fluidic chamber to a concentration of 3.6×10^{10} particles/mL in 100 mM KCl solution. The nanoparticle capturing events were observed using an inverted fluorescence microscope (IX73, Olympus)

with a LED light source (pE300, Cool LED) filtered through a U-FBNA filter set (Olympus). The optical signal was captured by a digital CMOS camera (OCRA-Flash4.0 LT, Hamamatsu) through a 40 \times dry objective (LUCPlanFL 40 \times /0.60 Ph2, Olympus).

III. EXPERIMENTAL RESULTS

A 10 \times 10 nanopore array with pore diameter of 80 nm was used to capture polystyrene nanoparticles of 100 nm diameter. Because the surface was carboxylic-modified, the nanoparticle was overall negatively charged in an electrolyte of pH=8.0. The SiN_x membrane surface was also negatively charged at this pH value. At a cross-nanopore bias voltage below 200 mV, no obvious capture of nanoparticle was observed. In this case, an electroosmotic flow streaming (originated by the positive ions attracted to the negatively charged SiN_x sidewall) in the opposite direction to the electrophoresis was presumably hindering a stable capture of nanoparticles. By increasing the bias voltage above 400 mV, an efficient capture process was observed. As shown in Figure 2, a set of fluorescence images taken at different time spots of a continuous video clip clearly reveal the capture process. As the confined electric field near the nanopore orifice is strong enough, the captured nanoparticles are mostly stable, as marked by the blue circles to show the temporally released ones in Figure 2. When the bias voltage was further increased above 600 mV and then kept for over 5 minutes, the capture became irreversible even when a reverse bias at 3 V was subsequently applied. This irreversible capture phenomenon is most likely caused by the predominated hydrophobic interaction between the polystyrene nanoparticles and the SiN_x surface.

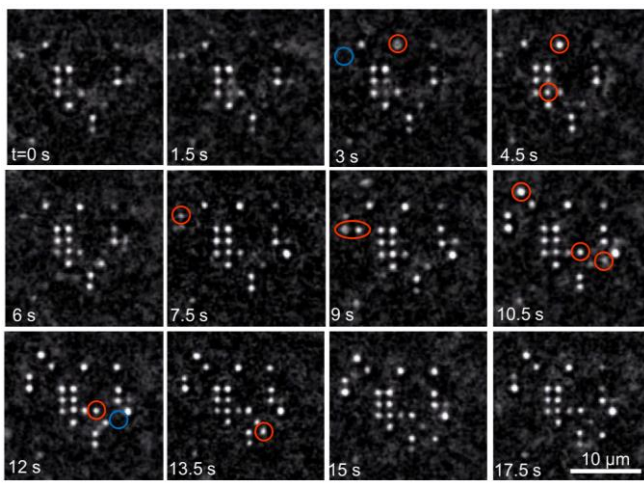


Fig. 2. Fluorescence images taken from a continuous video clip showing the capture of 100 nm fluorescent labeled, carboxylic-modified polystyrene nanoparticles in a 10 \times 10 nanopore array of 80 nm pore diameter at 600 mV bias voltage. In each frame, the red circles mark the newly captured nanoparticles compared with the previous image, while the blue circles show the temporally released nanoparticles.

Figure 3 shows typical SEM images of the captured nanoparticles on part of the nanopore array with 16 pores. At a bias voltage of 400 or 600 mV, a large fraction of captured nanoparticles is positioned in the center of the nanopore cavities with single particles. In this case, we regard the capture as a self-terminating process, mainly due to the high electric field in the pore being shut off by the captured nanoparticle thereby prohibiting further capture. However, at

1000 mV, capture of multiple particles by a pore occurs at higher rates, as a consequence of a stronger electric field in the pore due to leakage between the captured nanoparticle(s) and the nanopore wall. The statistical results show that over 50% of the single nanoparticle positioning on the arrayed nanopore structure is achieved at 600 mV bias voltage.

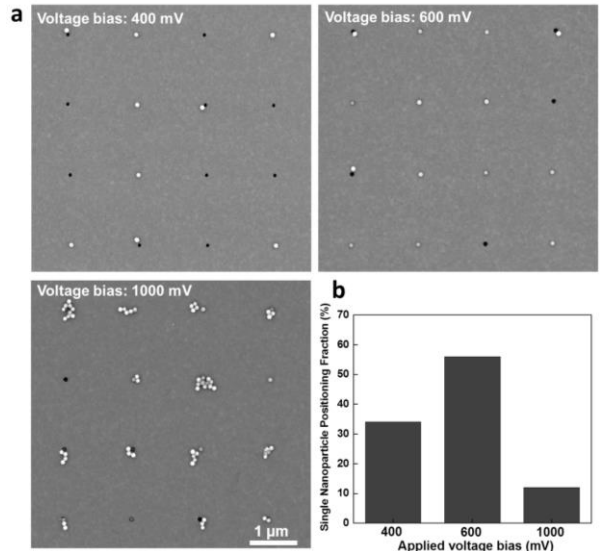


Fig. 3. a) SEM images of captured nanoparticles in the nanopore array at different bias voltages each for 5 minutes; b) Statistical results for the fraction of single nanoparticle positioning on the 10 \times 10 nanopore array at different bias voltages.

ACKNOWLEDGMENT

This work was supported by the Swedish Research Council (621-2014-6300). Shiyu Li is a scholarship recipient (201606100043) of the China Scholarship Council (CSC).

REFERENCES

- [1] T. Gilboa and A. Meller, "Optical sensing and analyte manipulation in solid-state nanopores," *Analyst*, vol. 140, pp. 4733-47, Jul 21 2015.
- [2] M. Wanunu, W. Morrison, Y. Rabin, A. Y. Grosberg, and A. Meller, "Electrostatic focusing of unlabelled DNA into nanoscale pores using a salt gradient," *Nat Nanotechnol*, vol. 5, pp. 160-5, Feb 2010.
- [3] M. Sugimoto, Y. Kato, K. Ishida, C. Hyun, J. Li, and T. Mitsui, "DNA motion induced by electrokinetic flow near an Au coated nanopore surface as voltage controlled gate," *Nanotechnology*, vol. 26, p. 065502, Feb 13 2015.
- [4] D. P. Hoogerheide, B. Lu, and J. A. Golovchenko, "Pressure-voltage trap for DNA near a solid-state nanopore," *ACS Nano*, vol. 8, pp. 7384-91, Jul 22 2014.
- [5] J. Larkin, M. Foquet, S. W. Turner, J. Korlach, and M. Wanunu, "Reversible Positioning of Single Molecules inside Zero-Mode Waveguides," *Nano Lett.*, vol. 14, pp. 6023-6029, Oct 2014.
- [6] V. Tabard-Cossa, M. Wiggin, D. Trivedi, N. N. Jetha, J. R. Dwyer, and A. Marziali, "Single-molecule bonds characterized by solid-state nanopore force spectroscopy," *ACS Nano*, vol. 3, pp. 3009-14, Oct 27 2009.
- [7] M. Tsutsui, K. Yokota, T. Nakada, A. Arima, W. Tonomura, M. Taniguchi, *et al.*, "Particle Capture in Solid-State Multipores," *ACS Sens*, Nov 13 2018.
- [8] D. Yoo, K. L. Gurunatha, H. K. Choi, D. A. Mohr, C. T. Ertsgaard, R. Gordon, *et al.*, "Low-Power Optical Trapping of Nanoparticles and Proteins with Resonant Coaxial Nanoaperture Using 10 nm Gap," *Nano Lett*, vol. 18, pp. 3637-3642, Jun 13 2018.

Improving reliability issue of HfO_2 -based memristors by protecting the switching materials against buffer layer deposition

B. Attarimashalkoubeh* and Y. Leblebici

Microelectronic System Laboratory (LSM)

École polytechnique fédérale de Lausanne (EPFL), Lausanne, Switzerland

* Corresponding author: Behnoush.attarimashalkoubeh@epfl.ch

Abstract—As the variability issue is considered to be the main hurdle in the commercialization of the memristor technology, further researches are encouraged to solve it. In this study, we fabricated different HfO_2 -based memristors and investigated their electrical properties. We demonstrated how the insertion of a thin layer (2nm) of TiO_2 between the Ti buffer layer and the oxide, could effectively reduce the uncontrolled formation of conductive filaments composed of oxygen vacancies and results in a better resistive switching performance. We assume the ALD deposited TiO_2 protected the oxide materials against penetration of PVD deposited Ti during the fabrication.

Index Terms—ReRAMs, Memristor, Oxygen Vacancy, HfO_2 -based memristors, Variation Issue, Buffer layer.

Investigation of single-event-transient effect in floating-gate junctionless double-gate field-effect-transistor

Avashesh Dubey,
Mridula Gupta*

Semiconductor Device Research
Laboratory, Department of Electronic
Science, University of Delhi South
Campus, New Delhi-110021, India
avasheshniiit@gmail.com;
mridula@south.du.ac.in

Rakhi Narang

Department of Electronics
Sri Venkateswara College, University
of Delhi, New Delhi-110021, India
rakhinarrang@gmail.com

Manoj Saxena

Department of Electronics
Deen Dayal Upadhyaya College,
University of Delhi,
New Delhi-110078, India
saxenamanoj77@yahoo.co.in

Abstract—In this paper, effects of single event transient on Floating gate junction-less double gate field effect transistor (FG JL DG FET) have been studied using TCAD simulation. The result shows that the drain current peak obtained after heavy ion strike is 2.69×10^{-4} A at LET value of 11 MeV cm^2/mg which is high as compared to the on-state current i.e. 1.06×10^{-4} A at ($V_{ds}=0.5$ V and $V_{gs}=1.0$ V). Collected charge with various LET has also been investigated. The findings are compared with floating gate double gate field effect transistor (FG DG FET).

I. INTRODUCTION

In space or aircraft applications, the effects of radiation on floating gate devices have been a main concern. The abundantly present heavy ion and other high energy particle at high altitude causes many soft errors like SEU and degradation in gate oxide of transistor due to total ionized dose effect (TID) [1]-[2]. We have reported FG Junction Less (JL) DG MOSFET as radiation dosimeter [3]. In this paper, we have investigated the effect of linear energy transfer (LET) in the FG JL DG MOSFET.

II. DEVICE ARCHITECTURE AND SIMULATION RESULTS

In order to check single effect transient effect in the device, the heavy ion model has been used [4].

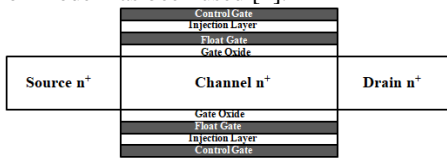


Fig.1. Cross sectional view of FG JL DG FET.

The single event upset occurs if the logic state of the circuit changes due to the heavy ion induced collected charge. The collected charge disturbs the circuits due to the formation of transient current. Figure 2 (a)-(b) shows the drain current transfer characteristics of the FG JL DG FET and FG DG FET with drain bias of 0.5 V. Figure 3 shows that the drain current transient increases as the heavy ion penetrates into the device and reaches to the maximum value for both the devices. The drain current peak for FG JL DG FET increases from 1.84×10^{-4} A at LET value of 1 MeV cm^2/mg to 2.69×10^{-4} A at LET value of 11 MeV cm^2/mg . This value of drain current peak is larger than the on-state current of the order of magnitude 1.06×10^{-4} A as shown in figure 2(a) at ($V_{ds}=0.5$ V and $V_{gs}=1.0$ V). A comparison of the drain current transient has been performed with FG DG FET. Figure 3 (b) shows that the transient drain current peak of FG DG FET due to heavy ion increases from 1.15×10^{-4} A at LET value of 1 MeV cm^2/mg to 2.36×10^{-4} A at LET value of 11 MeV cm^2/mg . This value of drain current peak is smaller than the on-state drain current of the order of 7.74×10^{-5} A as shown in figure 2(b). The

comparison of the results shows that the FG JL DG FET is more sensitive to heavy ion strike as compare to the FG DG FET thus it can lead to single event upset in the logic circuit.

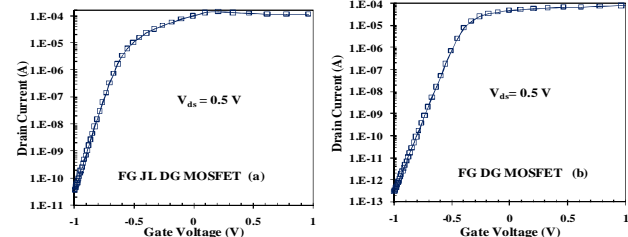


Fig.2. Drain current transfer characteristics for (a) FG JL DG FET and (b) FG DG FET at $V_{ds}=0.5$ V.

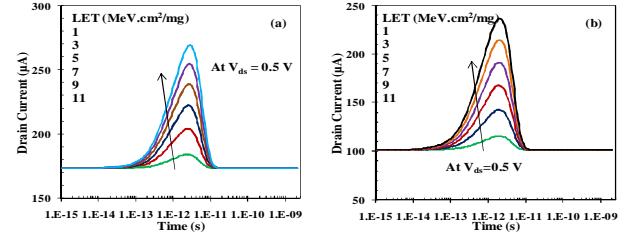


Fig.3. Drain current transient due to ion strike with various LET at 0.5 V drain bias for (a) FG JL DG FET and (b) FG DG FET

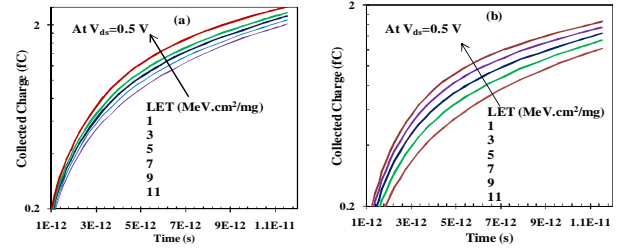


Fig.4. Charge collected after the heavy ion strike with different LET for (a) FG JL DG FET and (b) FG DG FET at drain bias of 0.5 V.

From figure 4, it is obtained that the collected charge exponentially increases for initial 5 ps and after that linearly increases with a linear energy transfer of 1 MeV cm^2/mg . It has been found that the magnitude of the collected charge for FG JL DG FET is higher than that of FG DG FET.

III. CONCLUSION

It has been concluded that FG JL DG FET is more sensitive to the linear energy transfer induced single event transient effects than FG DG FET. The collection of charges in both the device due to LET has also been investigated. The investigation demonstrates the problem of FG JL DG FET radiation reliability, which must be considered while design and development of the device.

REFERENCES

- [1] G. Cellere, et al., "A model for TID effects on floating gate memory cells," in *IEEE Transactions on Nuclear Science*, vol. 51, no. 6 II, pp. 3753–3758, 2004.
- [2] T. R. Oldham, et al., "SEE and TID Characterization of an Advanced Commercial 2Gbit NAND Flash Nonvolatile Memory," in *IEEE Transactions on Nuclear Science*, vol. 53, no. 6, pp. 3217-3222, Dec. 2006. doi: 10.1109/TNS.2006.885843
- [3] A. Dubey, et al., "Floating Gate Junction-Less Double Gate Radiation Sensitive Field Effect Transistor (RADFET) Dosimeter: A Simulation Study", *International Workshop on Physics of Semiconductor Devices. IWPSD-2017*, Springer Proceedings in Physics, vol-215, pp.571-576, 2019.
- [4] Synopsys Sentaurus TCADTools2016<<http://www.synopsys.com/products/tcad/tcad.html>>.

CBRAM devices with a water casted solid polymer electrolyte for flexible electronic applications

Prabir Mahato, Etienne Puyoo, Damien Deleruyelle
*Institut des Nanotechnologies de Lyon UMR CNRS 5270,
Institut National des Sciences Appliquées de Lyon,
Villeurbanne, France
prabir.mahato@insa-lyon.fr*

Sébastien Pruvost
*Ingénierie des Matériaux Polymères IMP, UMR CNRS 5223,
Univ Lyon, INSA Lyon,
Villeurbanne, France
sebastien.pruvost@insa-lyon.fr*

Abstract - In this work, an eco-friendly polymer consisting of Polyethylene Oxide (PEO) is employed to achieve the solid electrolyte layer of Conductive-Bridge Random Access Memory devices (CBRAM). In an attempt to move towards green solvent, water was used to fabricate the devices on polyimide substrates. The devices show promising electrical performance with low operating voltages (<2.0 V), endurance cycles together with high OFF/ON resistance ratio ($>10^4$) along with mechanical stresses. These results achieve a promising step toward the sustainable development of flexible electronic devices.

INTRODUCTION

Flexible electronics brings great opportunities for the development of smart embedded objects in domains such as wearables or large area electronics [1, 2]. Besides logic and sensing devices, memory devices are fundamental ingredients of any electronic system. Previous works [4-9] showed that a solid polymer electrolyte (SPE) could be employed to develop resistive switching memories such as CBRAM instead of metallic oxides [10, 11]. Following this approach, CBRAM devices using SPEs were demonstrated on various substrates such as silicon, glass or flexible substrates [4-9]. However, in most of the cases toxic and unsustainable solvents like acetonitrile or toluene are used to process the polymers [3-5, 7-9]. In this work, memory devices were fabricated using water as solvent on a flexible polyimide. After providing the fabrication details of the SPE layer and the memory device, electrical performances of the devices were investigated.

DEVICE FABRICATION

PEO thin film preparation: Poly(ethylene oxide), molecular weight 600 000, powder (Aldrich, Chemistry) is used for the preparation of thin PEO films. PEO powder was added in deionized water and kept on a hot plate at ~30°C for overnight stirring with a speed of 1000 rpm to completely dissolve the polymer powder. Solutions featuring various PEO concentration were prepared and spin cast on silicon substrates. Thin films were then dried in a vacuum drier at 80°C for 20 hours. Fig. 1 shows the variation of thickness with respect to spin coating parameters and concentration, keeping the time for spin coating constant at 60 seconds. The thickness of the polymer was assessed with a profilometer (DektakXT, Bruker) by making indentation with a scalpel at nine the substrates.

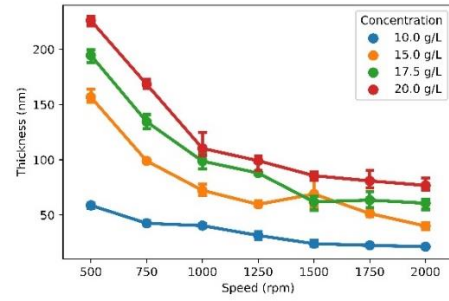


Fig. 1. Thickness of the PEO layer versus spin speed and concentration of the solution

As anticipated, the thickness decreases on increasing the concentration and decreasing the spin speeds leading to thicknesses ranging from 25 to 225 nm.

Memory device fabrication: Memory devices were fabricated using shadow masks (feature size ranging from 25 to 100 μ m) on a 125 μ m-thick kapton substrate. The substrates were cleaned with dry N₂ and then the adhesive layer Titanium (5 nm) and bottom Platinum (50 nm) electrode were deposited using the physical vapour deposition method. In the next step, the bottom electrode with the substrate was cleaned with Iso-propyl-alcohol (IPA), Ethanol and Acetone and dried with N₂. UV-Ozone treatment of the surface was performed for 20 minutes. The 150 nm-thick Solid Polymer Electrolyte (SPE) was then deposited from spin-casting 5 mL from a 20 g/L PEO solution. Finally the top Ag electrode was deposited by the electron beam evaporation method. Inset in fig. 2 shows the fabricated devices on kapton. Following a similar procedure, reference samples consisting of PEO (130nm) sandwiched between two Pt electrodes were fabricated to study the conduction mechanisms in PEO layers.

RESULTS AND DISCUSSION

IV Characteristics: Fig. 2 shows the I-V characteristics of the devices measured in the -2V/+2V range. The devices exhibit OFF/ON ratio exceeding 10^4 . Voltage statistics of set, reset and forming voltages was extracted in Fig. 3 evidencing switching voltages extending from -1.5 to 2.0V.

Conduction Mechanism: Pt\PEO\Pt reference samples were analyzed by means of IV measurements performed at

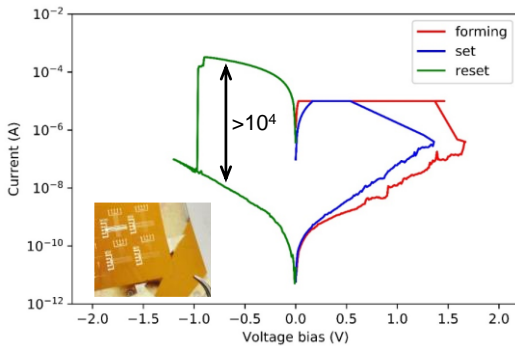


Fig. 2. IV-characteristics of the devices. Inset shows the fabricated devices on a flexible substrate- kapton. Compliance current was set to $10\mu\text{A}$.

temperatures ranging from 230 to 330 K in vacuum. As shown in Fig. 4, results evidenced Poole-Frenkel conduction type with a trap depth of 64 meV. Pt|PEO|Ag devices in the low resistance state (LRS) unambiguously exhibited ohmic type of conduction mechanism (not depicted here).

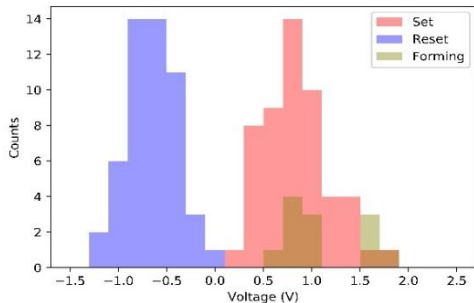


Fig. 3. Forming/Set/Reset voltage statistics measured on 12 devices.

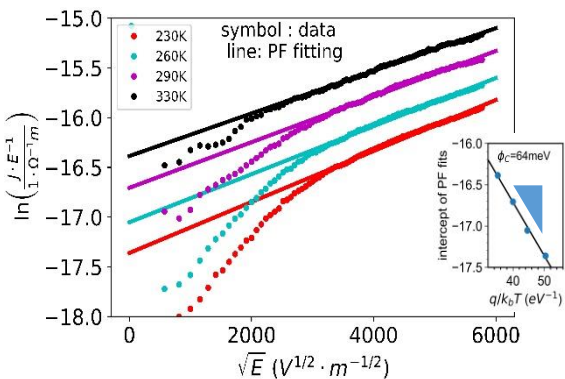


Fig. 4. Study of conduction mechanism in Pt|PEO|Pt reference samples: Poole-Frenkel plots and fitting at different temperatures between 230 and 330K. The inset shows the extracted trap barrier height of 64meV.

Reliability tests: 1R devices exhibited endurance exceeding 400 cycles when performed at current compliance of 10 to $100\mu\text{A}$ with high OFF/ON resistance ratio.

Devices were then subjected to mechanical stress reliability test through bending cycles performed at a radius of curvature of 0.5 cm. As shown in Fig. 5, devices still exhibit a $>10^4$ OFF/ON ratio after 10^4 bending cycles.

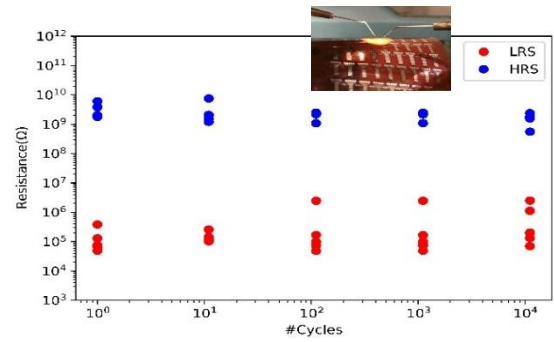


Fig. 5. Bending cycles on six devices. Inset shows the picture of the devices during IV characterization after they undergo bending cycles.

CONCLUSION

CBRAM devices featuring an eco-friendly Solid Polymer Electrolyte were fabricated on flexible substrates. Devices operate at low programming voltages and exhibited high OFF/ON resistance ratio together with excellent mechanical stress reliability tests. Withstanding the fact that the solid electrolyte layer is a water processed polymer - polyethylene oxide and fabricated on a flexible polyimide substrate, these results are very promising for the sustainable development of flexible electronic devices.

REFERENCES

- [1] Koydemir, H. C., & Ozcan, A. (2018). Wearable and Implantable Sensors for Biomedical Applications. *Annual Review of Analytical Chemistry*, 11(1), 127–146.
- [2] Stacey, W. C. & Litt, B. Technology insight: neuroengineering and epilepsy designing devices for seizure control. *Nature Clin. Pract. Neurol.* 4, 190–201 (2008).
- [3] Kaniappan K., & Latha, S. (2011). Certain investigations on the formulation and characterization of polystyrene/poly(methyl methacrylate) blends. *International Journal of ChemTech Research*, 3(2), 708–715.
- [4] Krishnan, K., Tsuruoka, T., Mannequin, C., & Aono, M. (2016). Mechanism for Conducting Filament Growth in Self-Assembled Polymer Thin Films for Redox-Based Atomic Switches. *Adv. Mat.*, 28(4), 640–648.
- [5] Ariga, K., Terabe, K., Tsuruoka, T., Wu, S., Hill, J. P., Aono, M., & Hasegawa, T. (2009). Development of polymer electrolytes based resistive switch. In *Second International Conference on Smart Materials and Nanotechnology in Engineering* (Vol. 7493, p. 749364).
- [6] Wu, S., Tsuruoka, T., Terabe, K., Hasegawa, T., Hill, J. P., Ariga, K., & Aono, M. (2011). A polymer-electrolyte-based atomic switch. *Advanced Functional Materials*, 21(1), 93–99.
- [7] Mohapatra, S. R., Tsuruoka, T., Hasegawa, T., Terabe, K., & Aono, M. (2012). Flexible resistive switching memory using inkjet printing of a solid polymer electrolyte. *AIP Advances*, 2(2).
- [8] Mohapatra, S. R., Tsuruoka, T., Krishnan, K., Hasegawa, T., & Aono, M. (2015). Effects of temperature and ambient pressure on the resistive switching behaviour of polymer-based atomic switches. *Journal of Materials Chemistry C*, 3(22), 5715–5720.
- [9] Krishnan, K., Aono, M., & Tsuruoka, T. (2016). Kinetic factors determining conducting filament formation in solid polymer electrolyte based planar devices. *Nanoscale*, 8(29), 13976–13984.
- [10] Ye, C., Deng, T., Zhang, J., Shen, L., He, P., Wei, W., & Wang, H. (2016). Enhanced resistive switching performance for bilayer HfO₂/TiO₂ resistive random access memory. *Semicond. Sci. and Technology*, 31(10).
- [11] Zhu, W., Chen, T. P., Yang, M., Liu, Y., & Fung, S. (2012). Resistive switching behavior of partially anodized aluminum thin film at elevated temperatures. *IEEE Trans. on Elect Devices*, 59(9), 2363–2367.

p-Heterogate Ge EHBTFET with asymmetric dielectric underlap pockets

1st Ashita

Dept. of Applied Sciences and Humanities

Jamia Millia Islamia

New Delhi, India

ashita1991@hotmail.com

2nd Sajad A. Loan

Dept. of Electronics and Communication Engineering

Jamia Millia Islamia

New Delhi, India

sloan@jmi.ac.in

3rd Mohammad Rafat

Dept. of Applied Sciences and Humanities

Jamia Millia Islamia

New Delhi, India

mrafat@jmi.ac.in

Abstract- In this work, we investigate a p-Ge Heterogate Electron Hole Bilayer Tunnel FET (p-HG-EHBTFET) with asymmetric underlaps and dielectric underlap pockets (UDPs). Such a structure blocks the ambipolar as well as OFF state parasitic leakage simultaneously. Further, the asymmetric UDPs overcome the constraint of longer underlaps, particularly required in Ge EHBTFETs. Even at scaled underlaps as low as 20nm, an OFF state leakage of less than 10pA/ μ m is achieved at $V_{DS}=V_{GS}=-0.5V$ with ambipolar current suppression of six orders over the entire voltage range of $0 < |V_{GS}| < 0.5V$.

Introduction- EHBTFETs exhibit vertical tunneling between n and p quantum wells formed inside a thin channel film [1]. Such a structure is a line based TFET [2] where tunnel junction is formed inside the channel, parallel to the gates using metal gates with selective workfunctions. Resultant parallel layers of 2D electron (2DEG) and hole (2DHG) gas formed are termed as bilayer. However, in low bandgap Ge based EHBTFETs, a large underlap length is required for suppression of leakage [3]. Therefore, in this work, we extended our previously reported idea of leakage suppression in Si based EHBTFET employing n-heterogate and asymmetric dielectric pockets with asymmetric underlaps lengths [4] to a p-heterogate based Ge EHBTFET (Fig. 1(b)) and it was observed to be an even better way of controlling leakage both in the OFF as well as ambipolar state particularly in Ge EHBTFET even after scaling the underlap down to 20nm from 50nm. A much better performance in terms of ambipolar leakage, SS, ON current and underlap scalability is obtained simultaneously.

Device Structure and Simulation Setup- A 2D TCAD study is performed on Sentaurus Device Simulator [5] taking the conventional structure from [1]. Quantum corrected Dynamic Non-Local Band-to-Band Tunneling (BTBT) Model parameters were taken from [6] with surface redistribution effects captured by tuning Density Gradient Model parameters to the initial carrier concentration obtained from 1D Schrodinger solver for a 10nm Ge film [1],[6-7]. Further, SRH recombination and Trap Assisted Tunneling models were also used.

Results and Discussion- For an underlap gate length $Lg3=50nm$, with asymmetrical drain and source underlaps of 50nm and 10nm respectively, using asymmetric UDPs of dimension $Lp1=15nm$, $Lp2=60nm$, $wp1=wp2=5nm$, a sharp SS of $\sim 24.72mV/dec$ is obtained over seven current decades with a suppression in the ambipolar conduction by six

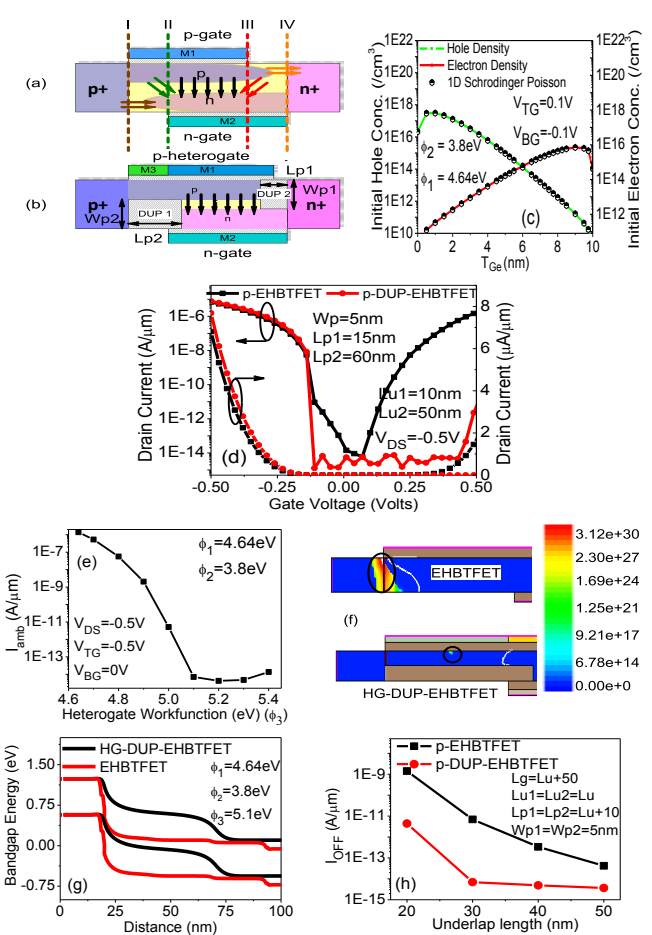


Fig. 1. a) EHBTFET showing all possible tunnel leakage paths, b) p-Ge HG-DUP-EHBTFET with asymmetric UDPs and underlaps, c) initial carrier concentration obtained with DG Model mapping. d) transfer characteristics comparison, e) variation of ambipolar current with underlap gate workfunction, f) BTBT and g) band profile comparison in ambipolar state. h) OFF current comparison for symmetric underlap symmetric pockets configuration at scaled underlap lengths.

orders to $\sim 5pA/\mu m$ at $V_{DS}=-V_{GS}=-0.5V$ (Fig. 1(d)). The device exhibits negligible conductivity between $\Phi_3=5.1-5.3eV$ due to the delay in the band alignment caused by the underlap gate in the reverse direction (Fig. 1(e)-(g)). Fig. 1(h) shows the OFF state leakage comparison with underlap length scaling. The DUPs along with p-heterogate improve underlap scalability due to suppression of misaligned leakage paths at the four interfaces shown in fig. 1(a).

Conclusion- Due to geometry, the overlap/underlap interfaces are highly sensitive to band alignment and create leakage at scaled underlaps. In such scenarios, using UDPs with a heterogate proves to be a better solution for leakage particularly with low bandgap materials in turn increasing the overall device size scalability.

REFERENCES

- [1] L. Lattanzio, L. D. Michielis, and A. M. Ionescu, "Complementary Germanium Electron–Hole Bilayer Tunnel FET for Sub-0.5-V Operation", *IEEE Electron Device Letters*, 2012, **33**, pp. 167-169.
- [2] Ashita, S. A. Loan, and M. Rafat, "A High-Performance Inverted-C Tunnel Junction FET With Source–Channel Overlap Pockets", *IEEE Transactions on Electron Devices*, 2018, **65**, pp. 763-768
- [3] J. L. Padilla, C. Alper, F. Gamiz, and A. M. Ionescu, "Assessment of field-induced quantum-confinement in heterogate germanium electron-hole bilayer field effect transistor", *Applied Physics Letters*, 2014, **105**, pp. 1-4
- [4] Ashita, S. A. Loan, A. G. Alharbi and M. Rafat, "Ambipolar leakage suppression in electron-hole bilayer TFET: investigation and analysis," in *Journal of Computational Electronics*, May 2018.
- [5] Sentaurus User Guide, J-2014.09
- [6] J. L. Padilla, C. Alper, A. Godoy, F. Gámiz, and A. M. Ionescu, "Impact of Asymmetric Configurations on the Heterogate Germanium Electron–Hole Bilayer Tunnel FET Including Quantum Confinement", *IEEE Transactions on Electron Devices*, 2015, **62**, pp. 3560-3566
- [7] L. Lattanzio, L. D. Michielis, and A. M. Ionescu, "The Electron-Hole Bilayer Tunnel FET", *Solid-State Electronics*, 2012, **74**, pp. 85–90

CNTFET Based Galois Design with Multi-valued Logic

Soheli Farhana

MIIT

Universiti Kuala Lumpur (UniKL)

Kuala Lumpur, Malaysia

farhanas@unikl.edu.my

Over the most recent couple of years, there has been an extensive increment in nanotechnology particularly Nanoelectronics. This paper presents Galois design of a carbon nanotube field-effect transistors (CNTFETs) based Multi-Valued Logic (MVL). MVLs have shown significant consideration in various circuits structure. MVLs are an option in contrast to regular practice parallel rationale, which generally has been extended from ternary (three-esteemed) rationale. Recreation results utilizing a SPICE model of 14nm CNT hub innovation to improve the power utilization of the MVL multiplier is $1.855\mu\text{S}$.

A. Introduction

To guarantee additional upgrades for CNTFET using single walled carbon nanotube (SWCNT) execution, therefore search is important for CNTFETs, that guarantees in conveying considerable preferred execution over current FETs. Nanotube based transistors innovation likewise stay effectively coordinated through mass corresponding MOS innovation over solitary IC and use a similar framework [1, 2]. Contrasted and parallel rationale, the different esteemed rationale (MVL) logic circuits give improved frequency and miniature IC [3].

B. CNTFET

a) *CNTFET Modeling*: CNTFETs have been supplanted with crude silicon gadgets. A CNTFET was effectively created at room temperature [4] using SWCNT. It has pulled in critical enthusiasm as the cutting edge gadget. A semiconducting or metallic one-dimensional single-walled carbon nanotube (SWCNT) that molecules characterized by their chirality, Ch and nanotube distance across, appeared in (1), (2) separately, where graphite grid steady is 0.249 nm and n_1, n_2 are certain whole numbers determine the chiral vector of cylinders. A SWCNT is moved up and combined along a roll in equation (1), where the unit vectors are a_1 and a_2 . The CNT is called crisscross if $n_1 = 0$, easy chair if $n_1 = n_2$, and chiral something else.

$$C_h = \sqrt{n_1 \cdot a_1 + n_2 \cdot a_2} \quad (1)$$

$$D_{cnt} = \frac{C_h}{\pi} \quad (2)$$

Bandgap is a significant asset of CNTFETs that is conversely corresponding with the nanotube as appeared in Equation (3).

$$E_g = \frac{0.84}{d(\text{nm})} \text{ ev} \quad (3)$$

As the obstruction stature decides the edge capability of a CNTFET, the CNTFET edge voltage can be communicated as Equation (4).

$$V_{th} = \frac{0.42}{d(\text{nm})} \text{ ev} \quad (4)$$

Substituting the channel of a customary FET by various semiconducting CNT with semiconducting properties in CNTFET as shown in Figure 1 [5].

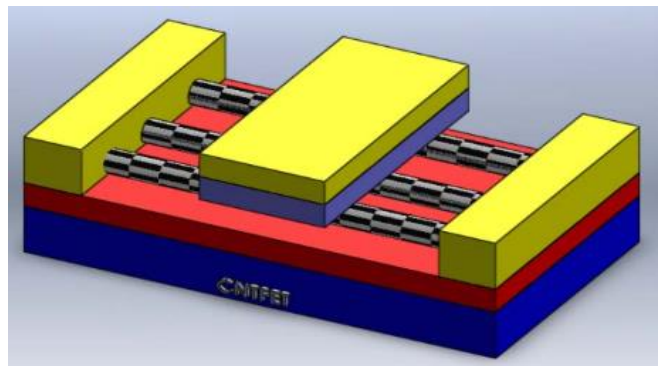


Fig. 1. A 3D model of CNTFET Schematic Diagram

b) *Proposed Design*: Galois circuits utilize a novel plan method for ternary rationale entryways dependent on CNTFETs that control every one of the ways by recognizing every mix of sources of info. The ternary-esteemed rationale Galois field multiplier and viper are presented in this paper.

Figure 2 demonstrates the designed Galois circuit of CNTFET structures to accomplish one limit voltage with the chirality of CNTs (25,0) [5]. The Galois voltage is V_{dd} in the configuration of 0.8 V . In the event that $V_{IN} = V_{TH} = 0.25$ and once the data voltage ascends to $V_{TH} = 0.25$, V_{IN} , $V_{TH} = 0.58$, simply the N-CNTFETs with $V_{TH} = 0.25$ are going to be killed. The P-CNTFETs with $V_{TH} = 0.58\text{ V}$ are going to be turned on and also the others will be killed. within the event that the data voltage rises more to $V_{IN} = V_{TH} = 0.58\text{ V}$, others are going to be activated and every one the P-CNTFETs off. Thus, breaking down our novel circuit structures demonstrates that yield voltages are the consequence of voltage divisions, that are delivered by dynamic transistors [6-7]. once IN_1 or IN_2 is below 0.25 within the novel number circuit configuration (Figure 6), CN_{T7} or CN_{T8} are going to be turned on and also the yield achieves zero as a result of the most dynamic association with the bottom. Whenever IN_1 and IN_2 are quite zero.25, CN_{T9} or CN_{T10} are going to be turned on and these can initiate the association with the foremost noteworthy voltage (V_{dd}). On the off probability that $(IN_1, IN_2) = (1, 1)$ or $(IN_1, IN_2) = (2, 2)$, at that time we've got the opposite dynamic associations with the bottom. We've got a voltage division to accomplish the conventional voltage on the yield hub. On the off chance that $(IN_1, IN_2) = (2, 1)$, just the association with the most noteworthy voltage is actuated and others are handicapped so we have $V_{out} = V_{dd}$.

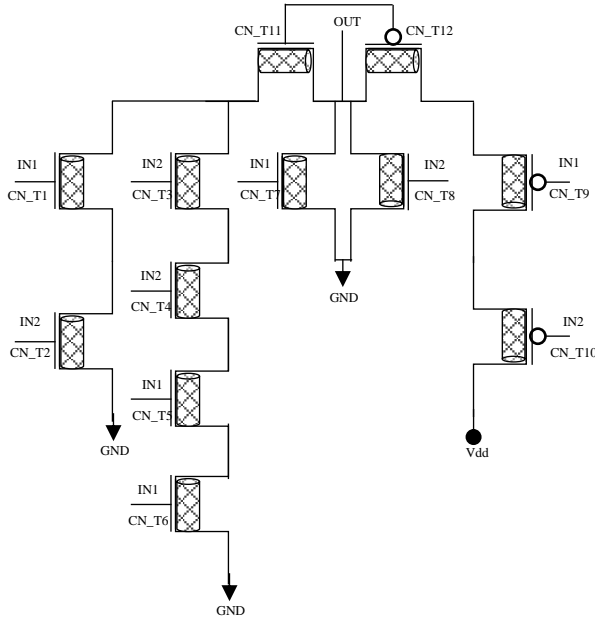


Fig. 2. Novel, efficient Galois field multiplier circuit

C. Simulation result

In this segment, the proposed plan is reproduced at various supply voltages SPICE. The normal engendering deferral and normal power utilization are estimated. By seeing impact of restriction varieties at supplied Vdd as described. The results had been discovered that for the most effective execution, the availability voltage should be set at around zero.8 V. alteration the availability voltage diminishes the ability utilization attributable to corresponding scaling however additionally influences the circuit deferral and PDP as shown in Figure 3.

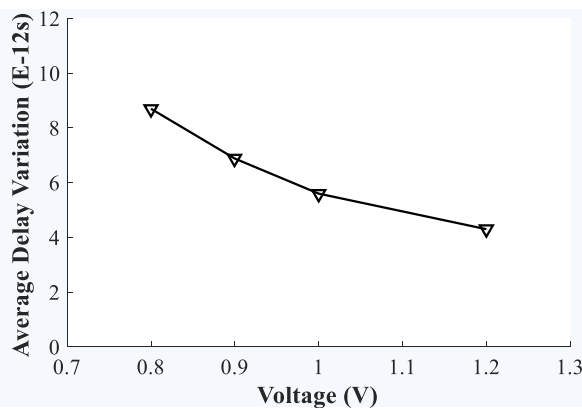


Fig. 3. Differences of delay vs supply voltage

As is appeared in Figure 4, the simplest power is at Vdd 0.8 V. The mathematician field multiplier factor is 43.25%, 63.4994%, and 83.7% a lot of too bad than the circuit set up in Vdd = 0.8 V for 0.9 V, 1.0 V, and 1.2 V, separately.

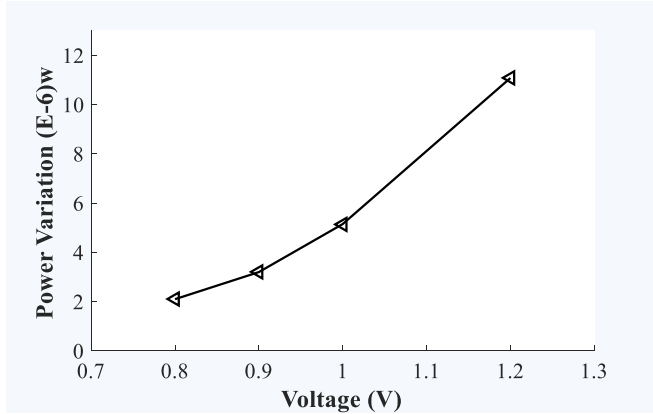


Fig. 4. Disparities of power with different supply voltage

Figure 5 outlines that we've got the simplest energy for number with Vdd = 0.8 V. The Evariste Galois field number is 22.9%, 43.9%, and 65.016% additional too bad than the circuit structure in Vdd = 0.8 V for 0.9 V, 1.0 V, and 1.2 V, distinctly.

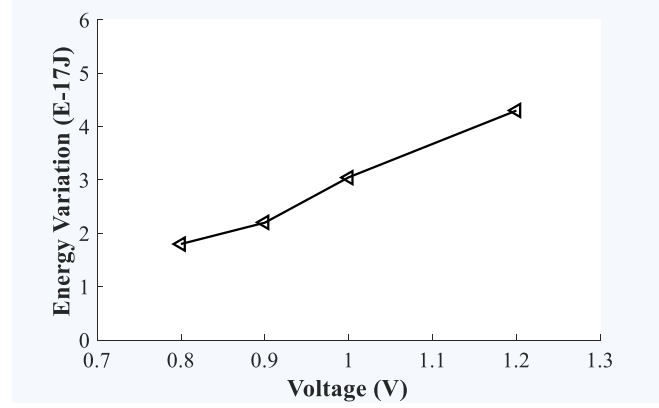


Fig. 5. Differences of energy vs supply voltage

REFERENCES

- [1] Z. Yao, H.W. Postma, L. Balents, C. Dekker. Carbon nanotube intramolecular junctions. *Nature*. 1999;402:273–276.
- [2] W. Li, S. Xie, L. Qian. Large scale synthesis of aligned carbon nanotubes. *Science*. 1996;274(5293):1701–1703.
- [3] M. Mukaidono. Regular ternary logic functions: ternary logic functions suitable for treating ambiguity. *IEEE Trans Computers*. 1986;C35(2):179–183.
- [4] S. Iijima. Helical microtubules of graphic carbon. *Nature*. 1991;345:56–58.
- [5] S. Farhana, AHM Z. Alam, S. Khan, and S. M. A. Motakabber. "CNTFET SPICE Model: Design of a Carbon Nanotube Field Effect Transistor." In 2014 International Conference on Computer and Communication Engineering, pp. 262–264. IEEE, 2014.
- [6] P. Keshavarzian, K. Navi. Efficient carbon nanotube Galois field circuit design. *IEIC Electronic Express*. 2009;6(9):546–552.
- [7] P. Keshavarzian, K. Navi. An improved CNTFET Galois circuit design as a basic MVL field. *Smart Nanocomposite*. 2010;1:2

1
2
3
4
5
6
7
8
9
10
11
12
13
14
15
16
17
18
19
20
21
22
23
24
25
26
27
28
29
30
31
32
33
34
35
36
37
38
39
40
41
42
43
44
45
46
47
48
49
50
51
52
53
54
55
56
57
58
59
60
61
62
63
64
65

NMDC 2019 1570564568

14th IEEE Nanotechnology Materials and Devices Conference

Stockholm, Sweden 27-30 October 2019

Structural Study of Silicon thins films doped with Cerium

BEKHEDDA Kheira[✉], BRIK Afaf, BENYAHIA Badra, MENARI Hamid, MANSERI Amar

Centre de Recherche en Technologie des Semi-conducteurs pour l'Energétique (CRTSE)

2 Bd Frantz Fanon, B.P.140 Alger-7 Merveilles, Algiers (Algeria), Tel & Fax: +213 21433511

Abstract

In this work, the structural properties of silicon thins films doped with cerium (Ce) were studied. The silicon films were prepared with low pressure chemical vapor deposition technique using NH₃/SiH₄ mixture. Ce films were obtained by evaporation of Cerium oxide (CeO₂) on Si layers and subsequently annealed within the temperature range of 800-1000°C in N₂ ambient.

Structural investigations were performed by Raman spectrometry experiments and scanning electron microscopy. Energy-dispersive X-ray spectroscopy (EDX) characterization results confirm the successful insertion of Ce³⁺ in the silicon at 900°C annealing for 1 hour.

The results presented in this study indicate that Silicon doped with cerium is a promising material candidate to the development of a silicon-based light source, particularly for visible light emitting applications and photovoltaic solar cells.

Keywords: Cerium, Silicon, evaporation.

[✉] bekhedda.tssm@gmail.com

Tel: 213 559 899 704

Fabrication of Self-organized InP Nanopillars by Ion-bombardment for Optoelectronic Applications

Ajith Padyana Ravishankar

Department of Applied Physics
KTH Royal Institute of Technology
Kista, Sweden
aprav@kth.se

Dennis Visser

Department of Applied Physics
KTH Royal Institute of Technology
Kista, Sweden
dvisser@kth.se

Gabriel Haddad

Department of Applied Physics
KTH Royal Institute of Technology
Kista, Sweden
ghaddad@kth.se

Juliana Jaramillo Fernandez

Catalan Institute of Nanoscience and
Nanotechnology (ICN2), CSIC and The
Barcelona Institute of Science and
Technology
Campus UAB, Barcelona, Spain.
jjf@kth.se

Srinivasan Anand

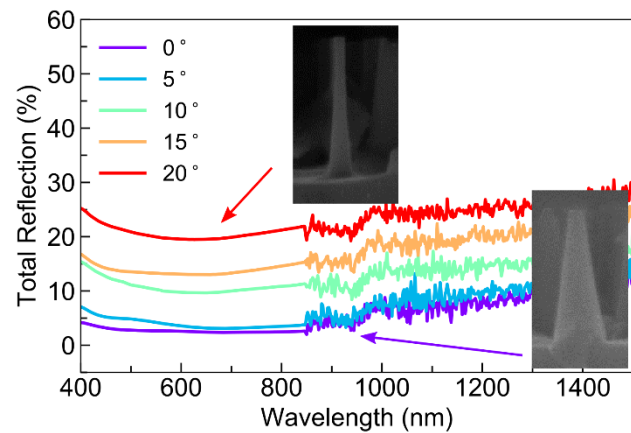
Department of Applied Physics
KTH Royal Institute of Technology
Kista, Sweden
anand@kth.se

Clivia Marfa Sotomayor Torres

Catalan Institute of Nanoscience and
Nanotechnology (ICN2), CSIC and The
Barcelona Institute of Science and
Technology
Campus UAB, Barcelona, Spain.
clivia.sotomayor@icn2.cat

Rapid progress in the field of nanofabrication has facilitated precise control over the physical aspects of nanostructures. Interesting optical properties such as broadband anti-reflection, resonant scattering or enhanced light-matter interactions are observed by tuning both the physical and material parameters of these nanostructures. Such optical properties can be obtained by realizing III-V semiconductor nanopillar/wire assemblies and are highly relevant for several optoelectronic devices such as solar cells, photodetectors, and light emitting diodes to increase their efficiencies and functionalities. In this work, a novel fabrication method is demonstrated to obtain wafer-scale, lithography-free, self-assembled nanopillars on InP substrates using nitrogen ion beam sputtering. Preferential etching of group V species (P) from the substrate leaves excess of group III species (In) which diffuse and coalesce to form self-assembled nano-masks. Elemental mapping on as-formed nanopillars shows an In-rich capping together with an amorphous jacket around crystalline InP stem. Using wet chemical etching (HF treatment), the crystalline stem of the nanopillar can be retained by removal of the In-rich cap and the amorphous sidewall layer. Fourier analysis on the spatial arrangement of the self-assembled nanopillars reveals a disordered distribution and nearest neighbor study shows that on an average the distances between the nanopillars are in subwavelength range. We investigate the influence of various etch conditions such as substrate temperature (150-270 °C), ion beam energy (200-600 eV), ion beam incidence angle (0-20°) and sputter duration (30sec – 40 min) on the geometrical parameters of the pillars such as diameter, height and shape (tapered to cylindrical). The diameters of the nanopillars can be tuned from 80 to 200 nm, whereas nanopillar heights up to 2500 nm can be realized by increasing etch durations. Optical

responses differ significantly with the change in geometrical properties of the pillars. Depending on the shapes and sizes of the pillars, reflection from the pillar assemblies can be reduced to as low as 4% in the wavelength range of 400-900 nm. μ-Raman measurements show strong variations in the Raman characteristics from pillars etched at different ion beam incidence angles. Furthermore, a clear influence of the metal-rich capping in the as-formed InP nanopillars on the Raman measurements is reported. Spectrophotometry results are systematically analyzed and modelled using a finite-difference time-domain (FDTD) simulation method to further explain the physical origin of the optical responses from these nanopillar assemblies.



Total reflection spectra from the self-assembled InP nanopillars (HF treated) etched at different ion beam incidence angle (0-20°). Inset shows the cross-sectional scanning electron microscopy (SEM) profiles of the pillars fabricated at 0° and 20° ion beam incidence angles. The tapered nanopillar structures (0°) clearly show reduction in the reflection compared to the less tapered nanopillar structures (20°).

Quantum yield enhancement of Si nanocrystals incorporated into thiol-ene polymer

1 Jingjian Zhou

2 Department of applied physics
 3 KTH-Royal Institute of Technology
 4 Stockholm, Sweden
 5 ORCID: 0000-0002-6623-2491

6 Hiroshi Sugimoto

7 Department of Electrical and
 8 Electronic Engineering
 9 Kobe University, Kobe, Japan
 10 ORCID: 0000-0002-1520-0940

11 Jing Huang

12 Department of applied physics
 13 KTH-Royal Institute of Technology
 14 Stockholm, Sweden
 15 ORCID: 0000-0001-6005-2302

16 Minoru Fujii

17 Department of Electrical and
 18 Electronic Engineering
 19 Kobe University, Kobe, Japan
 20 ORCID: 0000-0003-4869-7399

21 Tommy Haraldsson

22 Division of Micro and Nanosystems
 23 KTH-Royal Institute of Technology
 24 Stockholm, Sweden
 25 ORCID: 0000-0002-0441-6893

26 Ilya Sychugov

27 Department of applied physics
 28 KTH-Royal Institute of Technology
 29 Stockholm, Sweden
 30 ORCID: 0000-0003-2562-0540

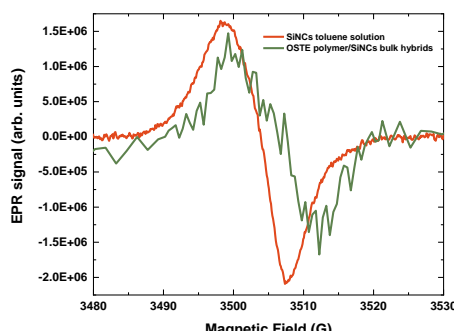
31 In this work, Thiol-ene polymer/Si nanocrystal (NCs) bulk
 32 hybrids were synthesized from Ester-passivated Si NCs
 33 toluene solution. Si NCs were encapsulated in a solid matrix
 34 of off-stoichiometry Thiol-ene (OSTE) polymer. As shown in
 35 Fig. 1, the electron paramagnetic resonance (EPR) results
 36 demonstrated that the concentration of unpaired electrons
 37 (dangling bonds) on Si NC surface is lower for polymer-
 38 embedded particles. This is due to the presence of chemically
 39 active radicals in the polymer, which can passivated dangling
 40 bonds. This, in turn leads to the activation of “dark” Si NCs,
 41 contributing to an increase on the photoluminescence
 42 quantum yield (PLQY) [1]. Since most light-converting
 43 applications requires solid state nanoparticles[2], this
 44 technique could be applied to raise efficiency of those devices,
 45 such as for the Luminescent Solar Concentrator[3].

46 From the EPR data a fraction of activated “dark”
 47 nanoparticles can be evaluated as B. A general trend of the
 48 PLQY enhancement by this method can be then evaluated.
 49 The following formula is proposed for estimating the PLQY
 50 enhancement (QY₂) after polymerization process when
 51 starting from QY₁ value for the Si NCs in the solution:

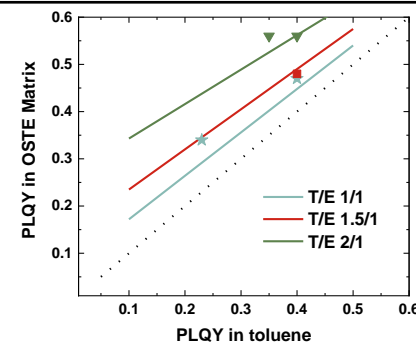
$$QY_2 = 1 - (1 - QY_1) \times B \quad (1)$$

52 Therefore, PLQY in the polymer depends on both the
 53 original PLQY in the solution and the B value. This means, in
 54 order to achieve higher quantum yield in the polymer, one
 55 could either raise the quantum yield of Si NCs in the solution
 56 or optimize B value by adjusting the composition of the two-
 57 component polymer compound.

58 For the purpose, the effect of thiol/allyl group ratio was
 59 also explored. It was found that the PLQY enhancement was
 60 proportional to the thiol excess. Meanwhile, the results
 61 confirmed the validity of the suggested formula.



62 Fig. 1. EPR spectra of Si NCs in the solution and polymer. Both spectra are
 63 normalized to the same amount of Si NCs.



64 Fig. 2. Effect of thiol/allyl group ratio. Three solid lines are plotted based on
 65 the formula 1 when knowing the B value by EPR. The B values of the blue,
 66 red and green line are 0.92, 0.85 and 0.73, respectively. The dash line
 67 represents no PLQY enhancement.

68 To conclude, Thiol-ene polymer/Si nanocrystal (NCs) bulk
 69 hybrids possessed better quantum yield than Si NCs in
 70 solution, owing to dangling bond passivation by active
 71 radicals. This effect can be utilized in enhancing efficiency of
 72 the light conversion using silicon and possibly, other
 73 nanocrystal quantum dots for various applications.

ACKNOWLEDGMENT

74 This project is supported by Swedish Energy Agency
 75 (46360-1), and Jingjian Zhou thanks the support from China
 76 Scholarship Council.

REFERENCES

- [1] A. Marinins, R. Zandi Shafagh, W. van der Wijngaart, T. Haraldsson, J. Linnros, J.G.C. Veinot, S. Popov, I. Sychugov, Light-Converting Polymer/Si Nanocrystal Composites with Stable 60–70% Quantum Efficiency and Their Glass Laminates, *ACS Appl. Mater. Interfaces*, vol. 9, pp. 30267-30272, 2017.
- [2] J. Lee, V.C. Sundar, J.R. Heine, M.G. Bawendi, K.F. Jensen, Full color emission from II-VI semiconductor quantum dot-polymer composites, *Adv. Mater.*, vol. 12, pp. 1102-1105, 2000.
- [3] F. Meinardi, S. Ehrenberg, L. Dhamo, F. Carulli, M. Mauri, F. Bruni, R. Simonutti, U. Kortshagen, S. Brovelli, Highly efficient luminescent solar concentrators based on earth-abundant indirect-bandgap silicon quantum dots, *Nat. Photonics*, vol. 11, pp. 177, 2017.

High Mobility *n*-type PdSe₂ Field Effect Transistors Enabled by Contact EngineeringArthur Bowman III[†], Kraig Andrews[†], Amanda Haglund[‡], David Mandrus^{‡,§}, and Zhixian Zhou[†][†]Physics and Astronomy Department, Wayne State University, Detroit, Michigan 48201, United States[‡]Department of Materials Science and Engineering, The University of Tennessee, Knoxville, Tennessee 37996, United States[§]Materials Science and Technology Division, Oak Ridge National Laboratory, Oak Ridge, Tennessee 37831, United States

Two-dimensional (2D) semiconductors such as transition metal dichalcogenides (TMDs) have emerged as a promising candidate for post-silicon electronics. One such material of interest is palladium diselenide, (PdSe₂) because of its high electron mobility and excellent chemical stability. However, in spite of its relatively small bandgap, the performance of few-layer PdSe₂ field-effect transistors (FETs) has been largely limited by the presence of a substantial Schottky barrier, which is likely due to Fermi-level pinning. In this work, we report the fabrication of high mobility *n*-type PdSe₂ FETs, using a new method to significantly reduce the barrier height at the semiconductor/metal interface. As a result, we observed an order of magnitude reduction of contact resistance in comparison with conventional metal contacts. The effective mobility also improved from 133 cm² V⁻¹ s⁻¹ to ~ 256 cm² V⁻¹ s⁻¹ at room temperature, and from 260 cm² V⁻¹ s⁻¹ to ~ 670 cm² V⁻¹ s⁻¹ at 77 K. We believe the significantly improved device performance enabled by this novel contact engineering technique will enable further studies of the intrinsic properties of PdSe₂ and other exciting new 2D material.

1 2 3 4 5 6 7 8 9 10 11 12 13 14 15 16 17 18 19 20 21 22 23 24 25 26 27 28 29 30 31 32 33 34 35 36 37 38 39 40 41 42 43 44 45 46 47 48 49 50 51 52 53 54 55 56 57 58 59 60 61 62 63 64 65 Effect of annealing Temperature on the Magnetic Properties of Nickel Ferrite Nanofiber prepared by Electrospinning Method

Suman Kumari, Lagen Kumar Pradhan, Murli Kumar Manglam and Manoranjan Kar

Department of Physics, Indian Institute of Technology Patna, Bihta, Patna, 801103, India

Email address: manoiitg@gmail.com

ABSTRACT

Grain size of Nickel ferrite increases with the increase of annealing temperature. However, the properties of Nickel ferrite nanofibre are very interesting. The magnetic properties of Nickel Ferrite nanofiber can be tuned by annealing at different temperatures. Nickel ferrite nanofiber has been fabricated by using the electrospinning method. The nanofibers were prepared by annealing the as-spun nanofiber at different temperatures (973K, 1073K and 1173K). The details of magnetic properties (magnetocrystalline anisotropy, saturation magnetization etc.) have been studied by employing the Law of Approach to Saturation. The magnetocrystalline anisotropy constant is found to be increase with the decrease in temperature.

KEYWORDS: Nanofiber, Spinel ferrite, Magnetocrystalline anisotropy and saturation magnetization.

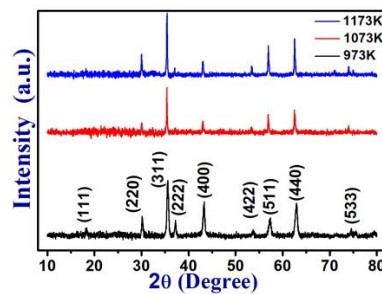


Fig. 1. XRD patterns of the nickel ferrite nanofiber annealed at 973K, 1073K and 1173K.

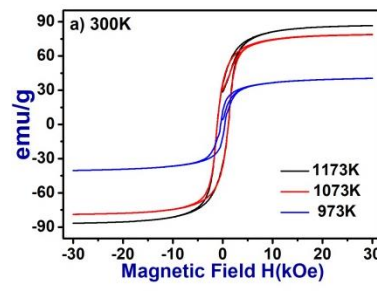


Fig. 2. Magnetic hysteresis loops at (a) 300K and (b) 60K of the nickel ferrite nanofiber with different annealing temperature (i.e. 973K, 1073K and 1173K).

REFERENCES

- [1]. Dan Li *et al.*, Magnetic nanofibers of nickel ferrite prepared by electrospinning, *Appl. Phys. Lett.* 83, 4586 (2003).
- [2]. J. Xiang *et al.* Electrospinning preparation, characterization and magnetic properties of cobalt–nickel ferrite ($Co_{1-x}Ni_xFe_2O_4$) nanofibers, *Journal of Colloid and Interface Science* 376, 57-61 (2012).

Interwell Carrier Transport in InGaN/(In)GaN Multiple Quantum Wells

1 R. Yapparov

2 Department of Applied Physics
 3 KTH Royal Institute of Technology
 4 Stockholm, Sweden
 5 Electrum 229, 16440 Kista

6 S. P. DenBaars

7 Materials Department
 8 University of California
 9 Santa Barbara, USA
 10 California 93106, USA

11 L. Y. Kuritzky

12 Materials Department
 13 University of California
 14 Santa Barbara, USA
 15 California 93106, USA

16 S. Nakamura

17 Materials Department
 18 University of California
 19 Santa Barbara, USA
 20 California 93106, USA

21 J. S. Speck

22 Materials Department
 23 University of California
 24 Santa Barbara, USA
 25 California 93106, USA

26 S. Marcinkevičius

27 Department of Applied Physics
 28 KTH Royal Institute of Technology
 29 Stockholm, Sweden
 30 Electrum 229, 16440 Kista

31 Efficiency of multiple quantum well (MQW) photonic devices, such as light emitting diodes (LED) and laser diodes, depends, to a large degree, on the carrier distribution between QWs. In case of a uniform distribution, each of the QWs contributes to the emission allowing to reach high output powers at carrier densities for which the detrimental Auger recombination is not yet impeding the quantum efficiency. However, simulations suggest that, because of the inefficient hole transport, only one or two QWs located closest to the p-side of an InGaN/GaN LED structure substantially contribute to the overall light emission or lasing [1, 2]. However, because of the complex nature of ternary nitride alloys with nm-scale band potential fluctuations and a possibility of percolation transport [3], simple simulations require an experimental verification. In addition, direct measurements would allow exploring relevance of different transport mechanisms, contribute to a better understanding of the limitations of typical MQW structures, and suggest ways to their improvement.

32 In this work, we have studied the interwell carrier transport by time-resolved photoluminescence (PL) with using an optical marker technique [4, 5]. InGaN/(In)GaN MQW structures with different well and barrier parameters were studied. The structures were grown on a c-plane sapphire substrate and consisted of a 6 μ m thick buffer layer, a 3 nm thick detector QW (DQW) with 18% In content, a region of three to eight 3 nm transport QWs (TQWs) with 12% In, and a 100 nm GaN cap layer. For different structures, the GaN barrier width was varied between 5.5 and 13.5 nm; for one structure 8.5 nm $\text{In}_{0.05}\text{Ga}_{0.95}\text{N}$ barriers were used. PL was excited by femtosecond pulses at 260 nm for which most of the excitation took place in the cap layer. The photoexcited carrier transport via the TQWs was monitored by measuring increase of the PL signal at the DQW wavelength. The photoexcited carrier concentration was much larger than the background electron concentration of $1 \times 10^{17} \text{ cm}^{-3}$; thus, the measured transport was limited by the slower holes.

33 Mechanism for the interwell hole transport was established by performing measurements at different temperatures (180 K and 340 K). The exponential increase of the number of carriers transferred to the DQW shows that the interwell transport occurs via sequential carrier capture and thermionic emission. For InGaN/GaN QW structures the transport times are long, ≈ 1 ns per well. Only a small fraction of carriers excited in the cap layer reach the detector QW indicating that the interwell carrier distribution is nonuniform.

34 For structures with wide barriers or a large number of TQWs no carriers were reaching the DQW at all. However, for the sample with barriers containing 5% indium, the transport time decreased by a factor of 4 and the hole thermionic emission energy - from 200 meV to 70 meV. This reduction is larger than the decrease of the barrier height for a spatially uniform InGaN alloy. This can be explained by a percolation transport of holes through nanoscopic band potential fluctuations in the InGaN barriers. Hence, the study shows that using InGaN barriers may be a promising pathway toward efficient high power InGaN LEDs.

REFERENCES

- [1] Y.-K. Kuo, T.-H. Wang, and J.-Y. Chang, *Appl. Phys. Lett.* **100**, 031112, 2012.
- [2] W. G. Scheibenzuber and U. T. Schwarz, *Appl. Phys. Express* **5**, 042103, 2012.
- [3] C.-K. Li, M. Piccardo, L.-S. Lu, S. Mayboroda, L. Martinelli, J. Peretti, J. S. Speck, C. Weisbuch, M. Filoche, and Y.-R. Wu, *Phys. Rev. B* **95**, 144206, 2017.
- [4] B. Deveaud, J. Shah, T. C. Damen, B. Lambert, and A. Regreny, *Phys. Rev. Lett.* **58**, 2582, 1987.
- [5] K. Fröjd, S. Marcinkevičius, U. Olin, C. Silfvenius, B. Stålnacke, and G. Landgren, *Appl. Phys. Lett.* **69**, 3659, 1996.

NMDC 2019 1570565456

Competition of Interfacial and Interlayer Dzyaloshinskii-Moriya Interactions

Elena Y. Vedmedenko

Physics Department

University of Hamburg

Hamburg, Germany

vedmeden@physnet.uni-hamburg.de

1

Many magnetic systems possess certain periodicity. The periodicity has at least two length scales—that of an atomic lattice, and that of a magnetic structure. Such structures, which consist of a periodic crystal, and an additional periodic modulation of some order parameter, are denoted as modulated structures. In centrosymmetric, magnetically ordered crystals the handedness of modulated structures is energetically degenerate. However, if the inversion symmetry is broken for some reasons, this degeneracy may be lifted, because the electronic spin-orbit scattering induces chiral asymmetry of exchange coupling known as the Dzyaloshinskii-Moriya Interaction (DMI). In such magnetic systems an additional order parameter – chirality of magnetization - might appear.

The DMI is particularly strong near magnetic surfaces or interfaces due to the interfacial symmetry breaking. This interfacial DMI leads to the formation of chiral structures with unique rotational sense within those interfaces, which can be used to store information. An example is given by the magnetic skyrmions or spin spirals (see Fig.1a) arising within single magnetic interfaces as well as in systems with several interfaces. Individual magnetic planes in multilayers are often coupled via the Ruderman-Kittel-Kasuya-Yoshida (RKKY) coupling ensuring collective magnetic behavior of all layers as shown in Fig.1a, where the chiral structure is identical in all layers, behaves like an entity and remains, therefore, two-dimensional. If, however, the DMI across a spacer exists, this collective spiral state can be destroyed and different scenarios can develop.

In this study, we employ analytical and atomistic Monte Carlo calculations to investigate the existence and potential properties of DMI coupling between two ferromagnetic layers across a nonmagnetic spacer. We find that such an interlayer DMI exists for many microscopic geometries. This coupling is not trivial and seeks to create a three-dimensional spin spiral across the complete system (see Fig.1b). Therefore, it might compete with the interfacial DMI and other energy contributions to create a three-dimensional magnetic chiral structure with different chiralities within and between the magnetic layers [2].

The microscopic characteristics of this interaction depend on the lattice geometry of magnetic layers, the spin-orbit coupling parameter, and on the lateral structure of the films. If the interlayer DMI is supported by RKKY interlayer coupling, it might further enhance the effective DMI, which could be most relevant for future technological breakthroughs: if the interlayer DMI competes with the

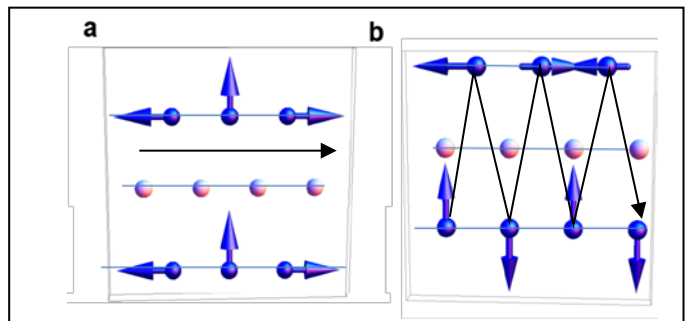


Fig. 1. Schematic representation of two magnetic layers with (a) dominating interfacial and (b) interlayer Dzyaloshinskii-Moriya interactions. The arrows represent magnetization vectors, while the light spheres represent the non-magnetic spacer mediating the Dzyaloshinskii-Moriya interactions. In (a) a clockwise cycloidal magnetic spiral along the path denoted by the black arrow is formed. This spiral is identical in both layers coupled by the ferromagnetic RKKY interaction. In (b) a counterclockwise magnetic spiral across the two layers along the black path is formed. Additionally, there is an alternation of counterclockwise and clockwise rotations along the vertical direction.

RKKY interlayer coupling, some unexpected phenomena like intrinsic separation of columnar skyrmions or spirals or three-dimensional frustration might emerge, which would enrich the landscape of possible spin structures, but might also complicate envisioned application scenarios.

Even in strongly ferromagnetic layers, this interaction leads to novel phenomena like chiral exchange bias [2], which appears due to the common action of the interfacial and interlayer DMI. The realization of systems integrating interlayer magnetic chiral interactions paves the way for the creation and manipulation of unprecedented magnetic effects in magnetic multilayers and synthetic antiferromagnets, for example the introduction of indirect—via the magnetic state of a neighbouring layer—control of asymmetric effects in the motion of domain walls and spin waves of a magnetic system. It is also of great relevance in the development of future three-dimensional spintronic systems.

REFERENCES

- [1] E. Y. Vedmedenko, P. Riego, J. A. Arregi, and A. Berger, “Interlayer Dzyaloshinskii-Moriya Interactions,” Phys. Rev. Lett. , in press.
- [2] A. Fernandez-Pacheco, E. Y. Vedmedenko, F. Ummelen, R. Mansell, D. Petit, and R. P. Cowburn, “Symmetry-breaking interlayer Dzyaloshinskii-Moriya interactions in synthetic antiferromagnets,” Nature Mater. , vol. 18, pp. 679-684, June 2019

Top-Down Fabrication of High Quality Gallium Indium Phosphide Nanopillar/disk Array Structures

Dennis Visser

Department of Applied Physics
KTH Royal Institute of Technology
Kista, Sweden
dvisser@kth.se

Marcin Swillo

Department of Applied Physics
KTH Royal Institute of Technology
Stockholm, Sweden
marcin@kth.se

Rinat Yapparov

Department of Applied Physics
KTH Royal Institute of Technology
Kista, Sweden
yapparov@kth.se

Eleonora De Luca

Department of Applied Physics
KTH Royal Institute of Technology
Stockholm, Sweden
eldl@kth.se

Saulius Marcinkevicius

Department of Applied Physics
KTH Royal Institute of Technology
Kista, Sweden
sm@kth.se

Yohan Désières

University of Grenoble Alpes
CEA, LETI, MINATEC
Grenoble, France
yohan.desieres@cea.fr

Srinivasan Anand

Department of Applied Physics
KTH Royal Institute of Technology
Kista, Sweden
anand@kth.se

In this work, top-down fabrication methods for fabricating high optical quality gallium indium phosphide (GaInP) nanopillar/disk arrays are investigated for optoelectronic applications. Time-resolved photoluminescence (TRPL) measurements are used to characterize the fabricated nanostructures and the results are compared to the properties of a reference GaInP ‘slab’. Photoluminescence (PL) spectra and carrier lifetimes are characterized for the fabricated GaInP structures embedded in a highly transparent film. Additionally, using GaInP structures on a gallium arsenide (GaAs) substrate the effect of a sulphur-oleylamine based surface passivation procedure is investigated. This was done for the purpose of improving the PL intensities, increase carrier lifetimes and prevent photodegradation by passivating the surface states.

GaInP and AlGaInP have been reported for a wide range of applications such as transistors [1], diodes [2], lasers [3], light emitting diodes (LEDs) [4], solar cells [5] and window layers in solar cells [6]. Important features for these applications are the optical and electrical properties of this material, for which the initial quality of the grown (Al)GaInP layer plays an important role. Patterning of this layer can be beneficial for several features, e.g., absorption enhancement, light extraction enhancement and/or improvement of carrier extraction. However, processing of the layer may lead to a degradation of the optical quality due to surface states and process induced defects. Therefore, it is important to investigate the effect of the fabrication methods on the material properties of GaInP by characterizing the optical/electrical quality of the structures.

GaInP nanopillar/disk arrays were fabricated from high quality epitaxially grown $\text{Ga}_{0.49}\text{In}_{0.51}\text{P}$ layers, on a GaAs substrate, having a direct bandgap emission wavelength of ~ 660 nm. As a reference, microdisks were fabricated to mimic a bulk-like GaInP slab. A stack layer of GaInP/GaAs was used in order to obtain substrate-free GaInP structures embedded in a polydimethylsiloxane (PDMS) film. A fabrication process based on a combination of colloidal lithography (CL) or optical lithography and inductively coupled plasma reactive ion etching (ICP-RIE) was used for obtaining the GaInP

structures; where CL was used for the nanopillar/disk structures and optical lithography for the (reference) microdisk. An initial GaInP layer of 1 μm thickness was used for the fabrication of the nanopillar arrays and the microdisks, whereas a 200 nm layer thickness was used for the fabrication of the nanodisk arrays; where the thickness of the layer determines the height of the structures. A thin (100 nm) GaAs sacrificial layer was provided below the GaInP layer. Substrate-free structures are then obtained by using a selective wet etching process to etch away the GaAs layer. For the CL, silicon dioxide (SiO_2) colloidal spheres, having a diameter of ~ 500 nm, were spin coated resulting in a close-packed hexagonal array; the original colloid diameter determines the hexagonal array period. The ICP-RIE etching of the GaInP/GaAs structures is based on a $\text{Cl}_2/\text{CH}_4/\text{H}_2$ -chemistry resulting in smooth sidewalls and a selectivity of ~ 4.1 with regard to the SiO_2 mask. For the (partial) sacrificial layer etch, a wet etch chemistry based on $\text{H}_3\text{PO}_4/\text{H}_2\text{O}_2/\text{H}_2\text{O}$ is used. To investigate the GaInP structures without the influence of the GaAs substrate, the fabricated substrate-free GaInP structures were embedded in a PDMS film which was subsequently peeled off from the substrate. The resulting nanopillar arrays have a height of 1 μm , hexagonal array period of ~ 500 nm and a top-bottom diameter of $\sim 150\text{--}350$ nm. The nanodisk arrays have a height of 200 nm, hexagonal array period of ~ 500 nm and a diameter of ~ 350 nm. The microdisk has a height of 1 μm and diameter of ~ 20 μm . For the sculpting and passivation of the structures, a sulphur-oleylamine based treatment was used. These studies were performed for the ICP-RIE etched GaInP structures still on the substrate.

For the TRPL measurements a harmonic generator was used with short pulses, having a pulse width of 140 fs and a repetition rate of 80 MHz, for two different excitation wavelengths: 450 and 532 nm; for average power densities of 57, 96 and 134 kW/cm^2 and a spot size of ~ 20 μm . The TRPL results for the GaInP structures embedded in PDMS, indicate carrier lifetimes of $\sim 2\text{--}3$ ns for the microdisk which indicates a good quality (bulk) material and $\sim 0.3\text{--}0.5$ ns for the nanopillar/disk arrays; which is quite good for nanopillar/disk structures. A slight improvement for the carrier lifetimes was

observed for lower excitation powers. A strong PL peak centred at \sim 660 nm is observed for the GaInP structures with a FWHM of \sim 15 nm. The nanopillar arrays show the highest PL intensity, attributed to better in and out coupling of light.

For both the non-passivated embedded structures and ICP etched structures on the substrate, a clear decrease in the PL intensity is observed with time when keeping the laser at the same spot. This degradation is attributed to photo-induced chemical modifications of the material in ambient air and appears to be irreversible; the PL and TRPL signals do not recover to their original values. GaInP structures passivated by a sulphur-oleylamine based solution indicate an improvement of both the PL intensity and carrier lifetimes. In addition, the passivated structures did not show any observable photo-induced PL degradation with time. This indicates that surface passivation (electronic and chemical) is beneficial for improving the material quality.

REFERENCES

- [1] R. Sridhara, S. M. Frimel, K. P. Roenker, N. Pan, and J. Elliott, "Performance Enhancement of GaInP/GaAs Heterojunction Bipolar Phototransistors Using DC Base Bias," *J. Light. Technol.*, vol. 16(6), pp. 1101–1106, June 1998.
- [2] D. Jung, C. A. Parker, J. Ramdani, and S. M. Bedair, "AlGaAs/GaInP heterojunction tunnel diode for cascade solar cell application," *J. Appl. Phys.*, vol. 74(3), pp. 2090–2093, June 1998.
- [3] A. Chen and S. J. Chua, "Two-dimensional AlGaInP/GaInP photonic crystal membrane lasers operating in the visible regime at room temperature," *Appl. Phys. Lett.*, vol. 90, pp. 011113, January 2007.
- [4] B. Wang, C. Wang, K. H. Lee, S. Bao, K. E. K. Lee, C. S. Tan, S. F. Yoon, E. A. Fitzgerald, and J. Michel, "Red InGaP light-emitting diodes epitaxially grown on engineered Ge-on-Si substrates," *Proc. of SPIE*, vol. 9768, pp. 97681J, March 2016.
- [5] Y. Wang, R. Zhang, Z. Zhang, B. Qiu, S. Wang, and X. Wu, "Efficiency improvement of GaInP solar cells by broadband omnidirectional antireflection through dielectric composite nanostructures," *Sol. Energy Mater. Sol. Cells*, vol. 169, pp. 33–39, May 2017.
- [6] J. Plá, M. Barrera, and F. Rubinelli, "The influence of the InGaP window layer on the optical and electrical performance of GaAs solar cells," *Semicond. Sci. Technol.*, vol. 22, pp. 1122–1130, September 2007.

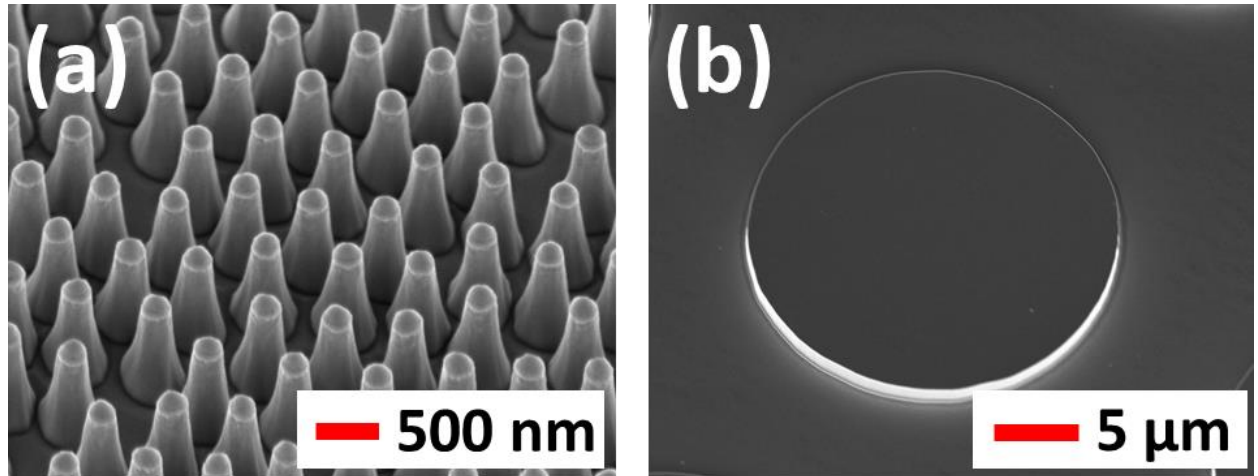


Fig. 1. Representative tilted (30°) top view scanning electron microscopy (SEM) images of the fabricated GaInP structures: (a) nanopillar arrays and (b) GaInP microdisk.

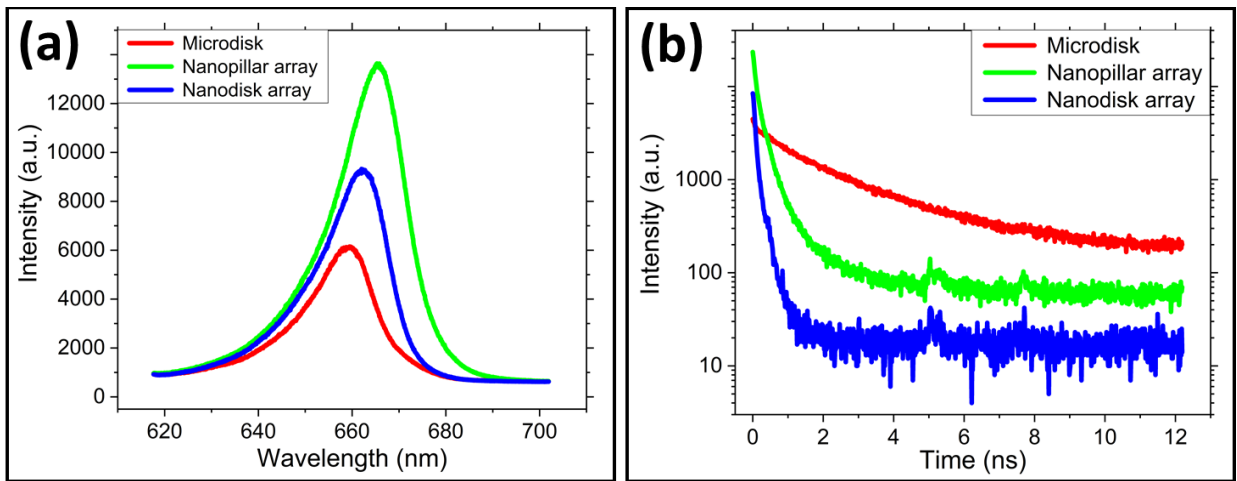


Fig. 2. (a) Photoluminescence (PL) spectra and (b) time-resolved PL (TRPL) spectra for the fabricated (non-passivated) GaInP micro- and nanostructures embedded in a PDMS film. The variations in the peak positions are due to non-uniformity in the wafer.

Three-Dimensional Printed Photoluminescent Polymeric Waveguides

10
11 *Gustavo González^{a,b}, Francesca Frascella^a, Paula Bosch^c, Angelo Angelini^a, Annalisa Chiappone^a, Marco Sangermano^a, Candido
12 Fabrizio Pirri^{a,b}, Ignazio Roppolo^{a*}*

13
14 ^aDepartment of Applied Science and Technology, Politecnico di Torino, Torino, Corso Duca degli Abruzzi 24, 10129, Italy

15
16 ^bCenter for Sustainable Future Technologies @Polito, Istituto Italiano di Tecnologia, Corso Trento 21, Torino 10129, Italy

17
18 ^cDepartamento de Química Macromolecular Aplicada, Instituto de Ciencia y Tecnología de Polímeros, Consejo Superior de
19
20 Investigaciones Científicas (CSIC), C/ Juan de la Cierva 3, Madrid, 28006, Spain

Abstract

21
22
23
24
25
26
27
28
29
30
31
32
33
34
35
36
37
38 In this work, we propose an innovative strategy for
39
40
41
42
43
44
45
46
47
48
49
50
51
52
53
54
55
56
57
58
59
60
61
62
63
64
65 obtaining 3D printed polymer waveguides and splitters
employing a light activated additive manufacturing
technology, specifically Digital Light Processing (DLP).
This technology is based on the spatially-controlled
solidification of liquid formulations through fast
photopolymerization reaction [1]. Typically, the
materials processed by DLP present 3 main ingredients:
monomers, photoinitiator and a dye. While the first one
will constitute the printed object and the second controls
the reactivity towards the light and so the printing rate,
the third one is added at low concentrations to control
the light penetration, allowing to obtain well-defined
structures. However, after the printing process is usually
useless, giving a residual colour, often undesired. [2]

66
67
68
69
70
71
72
73
74
75
76
77
78
79
80
81
82
83
84
85
86
87 Here [3] we exploit the necessary use of the dye for
88
89
90
91
92
93
94
95
96
97
98
99
100
101
102
103
104
105
106
107
108
109
110
111
112
113
114
115
116
117
118
119
120
121
122
123
124
125
126
127
128
129
130
131
132
133
134
135
136
137
138
139
140
141
142
143
144
145
146
147
148
149
150
151
152
153
154
155
156
157
158
159
160
161
162
163
164
165
166
167
168
169
170
171
172
173
174
175
176
177
178
179
180
181
182
183
184
185
186
187
188
189
190
191
192
193
194
195
196
197
198
199
200
201
202
203
204
205
206
207
208
209
210
211
212
213
214
215
216
217
218
219
220
221
222
223
224
225
226
227
228
229
230
231
232
233
234
235
236
237
238
239
240
241
242
243
244
245
246
247
248
249
250
251
252
253
254
255
256
257
258
259
260
261
262
263
264
265
266
267
268
269
270
271
272
273
274
275
276
277
278
279
280
281
282
283
284
285
286
287
288
289
290
291
292
293
294
295
296
297
298
299
300
301
302
303
304
305
306
307
308
309
310
311
312
313
314
315
316
317
318
319
320
321
322
323
324
325
326
327
328
329
330
331
332
333
334
335
336
337
338
339
340
341
342
343
344
345
346
347
348
349
350
351
352
353
354
355
356
357
358
359
360
361
362
363
364
365
366
367
368
369
370
371
372
373
374
375
376
377
378
379
380
381
382
383
384
385
386
387
388
389
390
391
392
393
394
395
396
397
398
399
400
401
402
403
404
405
406
407
408
409
410
411
412
413
414
415
416
417
418
419
420
421
422
423
424
425
426
427
428
429
430
431
432
433
434
435
436
437
438
439
440
441
442
443
444
445
446
447
448
449
450
451
452
453
454
455
456
457
458
459
460
461
462
463
464
465
466
467
468
469
470
471
472
473
474
475
476
477
478
479
480
481
482
483
484
485
486
487
488
489
490
491
492
493
494
495
496
497
498
499
500
501
502
503
504
505
506
507
508
509
510
511
512
513
514
515
516
517
518
519
520
521
522
523
524
525
526
527
528
529
530
531
532
533
534
535
536
537
538
539
540
541
542
543
544
545
546
547
548
549
550
551
552
553
554
555
556
557
558
559
5510
5511
5512
5513
5514
5515
5516
5517
5518
5519
5520
5521
5522
5523
5524
5525
5526
5527
5528
5529
5530
5531
5532
5533
5534
5535
5536
5537
5538
5539
5540
5541
5542
5543
5544
5545
5546
5547
5548
5549
55410
55411
55412
55413
55414
55415
55416
55417
55418
55419
55420
55421
55422
55423
55424
55425
55426
55427
55428
55429
55430
55431
55432
55433
55434
55435
55436
55437
55438
55439
55440
55441
55442
55443
55444
55445
55446
55447
55448
55449
55450
55451
55452
55453
55454
55455
55456
55457
55458
55459
55460
55461
55462
55463
55464
55465
55466
55467
55468
55469
55470
55471
55472
55473
55474
55475
55476
55477
55478
55479
55480
55481
55482
55483
55484
55485
55486
55487
55488
55489
55490
55491
55492
55493
55494
55495
55496
55497
55498
55499
554100
554101
554102
554103
554104
554105
554106
554107
554108
554109
554110
554111
554112
554113
554114
554115
554116
554117
554118
554119
554120
554121
554122
554123
554124
554125
554126
554127
554128
554129
554130
554131
554132
554133
554134
554135
554136
554137
554138
554139
554140
554141
554142
554143
554144
554145
554146
554147
554148
554149
554150
554151
554152
554153
554154
554155
554156
554157
554158
554159
554160
554161
554162
554163
554164
554165
554166
554167
554168
554169
554170
554171
554172
554173
554174
554175
554176
554177
554178
554179
554180
554181
554182
554183
554184
554185
554186
554187
554188
554189
554190
554191
554192
554193
554194
554195
554196
554197
554198
554199
554200
554201
554202
554203
554204
554205
554206
554207
554208
554209
554210
554211
554212
554213
554214
554215
554216
554217
554218
554219
554220
554221
554222
554223
554224
554225
554226
554227
554228
554229
554230
554231
554232
554233
554234
554235
554236
554237
554238
554239
554240
554241
554242
554243
554244
554245
554246
554247
554248
554249
554250
554251
554252
554253
554254
554255
554256
554257
554258
554259
554260
554261
554262
554263
554264
554265
554266
554267
554268
554269
554270
554271
554272
554273
554274
554275
554276
554277
554278
554279
554280
554281
554282
554283
554284
554285
554286
554287
554288
554289
554290
554291
554292
554293
554294
554295
554296
554297
554298
554299
554300
554301
554302
554303
554304
554305
554306
554307
554308
554309
554310
554311
554312
554313
554314
554315
554316
554317
554318
554319
554320
554321
554322
554323
554324
554325
554326
554327
554328
554329
554330
554331
554332
554333
554334
554335
554336
554337
554338
554339
554340
554341
554342
554343
554344
554345
554346
554347
554348
554349
554350
554351
554352
554353
554354
554355
554356
554357
554358
554359
554360
554361
554362
554363
554364
554365
554366
554367
554368
554369
554370
554371
554372
554373
554374
554375
554376
554377
554378
554379
554380
554381
554382
554383
554384
554385
554386
554387
554388
554389
554390
554391
554392
554393
554394
554395
554396
554397
554398
554399
554400
554401
554402
554403
554404
554405
554406
554407
554408
554409
554410
554411
554412
554413
554414
554415
554416
554417
554418
554419
554420
554421
554422
554423
554424
554425
554426
554427
554428
554429
554430
554431
554432
554433
554434
554435
554436
554437
554438
554439
554440
554441
554442
554443
554444
554445
554446
554447
554448
554449
554450
554451
554452
554453
554454
554455
554456
554457
554458
554459
5544510
5544511
5544512
5544513
5544514
5544515
5544516
5544517
5544518
5544519
55445100
55445101
55445102
55445103
55445104
55445105
55445106
55445107
55445108
55445109
55445110
55445111
55445112
55445113
55445114
55445115
55445116
55445117
55445118
55445119
55445120
55445121
55445122
55445123
55445124
55445125
55445126
55445127
55445128
55445129
55445130
55445131
55445132
55445133
55445134
55445135
55445136
55445137
55445138
55445139
55445140
55445141
55445142
55445143
55445144
55445145
55445146
55445147
55445148
55445149
55445150
55445151
55445152
55445153
55445154
55445155
55445156
55445157
55445158
55445159
55445160
55445161
55445162
55445163
55445164
55445165
55445166
55445167
55445168
55445169
55445170
55445171
55445172
55445173
55445174
55445175
55445176
55445177
55445178
55445179
55445180
55445181
55445182
55445183
55445184
55445185
55445186
55445187
55445188
55445189
55445190
55445191
55445192
55445193
55445194
55445195
55445196
55445197
55445198
55445199
55445100
55445101
55445102
55445103
55445104
55445105
55445106
55445107
55445108
55445109
55445110
55445111
55445112
55445113
55445114
55445115
55445116
55445117
55445118
55445119
55445120
55445121
55445122
55445123
55445124
55445125
55445126
55445127
55445128
55445129
55445130
55445131
55445132
55445133
55445134
55445135
55445136
55445137
55445138
55445139
55445140
55445141
55445142
55445143
55445144
55445145
55445146
55445147
55445148
55445149
55445150
55445151
55445152
55445153
55445154
55445155
55445156
55445157
55445158
55445159
55445160
55445161
55445162
55445163
55445164
55445165
55445166
55445167
55445168
55445169
55445170
55445171
55445172
55445173
55445174
55445175
55445176
55445177
55445178
55445179
55445180
55445181
55445182
55445183
55445184
55445185
55445186
55445187
55445188
55445189
55445190
55445191
55445192
55445193
55445194
55445195
55445196
55445197
55445198
55445199
55445100
55445101
55445102
55445103
55445104
55445105
55445106
55445107
55445108
55445109
55445110
55445111
55445112
55445113
55445114
55445115
55445116
55445117
55445118
55445119
55445120
55445121
55445122
55445123
55445124
55445125
55445126
55445127
55445128
55445129
55445130
55445131
55445132
55445133
55445134
55445135
55445136
55445137
55445138
55445139
55445140
55445141
55445142
55445143
55445144
55445145
55445146
55445147
55445148
55445149
55445150
55445151
55445152
55445153
55445154
55445155
55445156
55445157
55445158
55445159
55445160
55445161
55445162
55445163
55445164
55445165
55445166
55445167
55445168
55445169
55445170
55445171
55445172
55445173
55445174
55445175
55445176
55445177
55445178
55445179
55445180
55445181
55445182
55445183
55445184
55445185
55445186
55445187
55445188
55445189
55445190
55445191
55445192
55445193
55445194
55445195
55445196
55445197
55445198
55445199
55445100
55445101
55445102
55445103
55445104
55445105
55445106
55445107
55445108
55445109
55445110
55445111
55445112
55445113
55445114
55445115
55445116
55445117
55445118
55445119
55445120
55445121
55445122
55445123
55445124
55445125
55445126
55445127
55445128
55445129
55445130
55445131
55445132
55445133
55445134
55445135
55445136
55445137
55445138
55445139
55445140
55445141
55445142
55445143
55445144
55445145
55445146
55445147
55445148
55445149
55445150
55445151
55445152
55445153
55445154
55445155
55445156
55445157
55445158
55445159
55445160
55445161
55445162
55445163
55445164
55445165
55445166
55445167
55445168
55445169
55445170
55445171
55445172
55445173
55445174
55445175
55445176
55445177
55445178
55445179
55445180
55445181
55445182
55445183
55445184
55445185
55445186
55445187
55445188
55445189
55445190
55445191
55445192
55445193
55445194
55445195
55445196
55445197
55445198
55445199
55445100
55445101
55445102
55445103
55445104
55445105
55445106
55445107
55445108
55445109
55445110
5544

A Study on the Etching Residues of Nano-Patterns in C₄F₈/CH₂F₂/O₂/Ar Plasma

1 Byung Jun Lee

2 *Dept. of Control and Instrumentation*
3 *Engineering*
4 *Korea University*
5 Sejong 30019, Republic of Korea
6 byung_jun@korea.ac.kr

1 Yunho Nam

2 *Dept. of Control and Instrumentation*
3 *Engineering*
4 *Korea University*
5 Sejong 30019, Republic of Korea
6 yhnam09@korea.ac.kr

1 Jaemin Lee

2 *Dept. of Control and Instrumentation*
3 *Engineering*
4 *Korea University*
5 Sejong 30019, Republic of Korea
6 jaemin_lee@korea.ac.kr

12 Junmyung Lee

13 *Dept. of Control and Instrumentation*
14 *Engineering*
15 *Korea University*
16 Sejong 30019, Republic of Korea
17 lee_jm@korea.ac.kr

12 Kwang-Ho Kwon*

13 *Dept. of Control and Instrumentation*
14 *Engineering*
15 *Korea University*
16 Sejong 30019, Republic of Korea
17 kwonkh@korea.ac.kr

The demand for miniaturization and high integration of semiconductor devices has ever been increasing. In order to achieve the requirements of the semiconductor industry, plasma etching processes using fluorocarbon-based gases are being designed to have higher selectivity and more polymerizing [1 - 5]. In high aspect ratios (HARs) etching, the non-volatile passivation layer can control the slope of the etched silicon dioxide (SiO₂) contact hole pattern. These sidewall passivation layers play a important role in vertical HAR profiles, anisotropy etching, and lateral etching prevention [6 - 8]. Therefore, investigation of the chemical characteristics of the sidewall residues is vital for forming HAR SiO₂ contacts and to precisely control the anisotropy of the nano-patterns. Generally, the removal of etching residues formed inside the pattern after the etching process has a crucial effect on the performance of the semiconductor devices. As the pattern size becomes smaller, there is an area that cannot be cleaned by the conventional wet cleaning method. Recently, various dry cleaning techniques using plasma radicals and ions have been proposed [9 - 10]. For precise control and understanding of residue removal, a detailed compositional analysis of the etching residue must be performed. These studies are also very important in evaluating the effectiveness of dry-cleaning. However, little research has been done to investigate the characteristics of etching residues formed inside the nano-scale patterns. This is because it is difficult to analyze the surface composition in a small area.

In this work, we conducted a study on the characteristics of the etching residues formed inside the nano-scale patterns. A C₄F₈/CH₂F₂/O₂/Ar mixture gas plasma was used to form a high-aspect-ratio silicon dioxide contacts (HARCs) on a silicon wafer. The chemical compositions and binding states of etching residues inside the patterns were examined by an x-ray photoelectron spectroscopy (XPS) with angle changes in detail. To investigate the formation of etching residues, the plasma characteristics (i.e. radicals, ions and electrons) were examined in parallel using an optical emission spectroscopy (OES) and a Langmuir probe (LP) system.

As a result of the analysis, it was observed that the etching residues formed on the sidewalls of the hole patterns changed to the same tendency. At the same time, it was confirmed that

depending the etched depth, the composition of the residue on the sidewall of holes changed.

ACKNOWLEDGMENT

This work was supported by a Korea University Grant.

REFERENCES

- [1] Takahashi, Kunimasa, Masaru Hori, and Toshio Goto, "Fluorocarbon radicals and surface reactions in fluorocarbon high density etching plasma. I. O₂ addition to electron cyclotron resonance plasma employing CHF₃," *Journal of Vacuum Science & Technology A: Vacuum, Surfaces, and Films* 14.4 (1996): 2004-2010.J. Clerk Maxwell, *A Treatise on Electricity and Magnetism*, 3rd ed., vol. 2. Oxford: Clarendon, 1892, pp.68-73.
- [2] Kwon, B. S., et al, "Ultrahigh selective etching of SiO₂ using an amorphous carbon mask in dual-frequency capacitively coupled C₄F₈/CH₂F₂/O₂/Ar plasmas," *Journal of The Electrochemical Society*, 2010, D135-D141.
- [3] N. Ikegami, A. Yabata, T. Matsui, J. Kanamori, Y. Horii, "Characteristics of very high-aspect-ratio contact hole etching," *Japanese Journal of Applied Physics* 36, 1997, 2470.
- [4] S. Samukawa, T. Mukai, "High performance silicon dioxide etching for less than 0.1 μm high aspect contact holes," *Journal of Vacuum Science & Technology B* 18, 2000, 166.
- [5] P. Czuprynski, O. Joubert,"X-ray photoelectron spectroscopy analysis of silicon dioxide contact holes etched in a magnetically enhanced reactive ion etching reactor," *Journal of Vacuum Science & Technology B* 16, 1998, pp.1051-1058.
- [6] L. Ling, X. Hua, L. Zheng, G.S. Oehrlein, E.A. Hudson, P. Jiang, "Studies of fluorocarbon film deposition and its correlation with etched trench sidewall angle by employing a gap structure using C₄F₈/Ar and CF₄/H₂ based capacitively coupled plasmas," *Journal of Vacuum Science & Technology B* 26, 1989, 11
- [7] G.S. Oehrlein, K.K. Chan, M.A. Jaso, G.W. Rubloff, "Surface analysis of realistic semiconductor microstructures," *Journal of Vacuum Science & Technology A*, 7, 1989 , pp.1030-1034.
- [8] T.D. Bestwick, G.S. Oehrlein, "Reactive ion etching of silicon using bromine containing plasmas," *Journal of Vacuum Science & Technology A* 8, 1990, pp. 1696-1701.
- [9] Koh, Kyongbeom, et al, "Quasi atomic layer etching of SiO₂ using plasma fluorination for surface cleaning," *Journal of Vacuum Science & Technology A*, 2018, 01B106.
- [10] K.J. Kanarik, T. Lill, E.A. Hudson, S. Sriraman, S. Tan, J. Marks, V.Vahedi, R.A. Gottscho, "Overview of atomic layer etching in the semiconductor industry," *Journal of vacuum Science & Technology A* 33, 2015, 0208.

Study on the Etching properties by using Inductively Coupled CF₄/C₄F₈/O₂ & CF₄/CBr₂F₂/O₂ plasmas

1
2
3
4
5
6
7
8 Yunho Nam

Dept. of Control and Instrumentation
Engineering
Korea University
Sejong 30019, Republic of Korea
yhnam09@korea.ac.kr

Byung Jun Lee

Dept. of Control and Instrumentation
Engineering
Korea University
Sejong 30019, Republic of Korea
byung_jun@korea.ac.kr

Junmyung Lee

Dept. of Control and Instrumentation
Engineering
Korea University
Sejong 30019, Republic of Korea
lee_jm@korea.ac.kr

14 Jongchan Lee

Dept. of Control and Instrumentation
Engineering
Korea University
Sejong 30019, Republic of Korea
jongchanlee@korea.ac.kr

Kwamg-Ho Kwon*

Dept. of Control and Instrumentation
Engineering
Korea University
Sejong 30019, Republic of Korea
kwonkh@korea.ac.kr

In the modern semiconductor industry, nano-electronic devices have become very highly integrated, requiring the formation of complex nanostructures on the wafer. To fabricate nano-electronic devices, precise patterns must first be formed on the silicon substrate. Dry-etching techniques (i.e., plasma etching) have been widely applied in nano-patterning processes for precise pattern transfer by controlling chemically active neutrals and the energetic charged particle flux[1]. Heretofore, perfluorocarbon (PFC)-based gas chemistries, including CF₄, CHF₃, C₄F₈, and CH₂F₂, with O₂ and/or Ar, have been widely used for nano-patterning of both silicon and silicon-based intermetal dielectric (IMD) films (e.g., SiO₂, Si₃N₄, and SiON), owing to the high chemical reactivity of fluorine with Si. However, PFC gases generally have a high global warming potential (GWP) of more than 8,000 and have a significantly negative impact on the ozone layer [2, 3]. Recently, attempts have been made to replace, decompose, and/or recycle high-GWP PFC gas to reduce the greenhouse effect in nano-sized electronic devices [2]. To achieve this, low-GWP gases should be used for fabricating nano-sized electronic devices in industrial fields. They have low boiling points and/or exist as liquid sources in the atmosphere for easy recovery. Therefore, to overcome the environmental issues in the manufacturing process for nano-sized semiconductor devices, the process applicability of liquid-PFC (L-PFC) gases (i.e., CBr₂F₂, C₉F₂₀, and C₁₁F₂₀) should be further studied for fabricating nano-sized devices in advance.

CBr₂F₂ is a liquid at room temperature and has a boiling point of 22.8 °C. It has a molar mass of 209.8155 g/mol and a density of 8.7 g/cm³. L-PFC gas is advantageous, because it is easier than other gases to maintain a liquid state at room temperature and recover [4]. However, to replace conventional PFCs with L-PFC gases for fabricating nano-sized devices in advance, it is necessary to compare etching characteristics (e.g., etching rate, selectivity, and etching profile) with conventional PFC gases. However, until now, there have been few studies comparing the etching and surface

characteristics of silicon-based IMD materials using PFC and L-PFC gases for fabricating nano-sized devices.

In this study, we examine the etching characteristics and consequent changes in the SiON film-surface characteristics caused by the IMD etching process using CBr₂F₂ mixed plasma as an alternative to PFC gas. we evaluate the possibility of replacing existing perfluorocarbon gas with CBr₂F₂, which can be recovered in its liquid state from room-temperature air. We performed the plasma etching using CF₄+X+O₂ mixed gases, where X = C₄F₈, CBr₂F₂, and studied the process optimization conditions using various process parameters. To understand the etching mechanism, etching rates, selectivities, and profiles are examined using a surface profiler and field-emission scanning electron microscope (FE-SEM). the plasma diagnostics such as a double Langmuir probe(DLP) and optical emission spectroscopy(OES), were performed. Also, the surface characteristics investigated in detail by using X-ray photoelectron spectroscopy(XPS) and Atomic force microscopy(AFM).

ACKNOWLEDGMENT

This work was supported by the Korea Institute of Energy Technology Evaluation and Planning (KETEP) and the Ministry of Trade, Industry & Energy(MOTIE) of the Republic of Korea (No. 20172010105910).

REFERENCES

- [1] V.M. Donnelly, A. Kornblit, "Plasma etching: yesterday, today, and tomorrow," Journal of Vacuum Science & Technology A 31(5) (2013) 050825.
- [2] S. Nakamura, M. Itano, H. Aoyama, K. Shibahara, S. Yokoyama, M. Hirose, "Comparative studies of perfluorocarbon alternative gas plasmas for contact hole etch," Japanese Journal of Applied Physics 42 (2003) 5759-5764.
- [3] A. Sekiya, S. Misaki, "The potential of hydrofluoroethers to replace CFCs, HCFCs and PFCs," Journal of Fluorine Chemistry 101(2) (2000) 215-221.
- [4] T. Uchii, K. Suzuki, M. Shiiki, "System and method for gas recycling incorporating gas-insulated electric device," Google Patents, 2006.

Microstructure-Dependent Nanomechanics in Battery Relevant Nanomaterials

1 Md Ruhul Amin Shikder

2 Department of Mechanical and
3 Industrial Engineering
4 University of Illinois at Chicago
5 Chicago, IL 60607, USA.
6 mshikd2@uic.edu

7 Mathius Barua

8 Department of Mechanical and
9 Industrial Engineering
10 University of Illinois at Chicago
11 Chicago, IL 60607, USA.
12 mbarua2@uic.edu

13 Mahjabin Maksud

14 Department of Mechanical and
15 Industrial Engineering
16 University of Illinois at Chicago
17 Chicago, IL 60607, USA.
18 mmaksu2@uic.edu

19 Bryan W. Byles

20 Department of Materials Science and
21 Engineering
22 Drexel University
23 Philadelphia, PA 19104, USA.
24 bwb46@drexel.edu

25 Ekaterina Pomerantseva

26 Department of Materials Science and
27 Engineering
28 Drexel University
29 Philadelphia, PA 19104, USA.
30 ep423@drexel.edu

31 Arunkumar Subramanian

32 Department of Mechanical and
33 Industrial Engineering
34 University of Illinois at Chicago,
35 Chicago, IL 60607, USA.
36 sarun@uic.edu

Electrode mechanical degradation represents an important failure mode, which has impeded the use of several high-performance material candidates in lithium batteries. This causes fracture and dissolution of the electrode into its electrolyte thereby, resulting in a loss in charge storage capacity of the battery. In this paper, plastic recovery mechanisms in nanostructured materials, which are mediated by stress-induced dynamic recrystallization, will be investigated as a potential pathway to solve this problem. These results will be discussed in the context of two different phases of tunnel manganese dioxide nanowires [1], which offer a “green” and yet, high-performance alternative to the lithium cobalt oxide cathodes in current batteries. The two chosen phases contain microporous tunnels with varying unit-cell geometries, in order to highlight the impact of microstructure on mechanical stability.

A. $\text{Na}_{0.44}\text{MnO}_2$ and Todorokite-like MnO_2

The materials chosen for this effort contain porous tunnels, which are formed through the sharing of edges and corners between MnO_6 octahedral units. The size and cross-sectional shape of these porous tunnels are controlled to form the different phases of these materials. In this effort, the following tunnel manganese oxides were chosen (Fig. 1): (i) nanowires (NWs) in the $\text{Na}_{0.44}\text{MnO}_2$ phase or NMO-NWs, which contain Z-shaped tunnels, and (ii) nanobelts (NBs) in the todorokite-like MnO_2 phase or T-NBs, which contain $mx3$ rectangular tunnels (m and 3 denote the number of octahedral units in the cross-sectional width and height directions) [2].

B. Nanomechanical Testing

The T-NBs (or, NMO-NWs) were assembled on top of spatially separated pairs of gold electrodes on silicon chips, from their colloidal suspensions in alcohol using dielectrophoresis-based electric field driven assembly techniques. Once assembled, the NBs (or NWs) are anchored in place on the underlying gold electrodes using electron beam induced deposition of platinum metal lines inside a focused ion beam – scanning electron microscope system. This results in the formation of doubly clamped nanobeams. These beams are then subjected to atomic force microscopy (AFM) based three-point bending loading-unloading tests [3, 4]. At each point during this testing process, the force applied on the NW (F) and its flexural deflection (Z) are extracted.

C. Results

The F vs. Z curve of Fig. 1(c), which has been shown here with a T-NB as an example, indicates the following: (i) an

initial elastic segment, which starts with pure beam bending in the low deformation regime and then, extends to bending plus stretching in the large deformation regime, (ii) material ductility, which is indicated by a load-drop, when the load exceeds the yield limit for the material, (iii) reversibility of plastic deformation upon unloading via a retraction of the AFM tip. Reversibility of plastic deformation is further confirmed by a post-testing AFM scan (Fig. 1(d)), which shows no change in the NW height profile within the suspended trench region. In a recent report, we have discussed this reversibility mechanism in detail [2]. Specifically, this was attributed to plasticity occurring selectively within the larger width tunnel grains via increased inter-layer linking or recrystallization (to form smaller sized tunnel pores). At the same time, the smaller width tunnel grains undergo pure elastic deformation and the release of this elastic energy aids in the de-linking of layers to re-form the larger width tunnels during the unloading process. In this effort, we will extend these insights by performing large-deformation nanomechanics experiments on the NMO-NW phase. This study is anticipated to reveal the impact of tunnel microstructure on the mechanical properties of this material system.

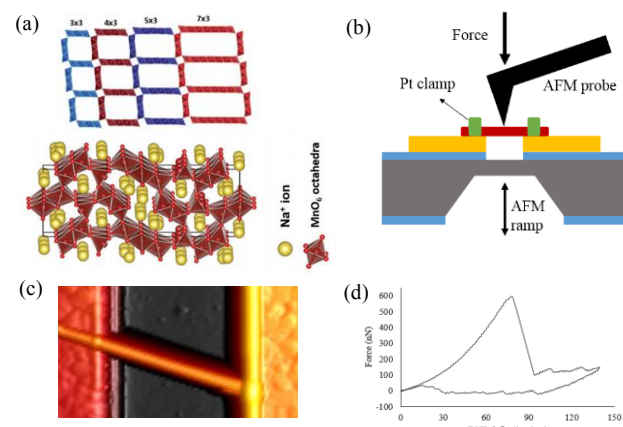


Figure 1: (a) Cross-sectional schematics of T-NBs (top) & NMO-NWs (bottom), showing their respective, MnO_6 octahedral tunnel network. (b) An illustration of the AFM based three-point bending test. (c) AFM micrograph of a T-NB. (d) Force-deflection data obtained from an AFM loading-unloading test done on the device of panel ‘c’.

D. Conclusion

This effort will present AFM nanomechanical investigations involving NWs and NBs based on the tunnel manganese oxide material system. Through these three-point bending tests, this study will reveal the impact of tunnel porosity and microstructure on its mechanical stability. Specifically, this paper will reveal the impact of microstructure on the mechanical stabilization of these battery-relevant nanomaterials.

ACKNOWLEDGMENT

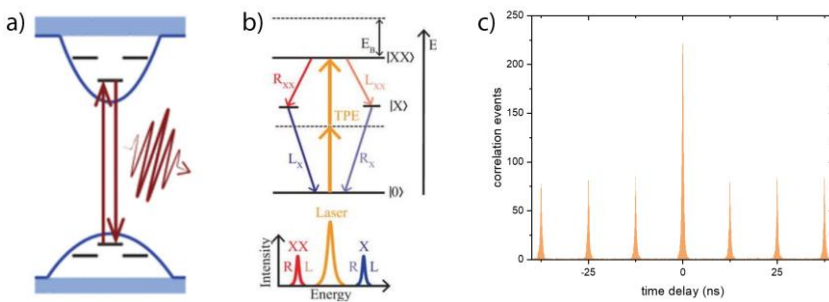
A. S, M. M., M. B., and M. R. A. S. acknowledge support for this work, in part, from the National Science Foundation under Grant No. 1655496. Use of the Center for Nanoscale Materials, an Office of Science user facility, was supported by the U.S. Department of Energy, Office of Science, Office of Basic Energy Sciences, under Contract No. DE-AC02-06CH11357. The authors would specifically like to thank Dr. Ralu Divan, Ms. Suzanne Miller, and Dr. Dafei Jin for the technical support and training associated with the use of nanofabrication and characterization capabilities at the Center for Nanoscale Materials.

REFERENCES

- [1] C. M. Julien and A. Mauger, "Nanostructured MnO₂ as Electrode Materials for Energy Storage", *Nanomaterials*, vol. 7, pp. 396, November 2017.
- [2] M. R. A. Shikder, M. Maksud, G. Vasudevamurthy, B. W. Byles, D. A. Cullen, K. L. More, E. Pomerantseva, and A. Subramanian, "Brittle fracture to recoverable plasticity: polytypism-dependent nanomechanics in todorokite-like nanobelts", *Nanoscale Adv.*, vol. 1, pp. 357, September 2018.
- [3] B. Wen, J. E. Sader, and J. J. Boland, "Mechanical Properties of ZnO Nanowires", *Phys. Rev. Lett.*, vol. 101, pp. 175502, October 2008.
- [4] M. Maksud, J. Yoo, C. T. Harris, N. K. R. Palapati, and A. Subramanian, "Young's modulus of [111] germanium nanowires" 2015 *APL Mater.*, vol. 3, pp. 116101, October 2015.

1 Resonance fluorescence vs. two-photon excitation with GaAs QDs
23 L. Schweickert^{1,*}, E. Schöll¹, L. Hanschke², K. D. Zeuner¹, M. Reindl³, S. F. Covre da
4 Silva³, T. Lettner¹, R. Trotta⁴, J. J. Finley², K. Müller², A. Rastelli³, V. Zwiller¹, and
5 K. D. Jöns¹6 1. Department of Applied Physics, Royal Institute of Technology, Albanova University
7 Centre, Roslagstullsbacken 21, 106 91 Stockholm, Sweden8 2. Walter Schottky Institut and Physik Department, Technische Universität München,
9 85748 Garching, Germany10 3. Institute of Semiconductor and Solid State Physics, Johannes Kepler University
11 Linz, 4040 Linz, Austria12 4. Dipartimento di Fisica, Sapienza Università di Roma, Piazzale A. Moro 1, I-00185
13 Roma, Italy

14 * Electronic address: lucassc@kth.se

15 Semiconductor quantum dots have proven to be versatile and highly performant single
16 photon sources for quantum information processing applications. Lately, remarkable
17 results have been shown with GaAs quantum dots grown via the droplet etching method:
18 second order coherence $g^{(2)}(0) = 7.5\text{E-}5$ [1], concurrence $C = 97\%$ [2], and two-photon
19 interference visibility $V_{\text{HOM}} = 95\%$ [3]. These excellent values have been achieved using
20 two different excitation methods: pulsed two-photon and strictly resonant excitation
21 methods. Here, we explore how switching from a) direct resonant excitation of the
22 exciton state to b) two-photon excitation of the biexciton state changes emission
23 characteristics of these quantum dots. By performing second-order intensity correlation
24 measurements, we gain insights in the intrinsic differences between a quantum
25 mechanical two-level system [4] and a three-level quantum ladder system.36
37 Figure 1: Excitation schemes for a) resonant and b) two-photon excitation. c) Bunching
38 for resonant 2P_i excitation of the exciton transition with $g^{(2)}(0) = 3.28 \pm 0.04$.39 [1] L. Schweickert et al., Appl. Phys. Lett. **112**, 093106 (2018).
4041 [2] D. Huber et al., Phys. Rev. Lett. **121**, 033902 (2018).
4243 [3] E. Schöll et al., Nano Lett. **19**(4), 2404–2410 (2019).
4445 [4] K. A. Fischer et al., Nat. Phys. **13**, 649–654 (2017).
46

Nanoscale (in)coherent optical excitations in the electron microscope

Albert Polman

Center for Nanophotonics, AMOLF, Amsterdam, the Netherlands
polman@amolf.nl

Abstract

We present time, polarization, and phase-resolved cathodoluminescence (CL) spectroscopy using two new SEM-CL microscopes that we have recently constructed. We derive the 3D phase profile of plasmonic scatterers by CL holography, determine the bandstructure of topological Si photonic crystals using CL momentum spectroscopy; and unravel the electron-induced $NV^0 \leftrightarrow NV^-$ state transfer of diamond NV centers using a novel pump-probe CL spectroscopy technique.

Broken Gate of $\text{In}_{0.53}\text{Ga}_{0.43}\text{As}$ TFET for Reduced OFF current and Gate Capacitance

1st Mohd Haris

Electronics and Communication Engineering
Jamia Millia Islamia
New Delhi, India
mohdharis@outlook.com

2nd Sajad A. Loan

Electronics and Communication Engineering
Jamia Millia Islamia
New Delhi, India
sajadiitk@gmail.com

3rd Mainuddin

Electronics and Communication Engineering
Jamia Millia Islamia
New Delhi, India
mainuddin@jmi.ac.in

Abstract- In this work, we propose broken gate $\text{InGa}_{0.53}\text{As}_{0.53}$ TFET (BG-TFET), in which the gate is not extended over the complete channel. The gate is present over the source-channel and the channel-drain tunnelling junctions, with a gap in between both the gates, thereby reducing the effective length of total gate. The BG-TFET exhibits suppressed off current with reduced total gate capacitance (C_{gg}) as compared to conventional $\text{In}_{0.53}\text{Ga}_{0.47}\text{As}$ TFET without reducing ON state performance. The BG-TFET provides > 1 order reduction in OFF current, 28% and 18% reduction in C_{gg} in OFF state and ON state respectively.

Introduction- Tunnel FET being a device with SS scalable SS below 60 mV/decade, is being projected as a potential alternative to MOS for beyond Moore's law era [1,2]. However, low ON current, increased gate capacitances and ambipolarity are major issues in TFET as compared to MOSFET[3]. Low band gap and tunnelling mass III-V TFET are apparent solution for low ON current [1], however issue of off state leakage ambipolar leakage, which may further increase the OFF current become more severe in them. Most of the architecture reported for ambipolar leakage suppression for point TFET either hamper the frequency performance or increases process complexity significantly [4,5]. Here, we propose the BG-TFET, which suppress the OFF current with reduced gate capacitance in both OFF and ON state, thus improving the frequency response by reducing the total gate capacitance with respect to conventional $\text{In}_{0.53}\text{Ga}_{0.47}\text{As}$ TFET.

Simulation parameters and methodology- Fig. shows the schematics of conventional $\text{In}_{0.53}\text{Ga}_{0.47}\text{As}$ TFET and the proposed Broken gate $\text{In}_{0.53}\text{Ga}_{0.47}\text{As}$ TFET. Non-local BTBT, CVT, SRH, BGN model has been used. Silvaco ATLAS [6] has been used to simulate the devices. The simulations have been. The electron and hole tunnelling masses are taken form [7]. Both devices have channel length of 50 nm. $L=50$ nm, $L_1=20$ nm, $L_2=10$ nm. $L_{GAP}=20$ nm.

Results and discussion- Fig. 1(a)-(c) shows the energy band diagrams, e^- tunnelling rate in OFF state ($V_{DS}=0.5$, $V_{GS}=0.0$), transfer characteristics for Conventional $\text{In}_{0.53}\text{Ga}_{0.47}\text{As}$ TFET, gate drain underlap $\text{In}_{0.53}\text{Ga}_{0.47}\text{As}$ TFET TFET (GDU-TFET) and the proposed $\text{In}_{0.53}\text{Ga}_{0.47}\text{As}$ TFET TFET. It is evident from the fig. 1(c) that SS and OFF current of GDU TFET degrades severely and the proposed TFET provides best I_{ON}/I_{OFF} among all three devices, without degrading the ON state performance. It is evident from the fig. 1(a)-(b) that BG-TFET exhibits higher tunnelling barrier and hence lower e^- tunnelling rate as compared to conventional TFET and GDU TFET at the drain-channel junction and the source-channel junction respectively (marked by circles) in OFF state. The highest e^- tunnelling rate in GDU TFET at source-channel junction can be attributed to the absence of complete depletion due to presence of gate only at source-channel junction. Further, the lower tunnelling rate in the proposed TFET as compared to conventional TFET at the

channel-drain junction in OFF state arises from lesser band banding in the middle of channel due to absence of gate over the region. The BG-TFET also exhibits lower gate capacitances due to reduced total gate length as compared to conventional TFET as shown in 2(a). Fig 2(b) shows that BG-TFET provides slightly better cut-off frequency due to reduced gate capacitance as shown in fig. 2(a). As BG-TFET provides reduced gate capacitance in both the OFF region and ON region, it can be expected to exhibit the lower propagation delay in the inverter circuit as compared to conventional TFET. The value of OFF current, ON current, C_{gg} and f_T in ON state ($V_{DS}=0.5$, $V_{GS}=0.7$) has been mentioned in the Table.

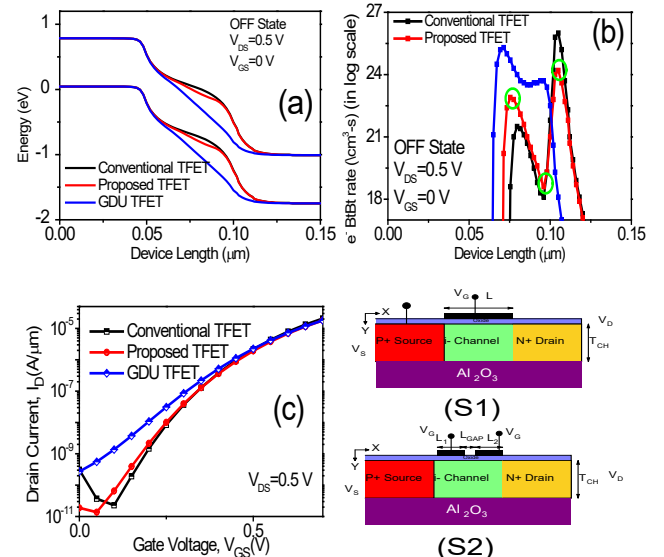


Fig. 1. Comparison of (a)Energy band diagrams, (b) e^- tunnelling rate, (c) Transfer characteristics obtained from conventional TFET, gate drain underlap (GDU) TFET and the proposed TFET, (S1) conventional TFET and (S2) Proposed TFET.

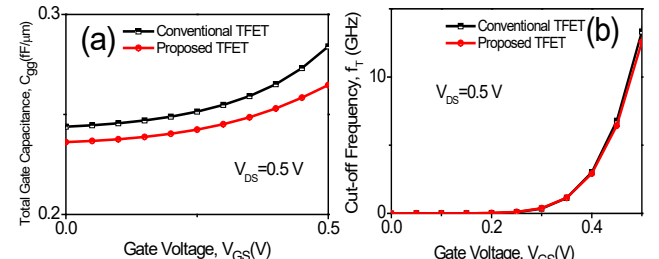


Fig. 2. Comparison of (a) C_{gg} (b) f_T between conventional TFET and Proposed TFET.

Table I

Device	Parameters		
	OFF current	C_{gg} (ON state)	f_T (ON state)
BG TFET	1.88×10^{-11}	2.90×10^{-16}	7.1×10^{10}
Conventional TFET	3.08×10^{-10}	3.54×10^{-16}	6.71×10^{10}

REFERENCES

- [1] A. M. Ionescu and H. Riel, "Tunnel field-effect transistors as energy-efficient electronic switches," *Nature*, vol. 479, no. 7373, pp. 329–337, Nov. 2011.
- [2] W. Y. Choi, B.-G. Park, J. D. Lee, and T.-J. K. Liu, "Tunneling field-effect transistors (tfets) with subthreshold swing (ss) less than 60 mv/dec," *IEEE Electron Device Letters*, vol. 28, no. 8, pp. 743–745, 2007.
- [3] S. Mookerjea, R. Krishnan, S. Datta and V. Narayanan, "Effective Capacitance and Drive Current for Tunnel FET (TFET) CV/I Estimation," in *IEEE Transactions on Electron Devices*, vol. 56, no. 9, pp. 2092-2098, Sept. 2009.
- [4] D. B. Abdi and M. Jagadish Kumar, "Controlling Ambipolar Current in Tunneling FETs Using Overlapping Gate-on-Drain," in *IEEE Journal of the Electron Devices Society*, vol. 2, no. 6, pp. 187-190, Nov. 2014
- [5] M. R. Uddin Shaikh and S. A. Loan, "Drain-Engineered TFET With Fully Suppressed Ambipolarity for High-Frequency Application," in *IEEE Transactions on Electron Devices*, vol. 66, no. 4, pp. 1628–1634, April 2019.
- [6] Silvaco's Atlas Version 5.19.20.R. [Online]. Available: <http://www.silvaco.com>
- [7] S. Sant and A. Schenk, "Methods to Enhance the Performance of InGaAs/InP Heterojunction Tunnel FETs," in *IEEE Transactions on Electron Devices*, vol. 63, no. 5, pp. 2169-2175, May 2016.

I

Effect of Stone-Wales Defects on transversely isotropic elastic properties of boron nitride nanotubes: a molecular dynamics study

Vijay Choyal*, V. K. Choyal and S. I. Kundalwal

*Applied and Theoretical Mechanics (ATOM) Laboratory, Discipline of Mechanical Engineering,
Indian Institute of Technology Indore, Simrol, Indore 453 552, India*

**Email: vijaychoyal26@gmail.com, +91-9303505188*

Abstract: - Current revolutions in the synthesis of boron nitride nanotubes (BNNTs) attracted researchers' attention for developing their nanocomposites. This is because BNNTs possess wide band gap (~ 5.5 eV, independent of geometry), strong hardness, thermally and chemically stable, and excellent piezoelectric properties than carbon nanotubes (CNTs). Besides, BNNTs have comparable mechanical and thermal properties compared to CNTs. As the first of its kind, this study reports the transversely isotropic elastic properties of pristine and Stone-Wales (SW) defected BNNTs within the framework of MD simulations using a Tersoff force field. This is achieved by imposing axial extension, twist, in-plane biaxial tension, and in-plane shear to the BNNTs. The study report that higher density of SW defect affect profoundly the axial Young's modulus, shear modulus, plane strain bulk and in-plane shear moduli of BNNTs and decrease their values by 9%, 7%, 1.5% and 5%, respectively. The present fundamental study highlights the significant role played by SW defected BNNTs in determining their mechanical behaviours as reinforcements in multifunctional nanocomposites.

Keywords: Boron nitride nanotubes, Stone Wales defects, Elastic properties and Molecular dynamics simulations

1
2
3
4
5
6
7
8
9
10
11
12
13
14
15
16
17
18
19
20
21
22
23
24
25
26
27
28
29
30
31
32
33
34
35
36
37
38
39
40
41
42
43
44
45
46
47
48
49
50
51
52
53
54
55
56
57
58
59
60
61
62
63
64
65

Thin Film Synthesis of Organometal halide Perovskite nanomaterial and MOF composite using inkjet printing technique.

Priyanshu Goel^{1,2}, Akash Deep^{1,2}, Sunita Mishra^{1,2*}

¹Central Scientific Instruments Organisation (CSIR-CSIO), Sector 30 C,
Chandigarh, 160030, India;

²Academy of Scientific and Innovative Research, CSIR-CSIO, Sector 30 C,
Chandigarh, 160030, india;

Email: *sunita_mishra@csio.res.in

Abstract

Organometal halide Perovskite(OHP) are widely known for their variety of optical and electronic properties. These properties lead their use in the fabrication of various optoelectronics devices such as LEDs, Solar cells, photodetectors, sensors and so on. However, OHP synthesis and their stability in the ambient conditions is still a challenge. Metal organic framework (MOF) is a class of materials having high porosity and high chemical and structural stability with tunable pore size. Due to their porous nature and the presence of the various organic groups MOF acts as promising template for host-guest chemistry. In this work, we synthesize methyl ammonium lead bromide and iodide perovskite composite with lead MOF (Pb-MOF) and MOF-5 (Zn-MOF) by simply inkjet printing the MOF Inks on to different substrate and then loading the perovskite precursor salts into these printed films. The thin films further studied and characterized by the X-ray diffraction, scanning electron microscopy and photo luminescence spectroscopy. Results shows high luminescence in the green region at round 520nm and the stability of composite in the ambient atmosphere for around 2months.

Area Selective Growth of MOF Thin Film Patterns in Micro-sized via Holes Promoted by Surface Covering of Cu Powders

Atsushi Shimizu

*Graduate School of Science.
Tokyo University of Science
Katsushika-ku, Tokyo, Japan
Nanoelectronics Research Institute
National Institute of Advanced
Industrial Science and Technology
Tsukuba, Ibaraki, Japan
1518524@ed.tus.ac.jp*

Kentaro Kinosita

*Graduate School of Science.
Tokyo University of Science
Katsushika-ku, Tokyo, Japan
kkinosita@rs.tus.ac.jp*

Yusuke Nakaune

*Graduate School of Science.
Tokyo University of Science
Katsushika-ku, Tokyo, Japan
1518535@ed.tus.ac.jp*

Hisashi Shima

*Nanoelectronics Research Institute
National Institute of Advanced
Industrial Science and Technology
Tsukuba, Ibaraki, Japan
shima-hisashi@aist.go.jp*

Makoto Takahashi

*Nanoelectronics Research Institute
National Institute of Advanced
Industrial Science and Technology
Tsukuba, Ibaraki, Japan
makoto.takahashi@aist.go.jp*

Yasuhide Naitoh

*Nanoelectronics Research Institute
National Institute of Advanced
Industrial Science and Technology
Tsukuba, Ibaraki, Japan
ys-naitoh@aist.go.jp*

Hiro Akinaga

*Nanoelectronics Research Institute
National Institute of Advanced
Industrial Science and Technology
Tsukuba, Ibaraki, Japan
akinaga.hiro@aist.go.jp*

We newly propose the epoch-making highly area-selective MOF (metal-organic- framework) crystal growth method, “Cu powder covering method”. We found that the Cu powders covering the substrate surface during the growth process improves the area-selectivity and yield. The MOF crystals can be grown even in the confined space such as the via-holes with the diameter of 1 μ m. The present achievement will strongly push forward the introduction of MOF into the electronic devices and semiconductor processes.

INTRODUCTION

Metal organic frameworks (MOFs) inherently involve the array structure of the periodic and dense nanoscale pores. Taking advantage of the outstanding features of such pores including the high structural design ability, various studies to realize electronic devices using MOFs [1] such as gas sensors [2], FETs [3], and solar cells [4] have been carried out. Toward the electronics application of this potentially useful material, the growth methods of MOFs require the compatibility with the conventional Si processes. However, most of the previously reported MOF growth methods still remain insufficient from this point of view. For example, HKUST-1, one of the most popular MOFs owing to its high stability in the atmosphere [5], is basically synthesized in solution. It is in general called the solvothermal method. However, this method usually results in the continuous thin film of granular MOFs and the location of the crystal growth is uncontrollable. Therefore, the solvothermal method is incompatible with the

semiconductor processes because it needs the precise alignment of the pattered thin films that constitute the electronic devices. There have been some attempts to control the locations of the HKUST-1 crystal growth on the substrate. Most of them require an insulating self-assembled monolayer (SAM) film as a seed layer [6], which is unfavorable from the aspect of the electric conduction. On the other hands, the “direct conversion from metals (DCM)” method reported by H. Ji *et al.* enables the selective growth of HKUST-1 without any SAM film. In their method, the Cu film deposited on the substrate determines the location of the HKUST-1 growth. Unfortunately, despite the above good aspect, the relatively thick Cu film with the thickness of 500 nm for instance is necessary to avoid the Cu exhaustion during the synthesis. It will become a drawback to the device size miniaturization.

In this study, we propose a new MOF growth method based on a hypothesis that both the supply of the sufficient Cu ions and the suppression of the solution convection just above the MOF growth point are the keys to prevent the Cu exhaustion observed in the DCM method. The area selective and high yield rate growth of HKUST-1 crystals in the via hole structure with the diameter of 1 μ m has been successfully demonstrated.

EXPERIMENTAL

We firstly prepared the multilayer structure of SiO_2 (27 nm)/Cu(50 nm)/Pt(20 nm)/TiN(20 nm) on the SiO_2/Si substrate. After that, the via hole with the diameter of 1 μ m

was fabricated by the conventional photolithography and reactive ion etching processes. The Cu layer is exposed at the bottom of the via hole (Figs. 1(a)-(c)). 1,3,5-Benzenetricarboxylic acid (BTC) of 0.12 g was dissolved into the mixed solution of ethanol of 1 ml and dimethylformamide (DMF) of 1 ml. After heating the solution to 50°C, we added Cu powders of 0.5 g and soaked the micro-fabricated substrate into the solution. Subsequently, we covered the substrate surface with Cu powders. After a predetermined period of time to synthesize HKUST-1, the Cu powders were removed from the substrate surface by ultrasonic cleaning with ethanol. Finally, the substrate surface was observed by SEM.

RESULTS & DISCUSSIONS

Figure 2 is the SEM image of the via hole after soaking a substrate in solution without Cu powders. A severe damage is observed right outside of the via hole. Such damage is probably caused by the Cu ion diffusion through the via hole because the low Cu ion concentration in the solution enhances the Cu dissolution. In this case, the Cu ions immediately flow away from the via hole. As a consequence, HKUST-1 was not synthesized. This result arises from the same causes as the entire consumption of Cu observed in the DCM method when the Cu thin film thickness is 100 nm [7].

The Cu powders in the present study are used in order to solve this problem (Fig. 3(a)). Namely, they can efficiently supply Cu ions into the solution because their surface area is quite large. As a result, the Cu ion concentration is sufficiently increased before soaking the substrate and hence the Cu ion outflow from the via holes is suppressed (Fig. 3(b)-(d)). Figure 3(e) is the SEM image of the substrate processed in this fashion. As we expected, the HKUST-1 crystals are stably grown only in the via holes. Concerning the role of the Cu powders, we suppose that they also serve efficiently to suppress the convection. It was confirmed in the control experiment shown in Figs. 3(a) and (f)-(i). In this case, the Cu powders were under the substrate during the synthesis, although the Cu ion concentration in the solution was increased in advance. As shown in Fig. 3(i), no HKUST-1 crystal was grown on the substrate. Therefore, from those results, both the sufficient Cu ion concentration and the suppression of the solution convection are indispensable for the stable HKUST-1 growth.

CONCLUSION

We have newly developed the Cu powder covering method that enables highly area selective growth of HKUST-1 crystals even in the confined space such as the via holes. The production yield of HKUST-1 is also quite high. This method accelerates the introduction of this material into Si processes.

REFERENCE

- [1] I. Stassen, N. Burch, A. Talin, P. Falcaro, M. Allendorf and R. Ameloot, "An updated roadmap for the integration of metal-organic frameworks with electronic devices and chemical sensors" *Chem. Soc. Rev.*, 2017, 46, pp. 3185-3241.
- [2] M.-S. Yao, W.-X. Tang, G.-E. Wang, B. Nath and G. Xu, "MOF Thin Film-Coated Metal Oxide Nanowire Array: Significantly Improved Chemiresistor Sensor Performance" *Adv. Mater.*, 2016, 28, pp. 5229-5234.
- [3] G. Wu, J. Huang, Y. Zang, J. He and G. Xu, "Porous Field-Effect Transistors Based on a Semiconductive Metal-Organic Framework" *J. Am. Chem. Soc.* 2017, 139, pp. 1360-1363.
- [4] C. J. Brabec, S. Gowrisanker, J. J. M. Halls, D. Laird, S. Jia, S. P. Williams, "Polymer-Fullerene Bulk-Heterojunction Solar Cells" *Adv. Mater.* 2010, 22, pp. 3839-3856.
- [5] S. S.-Y. Chui, S. M.-F. Lo, J. P. H. Charmant, A. G. Orpen, L. D Williams, "A Chemically Functionalizable Nanoporous Material $[Cu_3(TMA)_2(H_2O)_3]_n$ " *Science*, 1999, 283, 5405, pp. 1148-1150.
- [6] O. Shekhah, H. Wang, S. Kowarik, F. Schreiber, M. Paulus, M. Tolan, C. Sternemann, F. Evers, D. Zacher, R. A. Fischer and C. Wöll, "Step-by-Step Route for the Synthesis of Metal-Organic Frameworks" *J. Am. Chem. Soc.*, 2007, 129, 49, pp. 15118-15119.
- [7] H. Ji, S. Hwang, K. Kim, C. Kim and N. C. Jeong, "Direct in Situ Conversion of Metals into Metal-Organic Frameworks: A Strategy for the Rapid Growth of MOF Films on Metal Substrates" *ACS Appl. Mater. Interfaces*, 2016, 8, 47, pp. 32414-3242.

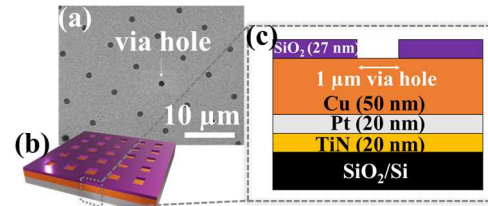


Fig. 1. (a) Top-view SEM image and (b, c) top and cross-sectional schematics of the processed substrate with via holes.

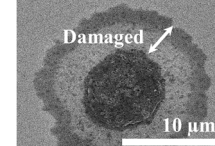


Fig. 2. A damaged via hole observed after soaking a substrate in solution without Cu powders.

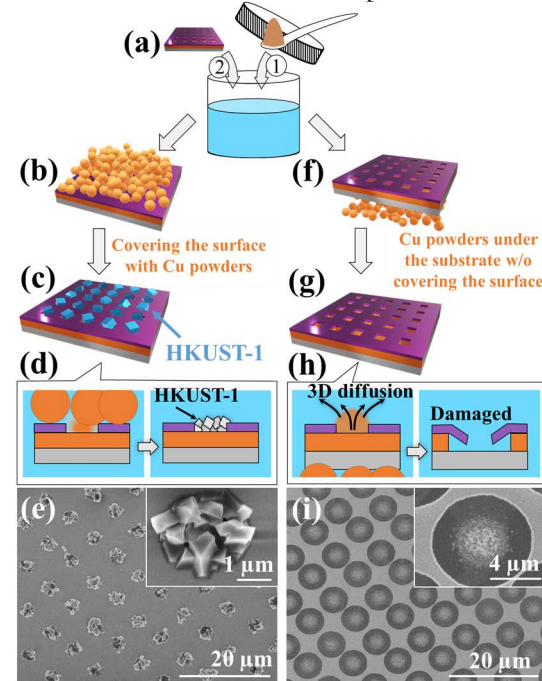


Fig. 3. Schimatic illustrations of flow of HKUST-1 synthesis with ((a)-(d)) and without ((a) and (f)-(h)) covering the surface of substrates with Cu powders, and top view of SEM images for the former (e) and the latter (i), respectively.

Optimizing The Crystal of Ta/TaN Diffusion Barrier for the Improve Resistance of Cu line

Kuo-Tzu Peng , Wei-Lin Wang , Yi-Wen Lu , Shih-His Chen , Hsien-Chang Kuo , Ming-Chen Lu , Chang-Che Chen , Pei-Chia Chen

Process Technology Development Division, Powerchip Technology Corporation,

No. 12, Li-Hsin Rd. 1, Hsinchu Science Park, Hsinchu, Taiwan

*Tel: +886-3-5795000 ext. 8672; E-mail: kcpeng@powerchip.com

Abstract

The crystal phase of Ta on TaN barrier depends on the underlying N concentration of TaN film. In this study, we have investigated the influences of the crystal phase of the Ta barrier at the via bottom on via resistance and reliability performance. PVD Ta/TaN bi-layer films, commonly used as diffusion barriers in Cu interconnects, have been deposited by SIP(self-ionized plasma) system. In amorphous TaN film with low N concentration, Ta film consists of α -phase Ta (α -Ta) and β -phase Ta (β -Ta). The sheet resistance of Ta film with the mixture of α -Ta and β -Ta is decreased by the increase of α -Ta content. The formation of pure α -Ta film can be achieved by increasing the N concentration of underlying amorphous TaN film. It has been reported that the electrical property and reliability of Cu interconnection structure have been investigated by utilizing various types of Ta/TaN diffusion barrier. The diffusion barrier fabricated by the combination of crystallized α -Ta and TaN with high N concentration efficiently reduces the K_R and improves the EM resistance of the Cu interconnection structure. These results indicate the influence of the phase of Ta in only the distribution of via-resistance.

bulk Ta metal is α -Ta which is body-centered cubic structure with resistivity about 15~60 $\mu\Omega\text{cm}$. The meta-stable phase, β -Ta, is tetragonal structure with resistivity in the range of 170~210 $\mu\Omega\text{cm}$ [5-6].

In the application for IC devices, β -Ta with much higher resistivity is certainly unfavorable. Thus, the fabrication of α -Ta film is the goal of practical applications. Previous studies presented several methods to achieve crystallized α -Ta film, including the adjustment of N2/Ar gas ratio, TaN surface treatment, graded Ta(N)/TaN under-layer, and the increment of the N concentration in TaN film [7-11]. In this study, we investigated the influence of crystal phase of Ta in Ta/TaN bi-layer barrier on via resistance. The influence of the N concentration in amorphous TaN under-layer on the microstructure of over-deposited Ta film was systematically investigated. Furthermore, the effect of amorphous TaN thickness on the crystalline property of Ta film was taken into comparative discussion.

I. Introduction

Cu wiring has been widely used for advanced integrated circuit(IC), because of its small resistivity and electromigration resistance performance compared with Al wiring[1-2]. In Cu interconnect process, Ta/TaN bi-layer is commonly used to prevent the diffusion of Cu into the dielectric oxide layer. Because of the multi-level interconnect process, Ta/TaN diffusion barrier layers are also deposited between Cu via bottoms and underlying Cu lines. Ta/TaN barrier is employed because it has high performance of barrier properties and a Ta film has good adhesion to Cu. For the adhesion with the dielectric oxide layer, TaN presents superior ability[3-4]. The resistance of the Ta/TaN diffusion barrier inevitably impacts the contact resistance (R_c) of the Cu interconnection structure. As IC devices are scaling down drastically, the R_c of Cu interconnection is expected to increase. For Ta metal, there are two types of crystal phases, including α -phase Ta (α -Ta) and β -phase Ta (β -Ta). Generally,

Single-step nanopatterning of GaAs via wet-based chemical etching with metal stamp

1 Kyunghwan Kim

2 School of Integrated Technology
3 Yonsei University
4 Incheon, Republic of Korea
5 kyunghwan.kim@yonsei.ac.kr

6 Bugeun Ki

7 School of Integrated Technology
8 Yonsei University
9 Incheon, Republic of Korea
10 bugeun.ki@yonsei.ac.kr

11 Keorock Choi

12 School of Integrated Technology
13 Yonsei University
14 Incheon, Republic of Korea
15 keorock.choi@yonsei.ac.kr

16 Seung Min Lee

17 School of Integrated Technology
18 Yonsei University
19 Incheon, Republic of Korea
20 sm.lee@yonsei.ac.kr

21 Jungwoo Oh

22 School of Integrated Technology
23 Yonsei University
24 Incheon, Republic of Korea
25 jungwoo.oh@yonsei.ac.kr

26 Semiconductor 3-dimensional nanopatterns are widely
27 used to enhance the performance of various devices such as
28 electronics, optics, and sensors.^[1] Most of semiconductor
29 nanopatterns are fabricated by photolithography and dry etch,
30 which are costly due to batch processing and complex
31 equipment.^[2] In addition, crystal defects caused by high
32 energy plasma ions during the dry etch are hardly recovered
33 especially in compound semiconductors acting as carrier
34 recombination sites, which eventually deteriorates the device
35 performances. As an alternative to photolithography,
36 nanoimprint lithography (NIL) has been studied
37 extensively.^[3] NIL fabricates nanopatterns after stamping
38 polymer resist with pre-defined stamp. NIL has been
39 spotlighted to simplify the lithography process. However, to
40 fabricate semiconductor nanopatterns, subsequent etching
41 processes are still required.

42 Chemical imprinting that combines NIL and metal-
43 assisted chemical etching (MacEtch) by single-step process,
44 has been recently introduced.^{[4]-[5]} As shown in Fig. 1 (a),
45 chemical imprinting fabricates semiconductor nanopatterns
46 by pressing and releasing of pre-defined metal stamp in
47 etchant composed of acid and oxidant. During the contact
48 between stamp and semiconductor in etchant, etching occurs
49 via the chemical reaction between metal, etchant and
50 semiconductor. Reduction caused by metal catalyst in an
51 oxidant generates electronic holes, which oxidize the GaAs.
52 The acid dissolve the oxidized GaAs. Through these processes
53 etching occurs in the contact area with the metal stamp, and
54 lithography and etching are performed concurrently.
55 Chemical imprinting is wet-based etching and fabricates
56 nanopatterns without crystal defects. Chemical imprinting is
57 expected to increase the productivity in the semiconductor
58 manufacturing by directly imprinting the patterns on
59 crystalline semiconductors in a single step.

60 In this study, we demonstrate the chemical stamping of
61 GaAs. Various 3D profiles are fabricated on the GaAs with
62 dopant types and oxidant compositions. Dopants in the GaAs
63 changed the junction profiles between the stamp and GaAs,
64 which determines the imprinted patterns. Fig. 1 (b)-(d) shows
65 the imprinted n-type and p-type GaAs substrates after using
66 the pillar stamps. In addition, the oxidant in etchant increased
67 the aspect ratio of the imprinted patterns. The excess holes
68 result in fast oxidation and removal of GaAs, indicating the
69 oxidation limited chemical imprinting.

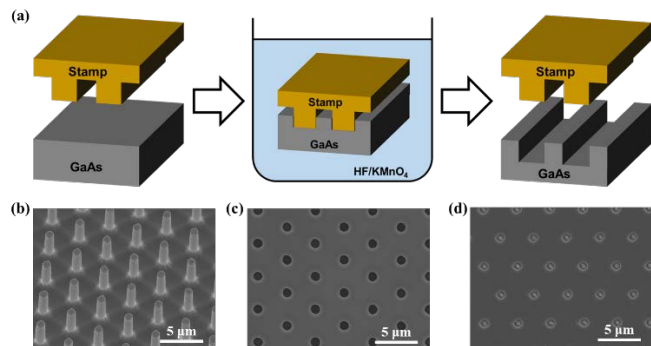


Fig. 1 (a) Schematic illustrates of chemical imprinting process. SEM images of (b) pillar patterned metal stamp. SEM images of hole patterned (c) n-type and (d) p-type GaAs imprinted by bar and pillar patterned metal stamp under the same process condition.

ACKNOWLEDGMENT

This research was supported by the MSIT(Ministry of Science and ICT), Korea, under the “ICT Consilience Creative Program” (IITP-2019-2017-0-01015) supervised by the IITP(Institute for Information & communications Technology Planning&Evaluation). This research was also supported by Basic Science Research Program through the National Research Foundation of Korea(NRF) funded by the Ministry of Education, Science and Technology(NRF-2016R1D1A1A09918647)

REFERENCES

- [1] K. Tomioka, M. Yoshimura, and T. Fukui, “A III-V nanowire channel on silicon for high-performance vertical transistor”, *Nature*, vol. 488, pp. 189–193, August 2012.
- [2] X. Liu, P. R. Coxon, M. Peters, B. Hoex, J. M. Cole, and D. J. Fray, “Black silicon: fabrication methods, properties and solar energy applications”, *Energy Environ. Sci.*, vol. 7, pp. 3223–3263, October 2014.
- [3] L. J. Guo, “Nanoimprint lithography: methods and materials requirements”, *Adv. Mater.*, vol. 19, pp. 495–513, February 2007.
- [4] B. Ki, Y. Song, K. Choi, J. H. Yum, and J. Oh, “Chemical imprinting of crystalline silicon with catalytic metal stamp in etch bath”, *ACS Nano*, Vol. 12, pp. 609–616, January 2018.
- [5] K. Kim, B. Ki, K. Choi, S. Lee, and J. Oh, “Resist-free direct stamp imprinting of GaAs via metal-assisted chemical etching”, *ACS Appl. Mater. Interfaces*, Vol. 11, pp. 13574–13580, April 2019.

Photonic Qubits emitted by semiconductor quantum dots for quantum network applications

K. D. Zeuner^{*1}, S. Gyger¹, K. D. Jöns¹, C. Nunez Lobato¹, C. Reuterskiöld Hedlund²,
S. Steinhauer¹, G. Vall Llosera³, K. Wang¹, M. Hammar² and V. Zwiller¹

1. KTH Royal Institute of Technology, Department of Applied Physics, Albanova University Centre,
Roslagstullsbacken 21, 106 91 Stockholm, Sweden

2. KTH Royal Institute of Technology, Department of Electronics, Electrum 229,
164 40 Kista, Sweden

3. Ericsson Research, Ericsson AB, Stockholm 16480, Sweden

* Electronic address: zeuner@kth.se

Quantum networks enable the distribution of quantum information between remote quantum computing nodes, as well as an intrinsically secure information transmission channel [1]. Many applications in this field require sources of quantum states of light to allow long-distance communication. Quantum dots emitting in the telecom C-band as sources of single [2] and entangled photons [3] are ideal candidates for fiber-based quantum networks.

Here, we present metal organic vapour phase epitaxy grown InGaAs quantum dots on GaAs, using a metamorphic buffer method to be able to create single photons and pairs of photons in the telecom C-band. We demonstrate the inclusion of our quantum source in a metropolitan scale quantum link based on commercial deployed fiber. The link is connecting KTH's laboratories in downtown Stockholm and Ericsson research labs in Kista, spanning a total distance of 36 km. We investigate the applicability and limitations of our quantum light source in this real-life test bed.

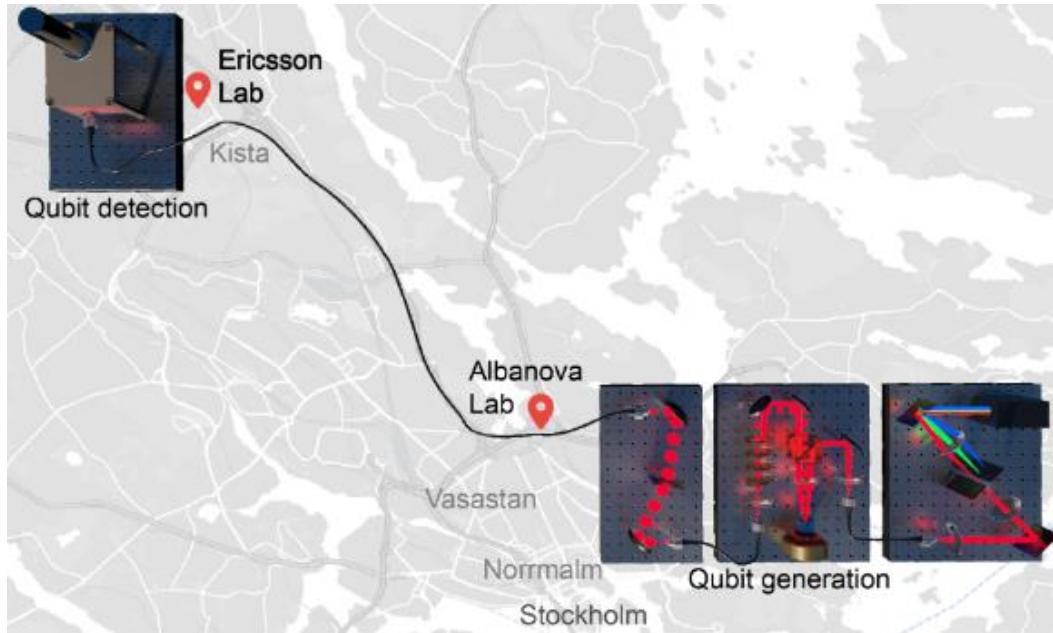


Figure 1: Artistic view of the Stockholm quantum link connecting quantum infrastructure in two research labs.

[1] H. J. Kimble, *Nature*. 453, 7198 (2008).

[2] M. Paul, et al., *Appl. Phys. Lett.* 111, 033102 (2017).

[3] F. Olbrich, et al., *Appl. Phys. Lett.* 111, 133106 (2017).

Super-resolved optical characterization of defects in 2D materials

1 Miao Zhang

2 *Laboratory of Nanoscale Biology*
 3 *Institute of Bioengineering, EPFL*
 4 *Dept. of Applied Physics, KTH*
 5 *Lausanne, Switzerland*
 6 *miao.zhang@epfl.ch*

1 Jean Comtet

2 *Laboratory of Nanoscale Biology*
 3 *Institute of Bioengineering, EPFL*
 4 *Lausanne, Switzerland*
 5 *jean.comtet@gmail.com*

1 Jiandong Feng

2 *Dept. of Chemistry*
 3 *Zhejiang University*
 4 *Hangzhou, China*
 5 *jiandong.feng@zju.edu.cn*

12 Aleksandra Radenovic

13 *Laboratory of Nanoscale Biology*
 14 *Institute of Bioengineering, EPFL*
 15 *lausanne, Switzerland*
 16 *aleksandra.radenovic@epfl.ch*

17 Defects in two-dimensional (2D) materials can
 18 significantly alter physical properties of the materials, such as
 19 electron mobility, photoluminescence, etc. Defects
 20 themselves also exhibit new and exciting properties. For
 21 example, nitrogen-vacancy related defects in monolayer
 22 hexagonal boron nitride (h-BN) have been reported to exhibit
 23 room temperature single photon emission, which can be
 24 potentially integrated to photonics devices for quantum
 25 communication [1]. Due to atomic-thickness of the 2D
 26 materials, defects in such hosting material are highly sensitive
 27 to their environment, therefore can be tuned externally [2] or
 28 be inversely used as sensing probes. Detailed crystalline and
 29 electronic structure of individual defects can be characterized
 30 by high-resolution aberration-correction electron tunneling
 31 microscope (TEM) and scanning tunneling microscope
 32 (STM). However, these methods suffer from tedious sample
 33 preparation, time-consuming imaging process, and small
 34 imaging area. The electrons of high energy in TEM can
 35 introduce defects in the material during the imaging process.
 36 With the rapid progress in large scale 2D material growth by
 37 chemical vapor deposition (CVD), there is a growing demand
 38 for development of a fast and large-scale characterization
 39 method of individual defects in 2D materials.

40 Our group has recently employed single molecule
 41 localization microscopy (SMLM) as a characterization
 42 technique for wide-field mapping of optically active defects in
 43 h-BN both spatially and spectrally. [3] [4].

44 Point defects in h-BN are often observed to have bright
 45 and narrow emission lines with energies ranging from 1.6 eV
 46 to 2 eV. Due to their intermittent emission, optical super-
 47 resolution reconstruction technique can be applied to localize
 48 temporally isolated point emitters in dense areas. Since the
 49 localization uncertainty scales inversely with square root of
 50 the number of the detected photons, bright emission and high
 51 photostability of these emitters allows in the ideal case to
 52 separate two emitters only 10 nm apart. With careful drift
 53 correction in the image plane, quantitative information such as
 54 defects density can be characterized throughout the whole
 55 field of view [3].

56 To identify the types of defects, we also developed
 57 simultaneous spectral characterization of individual emitters
 58 as part of the super-resolution imaging system. Here, a beam
 59 splitter is added in the emission path to evenly split the
 60

61 emission light into two paths. One path goes directly to the
 62 camera allowing for spatial mapping, while the light from the
 63 second path is dispersed by a prism and is projected next to
 64 the spatial image on the same camera. Two populations of
 65 emitters with distinct emission peaks at 1.94 eV and 2.12 eV,
 66 respectively, are found on CVD-grown h-BN. On irradiated
 67 exfoliated flakes only one type of defects is predominantly
 68 presented [4].

69 To further extend the capacity of SMLM to characterize
 70 defects in other 2D materials that are not intrinsic emitters at
 71 room temperature, we use chemically modified fluorophores
 72 to label the defects and allow for optical mapping. For the
 73 purpose of super-resolution reconstruction, intermittency of
 74 the labels is induced by using either self-blinking fluorophores
 75 or fluorescent labels that only bind to the defects transiently.
 76 We demonstrate this approach to image sulfur-vacancies in
 77 MoS₂ monolayer. Fluorophores modified with thiol tags are
 78 chosen to bind with sulfur-vacancies. The emission
 79 wavelength of the fluorophores is carefully selected to avoid
 80 overlapping with the photoluminescence from monolayer
 81 MoS₂. A dual-color system is employed to allow simultaneous
 82 observation of PL imaging from MoS₂ and defects labels.
 83 Preliminary results show that thiol-modified-fluorophores
 84 preferentially bind to grain boundaries of CVD-grown MoS₂,
 85 where a high density of sulfur-vacancies is expected.

86 In summary, our results demonstrate that super-resolution
 87 microscopy and spectroscopy can be used as a high-
 88 throughput tool for fast, room temperature characterization of
 89 defects in various 2D materials.

REFERENCES

- [1] A. Splendiani, L. Sun, Y. Zhang, T. Li, J. Kim, C. Chim, G. Galli, and F. Wang, "Emerging Photoluminescence in Monolayer," *Nano Lett.*, vol. 10, pp. 1271–1275, 2010.
- [2] N. Nikolay, N. Mendelson, N. Sadzak, F. Böhm, T. T. Tran, B. Sontheimer, I. Aharonovich, and O. Benson, "Very Large and Reversible Stark-Shift Tuning of Single Emitters in Layered Hexagonal Boron Nitride," *Phys. Rev. Appl.*, vol. 10, no. 1, p. 1, 2019.
- [3] J. Feng, H. Deschout, S. Caneva, S. Hofmann, and I. Lonc, "Imaging of Optically Active Defects with Nanometer Resolution," *Nano Lett.*, no. 18, pp. 1739–1744, 2018.
- [4] J. Comtet, E. Glushkov, V. Navikas, J. Feng, and V. Babenko, "Wide-Field Spectral Super-Resolution Mapping of Optically Active Defects in Hexagonal Boron Nitride," *Nano Lett.*, vol. 19, pp. 2516–2523, 2019.

Bowtie Nano-Antenna Simulation For Bio-sensing Applications and Rectenna Integration

Lina Tizani *System on Chip Center and EECS*
Khalifa University
Abu Dhabi, United Arab Emirates
lina.tizani@ku.ac.ae

Baker Mohammad
System on Chip Center and EECS
Khalifa University
Abu Dhabi, United Arab Emirates
mohd.rezeq@ku.ac.ae

Moh'd Rezeq
dept. of Physics and Electrical and System on Chip Center
Khalifa University
Abu Dhabi, United Arab Emirates
mohd.rezeq@ku.ac.ae

Jaime Viegas
System on Chip Center and EECS
Khalifa University
Abu Dhabi, United Arab Emirates
jaime.viegas@ku.ac.ae

Optical antennas represent an optical detector similar to radio frequency antennas but operating in the optical regime. Nowadays, optical antennas are attracting a lot of attention due to their enormous potential for applications ranging from nanoscale optical microscopy and spectroscopy over solar energy conversion, integrated optical Nano circuitry to ultra-sensing, etc.[1]. This gain focus is due to the progress in nano-manufacturing technologies, which makes it possible utilizing sub-wavelength plasmonic structures in different shapes and sizes [2]. Different shapes of the apertures are studied for bio-sensing and in infrared domain such as H-shape, cross shape as well as quad-triangles [3] and bowtie [4].

In this work, we present the interaction of bowtie nano-antenna with the background material to integrate it with terahertz detector for bio-sensing applications. This antenna will be integrated at a later stage along with a THz rectifying diode in order to fabricate an infrared rectenna. For a certain frequency of operation nano antenna design must be optimized in order to produce maximum field enhancement. Moreover, the high frequency of antenna leads to several challenges related to fabrication as well to the rectifying process since typical semiconductors based rectifiers do not have fast switching speed that enable them to rectify THz signal.

To examine the biomaterial effect on modeled nano-antenna, few conventional biomaterials has been selected and their effect on the signal transmission is analyzed. The structure is modeled using Finite Difference Time Domain (FDTD) simulation by the CST microwave studio.

A. Design

The structure studied in this work is a bowtie dipole using gold as metal and a gap of 12nm. This structure has been realized as per the schematic in "Fig.1". The first layer is a silicon dioxide layer that is used to increase the transmission of the THz signal to the underlying silicon substrate. a back layer of gold has been employed as a reflector to enhance coupling to the antenna from the substrate. The antennas are covered with a material of refractive index n . it is essential to consider such environment material where the antenna will be immersed in liquid to resemble bio-sensing applications [5]. If not specified otherwise, n is defined as 1. In order to analyze the nano antenna aperture we use CST microwave studio. A port waveguide was used as a feed source in the 3-D simulation.

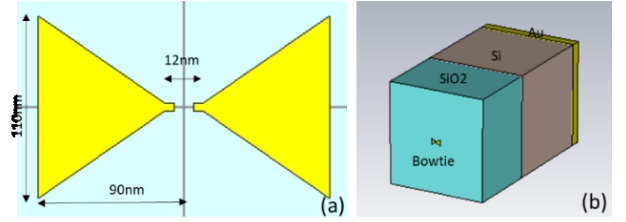


Fig. 1: (a) Dimensions of the proposed bow-tie antenna. (b) 3D perspective of the structure simulated.

B. Results and Discussion

In normal testing conditions ($n=1$), the nano-antenna has a resonance of 30.176 THz and the transmission pick is about 0.974. To examine the effect of biomaterial on nano-antenna, we selected the following conventional refractive indexes for materials widely used in bio-sensing applications: $n= 1.35, 1.43, 1.525, 1.627$ [2-4, 6, 7]. The resonance peak is shifted from 30.176THz to 28.934 THz with increasing refractive index as shown in "Fig.2". this could be interpreted as an increase in the capacitance that is correlated to a decrease in the resonance frequency due to the implementation of the external material [7].

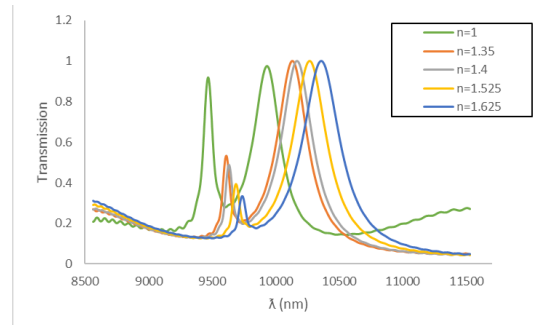


Fig. 2: Nano-aperture transmittance in presence of biochemical material. A decrease in resonance frequency is observed (increase in wavelength) as a function of increasing order of n .

CONCLUSION

In Current research, we design a bowtie nano-antenna for bio-sensing application. The current aperture will be fabricated using microfabrication techniques along with THz rectifier to form a THz rectenna.

REFERENCES

- [1] P. Biagioni, J.-S. Huang, and B. Hecht, "Nanoantennas for visible and infrared radiation," *Reports on Progress in Physics*, vol. 75, no. 2, p. 024402, 2012.
- [2] F. B. Zarrabi, M. Naser-Moghadasi, S. Heydari, M. Maleki, and A. S. Arezomand, "Cross-slot nano-antenna with graphene coat for bio-sensing application," *Optics Communications*, vol. 371, pp. 34-39, 2016.
- [3] A. Ahmadvand, R. Sinha, and N. Pala, "Hybridized plasmon resonant modes in molecular metallocdielectric quad-triangles nanoantenna," *Optics Communications*, vol. 355, pp. 103-108, 2015.
- [4] J. Calderón, J. Álvarez, J. Martínez-Pastor, and D. Hill, "Bowtie plasmonic nanoantenna arrays for polarimetric optical biosensing," in *Frontiers in Biological Detection: From Nanosensors to Systems VI*, 2014, vol. 8933, p. 89330I: International Society for Optics and Photonics.
- [5] H. Fischer and O. J. F. Martin, "Engineering the optical response of plasmonic nanoantennas," *Optics Express*, vol. 16, no. 12, pp. 9144-9154, 2008/06/09 2008.
- [6] M. N. Moghadasi, R. A. Sadeghzadeh, M. Toolabi, P. Jahangiri, and F. B. Zarrabi, "Fractal cross aperture nano-antenna with graphene coat for bio-sensing application," *Microelectronic Engineering*, vol. 162, pp. 1-5, 2016.
- [7] P. Jahangiri, F. B. Zarrabi, M. Naser- Moghadasi, A. Saeed Arezoomand, and S. Heydari, "Hollow plasmonic high Q-factor absorber for bio-sensing in mid-infrared application," *Optics Communications*, vol. 394, pp. 80-85, 2017.

MOCVD synthesis of 2D saturable absorbers for pulsed fiber lasers

Petr Kuznetsov¹, Galina Yakushcheva¹, Evgeny Savelyev¹, Dmitry Sudas², Vasily Yapaskyrt^{1,3}, Vasily Sherbakov^{1,3}, Konstantin Golant¹

¹ Kotel'nikov Institute of Radio Engineering and Electronics (Fryazino Branch) of RAS, Fryazino, 141190, Russia

² Peter the Great St. Petersburg Polytechnic University, Saint Petersburg, 195251, Russia

³ Moscow State University, Geological Faculty, Department of Petrology, Moscow, 119991, Russia

Corresponding author: Petr Kuznetsov (e-mail: pik218@ire216.msk.su)

Saturation absorption in a wide spectral range with the increase of the incident light intensity [1], and a very fast relaxation after de-excitation are unique properties of many 2D materials, in particular thin films of topological insulators Bi_2Se_3 and Bi_2Te_3 . The properties mentioned above can be widely used in quantum electronics and lasers. Metalorganic chemical vapor deposition (MOCVD) looks as a promising method for the fabrication of these 2D materials. However, up to the moment the application of the MOCVD for this purpose is not widespread.

In the current paper we present the results of the MOCVD technology application when depositing various 2D materials such as MoSe_2 , MoTe_2 , WSe_2 and topological insulators Bi_2Se_3 , Bi_2Te_3 , Sb_2Te_3 , as well as Bi and Sb bilayers on the surface of tapered sections of an optical fiber. The tapered sections 2-10 mm in length and 8-12 μm in diameter were prepared by chemical etch removal of the silica cladding using non-toxic NH_4F - $(\text{NH}_4)_2\text{SO}_4$ - H_2O solution. More details regarding the fabrication technology of the tapers one can find in [2].

In order to deposit thin films of the materials listed above on the surface of a fiber taper, we exploit a homemade tubular silica reactor heated by a resistance furnace. During the deposition, transmission spectra of the taper were monitored 'in situ' within 1-1.6 μm wavelength

range. We stopped the deposition process as soon as the transmission of the taper amounted to 90-70% at a wavelength of 1.56 μm . According to the conducted AFM study, the obtained coatings were discontinuous and film islands occupied only a small part of the taper's surface. The average height of the islands on all samples under study was less than 8 nm. Local energy dispersive X-ray and Raman spectroscopy confirmed the stoichiometry of the coating films. The obtained tapers covered with 2D materials were tested by installing them into a ring cavity of an erbium fiber laser as passive Q-switchers. The transition from CW to Q-switch oscillation mode was observed only for tapers having diameter smaller than 11 μm . The passively Q-switching mode in the ring erbium fiber lasers with thin film coated tapers of larger diameters installed in the cavity arose only in the case of additional outer covering of the tapers with the polydimethylsiloxane elastomer, having the refractive index of about 1.40 at a temperature of 20 $^{\circ}\text{C}$.

Fig. 1 shows two examples of Q-switch modes obtained with the help of the tapers coated with Bi_2Te_3 and MoSe_2 films. Comparison study of the effectiveness of the Q-switches based on fiber tapers having similar dimensions but different 2D coating materials is our immediate task.

This work is supported by Russian Science Foundation, Project #17-19-0157

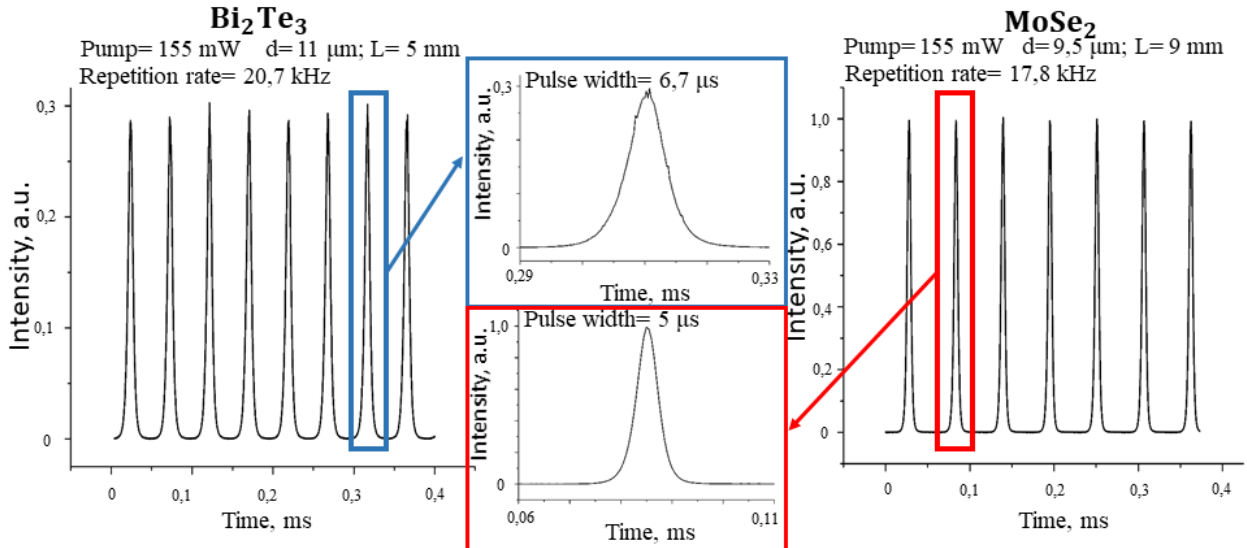


Fig. 1. Passively Q-switched oscillations in a ring erbium fiber laser. Trains of pulses shown at the left and at the right correspond to the lasers with Bi_2Te_3 and MoSe_2 coated tapers installed in the cavity, respectively. Taper sizes, coating materials, pulse durations and repetition rates are indicated in the figure.

[1] C Zhao, Y Zou, Y Chen, Z Wang, S Lu, H Zhang, S Wen, and D Tang, Opt. Express vol. 20 (25), 2012, pp. 27888–27895.

[2] P I Kuznetsov, V A Jitov, E I Golant, E A Savelyev, D P Sudas, G G Yakushcheva, and K M Golant, Phys. Scr., vol. 94, 2019, 025802 (6 pp).

Analytical Model of Band-to-Band Tunneling in ATLAS-TFET

Ahsan Ahamed
Department of EEE
Bangladesh University of Engineering
and Technology
Dhaka, Bangladesh
ahsan2313@gmail.com

Nusrat Jahan Ananna
Department of EEE
Bangladesh University of Engineering
and Technology
Dhaka, Bangladesh
ananna.nusrat.13@gmail.com

Quazi DM Khosru
Department of EEE
Bangladesh University of Engineering
and Technology
Dhaka, Bangladesh
qdmkhosru@eee.buet.ac.bd

Abstract— The atomically thin and layered semiconducting-channel tunnel field effect Transistor (ATLAS-TFET) is a recent development from the conventional TFET that exhibits a steep turn-on with minimum subthreshold swing (SS) of 3.9 millivolts per decade. In this paper, a semi-classical analytical model of the tunneling current of this device is derived. The electric field and charge concentration is calculated by solving Poisson's equation. The generation current is then obtained using Kane's generation model for band-to-band tunneling (BTBT) along with maximum electric field approximation (MEFA). Quantum mechanical factors are incorporated in our model using necessary correction factors. The results obtained from this model are compared with the experimental data and good agreement between the results is found.

Keywords— analytical model, band-to-band tunneling, Kane's Generation model, 2D MoS₂, TFET

I. INTRODUCTION

In recent times extensive research is ongoing with TFETs due to their below 60 mV/dec SS and low power consumption [1]. As a continuation to that researchers have developed a two dimensional/three dimensional TFET (2D/3D TFET) namely ATLAS-TFET [2], [3] constructed with a 2D MoS₂ channel and 3D Ge source. This device structure allows a minimum subthreshold swing of 3.9 millivolts per decade (mV/dec) and an average of 31.1 mV/dec for four decades of drain current at room temperature to be achieved. Thus it stands as a strong candidate for the next generation transistors.

ATLAS-TFET has a vertical hetero-structure that allows electrons tunneling vertically from source to channel to generate the current. This carrier transport is modulated by gate voltage. When the device is in OFF state, no tunneling phenomenon is observed. In ON state, the conduction band of channel is lowered below the valence band of source due to the applied gate voltage and tunneling ensues. The electrons accumulated in the channel surface then get swept to the drain.

In this paper, a semiclassical analytical model for the ATLAS-TFET is established and the transfer characteristics obtained from this model is shown with comparison with the experimental data which is in good agreement.

II. ANALYTICAL MODEL

A. Threshold Voltage

Assuming that tunneling begins when the conduction band of the channel is lowered below the valence band of source, we define the threshold voltage for this tunneling device as the value of gate to source voltage for which the conduction band of MoS₂ aligns with the valence band of Ge.

We have also considered drain-induced barrier lowering (DIBL) which is a short-channel effect in FETs referring originally to a reduction of threshold voltage of the transistor

at higher drain voltages. So, the expression for threshold voltage becomes –

$$V_T = V_{oxT} + \varphi_{ms} + \psi_{MoS2T} - V_{DS} \times DIBL \quad (1)$$

where V_{oxT} and ψ_{MoS2T} are the gate oxide potential drop and surface potential drop at threshold voltage respectively, φ_{ms} is the work function difference between metal and semiconductor and V_{DS} is the drain to source voltage.

B. Charge Distribution

Charge distribution and potential drops across the junction are calculated by solving Poisson's equation.

$$\frac{\partial^2 \psi_{MoS2}}{\partial x^2} = -\frac{q}{\epsilon_{MoS2}} [p(x) - n(x) + N_d^+ - N_a^-] \quad (2)$$

Here, $p(x)$ and $n(x)$ is the positive and negative charge concentration in the MoS₂ channel, while N_d^+ and N_a^- are the respective dopant ion concentration. Solving this equation assuming slightly n-doped MoS₂, we get an expression for the Electric field on the MoS₂ channel,

$$E_{MoS2} = \frac{\partial \psi_{MoS2}}{\partial x} = \sqrt{\frac{2kTN_d}{\epsilon_{MoS2}}} \times \left(e^{-\frac{q\psi_{MoS2}}{kT}} + \frac{q\psi_{MoS2}}{kT} - 1 \right) \quad (3)$$

By applying V_{GS} the electrons starts to accumulate in the MoS₂ channel, increasing E_{MoS2} , thus increasing electric field in Germanium, E_{Ge} . With sufficiently large E_{Ge} the tunneling kicks in with a surge of electrons tunneled into the MoS₂ channel, turning the device on.

C. Generation Current

ATLAS-TFET works using the vertical tunneling mechanism [4] of electrons from p-Ge source to MoS₂ channel. This tunneling is modulated using the gate-to-source voltage. When V_{GS} increases beyond threshold voltage, the conduction band of MoS₂ is lowered below the valence band of Ge which enables the electrons to tunnel from the filled energy states of Ge to the empty energy states of MoS₂. Due to this vertical tunneling, electrons accumulate in the channel which are in to the drain laterally via drift and diffusion. This flow of electrons gives rise to generation current.

Here, we have used Kane's generation model [5] for calculation of the generation rate of electrons along with the Maximum Electric Field Approximation (MEFA) [6] of direct BTBT Kane model. Using these, the generation rate is calculated as –

$$G = RA \frac{E_{Ge,max}^D}{\sqrt{E_g}} \exp \left(\frac{-BE_g^{\frac{3}{2}}}{E_{Ge,max}} \right) \quad (4)$$

Where, $E_{Ge,max}$ is the maximum electric field at the tunnel junction, A and B are Kane's parameters for Ge. D is an adjustable parameter. We have added R as a correction factor depended upon the gate voltage that corresponds to the

allowable tunneling electrons from the degenerately doped Germanium.

Using this generation rate, we solved ambipolar transport equation to get the generation charge density, Q'_g . Finally, we have derived the expression for generation current as follows-

$$I_{\text{generation}} = \int_0^{V_{\text{DS}}} W \mu_{\text{MoS}_2} (Q'_g) dV \quad (5)$$

where W is the channel width, μ_{MoS_2} is the electron mobility of MoS_2 .

D. Subthreshold Current

The current obtained in subthreshold region is the reverse saturation current of the p-n junction which is generated due to the diffusion of minority carriers in the depletion region.

$$I_{\text{subthreshold}} = WL(J_p + J_n) \quad (6)$$

where L is the channel length and J_p and J_n are the diffusion current densities in MoS_2 and Ge respectively.

III. RESULTS AND DISCUSSIONS

A. Simulation Results and Comparison with Experimental Data

1) Transfer Characteristics

The simulation results of drain current (I_{DS}) are plotted against gate voltage (V_{GS}) in figure (1).

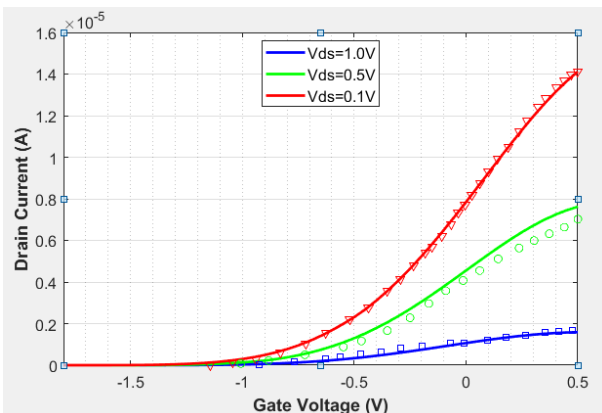


Figure 1: Drain Current as a function of Gate-to-Source Voltage. Solid line represents simulation results.

2) Subthreshold Swing

The drain current from our analytical model is also plotted in semi log scale against gate voltage (V_{GS}) in figure (2) for calculating the subthreshold swing (SS).

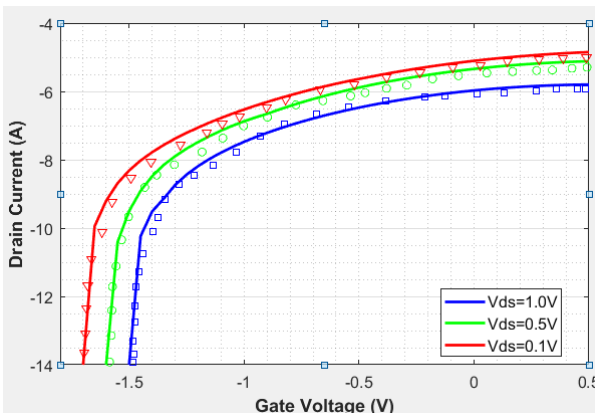


Figure 2: Drain Current (Log Scale) as a function of Gate-to-Source Voltage. Solid line represents simulation results.

B. Output Characteristics

We also calculate I_{D} for several values of V_{GS} within the range of -1 V to 0.5 V and obtain the relationship between drain current and drain voltage as shown in figure (3).

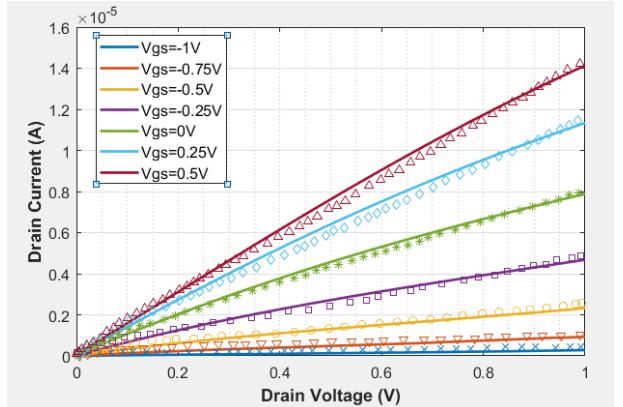


Figure 3: Drain Current as a function of Drain-to-Source Voltage. Solid line represents simulation results.

The comparison between the experimental data extracted from ATLAS-TFET[2] (marked by various symbols) and the data obtained from our analytical model show good match with very little discrepancy.

IV. CONCLUSION

Our analytical model is derived using charge distribution of the device and applying Kane's generation model for calculating the drain current. It is shown that after threshold voltage is crossed; BTBT mechanism dominates the current flow. Also, we show using our model that this device exhibits very low average subthreshold swing, low leakage current and high ON/OFF ratio compared to other conventional TFETs. The characteristics obtained from our analytical model are in close agreement with the experimental data of ATLAS-TFET.

ACKNOWLEDGMENT

The authors acknowledge the support and encouragement from the department of Electrical and Electronic Engineering of Bangladesh University of Engineering and Technology.

REFERENCES

- [1] W. Cao, J. Kang, D. Sarkar, W. Liu, and K. Banerjee, "2D Semiconductor FETs - Projections and Design for Sub-10 nm VLSI," IEEE Trans. Electron Devices, vol. 62, no. 11, pp. 3459–3469, 2015.
- [2] D. Sarkar et al., "A subthermionic tunnel field-effect transistor with an atomically thin channel," Nature, vol. 526, no. 7571, pp. 91–95, 2015.
- [3] K. Cao, W.; Kang, J; Banerjee, "2D/3D Tunnel-FET: Toward Green Transistors and Sensors," ECS Trans., vol. 77, no. 5, pp. 185–189, 2017.
- [4] K. K. Bhuwalka, S. Sedlmaier, A. K. Ludsteck, C. Tolksdorf, J. Schulze, and I. Eisele, "Vertical tunnel field-effect transistor," IEEE Trans. Electron Devices, vol. 51, no. 2, pp. 279–282, 2004.
- [5] E. O. Kane, "Theory of tunneling," J. Appl. Phys., vol. 32, no. 1, pp. 83–91, 1961.
- [6] L. H. Chien, Nguyen Dang; Shih, Chun-Hsing; Hoa, Phu Chi; Minh, Nguyen Hong; Hien, Duong Thi Thanh; Nhung, "Theoretical evaluation of maximum electric field approximation of direct band-to-band tunneling Kane model for low bandgap semiconductors," J. Phys. Conf. Ser., vol. 726, 2016.

Mathematical modelling of stresses in graphene polymer nanocomposites under static extension load

E Kirilova¹, T Petrova^{1,3}, W Becker², J Ivanova³

¹Institute of Chemical Engineering, Bulgarian Academy of Sciences, Acad. G. Bonchev str., Bl.103, 1113 Sofia, Bulgaria

² Institute of Structural Mechanics, TU Darmstadt, Franziska-Braun-Str. 7, L5|01 347a, 64287 Darmstadt, Germany

³ European Polytechnical University, 2300 Pernik, Bulgaria

Corresponding author e-mail: ivanova@imbm.bas.bg , eshopova@gmail.com

Abstract

In this study a two-dimensional theoretical model describing the interfacial stress transfer at adhesively bonded monolayered graphene/polymer nanocomposite subjected to static extension load, is presented. The governing forth order ordinary differential equation with constant coefficients for the axial stress in the first layer is obtained using a variational method. Other stresses in the remaining layers are obtained through the stress of the first layer and its derivatives. The analytical results for a given structure are illustrated in figures. The parametric analysis for influence of static load and geometry on the stresses in the considered structure is performed.

Key words: nanocomposite, graphene, polymer, interface shear stress transfer

High yield assembly of Cobalt nanowires using floating electrode dielectrophoresis

Sachin Kumar Singh

Department of Mechanical and
Industrial Engineering
University of Illinois at Chicago
Chicago, IL 60607, USA
ssing25@uic.edu

Jayasimha Atulasimha

Department of Mechanical and Nuclear
Engineering
Virginia Commonwealth University
Richmond, VA 23284, USA
jatulasimha@vcu.edu

Md Ruhul Amin Shikder

Department of Mechanical and
Industrial Engineering
University of Illinois at Chicago
Chicago, IL 60607, USA
mshikd2@uic.edu

Justin L. Drobitch

Department of Electrical and Computer
Engineering
Virginia Commonwealth University
Richmond, VA 23284, USA
drobitchjl@mymail.vcu.edu

Supriyo Bandyopadhyay

Department of Electrical and Computer
Engineering
Virginia Commonwealth University
Richmond, VA 23284, USA
sbandy@vcu.edu

Arunkumar Subramanian

Department of Mechanical and
Industrial Engineering
University of Illinois at Chicago
Chicago, IL 60607, USA
sarun@uic.edu

The isolation and manipulation of individual nanomaterials from macroscopic agglomerates and their integration into functional systems offer a pathway to realize devices in application areas spanning spintronics, nanoelectronics, energy storage, and sensing. Among different nanoassembly techniques reported so far, dielectrophoresis (DEP) enables device integration at a single nanowire (NW) or nanotube level [1]. In this paper, we will present results from a floating electrode dielectrophoresis (FE-DEP) methodology for assembly of Cobalt NWs.

On-chip DEP assembly involves the capture of NWs from its colloidal suspension using an electric field generated across arrays of nanoelectrode pairs. In this effort, the electric field is generated by applying an AC potential across lithographically defined gold nanoelectrode pairs. In FE-DEP [2,3], only one set of these electrodes is connected to an assembly bias (V_{AC}), while the opposing set of electrodes are held at a floating potential with respect to the underlying substrate, which is electrically grounded, as shown in Figure 1 (a). Figure 1(b) shows a representative image of a Cobalt NW deposited on a silicon chip using FE-DEP. While we have realized assembly of NWs through this methodology, the assembly yields, or the

percentage of electrode locations in the array that yield successfully bridging Co NWs, is low (less than 10%). In order to increase and optimize this yield, we will employ a 3D nano-electrokinetic model to establish the process parameters such as nanowire dimensions, electrode design, applied potential / frequency, deposition time, and suspension properties. This model will thereafter be leveraged to design and fabricate systems that advance the yield capability for single NW isolation on silicon chips using FE-DEP.

A. 3-D nanoelectrokinetic model

A 3D numerical model, which is based on a recent report [4], will be employed to examine the assembly of Co NW over FE-DEP based on-chip devices. This would involve a calculation of the electric field distribution within the chip system using a FEM model in COMSOL Multiphysics 5.4a. A representative electric field distribution around a FE-DEP electrode pair is shown in Figure 1(c). The largest electric field gradients are observed around the edges of the biasing electrode. This electric field distribution will thereafter be used in a MATLAB 2018b script to calculate the trajectory of a given NW around the electrode pair (using the methodology described in Singh et. al. [4]). This would involve evaluation of translational and rotational velocity, based on the DEP force and torque fields experienced by the NW in the vicinity of the electrode pair.

B. FE-DEP Predictions

The predicted trajectory of a representative 2 μm long and 20 nm diameter Co NW, which starts from 8 different locations in the FE-DEP workspace, is shown in Figure 2(a). It can be seen that for 5 of these starting locations, the NW is mainly in contact only with the biasing electrode. This is because of the asymmetry in FE-DEP electric field gradients, and therefore results in cantilevered (undesirable) NW assembly. The remaining 3 locations enable a bridging assembly of the NW between the two electrodes and is a desired outcome. Furthermore, most of the NWs in the region above the biasing electrode lead to deposition of NWs in the cantilevered mode, and NWs in region above the floating electrode are deposited in the bridging (i.e., desired) mode.

C. High yield single NW assembly using patterned resist layer

Based on the calculated trajectories for NWs starting from different locations in the computational domain, we can lithographically pattern a polymeric resist layer to control the volume from which a Co NW can be sourced. This would

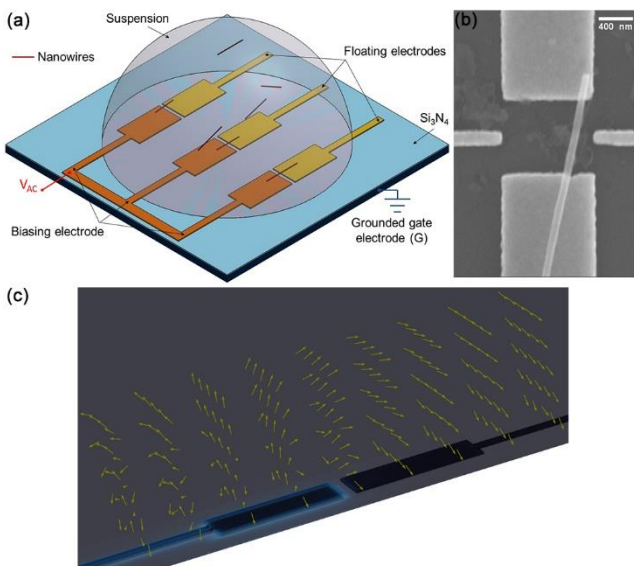


Figure 1: (a) Schematic illustration of the floating electrode (FE-DEP) chip design, (b) SEM image showing single Co NW deposited at an electrode site using FE-DEP, (c) electric field distribution around electrode pair along with normalized electric field vectors.

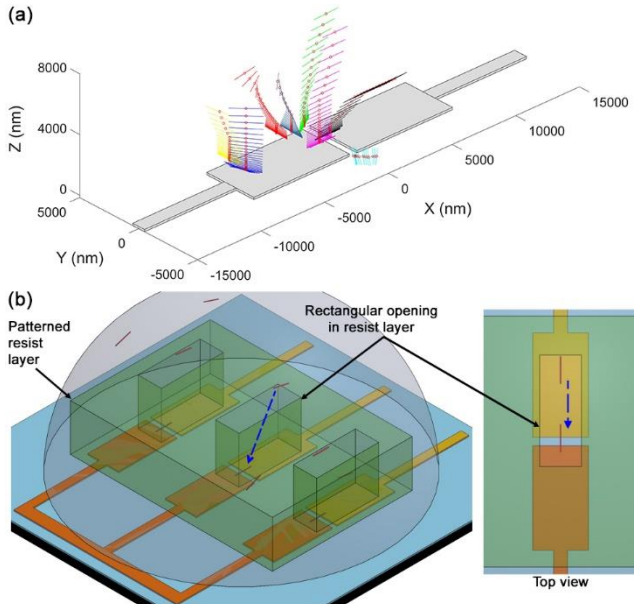


Figure 2: (a) Predicted trajectories for NWs starting from starting locations and their eventual deposition locations during FE-DEP, (b) design of patterned resist layer enabling high yield deposition of single NW using FE-DEP.

confine the NW deposition to occur only in the bridging mode and would prevent cantilevered deposition of NWs. This is achieved by physically masking the starting locations that remain within regions of the workspace that result in undesirable assembly. A representative patterned resist layer enabling high yield deposition of Co NW in bridging mode is schematically shown in Figure 2(b). It can be seen that the opening in reservoir needs to be positioned asymmetrically and have a larger overlap volume with respect to the floating electrode. Furthermore, by controlling the concentration of NWs in the suspension and by performing the FE-DEP for a predefined deposition time, we can ensure that only a single NW located within the patterned reservoir deposits in the bridging mode. This effort would result in assembly of single Co NW arrays, and achieve high yields similar to the other deposition approach outlined in Ref. [5]. In this paper, we will determine the appropriate resist pattern for high-yield assembly and then, determine the assembly process parameters.

D. Conclusions

A nanoelectrokinetic model will be presented to examine the assembly of Co nanowires onto pre-fabricated electrodes using FE-DEP. The model utilizes NW properties, dimensions, starting location, electrode design, applied electric field, suspension properties and deposition time to predict its trajectory and eventual deposition location. The model will thereafter be used to present a strategy for achieving high-yield assembly of single Co NWs.

ACKNOWLEDGMENT

The authors acknowledge support for this work, in part, from the National Science Foundation under Grant No. 1609303. Use of the Center for Nanoscale Materials, an Office of Science user facility, was supported by the U.S. Department of Energy, Office of Science, Office of Basic Energy Sciences, under Contract No. DE-AC02-06CH11357. The authors would specifically like to thank Dr. Ralu Divan, Ms. Suzanne Miller, and Dr. Dafei Jin for the technical support and training associated with the use of nanofabrication and characterization capabilities at the Center for Nanoscale Materials.

REFERENCES

- [1] Z. yang, M. Wang, Q. Zhao, H. Qiu, J. Li, Z. Li, and J. Shao, “Dielectrophoretic-assembled single and parallel-aligned Ag nanowire-ZnO-branched nanorod heteronanowire ultraviolet photodetectors”, *ACS Appl. Mater. Interfaces*, vol. 9, pp. 22837-22845, 2017.
- [2] B. R. Burg, V. Bianco, J. Schneider, and D. Poulikakos, “Electrokinetic framework of dielectrophoretic deposition devices”, *J. Appl. Phys.*, vol. 107, pp. 124308, 2010.
- [3] N. K. R. Palapati, E. Pomerantseva, and A. Subramanian, “Single nanowire manipulation within dielectrophoretic force field in the sub-crossover frequency regime”, *Nanoscale*, vol. 7, pp. 3109-3116, 2015.
- [4] S. K. Singh, N. Aryaan, M. R. A. Shikder, B. W. Byles, E. Pomerantseva, and A. Subramanian, “A 3D nanoelectrokinetic model for predictive assembly of nanowire arrays using floating electrode dielectrophoresis”, vol. 30, pp. 025301, 2019.
- [5] M. Collet, S. Salomon, N. Y. Klein, F. Seichepine, C. Vieu, L. Nicu, and G. Larrieu, “Large-scale assembly of single nanowire through capillary assisted dielectrophoresis”, *Adv. Mater.*, vol. 27, pp. 1268-1273, 2015.

Morphological analysis and size-based profiling of nanoscale vesicles by scanning electron microscopy

1 Sara Cavallaro

2 Department of Applied Physics
 3 KTH Royal Institute of Technology
 4 Stockholm, Sweden
 5 saracav@kth.se

6 Kristina Viktorsson

7 Department of Oncology/Pathology
 8 Karolinska Institutet
 9 Solna, Sweden
 10 kristina.viktorsson@ki.se

11 Federico Pevere

12 Department of Solid State Electronics
 13 The Ångström laboratory, Uppsala
 14 University
 15 Uppsala, Sweden
 16 federico.pevere@angstrom.uu.se

17 Petra Hååg

18 Department of Oncology/Pathology
 19 Karolinska Institutet
 20 Solna, Sweden
 21 petra.haag@ki.se

22 Jan Linnros

23 Department of Applied Physics
 24 KTH Royal Institute of Technology
 25 Stockholm, Sweden
 26 linnros@kth.se

27 Apurba Dev

28 Department of Solid State Electronics
 29 The Ångström laboratory, Uppsala
 30 University
 31 Uppsala, Sweden
 32 apurba.dev@angstrom.uu.se

33 Extracellular vesicles (EVs) are nanosized vesicles (30–
 34 2000 nm in diameter) released by cells and enclosed by a lipid
 35 bilayer.¹ Small EVs (sEVs), a subclass of EVs also called
 36 exosomes, are secreted from cells of different origin,
 37 including tumor cells, via the endolysosomal pathway. They
 38 have attracted considerable interest as a suitable biomarker
 39 for cancer diagnostics, because they reflect their cells of origin
 40 and are abundant in body fluids, offering a promising option
 41 for early cancer detection based on liquid biopsies.² The
 42 analysis of the EV size distribution can reveal useful
 43 information about their role³ in collective analyses, i.e.
 44 whether there is a link between the particle size and the role
 45 played in intercellular communication or cancer development,
 46 but also in single EV studies.³ Moreover, it may also enable to
 47 check the efficiency of the standard EV isolation procedures.⁴

48 Although different commercial techniques, such as
 49 Nanoparticle Tracking Analysis (NTA), flow cytometry and
 50 Tunable Resistive Pulse Sensing (TRPS),^{5–7} are already
 51 available on the market to analyze the EV size distribution,
 52 these methods are less accurate for sizes below 70 nm.⁷
 53 Furthermore, the resolution of these technologies are
 54 insufficient to distinguish between EVs and e.g. protein
 55 aggregates. In contrast, electron microscopy techniques, such
 56 as Scanning Electron Microscopy (SEM), offer far better
 57 resolution (~1 nm), allowing structural investigation of EVs
 58 with greater details. However, the low throughput of these
 59 methods has been a main drawback, preventing them to be
 60 used for size profiling of EVs. In addition, EV fixation, a
 61 critical step necessary to preserve the EV shape for SEM
 62 analysis, is often difficult to reproduce.

63 Herein, we present a method to improve the throughput
 64 and reproducibility of EV analysis by SEM. The technique is
 65 then used to accurately analyze the EV size distribution in the
 66 size range up to 500 nm. Parallel analysis with NTA shows
 67 good agreement for sizes larger than 80 nm. However, the

68 particles below 80 nm are clearly missing in the NTA profile,
 69 indicating a significant limitation in EV analysis. The
 70 proposed SEM approach could hence easily overcome such
 71 limitation and improve the EV characterization. Furthermore,
 72 the method can be calibrated for reliable estimation of particle
 73 counts.

74 In this study, we developed a technique to immobilize the
 75 EVs on a substrate in order to reduce the particle loss during
 76 the preparatory steps required for SEM imaging.⁷ The
 77 substrate, a Si wafer, was functionalized following the
 78 protocol reported by Dev et al.⁸ up to the Glutaraldehyde (GA)
 79 step. The EVs spotted afterwards on the functionalized wafer
 80 created a covalent bond with the GA molecules, remaining in
 81 place even after multiple washing steps. After immobilization,

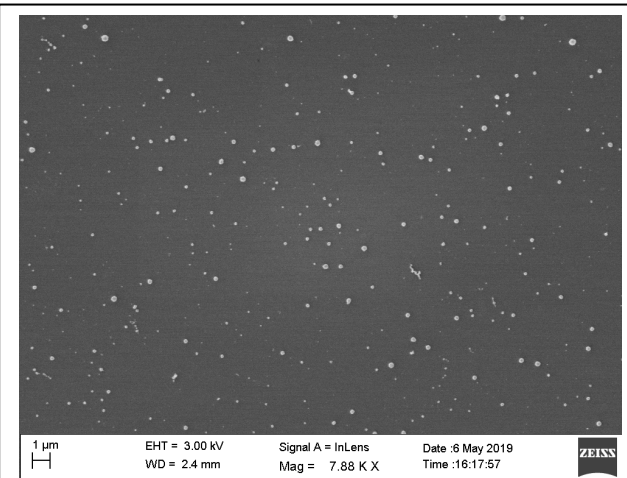


Fig. 1. SEM image of sEVs immobilized onto a GA-functionalized Si wafer and dehydrated using CPD. The sEVs were collected from the serum of a healthy patient and purified using a standard size exclusion chromatography method.

Critical Point Drying (CPD) was performed to dehydrate the biological specimens before SEM, while preserving their shapes.

Results

Fig. 1 shows a representative SEM image of the functionalized wafer and suggests that a large number of EVs remains attached to the substrate, even after many washing steps and CPD. This indicates that the functionalization protocol was efficient in keeping most particles attached, enabling size distribution analysis.

Fig. 2 compares the EV size distribution obtained with SEM and NTA. As shown, for EVs > 80 nm in diameter, the size peaks obtained with both techniques overlap, whereas for smaller EVs, the SEM showed peaks that could not be detected by NTA. These results suggest that SEM can be used to estimate the size distribution of the EVs over their entire size range, overcoming the intrinsic NTA limitations and improving on EV detection and characterization.

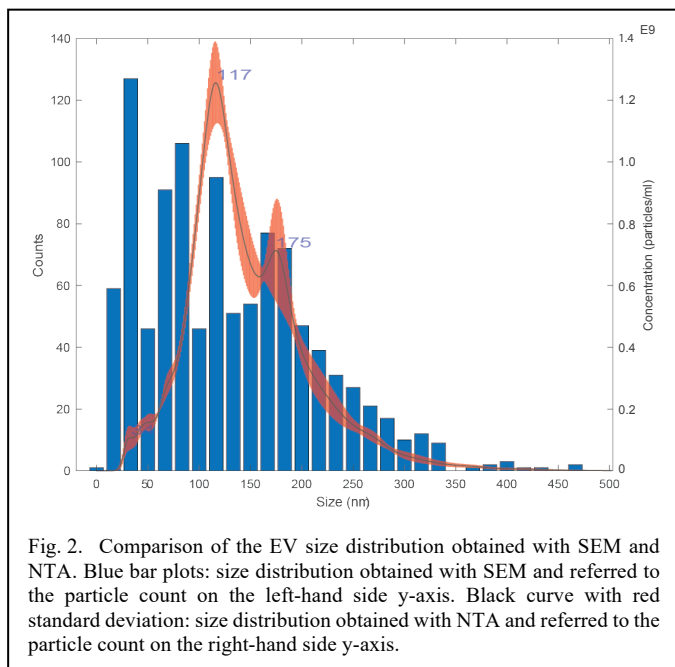


Fig. 2. Comparison of the EV size distribution obtained with SEM and NTA. Blue bar plots: size distribution obtained with SEM and referred to the particle count on the left-hand side y-axis. Black curve with red standard deviation: size distribution obtained with NTA and referred to the particle count on the right-hand side y-axis.

REFERENCES

- (1) El Andaloussi, S.; Mäger, I.; Breakefield, X. O.; Wood, M. J. A. Extracellular Vesicles: Biology and Emerging Therapeutic Opportunities. *Nat. Rev. Drug Discov.* **2013**, *12* (5), 347–357.
- (2) Cavallaro, S.; Horak, J.; Hägg, P.; Gupta, D.; Stiller, C.; Sahu, S. S.; Go, A.; Gatty, H. K.; Viktorsson, K.; Andaloussi, S. El; et al. Label-Free Surface Protein Profiling of Extracellular Vesicles by an Electrokinetic Sensor. *ACS Sensors* **2019**, *4*, 1399–1408.
- (3) Afm, U. C.; Sharma, S.; Rasool, H. I.; Palanisamy, V.; Mathisen, C.; Schmidt, K. M.; Wong, D. T.; Gimzewski, J. K. Structural-Mechanical Characterization of Nanoparticle Exosomes in Human Saliva, Using Correlative AFM, FESEM, and Force Spectroscopy. *ACS Nano* **2010**, *4* (4), 1921–1926.
- (4) Yáñez-Mó, M.; Siljander, P. R.-M.; Andreu, Z.; Bedina Zavec, A.; Borràs, F. et al. Biological Properties of Extracellular Vesicles and Their Physiological Functions. *Pdf. J. Extracell. Vesicles* **2015**, *4*, 27066 (1-60).
- (5) Momen-heravi, F.; Balaj, L.; Alian, S.; Tigges, J.; Toxavidis, V.; Ericsson, M.; Distel, R. J.; Ivanov, A. R.; Skog, J.; Kuo, W. P. Alternative Methods for Characterization of Extracellular Vesicles. *Front. Physiol.* **2012**, *3* (September), 1–8.
- (6) Akers, J. C.; Ramakrishnan, V.; Nolan, J. P.; Duggan, E.; Fu, C.; Hochberg, F. H.; Chen, C. C.; Carter, B. S. Comparative Analysis of Technologies for Quantifying Extracellular Vesicles (EVs) in Clinical Cerebrospinal Fluids (CSF). *CSF* **2016**, 1–11.
- (7) Pol, E. V. A. N. D. E. R.; Gardiner, C. Particle Size Distribution of Exosomes and Microvesicles Determined by Transmission Electron Microscopy, Flow Cytometry, Nanoparticle Tracking Analysis, and Resistive Pulse Sensing. *J. Thromb. Haemost.* **2014**, *12* (7), 1182–1192.
- (8) Dev, A.; Horak, J.; Kaiser, A.; Yuan, X.; Perols, A.; Björk, P.; Karlström, A. E.; Kleimann, P.; Linnros, J. Electrokinetic Effect for Molecular Recognition: A Label-Free Approach for Real-Time Biosensing. *Biosens. Bioelectron.* **2016**, *82*, 55–63.

Polarization Dependent Coloration in Metalo-Dielectric Nanopillars

Felix Vennberg

*Department of Applied Physics
KTH Royal Institute of Technology
Kista, Sweden
felixven@kth.se*

Ajith Padyana Ravishankar

*Department of Applied Physics
KTH Royal Institute of Technology
Kista, Sweden
aprav@kth.se*

Srinivasan Anand

Department of Applied Physics
KTH Royal Institute of Technology
Kista, Sweden
anand@kth.se

Optical metamaterials allows for manipulation of light through artificial sub-wavelength structures. Such materials can produce structural colors, where scattering and thin film interference, sometimes including absorption, generates the color. Furthermore, it has been demonstrated that the optical responses from dielectric and metallic metamaterials with asymmetrical structures are sensitive to the polarization of incoming radiation [1, 2]. Here we propose a polarization sensitive system of metalo-dielectric InP nanopillars produced by a single step, wafer scale fabrication process. Interesting optical properties have been observed from these nanopillar assemblies, such as structural colors and anti-reflection. These spectral characteristics in the reflectance are sensitive to the shape and dimensions of the nanopillars. In this work, we show that the reflected structural color from the pillars depend on incidence angle and polarization of the incoming radiation.

Self-assembled InP nanopillars are fabricated using ion beam assisted sputtering of InP [3]. The shape and dimensions of the nanopillars are controlled by tuning process parameters such as sputter duration, substrate temperature and ion energy. Additionally, tilted nanopillars can be obtained by changing the ion beam incidence angle. The fabricated nanopillars consist of an In rich cap on top of an InP stem and the spatial arrangement of the nanopillars is disordered.

Angle and polarization dependent optical reflectance measurements are performed and the results are explained with electromagnetic simulations using the finite difference

time domain method. For nanopillars with an average height of 420 nm and In cap radius \sim 90 nm the spectral dip position in the reflectance shifts with polarization of the incoming light and is more pronounced for higher incidence angles, shifting by as much as 200 nm at 45° incidence (see Fig. 1). Interestingly, the spectral dip position for the s-polarization blue shifts with increasing incidence angle, whereas it red shifts for the p-polarization. The shift is more dramatic for the s-polarization than for the p-polarization. The reflection is polarization independent at normal incidence due the radial symmetry of the pillars. To achieve polarization sensitivity in normal incidence we fabricate pillars that are tilted with respect to the substrate. Such pillars enable optical measurements with a larger span of incidence angles.

REFERENCES

- [1] Z. Li, Y. Chen, X. Zhu, et. al. “Polarization-dependent scattering properties of single-crystalline silicon nanocylindroids”, *Opt. Mater. Express* 8, 503-510, 2018
- [2] R. Verre, M. Svedendahl, N. Odebo Länk, Z. J. Yang, G. Zengin, T. J. Antosiewicz, and M. Käll, “Directional Light Extinction and Emission in a Metasurface of Tilted Plasmonic Nanopillars”, *Nano Lett.* 16 (1), 98-104, 2016
- [3] Sanatinia, R., Berrier, A., Dhaka, et. al. “Wafer-scale self-organized InP nanopillars with controlled orientation for photovoltaic devices”, *Nanotechnology*, 26(41), 2015

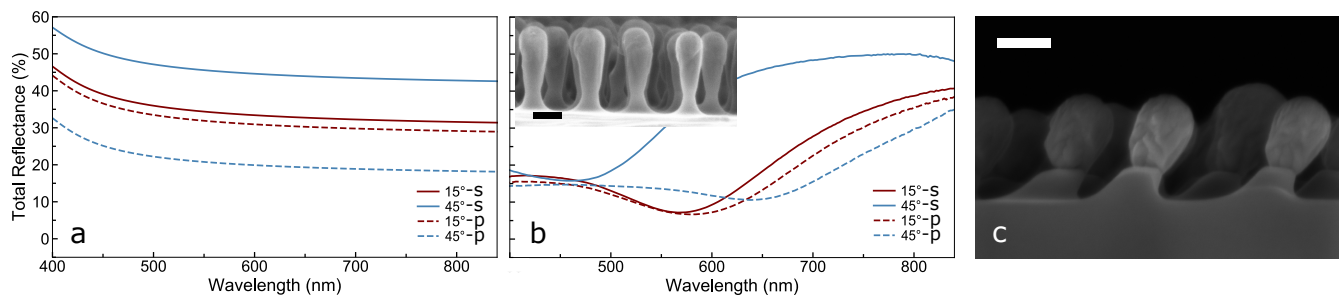


Figure 1. Influence of incident angle ($15^\circ, 45^\circ$), polarization (s,p) and surface structuring on the reflectance of InP. **a** Total reflectance from plain InP substrate. **b** Total reflectance from straight self-assembled In/InP nanopillars. Inset contains SEM image of nanopillars (scale bar 150 nm). **c** SEM image of tilted nanopillars (scale bar 200 nm).

1

2 Resonance fluorescence of GaAs/AlGaAs quantum dots with

3 near-unity photon indistinguishability

4
5
6
7
8
9
10
11
12
13
14
15
16
17
18
19
20
21
22
23
24
25
26
27
28
29
30
31
32
33
34
35
36
37
38
39
40
41
42
43
44
45
46
47
48
49
50
51
52
53
54
55
56
57
58
59
60
61
62
63
64
65
E. Schöll^{1*}, L. Hanschke², L. Schweickert¹, K. D. Zeuner¹, M. Reindl³,
S. F. Covre da Silva³, T. Lettner¹, R. Trotta⁴, J. J. Finley², K. Müller², A. Rastelli³,
V. Zwiller¹, and K. D. Jöns¹

10
11
12
13
14
15
16
17
18
19
20
21
22
23
1. Department of Applied Physics, Royal Institute of Technology, 106 91 Stockholm, Sweden
2. Walter Schottky Institut and Physik Department, Technische Universität München, 85748 Garching, Germany
3. Institute of Semiconductor and Solid State Physics, Johannes Kepler University Linz, 4040 Linz, Austria
4. Dipartimento di Fisica, Sapienza Università di Roma, I-00185 Roma, Italy

* Electronic address: escholl@kth.se

In recent years' single-photon based quantum technologies, offering the only reliable flying qubit to transmit quantum information, have gotten substantial attention not only from the scientific community but also from industrial stakeholders.

Since then GaAs quantum dots obtained by the Aluminium droplet etching technique have started to emerge as ideal candidates for these photonic quantum technologies, holding the record for the purest single-photon source [1], the brightest entangled photon pair source [2], the only on-demand source reaching entanglement fidelities near-unity [3], as well as showing quantum teleportation [4] and entanglement swapping [5,6]. However, another crucial parameter, near-unity indistinguishability of the emitted photons has proven to be elusive for these quantum emitters.

Here, we show for the first time [7] near-unity indistinguishability with a record-breaking raw visibility of $V = 95.0^{+5.0}_{-6.2}\%$ (Fig. 1a), without any data fitting nor correction for setup imperfections. We perform the first pulsed resonance fluorescence on these novel solid-state quantum emitters, revealing fast dynamics during the coherent control of the quantum mechanical V-system thanks to our low noise, high time resolution single-photon detectors (Fig. 1b).

Our results open the way for these emitters to be used as basic building blocks in quantum communication applications, such as sources for quantum repeaters.

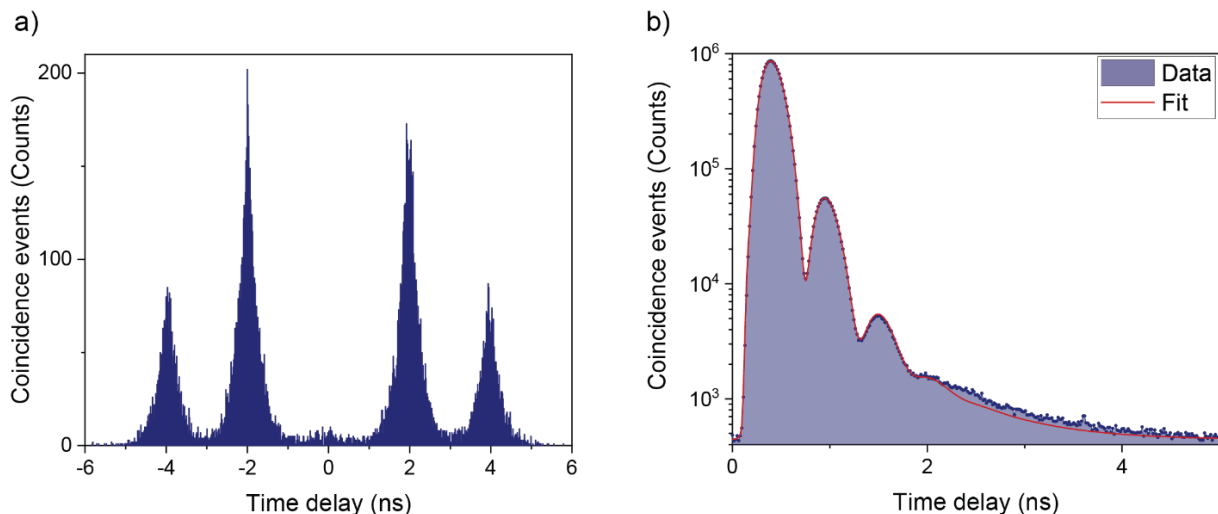


Figure 1: a) Hong-Ou-Mandel measurement under pulsed s-shell resonant excitation of the trion ($V = 95.0^{+5.0}_{-6.2}\%$), b) lifetime measurement (196 ± 2 ps) of the neutral exciton with oscillations due to the fine structure splitting ($7.44 \pm 0.05 \mu\text{eV}$).

[1] L. Schweickert et al., Appl. Phys. Lett. **112**, 093106 (2018).
[2] Y. Chen et al., Nature Communications **9**, 2994 (2018).
[3] D. Huber et al., Phys. Rev. Lett. **121**, 033902 (2018).
[4] M. Reindl et al., Sci. Adv. **4**, 4, eaau1255 (2018).
[5] F. Basso Basset et al., arXiv:1901.06646 (2019).
[6] M. Zopf et al., arXiv:1901.07833 (2019).
[7] E. Schöll et al., Nano Lett. **19**(4), 2404-2410 (2019).

Schrödinger Equation Based Quantum Corrections in Drift-Diffusion: A Multiscale Approach

Tapas Dutta, Cristina Medina-Bailon, Hamilton Carrillo-Nuñez, Oves Badami, Salim Berrada,

Vihar Georgiev, Asen Asenov

Device Modeling Group, School of Engineering

University of Glasgow, Glasgow G128LT, Scotland, UK.

E-mail: tapas.dutta@glasgow.ac.uk

Abstract—In this work, we report the development of a 3D drift-diffusion (DD) simulator for ultrascaled transistors with quantum corrections based on the solution of the Schrödinger equation. In a novel multi-scale simulation approach we use effective masses from tight-binding calculations, carrier mobility from the semi-classical Kubo-Greenwood formalism, and quantum corrections based on self-consistent Poisson-Schrödinger solution. This scheme has been implemented into the University of Glasgow TCAD tool NESS (Nano Electronic Simulation Software). The approach is validated in comparison to non-equilibrium Green's function (NEGF) simulations in the case of a nanowire field effect transistor with an elliptical cross section.

I. INTRODUCTION

Numerical transport solvers based on quantum formalisms have very high computational cost and are efficient for the simulation of devices with few nanometers in size. On the other hand, the classical drift-diffusion (DD) approach fails to reproduce the quantum confinement induced shift in the charge distribution in devices with scaled cross-sections like nanowire field effect transistor (NWFETs). A quantum corrected (QC) DD simulator provides a middle ground by ensuring a correct charge profile in the device at reduced computational costs. In this work, in order to facilitate the use of DD formalism to study nanodevices, we have developed and implemented a Poisson-Schrödinger based quantum corrected DD approach while considering the cross section dependence of the effective masses and the low-field carrier mobilities.

II. SIMULATION METHODOLOGY

Fig. 1(a) shows the device description and material parameters of a Si GAA NW MOSFET with elliptical cross-section used as an example device in this paper. Note that the simulator is capable of handling devices with different geometries. Fig. 1(b) summarizes the approach used in this work that has been integrated into the TCAD tool Nano-Electronic Simulation Software (NESS), developed at the University of Glasgow [1].

As semiconductor devices scale down, it is critical to take into account the dimension dependence of bandstructure and hence effective mass. The effective masses are calculated using full-band structure computed with the QuantumATK atomistic tool [2] and Effective Mass extractor module in NESS. The low-field mobility (which is input to the QC-DD simulator) for the NW is computed by means of the Kubo-Greenwood formalism [3] considering the most relevant 1D multisubband scattering mechanisms [4]. Then, the contributions of each mechanism are combined using the Matthiessen rule [5]. The DD simulator is a 3D tool based on the Scharfetter-Gummel discretization of the drift-diffusion equations using the Bernoulli functions. Different mobility degradation models are also implemented to capture the effects of doping (Masetti model [6]), and vertical and longitudinal electric

fields (Yamaguchi [7] and Caughey-Thomas [8] models respectively). For QC-DD we first solve self-consistently the 2D Schrödinger equation in planes perpendicular to transport and 3D Poisson equation in the whole device. The quantum charge is calculated using a top of the barrier approach [9]. Upon convergence, the resultant 3D quantum charge density is used to calculate a quantum correction term [10], [11]. This term is then used to generate a corrected potential which (instead of the classical potential obtained from Poisson equation) is used as a driving force in the continuity equation as illustrated in Fig. 2. Note that this approach does not use any fitting parameters unlike the density gradient or the effective potential methods.

III. RESULTS AND DISCUSSION

Fig. 3 shows the acoustic, optical, and total phonon limited low-field mobilities as a function of the sheet density. Within the gate bias range considered here, $0V < V_{GS} < 0.6V$, and their corresponding sheet density, the total mobility ranges from $650\text{-}757 \text{ cm}^2/\text{Vs}$. In Fig. 4 we show a comparison of the 2D charge distribution at the middle of the channel for the three cases: classical DD, QC-DD, and NEGF at convergence for $V_{GS} = 0.4V$, $V_{DS} = 0.05V$. The quantum nature of the QC-DD charge profile and its close match with the NEGF charge profile is evident.

We compare our current-voltage characteristics with those obtained from the more sophisticated coupled-mode space based NEGF solver in ballistic approximation [12] which is also implemented in NESS [1]. The results obtained are shown in Fig. 5. Using the baseline mobility from Kubo-Greenwood and typical parameters for the doping and field dependent mobility degradation models in the QC-DD provides reasonable predictions of the drain current at low drain bias. We obtain very close match with the ballistic NEGF current in the low and medium gate bias regime. At high gate bias, the ballistic NEGF current exceeds the QC-DD current, as expected. The QC-DD current remains lower than the classical DD current for the entire gate bias range.

IV. CONCLUSION

A Poisson-Schrödinger based quantum corrected drift-diffusion simulator has been implemented in our in-house 3D TCAD tool, NESS. The low-field mobility in the GAA nanowire FET is obtained from the 1D multisubband semi-classical module using the Kubo-Greenwood formalism. In addition to obtaining the correct charge profile, the carrier transport includes mobility models that take into account the impact of doping and electric field induced degradation. Our approach shows an excellent agreement in the weak and moderate inversion regimes when compared with NEGF simulations. At high drain bias the saturation velocity has to be calibrated in respect of multisubband 1D MC simulations which is the next objective in the NESS development.

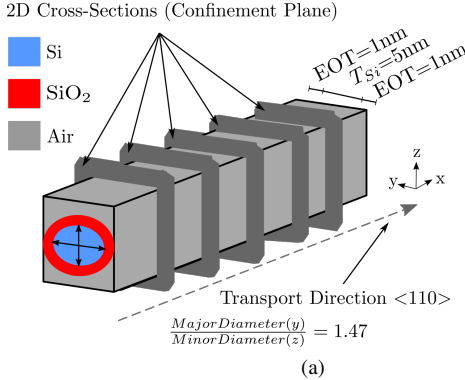


Fig. 1. (a) Sketch of an elliptical nanowire FET. The gate is 10 nm long and it is all-around the intrinsic region. The major and minor axis diameters are 5 nm and 3.4 nm. The transport occurs along the $\langle 110 \rangle$ crystallography direction. The source and drain are highly doped with $N_D = 10^{20} \text{ cm}^{-3}$. The oxide layer thickness is 1 nm. The device is at room temperature. (b) Scheme showing the flow of the approach proposed in this work. Once the nanowire effective masses are extracted, the low-field mobility is computed by means of the Kubo-Greenwood formalism. The mobility is then input in the DD equations for the charge and current and both are quantum corrected by including the impact of quantum confinement as described in Fig. 2.

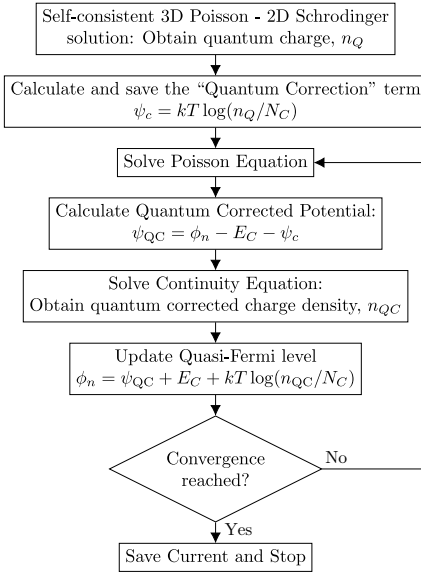


Fig. 2. Flow of the quantum-correction procedure. ψ_c , ψ_{QC} , and ϕ_n are respectively the quantum correction term, the quantum corrected potential, and the quasi-Fermi level. Note that all potential terms have the units of eV in this implementation.

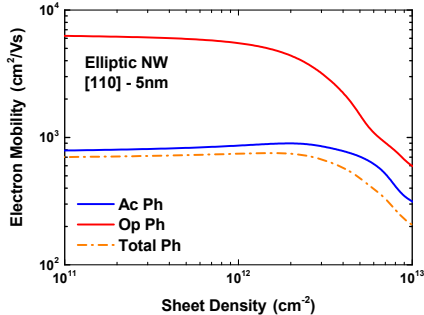


Fig. 3. Acoustic, optical and total low-field mobility as a function of the sheet density for the device in Fig. 1(a). The total mobility is calculated using the Matthiessen rule.

REFERENCES

- [1] S. Berrada, et al., SISPAD 2018
- [2] Quantum ATK version O-2018.06. Synopsys, Inc. 2018.
- [3] S. Jin, T.-W. Tang, and M. V. Fischetti, IEEE Trans. Elec. Dev., vol. 55, no. 3, 727-736, 2008.
- [4] T. Sadi et al., Materials, vol. 12, no. 124, 2019.
- [5] D. Esseni and F. Driussi, IEEE Trans. Elec. Dev., vol. 58, no. 8, pp. 2415-2422, 2011.
- [6] G. Masetti, et al., IEEE Trans. Elec. Dev., vol. 30, no. 7, pp. 764-769, July 1983.
- [7] K. Yamaguchi, IEEE Trans. Elec. Dev., vol. 26, no. 7, pp. 1068-1074, July 1979.
- [8] D. M. Caughey and R. E. Thomas, vol. 55, no. 12, pp. 2192-2193, Dec. 1967.
- [9] G. Fiori et al., IEEE Transactions of Nanotechnology, vol. 6, no. 5, pp. 524-529, Sept. 2007.
- [10] G. A. Kathawala and U. Ravaioli, IEEE IEDM, pp. 29.2.1-29.2.4., 2003.
- [11] A. Brown et al., Journal of computational electronics, vol. 9, no. 3, pp. 187-196, 2010.
- [12] A. Svizhenko et al., Journal of Applied Physics, vol. 91, pp. 2343, 2002.

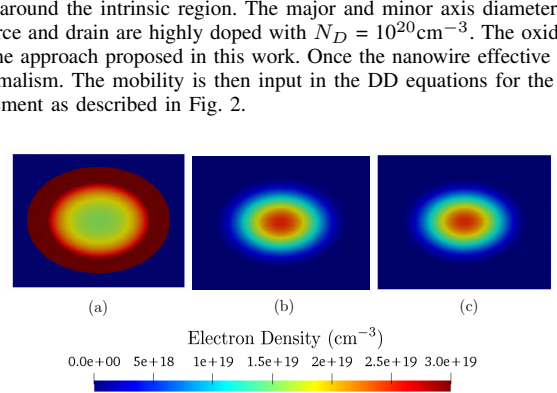
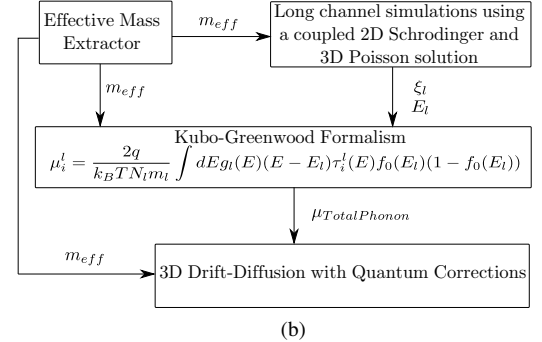


Fig. 4. 2D profile of electron density in the NWFET for (a) Classical DD, (b) QC-DD, and (c) NEGF in the plane normal to transport direction at the middle of the channel. $V_{GS} = 0.4$ V, $V_{DS} = 0.05$ V. In case of classical DD, the charge profile is maximum at the edges while for QC-DD and NEGF the maximum occurs at the center. A good match between the QC-DD and NEGF charge distributions is obtained.

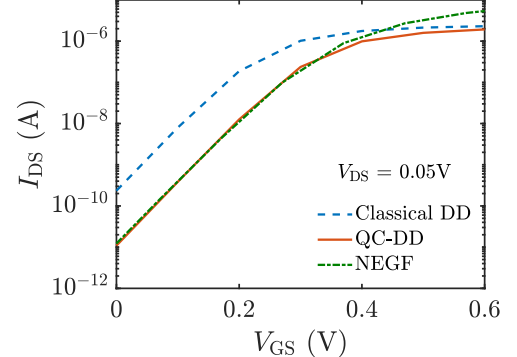


Fig. 5. $I_{DS} - V_{GS}$ characteristics computed using classical DD, QC-DD, and NEGF solvers. QC-DD matches very well with the NEGF current especially in weak and moderate inversion. At higher voltages, the QC-DD is noticeably lower than the ballistic NEGF current.

Observation of Highly Nonlinear Resistive Switching of $\text{Al}_2\text{O}_3/\text{TiO}_2$ -based Memristors at Cryogenic Temperature (1.5 K)

Yann Beilliard^{1,2*}, François Paquette^{1,2}, Frédéric Brousseau^{1,2}, Serge Ecoffey^{1,2}, Fabien Alibart^{1,2,3}, Dominique Drouin^{1,2}

¹Institut Interdisciplinaire d'Innovation Technologique (3IT), Université de Sherbrooke, Sherbrooke, Québec, Canada

²Laboratoire Nanotechnologies Nanosystèmes (LN2)—CNRS UMI-3463

³Institute of Electronics, Microelectronics and Nanotechnology (IEMN), Université de Lille, Villeneuve d'Ascq, France

*Correspondance: yann.beilliard@usherbrooke.ca – Orcid: <https://orcid.org/0000-0003-0311-8840>

Abstract—In this paper, we investigate the behavior and performance of $\text{Al}_2\text{O}_3/\text{TiO}_2$ -based memristors at cryogenic temperature, for future co-integration with silicon-based quantum systems. We report, for the first time, resistive switching of $\text{Al}_2\text{O}_3/\text{TiO}_2$ -based memristor devices at 1.5 K. The presence of negative differential resistance (NDR) is attributed to a metal-insulator-transition (MIT) of the Ti_4O_7 conductive filament at approximately 130 K. The selector-like characteristics induced by the MIT, involving an $I_{\text{ON}}/I_{\text{OFF}}$ ratio of 84, paves the way to selector-free cryogenic passive crossbars. The influence of metallic and insulating regimes on low resistance state and high resistance state is discussed. A thermal activation energy E_a of about 58 meV was found for the conduction mechanism below non-volatile switching regime.

A. Introduction

Continuous progress in silicon-based quantum technologies has led to promising high-quality silicon qubits working at cryogenic temperature. However, these increasingly complex quantum systems require cryogenic classical electronics to overcome scalability roadblocks [1]. In that scope, cryogenic memristors with reversible, non-volatile and highly non-linear resistance programming are desirable for co-integration of data storage units and crossbar-based computing paradigms on quantum devices. To this day, the lowest temperature at which HfO_2 and TiO_2 memristors were studied is 4 K [2]–[5]. In the present work, we investigate for the first time the current-voltage-temperature characteristics of $\text{Al}_2\text{O}_3/\text{TiO}_2$ -based memristors at temperature as low as 1.5 K.

B. Experiments

The devices studied in this work were fabricated through contact UV lithography. The 2 μm wide TiN bottom electrodes (BE) were realized with a BEOL-compatible damascene process in SiO_2 . The $\text{Al}_2\text{O}_3/\text{TiO}_2$ switching junction was deposited by ALD and PVD. The 2 μm wide Ti/Pt top electrodes (TE) were patterned using liftoff techniques. Electrical characterizations at ambient and cryogenic temperatures were carried out in a variable temperature insert (VTI) cryostat. 10 devices were wire bonded to a chip carrier and characterized from 1.5 to 300 K with an Agilent E5270B. The average resistances of BE and TE were measured at each temperature, allowing the calculation of the voltage V_{junction} seen by the switching junction, by subtracting the contribution of the electrodes to the total voltage V_{total} .

C. Results and Discussion

Fig. 1 shows I-V-T measurements of a memristor with V_{junction} in abscissa, demonstrating successful resistive switching at

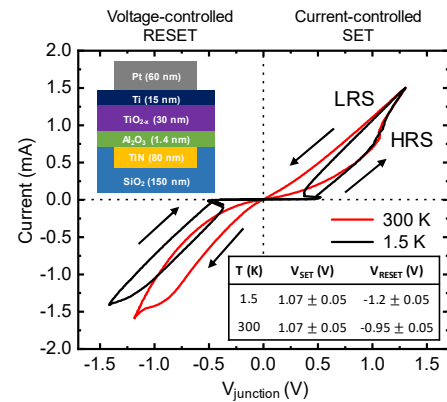


Fig. 1. Experimental resistive switching at 300 and 1.5 K. Negative differential resistance is visible at around 0.5 V. Insets show the devices cross-section and V_{SET} and V_{RESET} values as a function of temperature.

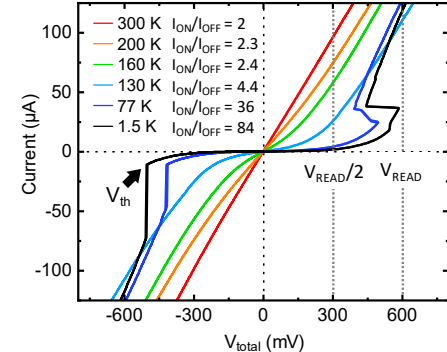


Fig. 2. I-V curves of a memristor in LRS between 300 and 1.5 K. The MIT of the filament appears between 160 and 130 K, associated to a threshold voltage V_{th} . $I_{\text{ON}}/I_{\text{OFF}}$ ratios measured at $V_{\text{READ}} = 0.6$ V and $V_{\text{READ}}/2$ are indicated. At 1.5 K, the $I_{\text{ON}}/I_{\text{OFF}}$ ratio is increased by a factor 42 compared to 300 K.

both 300 and 1.5 K. While progressive SET-RESET behavior, typical of TiO_2 -based memristors, is preserved at cryogenic temperature, only the RESET voltage V_{RESET} seems to be affected by temperature with a shift of around -0.25 V (see inset). Furthermore, the I-V curve at 1.5 K is highly non-linear and exhibits a negative differential resistance (NDR) behavior around 0.5 V. To further investigate these temperature-induced phenomena, we conducted back and forth low current/voltage sweeps on memristors in low resistance state (LRS) at various temperatures. The results are visible in Fig. 2, with the total voltage V_{total} in abscissa. We can first observe a decrease in current values with temperature, with a highly nonlinear I-V characteristics beginning at 130 K. From that critical temperature down to 1.5 K, one can clearly observe current-

controlled NDR effects and sudden jumps in current during voltage-controlled sweeps. This behavior seems to be related to volatile switching mechanisms, as no hysteresis are visible. It has been demonstrated that the conductive filament of TiO_2 -based memristors is made of Ti_4O_7 [6], [7]. This Magnéti phase of titanium oxide is known to undergo abrupt increases in resistance at temperatures ranging from 155 down to 120 K [8], [9]. We therefore attribute the drastic temperature-related modification of the I-V curves to a metal-insulator-transition (MIT) of the conductive filament assisted by Joule heating. The presence of NDR during voltage-controlled sweeps in Fig. 1 can thus be explained by a voltage redistribution during the MIT, leading to a decrease of V_{junction} . The threshold voltage V_{th} associated to the MIT in Fig. 2 is inversely proportional to temperature, as more power is needed to heat up the filament to a critical temperature range of 120-155 K [9]. Similarly to room temperature MIT-based access devices using VO_2 or NbO_2 [10], the high nonlinearity of $\text{Al}_2\text{O}_3/\text{TiO}_2$ -based memristor at cryogenic temperature induced by the thermoelectrically triggered MIT of Ti_4O_7 paves the way to selector-free cryogenic passive crossbar architectures. In that scope, we calculated the $I_{\text{ON}}/I_{\text{OFF}}$ ratio as a function of temperature, measured from Fig. 2 with read voltages $V_{\text{READ}} = 0.6$ V and $V_{\text{READ}}/2$. The obtained values range from 2 to 84 between 300 and 1.5 K, with a significant increase around 130 K. In order to evaluate the influence of MIT on the resistive switching performance, the average resistances in low resistance state R_{LRS} and high

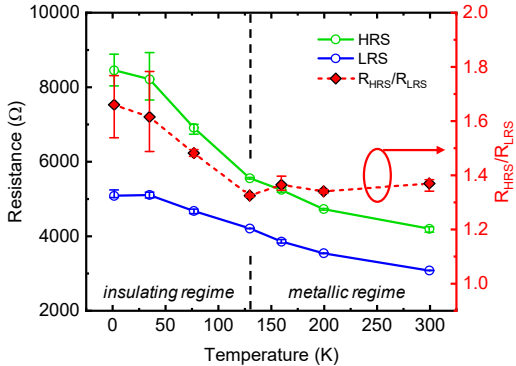


Fig. 3. Average resistance values of a device in LRS and HRS measured at $V_{\text{READ}} = 0.6$ V as a function of temperature. $R_{\text{HRS}}/R_{\text{LRS}}$ ratio values are plotted in red. Error bars represent minimum and maximum resistance and ratio values over multiple switching cycles.

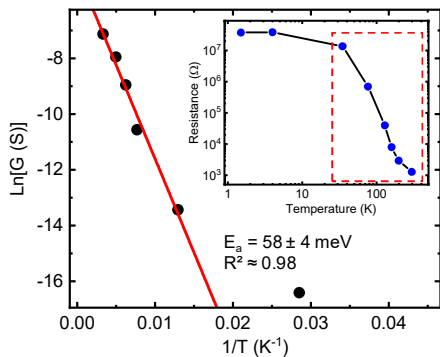


Fig. 4. Arrhenius plot of the logarithm of the zero-bias conductance of the switching junction in LRS between 300 and 77 K. The inset shows the plot of the associated zero-bias resistance of the junction from 300 to 1.5 K.

resistance state R_{HRS} were measured at $V_{\text{READ}} = 0.6$ V over multiple switching cycles. Fig. 3 shows the result along with $R_{\text{HRS}}/R_{\text{LRS}}$ values as a function of temperature. Two regimes can be distinguished, defined by the critical temperature of 130 K associated with the onset of MIT for our devices. When the filament is in metallic regime, $R_{\text{HRS}}/R_{\text{LRS}}$ has a relatively constant value of around 1.35, despite the slight increase of both R_{HRS} and R_{LRS} related to a temperature-dependant conduction mechanism. The insulating regime of the filament exhibits an increase of $R_{\text{HRS}}/R_{\text{LRS}}$ and higher variability of R_{HRS} values at lower temperatures. This raises the question of the impact of MIT on the stability of the SET processes, which should be investigated further. To better understand the influence of temperature on the conduction mechanism inside the junction below non-volatile switching regime, the Arrhenius plot of the zero-bias conductance of a device in LRS is shown in Fig 4. The inset shows the associated zero-bias resistances, calculated from I-V-T data with $V = V_{\text{junction}}$. The conduction mechanism follows the Arrhenius equation $G = G_0 \exp(-E_a/k_B T)$ with $R^2 \approx 0.98$ at temperatures ranging from 300 down to 77 K. The extracted thermal activation energy E_a is about 58 meV, which is in agreement with the work reported in [5]. Further studies should involve additional measurements of I-V-T data for in-depth investigations of switching mechanisms and conduction modes at cryogenic temperature.

ACKNOWLEDGMENT

This research was funded by Natural Sciences and Engineering Research Council of Canada (NSERC). We acknowledge financial supports from the EU: ERC-2017-COG project IONOS (# GA 773228).

REFERENCES

- [1] J. M. Hornibrook *et al.*, "Cryogenic Control Architecture for Large-Scale Quantum Computing," *Phys. Rev. Appl.*, vol. 3, no. 2, p. 024010, Feb. 2015.
- [2] S. Blonkowski and T. Cabout, "Bipolar resistive switching from liquid helium to room temperature," *J. Phys. D. Appl. Phys.*, vol. 48, no. 34, p. 345101, Sep. 2015.
- [3] C. Vaca *et al.*, "Study From Cryogenic to High Temperatures of the High- and Low-Resistance-State Currents of ReRAM $\text{Ni}-\text{HfO}_2-\text{Si}$ Capacitors," *IEEE Trans. Electron Devices*, vol. 63, no. 5, pp. 1877-1883, May 2016.
- [4] M. D. Pickett, J. Borghetti, J. J. Yang, G. Medeiros-Ribeiro, and R. S. Williams, "Coexistence of Memristance and Negative Differential Resistance in a Nanoscale Metal-Oxide-Metal System," *Adv. Mater.*, vol. 23, no. 15, pp. 1730-1733, Apr. 2011.
- [5] H. S. Alagoz, K. H. Chow, and J. Jung, "Low-temperature coexistence of memory and threshold switchings in $\text{Pt}/\text{TiO}_x/\text{Pt}$ crossbar arrays," *Appl. Phys. Lett.*, vol. 114, no. 16, p. 163502, Apr. 2019.
- [6] J. P. Strachan *et al.*, "Direct Identification of the Conducting Channels in a Functioning Memristive Device," *Adv. Mater.*, vol. 22, no. 32, pp. 3573-3577, Aug. 2010.
- [7] D.-H. Kwon *et al.*, "Atomic structure of conducting nanofilaments in TiO_2 resistive switching memory," *Nat. Nanotechnol.*, vol. 5, no. 2, pp. 148-153, Feb. 2010.
- [8] R. F. Bartholomew and D. R. Frankl, "Electrical Properties of Some Titanium Oxides," *Phys. Rev.*, vol. 187, no. 3, pp. 828-833, Nov. 1969.
- [9] A. D. Inglis, Y. Le Page, P. Strobel, and C. M. Hurd, "Electrical conductance of crystalline $\text{Ti}_{n-1}\text{O}_{2n-1}$ for $n=4-9$," *J. Phys. C Solid State Phys.*, vol. 16, no. 2, pp. 317-333, Jan. 1983.
- [10] G. W. Burr *et al.*, "Access devices for 3D crosspoint memory," *J. Vac. Sci. Technol. B, Nanotechnol. Microelectron. Mater. Process. Meas. Phenom.*, vol. 32, no. 4, p. 040802, Jul. 2014.

Conducting-Bridge RAM with metal containing ionic liquid filled in Artificially fabricated pore

Hiroshi Sato
Graduate School of Science
Tokyo University of Science
Katsushika-ku, Tokyo, Japan
Nanoelectronics Research Institute
National Institute of Advanced
Industrial Science and Technology
Tsukuba, Ibaraki, Japan
1519518@ed.tus.ac.jp

Hisashi Shima
Nanoelectronics Research Institute
National Institute of Advanced
Industrial Science and Technology
Tsukuba, Ibaraki, Japan
shima-hisashi@aist.go.jp

Toshiyuki Itoh
Graduate School of engineering
Tottori University
Tottori, Tottori, Japan
titoh@tottori-u.ac.jp

Kentaro Kinoshita
Graduate School of Science
Tokyo University of Science
Katsushika-ku, Tokyo, Japan
kkinosita@rs.tus.ac.jp

Yasuhide Naito
Nanoelectronics Research Institute
National Institute of Advanced
Industrial Science and Technology
Tsukuba, Ibaraki, Japan
ys-naitou@aist.go.jp

Yusei Honma
Nanoelectronics Research Institute
National Institute of Advanced
Industrial Science and Technology
Tsukuba, Ibaraki, Japan
yusei-honma@aist.go.jp

Hiroyuki Akinaga
Nanoelectronics Research Institute
National Institute of Advanced
Industrial Science and Technology
Tsukuba, Ibaraki, Japan
akinaga.hiro@aist.go.jp

Crosspoint structure of conducting-bridge RAM (CBRAM) with metal containing ionic liquid filled in artificially formed pore was fabricated successfully. Fast switching with low switching voltage (SV) and small SV dispersion were achieved. The high performance indicates the effectiveness of ionic liquids for memory applications.

INTRODUCTION

CBRAM is expected as a next generation memory and other applications such as neuromorphic devices. We previously reported that the switching endurance and the dispersion of operating voltages were improved by supplying ionic liquid (IL) to the polycrystalline metal oxide (poly-MO) layer of CBRAM with a Cu/poly-MO/Pt structure [1, 2]. The supplied IL is absorbed into gaps between crystal grains of the poly-MO layer due to capillary condensation and mediates the electrochemical diffusion of Cu. However, the gaps are naturally formed and their forms and surface properties are uncontrollable. Therefore, we fabricated a CBRAM device in which IL was filled in a pore artificially introduced in a solid memory layer and sandwiched between sputtered electrodes (IL-CBRAM). 0.4 M Cu-doped IL-CBRAM showed fast switching, $< 1.0 \mu\text{s}$, with low voltage, $< 3.0 \text{ V}$, and low SV dispersion, $< 0.6 \text{ V}$.

EXPERIMENT

Inset of Fig. 1 shows the schematic of IL-CBRAM device, which structure is Cu(50nm)/a memory layer with IL(30nm)/Pt(20nm)/Ta(1nm)/SiO₂. A pore with the diameter of 1 μm was fabricated in the memory layer by photolithography and filled the pore with IL. The Cu and Pt layers were deposited by DC sputter method, and the Ta layer by RF. As an IL, we selected Cu doped [bmim][Tf₂N], Cu[Tf₂N]₂ + [bmim][Tf₂N] (Cu-IL), where [bmim][Tf₂N] is one of the most popular ILs for electronic applications. We

prepared Cu-ILs with Cu concentrations, n_{Cu} , of 0.4 M. A voltage was applied to the Cu-electrode with the Pt-electrode grounded. Current-voltage (*I*-*V*) characteristics were measured using a semiconductor parameter analyzer (Agilent B1500A). For voltage sweep measurement, a current compliance value was fixed at 200 μA for set process. For pulse measurement, we inserted junction transistor (JFET) in series with a sample to limit the excess growth of filaments.

RESULTS AND DISCUSSION

A. Voltage sweep measurement

Fig. 1 show *I*-*V* characteristics of 0.4 M Cu doped IL-CBRAM, where 100 cycles out of 500 cycles were extracted. Bipolar resistive switching that set and reset occurred by applying positive and negative bias voltage, respectively, was observed. This indicates that IL-CBRAM is same stable operation as the conventional operation. Fig. 2 shows probability densities of V_{set} and V_{reset} for the IL-CBRAM. For comparison, probability densities of V_{set} and V_{reset} for a Cu/poly-HfO₂/Pt structure supplied with Cu 0.4 M IL [1]. Absolute values of both V_{set} and V_{reset} were smaller in the IL-CBRAM than in the Cu/poly-HfO₂/Pt. This suggests that Cu ions migrate on the surface of the pore. Since the artificially controlled pore contains no grain boundary, Cu ions can continuously migrate along the pore surface and switching voltages are reduced.

B. Pulse measurement

Figs. 3 shows how set speed(t_{set}) was evaluated. Figs. 3(a) and (b) show the height of applied voltage pulse and resistance after the pulse injection, respectively. First, at the pulse count of 1 (#1), a voltage pulse with the height of -2 V was applied to the IL-CBRAM and the resistance was reset to R_{HRS} , where the pulse width(t'_{w}) was fixed at 10^{-5} s . Next,

at the pulse #2-51, voltage pulses with a height from 0 V to 5.0 V in the increment of 0.1 V were applied as shown in Fig. 3(a). Here, the pulse width(t_w) was fixed at, ex., 10^{-6} s in this case. The resistance changed from high to low at the pulse #20 as shown in Fig. 3(b), showing that set switching occurred at the pulse height of 1.9 V for the t_w of 10^{-6} s. Repeating the series of measurements, ex., #52-102, we can obtain a set of pulse heights required to set IL-CBRAM and discuss them statistically. The same measurement was also performed for reset processes.

Fig. 4 shows pulse heights required to set and reset 0.4 M Cu doped IL-CBRAM, i.e., V_{set} and V_{reset} for pulse measurement, for various t_w . t_{set} and reset speed(t_{reset}) was 10^{-6} s for V_{set} of 2.4 V and 10^{-7} s for V_{reset} of 1.4 V, respectively. In particular, t_{reset} is more than two orders of magnitude faster than t_{set} if compared at the same absolute values of V_{set} and V_{reset} . For example, as shown by the green arrow in the figure, if the switching voltage is 1.4 V, t_{reset} was about three orders of magnitude faster than t_{set} . This is because metal ion solvated to IL strongly attracts the anion of IL. This prevent Cu ions from accessing the Cu electrode and inducing increased V_{set} [2] and may slow down t_{set} . Further improvement of switching speed can be expected by utilizing the high IL design to weaken the interaction of metal ions and anions that make up the IL.

SUMMARY

We fabricated a memory device in which an artificially controlled pore filled with ionic liquid was contained, IL-CBRAM. IL-CBRAM can operate with lower switching voltages than CBRAM with polycrystal grain boundaries, and high speed resistive switching less than 10^{-6} s was confirmed.

ACKNOWLEDGEMENT

This work was supported by NAGASE & CO., LTD. Colors & Advanced Processing Dept.

REFERENCES

- [1] K. Kinoshita, A. Sakaguchi, A. Harada, H. Yamaoka, S. Kishida, Y. Fukaya, T. Nokami and T. Itoh, "Improvement of switching endurance of conducting-bridge random access memory by addition of metal-ion-containing ionicliquid" Jpn. J. Appl. Phys. 56 04CE13, 2017.
- [2] H. Yamaoka, T. Yamashita, A. Harada, A. Sakaguchi, K. Kinoshita, S. Kishida, S. Hayase, T. Nokami and T. Itoh "Significantly Improved Performance of a Conducting-bridge Random Access Memory(CBRAM) Device Using Copper-containing Glyme Salt" Chem. Lett. 46, 1832-1835, 2017.

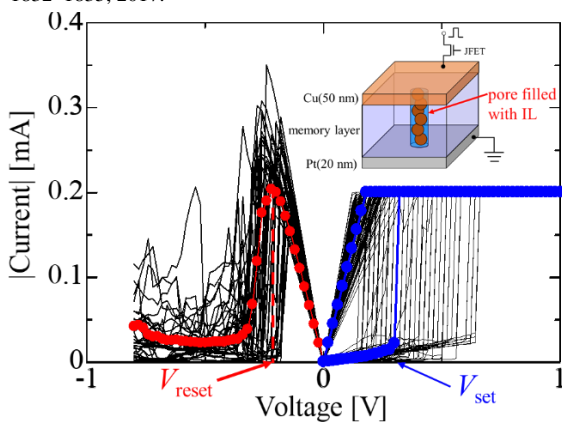


Fig. 1. I-V characteristics of 0.4 M Cu doped IL-CBRAM.
Inset: Schematic of memory structure.

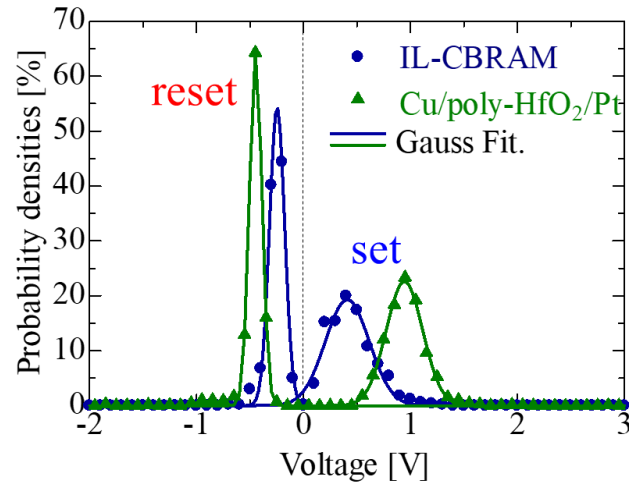


Fig. 2. Probability densities of V_{set} and V_{reset} for IL-CBRAM. Data for Cu/poly-HfO₂/Pt supplied with Cu 0.4 M IL [1] are shown for comparison.

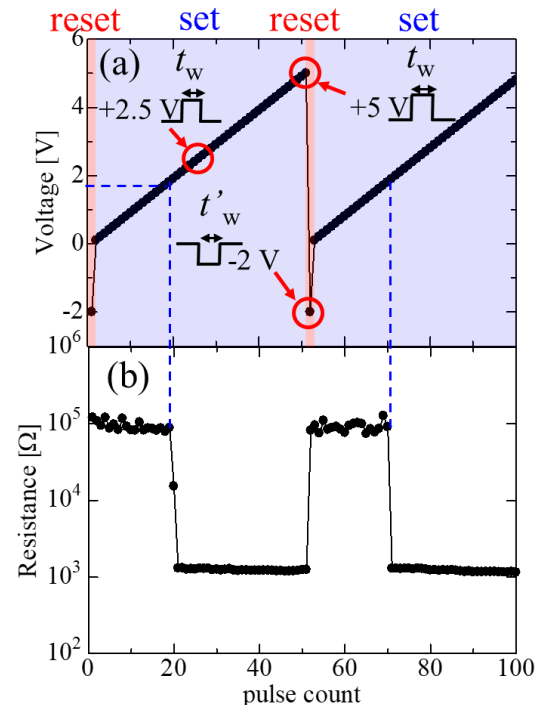


Fig. 3. (a) Height of applied voltage pulse and (b) resistance after the pulse injection.

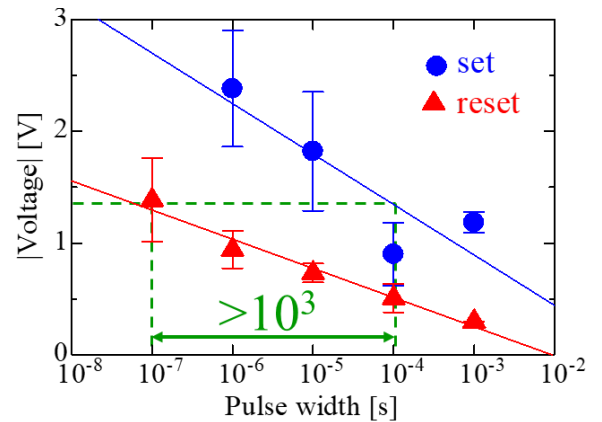


Fig. 4. Pulse heights vs. pulse width required to set and reset 0.4 M Cu doped IL-CBRAM

A novel miniaturized electrokinetic sensor applicable for biomarker detection

1 Hithesh Kumar Gatty

2 Department of engineering sciences
3 Uppsala University
4 Uppsala, Sweden
5 hithesh.gatty@angstrom.uu.se

6 Jan Linnros

7 Department of applied physics
8 KTH Royal Institute of Technology
9 Stockholm, Sweden
10 ORCID: 0000-0002-5260-5322

11 Apurba Dev

12 Department of engineering sciences
13 Uppsala University
14 Uppsala, Sweden
15 Apurba.dev@angstrom.uu.se

In this work, we present a novel electrokinetic biosensor chip fabricated on a silicon wafer. The novelty lies in the development of high pressure channel with integrated electrodes for the detection of biomarkers. The glass capping allows for a high-pressure input of the analyte up to 7 bar of pressure. In addition to biomarker detection, the sensor chip allows for multiplexed detection of biomarker when several sensors are used in parallel. Using this chip, we present the detection of Avidin molecule.

The enzyme-linked Immunosorbent Assay (ELISA) is a widely accepted clinical diagnostic tool for the detection and quantification of protein biomarker. However, in the modern world, robust technologies with personalized medicine are required to handle complex disease biomarkers. In addition, multiplexed detection of biomarkers with high sensitivity, selectivity and faster response time are required in the present day health care diagnostics. A capillary-based sensor for label-free and real-time detection of biomolecules has been demonstrated earlier [1,4]. Recently, electrical detection of cancer markers on a microchip using nanopore array has been demonstrated for several biomarkers [2]. Electrical detection of protein biomarkers was demonstrated by using functionalized beads and measuring the magnitude of resistance change across the microfluidic channel [3].

The concept and the detection principle is shown in Figure 1. Figure 2 describes the sensor chip design layout and assembly. The process flow is shown in figure 4 (a-f). A 100 mm silicon wafer with a 500 μ m thick is used as a substrate for processing the microchannels. Inlet and outlet ports are etched through using deep reactive ion etching (DRIE). Passivation of the surface of the walls is ensured by using thermal oxidation. The SiO₂ thus formed is also the active layer in the microfluidic channel. Sputter deposited platinum acts as electrodes of the sensor. Photograph of the fabricated chip showing three sensors on a die (Figure 2b). The sensor processing has a dimension of 20 μ m width, 9 μ m depth and 3 mm in length. The sensors are processed on a 11 mm \times 7 mm die chip. The

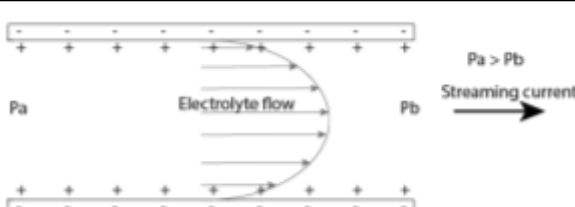


Fig 1: Schematic of electrolyte flow in a microchannel of the sensor. In a channel with a charged surface, a streaming current is generated when there is an electrolyte flow due to the pressure difference at the inlet and outlet ports. This streaming current is not only dependent on the surface charge but also on the size of the molecule present in the analyte. When a biomolecule binds to the surface of the channel, the streaming current is altered. This principle is used in the detection of biomolecules.

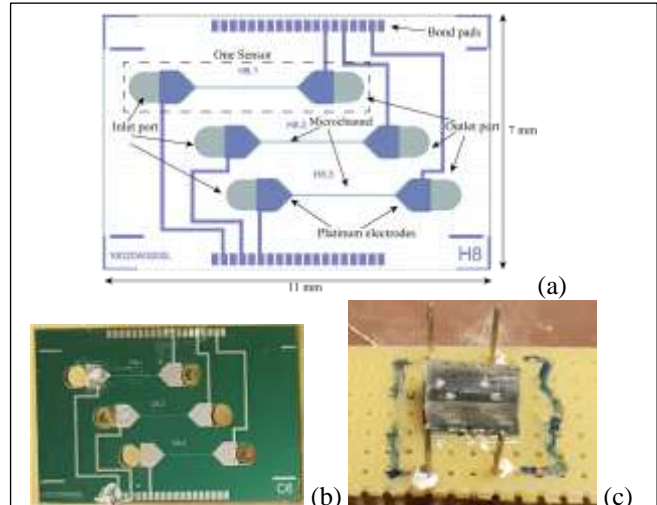


Fig 2: Electrokinetic biosensor (a) Schematic layout of the top view of the biosensor. There are three sensors that are processed and available for measurement. The platinum electrodes are placed at the inlet and outlet ports of the sensor. (b) Photograph of the fabricated chip showing three sensors on a die. The sensor has a dimension of 3000 μ m long rectangular microchannel, a width of 20 μ m and the depth of 9 μ m on the 11 mm \times 7 mm die chip. (c) Assembled chip showing the PDMS cover on a circuit board. The pins for electrical connections are shown are used for connecting with the external current measuring instrument.

Assembled chip showing the PDMS cover on a circuit board is shown in Figure 2c.

The measurement system consists of a fluid flow system which has PBS 0.1x solution and Avidin 9 nM that is switched

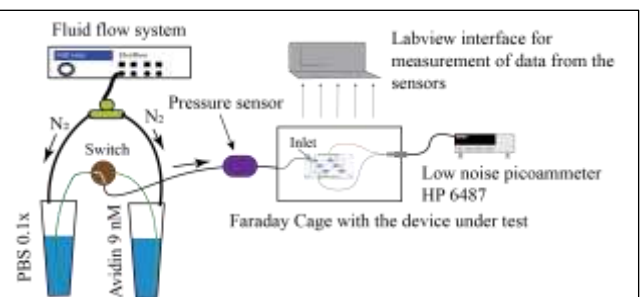


Fig 3: a Measurement system for detection of Avidin. The measurement system consists of PBS 0.1x solution and Avidin 9 nM that is switched alternately through the sensor. The sensor is sealed in a Faraday cage to avoid interference with external noise. A low noise Pico ammeter (Keithley HP6487) is used for measurement of low currents which, is then used for calculating the zeta potential. The fluid flow system controls the pressure of the analyte and buffers solution to the predetermined values.

alternately through the sensor as shown in figure 3. The sensor is sealed in a Faraday cage to avoid interference with any external noise. A low noise Picoammeter is used for measurement of currents in the range of picoamps. The fluid flow system controls the pressure of the analyte flowing

through the sensor.

Figure 5 presents the results of the characterization of the

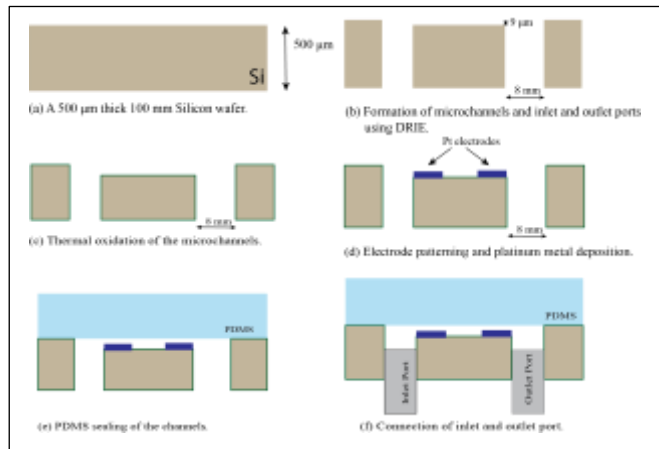


Fig 4 (a-f): Process flow for fabricating an electrokinetic sensor on a 100 mm silicon wafer. In order to get an individual sensor, the wafer is diced into 11 mm \times 7 mm chips. Each die contains three to four sensors.

sensor chip. The flow characterization of the sensor is shown in figure 5a. As expected a linear dependence on pressure vs the streaming current is observed as DI-water is pumped through the sensor. The slope is calculated to be 3.3pA/kPa. When PBS 0.1x solution is flown, the sensor response decrease to 0.85pA/kPa. This is due to reduced thickness of electric double layer at a higher salt concentration. In another measurement, the sensor was characterized with 9 nM concentration of Avidin. The response time for the

biomolecules to reach an equilibrium state was approximately 45 min. When PBS 0.1x is flown through the sensor after the equilibrium time has reached, the signal starts to decrease due to the unbinding of molecules present in the vicinity of the surface. The change in the zeta potential was calculated to be approximately 30 mV. The results show a promising step towards the detection and diagnosis of biomarkers. In addition, the effect of different oxide layer such as SiO_2 , Al_2O_3 and different channel dimension was investigated and the results show prospect for improved sensitivity as compared to our previously demonstrated commercial capillary based approach.

REFERENCES

- [1] A. Dev et al., "Electrokinetic effect for molecular recognition: A label-free approach for real-time biosensing," *Biosens. Bioelectron.*, vol. 82, pp. 55–63, Aug. 2016.
- [2] L. Duan and L. Yobas, "Label-Free Multiplexed Electrical Detection of Cancer Markers on a Microchip Featuring an Integrated Fluidic Diode Nanopore Array," *ACS Nano*, vol. 12, no. 8, pp. 7892–7900, Aug. 2018.
- [3] M. Javanmard, A. H. Talasaz, M. Nemat-Gorgani, F. Pease, M. Ronaghi, and R. W. Davis, "Electrical detection of protein biomarkers using bioactivated microfluidic channels," *Lab. Chip*, vol. 9, no. 10, p. 1429, 2009.
- [4] Sara Cavillaro et al "Label-Free Surface Protein Profiling of Extracellular Vesicles by an Electrokinetic Sensor", *ACS Sens.* 2019, 4, 5, 1399–1408.

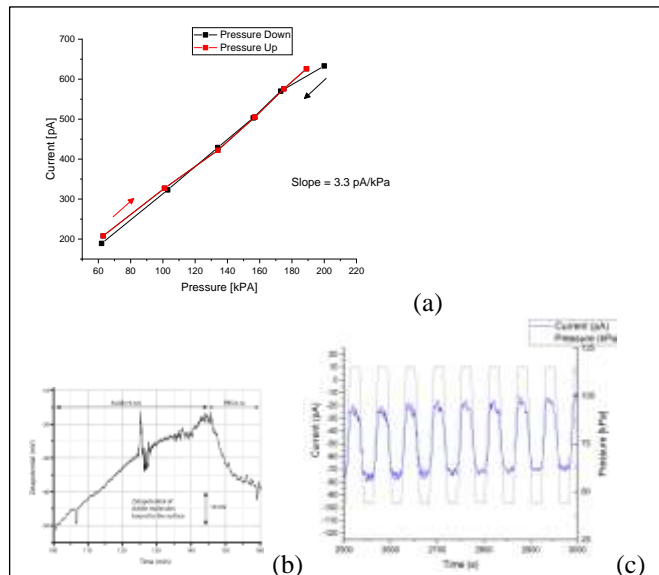


Fig 5: Graphs showing the characterization of the sensor. (a) The flow characterization of the sensor is shown in figure 5a. As expected a linear dependence on pressure vs the streaming current is observed as DI-water is pumped through the sensor. The slope is calculated to be 3.3pA/KPa. (b)Graph of the zeta potential vs time for Avidin at 9 nM concentration. The equilibrium time for the biomolecules to reach an equilibrium state is approximately 45 min. When PBS 0.1x is flown through the sensor after the equilibrium time has reached, the signal starts to decrease due to the unbinding of excessive molecules present in the vicinity of the surface. For 9 nM Avidin molecules approximately the signal is about 30 mV. (c) Graph shows the current vs pressure when a PbS 0.1x solution is flown through the sensor, response is approx. 0.85 pA/KPa

24GHz band printed silver nanowire radar antennas

Y. Kakuya
Research Division 2 Soken Inc.
14 Iwaya, Shimohasumi-cho, Nishio, Aichi
445-0012 Japan
E-mail: Yuuji_Kakuya@soken1.denso.co.jp

Dr H. Koga
The institute of Scientific and Industrial
Research Osaka University
8-1 Mihogaoka, Ibaraki, Osaka 567-0047,
Japan
E-mail: hkoga@eco.sanken.osaka-u.ac.jp

Dr K. Suganuma
The institute of Scientific and Industrial
Research Osaka University
8-1 Mihogaoka, Ibaraki, Osaka 567-0047,
Japan
E-mail: hkoga@eco.sanken.osaka-u.ac.jp

1. INTRODUCTION

Silver nanowires, a printable type of conductive material, are expected to be put into practical use in the field of printed electronics. We aim to realize a light transmitting 24GHz band radar antenna that can be mounted on a vehicle windshield using silver nanowires. However, since the conventional light transmission type antenna forms an antenna by stacking silver nanowires sparsely, the light transmittance and conductivity of the silver nanowire antenna have a trade-off relationship. Therefore the transmittance required for practical use in vehicles At 80%, there is a problem that the antenna performance is significantly deteriorated and can not be used as a radar. The purpose of this paper is to realize a 24GHz band silver nanowire radar antenna that can achieve both light transmittance and antenna performance.

2. METHOD

In order to achieve both light transmittance and antenna performance, first, the conductivity improvement of the silver nanowire material itself is realized. Specifically, we aim for a silver nanowire material with a transmission loss equivalent to bulk copper in the 24 GHz band. Next, the formation method of the silver nanowire antenna which can ensure antenna performance also in 80% of light transmittance is clarified.

2-1. Conductivity improvement of silver nanowire

It has been found that the conductivity of the silver nanowire wiring is proportional to the resistance R of the wiring. Here, the resistance can be expressed by Equation (1).

$$R = R_c + R_f + R_o \quad (1)$$

Where R is the DC resistance of the transmission line, and R_c is the resistance inherent to the material. R_f is the concentration resistance and R_o is the film resistance caused by contact between the materials.

We believed that removal of the Polyvinylpyrrolidone (PVP) covering the silver nanowire surface, which is the cause of film resistance, could make the film resistance $R_o \approx 0\Omega$. Therefore, we reveal the cleaning conditions of silver nanowires to remove PVP. [1][2]

The equation of concentration resistance R_f is given as Equation (2). [3]

$$R_f = \frac{\rho}{2a} \quad (2)$$

Where, ρ is the resistivity. a is the radius of contact between the silver nanowires. a can be thought of as a parameter

proportional to the total contact area between the silver nanowires.

Here, Hertz's equation is given as Equation(3).

$$a = \sqrt{\frac{3Pn(1-v^2)R}{4E}} \quad (3)$$

Where a is the contact radius of the silver nanowires, Pn is the applied pressure, R is the diameter of the silver nanowires, v is Young's modulus of silver, and E is Poisson's ratio.

Therefore, We clarify the condition of Pn that can reduce R_f .

2-2. Method of forming light transmissive radar antenna of silver nanowire.

An on-vehicle 24 GHz radar antenna is composed of an antenna element and Ground Plane (GND) (Fig. 1). When mounted on a windshield, it is essential to make the large GND area transparent from the viewpoint of the driver's visibility.

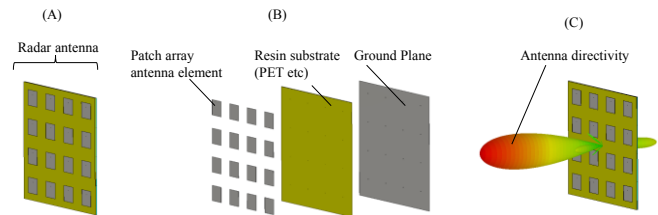


Fig. 1. (A) Radar antenna (B) Radar antenna structure (C) Radar antenna directivity

We considered that there is a GND area with high contribution to antenna performance and an area with low contribution. Therefore, we plan to increase the conductivity of only the GND area that has a high contribution to antenna performance.

First, the GND area having a high contribution to the antenna performance is clarified. For that purpose, electromagnetic field simulation is used to visualize the current on GND in the patch array antenna, and to clarify the area where the amount of current is large and the direction of the current (Fig. 2-A).

Next, in order to achieve both the transparency of the GND and the antenna performance, the GND is formed in the following configuration. That is, silver nanowires are stacked at a high density in an area having a large amount of current, and silver nanowires are stacked at a low density in an area having a small amount of current. Here, the GND

area where silver nanowires are stacked at low density is transparent, but the GND area where silver nanowires are stacked at high density is not transparent. Therefore, high conductivity thin line pattern made of silver nanowires are arranged in the current direction in the GND area where the current is concentrated (Fig. 2-B).

We clarify the condition of the pitch and width of the thin line pattern which can realize the antenna performance.

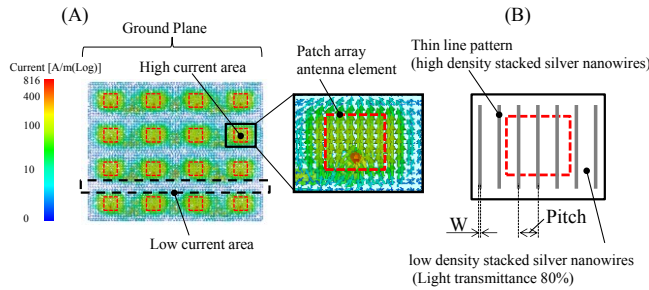


Fig. 2. (A) Current vector on the ground plane during antenna operation (B) Ground plane formation method for achieving both light transmittance and antenna performance

3. RESULT

A transmission line made of silver nanowire capable of realizing the same transmission loss as bulk copper in a frequency range of up to 40 GHz could be formed by washing removal (3,000rpm for 3min., 4 cycles) of PVP and pressure treatment (19MPa or more) (Fig. 3).

By arranging the conductive thin line pattern ($W = 20 \mu\text{m}$, $\text{Pitch} = 80 \mu\text{m}$) of the silver nanowires in the current direction, we revealed that the 24 GHz band silver nanowire radar antenna (80% light transmittance of GND) can operate as a radar (range measurement within 1 m of error, maximum detection distance 71 m @ 5.3 dBi)(Fig.4).

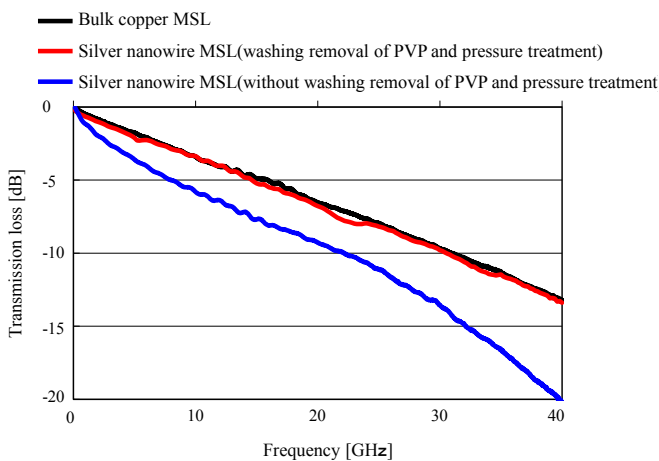


Fig.3. Transmission loss of printed silver nanowire microstrip line (MSL)

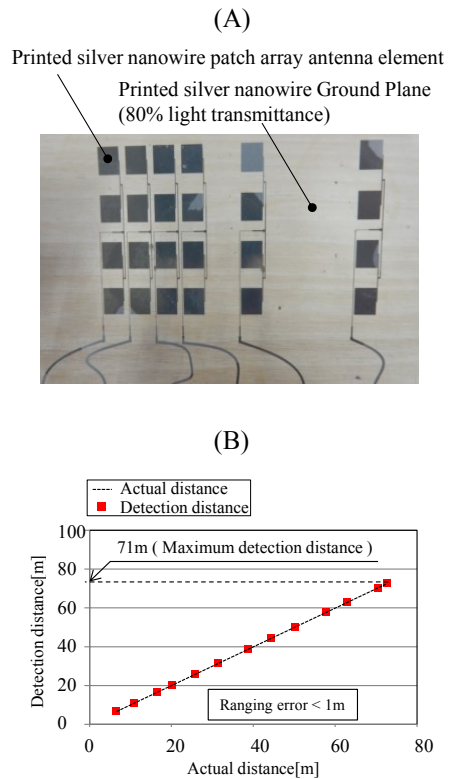


Fig. 4. (A) 24 GHz band silver nanowire radar antenna (B) Radar performance measured value

4. CONCLUSION

In the 24 GHz band, we clarified how to form a silver nanowire pattern that gives a same transmission loss as bulk copper. In addition, we clarified the antenna formation method of the silver nanowire which makes transparency and antenna performance compatible. This demonstrates that the 24GHz band radar antenna (the light transmittance of GND at 80%) can operate as a radar (range measurement within 1m of error, maximum detection distance of 71 m @ 5.3 dBi).

REFERENCES

- [1] J. Wang, "Silver Nanowire Electrodes: Conductivity Improvement Without Post-treatment and Application in Capacitive Pressure Sensors" Nano-Micro Lett. January 2015, vol 7, pp51-58
- [2] D. Langley, "Flexible transparent conductive materials based on silver nanowire networks: a review," Nanotechnology, 24, 45 (2013), 452001.
- [3] R. Holm, "Electric Contacts", 4th.Edit., pp60-71, Springer, New York(1967)

Wafer-level processing of a high aspect ratio single nanopore and measurement of DNA translocation

1 Hithesh Kumar Gatty

2 *Department of Engineering Sciences*
3 *Uppsala University*
4 *Uppsala, Sweden*
5 hithesh.gatty@angstrom.uu.se

6 Xuan Chung Nguyen

7 *Department of Applied Physics*
8 *KTH Royal Institute of Technology*
9 *Stockholm, Sweden*
10 nguyen2@kth.se

11 Miao Zhang

12 *Department of Applied Physics*
13 *KTH Royal Institute of Technology*
14 *Stockholm, Sweden*

15 Ilya Sychugov

16 *Department of Applied Physics*
17 *KTH Royal Institute of Technology*
18 *Stockholm, Sweden*

19 Jan Linnros

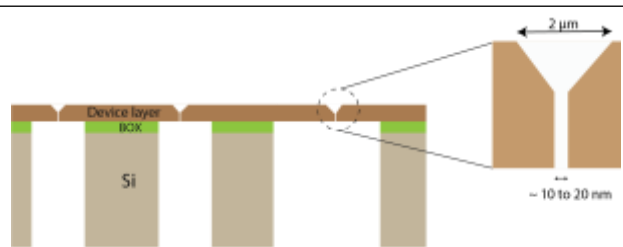
20 *Department of Applied Physics*
21 *KTH Royal Institute of Technology*
22 *Stockholm Sweden*
23 linnros@kth.se24 In this work, we present a two-step method for controlled
25 fabrication of high aspect ratio single nanopore on an SOI
26 substrate. An n-type device layer of 2 μm thick is used to
27 process nanopores in the range of 10 nm to 20 nm. The method
28 presented is repeatable, and can be processed on a large scale.
29 We use standard UV photolithography method on an SOI
30 wafer followed by electrochemical breakdown etching to
31 process nanopores. In addition, we present the electronic
32 measurement of DNA translocation through a single
33 nanopore.34 A low-cost method of fabricating a large scale high aspect
35 ratio nanopore down to 10 nm presents a unique opportunity
36 for measurements of DNA translocation. Controlled
37 fabrication of a nanopore using beam lithography is a well-
38 known method [1]. However, this method is expensive and is
39 slow in processing. Prior work on similar method has been
40 presented [2, 3]. In this method, a backside illumination is
41 used to induce the electrochemical etching together with an
42 applied bias. However, with several control elements that are
43 required to process the nanopores, it is often difficult to repeat
44 the process.45 In our work, we present an etching method without any
46 illumination called as breakdown electrochemical etching.
47 The controlled nanopore processing is achieved by
48 lithography on the surface of a 2 μm thick device layer
49 followed by a two-step etching method resulting in a high
50 aspect ratio nanopore with a diameter of approximately 10 to
51 15 nm as depicted in fig. 1. We have investigated and obtained
52 DNA translocation using these high aspect ratio nanopore
53 using a combination of electrical and optical methods.54 Each bias profile includes 2 regions: high bias (occurs
55 around first a few seconds) and low bias (occurs around a few
56 minutes later). The current during etching is also recorded. An
57 example of both voltage profile and current are showed in
58 fig 2 for a chip in the series.59 The SEM images in fig 3 show the single nanopores on the
60 backside of the device layer of some chips for different
61 voltage profiles. The amplitude of the low voltage region is
62 fixed at 5V for almost 15 mins. Both the amplitude and
63 duration of high bias region are important, and influence on
64 the diameter of these nanopores. By this method, the
65 nanopores of sizes of approximately 10 to 15 nm in diameter
are obtained. The nanopore diameters, as observed in the SEM
images, can be precisely controlled by varying the bias voltage
profile between the working and the counter electrode. This
method of processing nanopore is fast (~20 mins), requiresfewer control parameters (as compared to illumination
method).Using a single nanopore with the diameter of 25 to 30 nm
and an electrolyte with 0.1 M KCl, DNA strands of 1kbps
were translocated through a nanopore under an applied bias.
The bias threshold for translocation was approximate 300 mV.
Figure 4 shows the results of the translocation through the
nanopore when a bias of 800 mV was applied between the
nanopore. The background current was estimated to be 40 to
60 pA. The depth of the blockade current varies from 200 pA
to 2 nA. The translocation time was estimated to be in the
range of few milliseconds.

Fig. 1: Schematic cross section of the SOI wafer. The inset shows the schematic of a high aspect ratio nanopore obtained after electrochemical etching.

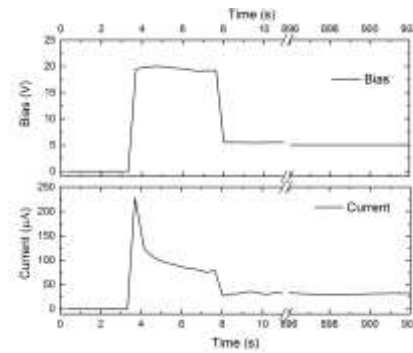


Fig. 2. A bias voltage profile and current dynamics during electrochemical etching. The two step etching incorporates two different voltages while etching.

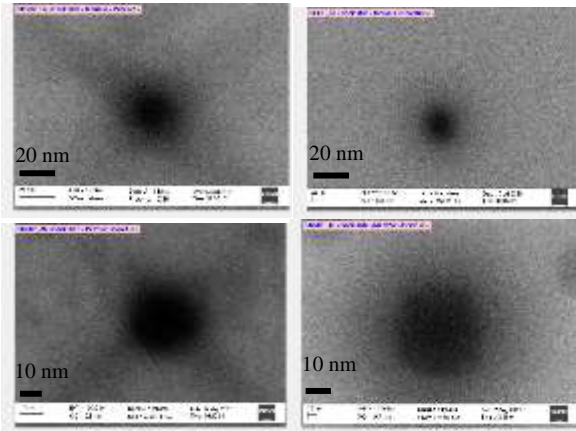


Fig. 3. SEM images of single nanopores at different voltage durations. The nanopores are approximately 10 to 15 nm in diameter.

ACKNOWLEDGMENT

The authors acknowledge the funding provided by Olle Engkvist for the purpose of Nanopore research.

REFERENCES

- [1] A. G. Ahmadi and S. Nair, "Geometry of nanopore devices fabricated by electron beam lithography: Simulations and experimental comparisons," *Microelectron. Eng.*, vol. 112, pp. 149–156, Dec. 2013.
- [2] T. Schmidt, M. Zhang, S. Yu, and J. Linnros, "Fabrication of ultra-high aspect ratio silicon nanopores by electrochemical etching," *Appl. Phys. Lett.*, vol. 105, no. 12, p. 123111, Sep. 2014.
- [3] P. Kleimann, J. Linnros, and S. Petersson, "Formation of wide and deep pores in silicon by electrochemical etching," *Mater. Sci. Eng. B*, vol. 69–70, pp. 29–33, Jan. 2000.

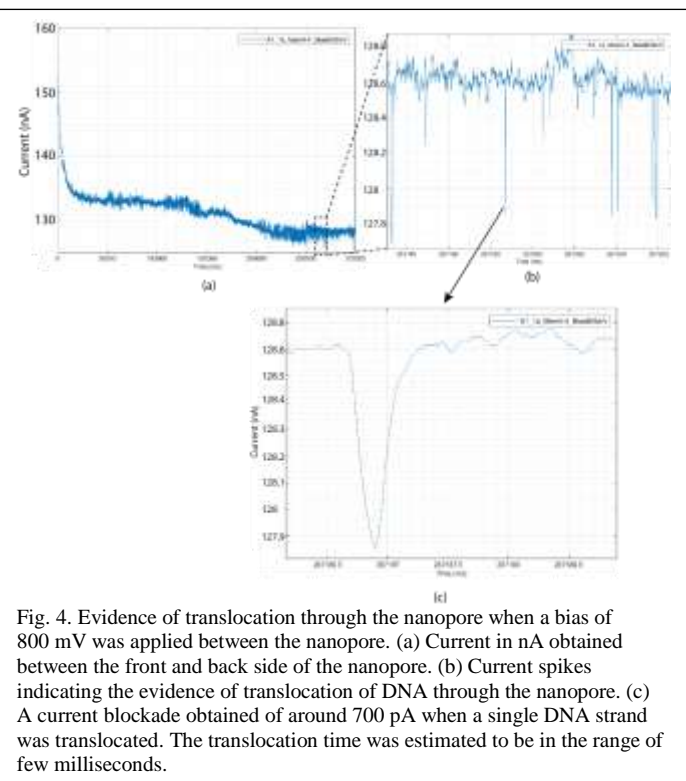


Fig. 4. Evidence of translocation through the nanopore when a bias of 800 mV was applied between the nanopore. (a) Current in nA obtained between the front and back side of the nanopore. (b) Current spikes indicating the evidence of translocation of DNA through the nanopore. (c) A current blockade obtained of around 700 pA when a single DNA strand was translocated. The translocation time was estimated to be in the range of few milliseconds.

Paper Title: Optimization of Device Performance Through Quantum Mechanical Analysis of a Single Layer 2D Transition Metal Dichalcogenide Material Based Vertical Heterojunction Tunnel FET.

Abstract: Two dimensional Transition Metal Dichalcogenide (TMD) material based tunnel FETs have been proposed a few years back to reach beyond thermionic limit of subthreshold slope as well as ensuring high on currents compared to conventional tunnel FETs. In this work, for a single layer n-doped MoS_2 and p-doped WTe_2 based vertical heterojunction tunnel FET, a well-organized quantum mechanical analysis has been performed to find the design criteria for low subthreshold swing keeping device length as short as possible. Real space model Hamiltonian of the device is formed by inter-coupling wave functions of the layers through coupling energy of WTe_2 valence band and MoS_2 conduction band in the overlap region. Non Equilibrium Green's Function formalism is applied to find current per unit width from valence band of WTe_2 layer to conduction band of MoS_2 layer. Here, self-consistent analysis is used to numerically solve the device by coupled schrodinger-poisson equations in MATLAB taking into account plane dependence of permittivity in 2D TMD material. For 15 nm channel overlap length and 15 nm gate extension length on both sides, subthreshold swing of 10 mV/decade has been obtained. For 20 nm channel overlap length, ON current of 18 $\mu A/\mu m$ has been obtained as well. Subthreshold swing and ON current can be further improved by increasing gate extension length and channel overlap length respectively until the device length crosses the upper limit. The effect of top gate extension, overlap length, chemical doping and dielectric layer thickness on ON and OFF state current transport can be explained quantum mechanically. Thus the framework presented in the work will help designers to optimize the device performance.

Ultrathin 2D Semiconductors Used as Contact Interlayer to Improve Performance of MoS₂ Transistors

Kraig Andrews*, Arthur Bowman*, Pai-Yen Chen[†], Zhixian Zhou*

*Department of Physics and Astronomy, Wayne State University, Detroit, MI, USA 48202

[†]Department of Electrical and Computer Engineering, University of Illinois at Chicago, Chicago, IL, USA 60607

Achieving low-resistance ohmic contacts in two-dimensional (2D) materials including transition metal dichalcogenides (TMDs) has been a major challenge to developing high-performance field-effect transistors (FETs). A substantial Schottky barrier (SB) is often present at the metal/2D-semiconductor interface largely due to the Fermi level pinning effect. To date, various strategies employed to reduce or eliminate the SB and ultimately reduce the contact resistance, such as substitutional and chemical doping are still deficient. Here, we present a simple, yet effective method to substantially reduce the SB height (SBH) in TMD-based FETs by inserting ultra-thin TMDs as an interlayer at the semiconductor-metal interface. Specifically, we observed a drastic reduction in the SBH from 100 meV to 25 meV by inserting TMD interlayers between the MoS₂ channel and the metal electrodes. Consequently, this reduction in the SBH results in over an order of magnitude decrease in the contact resistance. This method presents a significant advantage over previous works that utilize insulating interlayers because our method uses advantageous band alignments to reduce the SBH while circumventing a substantial tunneling barrier at the contacts.

Charges Distribution Analysis in the Body Cylindrical Gate-All-Around Nanowire Transistor

M. Kessi, A. Benfedila, A. Lakhelef, L. Belhimer and M. Djouder

The authors are within the Micro and Nanotechnology Research Group (MNRG), Faculty of Electrical Engineering and Computer Sciences, University M. Mammeri, Tizi-Ouzou, UMMTO DZ 15000, Algeria.

Abstract: Cylindrical Gate-All-Around (CGAA) MOSFET has been studied and the charges distribution are simulated and studied. MoreOver, the electric field, body potential, electron diffusion current density, total current density, electron and hole concentration, trap occupation, electric displacement field and electron conservative convective velocity are obtained using the finite element numerical method by solving Poisson's equation in the cylindrical coordinate system.

1. Introduction

As MOSFETs continue to get smaller between source and drain has led to an impending power crisis and reduces the capability of gate electrode to control the body potential and the charge distribution in the channel. The short-circuit from source and drain is facing serious problems, like Drain Induced Barrier Lowering (DIBL) and the threshold voltage roll off [1]. As a result the off state current increases and the On-Off current ration are degraded. Several designs structures (MuGFETs) have been developed, all of them are targeting the enhancement of the better channel control due to the action of multiple gate electrodes surrounding the channel [2]. Cylindrical Gate-All-Around MOSFETs have been regarded as a promising technology for sub-10-nm CMOS devices, because has provide the best short channel device performance, better gate controllability, suppressed floating-body, improved transport property and CMOS compatibility, compared with other non-classical device structures, because do not have corner effects due to the circular cross-section and cylindrical body [1-2]. Moreover, the charges distribution in the body of the CGAA structure has been investigated and the comparison is made with them.

2. Device Structure and Parameters

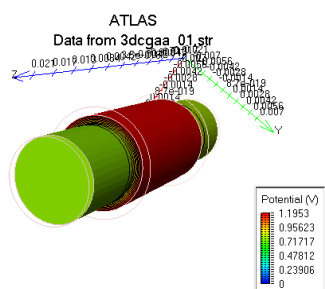


Fig. 1 Schematic structure of Cylindrical Gate-All-Around (CGAA) MOSFETs.

3. Results and Discussion

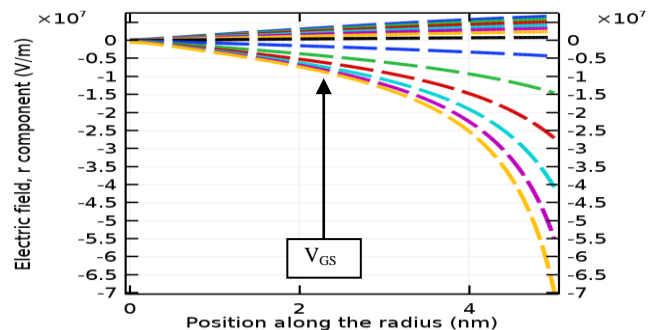


Fig.2 (a) electric field with position along the radius

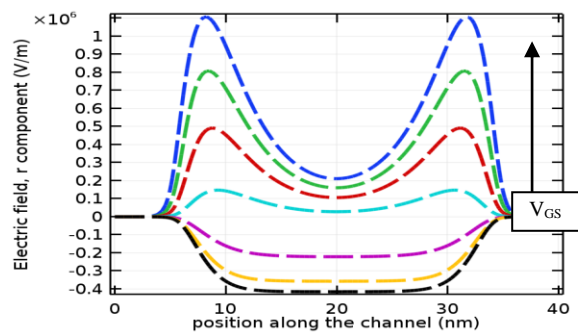


Fig.2 (b) Electric field, r component (V/m)

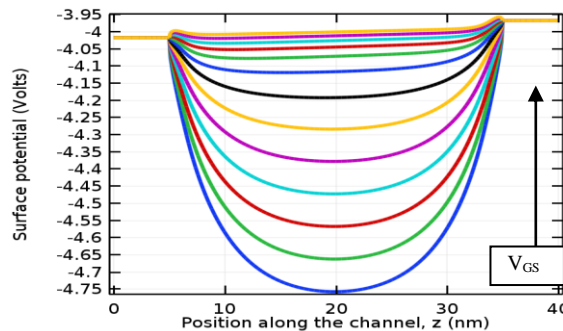


Fig. 3 (a) Surface potential along the channel length

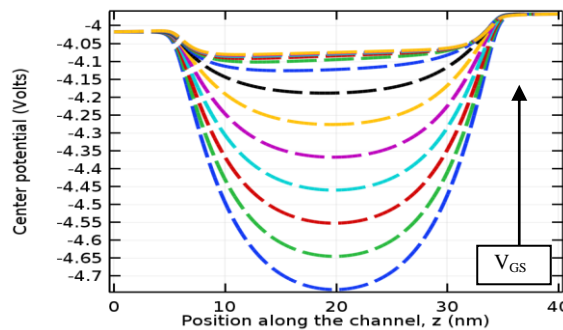


Fig. 3 (b) Center potential along the channel length.

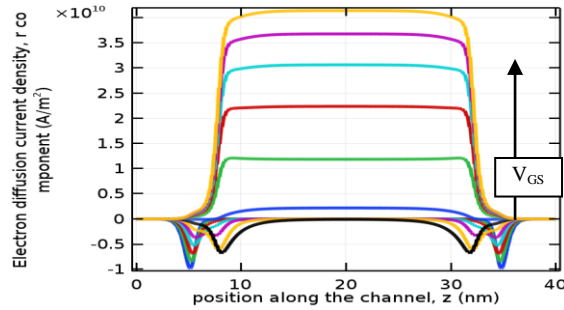


Fig. 4 (a) Electron diffusion current density, r component (A/m^2).

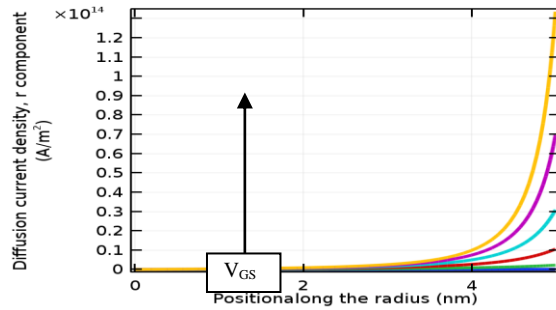


Fig. 3(b) Electron diffusion current density, r component (A/m^2)

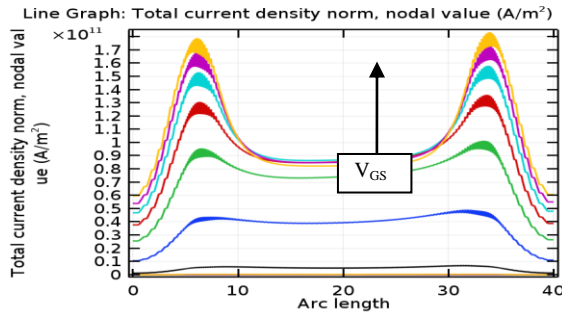


Fig. 3 (c) Total current density norm, nodal value (A/m^2)

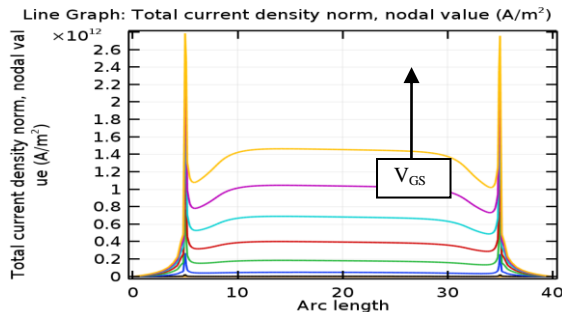


Fig. 3 (d) Total current density norm, nodal value (A/m^2)

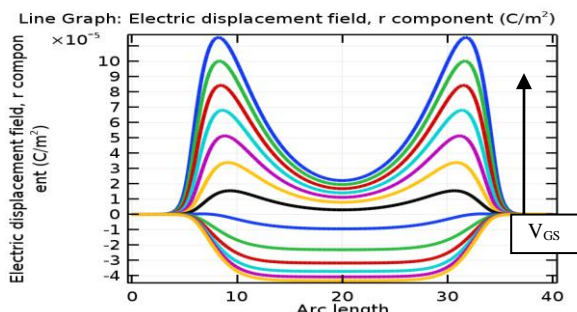


Fig. 5 (a) Electric displacement field, r component (C/m^2)

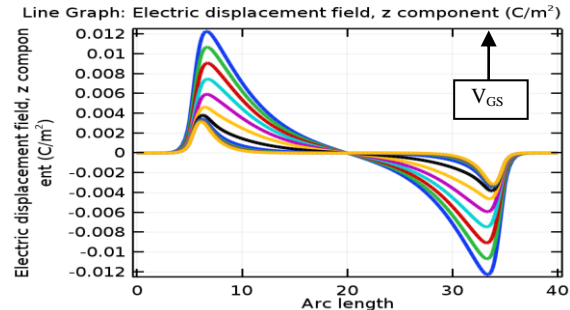


Fig. 5 (b) Electric displacement field, z component (C/m^2)

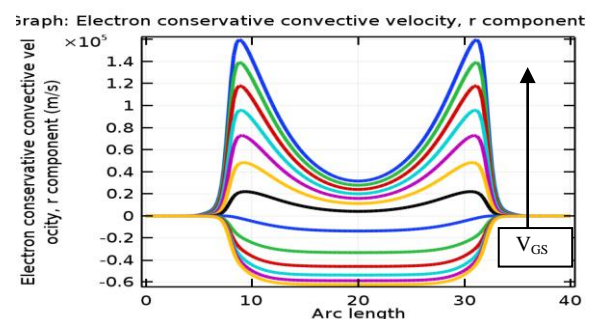
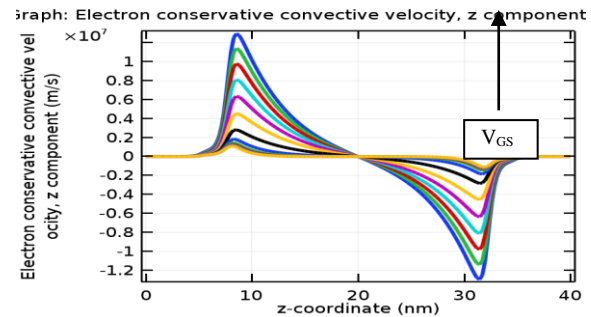


Fig. 6 (a) Electron conservative convective velocity, r component (m/s)



4. Conclusions

In this paper, we have studied the charges distribution in the body of the Cylindrical Gate-All-Around (CGAA) MOSFETs, using the finite element, numerical method by solving the Poisson's equation in the cylindrical coordinate system. The results show excellent accuracy comportment and good agreement with that obtained in the literature of the charges distribution in the channel of CGAA.

References

[2]. M. Kessi; A. Benfdila; A. Lakhlef "Investigation on cylindrical gate-all-around (GAA) tunnel FETs scaling", "P. ROC. 30th International Conference On Microelectronics (MIEL 2017), NIŠ, SERBIA, October, 9th-11th, 2017.

InGaN/GaN blue light emitting diodes grown on nanoimprint-based hollow patterned sapphire substrates

1 1st Young Hoon Sung2 Department of Materials Science and
3 Engineering
4 Korea University
5 Seoul, South Korea
6 azureshadow@naver.com7 2nd Jaemin Park8 Department of Materials Science and
9 Engineering
10 Korea University
11 Seoul, South Korea
12 qrwoals93@korea.ac.kr13 3rd Yuting Liu14 Department of Materials Science and
15 Engineering
16 Korea University
17 Seoul, South Korea
18 line 5: liuyuting0223@naver.com19 4th Dongwoo Chae20 Department of Materials Science and
21 Engineering
22 Korea University
23 Seoul, South Korea
24 superdw08@naver.com25 5th Jinhee Jeong26 Department of Materials Science and
27 Engineering
28 Korea University
29 Seoul, South Korea
30 jinheee1234@naver.com31 6th Heon Lee32 Department of Materials Science and
33 Engineering
34 Korea University
35 Seoul, South Korea
36 heonlee@korea.ac.kr

Three different conical-shaped hollow-patterned sapphire substrates (HPSSs) were fabricated and used as light emitting diode (LED) substrates. The HPSSs were fabricated on 2-inch diameter sapphire wafers by using the nanoimprint technique. Blue LED structures were grown on the HPSSs.

A. Figures

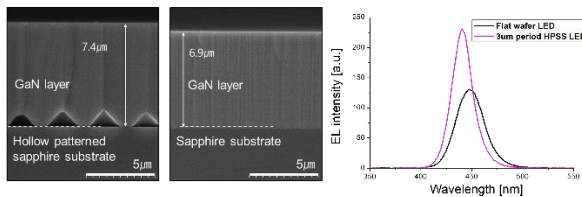


Fig. 1. SEM images and electroluminescence spectra of hollow patterned sapphire substrate and conventional flat sapphire substrate based blue LED.

Fig. 1 illustrates the cross sectional SEM images and electroluminescence(EL) spectra of blue LED structured hollow patterned sapphire substrate (HPSS) and conventional flat wafer. Conical-shaped hollow-patterned sapphire substrates (HPSSs) were fabricated in order to improve the light extraction efficiency of light emitting diodes. The HPSSs were fabricated on 2-inch diameter sapphire wafers by using the nanoimprint lithography. Blue LED structures were grown on the HPSSs. The photoluminescence (PL) and electroluminescence (EL) intensities of the LEDs were measured to confirm the effectiveness of the hollow-patterns on sapphire. An improvement in the luminescence efficiency was observed when HPSSs were used. 4.5 times higher PL intensity and 1.7 times higher EL intensity were observed for GaN LED structure grown on hollow-patterned sapphire wafer, compared to LED structure grown on conventional flat sapphire wafer.

ACKNOWLEDGMENT

This work was supported by the Technology Innovation Program (20000887, Development of self healing impact

resistant film coating material and process technology for rollable displays) funded by the Ministry of Trade, Industry & Energy (MOTIE, Korea). This work was supported by the Technology Innovation Program (N0002310) funded by the Ministry of Trade, Industry & Energy (MOTIE, Korea). This work was supported by the Technology Innovation Program (or Industrial Strategic Technology Development Program (10053288, Development of epitaxial wafer technology for Green LED/LD) funded By the Ministry of Trade, Industry & Energy(MOTIE, Korea).

REFERENCES

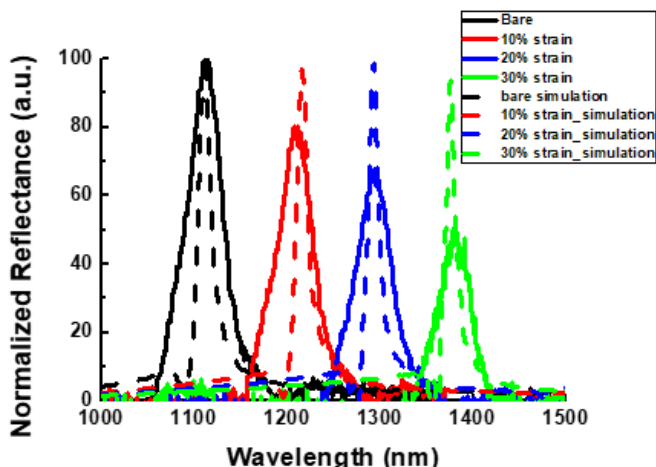
- [1] T. Sugahara et al., "Direct Evidence that Dislocations are Non-Radiative Recombination Centers in GaN," *Jpn. J. Appl. Phys.*, vol. 37, no. Part 2, No. 4A, pp. L398–L400, Apr. 1998.
- [2] T. Kozawa, T. Kachi, H. Kano, H. Nagase, N. Koide, and K. Manabe, "Thermal stress in GaN epitaxial layers grown on sapphire substrates," *J. Appl. Phys.*, vol. 77, no. 9, pp. 4389–4392, May 1995.
- [3] S. Zhou, S. Liu, and H. Ding, "Enhancement in light extraction of LEDs with SiO₂ current blocking layer deposited on naturally textured p-GaN surface," *Opt. Laser Technol.*, vol. 47, pp. 127–130, Apr. 2013.
- [4] C. M. Tsai et al., "High efficiency and improved ESD characteristics of GaN-based LEDs with naturally textured surface grown by MOCVD," *IEEE Photonics Technol. Lett.*, vol. 18, no. 11, pp. 1213–1215, Jun. 2006.
- [5] K.-J. Byeon et al., "Fabrication of photonic crystal structure on indium tin oxide electrode of GaN-based light-emitting diodes," *Phys. status solidi*, vol. 208, no. 2, pp. 480–483, Feb. 2011.
- [6] J.-Y. Cho and H. Lee, "Effect of the Shape of Nanometer-scaled Patterns on Sapphire Substrate on the Efficiency of Light Emitting Diode," *J. Photopolym. Sci. Technol.*, vol. 28, no. 4, pp. 541–545, May 2015.
- [7] K.-J. Byeon et al., "Enhancement of the photon extraction of green and blue LEDs by patterning the indium tin oxide top layer," *Semicond. Sci. Technol.*, vol. 24, no. 10, p. 105004, Oct. 2009.
- [8] K.-Y. Yang, K.-M. Yoon, S. Lim, and H. Lee, "Direct indium tin oxide patterning using thermal nanoimprint lithography for highly efficient optoelectronic devices," *J. Vac. Sci. Technol. B Microelectron. Nanom. Struct.*, vol. 27, no. 6, p. 2786, Dec. 2009.

Fabrication of fiber Bragg grating stretchable color filter by UV nanoimprint lithography

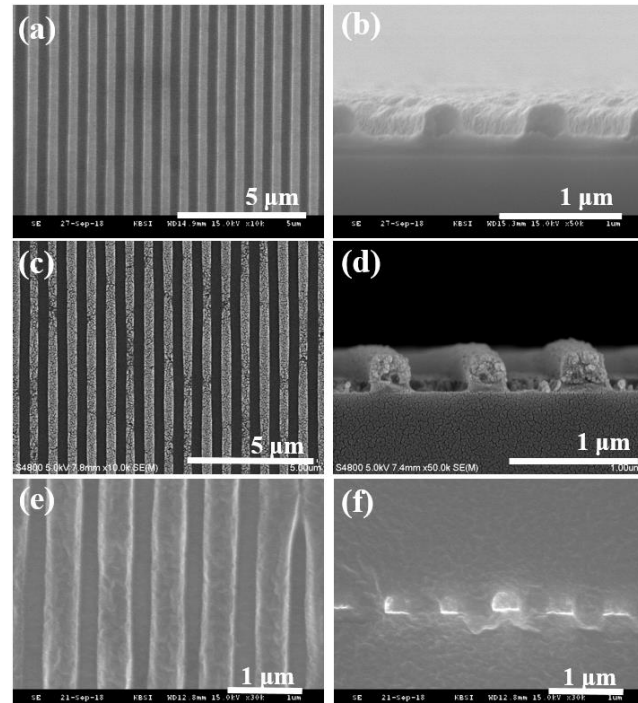
1 6 1st Wonjoong Kim2 7 Department of Material Science and
3 8 Engineering
4 9 Korea university
5 10 Seoul, Republic of Korea
6 11 kjw212212@korea.ac.kr2nd Daihong Huh3 Department of Material Science and
4 Engineering
5 Korea university
6 Seoul, Republic of Korea
7 huh324@korea.ac.kr3rd Sucheol Ju4 Department of Material Science and
5 Engineering
6 Korea university
7 Seoul, Republic of Korea
8 vxz091@korea.ac.kr12 13 4th Seungho Baek14 15 Department of Material Science and
16 Engineering
17 Korea university
18 Seoul, Republic of Korea
19 allpeople@korea.ac.kr5th Heon Lee14 Department of Material Science and
15 Engineering
16 Korea university
17 Seoul, Republic of Korea
18 heonlee@korea.ac.kr

In this study, we propose a color filter using the characteristics of fiber Bragg grating as a substitute for organic dye-based color filter that has low chemical stability [1, 2]. FBG is a reflector that reflects the light of a specific wavelength through periodic repetition of the refractive index inside the fiber [3]. When a strain is applied to an FBG, a red shift in the wavelength of the reflected light occurs [4]. To make fiber Bragg grating structure, periodic TiO_2 grating structure is formed by ultraviolet nanoimprint lithography with a TiO_2 nanoparticle dispersion resin [5]. The TiO_2 embedded PDMS color filter is completed using transfer printing by sacrificial layer [6]. The reflectance peak is measured by a UV-vis-NIR spectrophotometer under strain conditions. When strain is applied, a reflectance peak red shift of color filter occurs. And, the red shift in the FDTD simulation data and actually measured values occur at similar values, which suggests that the stretchable color filter is feasible.

37 Figures



54 **Figure 1.** Normalized reflectance and FDTD simulation of PDMS
55 with TiO_2 -nanoparticle grating structure under strain condition



56 **Figure 2.** SEM images of the grating structures using TiO_2 -
57 nanoparticle dispersion resin: (a), (b) after UV-NIL; (c), (d) after
58 RIE; (e) after PVA layer removal; and (f) after completing device

59 Figure 1 shows the comparison between the FDTD
60 simulation and the measured reflectance in the near-infrared
61 region from 1000 to 1500 nm. The solid and dotted lines
62 represent the actual device and the simulation data,
63 respectively. A comparison of the measured reflectance and
64 simulations show peak wavelength differences of 0, 5, 3, and
65 6 nm, respectively; however, the positions of the reflectance
peaks were similar in most cases.

ACKNOWLEDGMENT (Heading)

This work was supported by the Materials and Components Technology Development Program of MOTIE/KEIT. (10080352, Development of polymer-based adhesive light concentration film for solar cell with 85% light transmittance, 1m² area)

This research was supported by Creative Materials Discovery Program through the National Research Foundation of Korea(NRF) funded by Ministry of Science and ICT. (NRF-2018M3D1A1058972)

REFERENCES

- [1] R. W. Sabnis, "Color filter technology for liquid crystal displays," *Displays*, 1999, 20.3: 119-129.
- [2] T. W. Ebbesen, H. J. Lezec, H. F. Ghaemi, T. Thio, and P. A. Wolff, "Extraordinary optical transmission through sub-wavelength hole arrays," *Nature*, 1998, 391(6668) 667.
- [3] K. O. Hill, and G. Meltz, "Fiber Bragg grating technology fundamentals and overview," *Journal of lightwave technology*, 1997, 15(8) 1263-1276.
- [4] Y. J. Rao, "Fiber Bragg grating sensors: principles and applications," In *Optical fiber sensor technology*, 1998, (pp. 355-379). Springer Boston MA.
- [5] D. Huh, J. H. Shin, M. Byun, S. Son, P. H. Jung, H. J. Choi, Y. D. Kim, and H. Lee "Analysis of long-term monitoring data of PV module with SiO_x-based anti-reflective patterned protective glass," *Solar energy materials and solar cells*, 2017, 170 33-38.
- [6] C. H. Lee, D. R. Kim, and X. Zheng, "Transfer printing methods for flexible thin film solar cells: Basic concepts and working principles" *ACS nano*, 2014, 8(9) 8746-8756.

Polymer nanocomposites materials for passive daytime radiative cooling

1 6 1st Yuting Liu2 Department of Materials Science and
3 Engineering
4 Korea University
5 Seoul, Korea
67 liuyuting0223@naver.com8 2nd Pil-Hoon Jung9 Department of Materials Science and
10 Engineering
11 Korea University
12 Seoul, Korea
1314 feelsam21@naver.com15 3th Young Hoon Sung16 Department of Materials Science and
17 Engineering
18 Korea University
19 Seoul, South Korea
2021 azureshadow@naver.com22 4th Kwan Kim23 Department of Materials Science and
24 Engineering
25 Korea University
26 Seoul, Korea
2728 whoget@korea.ac.kr29 5th Heon Lee30 Department of Materials Science and
31 Engineering
32 Korea University
33 Seoul, Korea
3435 heonlee@korea.ac.kr

18 High temperature in summer induced by global warming
19 has significantly influenced human's study and work in recent
20 years. Space cooling, such as air conditioner, means that a
21 large amounts of energy consumption will be wasted in this
22 inevitable trend. Researchers around the world are looking for
23 method of cooling like passive daytime radiative cooling to
24 solve this problem, which is an appealing concept in this
25 century[1]-[3]. It is noted that heat transfer could occur in
26 three fundamental mechanisms, heat conduction, heat
27 convection, and thermal radiation. What's more, the thermal
28 radiation is the mission of electromagnetic waves from all
29 objects with temperature greater than absolute zero[4]. It is
30 also acknowledged that temperature of the outer space is much
31 lower than that of earth—a natural cold sink we can take
32 full advantage of, and fortunately, there is an atmospheric
33 transparency window between 8-13 μm [5], [6]. Objects with
34 high surface temperature can radiated from the clouds to outer
35 space through the atmospheric transparency window without
36 intermediate absorption and re-emission[3]. Although there is
37 also a transparent window in 16-24 μm , semi-transparent
38 specifically and it will disappear in coastal countries. In
39 summary, the whole process is named as passive radiative
40 cooling process[7].

41 Here, we experimentally demonstrate PDRC can be
42 achieved through polymer-inorganic composite materials on
43 the silver mirror. We proposed a simple double layer
44 composed of a top layer with the DPHA introduced Al_2O_3
45 nanoparticles (DPHA@ Al_2O_3 NPs) and Ag layer at the
46 bottom of DPHA@ Al_2O_3 NPs. This kind of radiative cooler
47 achieved obvious radiative cooling performance in sub-
48 ambient condition under direct sunlight (10.35 °C). Our work
49 demonstrated that without complex and expensive
50 metamaterial structures, PDRC also can be realized through
51 using inexpensive material and simple fabrication method.

A. Figures and Tables

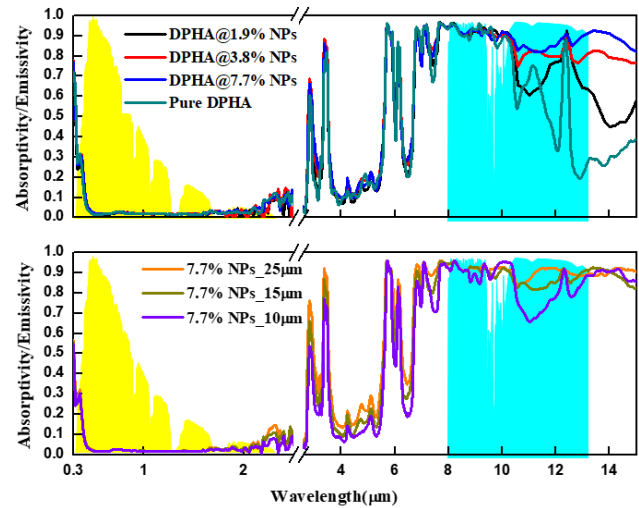


Figure 1. Absorptivity or emissivity of various formulations of DPHA@ Al_2O_3 NPs and pure DPHA at room temperature in the range of 0.3-15 μm

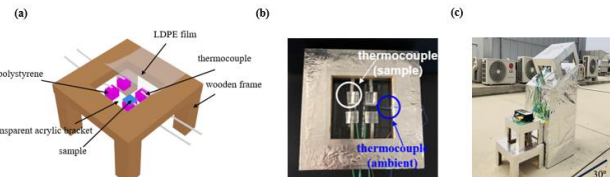


Figure 2. (a) Schematic diagram of chamber, (b) digital photo of fabricated chamber covered with Al foil and (c) experimental setting

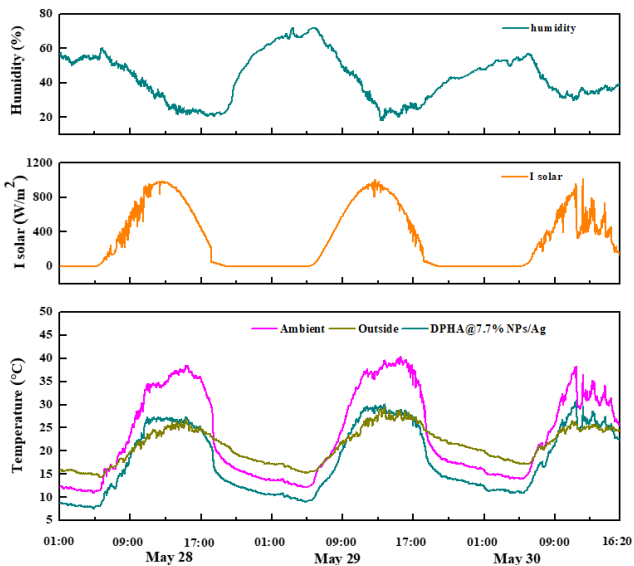


Figure 3. Outdoor humidity, solar radiance and temperature measurement for three consecutive days (from May 28 to May 30, 2019)

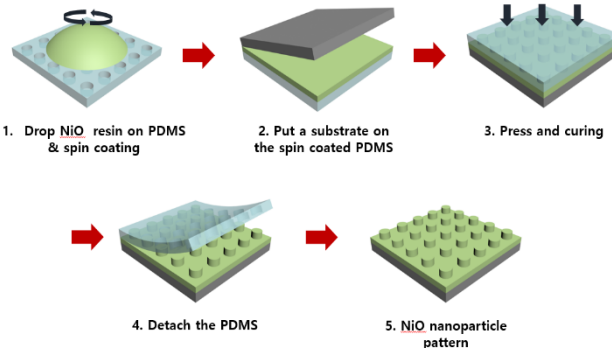
ACKNOWLEDGMENT

This research was supported by Creative Materials Discovery Program through the National Research Foundation of Korea(NRF) funded by Ministry of Science and ICT (NRF-2018M3D1A1058972)

REFERENCES

- [1] X. Wu and C. Fu, "RADIATIVE COOLING BY USING A SLAB OF HEXAGONAL BORON NITRIDE," in International Heat Transfer Conference 16, 2018, pp. 8263–8270.
- [2] B. Zhao, M. Hu, X. Ao, N. Chen, and G. Pei, "Radiative cooling: A review of fundamentals, materials, applications, and prospects," *Applied Energy*, vol. 236, pp. 489–513, Feb. 2019.
- [3] A. Hervé, J. Dréville, Y. Ezzahri, and K. Joulain, "Radiative cooling by tailoring surfaces with microstructures: Association of a grating and a multi-layer structure," *J. Quant. Spectrosc. Radiat. Transf.*, vol. 221, pp. 155–163, Dec. 2018.
- [4] Y. Zhai et al., "Scalable-manufactured randomized glass-polymer hybrid metamaterial for daytime radiative cooling," *Science (80-.)*, vol. 355, no. 6329, pp. 1062–1066, Mar. 2017.
- [5] M. M. Hossain and M. Gu, "Radiative cooling: Principles, progress, and potentials," *Advanced Science*, vol. 3, no. 7. 2016.
- [6] M. A. Kecebas, M. P. Menguc, A. Kosar, and K. Sendur, "Passive radiative cooling design with broadband optical thin-film filters," *J. Quant. Spectrosc. Radiat. Transf.*, vol. 198, pp. 179–186, Sep. 2017.
- [7] M. Zeyghami, D. Y. Goswami, and E. Stefanakos, "A review of clear sky radiative cooling developments and applications in renewable power systems and passive building cooling," *Solar Energy Materials and Solar Cells*, vol. 178, pp. 115–128, 2018.

Fabrication of various NiO patterns by thermal nanoimprint lithography*

1 6 1st Jinhee Jeong2 7 Department of Material Science and
3 8 Engineering
4 9 Korea University
5 10 Seoul, f Korea
11 jinheee1234@naver.com2nd Soomin Son3 Material science and Engineering
4 Korea university
5 Seoul, Korea
6 wavry3330@naver.com3rd Dongwoo Chae4 Material science and Engineering
5 Korea university
6 Seoul, Korea
7 dwc0808@korea.com12 4th Heon Lee13 Material science and Engineering
14 Korea university
15 Seoul, Korea
16 heonlee@korea.ac.kr

30 Fig 1. Schematic diagram of the fabrication process of NiO nano-
31 micro structure by thermal NIL.

33 This nickel oxide(NiO) is a substance widely used in the
34 field of photocatalyst, water splitting and electrochromic
35 device. This study looked at the thermal nanoimprint
36 lithography(NIL) that can fabricate structures of holes, pillars,
37 line, convex and cone using resins distributed with NiO
38 nanoparticles. Through this process, the refractive index,
39 crystallization and optical properties of various structures
40 made of NiO nanoparticles were measured.

41 Fig 1. Shows schematic illustration of thermal NIL process
42 using NiO nanoparticle. To fabricate nanoparticle structures,
43 polydimethylsiloxane(PDMS) is first applied on a master
44 stamp with the desired pattern to form a PDMS mold with the
45 inverse shape of the stamp pattern. After spin-coating resin
46 with dispersed NiO nanoparticles on PDMS mold, substrate
47 was slowly covered over the coated mold making as constant
48 contact as possible. When pressure and heat are applied
49 sequentially, the pattern is formed as the curing agent in the
50 nanoparticle resin is cured. When resin is completely cured,
51 the PDMS mold is removed from the NiO structure.

52 The morphological, structural and optical properties of
53 NiO structure were analyzed using Scanning Electron
54 Microscope(SEM), X-ray Diffractometer(XRD) and UV-
55 visible spectrometer. It was confirmed that nano-to-micro
56 structures were successfully formed on top of the glass
57 substrate and flexible polycarbonate(PC) film as shown in Fig
58 2. It was also confirmed that crystallinity was improved when
59 heat treatment was applied. In addition, the higher the
60 concentration of nanoparticle in resin, the higher the refractive
61 index.

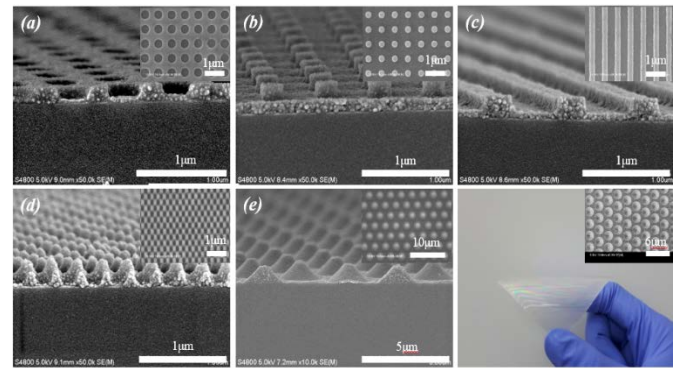


Figure 2 SEM images of (a) nano-hole pattern, (b) nano-pillar pattern, (c) nano-line pattern, (d) moth-eye pattern, (e) micro-cone pattern (f) NiO pattern on flexible substrate

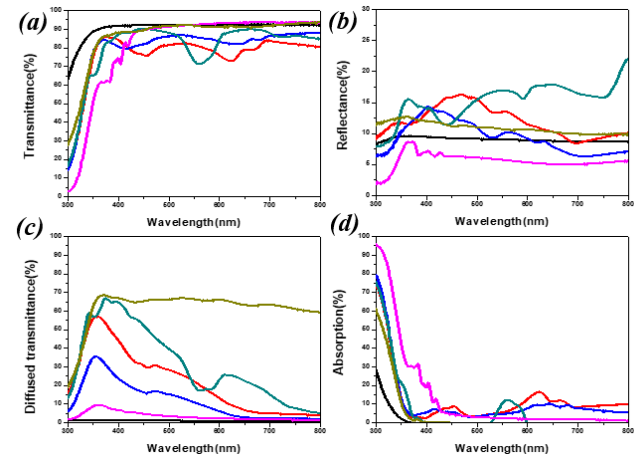


Figure 3. Optical properties of various patterns (a) transmittance, (b) reflectance, (c) diffused transmittance (d) absorption

index was. As shown in Fig 3, transmittance, reflectance and absorption measured by UV-vis showed that light scattered more when NiO pattern, especially micro-cone pattern, was on the substrate. In case of a moth-eye pattern, it was found that the reflectivity was very low due to a gradual change of the refractive index.

In this research, the possibility that the nanoimprint lithography could be used to make electrochromic device is also shown. NiO layer, electrochromic layer was simply patterned through nanoimprint lithography and it was

checked that the color switching occurred according to the direction of applied voltage.

ACKNOWLEDGMENT

This work was supported by the Technology Innovation Program (N0002310) funded by the Ministry of Trade, Industry & Energy (MOTIE, Korea).

This research was supported by Creative Materials Discovery Program through the National Research Foundation of Korea(NRF) funded by Ministry of Science and ICT (NRF-2018M3D1A1058972)

REFERENCES

[1] Jun, J.; Choi, H.; Moon, S.; Sung, Y.; Lee, H. Fabrication

Of SnO₂ Nano-To-Microscale Structures From SnO₂-Nanoparticle-Dispersed Resin Via Thermal Nanoimprint Lithography. *Journal of Nanoscience and Nanotechnology* 2016, 16, 11308-11312.

[2] Son, S.; Jung, P.; Park, J.; Huh, D.; Kim, K.; Lee, H.; Lee, H. Nano- And Micro-Sized Fe₂O₃ Structures Fabricated By UV Imprint Lithography. *physica status solidi (a)* 2018, 215, 1700948.

[3] Park, J.; Sung, Y.; Son, S.; Jun, J.; Huh, D.; Lee, H. Fabrication Of Al₂O₃ Nano-Micro Patterns By Al₂O₃ Dispersion Resin Using UV Imprint Lithography. *Thin Solid Films* 2018, 660, 428-433.

Effect of Embedded Patterns on Thermomechanical Property of Fan-out Package

Haksan Jeong, Kwang-Ho Jung, Choong-Jae Lee, Kyung Deuk Min, and Seung-Boo Jung*

School of Advanced Materials Science & Engineering

Sungkyunkwan University

Suwon, South Korea

*email : sbjung@skku.edu

Fan-out wafer level package has advantages such as lower power consumption and better thermal dissipation. However, warpage caused by CTE mismatch between different materials is critical issue. Therefore, effect of embedded pattern in epoxy mold compound (EMC) on warpage of fan-out package was investigated by shadow moiré method and finite element analysis. Warpage decreased with increasing area of pattern. When pattern was embedded in fan-in region, warpage decreased because CTE mismatch between EMC and Si decreased. When pattern was embedded in fan-out region, warpage decreased because warpage shape of fan-out region was opposite shape compared with that of fan-in region.

I. Introduction

The demands for faster performance, higher functionality and smaller size of electronic device has led to exceeding advances in package technology.[1] Among the 3D package technologies, fan-out wafer level package has many advantage such as thinner thickness, lower power consumption, better thermal dissipation with short interconnection of thin redistribution layer.[2] However, warpage caused by coefficient of thermal expansion (CTE) mismatch between different materials is critical issue.[3] Therefore, we evaluated the warpage of a fan-out package with various embedded patterns in epoxy mold compound (EMC) by shadow moiré method and finite element analysis (FEA).

II. Experimental procedure

Dimension of package component was designed as 14 mm x 14 mm x 0.3 mm with 8 mm x 8 mm x 0.1 mm embedding Si chip. First, Si chip was picked and placed on the laminated carrier. And Ag paste was printed on the other carrier. the Si chip and Ag pattern were molded with EMC molding process. Each carrier was detached from molded package, and then, redistribution layer (RDL) process was performed on the molded chip. Finally, package can be achieved after singulation process. The warpage behavior of fan-out package component was measured from 25°C to 260 °C using shadow moiré method and FEA in compliance with JESD22-B112A.

III. Result and Discussion

The warpage behavior of fan-out package component changed from convex to concave with increasing temperature. The warpage of component without embedded pattern at 25°C and 260 °C was 289 μm and 242 μm , respectively. Warpage of pattern 2, pattern 3, pattern 4 and pattern 5 was 130 μm ,

TABLE I. PATTERN IDENTIFICATION OF FAN-OUT PACKAGE COMPONENT WITH VARIOUS EMBEDDED PATTERNS

pattern identification	Pattern 1	Pattern 2	Pattern 3	Pattern 4	Pattern 5
Pattern design					

156.5 μm , 164.5 μm , and 181.5 μm , respectively. Warpage decreased with increasing area of embedded pattern.

Figure 1 (a) shows simulated warpage of fan-out package with various embedded patterns. The simulated warpage tended to decrease with increasing area of embedded pattern, too. When pattern was embedded in fan-in region such as pattern 2, pattern 3, and pattern 4, stiffness of whole materials increased because effective CTE mismatch between EMC and Si decreased with increasing embedded pattern. So, warpage decreased because the stiffness of the whole materials increased.[4] Figure 1 (b-e) shows the simulated warpage and simulated elastic stain distribution of pattern 1 and pattern 5. In case of pattern 5, whose pattern was located on fan-out region, the warpage shape of fan-out region was concave which is opposite warpage compared with that of fan-in region because CTE mismatch between embedded pattern and EMC.

IV. Conclusion

The fan-out package component was designed and fabricated with various embedded pattern in capping side of EMC. The measured and simulated warpage of fan-out package component was decreased with increasing area of embedded pattern. The effective CTE of EMC decreased with increasing area of embedded pattern when pattern was embedded on fan-in region. When pattern was embedded on fan-out region, the warpage of fan-out region was opposite side compared with that of fan-in region.

REFERENCES

- [1] M.M. Waldrop, "More than moore." *Nature*, vol. 530, no. 7589 2016: pp. 144-148.
- [2] T.G. Lim, D.S.W. Ho, E.W.L. Ching, Z. Chen, S. Bhattacharya, "FOWLP Design for Digital and RF Circuits" *Proc. Electron. Compon. Technol. Conf.(ECTC)*, 2019
- [3] Y. Niu, W. Wang, Z. Wang, K. Dhandapani, M. Schwarz, A. Syed, "Warpage Variation Analysis and Model Prediction for Molded Packages", *Proc. Electron. Compon. Technol. Conf.(ECTC)*, 2019
- [4] F.X. Che, D. Ho, M.Z. Ding, D.R.M. Woo, "Study on Process Induced Wafer Level Warpage of Fan-Out Wafer Level Packaging", *Proc. Electron. Compon. Technol. Conf.(ECTC)*, 2016

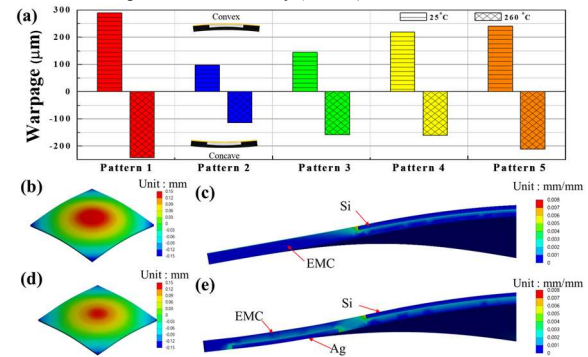


Fig. 1. (a) Simulated warpage of fan-out package component at 25 °C and 260 °C; Contour plots of (b,d) deformation and (c,e) equivalent elastic strain for fan-out component with (b,c) pattern 1 and (d,e) pattern 5 at 25 °C

TiO₂ nanoparticle based resistive switching memory on rigid and flexible substrate

*Note: Sub-titles are not captured in Xplore and should not be used

1 2 3 4 5 6 7 8 9 10 11 12 13 14 15 16 17 18 19 20 21 22 23 24 25 26 27 28 29 30 31 32 33 34 35 36 37 38 39 40 41 42 43 44 45 46 47 48 49 50 51 52 53 54 55 56 57 58 59 60 61 62 63 64 65 1st Jaemin Park

Department of Materials and Science
Engineering
Korea University
Seoul, Korea
qkrwoals93@korea.ac.kr

2nd Young Hoon Sung
Department of Materials and Science
Engineering
Korea University
Seoul, Korea
azureshadow@naver.com

3rd Soomin Son
Department of Materials and Science
Engineering
Korea University
Seoul, Korea
wavry3330@gmail.com

4th Wonjoong Kim

Department of Materials and Science
Engineering
Korea University
Seoul, Korea
kwj212212@korea.ac.kr

5th Heon Lee

Department of Materials and Science
Engineering
Korea University
Seoul, Korea
heonlee@korea.ac.kr

Resistive random access memory (ReRAM) using nanoparticles (NPs) as an active layer can be applied to flexible electronics devices, which require low-temperature processing. Since NPs are already crystallized, there is no need for high-temperature process. In this study, a solution – based direct printing process was used to fabricate nano-scale ReRAM via a simple method. The electrical characteristics of titanium dioxide NPs based nano ReRAM were measured using a conductive atomic force microscopy(c-AFM).

(1)

A. Figures and Tables

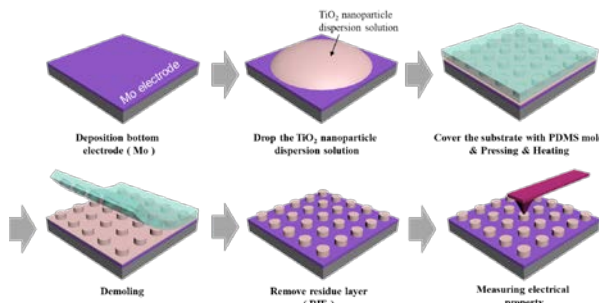


Fig1. A schematic diagram of TiO₂ nanoparticle based ReRAM fabrication process using direct printing.

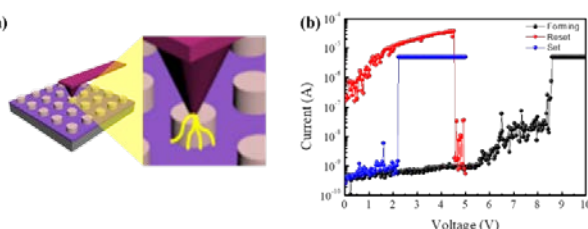


Fig 2. (a) A schematic diagram of measurement system using c-AFM (b) Forming and switching behavior of TiO₂ nanoparticle based ReRAM on Si substrate.

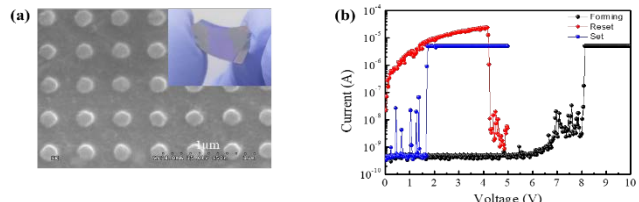


Fig3. (a) SEM image of the flexible TiO₂ nanoparticle based nano ReRAM on flexible PI film substrate. (b) Forming and switching behavior of TiO₂ NP based ReRAM on flexible PI substrate.

ACKNOWLEDGMENT (Heading)

This research was supported by Creative Materials Discovery Program through the National Research Foundation of Korea(NRF) funded by Ministry of Science and ICT (NRF-2018M3D1A1058972). Proin pharetra nonummy pede. Mauris et orci. Aenean nec lorem. In porttitor. Donec laoreet nonummy augue. Suspendisse dui purus, scelerisque at, vulputate vitae, pretium mattis, nunc. Mauris eget neque at sem venenatis eleifend. Ut nonummy. This work was supported by the Technology Innovation Program (20000887, Development of self healing impact resistant film coating material and process technology for rollable displays) funded By the Ministry of Trade, Industry & Energy(MOTIE, Korea)

REFERENCES

- [1] Sawa A, et al. "Resistive switching in transition metal oxides." Mater Today 11 28-36 2008
- [2] Chen J W, Hsin C L, Huang X W, Chiu C H, Huang Y T, Lin S J, Wu W W and Chen L J "Dynamic evolution of conducting nanofilament in resistive switching memories." Nano Lett 13 3671-7 2013..
- [3] Yang J J, Strukov D B and Stewart D R. "Memristive devices for computing." Nat. Nanotechnol. 8 13-24.
- [4] Ji L, Chang Y F, Fowler B, Chen Y C, Tsai T M, Chang K C, Chen M C, Chang T C, Sze S M, Yu E T, and Lee J C. "Integrated one diode-one resistor architecture in nanolillar SiOx resistive switching memory by nano sphere lithography." nano lett. 14 813-8 2014.

[5] Xia N, Villena M A, Yuan B, Chen S, Wang B, Elias M, Shi Y, Hui F , Jing X, Scheuermann A, Tang K, McIntyre P C and Lanza M “ Resistive random access memory cells with a bilayer TiO₂/SiO_x insulating stack for simultaneous filamentary and distributed resistive switching.” *Adv, Funct. Mater* 27 1-13 2017.

Optical Properties of Plasmonic Gold: An Application for Diagnosis of Cervical Cancer

Tejaswini Appidi

Dept. of Biomedical Engineering
Indian Institute of Technology
Hyderabad, India.
bm16resch11006@iith.ac.in

Rohit Srivastava

Dept. of Biosciences & BioEngineering
Indian Institute of Technology Bombay
Mumbai, India.
rsrivasta@iitb.ac.in

Dr. Aravind Kumar Rengan*

Dept. of Biomedical Engineering
Indian Institute of Technology
Hyderabad.
Hyderabad, India.
akr@iith.ac.in

Abstract

This paper reports the proof of concept for a novel qualitative technique for detection of cervical cancer using optical properties of gold nanoparticles formed with residual acetic acid collected after visual inspection with acetic acid (VIA). A colorimetric strategy employing the surface plasmon resonance of gold nanoparticles is proposed. The varying sizes of the gold nanoparticles formed in the presence of residual acetic acid collected from healthy and affected patients will result in different colors allowing the visual detection of malignancy. The proof of concept is demonstrated at laboratory level by detecting the different percentages of acetic acid and the reasons for the difference in color were evaluated. The quantification of acetic acid demonstrated the reliability and application potential of the proposed protocol for the detection. The proposed diagnosis technique shows great promise for in-field and point-of-care testing of cervical cancer. With the merits of simple procedures, short detection time and ideal portability, this platform could be extended with the existing visual inspection with acetic acid technique for rapid screening.

Keywords—Cervical cancer, surface plasmon resonance, gold nanoparticles, visual inspection with acetic acid (VIA).

I. INTRODUCTION

Cervical cancer is ranked the fourth most frequently diagnosed cancer and the fourth leading cause of cancer death in women. The disease was ranked second in incidence and mortality with an estimated 570,000 cases and 311,000 deaths worldwide for the year 2018. High-quality screening programs play a very important role in the prevention of cervical cancer. The WHO recommends the screening either through visual inspection with acetic acid in low-resource settings, Papanicolaou tests (cervical cytology) every 3 to 5 years, or HPV testing every 5 years among women aged 30 to 49 years [1].

The goal of cervical screening is to prevent mortality from invasive cancer and the existing screening techniques have their own strengths and limitations depending on the setting in which they are used. In the absence of HPV screening due to cost consideration and cytology not being practical to implement for universal screening, implementation of VIA screening to reduce the burden of the

disease is considered the currently available alternative in low resource settings [2]. Visual inspection entails application of either 3-5% acetic acid (VIA) on the cervix with direct treatment of screen-positive cervical sites several minutes later. Compared to Pap tests, these visualizations techniques have greater sensitivity but less specificity [3]. To address these constraints, a comprehensive approach for improvising the visual inspection technique is needed. There is an immediate need for the development of alternative strategies to support and improvise techniques that are low cost, effective, compatible with the socioeconomic realities, simple to perform, do not require laboratory infrastructure, and provide immediate results.

The various advances in nanotechnology led to the development of sensors based on the optical, physical and chemical characteristics of nanomaterials for more sensitive, specific and rapid analysis. Gold nanoparticles (Au NPs) have been brought to the forefront of research in recent years because of their facile synthesis and surface modification, strongly enhanced and tunable optical properties as well as excellent biocompatibility feasible for clinical settings [4].

A colorimetric sensing strategy employing gold nanoparticles and a paper-based analytical platform for the diagnosis of tuberculosis (TB) was reported by Tsai et. al. Detection limit of 1.95×10^{-2} ng/mL for TB DNA was reported with 60 min turnaround time for resource-limited settings [5]. Sina et al. used electrochemical and colorimetric techniques for developing an extremely simple, label free and naked eye platform that detects Methylscape biomarker from cancer genomes based on the level of gDNA adsorption on planar and colloidal gold surfaces respectively [6]. Luminol-reduced gold nanoparticles (LuReGNPs) were utilized as dual-response signal probes by Hui et.al. for the development of a colorimetric/chemi-luminescent immuno-chromatographic test strip (ITS) [7].

Researchers have developed various approaches and multiple mechanisms for disease diagnosis in resource-limited settings. Among the variety of sensing mechanisms, colorimetric assays that can be seen with the naked eye are particularly preferred [5]. Colorimetric assays are simple, inexpensive and do not require a sophisticated laboratory infrastructure for analysis.

We developed one such colorimetric technique which analyzes the residual acetic acid sample that will be collected after VIA procedure for the detection of cervical cancer. This employs the surface plasmon resonance property

of gold nanoparticles. The varying sizes of the gold nanoparticles formed in the presence of residual acetic acid collected from healthy and affected patients will result in different colors allowing the visual detection of malignancy.

II. RESULTS & DISCUSSION

In traditional VIA, the 5 % acetic acid application on the cervix results in reversible coagulation or precipitation of cellular proteins that can be visualized as aceto-white patches. Areas of high grade CIN & invasive cancer turn densely white, thick opaque on applying acetic acid, with well demarcated margins, while little/no coagulation occurs in the absence of CIN/cancer as superficial epithelium is sparsely nucleated.

An attempt to quantify the amount of the acetic acid used for protein coagulation by cells as a mode of detection is presented and discussed here. The residual acetic acid will be collected after VIA procedure and % of acetic acid will be evaluated by the technique mentioned below. The percentage of acetic acid left-over will indicate the presence/absence of malignancy. We have developed a technique to visually quantify the % of acetic acid. This was achieved by surface plasmon resonance of gold nanoparticles. Gold precursor salt when reduced in the presence of different percentages of acetic acid resulted in gold nanoparticles exhibiting different colors as shown in Figure 1.

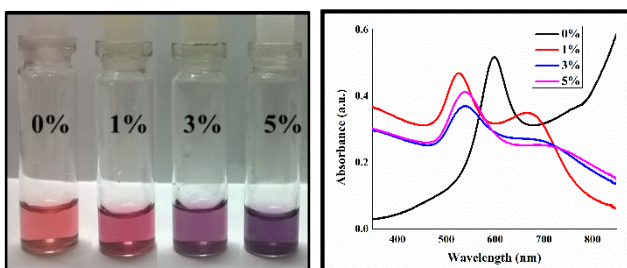


Figure 1: a) Colorimetric detection of % of acetic acid
b) UV-visible spectra.

The colors exhibited by these gold nanoparticles formed with different percentages of acetic acid were clearly distinct from one another. Investigating the reasons for the difference in color, absorption spectra and particle sizes of these gold nanoparticles formed in the presence of various % of acetic acid were studied using UV-visible spectroscopy and Dynamic light scattering. The differences in the absorption spectra corresponding to changes in size and structure of gold nanoparticles formed were recorded and shown in Figure 1b.

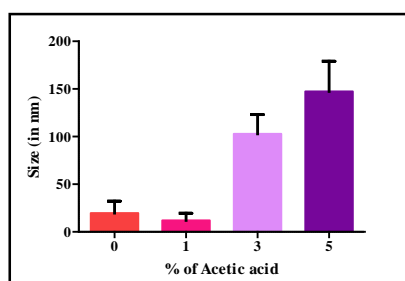


Figure 2: Size analysis of nanoparticles formed with different percentages of acetic acid.

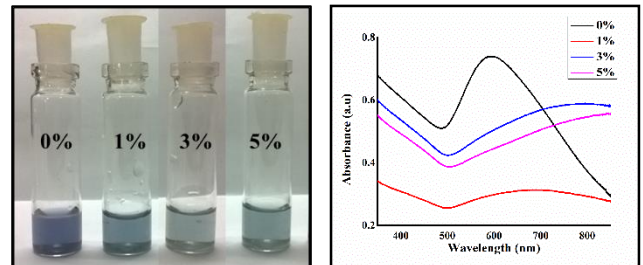


Figure 3: a) Colorimetric detection of % of acetic acid with liposome b) UV-visible spectra.

The size of these nanoparticles formed with different percentages of acetic acid was evaluated by dynamic light scattering system and is shown in Figure 2. The differences in structure of the nanoparticles were probed by Transmission Electron Microscopy (TEM). The quantification technique developed is sensitive in identifying the % of acetic acid compared to a simple pH strip and the colors were stable for longer durations.

The order of addition of reagents to achieve significant color difference with % of acetic acid is optimized. To further stabilize the quantification technique, liposome was added as a base material to identify the % of acetic acid. As can be seen from Figure 3, there is no clear difference in color as observed without liposome. Hence, the technique without any addition of liposome was taken forward for all the further experiments.

III. CONCLUSION

The proof of concept is demonstrated at laboratory level by detecting different percentages of acetic acid and the probable reasons for the difference in color were evaluated by UV-visible spectra, DLS and TEM. The quantification of acetic acid demonstrated the reliability and application potential of the proposed protocol for the detection. The proposed diagnosis technique shows great promise for in-field and point-of-care testing of cervical cancer. This platform could be extended with the existing visual inspection with acetic acid technique for rapid and reliable screening.

REFERENCES

- [1] Bray F, Ferlay J, Soerjomataram I, Siegel RL, Torre LA, Jemal A. Global cancer statistics 2018: GLOBOCAN estimates of incidence and mortality worldwide for 36 cancers in 185 countries. CA: a cancer journal for clinicians 2018;68:394-424.
- [2] Satyanarayana L, Asthana S, Bhambhani S, Sodhani P, Gupta S. A comparative study of cervical cancer screening methods in a rural community setting of North India. Indian journal of cancer 2014;51:124.
- [3] Vu M, Yu J, Awolude OA, Chuang L. Cervical cancer worldwide. Current problems in cancer 2018.
- [4] Huang X, El-Sayed MA. Gold nanoparticles: optical properties and implementations in cancer diagnosis and photothermal therapy. Journal of advanced research 2010;1:13-28.
- [5] Tsai T-T, Huang C-Y, Chen C-A, Shen S-W, Wang M-C, Cheng C-M, et al. Diagnosis of tuberculosis using colorimetric gold nanoparticles on a paper-based analytical device. ACS sensors 2017;2:1345-54.
- [6] Sina AAI, Carrascosa LG, Liang Z, Grewal YS, Wardiana A, Shiddiki MJ, et al. Epigenetically reprogrammed methylation landscape drives the DNA self-assembly and serves as a universal cancer biomarker. Nature communications 2018;9:4915.
- [7] Ouyang H, Wang M, Wang W, Fu Z. Colorimetric/chemiluminescent immunochromatographic test strip by using luminol-reduced gold nanoparticles as dual-response probes. Sensors and Actuators B: Chemical 2018;266:318-22.

Materials and Micro-Structure Design for Pyramidal Tactile Sensors

1 Haicheng Yao

2 Department of Materials Science and
3 Engineering, , , Singapore
4 National University of Singapore
5 Singapore
6 haicheng.yao@u.nus.edu

7 Benjamin C.K. Tee

8 Department of Materials Science and
9 Engineering
10 National University of Singapore
11 Singapore
12 benjamin.tee@nus.edu.sg

13 Zhuangjian Liu

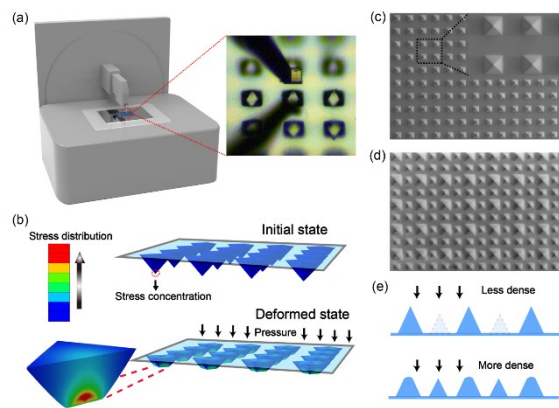
14 Institute of High Performance
15 Computing
16 A*STAR Research Entities
17 Singapore
18 liuzj@ihpc.a-star.edu.sg

19 Electronic-skin (e-skin) sensors enable robots and
20 biomedical devices to acquire highly intuitive skin-like
21 sensing abilities. To achieve ultra-high sensitivity,
22 microstructural designs such as micropyramids are
23 incorporated in the design of e-skin sensors. Prior research has
24 focused on investigating the effect of micropyramids on
25 sensitivity primarily at low load ranges, significantly limiting
26 the understanding of their behavior. Moreover, having
27 predictable pressure-induced electro-mechanical responses
28 are paramount for sensor designs and applications. Therefore,
29 systematic design principles for such microstructured sensors
30 are essential. Herein, we present for the first time, a search
31 engine-like system – SenSearch – to design micropyramidal
32 sensors across extensive applied load ranges. The
33 investigation combines numerical simulations, empirical
34 characterization and theoretical analysis. These validated
35 models allow for the rapid optimization of sensor performance
36 in relation to varying structures and materials properties. This
37 methodology could be used for sensor designs with tunable
38 sensitivity and desired mechano-electrical performance. The
39 Sensesearch platform can enable greater effectiveness in rapidly

40 In this work, we proposed a capacitive pressure (MPCP)
41 sensors made of polydimethylsiloxane (PDMS) by
42 characterizing various geometrical parameters and material
43 properties at the single micropyramid level. Their effects on
44 pressure response capability were explored through (i)
45 numerical simulations, (ii) empirical characterization and (iii)
46 theoretical analysis. (Fig. 1). First, the numerical simulations
47 informed the relationships between different parameters, e.g.
48 size of the micropyramids, sidewall angle of micropyramids,
49 PDMS Young's modulus, and their effect on sensing ability.
50 Next, empirical characterization provided correspondingly
51 matched results to show the validity of simulations.
52 Subsequently, we analyzed the theoretical relationship
53 between mechanical deformation and electrical response of
54 each single micropyramid. These combined enabled a
55 parameterized sensor design guidelines to deduce the
56 pressure response of MPCP sensors with varied adjustable
57 geometrical and material conditions across an extensive
58 applied load range. Finally, a search engine – SenSearch –
59 was built to enable custom sensor designs for desired sensor
60 performance.

61 In this study, the effects of various geometrical parameters
62 and material properties of PDMS-based micropyramids are
63 analyzed for adjustable and predictable sensing performance

64 of MPCP sensors. Derived equations yielded normalized
65 results, which could be used as parameterized guidelines for
66 deduction of sensor performance. Also, drawing inspiration
67 from the skin's sensing mechanism, real-time tunable sensing
68 was achieved using mix-sized micropyramids, which is allow
69 pressure sensors to adopt skin-like sensing behavior.
70 Additionally, theoretical analysis was presented for sensor
71 performance, relating mechanical and electrical sensing
72 responses. Based on these results, together the parameterized
73 guidelines, a programmable system (SenSearch system) was
74 built to optimize micropyramids. To do so, controllable
75 sensing design is achieved based on the requirements of
76 response performance. On-the-fly modification of sensor
77 parameters provides great design flexibility to overcome real-
78 world constraints of fabrication processes and cost. Our
79 systematic approach to elucidate structure-performance
80 relationships of micropyramidal sensors, coupled with the
81 SenSearch system, engenders immense possibilities for the
82 translation of MPCP sensors to robotics, prosthesis,
83 biomedical monitoring systems, promoting more widespread
84 integration of e-skin sensors in our daily lives



85 **Fig. 1.** Characterization of PDMS micropyramids, showing a)
86 Mechanical haracterization setup and schematic for single
87 micropyramid characterization. b) Numerical simulation of
88 stress distribution of micropyramid under compression. Stress
89 distribution at pyramid vertex leads to the high sensitivity. c)
90 Field Emission Scanning Electron Microscope (FESEM)
91 image of micropyramids array as dielectric layer for
92 capacitive pressure sensor. Each micropyramid has the size of
93 50 μ m and sidewall angle of 54.7°. d) FESEM image of mix-
94 sized micropyramids array. Micropyramids have size of both

50 μ m, 30 μ m and sidewall angle of 54.7°. e) Schematic of tunable pyramid density for mix-sized micropyramids.

Acknowledgement

The authors acknowledge funding from the NRF White Space: National Robotics Programme of Singapore (1722500063).

References

- [1] A. Chortos, J. Liu, Z. Bao, *Nat. Mater.* 2016, 15, 937.
- [2] B. C.-K. Tee, A. Chortos, A. Berndt, A. K. Nguyen, A. Tom, A. McGuire, Z. C. Lin, K. Tien, W.-G. Bae, H. Wang, P. Mei, H.-H. Chou, B. Cui, K. Deisseroth, T. N. Ng, Z. Bao, *Science*. 2015, 350, 313.
- [3] L. Y. Chen, B. C. Tee, A. L. Chortos, G. Schwartz, V. Tse, D. J. Lipomi, H. P. Wong, M. V. McConnell, Z. Bao, *Nat. Commun.* 2014, 5, 1.
- [4] B. C. K. Tee, J. Ouyang, *Adv. Mater.* n.d., 0, 1802560M. Liu, C. J. Castilho, R. H. Hurt, *Advanced Materials Letters*, 2018, 9, 8

Optically Stimulated Synaptic Device Based on the Hybrid Structure of Silicon Nanomembrane and Organolead Halide Perovskite

1
2
3
4
5
6
7
Lei Yin

State Key Laboratory of Silicon
Materials and School of Materials
Science and Engineering
Zhejiang University
Hangzhou, China
11726023@zju.edu.cn

8
9
10
11
12
13
14
Yiyue Zhu

State Key Laboratory of Silicon
Materials and School of Materials
Science and Engineering
Zhejiang University
Hangzhou, China
741542391@qq.com

15
16
17
18
19
20
21
Xiaodong Pi

State Key Laboratory of Silicon
Materials and School of Materials
Science and Engineering
Zhejiang University
Hangzhou, China
xdpi@zju.edu.cn

22
23
24
25
26
27
28
29
30
2 Deren Yang

State Key Laboratory of Silicon
Materials and School of Materials
Science and Engineering
Zhejiang University
Hangzhou, China
mseyang@zju.edu.cn

The Conventional von Neumann architecture faces the challenges of memory bottleneck and high power consumption due to constant data movements between the memory and the processor [1]. As an effective solution the hardware implementation of brain-inspired neuromorphic computing has attracted growing interests [2]. In particular, much attention has recently been paid to artificial synapses since they are the basic units of neuromorphic computing. Compared with synapses based on electrical stimulation, synapses based on optical stimulation are expected to further reduce the power consumption and increase the processing speed of neuromorphic computing because they require no sensing unit and feature less issues of interconnect [3-5].

In this work, we design and construct an optically-stimulated synaptic transistor based on the hybrid structure of silicon nanomembrane (Si NM) and organolead halide perovskite (MAPbI₃). The Si NM with efficient charge transport is used for the channel of the transistor. MAPbI₃ is coated on the Si NW as the light-absorbing layer. Transient photoresponse behaviors of the synaptic transistor are observed under lasers ranging from 375 to 808 nm at a constant intensity. It is shown that the decay of the photocurrent can be delayed after introducing MAPbI₃. Various synaptic behaviors are demonstrated for the synaptic transistors upon optical stimulation, e.g. excitatory postsynaptic current (EPSC) and paired-pulse facilitation (PPF). In addition, different synaptic plasticity can be realized, including short-term plasticity (STP), long-term plasticity (LTP), and the transition from STP to LTP. Furthermore, for device operation both the drain voltage and gate voltage are capable of regulating the photogenerated carriers and tuning the synaptic plasticity. The synaptic plasticity of the device

may be mainly attributed to the charge trapping/detrapping effect at the heterojunction interface. The power consumption of the synaptic device is very low (0.5 pJ), which is mainly due to the good carrier transport characteristics of Si NM [6] and the excellent optical absorption properties of perovskite[7].

Our current optoelectronic synapse is compatible with integrated circuit manufacturing process. This paves a way for the development of neuromorphic computing by taking the advantage of Si-based large-scale production.

REFERENCES

- [1] M. A. Zidan, J. P. Strachan, and W. D. Lu, "The future of electronics based on memristive systems," *Nat. Electron.*, vol. 1, no. 1, pp. 22–29, 2018.
- [2] Q. Wan, M. T. Sharbati, J. R. Erickson, Y. Du, and F. Xiong, "Emerging Artificial Synaptic Devices for Neuromorphic Computing," *Adv. Mater. Technol.*, vol. 4, no. 4, p. 1900037, Apr. 2019.
- [3] S. Qin et al., "A light-stimulated synaptic device based on graphene hybrid phototransistor," *2D Mater.*, vol. 4, no. 3, p. 35022, 2017.
- [4] H. Tan et al., "Broadband optoelectronic synaptic devices based on silicon nanocrystals for neuromorphic computing," *Nano Energy*, vol. 52, pp. 422–430, Jun. 2018.
- [5] Z. Ni et al., "Hybrid Structure of Silicon Nanocrystals and 2D WSe₂ for Broadband Optoelectronic Synaptic Devices," in 2018 IEEE International Electron Devices Meeting (IEDM), 2018, pp. 38.5.1-38.5.4.
- [6] J. A. Rogers and J. H. Ahn, *Silicon Nanomembranes*. Weinheim, Germany: Wiley-VCH Verlag GmbH & Co. KGaA, 2016.
- [7] S. De Wolf et al., "Organometallic Halide Perovskites: Sharp Optical Absorption Edge and Its Relation to Photovoltaic Performance," *J. Phys. Chem. Lett.*, vol. 5, no. 6, pp. 1035–1039, Mar. 2014.

Optoelectronic Devices Based on Silicon Nanocrystals

Xiaodong Pi

State Key Laboratory of Silicon Materials and School of Materials Science and Engineering, Zhejiang University, Hangzhou, Zhejiang 310027, China
xdpi@zju.edu.cn

Given the abundance and nontoxicity of silicon (Si) and their compatibility with existing Si technologies, Si nanocrystals (NCs) hold great promise for improving current Si-based applications and advancing the use of Si toward new fields such as neuromorphic computing. By taking advantage of the broadband absorption and localized surface plasmon resonance of Si NCs we have recently fabricated high-performance photodetectors with photodetection extended into the mid-infrared (MIR) region [1-3]. In these photodetectors Si NCs are coupled with graphene, which facilitates the charge transport in the device structures. Both optically and electrically stimulated optoelectronic synaptic devices have been realized by using the optical absorption and emission of Si NCs, respectively [4-6]. The realization of the bidirectional conversion between electrical and optical signals in synaptic devices may lead to the complete optoelectronic integration of artificial neural systems, helping fulfil the full potential of light in neuromorphic computing.

References

- [1] T. Yu, F. Wang, Y. Xu, L. L. Ma, X. D. Pi and D. Yang, *Graphene coupled with silicon quantum dots for high-performance bulk-silicon-based Schottky-junction photodetectors*, *Advanced Materials* **28**, 4912-4919 (2016).
- [2] S. C. Du, Z. Y. Ni, X. M. Liu, H. W. Guo, A. Ali, Y. Xu and X. D. Pi, *Graphen/silicon-quantum-dot/silicon Schottky-PN cascade heterojunction for short-wavelength infrared photodetection*, *International Electron Device Meeting (IEDM)*, 8.7.1-8.7.4 (2017), 2-6 Dec. 2017, San Francisco, USA.
- [3] Z. Y. Ni, L. L. Ma, S. C. Du, Y. Xu,*M. Yuan, H. H. Fang, Z. Wang, M. S. Xu, D. S. Li, J. Y. Yang, W. D. Hu, X. D. Pi and D. Yang, *Plasmonic silicon quantum dots enabled high-sensitivity ultra-broadband photodetection of graphene-based hybrid phototransistors*, *ACS Nano* **11**, 9854-9862 (2017).
- [4] H. Tan, Z. Y. Ni, W. B. Peng, S. C. Du, X. K. Liu, S. Y. Zhao, W. Li, Z. Ye, M. S. Xu, Y. Xu, X. D. Pi and D. Yang, *Broadband optoelectronic synaptic devices based on silicon nanocrystals for neuromorphic computing*, *Nano Energy* **52**, 422-430 (2018).
- [5] Z. Y. Ni, Y. Wang, L. X. Liu, S. Y. Zhao, Y. Xu, X. D. Pi and D. Yang, *Hybrid structure of silicon nanocrystals and 2D WSe₂ for broadband optoelectronic synaptic devices*, *International Electron Device Meeting (IEDM)*, 38.5.1-38.5.4 (2018), 1-5 Dec. 2018, San Francisco, USA.
- [6] S. Y. Zhao, Z. Y. Ni, H. Tan, Y. Wang, H. Jin, T. X. Nie, M. S. Xu, X. D. Pi and D. Yang, *Electroluminescent synaptic devices with logic functions*, *Nano Energy* **54**, 383-389 (2018).

Iodine intercalated graphene and its sensing properties towards NH₃ and NO₂ gas

Monica Jaiswal¹, Robin Kumar¹, Jagjiwan Mittal¹,

¹Amity Institute of Nanotechnology, Amity University, Noida Sector 125, Uttar Pradesh 201301, India
Email Id: mjaiswal@amity.edu

Abstract

Acceptor type graphite intercalation compounds (GICs) of transition metal oxides and chlorides have been widely studied in past [1] for their exceptional properties and potential applications in many areas. It has been found that Cl₂ can open the edges of graphene [2] and help in intercalation of metals [3]. In present study, Multi-layer graphene (MLG) is intercalated with Iodine using chloroform and exposure to UV light. XRD, SEM, EDX results support the intercalation of Iodine in MLG. A film of synthesized intercalated compound was deposited by drop and cast method to study its gas sensing properties. It was observed that sensor film shows a remarkable increase in electrical resistance with response of 183% towards NH₃ gas with exceptional detection time of 2 seconds at room temperature in air with 30 %RH. The same sensor can detect NO₂ and it was found that electrical resistance of the sensor decrease when exposed to NO₂ gas with a response of 36% at room temperature in air with 30% RH .The sensor show self-recovery on removal of NH₃ and NO₂.

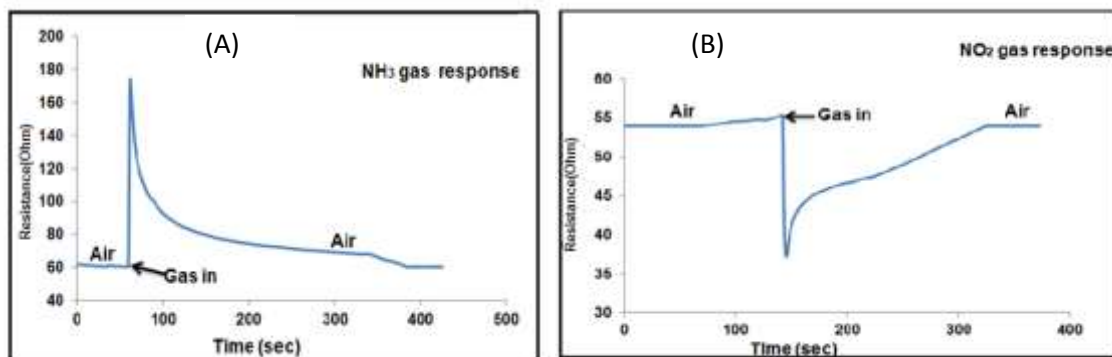


Fig 1. (A) shows the resistance change on exposure NH₃ and (B) change of resistance on exposure to NO₂

Table 1

Material	Gas	Response time (sec)	Recovery time (sec)	Response (S%)	Resistance
Iodine intercalated graphene	NH ₃	~2	~277	183% (200PPM)	Increase
	NO ₂	~2	~185	36% (200PPM)	Decrease

- [1] M. Inagaki, Applications of graphite intercalation compounds. *J. Mater. Res.* 4(1989)1560-8.
- [2] J. Mittal, H. Konno, M. Inagaki M. Synthesis of graphite intercalation compounds with Cr^{VI} compounds using CrO₃ and HCl at room temperature. *Synth. Met.* 96(1998) 103-8
- [3] J. Mittal and M. Inagaki, Effect of reaction of MoCl₅ with atmospheric water on its intercalation into graphite, *Solid State Ionics*, 121 (1999),183-18.

Engineering of Free-Free Type Micromechanical Resonators with Photonic Crystal Patterns for Gallium Arsenide-Based Cavity Optomechanics

Sushanth Kini Manjeshwar*, Karim Elkhouly*, Jamie M. Fitzgerald†, Martin Ekman†,
Shu Min Wang*, Philippe Tassin†, and Witlef Wieczorek*

*Department of Microtechnology and Nanoscience

Chalmers University of Technology
SE-412 96 Gothenburg, Sweden

Email: witlef.wieczorek@chalmers.se

†Department of Physics
Chalmers University of Technology
SE-412 96 Gothenburg, Sweden

Abstract—We present mechanically compliant, GaAs-based photonic crystal slabs for use in cavity optomechanics devices. The geometry of the slabs is chosen such to decrease clamping-induced mechanical dissipation. At the same time, the 100 nm-thick slab is patterned with a photonic crystal designed for increasing its out-of-plane reflectivity at telecom wavelengths. This particular design aims for maximizing the interaction between light and mechanical motion for future integration in multi-element cavity optomechanics devices.

Index Terms—optomechanics, micromechanical resonator, photonic crystal, gallium arsenide

I. INTRODUCTION

The interaction of light with mechanical motion in cavity optomechanical devices has lead to spectacular progress for controlling mechanical resonators, even down to the quantum regime [1]. An outstanding challenge in the field is reaching the single-photon strong coupling regime in chip-based devices. This regime would enable accessing the non-linearity of the optomechanical interaction that allows for direct generation of non-classical mechanical or optical states [2, 3]. The concept of multi-element optomechanics [4] has been proposed as a viable means to reach that regime. This concept exploits coupling of an intra-cavity optical field to multiple, independent mechanical resonators that exhibit a well-defined inter-element spacing. Recent experiments aim at implementing this concept using SiN-based mechanical devices [5–7].

II. RESULTS

In this work we present first steps towards realizing integrated multi-element optomechanics devices using crystalline aluminium gallium arsenide (AlGaAs) as material system. GaAs-based mechanical resonators [8–10] profit from epitaxial bottom-up material growth and precise top-down microfabrication. This processing technology results in devices of high mechanical and optical quality. Further, it allows to precisely

engineer the mechanical element's thickness and inter-element spacing as is required for feasibly implementing multi-element mechanical arrays [4].

The utilized mechanical resonators are of the free-free type geometry [8] to decrease undesired clamping loss to the substrate. The resonators are fabricated in a standard micro-fabrication process consisting of electron beam lithography, followed by dry and wet etching and finished by critical point drying. A scanning electron microscope image of a released device is shown in Fig. 1(a). Finite element simulation and corresponding mechanical mode tomography for the free-free type mechanical mode is shown in Fig. 1(b). Mechanical quality factors larger than 10^4 at room temperature have been measured. We expect an improvement of the quality factor by more than an order of magnitude when operating the slabs at temperatures of 4 K [10].

The mechanical resonator includes a photonic crystal pattern for maximizing its out-of-plane reflectivity, following Refs. [11, 12], see Fig. 1(a). Simulations based on rigorous coupled wave analysis show that an optical reflectivity exceeding 99.9% at the intended telecom wavelength range is feasible. First measurements of fabricated devices already indicate a reflectivity larger than 95%. Importantly, the reflectivity

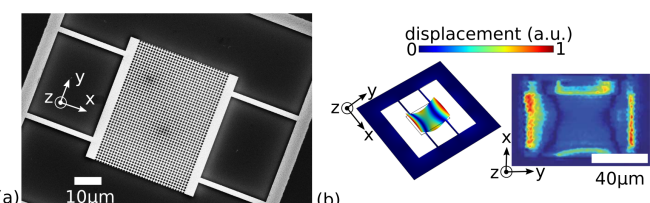


Fig. 1. Mechanical properties of GaAs-based photonic crystal reflectors. (a) Scanning electron microscope image of a suspended mechanical resonator with an inscribed photonic-crystal pattern. (b) Finite element modeling of the free-free oscillation mode of a mechanical resonator (left) and measured mechanical mode tomography (right).

depends on the size of the optical beam waist of the incident laser beam.

III. SUMMARY

We have successfully fabricated state-of-the art mechanical resonators in GaAs that exhibit a large out-of-plane reflectivity at telecom wavelengths. Future work aims at characterizing the devices at low temperatures with expected improvements in mechanical quality factor and further integration of the GaAs slab in a cavity optomechanical device.

ACKNOWLEDGMENT

We acknowledge fruitful discussions with Garrett D. Cole and Claus Gartner concerning microfabrication. We further acknowledge funding from Chalmers' Excellence Initiative Nano and from the Knut and Alice Wallenberg Foundation.

REFERENCES

- [1] M. Aspelmeyer, T. J. Kippenberg, and F. Marquardt, *Reviews of Modern Physics* **86**, 1391 (2014).
- [2] P. Rabl, *Physical Review Letters* **107** (2011).
- [3] A. Nunnenkamp, K. Borkje, and S. M. Girvin, *Physical Review Letters* **107** (2011).
- [4] A. Xuereb, C. Genes, and A. Dantan, *Physical Review Letters* **109** (2012).
- [5] B. Nair, A. Naesby, and A. Dantan, *Opt. Lett.*, **OL 42**, 1341 (2017).
- [6] P. Piergentili, L. Catalini, M. Bawaj, S. Zippilli, N. Malossi, Riccardo Natali, D. Vitali, and G. D. Giuseppe, *New J. Phys.* **20**, 083024 (2018).
- [7] C. Gartner, J. P. Moura, W. Haaxman, R. A. Norte, and S. Groblacher, *Nano Lett.* (2018).
- [8] G. D. Cole, I. Wilson-Rae, K. Werbach, M. R. Vanner, and M. Aspelmeyer, *Nature Communications* **2**, 231 (2011).
- [9] H. Yamaguchi, *Semicond. Sci. Technol.* **32**, 103003 (2017).
- [10] M. Hamoumi, P. Allain, W. Hease, E. Gil-Santos, L. Morgenroth, B. Gerard, A. Lematre, G. Leo, and I. Favero, *Phys. Rev. Lett.* **120**, 223601 (2018).
- [11] K. Makles, T. Antoni, A. G. Kuhn, S. Delglise, T. Briant, P.-F. Cohadon, R. Braive, G. Beaudoin, L. Pinard, C. Michel, V. Dolique, R. Flaminio, G. Cagnoli, I. Robert-Philip, and A. Heidmann, *Opt. Lett.* **40**, 174 (2015).
- [12] R. A. Norte, J. P. Moura, and S. Groblacher, *Phys. Rev. Lett.* **116**, 147202 (2016).

Type-II superlattice infrared detector development at IRnova: from eSWIR to VLWIR

L. Höglund, S. Naureen, M. Delmas, R. Ivanov, M. Pozzi, S. Almqvist, S. Becanovic, D. Rihtnesberg,
S. Smuk, W. Diel, S. Fattala, A. Smuk, E. Trybom and E. Costard

IRnova AB, Isafjordsgatan 22 C5, SE-16440 Kista, Sweden

InAs/GaSb and InAs/InAsSb Type-II superlattices (T2SLs) have proven to be excellent material for high end infrared (IR) detectors and are now competing with traditional state-of-the-art technologies, such as Indium Antimonide (InSb), Mercury Cadmium Telluride (MCT) and Quantum well infrared Photodetectors (QWIP). The desirable properties needed for good imaging performance, i.e. low dark current, high quantum efficiency (QE), low noise, high operability and good long-term stability are all fulfilled by the T2SL technology.

The high performance of T2SL detectors is enabled by high quality growth with molecular beam epitaxy (MBE) and by the flexibility to combine different lattice matched superlattices and bulk layers in the detector design. Positioning of wide bandgap barriers in the sensitive p-n junction region, act to reduce both generation-recombination (G-R) dark current as well as tunneling dark currents while allowing the desired photocurrent to flow unimpededly. This enables high photocurrent / dark current ratio in the infrared detectors based on these barrier designs.

Major investments in the T2SL technology have enabled rapid progress and now enables fabrication of megapixel detector arrays with maintained high performance and good manufacturability on up to 5" and 6" substrates. With this progress, T2SL detectors are now being qualified for major military programs¹ and are also challenging MCT for space applications². MW T2SL technology is currently also revolutionizing the market for low Size Weight and Power (low-SWaP) applications due to high operating temperatures (HOT) enabled with these devices^{3,4,5,6}.

In this paper, the basic physics of T2SL detectors will be discussed and an overview of the T2SL technology showing the different realizations of the technology will be given. Results from InAs/GaSb T2SL detector development at IRnova with detector cut-off wavelengths ranging from 2.4 μ m (eSWIR) to 14 μ m (VLWIR) will be demonstrated. The bandgaps (cut-off wavelengths) of the T2SL detectors were tailored to different wavelengths by individually varying the thickness and composition of the alternating layers in the SL. Absorption properties, quantum efficiencies and dark current densities will be compared for detectors with different cut-off wavelengths and the performance and imaging properties of T2SL FPAs will be demonstrated.

¹ Infrared Imaging News, August 2018 by Maxtech

² E. H. Steenbergen, C. P. Morath, D. Maestas, G. D. Jenkins, J.V. Logan, "Comparing II-VI and III-V infrared detectors for space applications", SPIE Proceedings Volume 11002, Infrared Technology and Applications XLV, 110021B (2019)

³ L. Höglund, S. Naureen, R. Ivanov, M. Pozzi, S. Almqvist, D. Rihtnesberg, S. Smuk, W. Diel, S. Fattala, A. Smuk, E. Trybom, E. Costard, "Type II superlattices: HOT MWIR production and development at IRnova", SPIE Proceedings 11002, Infrared Technology and Applications XLV, 110020U (2019)

⁴ D. Forrai et. al. "Implementing VISTA technology in a III-V detector foundry" Proceedings Volume 10177, Infrared Technology and Applications XLIII, 101770X (2017)

⁵ E. P. Smith et al. "III-V strained layer superlattice infrared detector characteristics and FPA performance", Proceedings Volume 10177, Infrared Technology and Applications XLIII, 101770V (2017)

⁶ See FLIR, Neutrino products

Operando observation of analog resistance change in metal / oxide junctions

Yuji Okuda

Graduate School of Science,
Tokyo University of Science
Katsushika-ku, Tokyo, Japan
AIST-UTokyo Advanced Operando-
Measurement Technology Open
Innovation Laboratory
National Institute of Advanced
Industrial Science and Technology
Tsukuba, Ibaraki, Japan
1518508@ed.tus.ac.jp

Junpei Kawakita

The Institute for Solid State Physics,
The University of Tokyo
Kashiwa, Chiba, Japan
AIST-UTokyo Advanced Operando-
Measurement Technology Open
Innovation Laboratory
National Institute of Advanced
Industrial Science and Technology
Tsukuba, Ibaraki, Japan
kawakita@issp.u-tokyo.ac.jp

Toshiyuki Taniuchi

The Institute for Solid State Physics,
The University of Tokyo
Kashiwa, Chiba, Japan
AIST-UTokyo Advanced Operando-
Measurement Technology Open
Innovation Laboratory
National Institute of Advanced
Industrial Science and Technology
Tsukuba, Ibaraki, Japan
taniuchi@issp.u-tokyo.ac.jp

Hisashi Shima

AIST-UTokyo Advanced Operando-
Measurement Technology Open
Innovation Laboratory
National Institute of Advanced
Industrial Science and Technology
Tsukuba, Ibaraki, Japan
Nanoelectronics Research Institute
National Institute of Advanced
Industrial Science and Technology
Tsukuba, Ibaraki, Japan
shima-hisashi@aist.go.jp

Atsushi Shimizu

Graduate School of Science.
Tokyo University of Science
Katsushika-ku, Tokyo, Japan
Nanoelectronics Research Institute
National Institute of Advanced
Industrial Science and Technology
Tsukuba, Ibaraki, Japan
1518524@ed.tus.ac.jp

Yasuhiba Naitou

AIST-UTokyo Advanced Operando-
Measurement Technology Open
Innovation Laboratory
National Institute of Advanced
Industrial Science and Technology
Tsukuba, Ibaraki, Japan
Nanoelectronics Research Institute
National Institute of Advanced
Industrial Science and Technology
Tsukuba, Ibaraki, Japan
ys-naitou@aist.go.jp

Kentaro Kinoshita

Graduate School of Science.
Tokyo University of Science
Katsushika-ku, Tokyo, Japan
kkinoshita@rs.tus.ac.jp

Hiro Akinaga

AIST-UTokyo Advanced Operando-
Measurement Technology Open
Innovation Laboratory
National Institute of Advanced
Industrial Science and Technology
Tsukuba, Ibaraki, Japan
Nanoelectronics Research Institute
National Institute of Advanced
Industrial Science and Technology
Tsukuba, Ibaraki, Japan
akinaga.hiro@aist.go.jp

Shik Shin

The Institute for Solid State Physics,
The University of Tokyo
AIST-UTokyo Advanced Operando-
Measurement Technology Open
Innovation Laboratory
Kashiwa, Chiba, Japan
National Institute of Advanced
Industrial Science and Technology
Tsukuba, Ibaraki, Japan
shin@issp.u-tokyo.ac.jp

We observed analog resistance changes in resistive random access memory (ReRAM) with metal / oxide junctions using laser-excited photoemission electron microscopy (Laser-PEEM). Laser-PEEM observations revealed that analog resistance change occurred in a whole of the device area in ReRAM elements before the occurrence of forming.

INTRODUCTION

ReRAM is a device with a simple structure consisting of an oxide layer with two electrodes at both ends [1]. It records data as its resistance that can be changed by voltage application. In particular, an analog resistance change, meaning that a resistance changes in a continuous manner against voltage stimulation, is expected to be suitable for the applications to neuromorphic computing [2]. However, the origin of an analog resistance change is not clear. So, what makes the difference between threshold and analog behaviors of resistance against voltage stimuli should be elucidated. The decrease of resistance is considered to occur by the generation of oxygen vacancies, which might cause a carrier doping. The oxygen vacancies are formed

by redox reactions caused when voltages are applied between electrodes. Accordingly, an analog behavior can be disturbed due to the local aggregation of oxygen vacancies, resulting in a threshold behavior. Therefore, the development of nanoscale analysis technology of real-space distributions of carriers will help us to establish the control method of analog resistance changes, visualizing the operating area.

Here we propose Laser-PEEM [3] as this analysis method. Laser-PEEM provides us with real-space information on density of states near the Fermi level of materials. So, fine changes in electronic states such as the increase and decrease of carrier density are observable. Furthermore, it is possible to observe changes in the oxide layers buried with the top electrodes without distraction, since probing depth is as large as tens of nanometers. Previously, we have detected that the carrier density of Ta_2O_5 -ReRAM rises at the moment of forming by using Laser-PEEM [4]. However, the operation area in the analog resistance changes has not been identified, because the analog resistance changes was not observed.

In this study, we performed *operando* observation of analog resistance changes and identified the operation area.

EXPERIMENTAL

The ReRAM stacking structure, consisting of Pt-top electrode (10 nm) / Ta_2O_5 (5 nm) / TiN-bottom electrode (20 nm), was deposited on a SiO_2/Si substrates by the method of RF sputtering in crossbar structure. This sample was loaded into the PEEM chamber with the electrical connections to a source measure unit (SMU) as Fig. 1. In this state, the voltage sweep caused the analog resistance change as shown in an I - V characteristics in Fig. 2. The I - V characteristics reached a current limit of 0.1 mA imposed by the SMU just after the occurrence of forming at -4.3 V. The analog resistance changes were observed from the sample normal with Laser-PEEM. We have calculated the differences in photoelectron intensity between images taken after sweep and the initial image for each. The differential images show only the changes of the photoelectron intensities due to the voltage sweep.

RESULTS & DISCUSSIONS

Figs. 3(a) and (b) show PEEM images at the initial and after sweeping a voltage to -4.3 V, respectively. Fig. 3(c) shows the differential image between these two images. We have found an increase in photoelectron intensity (red color spots) in a whole of the ReRAM device, suggesting the increase of carriers entirely over the device area. Figs. 4 (a) - (j) show differential images between images taken after each voltage sweep and the initial image, respectively. This suggests that the carrier density increases over the whole device area by voltage application. In the previous report, calculation by density functional theory predicted that energy levels originated in oxygen vacancies are generated just below the conduction band in Ta_2O_5 [5]. Considering this calculation result, the increase of conductivity observed in Fig. 2 might be due to the increase of carrier density as a result that the oxygen vacancies worked as electron donors. This scenario is consistent with the PEEM images shown in Figs. 3 and 4, since the introduction of donor level just below the conduction band pulls up the Fermi level to the bottom of the conduction band and it will make the PEEM intensity high. This is also consistent with the fact that the resistance before forming generally show temperature dependence of thermal activation type. Although an area at which a photoelectron intensity is high will be local not the whole of the device area, the similar phenomenon will be observed after the threshold switching as observed in our previous reports [4].

We expect that *operando* Laser-PEEM can observe of various devices other than ReRAM because of the capability of nondestructive *operando* carrier observation.

CONCLUSION

In this study, we succeeded in visualizing the operating area during the analog resistance change until the occurrence of forming in ReRAM. The results showed that analog resistance changes occur over a whole of the device area. It was also suggested that the PEEM intensity was related to the generation and repair of oxygen vacancies. This study will help us to establish the control method for analog resistance changes.

ACKNOWLEDGMENT

A part of this work was supported by Photon and Quantum Basic Research Coordinated Development Program from MEXT and JSPS KAKENHI 2522070.

REFERENCES

- [1] H. Akinaga, H. Shima, "Resistive random access memory (ReRAM) based on metal oxides," *Proc. IEEE*, vol. 98, no. 12, pp. 2237-2251, (2010).
- [2] S.-H. Jo, T. Chang, I. Ebong, B. B. Bhadviya, P. Mazumder, and W. Lu, "Nanoscale Memristor Device as Synapse in Neuromorphic Systems," *Nano Lett.* 10, 1297- 1301 (2010).
- [3] T. Taniuchi, Y. Kotani, and S. Shin, "Ultrahigh-spatial-resolution chemical and magnetic imaging by laser-based photoemission electron microscopy," *Rev. Sci. Instrum.* 86, 023701 (2015).
- [4] J. Kawakita, H. Shima, Y. Naitoh, H. Akinaga, T. Taniuchi, S. Shin, "Non-Destructive Observation of Chemical State in ReRAM by Laser-excited Photoemission Electron Microscopy," 49th *SSDM*, Sendai, Japan, PS-4-02 (Sep. 19-22, 2017).
- [5] R. J. Bondi, M. P. Desjarlais, A. P. Thompson, G. L. Brennecke, and M. J. Marinella, "Electrical conductivity in oxygen-deficient phases of tantalum pentoxide from first-principles calculations," *J. Appl. Phys.* 114, 203701 (2013).

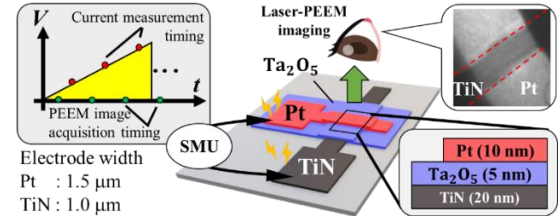


Fig. 1. Sample structure and *operando* observation geometry. The ReRAM of the actual device structure was observed in *operando*.

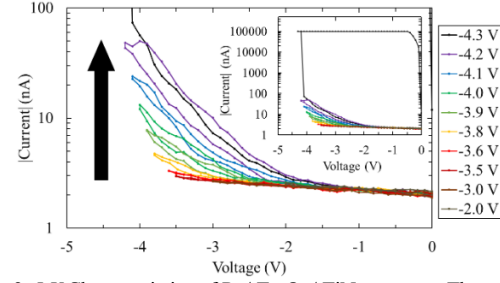


Fig. 2. I - V Characteristics of Pt / Ta_2O_5 / TiN structure. The resistance decreases as the maximum of the sweep voltage rises.

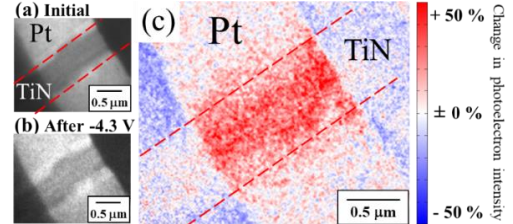


Fig. 3. (a) and (b) PEEM images at the initial and after -4.3 V sweep. (c) Differential image of photoelectron intensity between (a) and (b). Blue and red colors show the decrease and increase in photoelectron intensity, respectively.

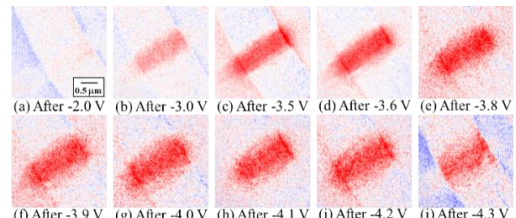


Fig. 4. Changes of the photoelectron intensity. (a)-(j) are differential images taken after applied voltages subtracted by the initial image. The applied voltage are indicated at the top of each image.

1
2
3
4
5
6
7
8
9
10
11
12
13
14
15
16
17
18
19
20
21
22
23
24
25
26
27
28
29
30
31
32
33
34
35
36
37
38
39
40
41
42
43
44
45
46
47
48
49
50
51
52
53
54
55
56
57
58
59
60
61
62
63
64
65

Doping of K-OMS-2 nano fibers with Ni and Cu for NH₃ and CO gas sensing

Robin Kumar¹, Monica Jaiswal¹ and Jagjiwan Mittal¹

¹Amity Institute of Nanotechnology, Amity University,

Sector125, Noida, Uttar Pradesh 201313, India

E-mail address: rkumar5@amity.edu

Carbon monoxide (CO) is a major pollutant in our environment and it is highly toxic to humans and animals. Ammonia is an important gas in various industrial and domestic applications. However, human body is severely affected by the exposure to the high concentration of gaseous ammonia. Irritation of the eyes, throat, skin and respiratory system are the major problems. As per US standard, >35ppm concentrations of CO exposure and ammonia may cause problems to humans and their high concentrations may lead to unconsciousness and death. Development of low cost selective and sensitive carbon monoxide (CO) and ammonia gas sensors are essential for industries, indoor and outdoor air quality monitoring. Metal doped Octahedral molecular sieves (M-OMS-2) nanofibers are attractive due to their easy and low-cost processing, good catalytic properties and high aspect ratio which provide high specific surface area for high adsorption for reducing gas [1]. Many attempts have been made to develop the CO and NH₃ sensors but either at high temperature, costly or low response. Due to better stability and good catalytic activity the synthesis, characterization, and applications of manganese oxide octahedral molecular sieves (OMS-2) have gained considerable research interest. Small doping of different elements (Ni, Cu, Fe, Co Ag, Nb, etc.) in OMS-2 changes its structural, catalytic, chemical and electronic properties. The coordination and crystal radii of the dopant cations determine where the doping occurs. The metal dopants can either replace some of the potassium ions or substitute the manganese into the octahedral framework of OMS-2

In the present work, K-OMS-2 was doped with small amount of Cu and Ni and the sensing ability of Cu-OMS-2 and Ni-OMS-2 towards CO and NH₃ was studied. Cu-OMS-2 showed the quick response of 18% and 33% in 55 sec when exposed to 10 ppm and 100 ppm of CO gas, respectively and recovered to the original value in ~42 sec after the removal of CO source. Ni-OMS-2 sensor showed strong response of 20% and 57% for 10 ppm and 50 ppm of NH₃ in just 60 seconds. No heating was required either for sensing or recovery in both cases. The sensor films displayed good repeatability for multiple exposures of respective gases at room temperature. The response and recovery time are compared with the undoped K-OMS2 nanofibers and sensing mechanism is proposed. Synthesis and characterization of Cu-OMS-2, Ni-OMS-2 and their sensing ability for carbon monoxide and NH₃ with related mechanism will be presented in the conference.

References

1. J. Luo, Q. Zhang, J.G. Martinez and S.L. Suib, *J. Am. Chem. Soc.* 130, 3198 (2008).

Analytical Modeling of Subthreshold Characteristics of Silicon-Nanotube-based Double Gate-All-Around (DGAA) FETs Incorporating Fringing Field Effects

Arun Kumar, P S T N Srinivas, and Pramod Kumar Tiwari

Department of Electrical Engineering, Indian Institute of Technology Patna, Bihta, Bihar, 801103, India

Email: arun.pee16@iitp.ac.in, surya_1821ee04@iitp.ac.in, pktiwari@iitp.ac.in

Abstract—In this paper, an analytical model of subthreshold characteristics of silicon-nanotube based DGAA FETs incorporating the fringing field effects have been developed. Pao-Sah's double integration method has been utilized for the formulation of the subthreshold current considering both drift and diffusion current components. Since the device structure is inherently asymmetrical in nature; so the effective conductive path due to both inner and outer channel surfaces has been formulated. The model of the subthreshold slope has also been presented in this work. The effects of the fringing field due to High-K dielectrics have been incorporated in the developed subthreshold current and subthreshold slope models. The effects of various device parameters such as channel thickness, effective oxide thickness, bias voltage variation, etc have been demonstrated. The accuracy of the proposed model has been verified by comparing with the numerical simulation results obtained from the device simulator VTCAD of Cogenda Int.

Keywords— DGAA MOSFETs, subthreshold current, subthreshold slope, fringing fields,

I. INTRODUCTION

To meet the end of ITRS roadmap and to continue the trend of scaling, many non-convention MOSFETs structures have been proposed, tested and fabricated by the researches, among these structures gate-all-around (GAA) found to be a most promising candidate for continuous device scaling [1]. GAA structures show excellent controllability of short channel effects (SCEs), but it suffers from the problem of low-drive current [1]. In order to overcome the problem of low drive current poised by GAA structure, double gate-all-around (DGAA) FETs structure has been presented [1]. DGAA FETs structures show a superb immunity to short channel effects along with high drive current as compared to GAA structure. In DGAA FETs, the circular channel region is surrounded by two gates, core gate (inner gate) and shell gate (outer gate) respectively. Thus the presence of two gates provides strong electrostatic control over the entire channel region.

Continuing with the ITRS roadmap of device downscaling, the device physical dimension such as channel thickness, source/drain thickness, oxide thicknesses are also scaled down. This scaling of oxide thickness approaches to the tunneling limit for electrons resulting in an enormous amount of gate leakage current. In order to resolve the problem of gate leakage, SiO_2 is replaced with alternative materials with higher permittivity and greater physical thickness as the gate dielectric material [2]. However, the use of high-K gate-dielectric material results in an increased gate-dielectric thickness comparable to the gate length of the

device. Such increment in gate-dielectric thickness results in an increased fringing field originating from the gate region to the source/drain regions of the device [2-3]. Many models have been developed so far as to estimate the fringing field capacitance for the conventional and non-conventional FETs [2-3]. In our earlier work, we have presented the analytical threshold voltage models dealing with the high-K dielectric induced fringing field effects for DGAA FETs [3].

In the present work, subthreshold current and subthreshold slope models for DGAA FETs. Including fringing field effects is developed. The device is assumed to be asymmetric in nature, so the effective conductive paths are also formulated. The model includes the parasitic fringing field induced charges in source and drain regions to improve the model accuracy. The channel length and the tube thickness are chosen in such a way that, the quantum-mechanical effect becomes negligible for the device. In order to check the accuracy of the proposed model, results obtained from the proposed model have been validated with TCAD results obtained from the VTCAD device simulator [4].

II. CONCLUSION

In this work, an analytical model of subthreshold characteristics of silicon-nanotube based DGAA FETs incorporating the fringing field effects has been developed. Pao-Sah's double integral method has been utilized in the formulation of the subthreshold current model of the device. The effects of the fringing field due to High-K dielectrics have been incorporated in the developed subthreshold current and subthreshold slope models. The accuracy of the proposed model has been tested and verified by numerical simulation results obtained from the device simulator VTCAD of Cogenda Int.

REFERENCES

- [1]. H. M. Fahad, C. E. Smith, J. P. Rojas, and M. M. Hussain, "Silicon nanotube field effect transistor with core-shell gate stacks for enhanced high-performance operation and area scaling benefits," *Nano Lett.*, vol.11, no. 10, pp. 4393-4399, Sep. 2011.
- [2]. M. J. Kumar, S. K. Gupta, V. Venkataraman, "Compact modeling of the effects of parasitic internal fringe capacitance on the threshold voltage of high-k gate-dielectric nanoscale SOI MOSFET", *IEEE Trans. Electron Devices*, vol. 52, no. 4, pp. 706-711, Apr. 2004.
- [3]. A. Kumar, P S T N Srinivas, S. Bhushan, S Dubey, Y K Singh and P. K. Tiwari "Threshold Voltage Modeling of Double Gate-All-Around Metal-Oxide-Semiconductor Field-Effect-Transistors (DGAA MOSFETs) Including the Fringing Field Effects", *J. Nanolectron. Optoelectron.*, Vol. 14, pp. 1-10, 2019
- [4]. Cogenda Pte, Singapore, Genius, 3-D Device Simulator, Version 1.9.0, Reference Manual, 2008.

Design and Fabrication of High-transmittance Electromagnetic Shielding Metallic Mesh Based on Randomly Distributed Mirco-Rings and Sub-Rings

1st Xi Lu

Ultra-precision Optical & Electronic
Instrument Engineering Center
Harbin Institute of Technology
Harbin, P. R. China
lucinda_lx@163.com

2nd Zhengang Lu

Ultra-precision Optical & Electronic
Instrument Engineering Center
Harbin Institute of Technology
Harbin, P. R. China
luzhengang@hit.edu.cn

3rd YiLei Zhang

Ultra-precision Optical & Electronic
Instrument Engineering Center
Harbin Institute of Technology
Harbin, P. R. China
zyl85602068@126.com

4th Heyan Wang

Ultra-precision Optical & Electronic
Instrument Engineering Center
Harbin Institute of Technology
Harbin, P. R. China
hitwhy@yeah.net

5th Jiubin Tan

Ultra-precision Optical & Electronic
Instrument Engineering Center
Harbin Institute of Technology
Harbin, P. R. China
jbtan@hit.edu.cn

The electromagnetic shielding technology of optical transparent component has important application value in many fields such as electronic displays, mobile communication devices and etc. An ideal shielding material for transparent component need to have high transmittance, uniform stray light distribution and strong electromagnetic shielding to obtain excellent imaging quality and anti-interference ability of equipment[1]. Among many kinds of high transmittance thin films, metallic mesh is one of the effective methods to achieve those comprehensive indexes at the same time[2,3].

This paper analyses and summarizes the different structural characteristics of existing metallic mesh. Based on this, a structural design scheme of metallic mesh based on randomly distributed micro rings and sub-rings is proposed. Based on scalar diffraction theory, the normalized diffraction intensity distribution model of metallic mesh is established and the transmittance is calculated. Based on the equivalent refractive index model of high-transmittance circular mesh and the structural characteristics of the metallic mesh designed in this paper, the equivalent reactance model is modified to make it suitable for the analysis of electromagnetic shielding efficiency of metallic mesh based on random rings and sub-rings. Then, considering the diffraction and electromagnetic shielding characteristics of metal mesh comprehensively, the parameters of metallic mesh based on random rings and sub-rings are analyzed and optimized. The simulation results show that the maximum diffraction intensity is reduced by at least 40% under the existing metallic mesh with the same transmittance[4].

The metallic mesh structure designed in this paper is processed by ultraviolet lithography technology, the influence of the parameters in each processing step on the quality was analyzed, and the final parameters were determined to produce a complete metallic mesh with the wire width in no more than 2.5 microns. The parameters of the metal mesh are tested by experiments. The experimental results show that the

metal mesh samples based on random rings and sub-rings had a high transmittance, depth homogenization of high-order diffraction and strong electromagnetic shielding efficiency in Ku band at the same time. All the indexes are in agreement with the simulation results, which proves the accuracy of the proposed diffraction model, electromagnetic shielding efficiency analysis model and the processing accuracy for random rings metallic mesh. The design method and sample of metallic mesh proposed in this paper can meet the performance requirements of precision optical instruments and equipment, and has a very broad application prospects.

ACKNOWLEDGMENT

We wish to thank the support from National Natural Science Foundation of China (NSFC). We also wish to express our sincere gratitude to CST Computer Simulation Technology GmbH, Germany, for providing a free package of CST Studio Suite® at the CST Training Center (Northeast China Region) in our university.

REFERENCES

- [1] I. B. Murray, V. Densmore, V. Bora, M. W. Pieratt, D. L. Hibbard, and T. D. Milster, "Numerical comparison of grid pattern diffraction effects through measurement and modeling with OptiScan software," Proc. SPIE 8016, 80160U (2011).
- [2] Z. Lu, H. Wang, J. Tan. Achieving an ultra-uniform diffraction pattern of stray light with metallic meshes by using ring and sub-ring arrays. Optics letters, 2016, 41(9): 1941-1944..
- [3] H. Wang, Z. Lu, Y. Liu, J. Tan, L. Ma, and S. Lin, "Double-layer interlaced nested multi-ring array metallic mesh for high-performance transparent electromagnetic interference shielding," Optics letters, 2017, 42, 1620-1623.
- [4] X. Lu, Y. Liu, Z. Lu, Y. Zhang, H. Wang, R. Ji, and J. Tan. High-transmittance double-layer frequency-selective surface based on interlaced multiring metallic mesh[J]. Optics letters, 2019,44(5):1253-1256.

Improved design and fabrication of HOT MWIR Type-II superlattices detectors at IRnova

S. Naureen, M. Pozzi, S. Almqvist, D. Rihtnesberg, L. Höglund, R. Ivanov, S. Smuk, W. Diel, S. Fattala, A. Smuk, E. Trybom and E. Costard

IRnova AB, Isafjordsgatan 22 C5, SE-16440 Kista, Sweden

Type-II superlattices (T2SL) have proven to be a mature technology for production of infrared focal plane arrays (FPAs). IRnova has been manufacturing midwave infrared (MWIR) FPAs since 2014 and has since then demonstrated excellent manufacturability of these FPAs with good stability, high operability, and narrow noise distribution. In the initial studies, the FPAs were operated at 85 K. However, during the past years, the improvements in the design and fabrication techniques with new passivation methods have enabled excellent performance up to 110 K.

The limiting factors, which initially prevented high operating temperatures (HOT) of these FPAs, were too high dark current, noise levels and too low quantum efficiency. In this paper we will demonstrate the importance of proper surface preparation and passivation techniques to reduce surface leakage currents. The surface states of III-V materials, which cause surface dark current and noise in the FPAs are directly related to the defect density. Moreover, etch by-products and other contaminations generated during dry etch for pixel isolation could also create extra interfacial states contributing to the dark current. Another important improvement in the T2SL devices at IRnova, is the new detector design, which helped to increase the detector quantum efficiency from 30 % to 55% in a single pass through the absorber material. This improved QE increased the ratio between the photogenerated current and dark current, which is the key for HOT devices. We will also demonstrate the importance of good hybridization techniques to get high operability of the devices, which now typically exceeds 99.8% for 640 x 512 FPAs with 15 μ m pitch. Finally, we will present results from these HOT FPAs and demonstrate imaging with FPAs integrated in F/4 IDDCAs with low Size, Weight and Power (SWaP), resulting in 20 mK noise equivalent temperature difference (NETD) for ca 10 ms integration time.

1
2
3
4
5
6
7
8
9
10
11
12
13
14
15
16
17
18
19
20
21
22
23
24
25
26
27
28
29
30
31
32
33
34
35
36
37
38
39
40
41
42
43
44
45
46
47
48
49
50
51
52
53
54
55
56
57
58
59
60
61
62
63
64
65

Synthesis, Processing and Characterization of Thermoelectric Thick Films

Bejan Hamawandi¹, Nuria Vicente^{1,2}, Martina Orlovska^{1,3}, Zulfiqar Shah¹, Muhammet S. Toprak¹

¹*KTH, Department of Applied Physics, School of Engineering Sciences, SE10691 Stockholm, Sweden*

²*Jaume I University, Department of Industrial Systems Engineering, ES12006 Castelló, Spain*

³*STU, Department of Inorganic Materials, Radlinského 9, 81237 Bratislava, Slovakia*

Abstract

Nano-structured thermoelectric (TE) materials and devices have developed tremendous interest for thermal management and harvesting waste heat energy. There is an increasing interest to fabricate flexible TE materials and devices with low cost and high efficiency, for emerging applications such as wearable TE power generators, health sensors, and powering small mobile wireless devices.

Fabrication of large-area TE materials has been a big challenge, which has been dealt with by the design of polymer-inorganic hybrid materials that can be applied by different schemes to conformably cover any surface. To date very few hybrid materials with decent TE performance have been developed, which has been limited due to the quality of the starting commercial TE powders as starting materials. The major challenge has been the formulation of the TE hybrid materials with good dispersion and viscosity characteristics.

Here, we report a complete process of fabricating TE thick films using colloidal chemistry principles. Microwave assisted synthesis method was developed and used for TE nanoparticles, which were then utilized to fabricate thick TE films using doctor blading technique. The most important feature of this technique is the processing speed, which takes only few minutes to synthesize desired n- and p-type TE nanomaterials by using developed microwave-assisted thermolysis route. These TE nanoparticles were then surface modified with N-methyl-2-pyrrolidone and mixed with PVDF before casting into hybrid TE films on solid or flexible substrates. This concept can also be referred to as “TE paint”. The fabricated n- and p-type TE films with pre-determined aspect ratios were evaluated for their transport properties as a function of process parameters and thickness. These flexible hybrid materials may have tremendous potential for flexible TE devices.

Analysis of T-shaped Plasmonic Nanogap Wavelength Filters

Geum-Yoon Oh, Jeong Beom Ko, Hyungchan Kim, and *Choon Keun Park

Bio Convergence Technology Group

Korea Institute of Industrial Technology

102 Jejudaehak-ro, Jeju-si, Jeju Special Self-Governing Province

*ckpark@kitech.re.kr

Photonic integrated circuits (PICs) have been a very active research area ever since the inception of integrated optics for the application of the wavelength division multiplexing networks. In this paper, we reported the T-shaped nano-gap resonator with the straight waveguide without the ring shape resonator, which is replaced with a straight waveguide, nano-metallic layer, T-shaped waveguide, and nano-gap. We investigated the resonant properties of the structure using the FDTD method. The results reveal that the proposed structure has the band-stop characteristic for PICs.

A. Introduction

Photonic integrated circuits (PICs) have been a very active research area ever since the inception of integrated optics for the application of the wavelength division multiplexing networks. One of the main size limitations to regular integrated optics based circuits is the weak optical confinement. This makes it very difficult to change the direction of optical waveguides in a very short distance with low loss. Photonic band gap based approaches offer promise of compact waveguide size that can be bent over very rapidly. However, wavelength dependence and the fabrication difficulty remain to be the challenges [1]. On the other hand, advances in nanofabrication and full-wave electromagnetic simulation techniques have permitted the design and realization of a wide variety of plasmonic waveguide structures as excellent candidates for future nanoscale electronic-photonic integrated circuits [2, 3]. However, a major problem in design of plasmonic waveguide-based devices is the inherent tradeoff between the propagation loss due to the high dissipation level of metals and the optical mode confinement. To overcome this problem, a few approaches have been proposed, including the long-range dielectric-loaded plasmonic waveguide and the Metal-Insulator-Metal (MIM) plasmonic waveguide [4]. According to previous studies, 2D MIM-based resonant structures suitable for filtering purposes can be mainly categorized as ring resonators, stubs and slots [5]. Of particular interest in this paper are square-shaped ring resonators which have been investigated as efficient resonating structures to realized band stop filters. Similarly to rectangular-shaped MIM resonators, square-shaped resonators provide high coupling efficiency due to the long coupling section between the waveguide and the resonator compared with circular rings.

In this paper, we propose a SOI-based novel resonator structure combining straight waveguide resonator with nanogap for application to highly tunable optical filters. In our design, the ring type resonator is replaced with a straight waveguide, nano-metallic layer, T-shaped waveguide, and nanogap. We use the finite difference time domain (FDTD) method to investigate the resonant properties of the structure.

The results reveal that the proposed structure has the band stop characteristic without the ring shape resonator.

B. The Device description and analysis

Figure 1 shows the schematic of the proposed SOI-based nanogap resonator with the straight waveguide and T-shaped waveguide. The structure parameters consist of the width of the waveguide (d), the gap width between the waveguide and the resonator (w_g), the width of the resonator (w_c), the height of the resonator (h_c), the width of the Ag layer (w_m) for resonance, the thickness of the Ag layer (t_m), and the thickness of the waveguide core (t_w).

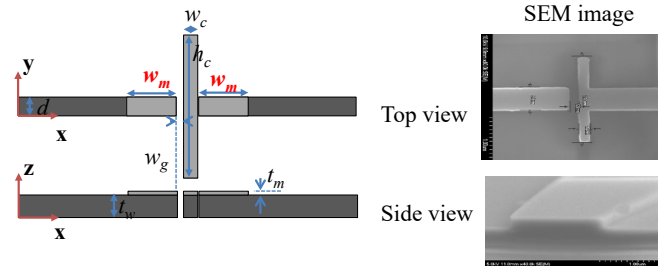


Fig. 1. Schematic of plasmonic nanogap resonator with top and side view.

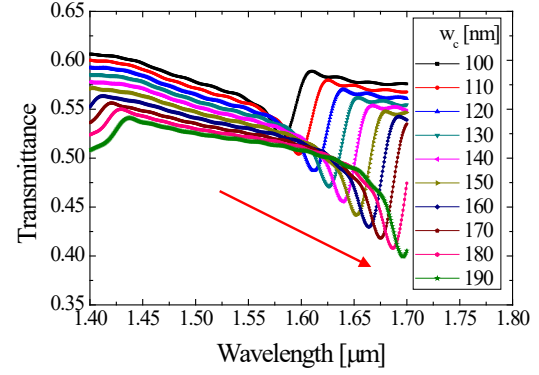


Fig. 2. Transmittance for resonator width variation (w_c).

Figure 2 illustrate transmittance of the structures with different resonator width, w_c . In order to find the change of the resonant wavelength according to the resonator width change, it can be seen that the resonance peak shifts to the long wavelength as the w_c increases. Also, the amount of output light decreases linearly as the area where the resonance occurs becomes wider. Surface plasmon polaritons are p-polarized optical surface waves that propagate along a metal-dielectric interface with fields that peak at the interface and decay exponentially away into both sides. Therefore, the TM mode wave cannot propagate into the waveguide due to the metallic

reflection and the coupling loss. In the TE mode case, when the propagating wave into the waveguide is arrived at metallic layer, the reflection is appeared gradually, which is similar to Fabry-Perot resonator mode as w_m variation.

More results will be presented.

ACKNOWLEDGMENT

This work was supported by the National Research Foundation of Korea(NRF) grant funded by the Korea government(MSIT) (No. NRF-2017R1D1A1B03030108).

REFERENCES

- [1] D. G. Kim, G. Y. Oh, W. K. Choi, H. J. Kim, S. H. Kim, H. C. Ki, S. T. Kim, H. J. Ko, T. U. Kim, M. H. Yang, H. J. Kim, J. C. Yi, Y. Chung, N. Dagli, and Y. W. Choi, "Extremely small multimode-interference coupled triangular resonator with sharp angle of incidence," *Opt. Exp.*, vol. 16, pp. 21053-21058, Dec. 2008.
- [2] E. Ozbay, "Plasmonics: Merging Photonics and Electronics at Nanoscale Dimensions," *Science*, vol. 311, pp. 189-193, Jan. 2006.
- [3] D. K. Gramotnev and S. I. Bozhevolnyi, "Plasmonics beyond the diffraction limit," *Nat. Photonics*, vol. 4, pp. 83-91, Jan. 2010.
- [4] V. S. Volkov, Z. Hua, M. G. Nielsen, K. Leosson, H. Keshmiri, J. Gosciniak, O. Albrektsen, and S. I. Bozhevolnyi, "Long-range dielectric-loaded surface plasmon polariton waveguides operating at telecommunication wavelengths," *Opt. Lett.*, vol. 36, pp. 4278-4280, Nov. 2011.
- [5] A. Hosseini and Y. Massoud, "Nanoscale surface plasmon based resonator using rectangular geometry," *Appl. Phys. Lett.*, vol. 90, pp. 181102, Apr. 2007.

NMDC 2019 1570569623

Macromolecular Gates

1
2
3
4
5
6
7
8
9
10
11
12
13
14
15
16
17
18
19
20
21
22
23
24
25
26
27
28
29
30
31
32
33
34
35
36
37
38
39
40
41
42
43
44
45
46
47
48
49
50
51
52
53
54
55
56
57
58
59
60
61
62
63
64
65
Andreas Dahlin
Dept. of Chemistry and Chemical
Engineering
Chalmers University of Technology
Gothenburg, Sweden
adahlin@chalmers.se

There is a steady need for new methods to detect, separate and analyze biomolecules using *in vitro* or “bottom-up” approaches. In this project we combine plasmonic nanopores[1] and polymer brushes with the long-term aim to develop new bioanalytical devices. Meanwhile we also address fundamental questions within the fields of macromolecules and supramolecular chemistry. Examples are interactions (or just repulsion) between different proteins and synthetic polymer chains. The combination of polymer brushes and nanopores offers unique possibilities to study brushes as barriers or selective filters. For one thing, interactions with the surface can be ignored as they do not influence the molecular transport through the brush. To complement the work with nanopores we also perform extensive analysis of the polymer brushes on planar surfaces using various tools, in particular surface plasmon resonance,[2-4] but also quartz crystal microbalance and electrochemical methods.

I will show recent results of plasmonic nanopores sealed by polymer brushes that either repel or attract proteins. Such pores enable new types of biomolecular filters whose properties are determined solely by the brush. The diameter of the pore in the solid material does not influence the permeability properties as long as the polymer brush is thick enough to seal the cross section (in essence equal to the radius). So far we have shown that a poly(ethylene glycol) brush can be an extremely strong barrier towards proteins while still allowing flow of water, ions and small molecules.[5] This is despite the fact that the brush consists mainly of water (>80%) and has no cross-links or self-interactions. Understanding brushes as barriers can lead to the development of ultrathin filters inspired by the remarkable selectivity of biological systems (Fig. 1).

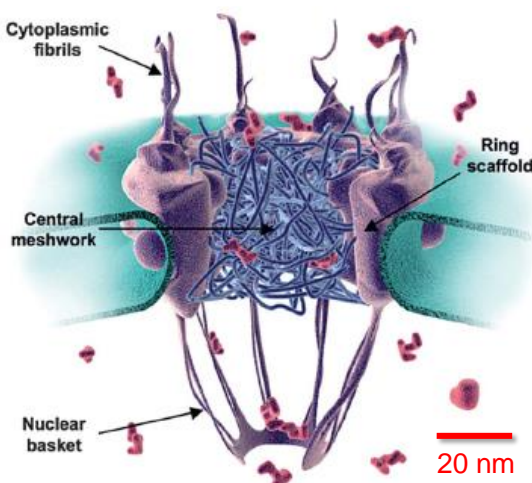


Fig. 1. Schematic representation of the nuclear pore complex. Image from Patel et al. *Cell* 2007, 129 (1), 83-96.

I will also describe different ways to achieve “gating”, i.e. morphology changes in the brush that make the sealed nanopores permeable to proteins on demand.[6] This could have applications in single molecule analysis by trapping proteins in a non-invasive manner under physiological conditions in volumes as small as one attoliter (a nanopore in a membrane). One can envision nanoscale reaction chambers where individual molecules and their interactions are analyzed by fluorescent techniques (Fig. 2).

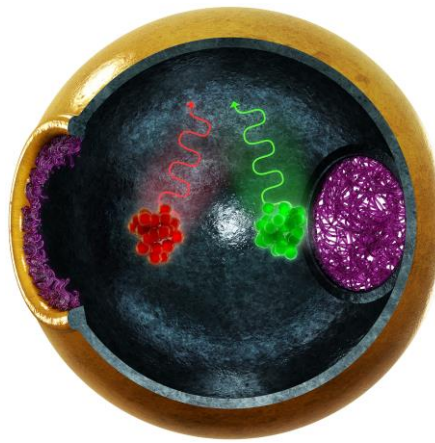


Fig. 2. Artistic description of a nanoscale reaction chamber for single molecule analysis, which is a possible future application of the macromolecular gates.

ACKNOWLEDGMENT

This work is financed by the Knut & Alice Wallenberg Foundation, the Erling-Persson Family Foundation and the Swedish Research Council.

REFERENCES

- [1] Dahlin, A. B. Sensing applications based on plasmonic nanopores: The hole story. *Analyst* **2015**, 140, 4748-4759.
- [2] Ferrand-Drake del Castillo, G.; Emilsson, G.; Dahlin, A. Quantitative analysis of thickness and pH actuation of weak polyelectrolyte brushes. *Journal of Physical Chemistry C* **2018**, 122, 27516-27527.
- [3] Emilsson, G.; Schoch, R. L.; Oertle, P.; Xiong, K.; Lim, R. Y. H.; Dahlin, A. B. Surface plasmon resonance methodology for monitoring polymerization kinetics and morphology changes of brushes - evaluated with poly(N-isopropylacrylamide). *Applied Surface Science* **2017**, 396, 384-392.
- [4] Emilsson, G.; Schoch, R. L.; Feuz, L.; Hook, F.; Lim, R. Y. H.; Dahlin, A. B. Strongly stretched protein resistant poly(ethylene glycol) brushes prepared by grafting-to. *ACS Applied Materials & Interfaces* **2015**, 7, 7505-7515.
- [5] Emilsson, G.; Xiong, K.; Sakiyama, Y.; Malekian, B.; Ahlberg Gagner, V.; Schoch, R. L.; Lim, R. Y. H.; Dahlin, A. B. Polymer brushes inside solid state nanopores form an impenetrable entropic barrier for proteins. *Nanoscale* **2018**, 10, 4663-4669.
- [6] Emilsson, G.; Sakiyama, Y.; Malekian, B.; Xiong, K.; Adali-Kaya, Z.; Lim, R. Y. H.; Dahlin, A. B. Gating protein transport in solid state nanopores by single molecule recognition. *ACS Central Science* **2018**, 4, 1007-1014.

Pressureless TLPS Bonding with Cu and Sn-58Bi Particles and Its Corrosion Behavior in 5% NaCl Solution

Kwang-Ho Jung, Kyung Deuk Min, Choong-Jae Lee, and Seung-Boo Jung*

School of Advanced Materials Science & Engineering

Sungkyunkwan University

Suwon-si, Gyeonggi-do

*sbjung@skku.edu

Recent trends for automotive technology has been getting verified with the advent of vehicle to everything (V2X), eco-friendly vehicles, sharing platform, etc. As the rapid trends for automotive technology is leading the increased portion of electronic system in an automobile, high-reliable electronic materials applicable to the harsh operating environments are getting more important [1]. Especially, alternative vehicles such as electric vehicles (EVs), hybrid electric vehicles (HEVs), plug-in hybrid electric vehicles (PHEVs), and fuel cell electric vehicles (FCEVs) strongly require stable power control system consisting of high-reliable materials and their operating temperature is commonly over 200 °C [2,3]. However, Sn alloy solder, the conventional interconnection materials in electronic packages, has critical problems of low re-melting temperature and awful reliability when being applicable in power electronics.

For these reasons, many studies have addressed alternative bonding technologies for high-temperature electronics, including high-temperature soldering, transient liquid phase (TLP) bonding, and sintering bonding [4]. Although the high-reliable interconnection technologies have advantages concerning high re-melting temperature and robust strength under harsh environments, there are technological barriers such as cost, high process temperature & pressure, void, brittleness, etc., which should be overcame. Transient liquid phase sintering (TLPS) bonding is advanced bonding technology combining TLP and sintering so that the weakness of both TLP and sintering bonding like the requirement of long time and high pressure process can be alleviated.

In our prior study, we developed TLPS paste consisting of Cu and Sn-58Bi particles for low-temperature (220 °C), short-time (under 90 min), pressureless bonding in order to minimize chip damage [4]. Bonding time and temperature indirectly indicating activation energy for interfacial reaction affected the formation of IMCs and voids. Also, the interfacial reaction further proceeded under high-temperature storage test (HTST) and the bonding characteristics of the TLPS joints could be changed. In this study, we fabricated the TLPS paste containing Cu (4 µm) and Sn-58Bi (35 µm) particles at three ratios of Cu to Sn-58Bi (1:9, 3:7, 5:5) and analyzed corrosion behavior in 5% NaCl solution for studying their electrochemical reliability.

The initial bonding strength of the TLPS joints was the strongest at higher content ratio of Sn-58Bi due to the active melting of the low-temperature solder (Sn-58Bi). However, the strength drastically decreased from about 45 MPa to 14 MPa with salt spray test for 96h. On the other hand, the

strength of the joint fabricated with the TLPS paste containing lower Sn-58Bi particles tended to maintain since the Sn remained little after bonding process and the electrochemical resistance of IMCs from corrosion is more noble than Sn residues. Cross-sectional SEM graph showed the corrosion behavior of TLPS joint and the active formation of corroded Sn residues was investigated in the content ratio of 1:9. We analyzed electrochemical characteristics of the respective TLPS paste with electrochemical impedance spectroscopy (EIS) and identified the inactiveness of the TLPS paste.

ACKNOWLEDGMENT (Heading)

This research was supported by Basic Science Research Program through the National Research Foundation of Korea(NRF) funded by the Ministry of Education(No. 2017R1D1A1B03035587 & No. 2019R1A6A1A03033215).

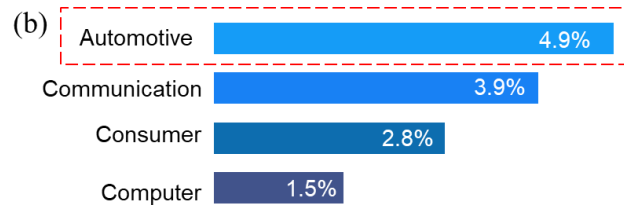
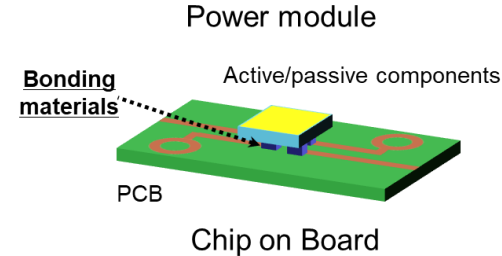
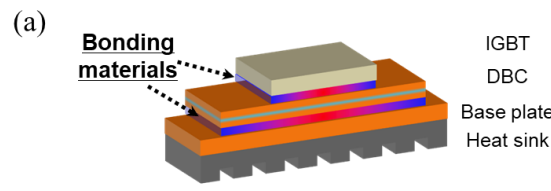


Fig. 1. (a) Schematic diagrams bonding materials in power electronics and mobile electronics, and (b) compound annual growth rate for electronics systems (2015-2020, IC Insights)

This work was supported by “Human Resources Program in Energy Technology” of the Korea Institute of Energy Technology Evaluation and Planning (KETEP), granted financial resource from the Ministry of Trade, Industry & Energy, Republic of Korea. (No. 20174030201800)

REFERENCES

- [1] K. Meier, M. Winkler, and K. Bock, “Fatigue Behaviour of Lead-Free Solder Joints Under Combined Thermal and Vibration Loads,” 2019 IEEE 69th Electronic Components and Technology Conference (ECTC).
- [2] T. Kadoguchi, N. Take, K. Yamanaka, and S. Nagao, “Highly thermo-stable joint of Cu/Ni plating/composite Sn-0.7Cu solder with added Cu balls for die attachment in power modules,” *J. Mater. Sci. Mater. Electron.* vol. 29, pp. 18290-18301, 2018.
- [3] R.W. Johnson, J.L. Evans, P. Jacobsen, J.R. Thompson, and M. Christopher, “The changing automotive environment: high-temperature electronics,” *IEEE Trans. Electron. Packag. Manuf.* vol. 27, 164e176, 2004.
- [4] K. H. Jung, K. D. Min, C. J. Lee, and S. B. Jung, “Pressureless die attach by transient liquid phase sintering of Cu nanoparticles and Sn-58Bi particles assisted by polyvinylpyrrolidone dispersant,” *J. Alloy. Compd.* vol. 781, pp. 657-663, 2019.

Design and Development of Quantum Dots Infused Films and an Optical Reader for Measurement of Blood Electrolytes

Pankaj Shihhare

Department of Biosciences &
Bioengineering

Indian Institute of Technology Bombay
Mumbai, India
pankaj.shihhare@iitb.ac.in

Sana Syeda Aliya

Department of Biosciences &
Bioengineering

Indian Institute of Technology Bombay
Mumbai, India
p15588@iitb.ac.in

Satyam Mohla,

Department of Electrical Engineering
Indian Institute of Technology Bombay
Mumbai, India
satyammohla@iitb.ac.in

Samarth Uttam

Department of Biosciences &
Bioengineering

Indian Institute of Technology Bombay
Mumbai, India
samarthuttam@iitdmj.ac.in

Prof. Rohit Srivastava

Department of Biosciences &
Bioengineering

Indian Institute of Technology Bombay
Mumbai, India
rsrivasta@iitb.ac.in

Abstract— A new method for blood plasma sodium and potassium monitoring and quantification is developed. MPA CdTe quantum dots, chromoionophore I and II, Potassium ionophore, Sodium ionophore, and cation exchanger and PVC is used to developed sodium and potassium sensor films. The sensor films produce fluorescence in the presence of blood plasma sodium or potassium. The excitation and emission wavelength of the quantum dots were programmed at 380nm and 600 nm, respectively. An optical reader was also developed for the quantification of the fluorescence-based sensor films.

Keywords—Quantum Dots, Blood Electrolytes, Point-of-care Devices, Optical Reader

I. INTRODUCTION

Blood electrolytes such as sodium and potassium are the fundamental ions as normal body functions depend on the right regulation of sodium and potassium both inside and outside of cells. Patients having medical conditions like central diabetes insipidus, hepatic cirrhosis, chronic kidney disorder, are prone to have the electrolyte imbalance. The monitoring of these ions in the blood plasma is quite critical and challenging. The common clinical techniques used for the detection of sodium are flame photometry and ion selective electrode (ISE) [1-3]. Recently, Optical based ions detection techniques have attracted much attention. Optical sensors have been widely used for quantitative measurement of the different analyte. They have various advantages over ISE such as no reference is required, minimal electrical interference, the output is insensitive to sample flow rate. Many absorbance based optical sensors for Na^+ , K^+ , Ca^+ and ammonium ions have been reported using optodes thin film assembly [2-5]. In the present report, a new method is proposed for the quantification of the sodium and potassium ions in blood plasma using Quantum Dots (QDs) infused sensor films and an optical reader.

II. MATERIAL AND METHODS

A. Materials

Cadmium Chloride monohydrate ($\text{CdCl}_2 \cdot \text{H}_2\text{O}$) (GR, >99.5%) was procured from Merck Pvt. Ltd., India. Tellurium powder (200 mesh, 99.8%), 1-Dodecanethiol (DDT) (98%),

Sodium Ionophore X (4-tert-Butylcalix[4]arenenetetraacetic acid tetraethyl ester), Chromoionophore-I (3-Octadecanoylimino-7-(diethylamino)-1,2 benzophenoxazine) and Sodium tetrakis [3,5-bis(trifluoromethyl)phenyl] borate were purchased from Sigma-Aldrich, USA. PolyVinyl Chloride (PVC) and Bis-2-Ethyl Hexyl Sebacate (97%) was obtained from Otto Chemicals, India. Tetrahydrofuran, acetone, sodium borohydride, sodium chloride, Mercaptopropionic acid (MPA) (puriss for synthesis, 99%) and other common laboratory reagents were obtained from SpectroChem Pvt. Ltd. All solvents and chemicals used in the experiments are of analytical grade. They were used as received without any further alteration and purification.

B. Synthesis of Quantum Dots and their Characterizations

Firstly, tellurium and cadmium precursors were synthesized in order to initiate the Quantum Dots preparation. In a round bottom flask, 10mmol $\text{CdCl}_2 \cdot \text{H}_2\text{O}$ was added in adequate amount of milliQ water to prepare cadmium precursor. The setup has the side openings to maintain the required temperature. Nitrogen purging was done in order to stabilize the solution. Then 210 μl of 24 mmol MPA was added into the above solution. The pH of the solution was raised from acidic to extremely basic condition (pH 11.5) using 2M NaOH [6-7]. Tellurium power and sodium borohydride were dissolved in milliQ to prepare tellurium precursor. Nitrogen purging was done in order to create the oxygen-free environment for the reaction. The temperature of the solution was maintained around 50°-60°C and the appearance of the purple colour was the indication of the reaction end-point. The purple colour appeared because of the formation of sodium telluride. After preparation of the required precursors, tellurium was introduced into the cadmium contained flask with almost care. In the absence of oxygen, the solution turned into the reddish-brown solution, which is the indication of the successful formation of the uniform and monodisperse QDs [7].

Small volumes of the formed QDs solution were taken at different time intervals for assessment. Once the reaction was ended, the QDs solution was immediately cooled to prevent further growth. The QDs solution was filtered and stored at 4°C for further use and characterizations.

C. QDs Infused PVC Polymeric Film Preparation

The sodium and potassium sensor films were prepared by evenly spreading 10 μ l of polymer solution onto a cleaned 5mm glass coverslips. The constituents of polymer solution were 0.1mg/ml CH-I, 0.2mg/ml potassium ionophore-X/ sodium ionophore-X, 0.1mg/ml cation exchanger, 0.2mg/ml CdTe-QDs, 150mg/ml PVC beads and 150mg/ml plasticiser mixed in 1ml of THF respectively. The solution was left to dry out at RT for 2 hours.

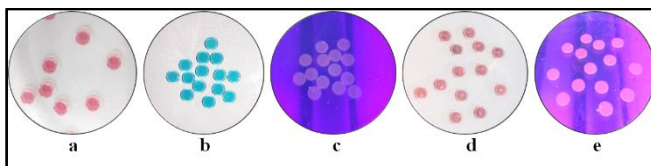


Figure 1. (a) Developed QD films (b) QD films after treatment with glycine HCl buffer (pH-4) under normal light (c) QD films after treatment with glycine HCl buffer (pH-4) under UV light (380 nm) (d) QD films changes its colour after incubation 5 min with 10 μ l of sodium standard solution, under normal light (e) QD films produces fluorescence after 5 min incubation with sodium solution, under UV light (380 nm)

III. CHARACTERIZATION OF THE QUANTUM DOT FILMS

A. FEG-Transmission electron microscopy (TEM) Imaging

10 μ l of prepared QDs solution was dispersed in Tetrahydrofuran (THF), loaded onto the TEM grid, and kept drying 10 μ l of organic QDs dispersed in toluene was loaded into TEM grid and kept for drying overnight.

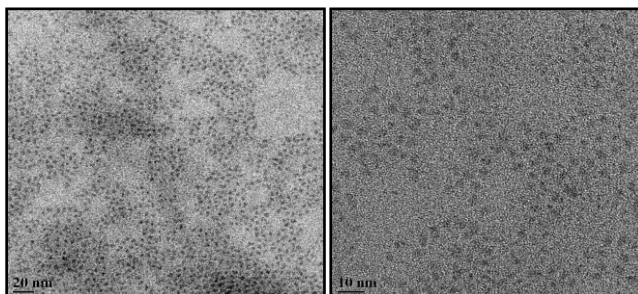


Figure 2. The average size of the prepared cadmium telluride quantum dots is 3.3 nm.

IV. DEVELOPMENT OF OPTICAL READER

An electronic reader was developed for the quantification of fluorescence of the sodium and potassium sensor films. The development of optical reader is divided into three parts; (a) Light illumination module, (b) Fluorescence sensing module, (c) Electronic hardware. The light illumination module consists of UV LEDs with uniform light radiation. The radiation wavelength of the UV led is selected based on the excitation wavelength of the sodium and potassium films and the QDs preparation. The developed QDs gives strong fluorescence when excited at 380 nm. The emission wavelength of the QDs is programmed in the range of 600 nm. We have selected a photodiode, which has a maximum spectral response at this range. The selected photodiode is highly sensitive light to digital value converter. It transforms light intensity into a digital signal output capable of the direct I2C interface. The high sensitivity of the photodiode enables to detect the smallest change in the fluorescence intensity.

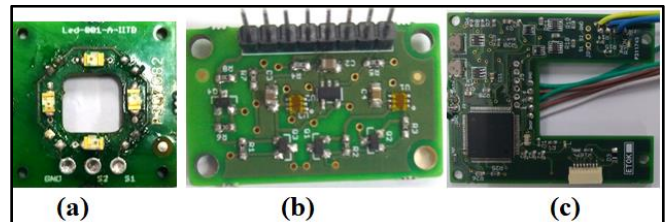


Figure 3. The electronic architecture of the optical reader.

V. RESULT AND DISCUSSION

The developed QDs fused sensor films for sodium and potassium were tested with the optical reader. The sensor films were tested with different concentration of the sodium and potassium standards. The results were compared with the results obtained from Synergy HTX Microplate reader.

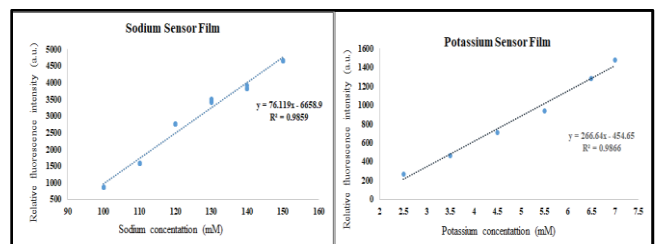


Figure 4. Testing of sodium and potassium sensor films with an optical reader.



Figure 5. Developed optical reader for the quantification of the QDs fused sodium and potassium sensor films

REFERENCES

- [1] Xie, X., Mistlberger, G., and Bakker, E. "Ultrasmall fluorescent ion-exchanging nanospheres containing selective ionophores," *Analytical chemistry*, 2013, vol. 85(20), pp. 9932-9938.
- [2] Xie, L., Qin, Y., & Chen, H. Y., "Direct fluorescent measurement of blood potassium with polymeric optical sensors based on upconverting nanomaterials," *Analytical chemistry*, 2013, vol. 85(5), pp. 2617-2622.
- [3] Dubach, J. M., Das, S., Rosenzweig, A., and Clark, H. A., "Optical nanosensors for intracellular sodium analysis," In *LEOS 2008-21st Annual Meeting of the IEEE Lasers and Electro-Optics Society IEEE*, November 2008, pp. 238-239.
- [4] Imoto, M., Sakaki, T., and Osakai, T., "Sophisticated Design of PVC Membrane Ion-Selective Electrodes Based on the Mixed Potential Theory," *Analytical chemistry*, 2013, vol. 85(9), pp. 4753-4760.
- [5] Bühlmann, P., and Chen, L. D., "Ion - Selective Electrodes With Ionophore - Doped Sensing Membranes," *Supramolecular Chemistry: From Molecules to Nanomaterials*, 2012.
- [6] Borse, V., and Srivastava, R., "Fluorescence lateral flow immunoassay based point-of-care nanodiagnostics for orthopedic implant-associated infection," *Sensors and Actuators B: Chemical*, 2019, vol. 280, pp. 24-33.
- [7] Borse, V., Sadawana, M., and Srivastava, R., "CdTe quantum dots: aqueous phase synthesis, stability studies and protein conjugation for development of biosensors," In *Nanophotonics VI, International Society for Optics and Photonics*, April-2016, vol. 9884, pp. 98842.

Towards a Microfabricated Flexible Graphene-Based Active Implant for Tissue Monitoring During Optogenetic Spinal Cord Stimulation

Andrada Iulia Velea^{1,2}, Sten Vollebregt², Vasiliki Giagka^{1,3}

¹*Bioelectronics Section and ²Electronic Components, Technology and Materials Section,*

Department of Microelectronics, Delft University of Technology, Mekelweg 4, 2628 CD, Delft, The Netherlands

³*Technologies for Bioelectronics Group, Department of System Integration and Interconnection Technologies, Fraunhofer Institute for Reliability and Microintegration IZM, Berlin, Germany*

A.I.Velea@student.tudelft.nl, S.Vollebregt@tudelft.nl, V.Giagka@tudelft.nl

Abstract – Our aim is to develop a smart neural interface with transparent electrodes to allow for electrical monitoring of the site of interest during optogenetic stimulation of the spinal cord. In this work, we present the microfabrication process for the wafer-level development of such a compact, active, transparent and flexible implant. The transparent, passive array of electrodes and tracks have been developed using graphene, on top of which chips have been bonded using flip-chip bonding techniques. To provide high flexibility, soft encapsulation, using polydimethylsiloxane (PDMS) has been used. Preliminary measurements after the bonding process have shown resistance values in the range of $k\Omega$ for the combined tracks and ball-bonds.

Keywords – Neural interface, optogenetic stimulation, active implant, graphene, PDMS.

I. INTRODUCTION

Epidural spinal cord stimulation (ESCS) has been proven to promote locomotion recovery in patients affected by spinal cord injuries (SCIs) [1]. However, optimization of the specifications for such therapies is still under research and identifying the mechanism of action could greatly benefit from parallel monitoring of the response of the biological tissue during stimulation. Usually, in ESCS, energy is injected into the tissue in the form of electrical pulses, leading to activation. Alternatively, energy in the form of light can also be used to activate the tissue, in a more spatially specific manner, using optogenetics.

Already available electrode arrays for ESCS feature opaque electrodes which limit electrical monitoring of the tissue response during optogenetic excitation [2]. Therefore there is the need to develop optically transparent, conductive, and flexible electrodes. This will allow for capturing the electrical activity of the neurons below the activation site at the time of stimulation. One potential material for these electrodes is graphene, as the material is optically transparent, bendable, potentially biocompatible, and has excellent electrical properties [3, 4]. Graphene microelectrode arrays have been previously reported as passive implants with Au tracks to interface the electrodes

with the outside active system [3]. However, for a smart implant, ultimately, active components, e.g. integrated circuits (ICs), have to be embedded with the electrodes to allow for signal acquisition, in-situ amplification and processing.

The aim of the current work is the development, by means of microfabrication, of a compact, flexible, graphene-based, active spinal cord monitoring implant for optogenetic stimulation.

II. MATERIALS AND METHODS

A microfabrication process has been used to ensure repeatability and maintain the small size of the implant while achieving high resolution. Fig. 1 depicts the process steps of the current work.

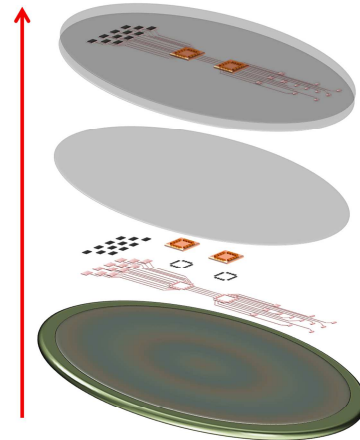


Fig. 1. Process steps of the proposed method. A molybdenum catalyst layer is used for graphene growth, on top of which chips are bonded and later, the complete structure is encapsulated in polymer.

Chemical vapor deposited (CVD) graphene tracks and electrodes have been microfabricated on a wafer level, using a pre-patterned 50 nm Mo layer as a catalyst, deposited on SiO_2 as described in detail in [5]. On top, 100 nm of Ti and 675 nm of Al have been deposited and patterned in order to create a bonding interface between graphene and the Au

stud bumps existent on the pads of the chips. Later, using a thermocompression flip-chip bonding technique, chips were bonded to the substrate. Next, 50 μm of Sylgard 184 polydimethylsiloxane (PDMS), 1:10 ratio, have been spin coated on top of the structure and cured at 90 $^{\circ}\text{C}$ for 1 hour. At this point, the complete structure had to be transferred or released from the original wafer in order to spin coat the final PDMS encapsulation layer. To do so, two approaches have been investigated, as illustrated in fig. 2.

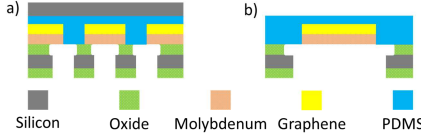


Fig. 2. Approaches used to transfer/ release the structure. In a), a wet transfer approach, using buffered hydrofluoric acid (BHF) 7:1 for oxide etching. In b), a “flex-to-rigid” (F2R) approach [6].

The approach in a) consists of the creation of through-silicon vias (TSV), before graphene growth, to increase the number of access points for the etchant, while the approach in b) consists of a deep reactive ion etching (DRIE) process for cm-size areas (that can later be coated with PDMS as final encapsulation), performed after having the complete structure on the wafer, an approach known as F2R [6].

III. RESULTS AND DISCUSSION

First, Raman spectroscopy was performed to ensure the presence of graphene (fig. 3). The ratio I_{2D}/I_G suggests that a multilayer graphene has been grown on the substrate, while the ratio I_D/I_G estimates the amount of defects present in the graphene layer (the greater the ratio, the more defects can be found). The defects originate from the growth process [5].

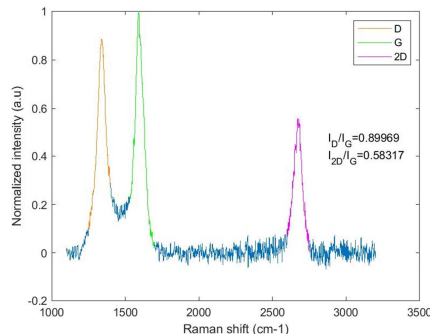


Fig. 3. Raman spectroscopy measurement, taken with a 633 nm laser. The 3 peaks indicate the presence of graphene.

A. “Wet” transfer of structure

BHF etching of the oxide layer from beneath the structure, has been tested. The expected etch rate was 150 nm/min and the total calculated etching time was 40 min. Yet, after 7 hours, no etching around the TSV has been observed. Possibly, DRIE of the TSV resulted in the deposition of a polymer layer which could not be removed by O₂-plasma treatment. To circumvent this, potassium hydroxide (KOH) etching was performed to widen the pathways for the BHF. However, after these long wet etching steps, the structures were highly damaged or even removed. Since later in the process, at this step, chips containing active components will also be present, wet transfer of the structure is to be avoided.

B. “Flex-to-rigid” approach

Fig. 4 shows the results obtained after the DRIE process, for silicon removal, in combination with wet etching of the remaining oxide layer. The complete area of the implant was successfully suspended and the membranes did not contain any significant wrinkles or damages.

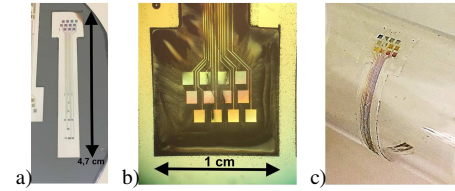


Fig. 4. Implant structure with Mo tracks after DRIE. In a), the complete suspended implant can be observed. In b), a detailed perspective of the PDMS membrane and tracks is presented. In c), the high flexibility of the structure is shown.

C. Flip-chip bonding

So far, no flip-chip bonding processes on graphene substrates have been reported in the literature and since our initial attempt showed that the adhesion between graphene and Au stud bumps is poor, the creation of a metal interface in between has been chosen as an alternative.

Fig. 5 a) depicts a visual representation of the structures before and after flip-chip bonding. In b), a computer tomography (CT) scan, after the bonding process is illustrated, while c) and d) show a preliminary 2-point measurement result. The resistance, $\sim 7.6 \text{ k}\Omega$, is the sum of the ball-bond resistance and 2 graphene tracks resistances (one graphene track indicated a resistance value of $\sim 3.7 \text{ k}\Omega$). Currently new devices are being fabricated which will allow the measurement of the flip-chip ball-bond only.

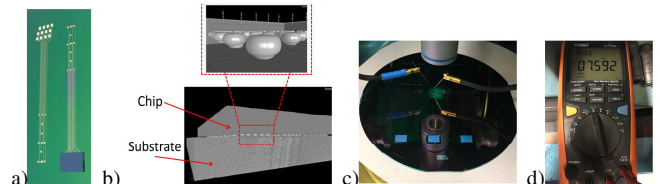


Fig. 5. Preliminary results after bonding. CT scans and 2-point measurements have been performed to ensure that the bonding process was successful.

IV. CONCLUSIONS

This work presents the process for developing flexible, active, graphene-based epidural spinal cord monitoring implant, by means of microfabrication only. It has been shown that F2R approach can be used to suspend large areas, thus avoiding as much as possible wet process steps that can damage the structures. Moreover, it has been demonstrated that flip-chip bonding of chips on a graphene substrate, using metal interfaces, is possible and initial measurements have shown that there is electrical conductivity after the bonding process. To the authors’ best knowledge, this is the first reported graphene-based active implant.

REFERENCES

- [1] R. van den Brand et al., *Science*, vol. 336, pp. 1182-1185, 2012.
- [2] V. Giagka et al., *Biomed. Microdev.*, vol. 17, pp. 106 – 118, 2015.
- [3] D. W. Park et al., *Nat. Commun.*, vol. 5, 2014.
- [4] J. Y. Hong et al., *ACS Nano*, vol. 10, 2016.
- [5] S. Vollebregt et al., *Proc. of IEEE-MEMS*, pp.17-20, 2016.
- [6] B. Mimoun et al., *IEEE Sensors*, vol. 13, pp. 3873-3882, 2013.

NMDC 2019 1570569720

Plasmonic Electronic Paper

1
2
3
4
5
6
7
8
9
10
11
12
13
14
15
16
17
18
19
20
21
22
23
24
25
26
27
28
29
30
31
32
33
34
35
36
37
38
39
40
41
42
43
44
45
46
47
48
49
50
51
52
53
54
55
56
57
58
59
60
61
62
63
64
65
1st Oliver Olsson

Dep. of Chemistry and Chemical
Engineering
Chalmers University of Technology
Gothenburg, Sweden
oliver@chalmers.se

2nd Marika Gugole

Dep. of Chemistry and Chemical
Engineering
Chalmers University of Technology
Gothenburg, Sweden
gugole@chalmers.se

3rd Jolie Blake

Dep. of Chemistry and Chemical
Engineering
Chalmers University of Technology
Gothenburg, Sweden
jolieb@chalmers.se

4th Kunli Xiong

Dep. of Chemistry and Chemical
Engineering
Chalmers University of Technology
Gothenburg, Sweden
kunil@chalmers.se

5th Andreas Dahlin*

Dep. of Chemistry and Chemical
Engineering
Chalmers University of Technology
Gothenburg, Sweden
adahllin@chalmers.se

When the power consumption in the world increases there is a need to develop more energy efficient products for our everyday life. The usage of electronic displays has increased strongly in the last decades. For instance, the average adult in the US spends more than 8 hours a day in front of a display according to the Q1 2018 Nielsen Total Audience Report. Emissive displays (LCD and LED) are already highly energy efficient and yet their energy consumption remains considerable in absolute numbers. Furthermore, a high fraction of the energy usage in a consumer device is associated with its display. By switching to a reflective display which does not emit light, also called electronic paper, the power consumption could be strongly reduced [1].

Structural color generation by plasmonics has been used for thousands of years to create vivid colors in glass [2]. Recently, there has been an interest in not only producing structural colors by plasmonic nanostructures, but also to actively tune them by electronic control [3]. In particular, conjugated polymers on the nanostructures can be used to change the color state with very low power consumption. In 2016, we presented the first work where this concept was used to create a new technology for electronic paper in full color [4].

In most work so far, we utilize that every color can be generated by modulating the reflection of three sub-pixels with either red, green and blue (RGB). Utilizing a plasmonic metastructure consisting of a silver or aluminium mirror, aluminium oxide and a thin gold or copper film to produce a Fabry-Perot cavity, highly reflective colored surfaces can be generated (Fig. 1). Further, nanoholes can be introduced in the gold by colloidal lithography to resonantly scatter light, thereby enhancing the coloration in the blue and green regions (Fig. 2) [4, 5].



Figure 1 Metasurfaces made by aluminum, aluminum oxide and gold. Blue and green are with nanoholes and red is without. Sample size is 18x24mm².

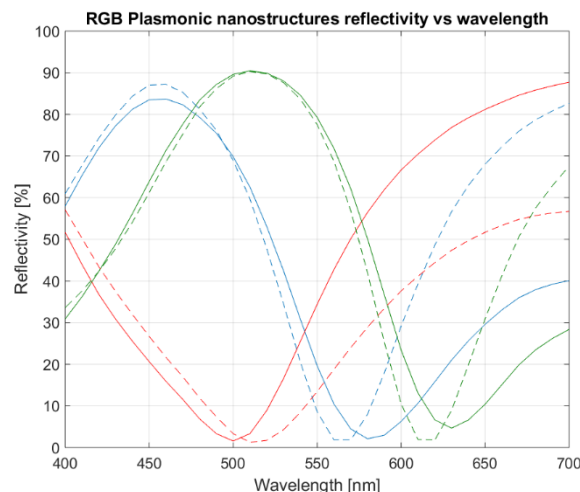


Figure 2 Spectra of plasmonic metastructures for red, green and blue. Dashed lines are with nanoholes and solid lines are without.

To be able to electronically modulate the reflection of the sub-pixels, both organic and inorganic electrochromic materials are used. Polymers are synthesized directly on electrodes using electropolymerization and can further be switched between different colors upon electrochemical doping of the polymer backbone [4]. One of the conjugated polymers which exhibits one of the highest contrasts (maximum 78%) with broad spectral tuning over the visible regime is dimethylpropylenedioxothiophene poly(ProDOT-Me2) [6]. Inorganic electrochromic materials such as tungsten trioxide have been well studied for its electrochromic properties. Although generally prepared by sputter coating, some work has shown good contrast (97%) on ITO prepared by pulsed electrodeposition [7].

We are currently comparing various organic and inorganic films with the aim to find the best candidate with respect to contrast, switching speed, power consumption and lifetime. This does not only involve the type of electrochromic material but also the electrolyte and the nanostructure. Examples of color switching are given in Fig. 3 which shows electrochromism of the metasurfaces with the conjugated polymer polypyrrole.

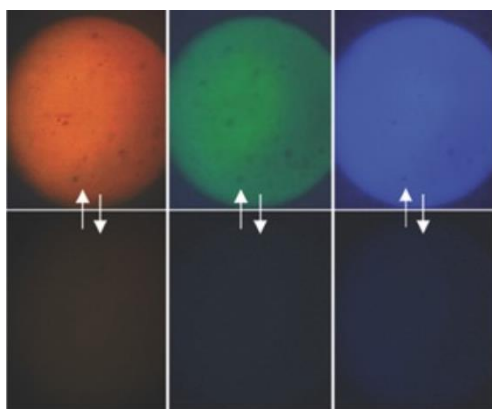


Figure 3 Electrochromic switching of colored metasurfaces [4].

ACKNOWLEDGMENT

Zeynep Adali., Gustav Ferrand-Drake Del Castillo, Timothy Robson, Bita Malekian, Justas Sirelis, John Andersson, Rebekah Hailes. Thanks for helping with miscellaneous tasks. Both work and non-work related.

REFERENCES

1. Fernández, M., E. Casanova, and I. Alonso, *Review of display technologies focusing on power consumption*. Sustainability, 2015. **7**(8): p. 10854-10875.
2. Kristensen, A., et al., *Plasmonic colour generation*. Nature Reviews Materials, 2016. **2**: p. 16088.
3. Xiong, K., et al., *Active control of plasmonic colors: emerging display technologies*. Rep Prog Phys, 2019. **82**(2): p. 024501.
4. Xiong, K., et al., *Plasmonic Metasurfaces with Conjugated Polymers for Flexible Electronic Paper in Color*. Adv Mater, 2016. **28**(45): p. 9956-9960.
5. Xiong, K., et al., *Switchable Plasmonic Metasurfaces with High Chromaticity Containing Only Abundant Metals*. Nano Lett, 2017. **17**(11): p. 7033-7039.
6. Welsh, D.M., et al., *Enhanced contrast ratios and rapid switching in electrochromics based on poly (3, 4 - propylenedioxythiophene) derivatives*. Advanced Materials, 1999. **11**(16): p. 1379-1382.
7. Cai, G., et al., *Ultra-large optical modulation of electrochromic porous WO₃ film and the local monitoring of redox activity*. Chem Sci, 2016. **7**(2): p. 1373-1382.

1
2
3
4
5
6
7
8
9
10
11
12
13
14
15
16
17
18
19
20
21
22
23
24
25
26
27
28
29
30
31
32
33
34
35
36
37
38
39
40
41
42
43
44
45
46
47
48
49
50
51
52
53
54
55
56
57
58
59
60
61
62
63
64
65

2D MXene for spintronic application

Mehroz Iqbal, Malika Rani, Ren-Kui Zheng,^c Syed Rizwan^{a*}

(Physics Characterization and Simulations Labs, School of Natural Sciences (SNS), National University of Sciences and Technology (NUST), Islamabad 54000, Pakistan. E-mail: syedrizwanh83@gmail.com)

Abstract: New family of two-dimensional materials called MXene, with general formula Ti_3C_2Tx , is successfully fabricated after etching from its bulk powder namely MAX. We have reported theoretical and experimental results on structural, optical and multiferroic properties of undoped and doped-MXene. The lattice parameters are changed after the doping, indicating adsorption-dominant properties. The magnetization vs. temperature curves, ferromagnetic hysteresis loops and existence of exchange-bias indicate the presence of ferromagnetic/antiferromagnetic phases together, making it a multiferroic material at low and room-temperatures. The results presented here are novel and is a first report on multiferroic properties of undoped Ti_3C_2 MXene and doped-MXene showing it to be a potential candidate for future magnetic data storage applications.

References:

- [1] J. Ran, G. Gao, F.-T. Li, T.-Y. Ma, A. Du, S.-Z. Qiao, Nat. Comm. 2017, 8: 13907-13909.
- [2] M. A. Iqbal, S. I. Ali, A. Tariq, M. Z. Iqbal, S. Rizwan, Preprints. 2018, 2018110386.
- [3] A. Tariq, S. I. Ali, D. Akinwande, S. Rizwan, ACS Omega, 2018, 3: 13828-13832.
- [4] I. R. Shein, A. L. Ivanovskii, Comp. Mater. Sci. 2012, 65: 104-114.

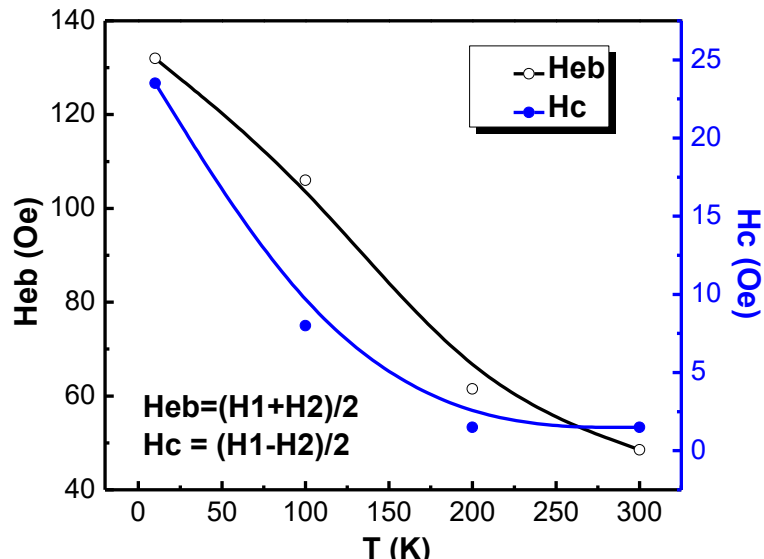


Figure. The trend of magnetic exchange-bias and coercivity as a function of temperature for pure and doped MXene.

Monolithic low temperature fabrication of 30 nm channel amorphous indium oxide thin-film transistors

¹Sunjin Kim, ²Gunwoo Lee, ²Hyungbeen Ju, ²Jiyoung Bang, ¹Heewon Yang, ¹Seong-Oh Yeom,
¹Gunwoo Ryu, ³Onejae Sul and ^{1,2,3}Seung-Beck Lee, *Member, IEEE*

Abstract— We report on a process that makes possible self-aligned and selective *n*-doping of insulating amorphous In_2O_3 thin-film. Hydrogen plasma treatment followed by low temperature rapid thermal annealing was used to heavily insert H^+ ions into selectively patterned insulating In_2O_3 thin-films. Low temperature (200°C) rapid thermal annealing allowed H^+ to locally diffuse between the contacts creating an *n*-type In_2O_3 channel with the H acting as shallow donors. We demonstrated the monolithic planar fabrication of 30-nm-channel In_2O_3 thin-film transistor with 10^6 On/Off current ratio and under $10^{-12}/\mu\text{m}$ leakage currents. The H self-aligned doping technique may make integrated oxide electronics a reality.

I. INTRODUCTION

In order to activate carriers in sputtered amorphous metal oxide thin-films, generally, post-deposition annealing or UV treatments are performed [1]. However, these processes can only be applied globally and cannot be used for selective doping at lithographically define locations which will be required for the monolithic fabrication of integrated circuits. By combining H plasma treatment and rapid thermal annealing (RTA), we have developed a fabrication process that makes possible selective *n*-doping of amorphous In_2O_3 insulating thin-films.

II. METHODS

The insulating amorphous In_2O_3 thin-film was deposited by sputter deposition on insulated (SiO_2 : 90 nm) $\text{p}++$ doped silicon substrate. For H insertion into the 10-nm-thick In_2O_3 , 30 W H plasma treatment. RTA was performed at 200°C for 20 min. Electron-beam lithography was used to pattern the nanoscale contact regions with various gaps, down to 30 nm. Source/drain contacts to the In_2O_3 thin-film transistors (TFTs) used thermally evaporated Ni/Au.

III. RESULTS

We found that the transfer characteristic of In_2O_3 TFTs with the channel *n*-doped by 60 s H plasma treatment and 20 min RTA was comparable to those produced by standard furnace thermal annealing (200°C for 60 min). This showed that H doping was able to produce *n*-type In_2O_3 comparable to that produced by oxygen vacancies at 1/3 of the time. After defining variously spaced regions in PMMA resist, H

insertion was performed using H plasma for 120 sec. This created heavily *n*-doped almost metallic contact regions. After contact metal deposition and resist removal, RTA was used to activate H diffusion between the contacts (see Fig.1(a)). We found that contacts separated by 200 nm and 100 nm gaps showed switching at ~ 30 V, which was due to oxygen vacancy generation (confirmed by XPS analysis). For 60 nm TFTs, we observe a lowering of the threshold voltage indicating that the H diffusion has formed an *n*-type channel between the contacts. The 30 nm In_2O_3 TFT shows characteristics similar to those with the channel directly doped by the H plasma treatment.

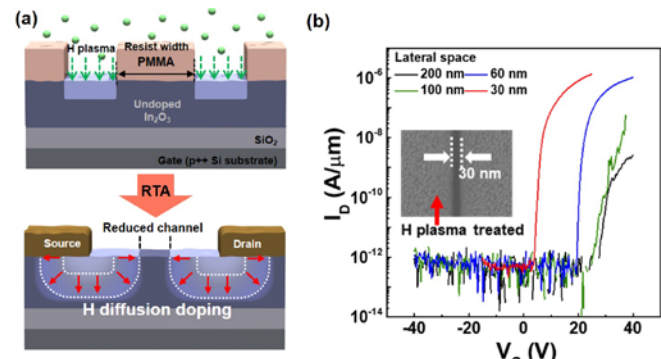


Figure 1. Monolithic fabrication of nanoscale In_2O_3 TFTs. (a) illustration of the H plasma insertion and the thermal diffusion process (b) transfer characteristics of the In_2O_3 TFTs with 200 nm, 100 nm, 60 nm, and 30 nm physical channel lengths. The inset shows the SEM image of the 30 nm gap between H doped contact regions before RTA.

IV. DISCUSSION & CONCLUSION

For the 30 nm channel, the H diffused regions seems to have overlapped. Since channel formation was observed with the 60 nm channel device, we believe that the 20 min RTA enabled 30 nm lateral diffusion of H into the insulating In_2O_3 from the heavily doped contact regions. This demonstrates that a monolithic self-aligned fabrication of nanoscale In_2O_3 integrated circuits may be possible.

ACKNOWLEDGMENT

This study was supported by the National Research Foundation of Korea (NRF) grant funded by the Korean Government (MEST) (NRF-2014M3A7B4049367 and NRF-2012R1A6A1029029).

REFERENCES

[1] Y.-H. Wang, Q. Ma, L.-L. Zheng, W.-J. Liu, S.-J. Ding, H.-L. Lu, and D. W. Zhang, IEEE Trans. Electron Devices, 63, 1893 (2016).

Bilayer Graphene/HgCdTe based self-powered mid-wave IR nBn Photodetector

Shonak Bansal¹, Krishna Prakash¹, Kuldeep Sharma¹, Prince Jain¹, Neha Sardana², Sanjeev Kumar³, Neena Gupta¹ and Arun K. Singh¹

¹Department of Electronics and Communication Engineering, Punjab Engineering College (Deemed to be University), Sector-12, Chandigarh, India

²Dept. of Metallurgical and Materials Engineering, IIT Ropar, India

³Department of Applied Science, Punjab Engineering College (Deemed to be University), Sector-12, Chandigarh, India

Abstract—In this work, we report on the photoelectrical performance of a bilayer graphene (BLG) and mercury cadmium telluride (Hg_{1-x}Cd_xTe: MCT) based unipolar n⁺-BLG/n⁻-Hg_{0.59}Cd_{0.41}Te/n⁺-Hg_{0.666}Cd_{0.334}Te (nBn) mid-wavelength infrared (MWIR: 2-5 μ m) photodetector as shown in Fig.1(a). The nBn photodetector removes the undesirable valence band discontinuity that is currently limiting the performance of conventional nBn photodetectors. The two dimensional model of n⁺-BLG/n⁻-MCT/n⁺-MCT heterojunction photodetector for the operation in MWIR region have been designed and analyzed at 77 K using Silvaco TCAD software. The drift- diffusion approach is used for the simulation of the device. Different recombination mechanism models such as Shockley-Read-Hall, Auger, and optical are considered for computing dark current [1], [2]. The photodetector exhibits low self-powered (i.e. zero biased) dark current and photocurrent density of 4.3×10^{-11} and $9.7 \times 10^{-5} \mu\text{A}/\text{cm}^2$, respectively (Fig. 1b). The proposed nBn device exhibits external quantum efficiency, responsivity, specific detectivity and noise equivalent power (NEP) of 53.86%, 1.82 A/W, $1.07 \times 10^{18} \text{ cmHz}^{1/2}/\text{W}$, $5.92 \times 10^{-22} \text{ W}$, respectively at self-powered mode. Bias-dependent photoresponse is observed in MWIR region with a cut-off wavelength of 4.2 μ m (Fig. 1c). The proposed unipolar barrier infrared photodetector exhibits quantum efficiency of 54.08%, responsivity of 1.83 A/W, specific detectivity of $1.07 \times 10^{18} \text{ cmHz}^{1/2}/\text{W}$, and NEP of $5.9 \times 10^{-22} \text{ W}$ at -0.5 V, confirms the suitability of proposed barrier photodetector for low noise applications.

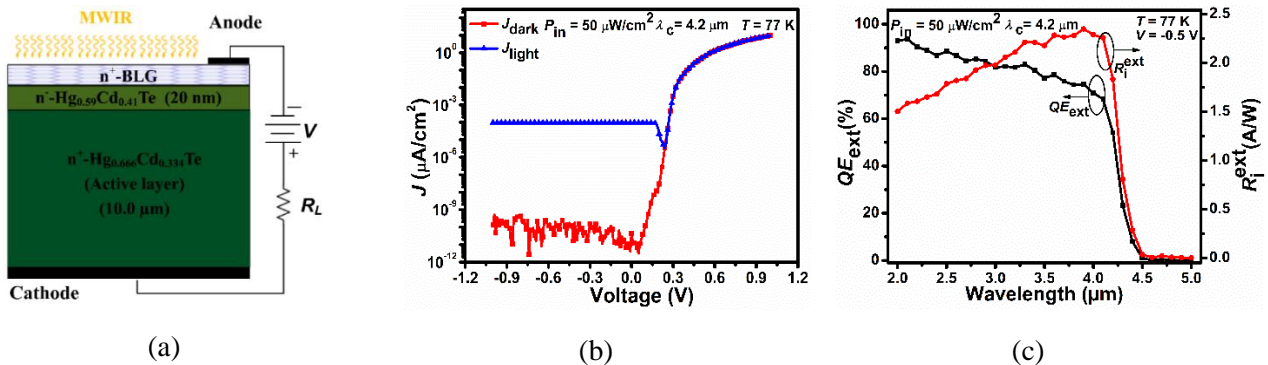


Fig. 1. nBn infrared photodetector (a) The schematic diagram, (b) Current density versus voltage characteristics, (c) External quantum efficiency and responsivity versus wavelength.

- [1] S. Bansal, K. Sharma, P. Jain, N. Sardana, S. Kumar, N. Gupta and A. K. Singh, “Bilayer Graphene/HgCdTe Based Very Long Infrared Photodetector with Superior External Quantum Efficiency, Responsivity, and Detectivity”, RSC Advances, vol. 8, pp. 39579–39592, 2018.
- [2] S. Bansal, P. Jain, N. Kumar, S. Kumar, N. Sardana, N. Gupta, and A. K. Singh, “A Highly Efficient Bilayer Graphene-HgCdTe Heterojunction Based p+-n Photodetector for Long Wavelength Infrared (LWIR)”, 2018 IEEE 13th Nanotechnology Materials and Devices Conference (NMDC), Portland, OR, USA, pp. 1-4, October 14–17, 2018.

Triple Band Polarisation Insensitive Metamaterial Absorber for Terahertz Applications

Prince Jain¹, Arvind K. Singh¹, Shonak Bansal¹, Neha Sardana², Sanjeev Kumar³, Neena Gupta¹ and Arun K. Singh¹

¹Department of Electronics and Communication Engineering, Punjab Engineering College (Deemed to be University), Sector-12, Chandigarh, India

²Dept. of Metallurgical and Materials Engineering, IIT Ropar, India

³Department of Applied Science, Punjab Engineering College (Deemed to be University), Sector-12, Chandigarh, India

Abstract—In this work, we have designed and simulated the metamaterial absorber (MMA) for triple band applications in terahertz frequencies using HFSS software. The metamaterial absorber consists of Al/GaAs/Al materials from the top to the bottom as shown in Fig. 1 (a). The top and bottom metallic layers are of $0.35\text{ }\mu\text{m}$ thick Aluminum (Al), with a conductivity (σ) of $3.3 \times 10^7\text{ S/m}$. The dielectric substrate is of Gallium Arsenide (GaAs) with a thickness and dielectric constant of $5\text{ }\mu\text{m}$ and 12.9, respectively. The absorption rates of 98.71, 99.6 and 90.5% have been achieved at 1.71, 3.16 and 4.89 THz, respectively, as shown in Fig. 1 (b). The proposed triple band MMA can be utilized for wide variety of applications such as sensing, cloaking and imaging due to thin and near-perfect absorbing structures [1], [2].

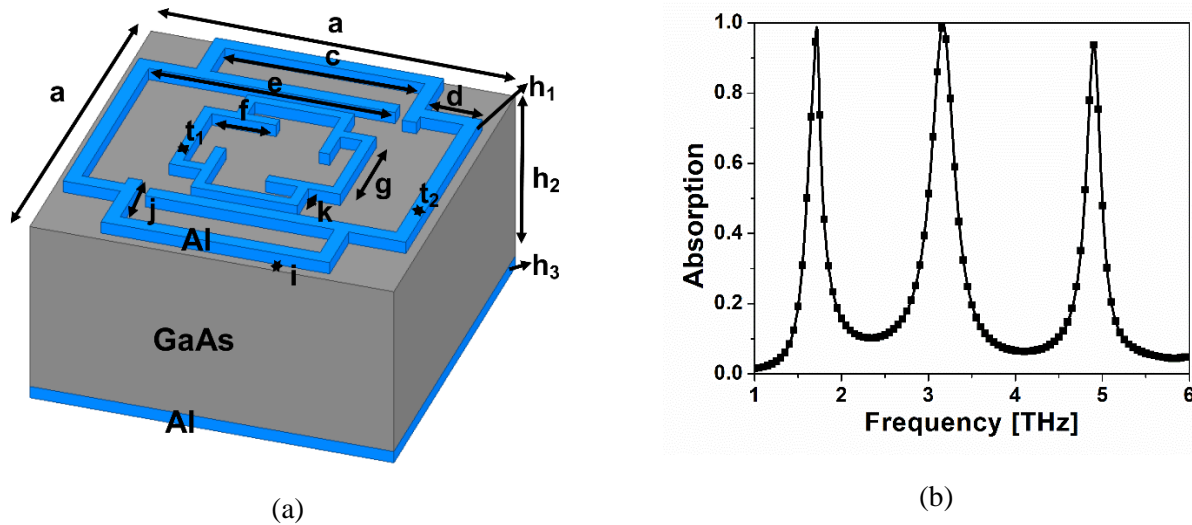


Fig. 1. (a) Three-dimensional (3D) structure of the metamaterial absorber (MMA) with geometric parameters: $a=10.2$, $c=6.4$, $d=1.6$, $e=6.9$, $f=1.8$, $g=3$, $i=0.3$, $j=5$, $k=1.6$, $t_1=0.4$, $t_2=0.3$, $h_1=h_3=0.35$, $h_2=5$ (all dimensions are in μm), (b) Simulated absorption characteristics demonstrating perfect absorption at 1.71, 3.16 and 4.89 THz.

- [1] N. I. Landy, S. Sajuyigbe, J. J. Mock, D. R. Smith, and W. J. Padilla, “Perfect metamaterial absorber,” *Phys. Rev. Lett.*, vol. 100, no. 20, 2008.
- [2] P. Jain, S. Garg, A. K. Singh, N. Sharma, S. Kumar, N. Sardana, S. Bansal, K. Prakash, N. Gupta, and A. K. Singh, “Dual Band Graphene Based Metamaterial Absorber for Terahertz Applications,” *IEEE 13th Nanotechnology Materials and Devices Conference (NMDC)*, Portland, OR, USA, October 14–17, 2018.

Drift diffusion modelling of three branch junction (TBR) based nano-rectifier

Krishna Prakash¹, Priyanka Thakur¹, Shonak Bansal¹, Kuldeep Sharma¹, Prince Jain¹, Sanjeev Kumar², Neena Gupta¹ and Arun K. Singh¹

¹Department of Electronics and Communication Engineering, Punjab Engineering College (Deemed to be University), Sector-12, Chandigarh, India

²Department of Applied Science, Punjab Engineering College (Deemed to be University), Sector-12, Chandigarh, India

Abstract— In this paper, we demonstrate the nonlinear electrical characteristics of three branch junction (TBR) based nanoelectronic rectifier utilising Silvaco TCAD software. The proposed device is based on graphene material and has three terminals named as source, drain and centre terminal as shown in Fig. 1(a). The input signals (DC and /or AC) are applied between source and drain terminals either in push-pull or push-fixed configurations, however, the rectified output is measured at centre terminal. The drift-diffusion model in combination with field mobility model and Shockley-Read-Hall Recombination model has been implemented in order to simulate the electrical characteristics at different temperatures varying from 4 to 300 K as shown in Figs. 1(b) and (c). The planar architecture of the device exhibits less parasitics, hence, enabling very high speed operation [1], [2].

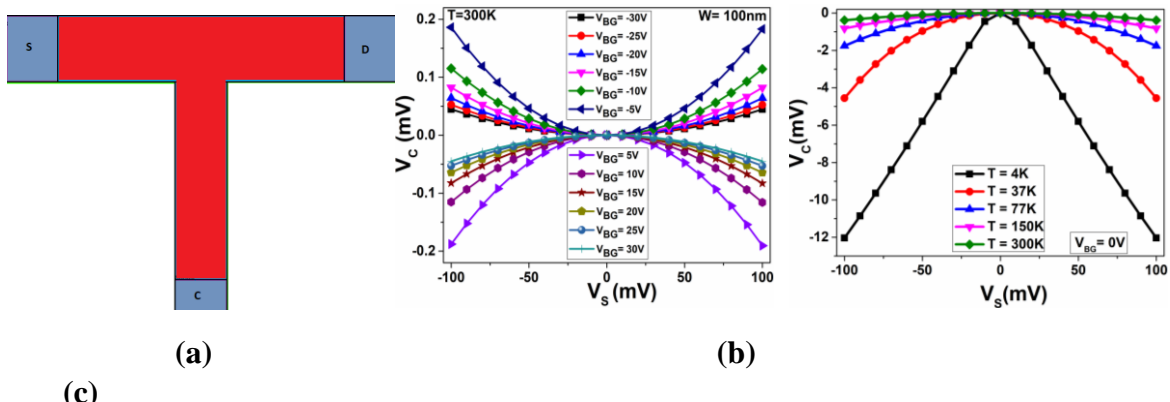


Figure 1 (a) Three branch junction based nanoelectronic rectifier. (b) The output voltage as a function of applied input voltage of 0.1 V at source terminal in push-fixed configuration at different back gate voltages. (c) The voltage output voltage of the device for different temperatures varying from 4 to 300 K at $V_{BG} = 0\text{ V}$.

- [1] A. Jacobsen, I. Shorubalko, L. Maag, U. Sennhauser, and K. Ensslin, “Rectification in three-terminal graphene junctions,” *Appl. Phys. Lett.*, vol. 97, no. 3, p. 032110, 2010.
- [2] A. Garg, N. Jain, and A. K. Singh, “Modeling and Simulation of Graphene based Three Terminal Junction Rectifier,” *J Comput Electron*, vol. 17, 562–570, 2018.

Molecular size and charge dependent sensitivity in electrokinetic biosensing

1 Siddharth Sourabh Sahu

2 *Division of Solid State Electronics*
 3 *Department of Engineering Sciences*
 4 *The Angstrom Laboratory*
 5 *Uppsala University*
 6 *Uppsala, Sweden*
 7 siddharth.sahu@angstrom.uu.se

1 Christiane Stiller

2 *Department of Protein Science*
 3 *School of Chemistry, Biotechnology,*
 4 *and Health (CBH)*
 5 *KTH Royal Institute of Technology*
 6 *Stockholm, Sweden*
 7 cstiller@kth.se

1 Sara Cavallaro

2 *Department of Applied Physics*
 3 *School of Engineering Sciences*
 4 *KTH Royal Institute of Technology*
 5 *Kista, Sweden*
 6 saracav@kth.se

12 Amelie Eriksson Karlström

13 *Department of Protein Science*
 14 *School of Chemistry, Biotechnology,*
 15 *and Health (CBH)*
 16 *KTH Royal Institute of Technology*
 17 *Stockholm, Sweden*
 18 amelie@biotech.kth.se

12 Jan Linnros

13 *Department of Applied Physics*
 14 *School of Engineering Sciences*
 15 *KTH Royal Institute of Technology*
 16 *Kista, Sweden*
 17 linnros@kth.se

12 Apurba Dev*

13 *Division of Solid State Electronics*
 14 *Department of Engineering Sciences*
 15 *The Angstrom Laboratory*
 16 *Uppsala University*
 17 *Uppsala, Sweden*
 18 apurba.dev@angstrom.uu.se

19 Electrokinetic methods are well known techniques for
 20 sensitive surface characterization[1], and they have recently
 21 been adapted for detection of bio-molecules, ranging from
 22 small (~ 1 nm) biological species such as proteins, DNA to
 23 large particles such as extracellular vesicles [2,3]. The
 24 diversity of the sizes of the molecules and their surface charge
 25 distribution obviously rises a question as to what extent these
 26 physical properties influences the signal. Well-developed
 27 theoretical models exist, that relate the influence of the size
 28 and charge of the particles to their electrokinetic response, but
 29 there is lack of experimental validation of these models for
 30 particles in the size range of proteins in the range of 1 - 3 nm,
 31 that is imperative for biosensing. In this study, we investigate
 32 the influence of size and charge on the apparent zeta potential
 33 of the sensor surface, ζ^* for a set of proteins in the range of
 34 1.3-3.5 nm radius, bearing positive, neutral and negative
 35 surface charge. We followed the scheme from our previous
 36 article [2].

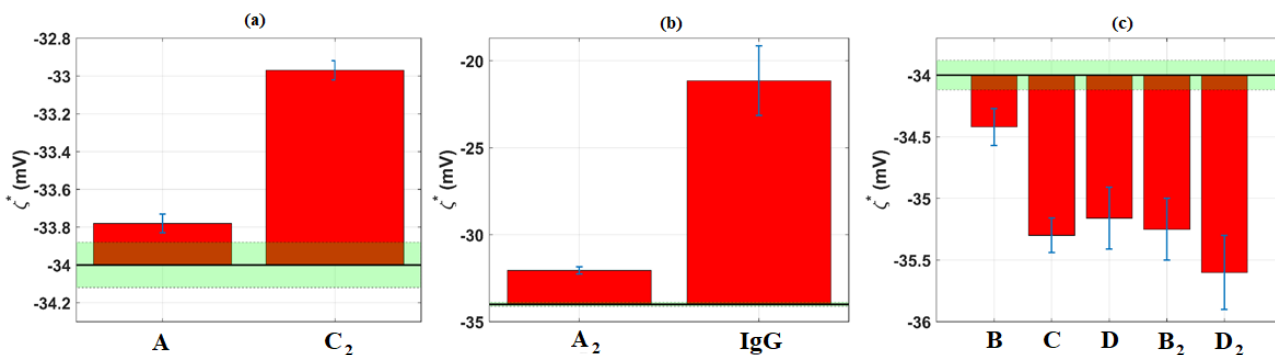
37 The experiments were performed with a set of four
 38 different recombinant affibodies in both monomeric and
 39 dimeric forms, and a standard antibody. The affibodies, all
 40 being derived from the same protein domain, had the same
 41 secondary structure. However, owing to different amino acid
 42 sequences, they had different surface charge, which was
 43 quantified through their surface zeta potential, ζ_p , measured
 44 using electrophoresis. Their size and charge details are
 45 provided in table 1. All the particles were then made to bind
 46 irreversibly to a glutaraldehyde (GA) functionalized sensor
 47 surface through their amine groups. The change in ζ^* was

48 recorded when the sample was injected in between two stable
 49 baselines of the measurement buffer.

50 Table 1: Size and charge of the various particles studied. The ζ_p values were
 51 measured by electrophoresis.

Bio-molecule	Construct	Symbol	Hydrodynamic radius (nm)	Surface zeta, ζ_p (mV)
Affibody A	monomer	A	1.4	-0.2
	dimer	A₂	1.7	2.7
Affibody B	monomer	B	1.4	-7.4
	dimer	B₂	1.7	-7.5
Affibody C	monomer	C	1.4	-1.5
	dimer	C₂	1.7	-0.3
Affibody D	monomer	D	1.4	-8.7
	dimer	D₂	1.7	-9.2
Antibody	--	IgG	3.5	1.5

52 The sensor response is shown in Fig. 1 in terms of ζ^* for the
 53 attachment of positive, neutral and negatively charged
 54 particles on a negatively charged GA surface. The influence
 55 of charge is clearly visible, with the response being the
 56 strongest for positive, and weakest for neutral particles. To
 57 verify this behaviour for a single particle, we measured
 58 affibody A in three different pH buffers. It is positive in pH
 59 6.4, negative in pH 8.4 and neutral in pH 7.4 (see Fig. 2(a) for
 60 the bar plots and ζ_p values) and the ζ^* response from its
 61 attachment to the surface is according to its net surface charge
 62 in the buffer in each case. Moreover, to check the variation of
 63 the sensitivity of the sensor with different kind of particles, we



64 Fig. 1. Bar plots show the sensor response, ζ^* for (a) neutral particles, (b) positively charged particles, and (c) negatively charged particles. The shaded area
 65 indicates a noise floor of 0.12 mV on both sides of the baseline value of -34 mV.

selected **IgG**, **A₂** and **B₂**. While **IgG** and **A₂** had the same sign of charge (positive) but different size, **A₂** and **B₂** had the same size but opposite charge. As can be seen in Fig. 2(b), the sensitivity is the highest for **IgG** and lowest for **B₂**.

Simulations based on a rigorous theoretical model developed by Adamczyk and coworkers [4] were used to explain the varying sensor response based on the size and

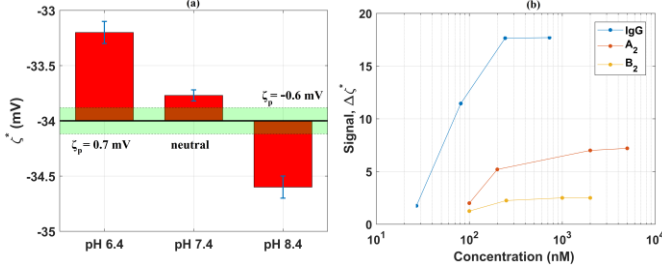


Fig. 2. (a) pH dependent study of the binding signal in the case of A. (b) Sensor response for different types of target proteins: semi-logarithmic plot of the signal vs. concentration of the positively charged **IgG** and **A₂**, and the negatively charged **B₂**.

charge of the attached particles. These results can be used to predict the performance of the sensor in relation to the physical properties of the target molecule.

ACKNOWLEDGMENT

The entire study was supported by a grant from the Erling Persson Family Foundation. A.D. and S.S.S. acknowledge also the grant funded by the Swedish Research Council (Contract No. 621-2014-5591).

REFERENCES

- [1] Hunter, R. J. *Zeta potential in colloid science: principles and applications*.
- [2] Dev, A. et al. *Electrokinetic effect for molecular recognition: A label-free approach for real-time biosensing.*, *Biosens. Bioelectron.* 82, 55–63 (2016).
- [3] Cavallaro, S. et. al. *Label-Free Surface Protein Profiling of Extracellular Vesicles by an Electrokinetic Sensor*, *ACS Sensors* 4, 1399 – 1408.
- [4] Adamczyk, Z. et al. *Streaming potential studies of colloid, polyelectrolyte and protein deposition.*, *Adv. Colloid Interface Sci.* 153, 1–29 (2010).

1 Nanometer-sized Break Junction in Bimetallic Nanowires for Nanoelectronics
2
3
4
5
6
7
8
9
10

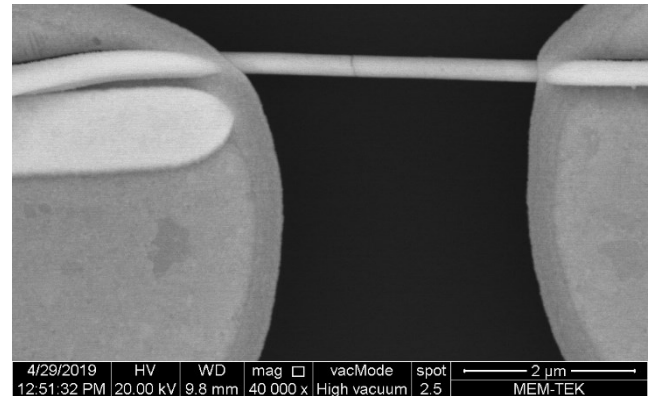
1 Ramazan KIZIL
2 Chemical Engineering Dpt.
3 Istanbul Technical University
4 Istanbul, Turkey
5 kizilr@itu.edu.tr

6 Creation of nanometer-sized separated metallic leads is
7 the prime need in nanoelectronics, especially molecular
8 electronics. Fabrication of nanogap electrodes in a cheap and
9 reproducible manner at large scale has long been a challenge
10 in nanotechnology. We use a hybrid technology to produce
11 on-chip nanowire nanogap devices by electrofluidically
12 addressing 7 micrometer long, 320 nm diametered Au-Ag-Au
13 nanowires onto lithographically predefined Au pads.
14 Nanogap in these nanowires were created either by chemical
15 etching the Ag strip of the wire or feedback controlled
16 electromigration. The key in this approach to make nanogap
17 electrodes is the thickness of the Ag segment in the middle of
18 the nanowire. Stripping patterns of the wires were controlled
19 by galvanostatic deposition of the metals from their plating
20 solutions. Electric field assisted direction of the stripped
21 nanowires was followed to align them between Au pads on a
22 microelectrode array patterned chip. A parallel electrofluidic
23 alignment of nanowires onto 5x10 microelectrode pairs were
24 achieved at 70% yield. SEM image of a single aligned Au-
25 Ag-Au nanowire across Au electrodes is shown in Fig.1. The
26 Ag segment in the middle of the wire has thickness as small
27 as 2 nm was created reducing the electrodeposition time to 12
28 seconds. An additional Au layer deposition was used to clamp
29 nanowires bridging two Au pads.

30 Nanogap in these segmented nanowires was prepared in
31 parallel by direct chemical etching of the Ag part using
32 diluted nitric acid followed by thermal annealing. The anchor
33 Au layer helps keep nanowires intact after etching. Feedback
34 controlled electromigration was also used to form break
35 junction at the Au-Ag interconnect point in series. Break
36 junctions were evaluated using I-V measurements of short
37 and open responses from the wires before and after Ag
38 removal either by etching or electromigration.

39 Nanowires based nanogap electrodes created using our
40 hybrid technology were tested detecting the electrical
41 responses of a metallic nanoparticle and alkanthiol
42 molecules. Self-assembly of alkanthiols on Au approach was
43 used to close the gap, which allowed to make current readouts
44 at low bias voltages (± 1.0 V). Another approach to close the
45 nanogap was capturing of naked and mercaptoundeconic
46 acid capped 13 nm Au nanoparticles.

47 The talk will cover the chemical and electrical approaches
48 used to synthesize segmented nanowires, align nanowires and
49 create nanogaps. I-V behavior of molecules detected using
50 the proposed nanowire nanogap devices and its
51 reproducibility will be discussed.



52 Fig. 1. Au-Ag-Au nanowire aligned on Au pads with a tiny Ag segment in
53 the middle to create a break junction.

Transfer-free Graphene-based Differential Pressure Sensor

Raghutham Ramesha¹, Sten Vollebregt¹, and Pasqualina M Sarro¹

¹ Laboratory of Electronics Components Technology and Materials , Faculty of Electrical Engineering, Mathematics and Computer Science, Delft University of Technology, Feldmannweg 17, 2628CT, Delft, The Netherlands
Email: s.vollebregt@tudelft.nl

Abstract — Graphene is an attractive material to be used for pressure sensors. One of the issues with processing graphene is scalability which is limited by the transfer process that is required for CVD graphene. We employed a novel, transfer-free approach to realize the devices [1]. The devices were successfully fabricated, and the samples were observed under Raman Spectroscopy. The average sheet resistance was 1.324 k Ω /sq.

Index Terms — *graphene, MEMS/NEMS Sensor, piezoresistance, Raman spectroscopy*

I. INTRODUCTION

Graphene, first isolated in 2004, is a promising material in the world of MEMS owing to its excellent mechanical, electrical, optical and chemical properties. The sp² hybridised C-C atoms form covalent bonds and these are responsible for its high in plane strength [2]. Some studies have shown CVD graphene to have a piezoresistive gauge factor around 18000 [3]. These factors make graphene a promising material for pressure sensors.

The current state of the art in the area of graphene based pressure sensor uses graphene membranes that are transferred on to thin dielectric films[4] or for dimensions smaller than 50um, some researchers have made use of free standing graphene membranes made from transferred graphene [5]. Though for the first case the mechanical properties are defined by the dielectric rather than graphene, this makes the sensor to withstand more pressure across the membrane since graphene is not structurally strong in the out-of-plane direction. In both case graphene transfer is used, a process which introduces polymer contamination, wrinkles and scaling challenges [6]. In addition, during transfer, there are chances of inducing pin holes in the graphene membrane with might compromise their structural integrity.

In this paper, we present a novel transfer-free method to fabricate graphene-based bulk micro-machined pressure sensors. This method is based on previous results by Vollebregt et al [1], which we extended for the first time with bulk micro-machined Si₃N₄ membranes. The devices were observed under a Raman spectroscopy and the sheet resistance of the graphene membrane was measured.

II. DESIGN

the device, the mechanical properties are dominated by the 300nm thick Si₃N₄ membrane. Simulations were performed on COMSOL Multiphysics and coherence was seen in the

deflection as a function of differential pressure between the theoretical calculation and the simulation[7]. The deformation in the silicon nitride membrane also causes a deformation in the graphene film. This deformation in the graphene film increases the strain. Hence, the resistance across the graphene film is also increased.

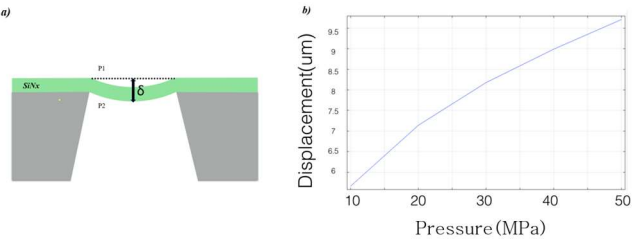


Fig 1. a) The deflection of the membrane due to the difference in pressure P_1 and P_2 . b) COMSOL simulation for a differential pressure up to 50MPa.

The area of the membrane was varied and membranes with side of 100um, 200um, 425um, 500um and 525um are included in the final mask.

III. EXPERIMENTAL

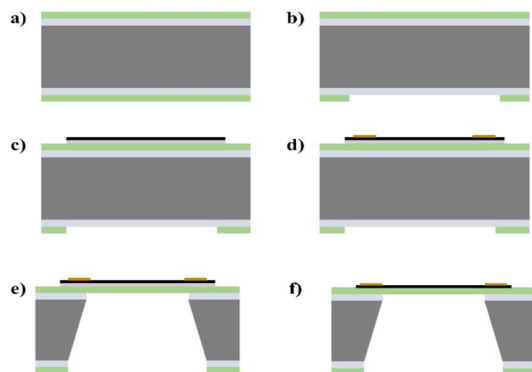


Figure 2. The various process steps involved in the fabrication of the device.

The processing is described in Figure 2. We use 500 μ m thick dual-sided polished 100 mm Si (100) substrates. First, a 300 nm thick oxide was grown using dry thermal oxidation. This was followed by a 300 nm thick LPCVD deposition of Si₃N₄ (Fig 2a). Using plasma etching a window was etched in the backside (Fig 2b). Further, a 50nm thick Molybdenum (Mo)

layer was sputtered on the specific areas for graphene. Mo is used here as a catalyst for CVD graphene growth. Graphene was then grown on the catalyst using an AIXTRON BlackMagic at 915 °C (Fig 2c). After this Cr/Au electrodes were defined using a lift-off process (Fig 2d). In the following step, the silicon oxide was removed by BOE and this was followed by KOH etching, which was further followed by a second BOE step to remove the oxide on the (Fig 2e). The final step involved the removal of the Mo catalyst by H₂O₂.

IV. RESULTS AND DISCUSSION

a) Raman Spectroscopy

The samples were analyzed under Raman spectroscopy during multiple stages of fabrication and a 633nm laser was used.

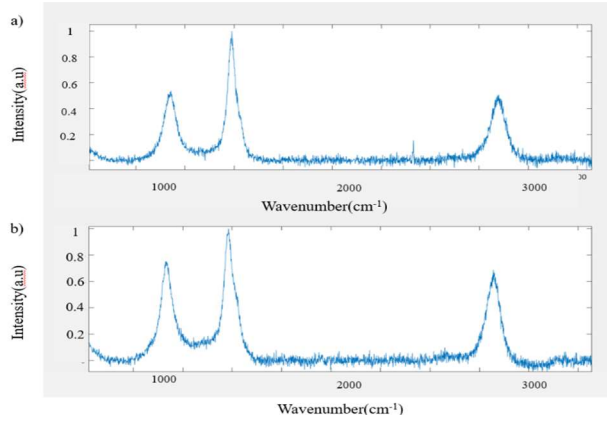


Fig 3. (a) Raman spectroscopy of membrane just after growth. (b) After complete fabrication

The Raman spectra of graphene has a G peak at 1580 cm⁻¹ that represents a primary in plane vibration mode, a D peak at 1350 cm⁻¹ and it's 2nd order overtone at 2690 cm⁻¹. Fig 3a represents the Raman spectrum just after graphene deposition. By comparing the intensity counts of the G and the 2D peaks, the graphene membrane is multi-layered. The ratio I_D/I_G indicates the order of disorder present in the graphene membrane [8]. By comparing Fig 3a and Fig 3b, we can concur that there is an increase in disorder after the graphene membrane is processed.

b) SEM and Optical Observations

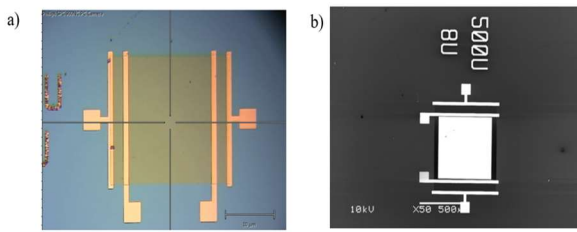


Fig. 4. a) Optical image of the top view of the device. The Si₃N₄ membrane with graphene (green square) and the four Au electrodes are visible. b) SEM image of the top view of the device.

c) Electrical Measurements

Using a four-point probe, the sheet resistance of the graphene membrane was measured.

Side Length(um)	Current(mA)	Voltage (V)	Resistance(kΩ/sq)
500	10	13.27	1.327
500	10	13.22	1.322

Table 1. Sheet resistance of graphene membrane.

The measurement was performed on multiple devices and the average sheet resistance was found to be 1.324 kΩ/sq. This value is comparable to the values sheet resistance of CVD graphene reported in literature [9].

d) Future Work

Further characterization of the device as a function of pressure will be performed.

V. CONCLUSION

We have successfully designed and fabricated transfer-free, bulk micromachined graphene-based pressure sensor. Raman spectroscopy was performed at multiple stages during the process and the effect of processing on the graphene membrane was noted. Further, the sheet resistance of the membrane was measured, and it agrees to the reported value of sheet resistance for CVD graphene.

Through this approach, graphene processing is streamlined into bulk micromachining. The risks of polymer contamination of graphene and other disadvantages that are induced by the “transfer” process can be minimized. Also, with the integration of graphene processing into standard semiconductor processing, better scalability and throughput is achieved.

ACKNOWLEDGMENT

The authors are grateful to the engineers and staff of Else Kooi Lab, TU Delft for their support during fabrication.

REFERENCES

- [1] S Vollebregt et al, IEEE MEMS 2016
- [2] Geim AK, et al., Nature Journals 2010 (pp. 11-19).
- [3] Hosseinzadeh H, et al., In2012 IEEE 25th international conference on micro electro mechanical systems (MEMS) 2012 Jan 29 (pp. 611-614). IEEE.
- [4] Zhu SE et al., Applied Physics Letters. 2013 Apr 22;102(16):161904.
- [5] Smith AD et al., ACS nano. 2016 Nov 7;10(11):9879-86.
- [6] S. Wagner et al., Microelectron. Eng., vol. 159, pp. 108-113, 2016
- [7] Maier-Schneider D et al., Journal of microelectromechanical systems. 1995 Dec;4(4):238-41
- [8] Childres Isaac, et al., *New developments in photon and materials research* 1 (2013).
- [9] Jo G, et al, Nanotechnology. 2012 Feb 28;23(11):112001.

1 2 3 4 5 6 7 8 9 10 11 12 13 14 15 16 17 18 19 20 21 22 23 24 25 26 27 28 29 30 31 32 33 34 35 36 37 38 39 40 41 42 43 44 45 46 47 48 49 50 51 52 53 54 55 56 57 58 59 60 61 62 63 64 65 Atomic-scale vdW Heterostructures Formed by Gold Clusters and Graphene for Thermoelectric Energy Recovery and Cooling

Sara Sangtarash

*Physics Department,**Lancaster University,**Lancaster, UK**s.sangtarash@lancaster.ac.uk*

Hafez Sadeghi

*Physics Department,**Lancaster University,**Lancaster, UK**h.sadeghi@lancaster.ac.uk*

Quantum engineering of electrical properties of nanoscale materials is fundamental to the development of high performance thermoelectric devices for the conversion of waste heat into electricity and cooling. Here, we demonstrate that quantum interference can be utilized to improve the room temperature thermoelectric efficiency of atomic-scale vdW heterostructures formed by metallic clusters and graphene electrodes. We study systematically the electronic and thermoelectric properties of gold clusters consisting of $N = 3, 4, 5, 6$ gold atoms (Au_N) sandwiched between graphene electrodes. We obtain a high Seebeck coefficient in the range of $100\text{--}500\mu\text{V/K}$ in this heterostructures which is higher than that of the best molecular scale junctions. Resonance transport at graphene electrodes Fermi energy through atomic scale gold nanoparticles leads to a significant improvement of both electrical conductance and Seebeck coefficient. Our finding shows that gold nanoparticle / graphene heterostructures are promising platform for thermoelectric energy harvesting and cooling.

Currently nearly 10% of the world's electricity is used by computers and the internet and converted to heat. This waste heat could be used to generate electricity economically, provided materials with a high thermoelectric efficiency could be identified [1]. Conversely, efficient Peltier cooling using such materials would have applications to on-chip cooling of CMOS-based devices [1]. The demand for new thermoelectric materials has led to a worldwide race to develop materials with a high thermoelectric efficiency [2]. The efficiency of a thermoelectric device is proportional to its power factor $PF = \sigma S^2$ [3] where σ is the electrical conductivity and S is the Seebeck coefficient (thermopower) [4]. Therefore high conductance and high Seebeck coefficient materials are needed for efficient conversion of heat into electricity. However, the interdependency of σ and S constrains the options for materials design and makes optimisation a difficult task.

The state-of-the-art room-temperature S at single-molecules is ranging in magnitude from ca. 1 to $50\mu\text{V/K}$. For example, the measured values include $8.7, 12.9$ and $14.2\mu\text{V/K}$ for benzenedithiol, dibenzenedithiol, and tribenzenedithiol, respectively [2], -12.3 to $13.0\mu\text{V/K}$ for a

series of amine-Au and pyridine-Au linked molecules [5] and -8.9 to $-33.1\mu\text{V/K}$ for fullerene-based single-molecule junctions [5], [6]. These S values are not sufficient to create a viable technology platform for thermoelectricity. Nevertheless, it was demonstrated recently that molecular wires can mediate long-range phase-coherent tunnelling over sub nanometer distances even at room temperature [7]. This creates the possibility of using quantum interference (QI) at atomic scale [8]–[11] to engineer enhancement of thermoelectricity in molecular materials [12], [13].

In this paper, we aim to demonstrate that room-temperature QI of electrons can be employed to obtain high S and G materials in cross-plane heterostructures formed by gold clusters sandwiched between graphene electrodes. We use density functional theory (DFT) to obtain ground state geometry of atomic-scale vdW heterostructures. To study electron transport through these heterostructures, we obtain the ground state mean field Hamiltonian from optimized geometries of each structure using SIESTA [14] implementation of DFT. We

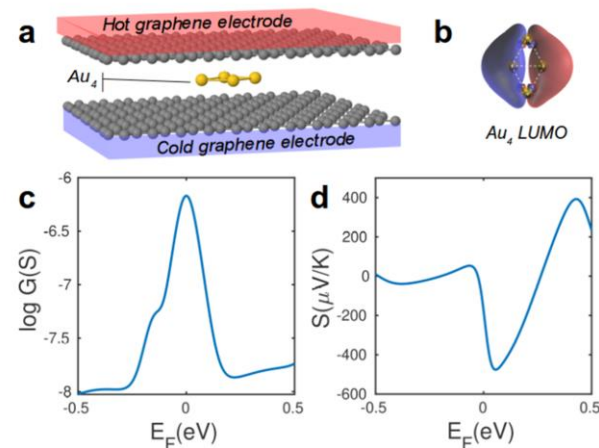


Fig. 1. Thermoelectric properties of Au_4 gold cluster between graphene electrodes. (a) An example of molecular structure of atomic scale vdW heterostructure formed by Au_4 gold cluster sandwiched between two graphene electrodes. Electron transport is perpendicular to the plane. (b) Lowest unoccupied molecular orbital (LUMO) of Au_4 . (c) Electrical conductance and (d) Seebeck coefficient versus Fermi energy of graphene electrodes.

then calculate the transmission probability [3] $T_e(E)$ of electrons with energy E traversing through Au clusters using our implementation of non-equilibrium Green's function method [3], [15]. G and S are then obtained from $T_e(E)$ as:

$$G = G_0 L_0 \quad (1)$$

and

$$S = -L_0/eT L_0 \quad (2)$$

where the momentums $L_n(T) = \int_{-\infty}^{+\infty} dE (E - E_F)^n T_e(E) (-\partial f / \partial E)$ and $f = (e^{(E-E_F)/k_B T} + 1)^{-1}$ is the Fermi distribution function, k_B is Boltzmann constant, T is the temperature, E_F is the Fermi energy, $G_0 = 2e^2/h$ is the conductance quantum, e is electron charge and h is the Planck's constant.

We study the electronic and thermoelectric properties of gold clusters consisting of $N = 3, 4, 5, 6$ gold atoms (Au_N) sandwiched between graphene electrodes. Figure 1 shows an example of these gold clusters formed by four gold atoms (Au_4) which is stable at room temperature [16]. The electrical conductance versus Fermi energy of graphene electrodes at room temperature is shown in figures 1c. At DFT Fermi energy ($E_F = 0eV$), a high electrical conductance of $10^{-6.1}$ Siemens is obtained per Au_4 cluster. The size of each cluster is ca. $0.2 \times 0.5 \text{ nm}^2$. To avoid interaction with neighboring clusters, a foot print of 1 nm^2 is considered to estimate electrical conductivity. This yield to electrical conductivity of $\sigma = 234 \text{ S/m}$. This relatively high electrical conductivity arise from a resonance transport due to the lowest unoccupied molecular orbital (fig. 1b) of Au_4 .

Figure 1d shows the room temperature Seebeck coefficient versus Fermi energy of graphene electrodes. A high S of ca. -0.5 mV/K is obtained in the vicinity of DFT Fermi energy which is higher than the best molecular junction, gold/C60/gold [17]. These simultaneous enhancement of electrical conductance and Seebeck coefficient lead to a high power factor of $P = \sigma S^2 = 59 \mu\text{W/mK}^2$. This is higher than power factors of other molecular materials such as polyaniline ($0.016 \mu\text{W/mK}^2$), polypyrole ($0.045 \mu\text{W/mK}^2$) and PEDOT:PSS ($12 \mu\text{W/mK}^2$) [18], [19].

ACKNOWLEDGMENT

S.S acknowledges the Leverhulme Trust for Early Career Fellowship no. ECF-2018- 375. H.S. acknowledges the UKRI for Future Leaders Fellowship number MR/S015329/1.

REFERENCES

[1] F. J. Disalvo, "Thermoelectric cooling and power generation," *Science*, vol. 285, no. 5428, pp. 703–706, 1999.

- [2] P. Reddy, S. Y. Jang, R. A. Segalman, and A. Majumdar, "Thermoelectricity in molecular junctions," *Science*, vol. 315, no. 5818, pp. 1568–1571, 2007.
- [3] H. Sadeghi, "Theory of electron, phonon and spin transport in nanoscale quantum devices," *Nanotechnology*, vol. 29, no. 37, p. 373001, 2018.
- [4] N. Sergueev, S. Shin, M. Kaviany, and B. Dunietz, "Efficiency of thermoelectric energy conversion in biphenyl-dithiol junctions: Effect of electron-phonon interactions," *Phys. Rev. B - Condens. Matter Mater. Phys.*, vol. 83, no. 19, p. 195415, 2011.
- [5] J. R. Widawsky, P. Darancet, J. B. Neaton, and L. Venkataraman, "Simultaneous determination of conductance and thermopower of single molecule junctions," *Nano Lett.*, vol. 12, no. 1, pp. 354–358, 2012.
- [6] S. K. Yee, J. A. Malen, A. Majumdar, and R. A. Segalman, "Thermoelectricity in fullerene-metal heterojunctions," *Nano Lett.*, vol. 11, no. 10, pp. 4089–4094, 2011.
- [7] G. Sedghi *et al.*, "Long-range electron tunnelling in oligo-porphyrin molecular wires," *Nat. Nanotechnol.*, vol. 6, no. 8, pp. 517–523, 2011.
- [8] S. Sangtarash *et al.*, "Searching the Hearts of Graphene-like Molecules for Simplicity, Sensitivity, and Logic," *J. Am. Chem. Soc.*, vol. 137, no. 35, pp. 11425–11431, 2015.
- [9] H. Sadeghi, S. Sangtarash, and C. J. Lambert, "Electron and heat transport in porphyrin-based singlemolecule transistors with electro-burnt graphene electrodes," *Beilstein J. Nanotechnol.*, vol. 6, no. 1, pp. 1413–1420, 2015.
- [10] H. Sadeghi *et al.*, "Conductance enlargement in pico-scale electro-burnt graphene nanojunctions," *Proc. Natl. Acad. Sci. USA*, vol. 112, no. 9, pp. 2658–63, 2016.
- [11] H. Sadeghi, S. Sangtarash, and C. J. Lambert, "Enhanced Thermoelectric Efficiency of Porous Silicene Nanoribbons," *Sci. Rep.*, vol. 5, no. May, p. 9514, 2015.
- [12] R. Miao *et al.*, "Influence of Quantum Interference on the Thermoelectric Properties of Molecular Junctions," *Nano Lett.*, vol. 18, no. 9, pp. 5666–5672, 2018.
- [13] S. Sangtarash, H. Sadeghi, and C. J. Lambert, "Connectivity-driven bi-thermoelectricity in heteroatom-substituted molecular junctions," *Phys. Chem. Chem. Phys.*, vol. 20, no. 14, pp. 9630–9637, 2018.
- [14] J. M. J. M. Soler *et al.*, "The SIESTA method for ab initio order-N materials simulation," *J. Phys. Condens. Matter*, vol. 14, no. 11, pp. 2745–2779, Mar. 2002.
- [15] J. Ferrer *et al.*, "GOLLUM: A next-generation simulation tool for electron, thermal and spin transport," *New J. Phys.*, vol. 16, p. 093029, 2014.
- [16] D. Schooss, P. Weis, O. Hampe, and M. M. Kappes, "Determining the size-dependent structure of Ligand-free gold-cluster ions," *Philos. Trans. R. Soc. A Math. Phys. Eng. Sci.*, vol. 368, no. 1915, pp. 1211–1243, 2010.
- [17] C. Evangelisti *et al.*, "Engineering the thermopower of C60 molecular junctions," *Nano Lett.*, vol. 13, no. 5, pp. 2141–2145, 2013.
- [18] H. Shi *et al.*, "Electrochemical Fabrication and Thermoelectric Performance of the PEDOT:PSS Electrode Based Bilayered Organic Nanofilms," *Int. J. Electrochem. Sci.*, vol. 9, no. 12, pp. 7629–7643, 2014.
- [19] Q. H. Al-Galiby, H. Sadeghi, L. A. Algharagholy, I. Grace, and C. Lambert, "Tuning the thermoelectric properties of metallo-porphyrins," *Nanoscale*, vol. 8, no. 4, pp. 2428–2433, 2016.

Nanoscale Three-Independent-Gate Transistors: Geometric TCAD Simulations at the 10 nm-Node

Patsy Cadareanu and Pierre-Emmanuel Gaillardon, *Senior Member, IEEE*

Laboratory for NanoIntegrated Systems
University of Utah, Salt Lake City, UT, USA
patsy.cadareanu@utah.edu

Abstract—*Three-Independent-Gate Field-Effect Transistors* (TIGFETs) are Schottky-barrier-based devices which can be reconfigured to be either *n*- or *p*-type allowing for innovative compact logic gate implementations. In this paper, we present an aggressively scaled 10-nm gate-all-around silicon-nanowire TIGFET device evaluated with *Synopsys Sentaurus* at a 0.7 V nominal supply voltage as typically used at this technology node. When considering a pure silicon channel, the maximum TCAD simulated current drive is 90.20 $\mu\text{A}/\mu\text{m}$ and 89.25 $\mu\text{A}/\mu\text{m}$ for *n*- and *p*-type operation respectively, and these simulations are verified using device physics calculations. In order to achieve higher current drives, we also consider a germanium-nanowire device which results in current drives more than 14 \times higher compared to the silicon-nanowire devices, thus making TIGFET devices competitive with FinFET technology at the 10-nm node.

I. INTRODUCTION

Conventional drive in the semiconductor industry has been based on the improvement of device performance and the scaling of these devices, as exemplified by Moore's scaling law. However, as the physical sizing limits of contemporary manufacturable transistors are being reached, Moore's law is coming to an end and innovations on standard *Fin Field-Effect Transistor* (FinFET) technology are necessary.

Reconfigurability refers to the capability of a single transistor to alternate between *n*-type and *p*-type behaviors after fabrication. Devices built based on this principle are a viable alternative to scaling due to their ability to enhance system functionality by simplifying logic gate implementations [1], [2]. The *Three-Independent-Gate Field Effect Transistor* (TIGFET) is an experimentally demonstrated reconfigurable device [3]–[5] whose dual-switching ability originates from electrostatic modulation of Schottky barriers at the source and drain contacts using additional gate terminals called *Polarity Gates* (PG).

This paper introduces TCAD simulations performed using *Synopsys Sentaurus* for 10 nm-gate TIGFET silicon-nanowire and germanium-nanowire devices designed to operate at the industry standard supply voltage V_{DD} of 0.7 V. These simulations are intended to verify TIGFET device performance at the 10 nm node, thus defining the device's validity for use alongside contemporary devices.

II. TIGFET OPERATION

A TIGFET device requires a channel made of a semiconductor material, metallic source and drain contacts, and three gate electrodes: the *Control Gate* (CG), and two symmetric PGs at

This work was supported by the NSF Career Award #1751064 and the SRC Contract 2018-IN-2834.

the source and drain to act as electrostatic doping means at the Schottky barrier interfaces. The device structure is illustrated in Fig. 1-a. Fig. 1-b shows a band diagram of combined *n*- and *p*-type operation at equilibrium. The chosen PG voltages determine which carriers will dominate in the channel: if the PGs are increased to the supply voltage, the device will be *n*-type (electron) carrier-dominated, as seen in Fig. 1-c and Fig. 1-d, whereas if the PGs are grounded, the device will be *p*-type (hole) carrier-dominated, as seen in Fig. 1-e and Fig. 1-f. The state of the CG determines whether the selected carriers will pass through, thus effectively turning the device on or off.

III. OVERVIEW OF THE TCAD SIMULATIONS

A. Silicon-nanowire Design

The Schottky barrier in the TCAD simulations was created by a *Nickel Silicide* (NiSi)-to-semiconducting material contact. NiSi is a mid-gap metal and can thus provide symmetric switching between *n*- and *p*-type carriers. The nanowire configuration was chosen due to its superior electrostatic control over the channel when compared to FinFET technology at the same node [6]. A 7 nm *Hafnium Dioxide* (HfO₂) layer was used as the gate dielectric. Modifications specific to the silicon-nanowire structure were made. These include elevating the *p*-type body doping to $1 \cdot 10^{16} \text{ cm}^{-3}$, and the assumption of strained $\langle 111 \rangle$ silicon, edited to effectively make *p*-type carriers 81% faster and *n*-type carriers 58% faster. The NiSi workfunction used in the silicon-nanowire simulation was 4.755 eV, and the corresponding silicon semiconductor work function was 4.59 eV.

Symmetric maximum current drives are achieved at the maximum supply drive of $V_{DD} = 0.7$ V for *n*- and *p*-configurations, as seen in Fig. 1-h. The maximum current drive for *n*-type operation is 90.20 $\mu\text{A}/\mu\text{m}$ and for *p*-type is 89.25 $\mu\text{A}/\mu\text{m}$. Due to the Schottky barrier cutoff, I_{OFF} is extremely low at 3.3 nA/ μm and 1.16 nA/ μm for *n*- and *p*-type operation respectively.

Assuming a diameter of 10 nm, calculations using the standard Eq. (1) for determining the maximum current at the Schottky barriers are performed to determine the validity of these simulated results [7]:

$$J_{ms} = \left(\frac{4\pi m^* q k^2}{h^3} \right) \cdot T^2 \cdot e^{\frac{-q \cdot \phi_{Bp}}{kT}} \cdot \left(e^{\frac{-q \cdot V_{DD}}{kT}} - 1 \right). \quad (1)$$

This results in a calculated maximum current drive of 196.21 $\mu\text{A}/\mu\text{m}$ which is approximately 2 \times the simulated maximum current drive for these devices. This difference is due to Eq. (1) calculating the theoretical current limit of a

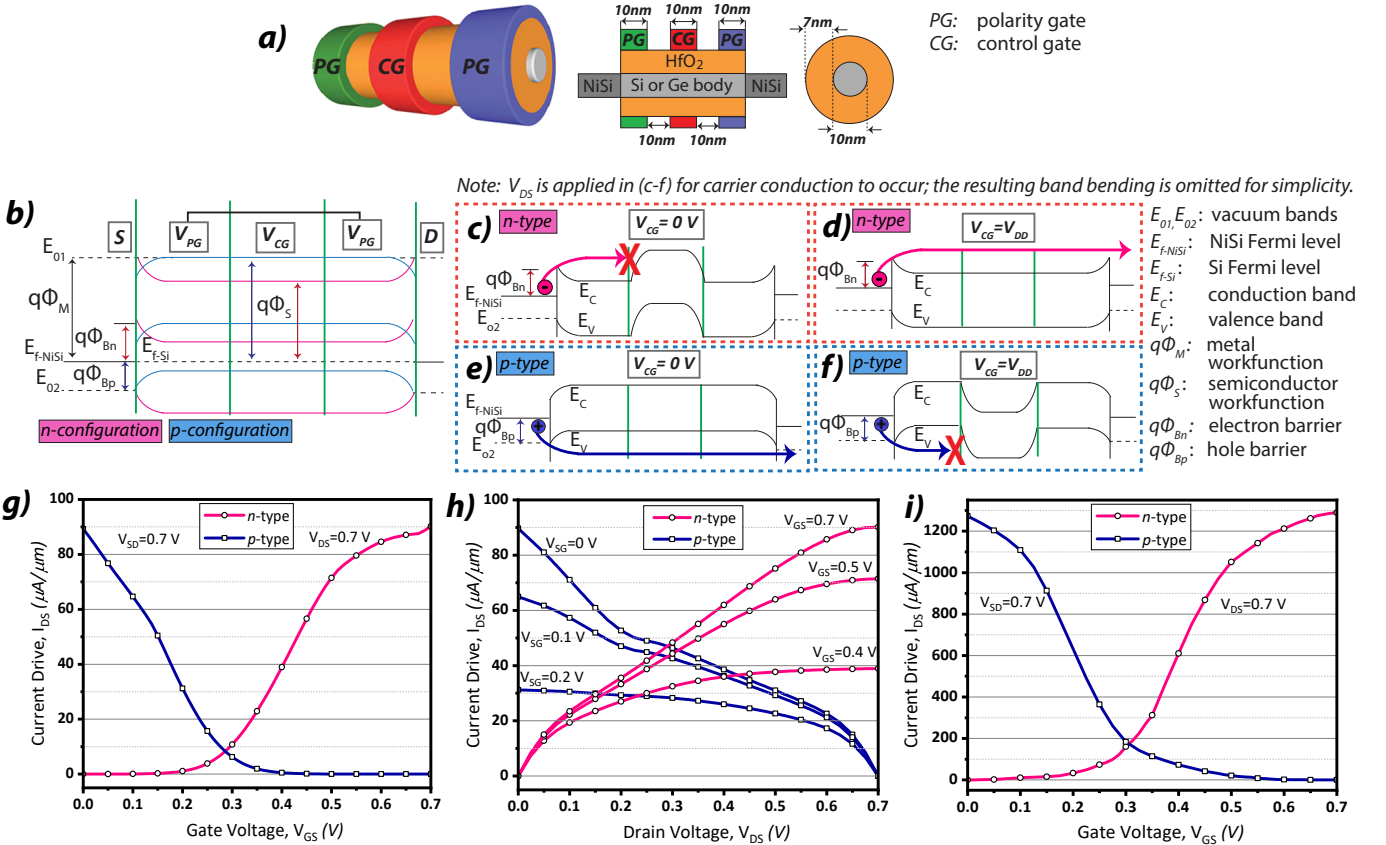


Fig. 1: (a) The structure of the designed device with 10 nm gate lengths and spacings. (b) Band diagram assuming the same bias for both polarity gates (pink lines correspond to *n*-type operation, $V_{PG}=V_{DD}$; blue bands correspond to *p*-type operation, $V_{PG}=0$ V) at equilibrium (no V_{GS} applied). (c) For the *n*-configuration, when $V_{CG}=0$ V the OFF condition occurs, blocking the electron-carrier flow. (d) For the *n*-configuration, when $V_{CG}=V_{DD}$ the ON condition occurs, allowing the electron-carrier flow. (e) For the *p*-configuration, when $V_{CG}=0$ V the ON condition occurs, allowing the hole-carrier flow. (f) For the *p*-configuration, when $V_{CG}=V_{DD}$ the OFF condition occurs, blocking the hole-carrier flow. (g) I_D - V_{GS} characteristics of the silicon-nanowire device at $V_{DD}=0.7$ V. (h) I_D - V_{DS} characteristics of the silicon-nanowire device. (i) I_D - V_{GS} characteristics of the germanium-nanowire device at $V_{DD}=0.7$ V.

single Schottky barrier, whereas the simulated TIGFET device consists of two Schottky barriers as well as the standard *p*-*n* junctions associated with the CG.

Fig. 1-h shows the current drive as a function of drain voltage for the *n*- and *p*-configurations. Symmetric characteristics are seen for both *n*-type and *p*-type carriers, with the switching centered around $V_D=0.3$ V. Saturation is seen for all *n*-type configuration and punchthrough is seen for the device biased *p*-type at $V_{sg}=0$ V and 0.1 V. Punchthrough occurs in short-channel devices such as this simulation due to the simulated depletion regions of the source and drain reaching each other which in turn lowers the potential and facilitates current flow near the surface of the device.

B. Germanium-nanowire Design

A germanium-nanowire 10-nm TIGFET simulation is considered as a higher-current alternative to the silicon-nanowire. The metal and semiconducting workfunctions used are 4.46 eV and 4.13 eV, respectively. As seen in Fig. 1-i, the maximum current drive achieved with this simulation is 1289.18 μ A/ μ m for *n*-type operation and 1272.65 μ A/ μ m for *p*-type operation. Eq. (1) is evaluated for the germanium-nanowire and results in a maximum expected current drive of 1990.65 μ A/ μ m,

which is on the same scale as our simulations. The simulated germanium-nanowire TIGFET current drive is on the same scale as 1550 μ A/ μ m, the reported current drive for modern FinFET technology [8]. The trade-off for this 14 \times drive current improvement over the silicon-based simulations are I_{OFF} values of 7.51 μ A/ μ m for *n*-type, and 4.52 μ A/ μ m for *p*-type operation.

REFERENCES

- [1] S. Rai *et al.*, *Emerging reconfigurable nanotechnologies: can they support future electronics?*, ICCAD, 2018.
- [2] J. Romero-Gonzalez *et al.*, *An Efficient Adder Architecture with Three-Independent-Gate Field-Effect Transistors*, ICRC, 2018.
- [3] M. De Marchi *et al.*, *Polarity control in double-gate, gate-all-around vertically stacked silicon nanowire FETs*, IEDM, 2012.
- [4] J. Zhang *et al.*, *Configurable Circuits Featuring Dual-Threshold-Voltage Design With Three-Independent-Gate Silicon Nanowire FETs*, IEEE TCAS I, 61(10): 2851–2861, 2014.
- [5] J. Trommer *et al.*, *Reconfigurable nanowire transistors with multiple independent gates for efficient and programmable combinational circuits*, DATE, 2016.
- [6] A. Bachtold *et al.*, *Logic Circuits with Carbon Nanotube Transistors*, Science 294(5545): 1317–1320, 2001.
- [7] S.M. Sze and K.K. Ng, *Physics of Semiconductor Devices*. 3rd ed, 2006.
- [8] Intel Corporation, *A 10nm High Performance and Low-Power CMOS Technology Featuring 3rd Generation FinFET Transistors, Self-Aligned Quad Patterning, Contact over Active Gate and Cobalt Local Interconnects*. IEDM, 29.1.129.1.4, 2017.

On-demand W/O droplet generation using ECF (electro-conjugate fluid) micropump

1
2
3
4
5
6
7
8
9
10
11
12
13
14
15
16
17
18
19
20
21
22
23
24
25
26
27
28
29
30
31
32
33
34
35
36
37
38
39
40
41
42
43
44
45
46
47
48
49
50
51
52
53
54
55
56
57
58
59
60
61
62
63
64
65
Zebing Mao

Department of Mechanical Engineering
School of Engineering, Tokyo Institute of
Technology
Tokyo, Japan

Kazuhiro Yoshida

Laboratory for Future Interdisciplinary
Research of Science and Technology
(FIRST)
Tokyo Institute of Technology
Tokyo, Japan

Joon-wan Kim

Laboratory for Future Interdisciplinary
Research of Science and Technology
(FIRST)
Tokyo Institute of Technology
Tokyo, Japan
woodjoon@pi.titech.ac.jp

Droplet-based microfluidics has been utilized in biomedical applications. Droplets with different volumes are required in some application such as multi-volume droplet polymerase-chain-reaction (PCR). To realize this, we need more sophisticated techniques to control the generation of droplets except for the extensively utilized methods (two syringe pumps in Fig. 1a). The reported methods (magnetic, optical, thermal, acoustic, mechanical and electrical methods), exerted additional forces on the dispersed streams and can negatively influence the droplets, like the viability of cells or organisms in the droplets [1]. Aiming to solve the problem, we propose a novel T-junction generator by integrating an ECF (electro-conjugate fluid) micropump on a chip. ECF is a kind of functional and dielectric oil, which can generate a strong flow (ECF jet) when its corresponding electrodes are applied to high DC voltages [2]. The ECF micropump composed of TPSEs (triangular prism and slit electrode pairs in Fig. 1b) can control flow rate precisely. Therefore, we can adjust the droplet size accurately on a chip (Fig. 1b), by utilizing our ECF micropump.

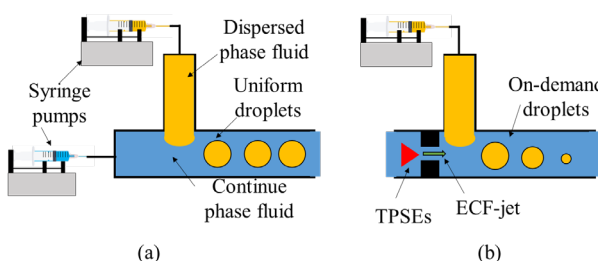


Fig. 1 (a) Uniform droplet generation. (b) On-demand droplet generation in this work

1. Materials, Design, and fabrication

In our case, the mixture of DBD and Span 80 (3.0 wt. %) is used as the continuous phase fluid and DI water with red dye is utilized as the dispersed phase fluid. We design the electrodes based on the modular concept of TPSEs, whose distribution is nine TPSEs in parallel and two ones in series, which can provide enough flow rate (powerful ECF jet). As for the T-junction geometry, the width of the continuous phase and the dispersed flow channel are 0.40 mm and 0.20 mm, respectively.

We fabricated the device by forming the TPSEs based on the UV-LIGA process and the fluidic channels based on the UV patterning of a thick photoresist of SU-8. The thickness was 0.30 μ m on average. The fabrication result is shown in Fig. 2.

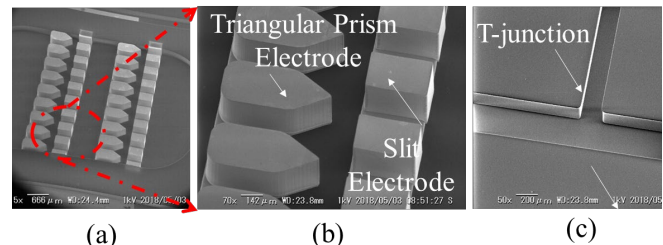


Fig. 2 (a) ECF micropump. (b) Triangular prism electrodes and slit electrodes. (c) SU-8-made T-junction.

2. Experimental results

To investigate the feasibility of the on-demand droplet generation, we changed the applied voltages (V_c) for the ECF micropump. The flow rate (Q_d) of DI water was set at 10 μ L/min. In Fig. 3a, we could obtain stable droplets with the same sizes under the situation: $V_c = 2.0$ kV, $Q_d = 10$ μ L/min. In Fig. 3b, the droplet size decreased, when applied voltage (V_c) was gradually changed from 1.0 kV to 2.0 kV. On the contrary, the droplet size increased with the change of V_c from 2.0 kV to 0 kV, as shown in Fig. 3c. The experiments showed we could control droplet size on a chip by tuning the applied voltages on the ECF micropumps.

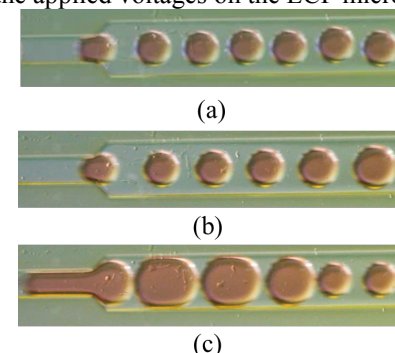


Fig. 3 (a) Stable generation: $V_c = 2.0$ kV, $Q_d = 10$ μ L/min. (b) Droplet size decreasing: V_c was gradually changed from 1.0 kV to 2.0 kV. (c) Droplet size increasing: V_c was gradually changed from 2.0 kV to 0 kV.

References

- [1] Zhu, Pingan, and Liqui Wang. Passive and active droplet generation with microfluidics: a review. *Lab on a Chip*, vol. 17, pp. 34-75, 2017.
- [2] Kim, J. W., Suzuki, T., Yokota, S., & Edamura, K. Tube-type micropump by using electro-conjugated fluid (ECF). *Sensors and Actuators A: Physical*, vol. 174, pp. 155-161, 2012.

1
2 Effect of Optical Photons on Hybrid Semiconductor-Superconductor Josephson Junctions
3
4
5
6
7
8
9
10
11
12
13
14
15
16
17
18
19
20
21
22
23
24
25
26
27
28
29
30
31
32
33
34
35
36
37
38
39
40
41
42
43
44
45
46
47
48
49
50
51
52
53
54
55
56
57
58
59
60
61
62
63
64
65

Understanding and controlling the interaction between superconducting circuit elements and optical frequency photons is key to interfacing emerging superconductivity based quantum technologies with quantum optics and long-distance telecommunication, and can further lead to novel techniques generating and detecting quantum states of light. Here we present a systematic study of the effect of optical frequency illumination on the current-voltage characteristics of Josephson junctions based on highly n-doped InAs nanowires proximitized by aluminum contacts. Three Josephson junctions were studied in detail under DC laser illumination at three wavelengths: 532nm, 790nm (near rubidium transition), and 1550 (for telecom). We find that, for this system, the effect of the laser on the supercurrent can be modeled as local heating of the junction, while the normal state conductance shows non-monotonic change with increasing laser power.

Ultra-high Vacuum Fabrication of Ordered Nanoparticles and Their Device Applications

1
2
3
4
5
6
7
8
9
10
11
12
13
14
15
16
17
18
19
20
21
22
23
24
25
26
27
28
29
30
31
32
33
34
35
36
37
38
39
40
41
42
43
44
45
46
47
48
49
50
51
52
53
54
55
56
57
58
59
60
61
62
63
64
65 Biswajit Das

Department of Electrical and Computer Engineering
University of Nevada
Las Vegas, USA
Biswajit.Das@unlv.edu

Nanoparticles are important for the implementation of a variety of photonic and electronic devices with new functionalities and improved performances. While multiple photonic devices using nanoparticles have been successfully implemented, the use of nanoparticles in electronic devices have significantly lagged; one of the primary reasons being the more stringent material and surface purity requirements for such devices. While the feasibility of a variety of electronic devices based on nanoparticles have been demonstrated in the laboratory, such as nanoparticle flash memory and single electron transistors, the fabrication technique employed is electron-beam lithography, which unfortunately is not suitable for large scale manufacturing. For most electronic devices, it is typically required that the nanoparticle dimensions be in the 1 nm to 10 nm range with size variations of 10% or less. Current photolithographic techniques are not suitable for the implementation of such nanoparticles, and nonlithographic techniques are typically used for their fabrication. However, most nonlithographic techniques are based on natural self-organization and suffer from a lack of flexibility or a lack of engineering control. Among the various nonlithographic techniques, the predominant ones are solution based, which require complex surface passivation involving capping molecules to prevent aggregation. These capping molecules modify the electrical surface properties of the nanoparticles making charge injection/extraction difficult. In addition, the solution based synthesis techniques are not compatible with the silicon integrated circuit (IC) process, in particular the Complementary Metal Oxide Silicon (CMOS) process, which is the predominant manufacturing process for electronic devices. It is widely believed that the availability of a CMOS compatible nanoparticle fabrication technique can greatly increase the viability of nanoparticle based electronic devices.

We have developed a CMOS compatible ultra-high vacuum system (Fig. 1) for the implementation of nanoparticle based electronic devices that addresses the above issues. The system consists of (i) a nanoparticle unit that provides the capability to deposit nanoparticles of any metal, semiconductor or insulator of diameters as low as 1 nm with less than 5% size variation on an arbitrary substrate, (ii) a 4-pocket electron-beam evaporation unit that allows the in-situ deposition of four different materials (metals or insulators) with less than 5% thickness uniformity, and (iii) a UHV pulsed DC sputter source that allows the in-situ deposition of thick layers of insulators (semiconductors or metals) including isolation dielectrics. The nanoparticle deposition unit, the ohmic contact metallization unit and the

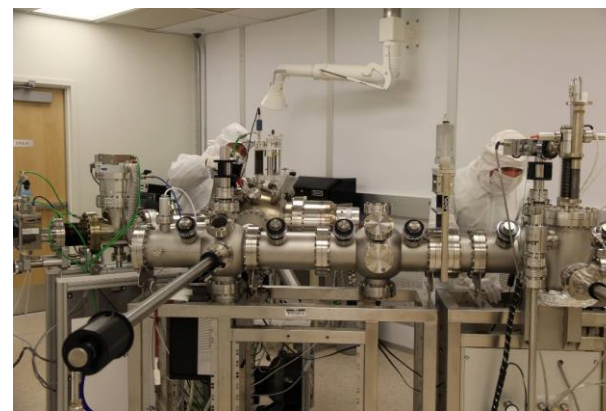


Fig. 1. Cluster tool developed for the fabrication of electronic and photonic devices incorporating nanoparticles

isolation dielectric deposition unit are all housed inside an ultra-high vacuum (10^{-10} torr) chamber to ensure high purity and good surface properties of the nanoparticles.

The nanoparticle deposition system is based on sputtering, thus making it possible to deposit nanoparticles of any material that can be sputtered. In addition, nanoparticle deposition can be carried out at room temperature, making it possible to deposit the nanoparticles on a variety of substrates including flexible substrates. Size selection of nanoparticles is achieved by using a quadrupole mass filter with the capability to provide as low as 2% size control. One advantage of the system is that ohmic contacts and isolation dielectrics can be formed in an integrated manner without breaking vacuum, which is important for electrical continuity. In addition, the deposited nanoparticles can be embedded in, or coated with, metallic, semiconducting or insulating layers without breaking vacuum, thus making complex multi-layered structures possible that can have applications in a variety of fields including nanoscale detectors, nano-optics, nano-sensors, field-emitters etc.

For nanoparticle based electronic devices to function properly, it is essential that the nanoparticles are physically separated from each other. In addition, if the nanoparticles can be ordered in a periodic manner, it can significantly improve device reliability and performance. To address these issues, we have developed a technique for the electrical ordering of the nanoparticles that can be carried out in-situ without breaking vacuum (Fig. 2). The ordering process is rapid, does not require physical contact with nanoparticles and thus prevents contamination.

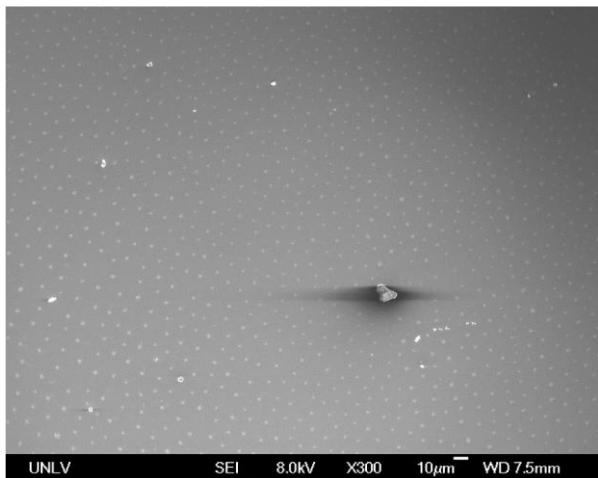


Fig. 2. Example of ordered nanoparticles deposited on a silicon substrate

We have used the system and technique for the deposition of a variety of nanoparticles of metals and semiconductors including Ni, Fe, Co, Au, Ag, Cu, Si, CdTe, CdSe, ZnS on a variety of substrates including silicon, silicon dioxide coated Si, metal coated silicon, quartz, sapphire. We have also fabricated complex structures containing nanoparticles for various applications. In this presentation, we will provide details of the apparatus, fabrication process, experimental results as well some of the nanoparticle based electronic devices currently being developed.

Optical absorption in superlattices of nanocrystals

1 Christophe Delerue

2 IEMN

3 ULille, CNRS, Centrale Lille, ISEN,
4 UPHF
5 UMR 8520, Lille, France
6 ORCID: 0000-0002-0427-3001

7 Maryam Alimoradi Jazi

8 Debye Institute for Nanomaterials
9 Science
10 University of Utrecht
11 Utrecht, The Netherlands
12 ORCID: 0000-0002-9244-8739

13 P. Tim Prins

14 Debye Institute for Nanomaterials
15 Science
16 University of Utrecht
17 Utrecht, The Netherlands
18 ORCID: 0000-0002-8258-0074

19 Niall A. Killilea

20 Materials Science Department
21 Friedrich-Alexander Universität
22 Erlangen-Nürnberg
23 Nürnberg, Germany

24 Wiel H. Evers

25 Department of Chemical Engineering
26 Delft University of Technology
27 Delft, The Netherlands
28 ORCID: 0000-0002-3413-5128

29 Wolfgang Heiss

30 Materials Science Department
31 Friedrich-Alexander Universität
32 Erlangen-Nürnberg
33 Nürnberg, Germany
34 ORCID: 0000-0003-0430-955

35 Zeger Hens

36 Department of Chemistry
37 University of Ghent
38 Belgium
39 ORCID: 0000-0002-7041-3375

40 Peter Geiregat

41 Department of Chemistry
42 University of Ghent
43 Belgium
44 ORCID: 0000-0001-7217-8738

45 Arjan Houtepen

46 Department of Chemical Engineering
47 Delft University of Technology
48 Delft, The Netherlands
49 ORCID: 0000-0001-8328-443X

50 Daniel Vanmaekelbergh

51 Debye Institute for Nanomaterials
52 Science
53 University of Utrecht
54 Utrecht, The Netherlands
55 ORCID: 0000-0002-3535-8366

56 Semiconductor nanocrystals capped with a ligand shell are
57 now routinely synthesized in colloidal solutions and are
58 intensively studied for their tunable optical properties. These
59 latter not only depend on the semiconductor compound but
60 also on the nanocrystal size and shape due to strong quantum
61 confinement effects. This remarkable tunability is presently
62 exploited for light-emitting applications, in particular in
63 commercial TVs.

64 Beyond these applications, semiconductor nanocrystals are
65 now increasingly seen as building blocks for the
66 fabrication of more complex materials. For example,
67 nanocrystals can be assembled into monolayers which, in the
68 best conditions, form well-ordered two-dimensional lattices
69 with hexagonal symmetry. However, in these lattices, the
70 nanocrystals are still separated by their ligand shell and
71 therefore the electronic coupling between neighbor
72 nanocrystals remains weak. In other words, the electronic
73 states in these systems are close to those of the individual
74 nanocrystals.

75 The situation is considerably different in two-dimensional
76 superlattices made of epitaxially-connected nanocrystals.
77 Recent progress in colloidal chemistry has enabled the
78 fabrication of such superlattices of PbX ($\text{X}=\text{Se, S, Te}$)
79 nanocrystals with square or honeycomb geometry [1-3]. In
80 addition, superlattices based on CdX semiconductors can be
81 derived from PbX nanocrystal superlattices using cation
82 exchange process [4]. In these artificial materials, the
83 electronic coupling between neighbor nanocrystals is strong,
84 leading to the formation of electronic mini-bands in which the
85 energy dispersion is strongly influenced by the lattice
86 geometry [5-7]. Two-dimensional superlattices exhibit much
87 higher electrical conductivities than self-assembled
88 monolayers [8,9].

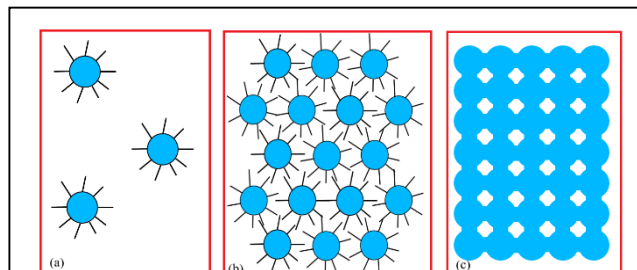


Fig. 1 : Semiconductor nanocrystals in solution (a), in hexagonal self-assembled lattice (b), in square epitaxially-connected superlattice (c).

89 In this vivid context, the comparison between the optical
90 properties of the nanocrystals placed in these different
91 configurations is of high interest. In the present talk, the
92 following questions will be addressed. How much light can be
93 absorbed per nanocrystal unit? How does it depend on its
94 dielectric environment and the electronic coupling with its
95 neighbor nanocrystals? How does it compare with the optical
96 absorption in two-dimensional materials such as
97 semiconductor thin films or graphene?

98 Different aspects of the physics of the optical absorption
99 process in these materials will be discussed. The optical
100 absorption in self-assembled lattices (Fig. 1b) can be increased
101 by a factor ~ 2 to ~ 6 compared to nanocrystals in solution (Fig.
102 1a) due to dipolar interactions between neighbor nanocrystals
103 [10]. We present new experimental and theoretical studies
104 which demonstrate that the absorptance of superlattices is
105 considerably enhanced due to the epitaxial connections
106 between neighbor nanocrystals. The measured and calculated
107 values are compared to the quantum absorptance found in
108 epitaxial two-dimensional films (quantum wells) [11] or in
109 graphene [12]. We discuss the main physical mechanisms
110 governing the variations of the absorption from isolated
111 nanocrystals to closely-packed situations, i.e., hexagonal

lattices of nanocrystals, epitaxial superlattices, to the quantum well limit.

REFERENCES

- [1] M. P. Boneschanscher et al. “Long-range orientation and atomic attachment of nanocrystals in 2D honeycomb superlattices,” *Science* 344, pp. 1377-1380, 2014.
- [2] C. Schliehe et al. “Ultrathin PbS Sheets by Two-Dimensional Oriented Attachment,” *Science* 329, pp. 550-553, 2010.
- [3] J. L. Peters et al. “Mono- and Multilayer Silicene-Type Honeycomb Lattices by Oriented Attachment of PbSe Nanocrystals: Synthesis, Structural Characterization, and Analysis of the Disorder,” *Chem. Mater.* 30, pp. 4831-4837, 2018.
- [4] W.H. Evers et al. “Low-Dimensional Semiconductor Superlattices Formed by Geometric Control over Nanocrystal Attachment,” *Nano Lett.* 13, pp. 2317-2323, 2013.
- [5] E. Kalesaki, W.H. Evers, G. Allan, D. Vanmaekelbergh, and C. Delerue, “Electronic structure of atomically coherent square semiconductor superlattices with dimensionality below two,” *Phys. Rev. B* 88, 115431, 2013.
- [6] E. Kalesaki et al. Dirac Cones, Topological Edge States, and Nontrivial Flat Bands in Two-Dimensional Semiconductors with a Honeycomb Nanogeometry. *Phys. Rev. X* 4, 011010, 2014.
- [7] A. Tadjine and C. Delerue, “Colloidal nanocrystals as LEGO® bricks for building electronic band structure models,” *Phys. Chem. Chem. Phys.* 20, pp. 8177-8184, 2018.
- [8] W.H. Evers et al. “High charge mobility in two-dimensional percolative networks of PbSe quantum dots connected by atomic bonds,” *Nat. Commun.* 6, pp. 8195, 2015.
- [9] M. Alimoradi Jazi et al. “Transport Properties of a Two-Dimensional PbSe Square Superstructure in an Electrolyte-Gated Transistor,” *Nano Lett.* 17, pp. 5238-5243, 2017.
- [10] P. Geiregat, Y. Justo, S. Abe, S. Flamee, and Z. Hens, “Giant and Broad-Band Absorption Enhancement in Colloidal Quantum Dot Mono layers through Dipolar Coupling,” *ACS Nano* 7, pp. 987-993, 2013.
- [11] H. Fang et al. “Quantum of optical absorption in two-dimensional semiconductors,” *P. Natl. Acad. Sci. USA* 110, pp. 11688-11691, 2013.
- [12] R. R. Nair et al. “Fine structure constant defines visual transparency of graphene,” *Science* 320, pp. 1308-1308, 2008.

Study of Non-linearity of the Bilayer Graphene Field Effect Transistors

1
2
3
4
5
6
7
8
9
10
11
12
13
14
15
16
17
18
19
20
21
22
23
24
25
26
27
28
29
30
31
32
33
34
35
36
37
38
39
40
41
42
43
44
45
46
47
48
49
50
51
52
53
54
55
56
57
58
59
60
61
62
63
64
65
MUNINDRA

Department of Electronics and Communication Engineering
Delhi Technological University
Delhi, INDIA
kumar.muninder90@gmail.com

DEVA NAND

Department of Electronics and Communication Engineering
Delhi Technological University
Delhi, INDIA
devkamboj07@gmail.com

Abstract: Bilayer graphene Field Effect Transistors (Bi-GFETs) could be one of the best emerging nanotech electronic devices, as follows the van der Walls heterostructure and graphene/hBN heterostructure. Simple and easy to fabricate bilayer GFETs could add a new dimension to the electronics device world and ready for replacement of conventional silicon technology. This work presents the non-linear behavior and characteristic of the bilayer GFET through output i.e. negative drain current versus drain to source voltage. Furthermore, the closed expression for the first, second and third order harmonic distortions (HD) of the drain current would be explained.

INTRODUCTION

The bi-layer and trilayer graphene in a controlled stacking way could be the optimal candidate for the post-silicon semiconductor industries and fabrication foundries. However, it can be very easily noticed that there are only a few dedicated GFETs model, which describes the bilayer or more layer graphene FET mathematically. Especially the non-linearity of Bi-layer GFET models is not very clear from the available literature. The non-linear behavior of a particular electronic device can decide by the characteristic curve of that device or by the output characteristic equation of that modelled device. In the same manner, here output drain current will be used to define non-linearity of Bi-GFETs. Taylor series expansion of the drain current as given below would explain the non-linearity of Bi-GFET where V_{GS} is the input applied voltage to the gate and source.

$$I_{DS} = \epsilon_1 V_{GS} + \epsilon_2 V_{GS}^2 + \epsilon_3 V_{GS}^3 + \dots + \epsilon_n V_{GS}^n \quad (1)$$

Drain current for the Bilayer Graphene channel can be formulated as follows as given in [7]. Where L is the length, μ is the mobility in bilayer graphene flack and W is the width of the Bi-GFET, V_{ds} is the applied voltage to the drain and source, $Q_{(n,p)}$ is the total charge contributed by the holes as well as electron, V_{sat} is the saturation velocity in the bilayer graphene, and $n_{(puddle)}$ is the charge contributed by the residual charge carrier.

$$I_{DS} = q\mu_{(n,p)} W \frac{\int_0^{V_{ds}} (|Q_{(n,p)}| + q n_{(puddle)/2}) dV}{L + \mu \int_0^{V_{ds}} \frac{1}{V_{sat}} dV} \quad (2)$$

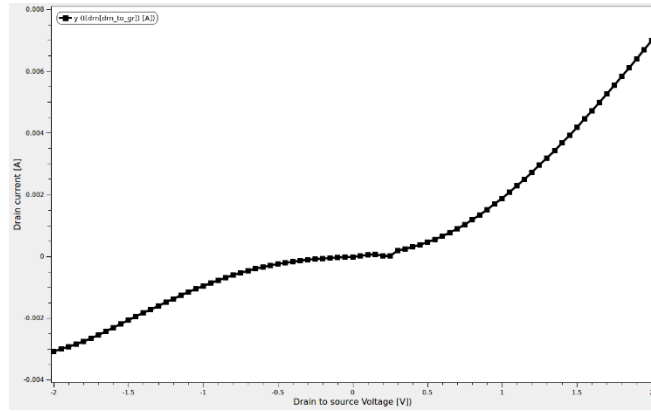


Figure 1: Non-linear behavior of the bilayer graphene field effect transistors (GFET) shown with help of output characteristic curve at i.e. negative drain current vs negative drain to source voltage at constant gate voltage of 1 V.

REFERENCES

- [1] S. Rodriguez, A. Smith, S. Vaziri, M. Ostling, M. C. Lemme and A. Rusu, "Static Nonlinearity in Graphene Field Effect Transistors," *IEEE Transactions on Electron Devices*, Vol. 61. No. 8, pp. 3001-3003, 2014.
- [2] A. Ul Alam, K. D. Holland, M. Wong, S. Ahmed, D. Kienle, and M. Vaidyanathan, "RF Linearity Performance Potential of Short-Channel Graphene Field Effect Transistors," *IEEE Transactions on Microwave Theory and Techniques*, Vol. 63. No. 12, pp. 3874-3887, 2015.
- [3] T. Ohta, A. Bostwick, T. Seyller, K. Hor, and E. Rotenberg, "Controlling the Electronic Structure of Bilayer Graphene," *Science* Vol. 313, pp. 951-954, Aug. 2006.
- [4] K. A. Jenkins, D. B. Farmer, S.-J. Han, C. Dimitrakopoulos, S. Oida, and A. Valdes-Garcia, "Linearity of Graphene Field Effect Transistors," *APPLIED PHYSICS LETTERS* 103, 173115, 2013.
- [5] G. Vincenzi, G. Deligeorgis, F. Coccetti, M. Dragoman, L. Pierantoni, D. Mencarelli, and R. Plana, "Extending ballistic graphene FET lumped element models to diffusive devices," *Solid-state Electron.*, Vol. 76, pp. 8-12, OCT 2012.
- [6] B. N. Szafranek, G. Fiori, D. Schall, D. Neumaier, and H. Kurz, "Current Saturation and Voltage Gain in Bilayer Graphene Field Effect Transistors," *Nano Lett.*, Vol. 12, issue 3, pp. 1324-1328, 2012.
- [7] J. Daniel, A. Morales, S. Frégonèse, C. Mukherjee, C. Maneux, and T. Zimmer, "An Accurate Physics-Based Compact Model for Dual-Gate Bilayer Graphene FETs," *Transactions on Electron Devices*, Vol. 62. No. 12, pp. 4333-4339, 2015.

Precisely Control of Chemical Luminescence Detection Using Quantitative Injection by Microfluidic Chip

Bongsu Kang^a, Moon Kyu Kwak^a, and Hosup Jung^{b*}

^a School of Mechanical Engineering, Kyungpook Nat. Univ.

^b*Center for Food and Bioconvergence, Dept. of Food Science and Biotechnology, Seoul Nat. Univ

1. Introduction

Microfluidics is an engineering field that focuses on controlling small volumes of target fluids according to their purpose and applies them to other disciplines.^[1,2] Chemical luminescence method^[3,4] is used in optical analysis to detect concentration and content of target materials by evaluating the luminescent reaction generated from a mixture of the luminescent reagent and the unknown reagent containing the target material. Chemical luminescence detection is an accurate and rapid analysis method that uses only a small amount of reagents; this method exhibits higher detection precision than other similar optical analysis techniques, such as adsorption spectroscopy and fluorescence analyses.^[5]

This paper reports a microfluidic chip system with small amount of reagents and small-sized equipment for chemical luminescence detection by controlling microfluids. Thus far, the application of microfluidic chip for miniaturizing and simplifying the scale of chemical luminescence experiments has not been universal. We performed experiments using a simple mechanism of luminol reaction to confirm the possibility of chemical luminescence detection using microfluidic chips. Experiment results confirmed the feasibility of quantitative classification and injection. The concentration of the target material was also detected by measuring luminol chemical luminescent reactions inside the microfluidic chips. The proposed highly portable and simple to use microfluidic chips can be used to quantify and inject reagents through microflow control of syringe pressure, not through a micro pump system, in various fields.

2. Experimental

2.1. Fabrication of microfluidic chip

Three types of channel were used to fabricate hierarchical structured microfluidic chips. To fabricate microfluidic and floor channels, we decreased the surface energy of the mold by using self-assembled monolayer (SAM) surface treatment. Polydimethylsiloxane (PDMS) was poured onto the

mold, which was then heat cured in an oven at 70 °C for 1 hour. (Figure 1).



Figure 1. Fabrication of hierarchical structured microfluidic chip. (a) Fabrication of microfluidic channel. (b) Fabrication of floor channel. (c) Bonding process of the three fabricated channels by oxygen plasma treatment and heat curing. (d) Fabricated hierarchical structured microfluidic chip.

2.2. Mechanism of quantitative injection using PDMS microfluidic chip

Channels A and B were controlled by the following steps to classify uniform quantity of chemical luminescence reagents (Figure 2).

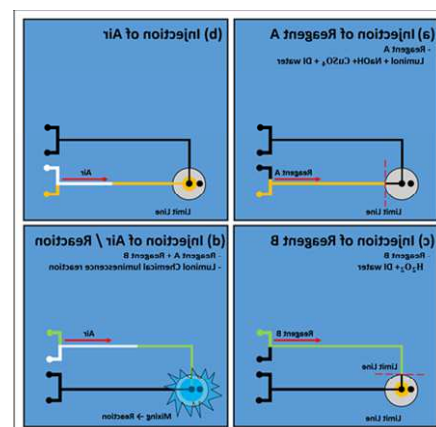


Figure 2. Schematic of the quantitative fluid injection mechanism. (a) Injection of reagent A (b) Injection of air for injecting reagent A into the chamber. (c) Injection of reagent B. (d) Luminol chemical luminescent reaction of the two reagent mixtures.

2.4. Set up of chemical luminometric device capable of microfluidic chip control and chemical

luminescence monitoring

A chemical luminometric device was set up for processing chemical luminescence in the microfluidic chip. On the second floor, a dark room is located for installing microfluidic chip and blocking external light source and pistons to control the syringe pressure (Figure 3).

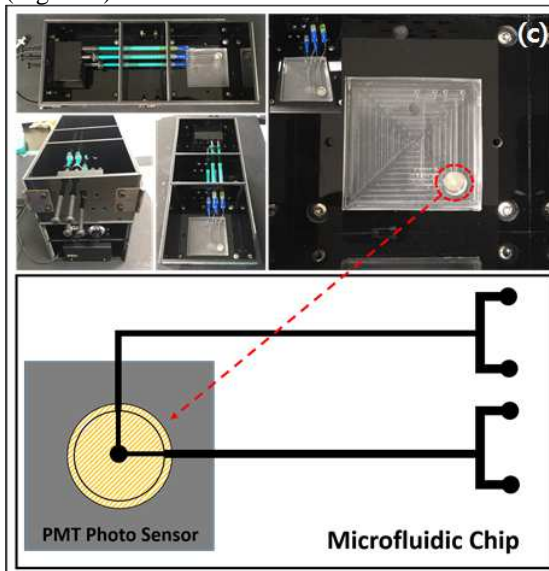


Figure 3. Photograph and schematic of microfluidic chip mounted on the chemical luminometric device. (a) 3D and 2D views of the device. (b) Schematic of the device. (c) Photograph of the set up device. (d) Schematic of the mounted microfluidic chip on the PMT sensor.

3. Result and Discussion

3.1. Monitoring the performance of the microfluidic chip and the chemical fluorometric device

Performance evaluation of the microfluidic chip and device was conducted focusing on the capability to detect change in C.L. intensity according to changes in the reagent concentration. Experiment results indicated that the C.L. intensity increased with increasing luminol concentration

3.2. Measurements of luminol chemical luminescence reaction inside the PDMS microfluidic chip by using the chemical luminometric device

To analyze the overall tendency of chemical luminescent reactions, we performed measurement for 60 seconds and for five times for each concentration. The C.L. intensity rapidly increased within the concentration range of 0.003–0.01 g/200 ml according to the luminol concentration but slowly increased within the range of 0.02–0.1 g/200 ml. Based on the overall tendency, the C.L. intensity increased proportionally with increasing luminol concentration under a fixed condition of reagent, except for luminol concentration. After a specific concentration, the C.L.

intensity decreased (Figure 4).

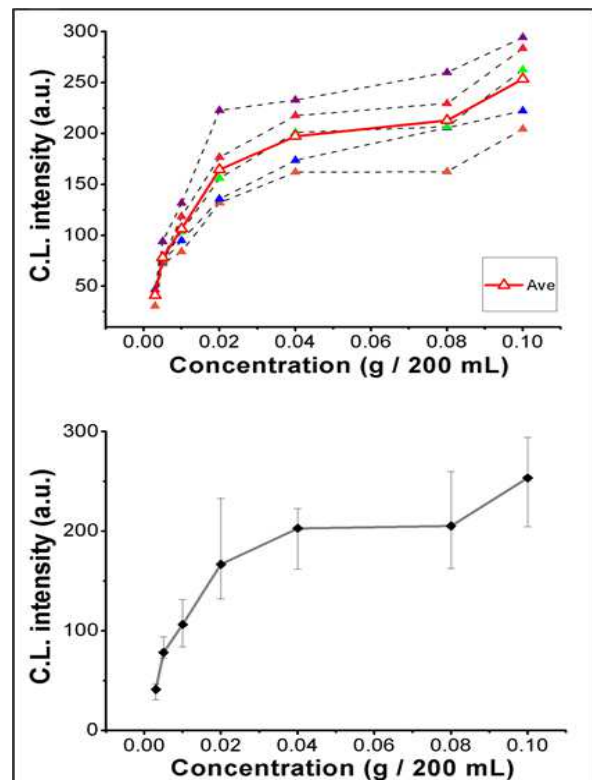


Figure 4. Graph of C.L. intensity according to changes in luminol concentration.

4. Conclusion

In this study, we fabricated a PDMS microfluidic chip for uniform quantitative classification and injection and developed a chemical fluorometric device for detecting chemical luminescence inside the microfluidic chip.

5. References

- [1] R.M. van Dam. "Solvent-Resistant Elastomeric Microfluidic Devices and Applications", In Partial Fulfillment of the Requirements for the Degree of Doctor of Philosophy, California Institute of Technology Pasadena, California, August, 2005
- [2] Lisa R. Volpati, Ali K. Yetisen, "Commercialization of microfluidic devices", Trends in Biotechnology July, 2014
- [3] S.C. Terry, J.H. Jerman, J.B. Angell, "A Gas Chromatographic Air Analyzer Fabricated on a Silicon Wafer", IEEE Trans.Electron Devices,ED-26,12(1979)1880–1886.
- [4] H. Lorenz, M. Despont, N. Fahrni, J. Brugger, P. Vettiger, P. Renaud, "High-aspect-ratio, ultrathick, negative-tone, near-UV photoresist and its application for MEMS", Sensors and Actuators A 64 (1998) 33-39
- [5] A del Campo, C. Greiner, "SU-8: a photoresist for high-aspect-ratio and 3D submicron lithography", J. Micromech. Microeng. 17 (2007) R81–R95

determination of glucose and uric acid", Lab Chip

Reliability and Thermal Stability of MoS₂ FETs with Ultrathin CaF₂ Insulators

Yu.Yu. Illarionov^{1,2}, A.G. Banshchikov², D.K. Polyushkin¹, S. Wachter¹, M.I. Vexler², N.S. Sokolov², T. Mueller¹, T. Grasser¹

¹TU Wien, Vienna, Austria ²Ioffe Institute, St-Petersburg, Russia

Two-dimensional (2D) materials can potentially provide a route to overcome the limitations of Si technologies by enabling nanoscale more than Moore FETs. Fabrication of these devices requires *i*) 2D semiconductors with sizable bandgaps and high carrier mobilities and *ii*) competitive insulators to separate the channel from the gate. However, up to now attention has been mostly paid to the channel materials, while insulators fully suitable for 2D FETs have not been identified. For instance, native oxides of 2D semiconductors, which would go along with them as well as SiO₂ goes with Si, either do not exist or cannot be easily synthesized. As a result, 2D FETs currently face the same problems as many other emerging technologies (e.g. Ge, III-V or GaN FETs), and commercial devices do not yet exist.

The absence of native insulators for 2D FETs requires the use of other materials. The most obvious of them are oxides known from Si technologies (e.g. SiO₂, Al₂O₃, HfO₂), which have been used in most 2D FETs. However, despite a respectable performance of some devices, the typical thickness of the oxides used ranges from tens to even hundreds of nanometers. When being scaled down to the equivalent oxide thicknesses (EOT) below 1nm, as required for end-of-the-roadmap devices, these oxides become amorphous. Thus, their interfaces with 2D channels are of poor quality and contain numerous defects which degrade the performance and reliability of 2D FETs. Another solution is the use of 2D insulators which form well-defined van der Waals interfaces with 2D channels. The best known of them is hBN which indeed resulted in the improvement of 2D FETs. However, when scaled down to several nanometers thickness, hBN exhibits significant tunnel leakage currents. This is due to the moderate dielectric properties ($\epsilon < 5$, $E_G = 6$ eV) of hBN, which appears to be unsuitable for scaling. As for other 2D insulators, such as mica or oxide nanosheets, their usability in devices has not been demonstrated.

As an alternative, we have recently suggested to use calcium fluoride (CaF₂) as an insulator for 2D devices [1]. Few-nanometers thin CaF₂ layers can be grown on Si(111) by molecular beam epitaxy (MBE) which forms an F-terminated inert surface with no dangling bonds [2]. This results in a quasi van der Waals interface with 2D materials (Fig.1a), similar to those formed by hBN. Furthermore, due to its good dielectric properties ($\epsilon = 8.43$, $E_G = 12.1$ eV), the tunnel currents through CaF₂ are lower than for most high-k oxides with equal EOT, not to mention SiO₂ and hBN.

We fabricated hundreds of CVD-grown MoS₂ FETs with epitaxial CaF₂ insulators of record-small thickness of only about 2 nm (EOT less than 1nm), see Fig.1b. The gate currents in our devices are small compared to the drain current (Fig.1c). Thus, already in the first bare channel prototypes we achieve competitive on/off current ratios of up to 10⁷ and SS down to 90 mV/dec (Fig.2a). At the same time, the hysteresis in our devices is even smaller than in Al₂O₃ encapsulated SiO₂(25nm)/MoS₂ FETs [3] (Fig.2b). In Fig.2c we compare the hysteresis widths normalized by the insulator field factor $\Delta V_G/d_{ins}$, where ΔV_G is the width of the gate voltage sweep range and d_{ins} the insulator thickness. For CaF₂ the hysteresis is comparable to that in Si/high-k FETs.

In Fig.3 we show the results for bias-temperature instabilities (BTI) in our CaF₂(2nm)/MoS₂ FETs. The negative BTI (NBTI, Fig.3a) and positive BTI (PBTI,

Fig.3b) at insulator fields which are typically used for 2D FETs (2.5 to 5MV/cm) are relatively weak. This is likely due to the lack of insulator defects in the crystalline CaF₂ insulator. However, PBTI stress at the insulator field of 7.5MV/cm leads to a negative drift of the threshold voltage (Fig.3c). This kind of degradation has never been observed for 2D FETs with thick insulators, which routinely operate at lower insulator fields. Recently we found that the negative V_{th} shift after PBTI stress observed in our CaF₂/MoS₂ FETs is very similar to that in MoS₂ FETs with 4nm thick hBN insulators [4]. Thus, we suggest that this is due to the activation of breakdown mechanisms in ultrathin insulators. However, we note that a reasonable on current in our CaF₂/MoS₂ FETs can be achieved already at a gate voltage of 1V (F_{ins} of 5MV/cm), allowing safe device operation.

We also analyzed the thermal stability of our devices and found that it strongly depends on the quality of the MoS₂ channel. If the CVD-grown MoS₂ film is formed by few nanometers sized grains (Process 1, Fig.4a), baking of the devices at 100°C introduces a strong hysteresis (Fig.4b). However, this hysteresis is observed only when using small sweep times t_{sw} and disappears for slow sweeps (Fig.4c). We suggest that the origin of this behavior is thermally enhanced creation of S vacancies in MoS₂. These S vacancies can cause a hysteresis when interacting with adsorbates [5], which can penetrate to the CaF₂/MoS₂ interface through the numerous grain boundaries in the small grain MoS₂. In contrast to charge trapping by slow insulator defects, which seems to be missing in CaF₂, interaction between S vacancies and adsorbates is a fast process. This explains the fast sweep hysteresis which we observe. In contrast, in the CaF₂/MoS₂ FETs with larger grains of the MoS₂ film (Process 2, Fig.5a) the hysteresis remains small even after baking at 165°C (Fig.5b), though a negative shift of V_{th} attributed to the creation of S vacancies is present. However, these S vacancies remain passive, since the number of grain boundaries in large grain MoS₂ is small and thus the penetration of adsorbates to the interface is less efficient. At the same time, the number of active defects in crystalline CaF₂ is small, independently of the MoS₂ quality. Thus, the hysteresis in our Process 2 devices remains small within the whole range of sweep times, while being smaller than in Al₂O₃ encapsulated SiO₂(25nm)/MoS₂ FETs (Fig.5c).

In summary, we examined the reliability and thermal stability of the MoS₂ FETs with CaF₂ insulators of record small 2nm thickness. We found that the virtually defect-free nature of CaF₂ insulators leads to a small hysteresis and BTI, while the thermal stability of our devices strongly depends on the quality of the MoS₂ channel.

- [1] Yu.Yu. Illarionov *et al*, “Ultrathin calcium fluoride insulators for two-dimensional field-effect transistors”, *Nature Electron.*, 2019.
- [2] A. Koma *et al*, “Heteroepitaxy of a two-dimensional material on a three-dimensional material”, *Appl. Surf. Sci.*, vol. 41, 451–456, 1990.
- [3] Yu.Yu. Illarionov *et al*, “Improved Hysteresis and Reliability of MoS₂ Transistors with High-Quality CVD Growth and Al₂O₃ Encapsulation”, *IEEE Electron Device Lett.*, vol. 38, 1763–1766, 2017.
- [4] Yu.Yu. Illarionov *et al*, “Reliability of scalable MoS₂ FETs with 2 nm Crystalline CaF₂ Insulators”, *2D Mater.*, 2019.
- [5] A. Di Bartolomeo *et al*, “Hysteresis in the transfer characteristics of MoS₂ transistors”, *2D Mater.*, vol. 5, 015014, 2017.

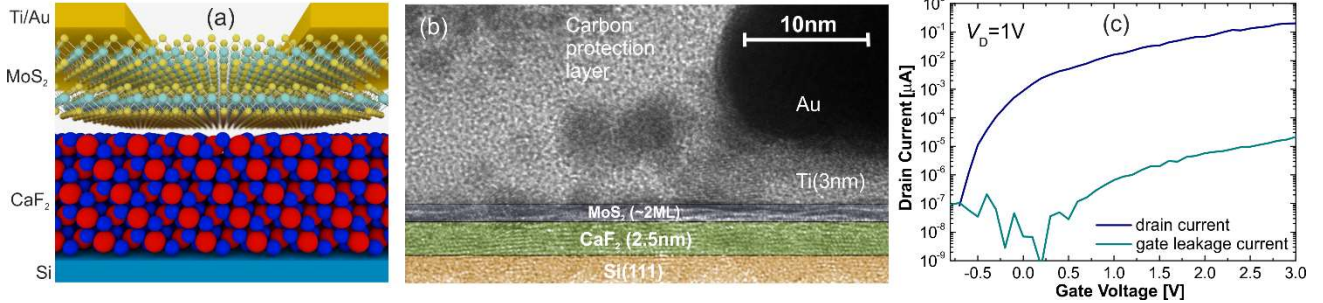
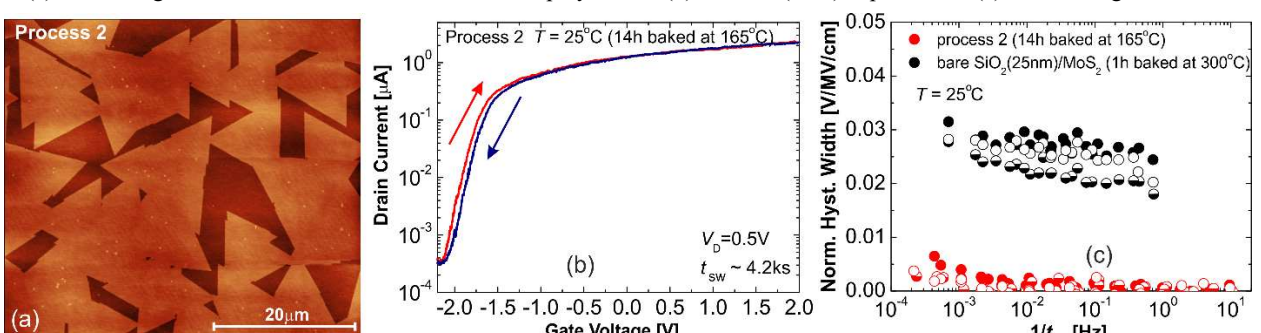
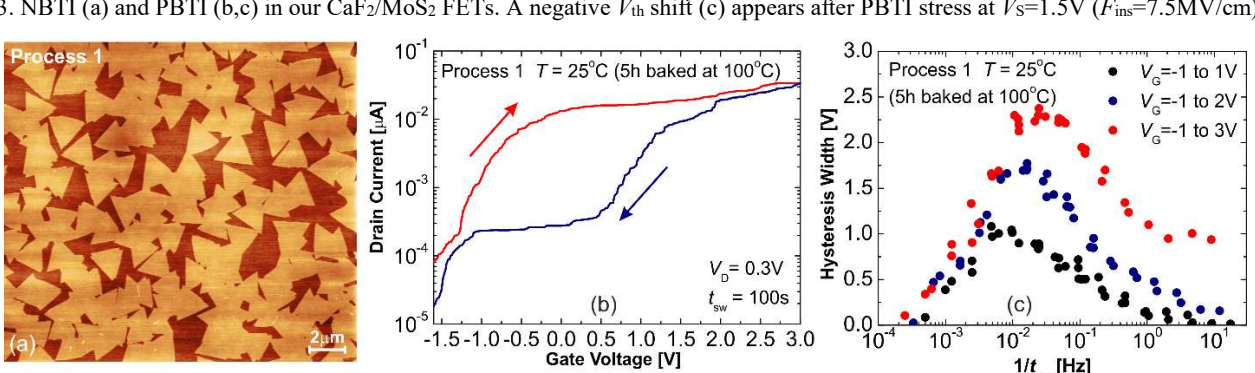
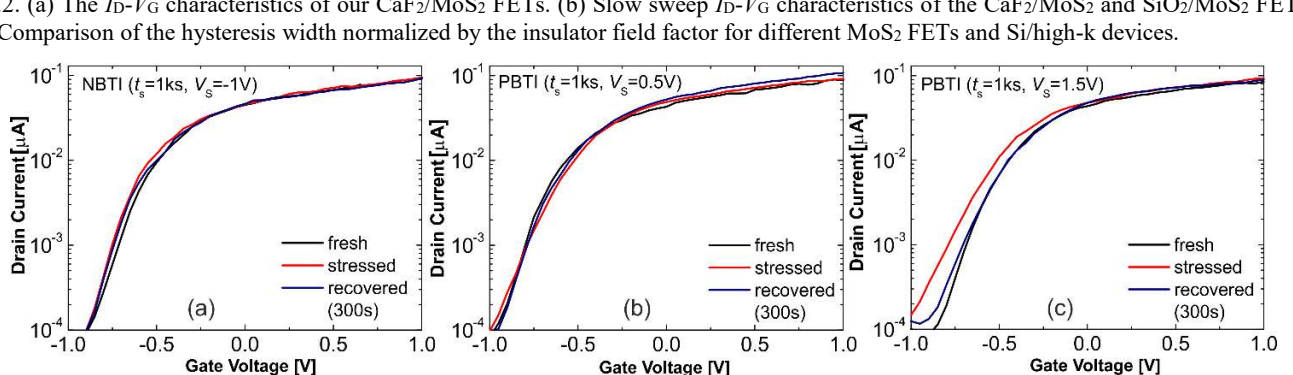
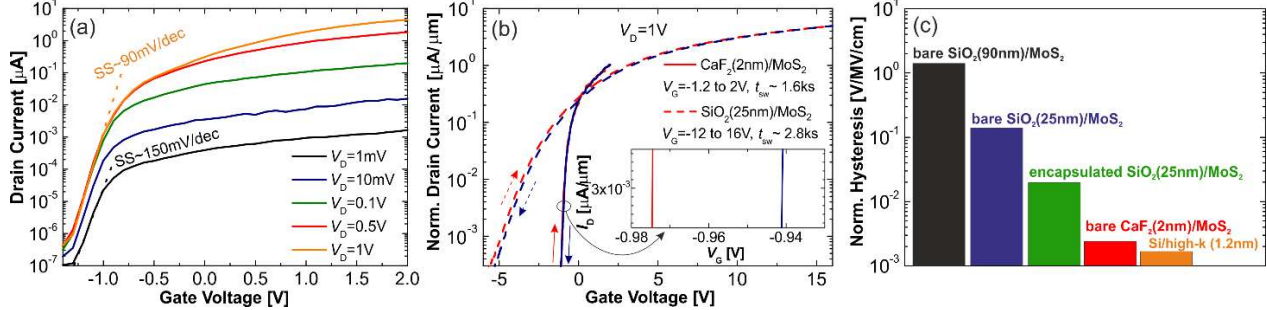


Fig.1. (a) Schematic device layout. (b) TEM image of the channel area. (c) Drain current and gate leakage current vs. gate voltage.



1 A High FoM Graphene Nano-composites for Supercapacitors Applications

2 K. R. Abidi

3 dept. of electronics engineering
4 AMU, Aligarh, India
5 krabidi@myamu.ac.in

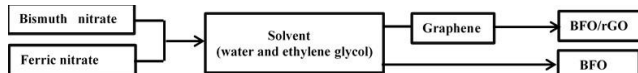
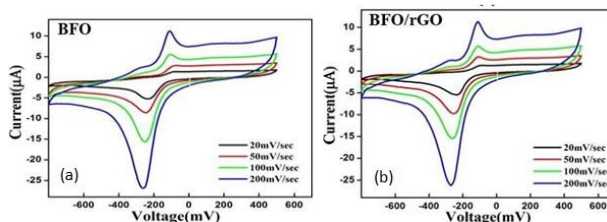
6 M.S Alam

7 dept. of electronics engineering
8 AMU, Aligarh, India
9 msalam.el@amu.ac.in

10 A. Azam

11 dept. of applied physics
12 AMU, Aligarh, India
13 aazam.ap@amu.ac.in14 **Keywords:** FoM, Supercapacitor, Quantum ATK15 A new figure-of-merit (FoM) has been proposed in this
16 work to evaluate the performance of supercapacitors. Key
17 parameters such as specific capacitance C (F/g), specific
18 energy E (WhKg⁻¹), specific power P (WKg⁻¹), potential
19 window P_w (V), capacity retention (η), series resistance R
20 (Ω) and fabrication cost (FC) were used individually,
21 which makes the performance comparison cumbersome
22 [1]. Therefore, in this work, a new FoM involving these
23 parameters has been proposed, which is defined as:

24
$$25 \text{FoM} = \frac{C \times E \times P \times P_w}{R \times FC} \quad (1)$$

26 The cobalt selenide (CoSe) (due to high C in contrast to
27 other metal chalcogenides [2]) and (CoSe-G) is studied
28 here due to their high FoM for supercapacitors applications
29 [2]. Both experimental and computational studies of CoSe-G
30 are carried as they are not thoroughly investigated in the
31 literature and its performance comparison with graphene
32 composite of bismuth ferrite (BFO/rGO) using the
33 experimental setup at the authors' institute is carried out.
34 The basic outline for the setup used for BFO and BFO/rGO
35 is outlined in Fig. 1.37 Fig. 1. Experimental setup used to develop BFO and BFO/rGO using the
38 sol-gel technique.39 Cyclic voltammetry (CV) tests for BFO and its
40 nanocomposite with graphene (BFO/rGO) at different scan
41 rates, were experimentally performed, as shown in Fig.
42 Fig. 2(a) and Fig. 2(b), respectively.

44 Fig. 2. Cyclic voltammetry test results for (a) BFO (b) BFO/rGO

45 Using the following equation on experimental results
46 shown in Fig 2, C (F/g) for BFO/rGO can be calculated as

47 [3]:
$$48 C = \frac{1}{mv(V_a - V_b)} \int_a^b IdV \quad (2)$$

49 Where,

50 m = weight of the nano-composite coated in one of the
51 electrodes (g)52 v = scan rate (mV s⁻¹)53 $V_a - V_b = \text{potential window } P_w \text{ (V); } I = \text{current (A).}$ 54 Experimentally, the specific energy is evaluated by
55 cyclic voltammetry (E_{CV}) and constant current
56 charge-discharge approach (E_{CCCD}) as [1]:

57
$$E_{CV} = \frac{1}{2} C(P_w)^2 \quad (3)$$

58
$$E_{CCCD} = \int_0^Q V_o dq = \frac{1}{2} V_o Q = \frac{1}{2} V_o It_c \quad (4)$$

59 Where, Q = net charge; V_o = peak potential value and
60 t_c (or t_d) = charging time (or discharging time).61 Cyclic voltammetry, CCCD and electrochemical
62 impedance spectroscopy (EIS) data are used to determine
63 specific power using either cyclic voltammetry (P_{CV}) or
64 CCCD (P_{CCCD}) as:

65
$$P_{CV} = \frac{1}{2} C(P_w) v = \frac{1}{2} \left(\frac{Q}{mv_o} \right) V_o \left(\frac{V_o}{s} \right) = \frac{1}{2} V_o I \quad (5)$$

66
$$P_{CCCD} = \frac{E_{CCCD}}{t_c \text{ (or } t_d \text{)}} \quad (6)$$

67 The series resistance R is obtained from the CCCD
68 voltage drop and impedance spectrum of EIS by using
69 E/P=RC. Similar procedure as described in Eq. (2) was
70 followed to determine C for CoSe-G. From Table I, it can
71 be observed that there is an enormous difference between
72 C for CoSe-G (C_{CoSe-G}=1016 F/g) and C for BFO/rGO
73 (C_{BFO/rGO}=211 F/g), which suggest CoSe-G offer
74 significant potential to realize supercapacitor.75 Using experimental data [4]-[9] and formulation
76 described in Eqs. (3)-(6), other parameters of the FoM
77 were determined for CoSe-G [10] and BFO/rGO (See
78 Table I). It can be observed from Table-I that FoM for
79 CoSe-G (FoM_{CoSe-G}) is significantly higher than FoM for
80 BFO/rGO (FoM_{BFO/rGO}). Therefore, the new graphene
81 nanocomposite material proposed in this paper offers
82 massive potential for supercapacitor applications, a
83 detailed investigation for physical and chemical properties
84 are required to ascertain reasons for such high FoM.
85 Usually, in the literature, rigorous experimental studies are
86 carried out the design and develop the new materials for
87 supercapacitor [4]-[9]. Therefore, experimental study
88 approach is cumbersome. Moreover, transport properties at
89 the atomistic level are not possible to determine using
90 experimental approach. Therefore, first principles
91 QuantumATK is used to investigate the physical and
92 chemical properties of the materials and composites
93 structures at the atomic level prior to their synthesis [11].
94 Furthermore, the theoretical basis for high performance for
95 the proposed nanocomposite materials is added to support
96 the simulation results, which well correlate with
97 experimental results given in Table I. The first principles
98 tool [11] utilized density functional theory (DFT) for
99 evaluation of parameters interest. DFT calculations are

accurate, as it investigates at the atomistic level, which is not possible in experimentally study; therefore, DFT is the back-end engine for most of the first principles tool [12]. The theoretical insight for various parameters used in FoM and their simulated results using ATK [11] are summarized in Table I.

TABLE I: FoM COMPARISON OF MATERIALS AND THEIR NANOCOMPOSITE

Nano-Materials	C [Fg $^{-1}$]	E [Whkg $^{-1}$]	P [Wkg $^{-1}$]	P_w [V]	η [%]	R [Ω]	FoM
Parameters Used in FoM determined Using Experimental data [4]-[9]							
BFO	152	6.6	3295	1.4	82	2.1	1824
CoSe	708	21.1	400	1.6	74	0.8	8843
BFO/rGO	211	1.9	18750	1.4	99	0.5	1041
CoSe-G	1016	45.5	1100	1.6	88	0.1	800000
Parameters Used in FoM determined Using Quantum ATK [11]							
BFO	155	7.1	3485	1.4	85	1.5	1890
CoSe	751	23	382	1.6	80	0.4	9557
BFO/rGO	248	1.8	17590	1.4	95	0.2	1104
CoSe-G	1120	47	1150	1.6	85	0.1	850000

A. Specific Capacitance

Using the fixed band structure approximation, the quantum capacitance C_Q was determined, although variable band structure is more accurate, the former gives quick response [13]. By using fixed band structure approximation and induced charge after applying a finite bias voltage, a net positive/negative charges Q on the surface (Also named as Mulliken population) are induced [10], which can be determined as:

$$Q = e \int_{-\infty}^{+\infty} DOS(E) \times f(E) dE \quad (7)$$

Where,

$f(E)$ = Fermi-dirac functions of the electrons, expressed as:

$$f(E) = \frac{1}{1 + \exp(E/kT)} \quad (8)$$

E = relative energy with respect to Fermi level

DOS = density of state. If φ is the applied voltage, then C_Q is evaluated as:

$$C_Q = e^2 \int_{-\infty}^{+\infty} DOS(E) \times \frac{\operatorname{sech}^2((E - e\varphi)/2kT)}{4kT} dE \quad (9)$$

After C_Q is obtained, the specific capacitance can be determined by knowing the number of atoms on the electrode surface.

B. Specific Energy and Power

Specific energy and power are evaluated by the ATK [11] by first determining the charge density σ (C/m^2) as [12]:

$$\sigma = e \int_{-\infty}^{+\infty} DOS(E) \times [f(E) - f(E - e\varphi)] dE \quad (10)$$

Further, DFT calculations were performed on the generalized gradient approximation (GGA) of Perdew, Burke and Ernzerh of exchange correlation (PBE) along with hybrid functional and executed by employing Quantum-wise ATK [11] Under the same conditions, DOS and the carrier transport in the materials are evaluated and used to assess the FoM.

C. Capacity Retention and Series Resistance

The capacity retention model is developed in ATK for simulation studies of these parameters. It is primarily based on the loss of charges on the surface, which result in rising of electrode series resistance. Furthermore, the

model controls the charge/discharge time and estimates the voltages as a function of cycle number. Authors' propose to carry out an experimental study of the new nanocomposite materials to authenticate simulation results, and its brief outline is shown in Fig. 3.

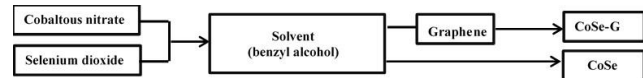


Fig. 3. Experimental setup to develop CoSe and CoSe-G using salvo thermal technique

The proposed study reveals that the parameters determined experimentally are in good agreement with the ATK simulated results, which establishes the accuracy of the first-principle tool. The high FoM of the new graphene nanocomposite demonstrates its suitability to design and develop high performance supercapacitor.

REFERENCES.

- [1] S.Ratha, A.K Samantara, Supercapacitor: instrumentation, measurement and performance evaluation techniques," SpringerBriefs in materials. Singapore 2018, pp. 18-21.J. Clerk Maxwell, A Treatise on Electricity and Magnetism, 3rd ed., vol. 2. Oxford: Clarendon, 1892, pp.68–73.
- [2] N. Mahmood, C.Zhang, H. Yin, Y.Hou "Graphene-based nanocomposites for energy storage and conversion in lithium batteries, supercapacitors and fuel cells", J. Mater. Chem. A, 2014, vol. 2, pp. 2- 15.
- [3] Electronic Supplementary Material (ESI) for RSC Advances This journal is © The Royal Society of Chemistry 2013, 21-27.
- [4] V.V Jadhav, M.K Zate, S.Liu, Mu. Naushad, R.S. Mane, K.N. Hui, S.H Han, "Mixed phase bismuth ferrite nanoflake electrodes for supercapacitor application", Appl Nanosci 2016, 6: pp. 511-519.
- [5] C.D.Lokhande, T.P Gujar, V.R Shinde, R.S.Mane, S.H.Han "Electrochemical supercapacitor application of perovskite thin films", Electrochemistry communications 9, 2007, pp. 1805-1809.
- [6] A. Sarkar, A.K Singh, D. Sarkar, G.G Khan, K.Mandal "Three dimensional nanoarchitecture of BiFeO₃ anchored TiO₂ nanotube arrays for electrochemical energy storage and solar energy conversion", ACS Sustainable Chem. Eng. 2015, 3, 2254-2263.
- [7] A. Soam, C. Mahender, R.Kumar, M. Singh, "Power performance of BFO-graphene composite electrodes based supercapacitor", Mater. Res. Express. 2018
- [8] H. Peng, G Ma, K. Sun, Z. Zhang, J. Li, X. Zhou, Z. Lei, " A novel aqueous asymmetric supercapacitor based on petals like cobalt selenide nanosheets and nitrogen doped porous carbon electrodes", Journal of power sources 297, 2015, pp. 351-358.
- [9] B. Kirubasankar, V. Murugadoss, S. Angaiah, "Hydrothermal assisted in situ growth of CoSe onto graphene nanosheets as a nanohybrid positive electrode for asymmetric supercapacitors", RSC Adv., 2017, 7, pp. 5853-5862
- [10] J. Theerthagiri, K. Karuppasamy, G. Durai, A.H.S. Rana, P. Arunachalam, K. Sangeetha, P. Kuppusami, H.S Kim, "Recent advances in metal chalcogenides (MX; X = S, Se) nanostructures for electrochemical supercapacitor applications: a brief review", Nanomaterial, 2018, 8, 256.
- [11] QuantumATK-2019 <https://www.synopsys.com/quantumatk.html>
- [12] D. G. Ladha. "A review on density functional theory based study on two dimensional materials used in batteries", Materials Today Chemistry 11, 2019, pp. 94-111.
- [13] F. Su, L.Huo, Q.Kong, L. Xie, C. Chen, " Theoretical study on the quantum capacitance origin of graphene cathodes in lithium ion capacitors", Catalysts 2018, 8, 444.

Environmental networks in aging society traveler for health services center, Bangkok Thailand

Material as environmental networks in aging society traveler for health services, Bangkok Thailand is education, health activities, aging society in the situation of aging society (supporting factors and obstacles) in the urban community. To study factors supporting travel and obstacles during the way to receive health services of aging society in Bangkok are survey research. The tool used is questionnaires and interview forms from the elderly population which select a sample group in the area by conducting field surveys. That information used to analyze descriptive and quantitative data using frequency percentage.

The results of the study showed that the analysis of material as environmental networks for older society with travel patterns in urban communities Bangkok. The changing travel behavior from using personal vehicles to using mass transit systems has resulted in a much higher energy price. The development direction therefore focuses on the development of mass transit systems. For the analysis of factors related to travel, receiving health services for the elderly in the urban community around Sirinthon Hospital, Bangkok in accordance with the rules and management of infrastructure of the urban community. The development direction in the next phase will encourage the support of education and technology research in order to develop the infrastructure in the next phase.

Keywords—Environmental networks in aging society; Travel communication; Urban structure application

Towards Highly Doped Si Single Crystal Cylindrical Nanowire Fabrication

1
2
3
4
5
6
7
8
9
10
11
12
13
14
15
16
17
18
19
20
21
22
23
24
25
26
27
28
29
30
31
32
33
34
35
36
37
38
39
40
41
42
43
44
45
46
47
48
49
50
51
52
53
54
55
56
57
58
59
60
61
62
63
64
65
Raul Back Campanelli

Institute of Physics "Gleb Wataghin"
Universidade Estadual de Campinas
Campinas, Brazil
raulbacam@gmail.com

Marcos V. Puydinger dos Santos
Institute of Physics "Gleb Wataghin"
Universidade Estadual de Campinas
Campinas, Brazil
puyding@ifi.unicamp.br

Fanny Béron
Institute of Physics "Gleb Wataghin"
Universidade Estadual de Campinas
Campinas, Brazil
fberon@ifi.unicamp.br

Kleber R. Pirota
Institute of Physics "Gleb Wataghin"
Universidade Estadual de Campinas
Campinas, Brazil
krpirota@ifi.unicamp.br

Abstract—This work reports on the fabrication on doped Si bulk and nanowire crystals. They were obtained through the Metal Flux Nanonucleation technique, where a nanoporous alumina template was used to define the nanowire shape, and Ga was used as flux, to lower the Si melting point. Results show that Ga was successfully incorporated in the Si crystal, and induced superconducting-like behavior.

Keywords—*Silicon, doped semiconductors, nanowires, single crystals, Gate-all-around transistor*

I. INTRODUCTION

Low-dimension materials are currently under the scope of both academia and industry. As a general classification, such materials can be described as 0-dimensional (such as quantum dots), 1-dimensional (like nanowires), 2-dimensional (thin films) and 3-dimensional. Such materials are of particular interest due to their distinct properties when compared to bulk materials, as well as for their potential for application in devices - such as transistors - and large scale production.

Among those, nanowire represents a shape that naturally incorporates into novel devices. However, distinction should be made between nanowires, taken as cylindrical, from nanoribbons, which exhibit a rectangular cross-section. While the later are commonly fabricated by lithography, their anisotropic cross-section may interfere with their behaviour. On the other side, cylindrical nanowires suffer the additional step of nanomanipulation before their integration in a device.

Regarding transistor technology, efforts have been made towards the fabrication of architecture called “gate-all-around” (GAA) [1], due to the presence of two channels. It consists of a cylindrical silicon nanowire upon which the gate is wrapped around. Therefore, the previous fabrication of high quality cylindrical nanowires for GAA transistor may overcome the extra cost of their afterwards integration.

In this context, this work focuses on the attempt of fabricating highly doped silicon cylindrical nanowires. The chosen technique, the Metal Flux Nanonucleation (MFNN), developed and patented in 2014 [2], already proved to achieve high quality GdIn_3 [3], Fe_3Ga_4 [4] and Ga [5] nanowires. Therefore, it provides a promising fabrication route for silicon cylindrical nanowires.

II. CRYSTAL FABRICATION

The Metal Flux Nanonucleation (MFNN) is based on the nucleation of single crystal nanowires from melt, mediated by the pore geometry of an nanoporous alumina template. Such templates, obtained through hard anodisation, exhibit nanopores that are cylindrical, regularly distributed, passing through the whole template thickness, and with diameter of 150 nm. The melt is made by adding a low melting point metal - called flux - that dissolves the desired element, and subsequently allows it to precipitate as crystals, acquiring the alumina template nanopore geometry. cylindrical nanowires for GAA transistor may overcome the extra cost of their afterwards integration.

For this particular work, gallium was selected as flux for its pronounced depression on the melting point of the Si-Ga binary, as well as its potential for high doping amounts in silicon. The fabrication route consisted of heating a sealed 1:10 combination (atomic ratio) of Si and Ga up to 1200 °C, followed by slowly cooling it down to 700 °C, when Si is a crystalline solid, and Ga is a removable liquid. Both macroscopic crystals and embedded Si nanowires are obtained at the end of the process

In this work, we present the newly synthesized silicon nanowires via MFNN. Average nanowire diameter is of 125 nm. It is concluded that MFNN offers a cost-effective fabrication route for silicon nanowires.

III. Si CRYSTALS

While the bulk Si crystals are free and few millimetres in size, the nanowires are retrieve lying of the alumina template surface. The average nanowire diameter is a little smaller than the pores, being around 125 nm, for several microns long. Energy-dispersive spectroscopy (EDS) confirmed their Si composition.

For practical reasons, the bulk crystals were firstly investigated. The X-ray diffraction (XRD) measurement yielded the expected diamond crystalline structure, without extra phases. The doping level was probed by resistivity measurements, performed in a PPMS platform. While the electrical resistivity increases when cooling the temperature, it exhibits a maximum around 90 K, before decreasing until zero. Similar superconducting-like behaviour was observed through magnetic measurements, where magnetization drops around 6-7 K.

Doping-induced superconductivity in covalent semiconductors from the group IV elements has been recently experimentally observed and theoretically investigated [6]. Therefore, our results suggest that the Si crystals are highly doped by Ga, which was incorporated during the crystal growth.

ACKNOWLEDGMENT

The authors are grateful to the Center for Semiconductor Components and Nanotechnologies (CCSNano) at the University of Campinas (UNICAMP) for the experimental support. This work was partially funded by the Brazilian funding agency *Fundação de Amparo à Pesquisa do Estado de São Paulo* (FAPESP) (project #2017/10581-1).

REFERENCES

- [1] J. P. Colinge, M. H. Gao, A. Romano-Rodriguez, H. Maes, and C. Claeys, "Silicon-on-insulator'gate-all-around' device", International Technical Digest on Electron Devices, vol. 90, pp. 595-598, December 1990.
- [2] Pirota, K. R. et al. BR patent 10 2014 019794 0, issued 11 Aug. 2014.
- [3] P.F.S. Rosa, L.A.S. de Oliveira, C.B.R. de Jesus, K.O. Moura, C.Adriano, W. Iwamoto, T.M. Garitezi, E.Granado, M.E.Saleta, K.R.Pirota, and P.G.Pagliuso, "Exploring the effects of dimensionality on the magnetic properties of intermetallic nanowires", Solid State Communications, vol. 191, pp. 14-18, August 2014.
- [4] K. O. Moura, L. A. S. de Oliveira, P. F. S. Rosa, C. B. R. Jesus, M. E. Saleta, E. Granado, F. Béron, P. G. Pagliuso, and K. R. Pirota, "Dimensionality tuning of the electronic structure in Fe₃Ga₄ magnetic materials", Scientific Reports, vol 6, pp. 28364, June 2016.
- [5] K. O. Moura, K. R. Pirota, F. Béron, C. B. R. Jesus, P. F. S. Rosa, D. Tobia, P. G. Pagliuso, and O. F. de Lima, "Superconducting Properties in Arrays of Nanostructured β -Gallium", Scientific Reports, vol 7, pp. 15306, November 2017.
- [6] X. Blase, E. Bustarret, C. Chapelier, T. Klein, and C. Marcenat, "Superconducting group-IV semiconductors", Nature Materials, vol. 8, pp. 375-382, May 2009.

Ni Nanowire Alignment Optimization During Dielectrophoresis Through External Magnetic Field

1
2
3
4
5
6 Bruno Luís Segat Frare

*Institute of Physics "Gleb Wataghin"
Universidade Estadual de Campinas
Campinas, Brazil
brunofrare@bol.com.br*

7
8
9
10
11
12
13
14
15 Fanny Béron

*Institute of Physics "Gleb Wataghin"
Universidade Estadual de Campinas
Campinas, Brazil
fberon@ifi.unicamp.br*

16
17
18
19
20
21
22
23
24
25
26
27
28
29
30
31
32
33
34
35
36
37
38
39 Marcos V. Puydinger dos Santos

*Institute of Physics "Gleb Wataghin"
Universidade Estadual de Campinas
Campinas, Brazil
puyding@ifi.unicamp.br*

40
41
42
43
44
45
46
47
48
49
50
51
52
53
54
55
56
57
58
59
60
61
62
63
64
65 Kleber R. Pirota

*Institute of Physics "Gleb Wataghin"
Universidade Estadual de Campinas
Campinas, Brazil
krpirota@ifi.unicamp.br*

Abstract—This work reports on the optimization of Ni nanowire alignment between electrodes. The nanowires were manipulated through dielectrophoresis, while an external magnetic field was applied to help their precise alignment. Results show that the magnetic torque is preponderant at heights above 40 μm from the electrodes, while the electric one overcomes it only in a radius of about 250 nm around them.

Keywords—Dielectrophoresis, nanowires, magnetic field

I. INTRODUCTION

Nanowires offer a wide range of advantages for several types of applications, such as detectors and sensors. In particular, their high aspect ratio yields a high sensitivity to their environment, while they present a low power consumption due to their small dimensions. The dielectrophoresis (DEP) technique can be used to manipulate at low cost the conducting nanowires during their integration in the devices [1]. The application of an alternate electric field polarizes the nanowires that are suspended in a dielectric solution, which creates a force towards the electrodes. However, even if an electrical contact is obtained, the DEP technique does not yield a precise alignment of the manipulated nanostructures, which may be crucial for several nanowire-based devices.

In this work, we report on the consequences of adding an external magnetic field during the DEP procedure of magnetic nanowires [2]. Due to their low fabrication cost when electrodeposited and their good electrical conduction, the alignment experiments were conducted using Ni nanowires.

II. METHODOLOGY

In order to maintain a low-cost technique, the magnetic field was applied using two rare earth magnets, symmetrically localised around the substrate. The magnetic field intensity (up to 80 kA/m) was varied by adjusting their distance. The DEP was performed by applying a peak-to-peak voltage of 3 V, at a 100 kHz frequency, as previously calibrated for 35 nm diameter and 4 μm long Ni nanowires and 2 μm wide electrode gap [3]. Statistical distributions were obtained by repeating at least three times the procedure for each conditions. The angle between each deposited nanowire and the electrodes was extracted from scanning electronic microscope images.

We combined the experimental procedure with calculated magnetic torque, using Keshoju et al. model [4], and simulated electric torque, through the use of COMSOL software.

III. NANOWIRE ALIGNMENT

In order to understand the consequences of each torque, magnetic and electric, acting of the nanowire rotation, we conducted the deposition under four distinct conditions: without any field, with only one applied field, and finally when applying both fields.

Taken alone, the DEP force slightly rotates the nanowires. Its application causes to pass from an almost random angle distribution to a wide normal one, with a standard deviation of 39°. On the other side, even small magnetic field (below 10 kA/m) achieves to align the nanowires, but without yielding a normal distribution. The percentage of nanowires positioned at angles between 0° and 10° quickly increases until stabilizing around 60% for magnetic field between 30 and 60 kA/m. When combining the effects of both the electric and magnetic field, we observed that the DEP slightly improves the nanowire alignment for magnetic field below 60 kA/m. However, the most noticeable result is the removal of a decay in the aligned nanowire percentage at high field (80 kA/m), which was present under the application of solely a magnetic field. This decay was attributed to nanowires that ended up magnetized in off-axis directions by the strong magnetic field. Our results suggests that the DEP force was sufficient to rectify the alignment of these nanowires.

Finally, the comparison of theoretical and simulated applied torques allowed us to understand in which region which torque was preponderantly acting. The magnetic torque was estimated to be around 10^{-17} to 10^{-16} N·m, depending of the magnetic field intensity. It is important to point out that these values are several orders of magnitude higher than the torque that would be created by the thermal energy (approximately 10^{-21} N·m). On the other side, the electric torque quickly decreases when moving away from the electrodes. Very near them (in a 250 nm radius), it overcomes the magnetic torque from a factor of 10, thus creating a small regions near the electrodes where the DEP torque is preponderant on the magnetic one.

In conclusion, the application of a small magnetic field greatly improves the percentage of aligned nanowires while performing dielectrophoresis. It is mainly due to the strong

torque exerted by the magnetic field on the nanowires in solution during most of the deposition time. However, the DEP torque is the most intense very near the electrodes. This may help to rectify the alignment of nanowires for which their magnetization was switched by intense magnetic field.

ACKNOWLEDGMENT

The authors are grateful to The authors are grateful to the staff of the Institute of Physics "Gleb Wataghin" (IFGW) and the Center for Semiconductor Components and Nanotechnologies (CCSNano) at the University of Campinas (UNICAMP) for the experimental support. This work was partially funded by the Brazilian funding agency *Fundação de Amparo à Pesquisa do Estado de São Paulo* (FAPESP) (project #2017/10581-1).

REFERENCES

- [1] B. C. Gierhart, D. G. Howitt, S. J. Chen, R. L. Smith, and S. D. Collins, "Frequency Dependence of Gold Nanoparticle Superassembly by Dielectrophoresis", *Langmuir*, vol. 23, pp. 12450, October 2007.
- [2] B. L. S. Frare, M. V. Puydinger dos Santos, F. Béron, "Alignment Optimization of the Dielectrophoresis of Ni Nanowires Through External Magnetic Field", *IEEE Magnetics Letters*, vol. 10, pp. 1-5, December 2019.
- [3] M. V. Puydinger dos Santos, L. P. B. Lima, R. A. Mayer, F. Béron, K. R. Pirota, and J. A. Diniz, "Dielectrophoretic manipulation of individual nickel nanowires for electrical transport measurements," *Journal of Vacuum Science Technology B*, vol. 33, pp. 031804, 2015.
- [4] K. Keshoju, H. Xing, and L. Sun, "Magnetic field driven nanowire rotation in suspension, *Applied Physics Letters*, vol. 91, pp. 123114, 2007.

Light-emission from gold nanoclusters and their ensembles

Jan Valenta¹, Ondrej Pavelka¹, Anna Fucikova¹, Goutam Pramanik² and Petr Cigler²

¹ *Charles University, Faculty of Mathematics and Physics, Prague 2, Czechia*

² *Institute of Organic Chemistry and Biochemistry, Czech Academy of Sciences, Prague 6, Czechia*

Gold (and other metals) particles are known for their interesting localized surface plasmon resonances (LSPR). However, when the size of particle is reduced below about two nanometers, LSPR disappears and such cluster start to behave like a molecule. For practical applications a cluster must be well passivated using various organic molecules – most often bonded to gold atoms through a thiol group. We fabricate and investigate gold nanoclusters of about 24 atoms with various passivation showing efficient near-infrared photoluminescence (NIR PL) with external quantum yield up to about 20%. Our complex optical investigation indicates that the exceptionally broad PL band (FWHM up to 0.48 eV) with slow decay kinetics (a few microseconds) is due to metal-to-ligand charge transfer states. Finally, we fabricate and investigate dimers of gold nanoclusters linked using DNA or other molecular chains.

1 2 3 4 5 6 7 8 9 10 11 12 13 14 15 16 17 18 19 20 21 22 23 24 25 26 27 28 29 30 31 32 33 34 35 36 37 38 39 40 41 42 43 44 45 46 47 48 49 50 51 52 53 54 55 56 57 58 59 60 61 62 63 64 65 Donor and Acceptor Pair Luminescence in Colloidal Silicon Quantum Dots

Minoru Fujii and Hiroshi Sugimoto

Graduate School of Engineering, Kobe University, Rokkodai, Nada, Kobe 657-8501, Japan
E-mail: fujii@eedept.kobe-u.ac.jp, sugimoto@eedept.kobe-u.ac.jp

We studied the luminescence property of a methanol solution of almost monodispersed silicon (Si) quantum dots (QDs) that are heavily doped with boron and phosphorus. A very narrow size distribution enabled us to extract doping-induced phenomena clearly. The degree of doping-induced shrinkage of the optical band gap was studied in a wide size range (3 nm to 10 nm in diameter). The lowest luminescence energy achieved by controlling the QD size and the doping concentration was ~ 0.9 eV. Comparison of the luminescence energy with theoretical calculations in a literature allowed us to estimate the number of active donor–acceptor pairs in a QD. We show that doping small number of boron and phosphorus atoms is an effective route to control the luminescence energy of Si-QDs beyond the range of the quantum size effect. In codoped Si-QDs, majority of doped impurities are accumulated on or near the surface and electrically inactive. These inactive surface dopants induce negative surface charges, and make Si-QDs dispersible in polar solvents. Because of the organic-ligand-free bare surface, codoped Si-QDs can exchange carriers with molecules in a solution efficiently. We discuss various charge transfer induced phenomena including photocatalytic activity of codoped Si-QDs.

A Silicon (Si) quantum dot (QDs) is an environmentally friendly nano-functional material potentially suitable for bio-photonics applications. Recently, we have developed a new type of all-inorganic Si QDs that can be dispersed in alcohol and water almost perfectly without organic ligands and exhibit size-dependent photoluminescence (PL) in the near-infrared range in water [1-2]. The unique property of the QDs arises from the unique structure. The QD has a core-shell structure; the core is heavily boron (B) and phosphorus (P) codoped crystalline Si and the shell is an amorphous layer composed of B, Si and P [3]. The shell induces negative potential on the surface and prevents agglomeration of Si QDs in polar solvents. To the ligand-free surface of codoped Si QDs, molecules in a solution can access easily, and thus a variety of charge-transfer-induced processes such as a photocatalytic effect and chemical doping are expected [4-5]. Furthermore, doping of B and P in a crystalline Si core modifies the luminescence property. In this presentation, we will discuss the relationship between the doping concentration and the PL

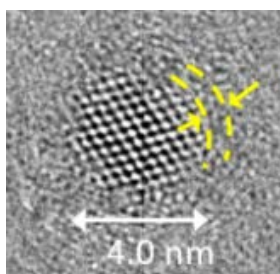


Fig.1 TEM image of a B and P codoped Si QD.

catalytic effect and chemical doping are expected [4-5]. Furthermore, doping of B and P in a crystalline Si core modifies the luminescence property. In this presentation, we will discuss the relationship between the doping concentration and the PL

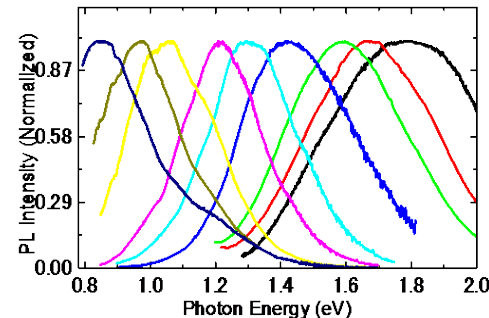


Fig.2 PL spectra of B and P codoped Si QDs in methanol.

property of Si QDs.

Figure 1 shows a typical TEM image of a B and P codoped Si QD [3]. The lattice fringe corresponds to {111} planes of crystalline Si. On the surface of the crystalline core, an amorphous shell is formed. The shell is composed of Si, B and P, the concentration of B and P being in the range from a few % to 10 at.%.

Figure 2 shows PL spectra of codoped Si QDs dispersed in methanol [6]. The PL energy can be controlled in a wide energy range and the controllable range extends below the bulk Si band gap (1.12 eV). This suggests that the PL arises from donor-acceptor pairs in Si QDs. Figure 3 shows the relation between the PL peak energy and the diameter of Si QDs [7]. The data of undoped Si QDs [8] and codoped Si QDs with different doping concentration are shown. The data of undoped Si QDs is well-explained by the effective mass approximation. The PL energy of codoped Si QDs is lower than that

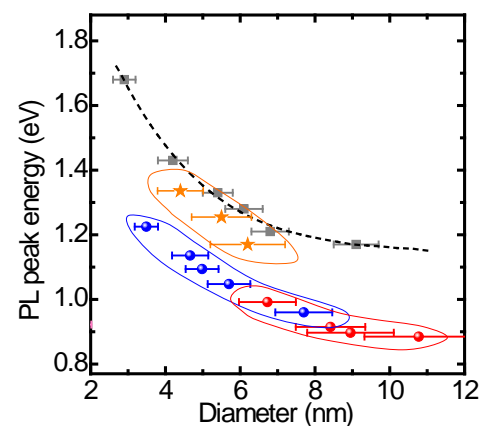


Fig.3 Relation between PL peak energy and Si QD diameter. The data of undoped Si QDs [8] and codoped Si QDs with different doping concentration are shown.

of undoped Si QDs with the same size. Furthermore, the PL energy depends strongly on the doping concentration; heavier doping results in lower energy shift of the PL energy. By comparing the PL energy with those obtained by theoretical calculations [9], we estimate the number of active B and P pairs in Si QDs. The comparison reveals that two B and P pairs are involved in the PL of lower concentration doped samples, while 5-10 active B and P pairs are involved in higher concentration doped samples.

References

- [1] M. Fujii, H. Sugimoto, and S. Kano, *Chem. Commun.*, Vol. 54, 4375 (2018).
- [2] M. Fujii, H. Sugimoto, and K. Imakita, *Nanotechnology*, Vol. 27, 262001 (2016).
- [3] H. Sugimoto, et al., *Nanoscale*, Vol. 10, 7357 (2018).
- [4] T. Kojima, H. Sugimoto, and M. Fujii, *J. Phys. Chem. C*, Vol. 122, 1874 (2018).
- [5] K. Inoue, T. Kojima, H. Sugimoto, and M. Fujii, *J. Phys. Chem. C*, Vol. 123, 1512. (2019).
- [6] H. Sugimoto, et al., *J. Phys. Chem. C*, Vol. 117, 11850 (2013).
- [7] H. Sugimoto, et al., *Nano Letters*, Vol. 18, 7282 (2018).
- [8] Y. Yu, et al., *J. Phys. Chem. C*, Vol. 121, 23240 (2017).
- [9] C. Delerue, *Phys. Rev. B*, Vol. 98, 045434 (2018).

Nanomechanical Sensing with 2D Materials

Peter G. Steeneken

Dept. of Precision and Microsystems Engineering &

Kavli Institute of Nanoscience

Delft University of Technology

Mekelweg 2, 2628 CD Delft, the Netherlands

p.g.steeneken@tudelft.nl

Since the discovery of graphene a large range of layered 2D materials have been studied. The two-dimensional nature of these compounds allows them to be made extremely thin, which opens new opportunities in the field of nanomechanical systems. With the field of MEMS becoming mature, 2D materials provide a route towards improved performance with 2D nanomechanical systems (2D NEMS) by reducing layer thicknesses down to the single atom limit. These ultrathin layers also open up completely novel device concepts.

In this work, recent achievements on the route from MEMS to 2D NEMS will be discussed. After introducing fabrication and characterization methods for studying the static¹ and dynamic² motion of suspended ultrathin membranes, several concepts for sensing gas pressure using atomically thin membranes are demonstrated, including static, resonant and Pirani pressure sensing³⁻⁵. Challenges to meet requirements on yield, sensitivity and lifetime are discussed and advances in optical⁶ and electronic calibration and readout methods using commercial low-cost electronics are discussed, aiming towards commercially viable graphene pressure sensor products as part of the Graphene Flagship sensors workpackage. Gas sensing concepts for analyzing gas composition based on permeation of gases through graphene nanopores are discussed and the feasibility of graphene gas pumps⁷ is shown.

Interestingly, optothermomechanical analysis of the dynamics of the suspended layers also provides a useful method to analyze the mechanical⁸ and thermal^{9,10} properties of the materials. When driving the membranes to large amplitudes, their dynamics becomes nonlinear already at amplitudes of a few nanometers. The combination of nonlinear dynamics and thermal motion of the membranes leads to stochastic switching¹¹ and parametric resonance¹².

Finally, a recent method for creating ultrathin membranes of complex oxides, like SrTiO₃ and SrRuO₄ is presented. Characterization of the resonances in membranes of these complex oxides¹³ enables the study of the strong electric and magnetic degrees of freedom in these materials with their mechanical properties. It can also lead to novel device architectures that can complement those of 2D materials.

Acknowledgements:

The presentation is an overview of contributions from the authors of references 1-13 below, who are gratefully acknowledged. The research received funding from the European Union's Horizon 2020 research and innovation programme under Grant Agreement No.785219 Graphene Flagship.

References:

1. Cartamil-Bueno, S. J. *et al.* Colorimetry technique for scalable characterization of suspended graphene. *Nano letters* **16**, 6792–6796 (2016).
2. Davidovikj, D. *et al.* Visualizing the motion of graphene nanodrums. *Nano letters* **16**, 2768–2773 (2016).
3. Davidovikj, D., Scheepers, P. H., van der Zant, H. S. & Steeneken, P. G. Static capacitive pressure sensing using a single graphene drum. *arXiv preprint arXiv:1708.05952* (2017).
4. Dolleman, R. J., Davidovikj, D., Cartamil-Bueno, S. J., van der Zant, H. S. & Steeneken, P. G. Graphene squeeze-film pressure sensors. *Nano letters* **16**, 568–571 (2015).
5. Romijn, J. *et al.* A Miniaturized Low Power Pirani Pressure Sensor Based on Suspended Graphene. in *2018 IEEE 13th Annual International Conference on Nano/Micro Engineered and Molecular Systems (NEMS)* 11–14 (2018). doi:10.1109/NEMS.2018.8556902
6. Dolleman, R. J., Davidovikj, D., van der Zant, H. S. J. & Steeneken, P. G. Amplitude calibration of 2D mechanical resonators by nonlinear optical transduction. *Appl. Phys. Lett.* **111**, 253104 (2017).
7. Davidovikj, D., Bouwmeester, D., Zant, H. S. J. van der & Steeneken, P. G. Graphene gas pumps. *2D Mater.* **5**, 031009 (2018).
8. Davidovikj, D. *et al.* Young's modulus of 2D materials extracted from their nonlinear dynamic response. *arXiv preprint arXiv:1704.05433* (2017).
9. Dolleman, R. J. *et al.* Optomechanics for thermal characterization of suspended graphene. *arXiv preprint arXiv:1702.06730* (2017).
10. Dolleman, R. J., Lloyd, D., Bunch, J. S., van der Zant, H. S. J. & Steeneken, P. G. Transient thermal characterization of suspended monolayer MoS₂. *arXiv:1806.10769 [cond-mat]* (2018).
11. High-Frequency Stochastic Switching of Graphene Resonators Near Room Temperature | Nano Letters.
12. Dolleman, R. J. *et al.* Opto-thermally excited multimode parametric resonance in graphene membranes. *Scientific Reports* **8**, 9366 (2018).
13. Davidovikj, D. *et al.* Ultrathin complex oxide nanomechanical resonators. *arXiv:1905.00056 [cond-mat, physics:physics]* (2019).

Photodetectors, Transistors and Memristors based on MoS₂/semiconductor Heterostructures

Max C. Lemme

RWTH Aachen University, Chair of Electronic Devices, Otto-Blumenthal-Str. 2, 52074 Aachen, Germany

AMO GmbH, Advanced Microelectronic Center Aachen (AMICA), Otto-Blumenthal-Str. 25, 52074 Aachen, Germany

Transition metal dichalcogenides (TMDs) are among a large family of two-dimensional (2D) layered materials. They can generically be described by the formula MX₂, where M is a transition metal such as molybdenum (Mo), tungsten (W), niobium (Nb) etc., and X is a chalcogen element like sulfur (S), selenium (Se), or tellurium (Te). “Bulk” TMDs are formed by vertically stacking of 2D-layers. The layers are connected via van der Waals forces. Molybdenum disulfide (MoS₂) is a semiconducting TMD material with a band gap ranging from 1.3 eV in bulk to 1.88 eV as a monolayer. The material is a potential candidate for applications in nanoelectronics, optoelectronics and neuromorphic computing [1]–[4]. In this talk, I will discuss recent results of electronic and optoelectronic devices based on heterostructures of MoS₂ and conventional three-dimensional semiconductors. I will present the principles of scalable growth through thermal conversion of metals (Fig 1., [5]). I will then discuss photodetectors based on MoS₂/silicon [6] and MoS₂/amorphous silicon, which show responsivity in the infrared regime (Fig. 2, [7]). Then, electronic devices from conventional field effect transistors to memristors based on MoS₂ will be shown (Fig. 3). The latter operate in vertical direction based on the tuning of energy barriers at MoS₂/semiconductor Schottky junctions through mobile ions [8], [9].

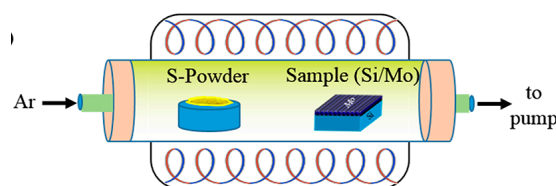


Fig. 1: Schematic of a setup for thermally assisted conversion of transition metals into 2D materials.

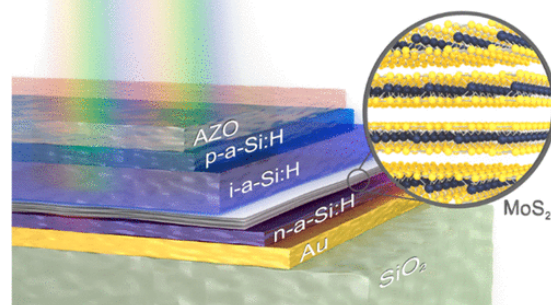


Fig. 2: Schematic of a MoS₂/a-Si photodetector.

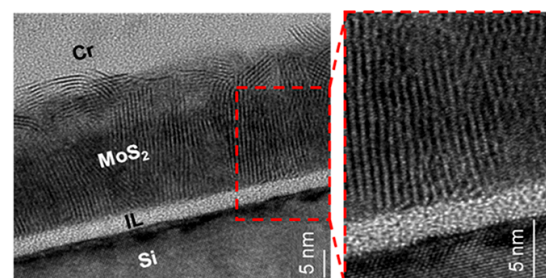


Fig. 3: TEM image of vertically aligned MoS₂ films.

References

- [1] K. F. Mak, C. Lee, J. Hone, J. Shan, and T. F. Heinz, “Atomically Thin MoS₂: A New Direct-Gap Semiconductor,” *Phys. Rev. Lett.*, vol. 105, no. 13, p. 136805, Sep. 2010.
- [2] B. Radisavljevic and A. Kis, “Mobility engineering and a metal-insulator transition in monolayer MoS₂,” *Nat. Mater.*, vol. 12, no. 9, pp. 815–820, Sep. 2013.

- [3] A. Bablich, S. Kataria, and M. C. Lemme, “Graphene and Two-Dimensional Materials for Optoelectronic Applications,” *Electronics*, vol. 5, no. 1, p. 13, Mar. 2016.
- [4] V. K. Sangwan *et al.*, “Multi-terminal memtransistors from polycrystalline monolayer molybdenum disulfide,” *Nature*, vol. 554, no. 7693, pp. 500–504, Feb. 2018.
- [5] S. Kataria *et al.*, “Growth-Induced Strain in Chemical Vapor Deposited Monolayer MoS₂: Experimental and Theoretical Investigation,” *Adv. Mater. Interfaces*, vol. 4, no. 17, p. 1700031, Sep. 2017.
- [6] C. Yim *et al.*, “Heterojunction Hybrid Devices from Vapor Phase Grown MoS₂,” *Sci. Rep.*, vol. 4, Jun. 2014.
- [7] A. Bablich *et al.*, “Few-Layer MoS₂/a-Si:H Heterojunction Pin-Photodiodes for Extended Infrared Detection,” *ACS Photonics*, vol. 6, no. 6, pp. 1372–1378, Jun. 2019.
- [8] M. Belete *et al.*, “Dielectric Properties and Ion Transport in Layered MoS₂ Grown by Vapor-Phase Sulfurization for Potential Applications in Nanoelectronics,” *ACS Appl. Nano Mater.*, vol. 1, no. 11, pp. 6197–6204, Nov. 2018.
- [9] M. Belete, O. Engstrom, S. Vaziri, S. Kataria, and M. C. Lemme, “Electron Transport across Vertical Silicon / Molybdenum Disulfide (MoS₂) / Graphene Heterostructures,” *submitted*.

1
2 Wood and cellulose nanotechnology for photonics and other functional materials
3
4

5 Lars Berglund
6 KTH Royal Inst of Technology
7 Dept of Fiber and Polymer Technology
8 Wallenberg Wood Sci Ctr
9 SE-100 44 Stockholm, Sweden
10
11 blund@kth.se
12

13 Bottom-up nanotechnology is of great technical importance and offers exceptional nanoscale
14 control. For larger load-bearing structures, nanostructured cellulosic materials including wood
15 are of interest for several reasons: renewable resource origin, mechanical properties, low
16 cost, high specific surface area, chemically active surfaces and the possibility to add functional
17 components to form nanostructured polymeric or inorganic/organic hybrid composites. In
18 addition, the native hierarchical structures of wood or wood fibers are anisotropic and
19 combine pore channels designed for liquid flow at the scale of 20-100 micrometers, with cell
20 wall nanoporosity at the scale of nanometers. The structures can also be carbonized and even
21 used as templates for infiltration by ceramic material precursors, while the cell wall
22 nanostructure is preserved. Applications include magnetic materials, composites for energy
23 storage, catalysis and filtration.
24

25 Recent work on optically transparent cellulosics includes transparent wood. Light
26 absorbing components in the structure are removed chemically, and pore space is filled by a
27 polymer with a refractive index matching cellulose. The structure shows anisotropic light
28 scattering, and scattering mechanisms are important for the functionalization potential.
29 Transparent wood has been used in solar cells, electrochromic windows and even as a heat
30 storage materials, where the function is provided by a phase change component distributed
31 at nanoscale. From a nanomaterials viewpoint, the distribution of silicon nanoparticles was
32 successfully controlled so that a luminescent material was formed. In addition, lasing was
33 demonstrated in a transparent wood composite functionalized by organic dye molecules.
34 Interestingly, the materials represents an anisotropic structure which is neither ordered nor
35 random, a feature which has not been widely analyzed.
36

37 Biological structures are of interest as templates for functional materials, where the
38 challenges of hierarchical structuring have already been met by the biological organism, using
39 sophisticated self-assembly. Multidisciplinary efforts at interfaces between disciplines are
40 likely to lead to new and interesting concepts for functional materials. Many materials
41 synthesis steps can be carried out in sequence, to build complex multifunctional composites
42 with new functionalities and/or expanded property range.
43
44
45
46
47
48
49
50
51
52
53
54
55
56
57
58
59
60
61
62
63
64
65

Graphene-Based Anisotropic Conductive Adhesives

1
2
3
4
5
6
7
8
9
10
11
12
13
14
15
16
17
18
19
20
21
22
23
24
25
26
27
28
29
30
31
32
33
34
35
36
37
38
39
40
41
42
43
44
45
46
47
48
49
50
51
52
53
54
55
56
57
58
59
60
61
62
63
64
65
Marcus Gårdin
Research Institutes of Sweden (RISE)
Stockholm, Sweden
marcus.gardin@ri.se

Mats Sandberg
Research Institutes of Sweden (RISE)
Norrköping, Sweden
mats.sandberg@ri.se

Astrid Armgård
Research Institutes of Sweden (RISE)
Norrköping, Sweden
astrid.armgarth@ri.se

Olof Öberg
Research Institutes of Sweden (RISE)
Stockholm, Sweden
olof.oberg@ri.se

Mats Ahmadi Götelid
Royal Institute of Technology (KTH)
Stockholm, Sweden
gothelid@kth.se

Qin Wang
Research Institutes of Sweden (RISE)
Stockholm, Sweden
qin.wang@ri.se

Cancer is one of the most severe diseases, causing 9.6 million deaths worldwide in 2018. The annual cost of cancer treatment was in 2010 estimated to be approximately \$US 1.16 trillion, according to the World Health Organization (WHO) [1]. A cancer treatment method commonly used is radiation therapy where a patient is irradiated by an x-ray beam focused on a cancer active area. If the treatment is successful, the DNA of the cancer cells is severely damaged and cannot divide nor survive.

When a patient is diagnosed with cancer, a treatment planning system (TPS) is made where the dosage of ionizing radiation is calculated. The TPS undergoes a quality assurance (QA) by comparing the delivered and calculated radiation dosage. This can either be done through the patient, in-vivo, or by using a phantom consisting of radiation diodes, in-vitro. The radiation sensors on the phantom used in the QA are connected currently by metallic connections with a wire bonding manually, which is not desirable for industrial scale manufacture. Thus, a flip chip bonding (FCB) approach for diodes connected directly onto a designed substrate through conductive bumps would be appreciated. As known, the flip-chip packaging technique, commonly applied in electronic fabrication, utilizes metal bumps, such as Au, AuSn, SnPb or epoxy based anisotropic conducting adhesives (ACA) with embedded metal particles for connecting the components on their substrate with corresponding contact pads [2-3].

However, when irradiating a heavy element such as the metal bumps in the connections of the sensors with a high energy beam, a secondary electron scattering causes an unwanted photocurrent that distort the QA of the TPS. A need to replace the heavy metal connections with a low weight conducting material is therefore necessary to reduce the unwanted photocurrent present in the QA.

This work considers the possibility utilizing in house developed lighter graphene-based ACA to FCB the radiation diodes on its substrate. Although the graphene-based ACA has lower conductivity owing its contact resistance of several orders of magnitudes larger compared to the metal-based adhesives [4], it was found still acceptable in our application due to sensing currents having a low order of magnitude in operation.

A test structure illustrated in the inset of figure 1 was made by placing a diode with two Al contact pads FCB over their corresponding tracks made of copper on the substrate. Connecting the contact pads of the diode with the copper tracks is the ACA with fillers of either metallic- or graphene-based fillers.

Then, current-voltage (I-V) measurements of the diodes FCB by graphene-based ACA, metal-based ACA and the

reference diode without using ACA were conducted. Results from the I-V measurements, found in figure 1, indicate that an exchange of fillers from metallic- to graphene-based fillers in the ACA conserves the I-V characteristics of the diode in a general sense.

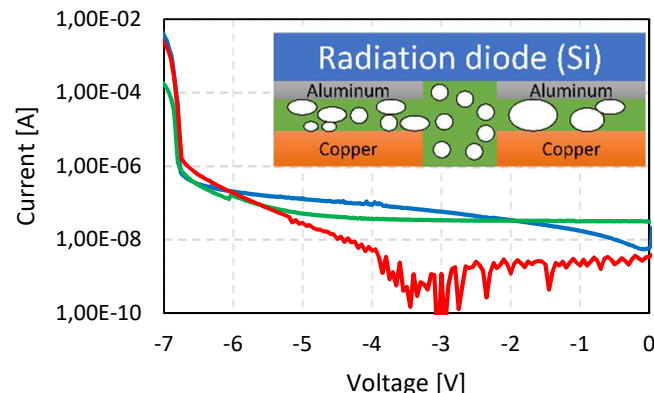


Figure 1: I-V measurements in reverse bias of the graphene-based ACA (blue), metal-based ACA (green) and the diode alone (red). The I-V measurement structure is illustrated in the inset.

This work also discusses and compares the thermal effect of the contact resistance of the graphene-based fillers under different temperatures. Their mechanical stability in various shearing test scenarios were also verified. Interpreted from the results a conclusion was made that our graphene-based ACA demonstrated promising as FCB bumps to connect the radiation diodes on the substrate.

ACKNOWLEDGMENT

The authors would like to thank Sweden's innovation agency (Vinnova) for financial support through Graphene Strategic Innovations Program (SIO Grafen) under Grant Agreements 2018-01491. Further thanks to Dr. Ingemar Petermann from RISE for his help on measurement assistance and Kjell Lundgren from ScandiDos AB for discussions.

REFERENCES

- [1] World Health Organisation (2018). *Latest global cancer data: Cancer burden rises to 18.1 million new cases and 9.6 million cancer deaths in 2018.*
- [2] Y. Wei and E. Sancaktar, "Dependence of electrical conduction on the film thickness of conductive adhesives: Modeling, computer simulation, and experiment," *Journal of Adhesion Science and Technology*, vol. 10, no. 11, pp. 1199-2219, 1996.
- [3] J. Jagt, "Reliability of electrically conductive adhesive joints for surface mount applications: a summary of the state of the art," *IEEE Transactions on Components, Packaging, and Manufacturing Technology: Part A*, vol. 21, no. 2, pp. 215-225, 1998.
- [4] G. Wu, K. Kou, N. Li, H. Shi and M. Chao, "Electrically conductive adhesive based on bismaleimide - triazine resin filled with microcoiled carbon fibers," *Applied Polymer Science*, vol. 128, no. 2, pp. 1164-1169, 2012.

CVD graphene-based resistive amphetamine sensor

1 2 3 4 5 6 7 8 9 10 11 12 13 14 15 16 17 18 19 20 21 22 23 24 25 26 27 28 29 30 31 32 33 34 35 36 37 38 39 40 41 42 43 44 45 46 47 48 49 50 51 52 53 54 55 56 57 58 59 60 61 62 63 64 65 1st ÜlleLinda Talts

Research Institutes of Sweden (RISE)
Stockholm, Sweden
ulle-linda.talts@ri.se

2nd Arne Quellmalz

Micro and Nanosystems
KTH Royal Institute of Technology
Stockholm, Sweden
arneq@kth.se

3rd Olof Öberg

Research Institutes of Sweden (RISE)
Stockholm, Sweden
olof.oberg@ri.se

4th Simon Dunne

The Swedish National Forensic Centre
Linköping, Sweden
simon.dunne@polisen.se

5th Louise Elmlund

The Swedish National Forensic Centre
Linköping, Sweden
louise.elmlund@polisen.se

6th Qin Wang

Research Institutes of Sweden (RISE)
Stockholm, Sweden
qin.wang@ri.se

Nanotechnology-based sensors enable highly sensitive and specific detection at a low cost. Due to its high surface-to-volume ratio and exotic electrical properties, graphene-based transduction mechanisms have been the focus of numerous studies. This approach has been particularly interesting for developing chemical sensors that allow detection of low concentration substances. Among multiple areas that could greatly benefit from advancements in this field is forensic science. Sensors based on epitaxial graphene on SiC have been proposed for on-site analysis of seized drugs [1] but a more cost-effective alternative is required for commercial use [2]. Here, we investigate the suitability of chemical vapour deposited (CVD) graphene for drug detection.

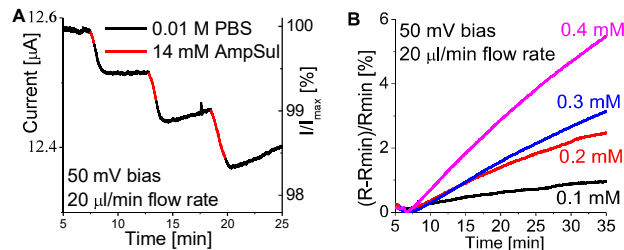
This study provides a proof-of-concept for resistive, non-specific sensors for detecting a commonly abused neurostimulant like amphetamine. Most often, the drug is seized in the format of amphetamine sulphate non-volatile salt that readily dissolves in water. This has been utilized in our previous work where pre-selectivity method in aqueous medium is introduced [1]. For detection, the aromatic and amine functionality of amphetamine molecules can be exploited. The aromatic functionality has an inherent affinity to graphene due to π - π electron stacking [3] while the amine functional group acts as n-type dopant due to the electron donating nature of nitrogen atoms [4]. These properties give a theoretical basis for electrical signal generation upon adsorption of amphetamine molecules on graphene.

The sensors investigated here detect changes in graphene resistance when exposed to amphetamine sulphate solution in 0.01 M phosphate buffered saline (PBS). The sensors were fabricated by deposition of Au electrodes on top of an oxidized silicon wafer. Subsequently CVD graphene (Graphenea Inc.) was transferred to the substrate using a wet transfer method [5]. For characterization, a fluidic chamber was mounted on top of the graphene and the electrodes were connected to an acquisition unit.

Exposure to 0.1-14 mM concentrations of amphetamine sulphate in 0.01 M PBS showed distinctive response through an increase in device resistance (Fig. 1). Repeated resistance change can be seen for increasing analyte exposure period with conductance recovery in buffer flow between the intervals (Fig. 1A). Furthermore, the increase in resistance becomes more rapid with increasing analyte concentration (Fig. 1B). It can be postulated that the inherently p-type doped CVD graphene on SiO_2 undergoes electron-hole recombination when electron donating amine groups interact with the surface. As charge carrier mobility in graphene remains relatively constant under heavy doping, we infer that

the response results from a reduction of majority carriers which increases the resistance [4]. Nonselective interaction with the analyte of interest can be detected by changes in the resistive properties of graphene.

Fig. 1. Sensor response to different concentrations of amphetamine sulphate in 0.01 M PBS at 50mV bias and 20 $\mu\text{l}/\text{min}$ flowrate A) Cyclic current response to 14 mM concentration. B) Relative resistance change to 0.1-0.4 mM.



This first study on recording amphetamine sulphate adsorption kinetics through resistive chemical graphene sensors hints at the future potential of these devices for qualitative forensic analysis. The analysis of the adsorption kinetics compared to the resistance increase allows quantitative detection of amphetamines which might be utilized in low-cost sensors. However, for practical application further studies of the selectivity and sensitivity must be conducted.

ACKNOWLEDGMENT

The authors would like to thank Sweden's innovation agency (Vinnova) for financial support through Graphene Strategic Innovations Program (SIO Grafen) under Grant Agreement 2018-01679. Further thanks to Dr. Per Björk, Dr. Ingemar Petermann from RISE and Prof. Mats Ahmadi Götelid from KTH for their help on measurement assistance and discussions.

REFERENCES

- [1] M. Karlsson *et al.*, 'Chemical sensors generated on wafer-scale epitaxial graphene for application to front-line drug detection', *Sensors*, vol. 19, no. 10:2214, pp 1-14 Jan. 2019.
- [2] K. S. Novoselov, V. I. Fal'ko, L. Colombo, P. R. Gellert, M. G. Schwab, and K. Kim, 'A roadmap for graphene', *Nature*, vol. 490, no. 7419, pp. 192-200, Oct. 2012.
- [3] H. Hafizi, A. Najafi Chermahini, G. Mohammadnezhad, and A. Teimouri, 'A theoretical study on the interaction of amphetamine and single-walled carbon nanotubes', *Appl. Surf. Sci.*, vol. 329, pp. 87-93, Feb. 2015.
- [4] F. Schedin *et al.*, 'Detection of individual gas molecules adsorbed on graphene', *Nat. Mater.*, vol. 6, no. 9, pp. 652-655, Sep. 2007.
- [5] A. Quellmalz *et al.*, 'Influence of humidity on contact resistance in graphene devices', *ACS Appl. Mater. Interfaces*, vol. 10, no. 48, pp. 41738-41746, Dec. 2018.

NMDC 2019 1570604978

Graphene In-Plane double gate transistor for the RF application

1
2
3
4
5
6 Nazir Hossain, Member IEEE
7 Department of Electrical Engineering
8 University of Massachusetts Lowell
9 Lowell, MA, USA
10 abuhenamuhammad_nazirhossain@stu
11 dent.uml.edu

1
2
3
4
5
6 JF Millithaler, Member IEEE
7 Department of Electrical Engineering
8 University of Massachusetts Lowell
9 Lowell, MA, USA
10 JeanFrancois_Millithaler@uml.edu

1
2
3
4
5
6 Martin Margala, Member IEEE
7 Department of Electrical Engineering
8 University of Massachusetts Lowell
9 Lowell, MA, USA
10 Martin_margala@uml.edu

13 **Abstract**— In this study, we designed and fabricated in plane
14 transistor based on graphene material system in which the
15 channel current modulated by lateral electric field from two
16 gates separated by high k dielectric Al_2O_3 and HfO_2 . We
17 achieved record low contact resistance at the source and drain
18 $\sim 75\Omega\cdot\mu\text{m}$ and strong electric field controlled in lateral direction
19 by using metal stack of Ti/Au 25/80nm. The graphene based
20 planar devices structure allows lowering the gate capacitance
21 reduction to ~ 0.5 to 0.9aF due to the fact that the low carrier
22 coupling between channel at the gate carrier presence along
23 with thinner sheet of conducting layer which is about ~ 0.3
24 0.8nm for the single layer graphene.

INTRODUCTION

25 The biggest challenge for the next generation electronics
26 devices are to operate very high frequency with higher density
27 of transistor. The higher density of transistor and integration
28 of digital, power and front-end module not only generate
29 parasitic elements but also carried out significant amount of
30 power dissipation in the form of capacitive load [1]. Scaling
31 down the transistor change the paradigm shift of carrier
32 transport inside the transistor channel path from diffusive to
33 ballistic regime due to the fact that the reduction of scattering
34 length allow carrier to follow longer path without losing any
35 emerging in the form of resistance [3].

36 Higher current density is the fundamental requirement of
37 device to drive high frequency of operation. Scale down the
38 transistor size allow generating more current but requires
39 higher width to trade-off the total current. To improve the
40 device performance, it is imperative to alternate the channel
41 material which permit higher mobility of carrier transport to
42 generate proportionate drive current with significant current
43 gain [4].

44 In this paper, we used state of art graphene material to
45 fabricate our device structure which is called double gated in
46 plane RF technology. The unique property of this transistor
47 structure is that it requires only ohmic contact and
48 insignificant carrier coupling between source to the gate.

DEVICE FABRICATION

49 In this project we used, commercially available graphene
50 wafer from graphene supermarket. These graphene wafers
51 have precise thickness for different layers and the quality of
52 graphene film is measured by Raman Spectroscopy. The
53 graphene coverage of this product is about 98% which is
54 verified by energy spectral density characterization. Although
55 the graphene film layers are continuous, but we observe minor
56 holes and organic residues during scanning electron
57 spectroscopy. In Raman spectroscopy investigation we found
58 that each graphene film is predominantly single layer which is

59 about 95% along with less than 5% bilayers. Graphene layers
60 are polycrystalline in nature which consists of grains with
61 different crystallographic orientation. The graphene layer we
62 used in this experiment are randomly oriented with respect to
63 each other and the measured sheet Resistance roughly 200-
64 600 Ω/sq that we found from Vander paw techniques.

65 After characterizing the surface morphology of the
66 graphene material properties, the fabrication process started
67 by doing oxygen plasma etching about 5s at very low power.
68 A 400nm of PMMA 495/950K photoresist has been coated
69 immediate after dried out on the hot plate about 160 second.
70 To get higher resolution electron beam lithography to pattern
71 transfer, we optimized a prebaked time about 120s.

72 The fabrication process involves two step electron beam
73 lithography at 10keV. In first step, we patterned source and
74 drain and the second step lithography to pattern gate electron
75 after depositing HfO_2 about 10nm.

RESULTS AND DISCUSSION

76 Graphene on SiO_2 verified from Raman spectroscopy and
77 AFM metrology which is shown in Fig. 1. In graphene the
78 charge carriers can be either electrons or holes with the
79 application of gate electrostatics. We fabricated L_g/W
80 100nm/4um proof of concept device due to low field
81 interaction in highly scaled GFET shown in Fig 2. In order to
82 determine the device performance, we utilized the
83 transmission line measurement method and to determine the
84 carrier mobility and concentration hall bar structure is used
85 [2]. We measure drain current (I_d) at source-drain voltage V_{sd}
86 = 200mV to operate the device in linear region which is shown
87 in Fig 2.

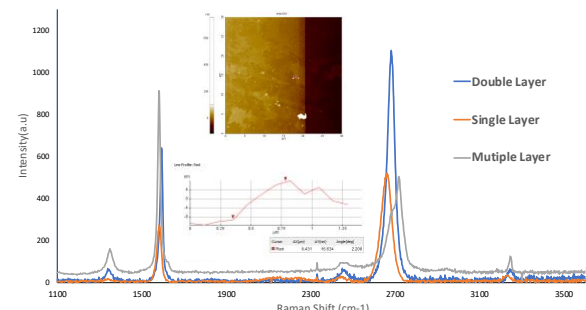


Fig 1. shows the Raman spectroscopy results, where a weak D band peak at 1340 cm^{-1} a G band peak at 1583 cm^{-1} and a sharp 2D band peak at 2682 cm^{-1} . Inset: atomic-force microscopy (AFM) image of graphene on SiO_2 . The thickness of the piece is $3\text{-}8\text{ \AA}$ suggesting that the growth takes place at the same rate on both SiO_2 and graphene.

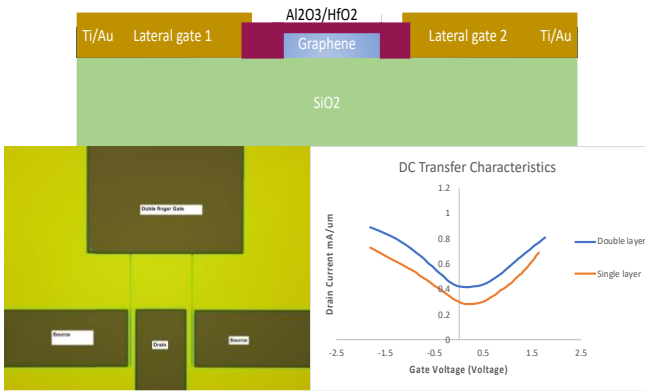


Fig. 2 Top. Cross section of the RF device structure in which the graphene layer buried below the HfO_2 high dielectric material. Bottom left is the optical image of the double gate RF structure. Bottom right represent the Transfer characteristics of transistor when $V_{ds}=0.2\text{V}$ for single layer and bilayer graphene.

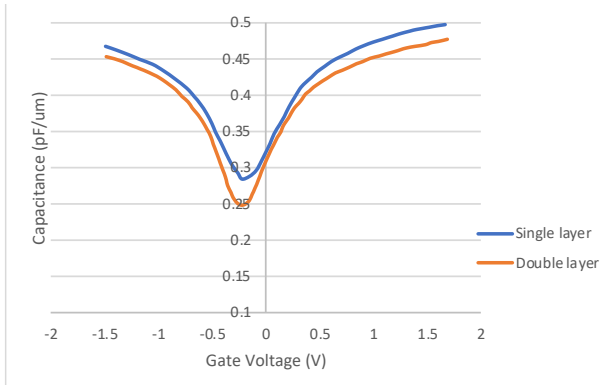


Figure 3. Room temperature small signal $V_{ac}=50\text{mV}$ capacitance measurement.

The devices are characterized in room temperature using a capacitance Analyzer E4981A connected to Microtech probe

station at room temperature. The peak-to-peak amplitude of the AC voltage is 50 mV to excite the carrier and the frequency 1MHz. We apply a DC bias in the range of -1.50 to $+1.50$ Which corresponds to average electron and hole densities of $n_c = 0 \pm 1 \times 10^{12} \text{ cm}^{-2}$, in order to study the gate capacitance in both the positive and negative regions.

In conclusion, the demonstration of graphene in plane RF structure provide the large current density about $0.9\text{mA}/\mu\text{m}$ with sharp slop of hole conduction. This in plane RF structure have low gate coupling to the source terminal and the current modulation through lateral electrostatic field tends to better frequency response in small signal analysis.

REFERENCE

- [1] Ullmann, B. & Grasser, T. Elektrotech. Inftech, “Transformation: nanotechnology—challenges in transistor design and future technologies”, <https://doi.org/10.1007/s00502-017-0534-y>
- [2] N. Hossain, J-F JF Millithaler, Martin Margala, “Graphene-Metal Contact Optimization for Ballistic RF Transistor Application”, CSW2018.
- [3] J. Nieder, A. D. Wieck, P. Grambow, H. Lage, D. Heitmann, K. V. Klitzing, and K. Ploog, “One-dimensional lateral-field-effecttransistor with trench gate-channel insulation,” Appl. Phys. Lett., vol. 57,no. 25, 73.
- [4] D. K. de Vries, P. Stelmaszyk, and A. D. Wieck, “Intrinsic and extrinsic capacitances of in-plane-gated transistors,” J. Appl. Phys., vol. 79, no. 10,p. 8087, 1996.